Carbonates from Olduvai Gorge, Tanzania: palaeohydrology and geochronology

UNIVERSITY OF LIVERPOOL

Thesis submitted in accordance with the requirements of the University of Liverpool for the degree of Doctor of Philosophy

By

Elisabeth Diane Rushworth

September 2012

Carbonates from Olduvai Gorge, Tanzania: palaeohydrology and geochronology

By Elisabeth Diane Rushworth

Abstract

Carbonates are abundant in the Pleistocene sedimentary sequence at Olduvai Gorge, Tanzania. This study reports their potential for investigating palaeoenvironments and for radiometric dating using U-Pb geochronology. Using their textural characteristics the, commonly nodular, terrestrial carbonates have been placed in one of five groups. By using multiple textural and geochemical analytical techniques, the palaeohydrological origin of each group has been proposed. When referenced to the geographical and stratigraphic framework at the eastern lake margin, the carbonates have been used to identify the palaeohydrological conditions beneath specific land surfaces and how it changed through time. The results identify the onset of synsedimentary faulting below Tuff IB, the palaeohydrological significance of fault control in landscape development, and the persistence of water in discrete settings. This helps to explain why hominin activity is located in certain areas in a fault compartment. The study has proved that detailed investigation of carbonates offers an effective method for understanding the wider palaeohydrology at exposure surfaces and the factors influencing hominin exploitation at particular locations and has the potential to provide a predictive tool for future archaeological investigations. Two types of dolomite are found at different stratigraphic levels, identifying episodes of high Mg/Ca ratios in the lake, and dolomite precipitation occurring in both a basinal and a lake marginal setting. Sand-sized calcite crystals formed in the shallow sub-surface sediments on the lake floor and lake margins under anoxic to sub-oxic conditions. ^{238}U - ^{206}Pb dating of these zoned calcite crystals using Laser Ablation MC-ICP-MS and has produced dates only a little older than those using ^{40}Ar/^{39}Ar on tuffs in the same stratigraphic intervals. ^{234}U/^{238}U activity ratios of the Pleistocene crystals indicate that different levels are more affected by open system behaviour than others. Early-diagenetic, authigenic calcite crystals show exciting promise for directly dating saline, alkaline lake sediments which may be useful in similar hominin sites where geochronology is less well constrained.

Acknowledgements

This thesis would not have been possible without the help and guidance of very many friends and colleagues. My supervisors, Jim Marshall, Ian Stanistreet and Randy Parrish have been an inspiration to me, and their solid and unwavering support has been invaluable. My thanks go to Jim for his door being always open, for guiding my understanding of the complexities of carbonate textures and geochemistry, and for pushing me that little bit harder each time we met. I am grateful to Ian for introducing me to the stratigraphy and history of Olduvai Gorge, and the incomparable experience of working there. Finally, my appreciation goes to Randy for allowing me to learn new science and then helping me to understand what it all means.

I truly value the opportunity to have worked with many other scientists during this research. My research at the University of Liverpool has been enlightened many times by thoughtful discussion and practical support from Steve Crowley and for analytical support from Jim Ball. My thanks also go to John Kavanagh who knows all about everything in the geology department and how to get everything done. I appreciate the opportunity and the support of the Olduvai Landscape Paleoanthropology Project, and my thanks go to all the scientists with whom I had the pleasure to work and who took such an interest in my carbonates; including Rob Blumenschine, Harald Stollhofen, Jackson N'jau, Fidelis Masao, Marion Bamford, Rosa Albert, Mike Pante, Ignacio de la Torre, and Lindsay McHenry. I am also grateful to the many Tanzanian people who made me so welcome, particularly Millau, my Maasai guide who kept me safe and helped to carry my many samples! My thanks go to all the staff from the NERC Isotope Geosciences Lab who helped me through the complexities of U-Pb geochronology; especially Dan Condon, Matt Horstwood, Steve Noble and Vanessa Pashley; for their advice on both the correct methods of analysis of the samples and for understanding the data once it was collected. In particular I am grateful for their analyses that help to show the value of the laser ablation work, to Matt for his help with the laser ablation data, and to Dan for his invaluable help with my geochronology chapter. I sincerely thank Bill Perkins from Aberystwyth University for allowing me to have access to analyses without which it would have been much more difficult to obtain the depth of scientific data I needed. My thanks also go to James Ebert for the use of his invaluable GIS data to construct the maps in the thesis.

I would like to thank the Tanzanian authorities for the necessary permissions to study and sample at Olduvai Gorge, in the Ngorongoro conservation Area, and at Lake Natron; the Tanzania Commission for Science and Technology, the Tanzania Antiquities Department of the Ministry of Natural Resources and Tourism, and the Ngorongoro Conservation Area Authority. My thanks for funding for my PhD go to NERC, and I am also grateful to The Leakey Foundation and the International Association of Sedimentologists, as without their support I would not have had a second, important, field season. Finally, I am grateful for the support of the NERC isotope geosciences lab for funding the geochronology analyses.

During this research I have been incredibly fortunate to have had friends who believed in me when I struggled to believe in myself, and who made me work harder and work better as time went on. Thanks go to all my many postgraduate friends at Liverpool whose commitment to their own research, and huge enthusiasm for science, has been a true inspiration to me. My love and thanks go to my great friends Kirstie, Lesley, Hilary, the Panini ladies Janet, Linda and Jane, and to my sisters and brothers-in-law Jennifer and David and Kathryn and Jamie. They gave me endless tea, cakes, emergency pink shrimps, yum-yums, a sympathetic shoulder, and the chance to talk about my science, and kept me involved with the real world.

Last, but not least, my love and gratitude go to my wonderful husband Simon Rushworth and my two lovely daughters Christine and Jessica, who have encouraged me constantly, and who are proud of me.

Table of Contents

Table of Figures

Table of Abbreviations

ELM	Eastern lake margin
WLM	Western lake margin
AF	Alluvial fan
$\delta^{13}C$	10^3 $\delta^{13}C$
$\delta^{18}O$	10^3 $\delta^{18}O$
CL	Cathode-luminescence
SEM	Scanning electron microscope
SEM-SE	Scanning electron microscope operating in secondary electron mode
SEM-BS	Scanning electron microscope operating in back scatter mode
EDX	Energy Dispersive X-Ray Spectroscopy
XRD	X-ray diffraction analysis
(solution) ICP-AES	Inductively coupled plasma atomic emission spectroscopy - sample delivery via solution
(Solution) ICP-MS	Inductively coupled plasma mass spectroscopy - sample delivery via solution
LA ICP-MS	Laser ablation Inductively coupled plasma mass spectroscopy - sample delivery via laser ablation of specimen
ID	Isotope dilution analysis
REE	Rare earth elements
LREE	Lighter rare earth elements: lanthanum to neodymium
HREE	Heavier rare earth elements: samarium to lutetium
PPL	Plain polarised light
XPL	Crossed polarised light (crossed Nichols)
EPS	Extra-cellular polymeric substances
NASC	North American Shale Composite
U^*	Total uranium concentrations measured by LA MC-ICP-MS
T-W	Tera-Wasserburg

Chapter 1: Introduction and research aims

1.1 Research questions

Olduvai Gorge, Tanzania, is the site of one of the most important archives of hominin evolution. The early Pleistocene sediments contain fossils of A*ustralopithecus boisei*, *Homo habilis,* and *Homo erectus,* and Oldowan and Acheulian stone tool artefacts (Leakey, 1971). Understanding palaeoenvironmental conditions, within a well-constrained time-frame, is vital for our understanding of hominin evolutionary progress (Kingston et al., 2007; Potts, 1998).

Reconstruction of the palaeoenvironment and palaeoecology at Olduvai has previously been investigated using lithology (Ashley, 2007; Ashley et al., 2010a, b; Ashley and Hay, 2002; Blumenschine and Masao, 1991; Blumenschine et al., 2008; Blumenschine and Peters, 1998; Blumenschine et al., 2003; Blumenschine et al., 2011b; Copeland, 2007; Deocampo, 2004; Deocampo et al., 2002; Hay, 1976, 1990; Liutkus and Ashley, 2003; Sikes and Ashley, 2007), the micro-mammal (Fernández-Jalvo et al., 1998) and micro-fossil record (Liutkus and Ashley, 2003), changes in the species of flora (Albert et al., 2009; Bamford, 2005; Bamford et al., 2006; Bamford et al., 2008), and the stable isotope record of carbonate deposits (Cerling and Hay, 1986; Hay, 1976; Hay and Kyser, 2001; Liutkus et al., 2005; Sikes, 1994). Although carbonates are abundant throughout the sedimentary succession, the potential for using their crystal textures, combined with their geochemical data, to interpret the depositional processes operating during their formation (Mount and Cohen, 1984; Wright, 2008) has not been fully exploited.

Accurate dating at Olduvai, and similarly important Early and Middle Pleistocene hominin archaeological sites, is usually dependent upon the presence of volcanic sediments. The stratigraphic ages at Olduvai have been defined using $^{40}Ar/^{39}Ar$ analyses of the volcanic deposits, (Blumenschine et al., 2003; Manega, 1993; Walter et al., 1992), apart from Tuff IF whose date is defined by the base of the Olduvai subchron (Hay and Kyser, 2001). However, where the volcanic deposits have been chemically altered, reworked, or are not present, there are few options for direct dating of fossil-bearing sediments here or elsewhere. Although carbonates have been successfully dated using the uranium-lead decay series (van Calsteren and Thomas, 2006), very specific criteria are needed when using this method for Early Pleistocene specimens. However, the success of this method potentially offers the development of a hominin chronology in previously poorly dated locations.

The dissertation, in part, builds on a pilot study (Bennett et al., 2012) which identified the significant potential of carbonates to provide highly detailed information about depositional settings. It considers some key questions about the carbonates at Olduvai.

The first questions focus on the investigation of the carbonates found in the terrestrial sediments at Olduvai:

- Using their textures and geochemistry, is it possible to use the carbonates from the terrestrial sediments as palaeohydrological indictors?
- Can the terrestrial carbonates then be used as predictive tools for palaeohydrological and palaeoenvironmental investigations at Olduvai Gorge, and potentially elsewhere?

The second considers the lacustrine carbonates at Olduvai:

- What is the genesis of the lacustrine carbonates and what information can they offer us in terms of palaeoenvironmental reconstruction?

The third investigates dating of the carbonates using the uranium-lead decay series:

- Can the lacustrine and terrestrial carbonates be accurately dated using the uranium-lead decay series, and so potentially provide a novel dating tool both at Olduvai and also at other, similar, hominin locations?

The involvement of multidisciplinary teams including geologists, geochemists, palaeobotanists, micro-mammal experts, taphonomists, and geochronologists has increased our ability to reconstruct the palaeoenvironment across Olduvai Gorge, and fieldwork for this study was completed in collaboration with the Olduvai Landscape Paleoanthropology Project (OLAPP).

1.1.1 Carbonate textures

Continental carbonates can be precipitated in soils, mudflats, and vegetated mires, both at or below the water table, or within a water column (Figure 1-1) (Arenas-Abad et al., 2010; Wright, 2008). Their formation from carbonate supersaturated water in shallow terrestrial sedimentary environments or lakes can occur through a variety of biogenically mediated and abiotic processes, which control the mineralogy and crystal habit of the carbonates (Chafetz and Guidry, 1999; Chafetz et al., 1991; Henderson et al., 1987; Pedley et al., 2009; Wright, 2008). Investigating the calcite crystal textures can, therefore, be used to interpret the formation process involved.

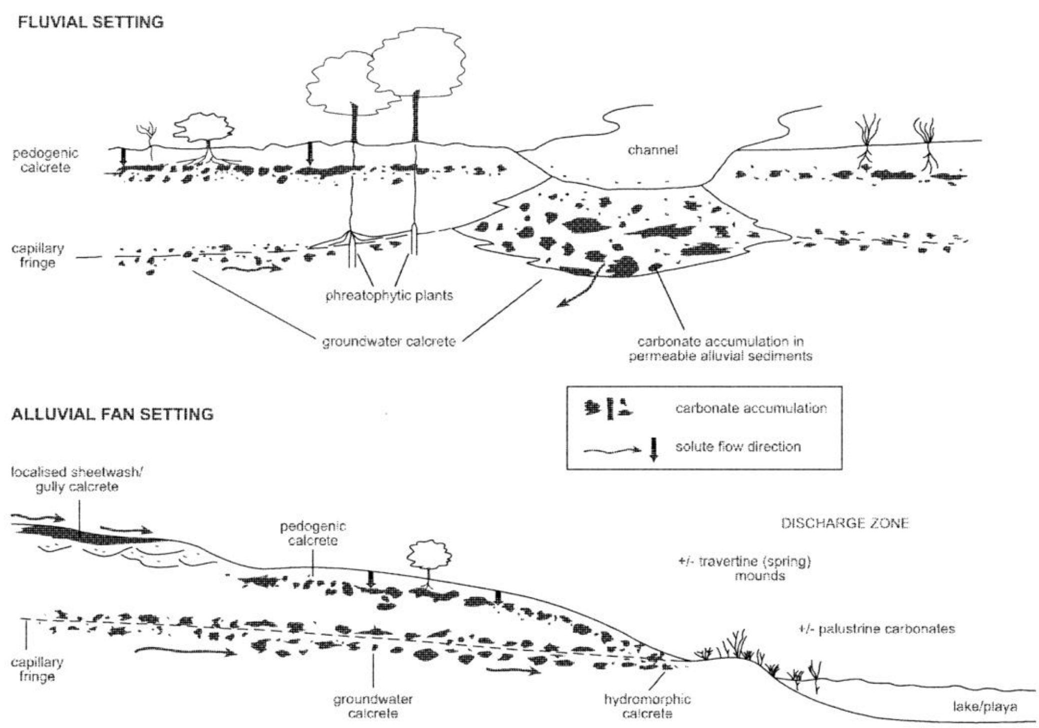

Figure 1-1: Potential settings where carbonate formation can occur (Wright, 2008). Continental carbonates form in pedogenic and non-pedogenic, vadose and phreatic settings; in soils, mudflats, and vegetated mires, both at or below the water table, or within a water column.

Interpreting the textures, however, can be complicated where different processes produce similar textures. For example, although carbonates formed in sediments are often associated with pedogenesis this is not always the case (Retallack, 2001; Wright, 2008). Carbonate micro-textures can be described using two end-members; Alpha and Beta fabrics. The alpha fabric has a crystalline matrix with nodules, complex cracks filled or partially filled with calcite cement, and calcite rhombs whereas the beta fabric has alveolar septal fabrics, calcified plant cells, needle fibre calcite (Wright, 2008; Wright and Tucker, 1991) (Figure 1-2). Beta fabrics are interpreted to have formed with a higher degree of biological activity than carbonates with an alpha fabric, although both fabrics may be the result of pedogenesis (Wright, 2008; Wright and Tucker, 1991).

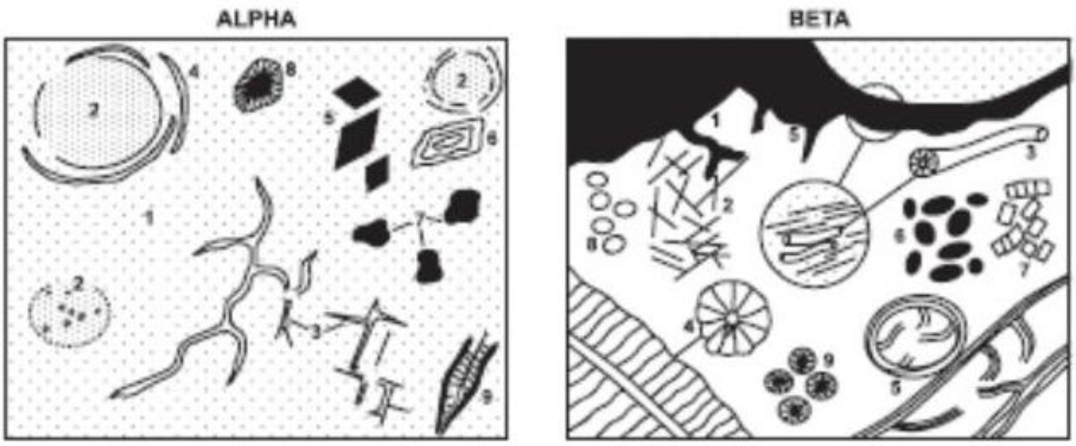

Figure 1-2: The Alpha and Beta micromorphological end-member fabrics of calcretes (Wright, 1991, 2008). Alpha fabrics: 1. Dense groundmass of micrite-microspar, 2. Nodules, 3. Complex cracks and crystallaria, 4. Circumgranular cracks, 5. Rhombic calcite crystals, 6. Etched and corroded calcite crystals, 7. Floating sediment grains, 8. Bladed calcite around grains, 9. Displacive calcite. Beta fabrics: 1. Microbial coatings and ooids, 2. Needle fibre calcite, 3. Calcified tubules, 4. Microcodium, 5. Alveolar-septal fabric, 6. Calcified pellets, 7. Calcified plant cells, 8. Calcispheres, 9. Spherulites.

Multiple textural characteristics of both the carbonate body and its relationship to host sediments should be employed to avoid erroneous categorisation (Alonso-Zarza and Wright, 2010b; Retallack, 2001; Sheldon and Tabor; Wright, 2008).

1.1.2 Carbonate geochemistry

Trace elements

Many trace elements can be incorporated either within a carbonate lattice, or interstitially, and their abundance is a function of: the redox conditions of the supply water and so the availability of redox sensitive elements; the pH of the supply fluid; the trace element partitioning in the calcite; and the rate of precipitation (Arenas-Abad et al., 2010; Bjørlykke and Bjørlykke, 2010; Curti, 1999; Machel, 2000).

The intensity of the luminescence of carbonate samples viewed using cathode-luminescence microscopy is primarily a function of the balance between Mn and Fe, although REEs can contribute as either activators and quenchers (Barnaby and Rimstidt, 1989; Habermann, 2002; Habermann et al., 1998; Machel, 2000). Consequently, although this is only a qualitative technique, the brightness of the CL has been used to indicate the redox conditions of the water supply during carbonate precipitation and so the hydrology of the depositional setting (Arenas-Abad et al., 2010; Barnaby and Rimstidt, 1989). These interpretations can be supported by comparing the luminescence with quantitative data obtained using mass spectrometry (Barnaby and Rimstidt, 1989; Machel, 2000).

Trace element partitioning during calcite growth is a function of the size and chemical properties of the metal and the mechanism of its incorporation in the calcite lattice. This can be expressed as the distribution coefficient; the concentration of a particular trace element, relative to Ca^{2+}, in the calcite lattice and the concentration of that trace element in the supply fluid (Machel, 2000). For example, the distribution coefficient of Mn and Fe is > 1, whereas that for Sr is < 1 and so Mn and Fe will preferentially substitute for calcium in the lattice compared to Sr. The rate of precipitation (Brand and Veizer, 1980; Curti, 1999; Lorens, 1981) also influences the incorporation of trace elements, and Sr is more likely to be incorporated at rapid precipitation rates compared to Mn.

Both quantitative and qualitative analyses of the trace elements in carbonates from Olduvai will improve the understanding of the palaeohydrology operating during carbonate formation. This is the first study of the carbonates at Olduvai that incorporates such data in the interpretations of their formation.

Stable isotopes

The $\delta^{18}O$ and $\delta^{13}C$ of carbonates have been used extensively to interpret the evolution of the water source. $\delta^{18}O$ isotopic composition of the fluid is principally affected by the local and regional climate, the drainage basin size and lithology, and the residence time of the water in lakes and other water bodies (Alonso-Zarza and Wright, 2010b; Casanova and Hillaire-Marcel, 1992; Hillaire-Marcel and Casanova, 1987; Levin et al., 2009; Tanner, 2010; Wright, 2008; Wright and Tucker, 1991). The $\delta^{13}C$ in groundwater has a similarly complex history as it is derived from the combined influences of the pCO_2 exchange between the water body and the atmosphere, input from any mineral source, biological activity including C3 and C4 photosynthesis and bacterial productivity of the soil (Farquhar et al., 1989; Jones and Renaut, 2010; Levin et al.; Sikes, 1994; Sikes and Ashley, 2007). Consequently, the evolution of the water in lake and lake margin settings is complex.

Previous studies of $\delta^{18}O$ and $\delta^{13}C$ of carbonates from Olduvai Gorge have used single spot samples of individual specimens taken from multiple positions within a sedimentary succession. The variations in oxygen values have been interpreted as exclusively produced by changes in the climate, with carbon values interpreted as the result of changes in the dominance of C3 and C4 vegetation driven by climate change (Ashley, 2000; Blumenschine et al., 2003; Cerling and Hay, 1986; Cerling et al., 1977; Hay, 1976; Sikes, 1994; Sikes and Ashley, 2007). Other studies, however, have interpreted a similar range of isotope values of multiple samples within individual carbonate specimens as variations in the dominance of lake water and meteoric water at the margins of Palaeolake Olduvai (Bennett et al., 2012; Liutkus et al., 2005).

Multiple, different, possibly repeating, palaeohydrological regimes may be involved during the formation of individual carbonate bodies as a consequence of duration of growth and fluctuating hydrological conditions. These factors emphasise the need to consider the potential sources of groundwater, in addition to the influences on their evolution, in any interpretations based on the $\delta^{18}O$ and $\delta^{13}C$ ratios.

Diagenesis

Diagenesis, that is, cementation, recrystallisation, or replacement of the original minerals, may have significantly altered the primary geochemical composition, and may only reflect the most recent source of ions, stressing the importance of linking the petrographic analysis of the specimen textures to their geochemistry (Deocampo, 2010; Mount and Cohen, 1984). However, other than the pilot study to this project there have been few reports applying petrographic analyses of carbonates from Olduvai as a screening tool prior to geochemical analysis of carbonates (Sikes and Ashley, 2007), and there are only two published papers incorporating details of the petrographic textures (Ashley, 2000; Bennett et al., 2012).

1.1.3 Uranium-lead dating

In aqueous systems uranium and its daughter products are efficiently fractionated during carbonate formation. In oxic and carbonate-rich water uranium in its +6 valent state is soluble as the uranyl ion $[UO_2]^{2+}$, and because the daughter products are not soluble, only the uranyl ion can be incorporated into the calcite lattice (Kelly et al., 2006). Provided that the original system is in "secular equilibrium" (see below), and the system remains closed with no subsequent diagenetic alteration, this effectively re-sets the radiometric clock to zero in the calcite lattice (van Calsteren and Thomas, 2006). Consequently the U-series decay pathways (Figure 1-3, Table 1) potentially offer a useful method for direct dating of carbonate-containing sediments. Recent studies have successfully dated Pleistocene speleothems, cave deposits and tufas using ^{238}U-^{206}Pb by MC-ICP-MS, TIMS and αspectrometry (Leeder et al., 2008; Richards et al., 1998; Walker et al., 2006; Woodhead et al., 2006).

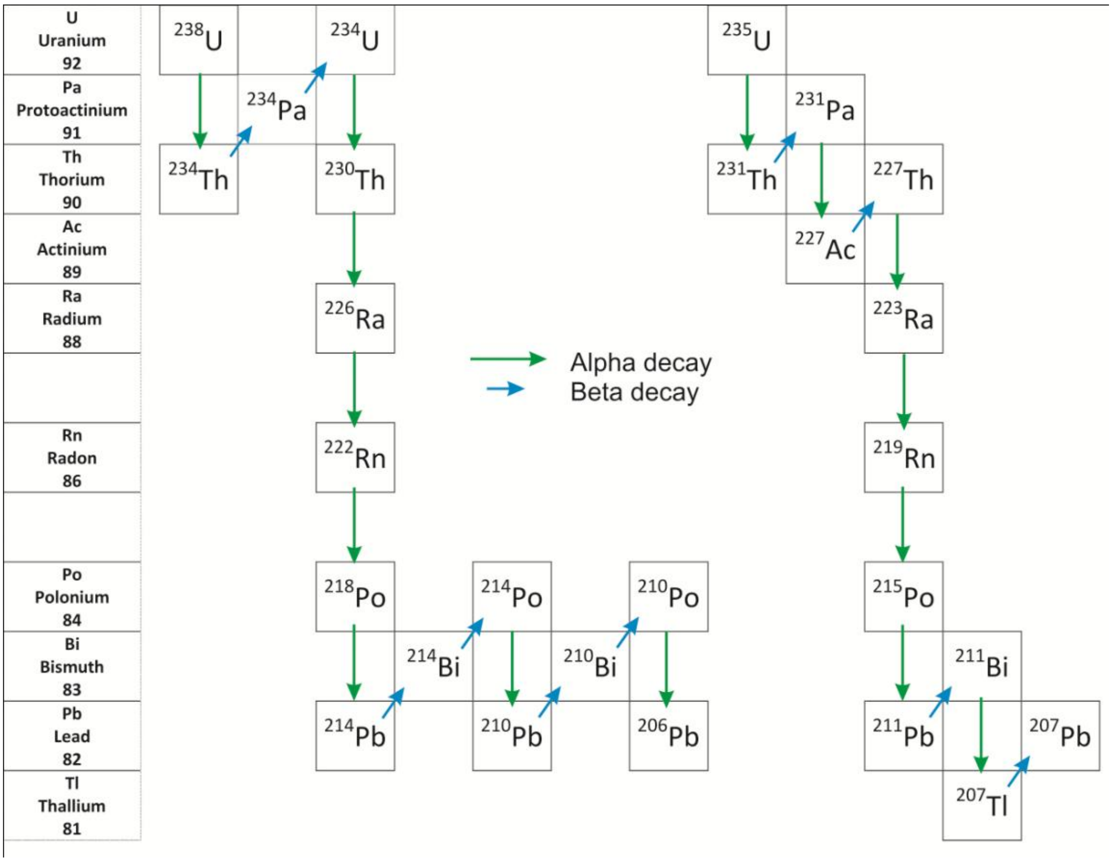

Figure 1-3: Uranium series decay pathways (Bourdon et al., 2003).

^{238}U Decay chain	Half life	^{235}U Decay chain	Half life
^{238}U	4.47 x 10^{9} y	^{235}U	7.04 x 10^{8} y
^{234}Th	24.1 d	^{231}Th	1.06 d
^{234}Pa	6.69 h	^{231}Pa	3.28 x 10^{4} y
^{234}U	2.45 x 10^{5} y	^{227}Ac	21.8 y
^{230}Th	7.5 x 10^{4} y	^{227}Th	18.7 d
^{226}Ra	1599 y	^{223}Ra	11.4 d
^{222}Rn	3.823 d	^{219}Rn	3.96 s
^{218}Po	3.04 min	^{215}Po	1.8 x 10^{-3} s
^{214}Pb	26.9 min	^{211}Pb	36.1 min
^{214}Bi	19.7 min	^{211}Bi	2.14 min
^{214}Po	1.6 x 10^{-4} s	^{207}Tl	4.77 min
^{210}Pb	22.6 y	^{207}Pb	Stable
^{210}Bi	5.01 d		
^{210}Po	138.4 d		
^{206}Pb	Stable		

Table 1: Half lives of isotopes in the uranium series decay pathways (Bourdon et al., 2003).

The geological clock in a closed system is said to be in secular equilibrium, or steady state of decay, after a time equivalent to six to eight times the longest daughter half life (Table 1) (Bourdon et al., 2003). Age determination rests on the state of disequilibrium, that is, how far away from secular equilibrium the nuclide balances of the decay chains are. Differing parts of the decay pathways can be used to determine the age of a sample and the part used depends upon its expected age. Generally different decay pathways are cross referenced with both each other and constants in the system such as ^{204}Pb and ^{232}Th to reduce errors caused by criteria such as sample contamination by detrital components, very small sample sizes, and ^{234}U enrichment of ground water.

1.1.4 Local geology

Olduvai Gorge, Tanzania is located on the boundary between the Serengeti Plain and the Volcanic Highlands, on the western edge of the Gregory Rift, East Africa (Figure 1-4 A, B).

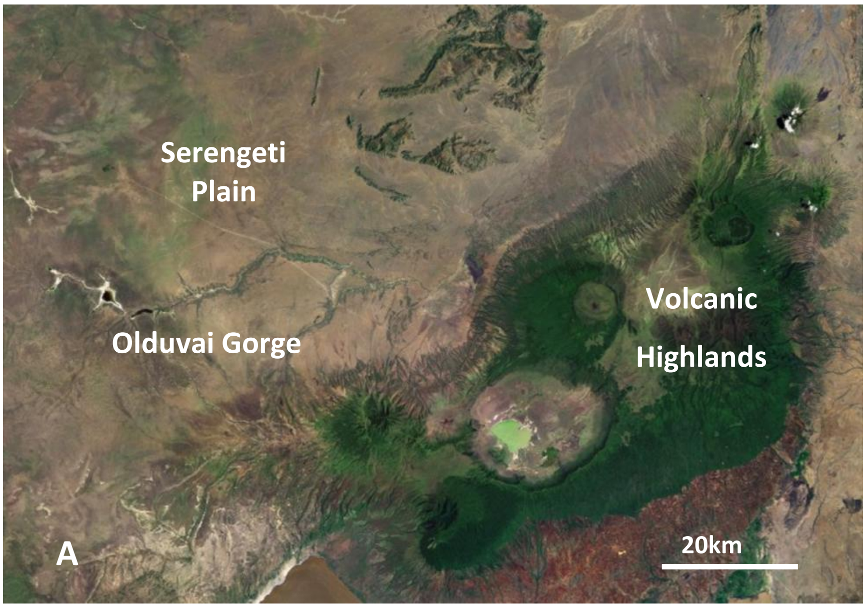

Figure 1-4 A Olduvai Gorge, Tanzania, East Africa: Olduvai Gorge, Tanzania is located on the boundary between the Serengeti Plain and the Volcanic Highlands, on the western edge of the Gregory Rift, East Africa (Google Earth 2010).

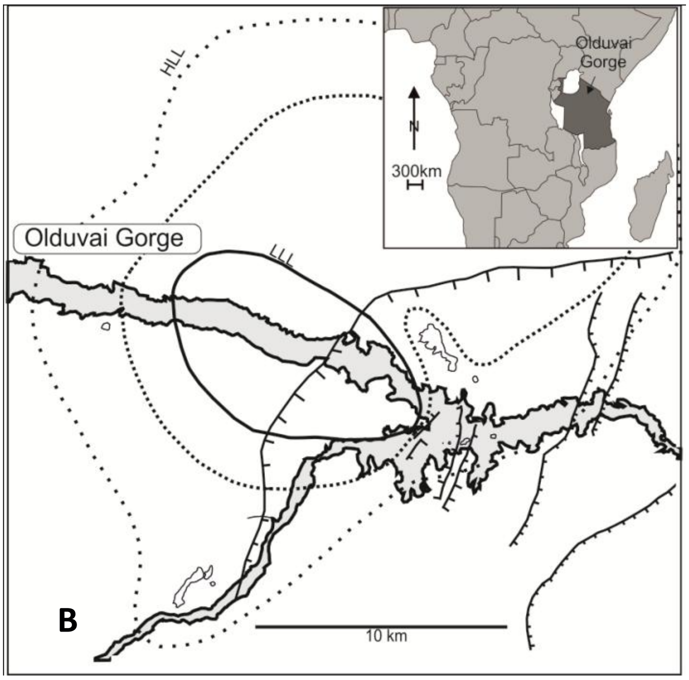

Figure 1-4 B: Olduvai Gorge, Tanzania, East Africa. The gorge is a primarily Late Pleistocene and Holocene fluvial incision into Pleistocene sediments, and is identified in grey. The positions of the major faults are identified by lines with ticks on the downthrow side. The variable extent of Palaeolake Olduvai is identified as LLL (Low Lake Level) and HLL (High Lake Level) using the palaeogeographical reconstruction immediately above Tuff IF (Hay, 1976).

The sedimentary succession of interbedded clays, sandstones and volcanic deposits was formed in and around a now extinct shallow, saline-alkaline lake formed in a rift-shoulder basin, termed Palaeolake Olduvai (Dawson, 1992; Hay, 1976). The clays were derived largely by alteration of volcaniclastic material (Deocampo, 2002; Hay, 1976; Mees et al., 2007), the sandstones were supplied by fluvial systems (Hay, 1976), and the volcanic deposits, which include multiple tuffs, ignimbrites, and a basalt bed, were sourced from the eastern volcanic complex (McHenry et al., 2008; Mollel, 2007; Mollel et al., 2009; Stollhofen et al., 2008). Carbonates are abundant throughout the stratigraphy.

The fossil record and the geology at Olduvai were first investigated in the major trenches of Mary Leakey and at more than 200 measured sections, distinguished by using ‘Loc’ numbers of Leakey, Hay and co-workers (Hay, 1976; Leakey, 1971). A further 150 trenches throughout the gorge have subsequently been excavated since 1994 by the Olduvai Landscape Paleoanthropology Project (OLAPP) distinguished by using ‘Tr’ numbers. Carbonates used for this study have been sampled from both

Loc and Tr sites. Previous work on the stratigraphy and sedimentology at Olduvai has identified the lacustrine setting and three principal partial or non-lacustrine depositional settings, each with different hydrological characteristics, the alluvial fan, the eastern lake margin, and the western lake margin (Figure 1-5) (Hay, 1976; Hay, 1996; Hay and Kyser, 2001; Peters and Blumenschine, 1995).

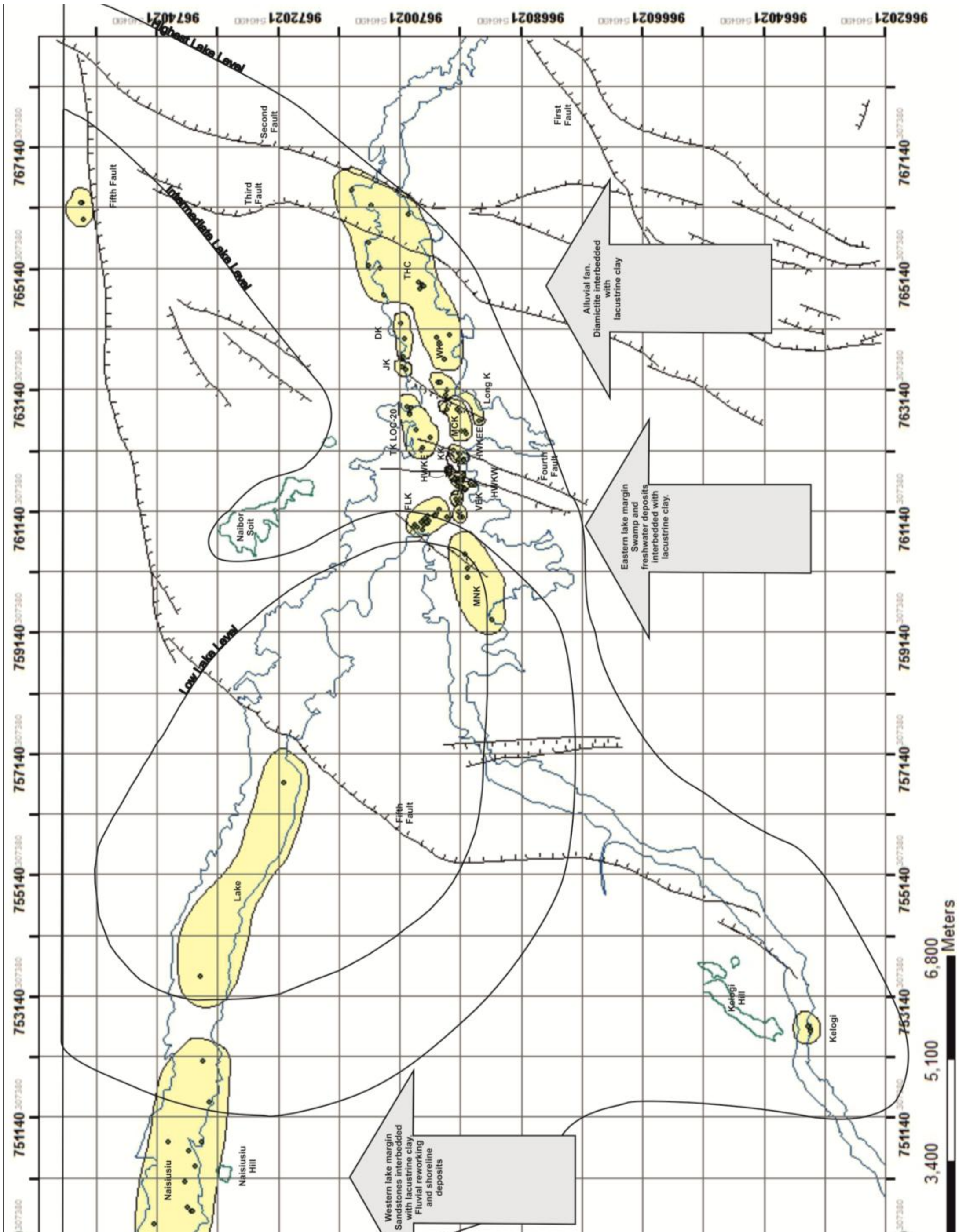

Figure 1-5: A map of Olduvai Gorge identifying important terrestrial depositional settings and interpreted Palaeolake levels (Hay, 1976). Constructed using data from Dr James Ebert, Ebert and Associates, Albuquerque. Olduvai Gorge is shown in blue. The principal terrestrial depositional settings and sediments have been marked using the large arrows: the western lake margin, eastern lake margin and the alluvial fan. The archaeological complexes within these settings are shown as yellow areas. They are categorised by their fossil and sedimentary records and are identified by letters, e.g. FLK at the eastern lake margin (Hay, 1976; Leakey, 1971). Sampling locations for this study are identified by the green diamonds.

The sequence has been divided into eight beds (Hay, 1976) (Figure 1-6). This study concentrates on the older part of the sequence, which includes Bed I and Bed II between ~2Ma and 1.4Ma, as it has produced the most important fossil record at Olduvai and has been the main focus of previous investigations.

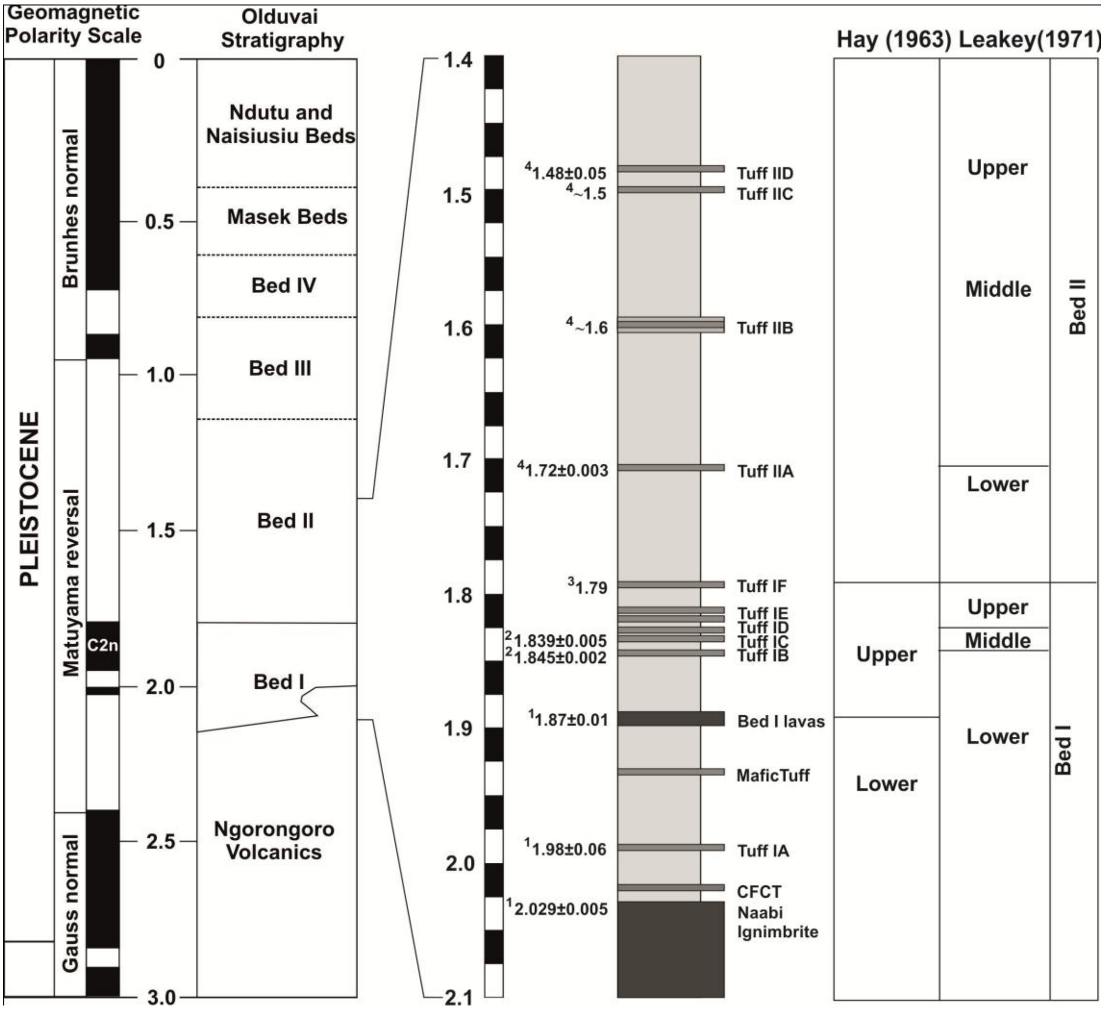

Figure 1-6: Generalised stratigraphy of the Olduvai beds (Stollhofen et al., 2008), including archaeological bed divisions for Bed I and Lower Bed II (Leakey, 1971) and geological bed divisions (Hay, 1976). This study is focussed on the stratigraphy between ~2.0Ma and 1.4Ma. The generalised stratigraphic succession comprises interbedded clays, sandstones and volcanic sediments. Published dates were determined using $^{40}Ar/^{39}Ar$ single crystals analyses of tuffs and one date defined by the base of the Olduvai Subchron. 1) (Walter et al., 1992), 2) (Blumenschine et al., 2003), 3) (Hay and Kyser, 2001), 4) (Manega, 1993).

1.2 Thesis structure

The thesis chapters are written as six papers, developed to investigate four key research questions as detailed on page 3.

Chapters 2 and 3 specifically address the potential for terrestrial carbonates to be used as palaeohydrological indicators. Importantly, this is achieved using a combination of several standard petrographic and geochemical methods. The carbonates are separated into seven groups by their textural characteristics, most of which are easily identifiable in hand specimens. Chapter 2 discusses the characteristics of two groups of carbonates with radial crystal textures, and chapter 3 details the characteristics of three groups of non-radial carbonates. The data are then used to interpret the processes operating during carbonate formation, the implication of variations within an individual carbonate specimen, and they are then used to infer a specific palaeohydrological setting for each group of carbonates.

Chapter 4 describes how the carbonate types, and their location on a sedimentary log, are used to interpret the palaeohydrology at a specific geographical position and stratigraphic level. Where multiple stratigraphic logs are correlated between locations the carbonates are then used to interpret the palaeohydrology across a wide geographical area at specific stratigraphic levels associated with hominin fossils. The results are compared to existing palaeoenvironmental data to assess its potential as a predictive palaeohydrological tool.

Chapters 5 and 6 detail the characteristics of two types of lacustrine carbonates; sand-sized calcite crystals and dolomite beds, using a combination of textural and geochemical techniques. Chapter 5 addresses the genesis of the calcite crystals, and their potential to be dated using the uranium-lead decay series. In particular it concentrates on the trace elements incorporated into the crystal lattice and the geochemical zoning seen under cathode-luminescence. Chapter 6 investigates three dolomites, and the potential for different formation processes operating in different beds. These inferences are then used to indicate possible lake conditions at two different stratigraphic levels.

Chapter 7 documents the results of dating the lacustrine calcite crystals using the uranium-lead decay series, and the exciting potential for using this method at other, similar, less well-dated sites.

The author intends that individual chapters will form the basis for jointly submitted papers with thesis supervisors and other groups involved in the analytical work.

1.3 Author contribution

Stratigraphic logging and sample collection: stratigraphic logs were drawn, and samples were collected, by the author during two field seasons 2010 and 2011, which supplemented an extensive collection of logs and samples previously collected by Professor Ian Stanistreet (University of Liverpool) during field seasons between 2000 and 2011.

Water sampling and analysis: modern lake water and shoreline sediments were collected by the author and the OLAPP team during two field seasons in 2010 and 2011.

Textural analyses: the author is responsible for all textural analyses at the University of Liverpool. Thin sections were prepared by the University of Birmingham and the University of Manchester, and all other sample preparation was performed by the author.

Trace element analyses: sample preparation and trace element analyses by Laser ablation MC ICP-MS at the University of Aberystwyth were carried out by the author. Solution ICP-MS analyses, other than calcite crystal separation and cleaning, including standard preparation, were prepared and analysed by Professor Bill Perkins at the University of Aberystwyth. Solution ICP-AES analyses were prepared by the author and standards prepared and samples analysed at the University of Manchester.

X-ray diffraction analyses: sample preparation for X-ray diffraction analysis was by the author, and the analyses were carried out by Dr. S. F. Crowley at the University of Liverpool.

Stable isotope analyses: both sample preparation and the analyses for stable isotopes of calcite samples were carried out at the University of Liverpool, in part by the author and in part by Mr. J. Ball and Dr. S. F. Crowley. The preparation of dolomite samples was performed by the author, and the sample digestion and stable isotope analyses were performed at the University of Liverpool by Dr. S. F. Crowley.

Uranium-lead dating analyses: The author is responsible for sample preparation and the uranium-lead series dating of carbonates by laser ablation MC ICP-MS at the NERC Isotope Geosciences Laboratory (NIGL). The author's operation of the mass spectrometer, data reduction calculations, and production of appropriate final graphs were supported and provided by Dr M. Horstwood and Dr. V Pashley (NIGL). Other than calcite crystal separation and cleaning, sample preparation and isotope dilution analyses using Thermal ionisation mass spectrometry (TIMS) and MC-ICP-MS were carried out by Dr D. Condon (NIGL). $^{234}U/^{238}U$ ratios were determined using the Neptune plus MC-ICP-MS, and corresponding calculations of initial uranium disequilibrium for the Pleistocene crystals, by Dr. S Noble (NIGL). Disequilibrium correction calculations for the U-Pb ages were supplied by Dr. D. Condon (NIGL).

Data interpretations are the responsibility of the author.

Chapter 2: The origins of radial calcite, Bed I and Lower Bed II, Olduvai Gorge, Tanzania

2.1 Overview

Two types of carbonates with a radial structure have been identified using their macromorphology and micromorphology; spherulitic clusters and sparry nodules. Spherulites occur in clusters of either one of two modal sizes, <0.5mm or ~2mm diameter, and are composed of several crystals of low-Mg calcite radiating from a central nucleus, often exhibiting inclusion-defined growth bands. Sparry nodules are up to 18 cm in diameter, although typically between 3 and 5cm, and have multiple concentric, radial, sparry bands of columnar low-Mg calcite around a central nucleus.

The calcite deposition is interpreted to be primarily abiotic in a terrestrial setting, and groundwater evolution is inferred to be driven by evaporation and the mixing of more dilute, meteoric, and fluvial water with more concentrated saline, alkaline lake water. Models for their formation have been proposed based on their textures and geochemistry. Spherulitic clusters are interpreted to have formed within the sediment from highly carbonate supersaturated water, in the capillary fringe immediately above the water table. Sparry nodules formed within the sediment and comprise three texturally different zones; the nucleus formed by recrystallisation of an original mineral by meteoric water; the sparry bands formed primarily in the shallow phreatic zone from groundwater increasingly influenced by lake water during their growth; and the cortex formed in the capillary and vadose zones under high levels of evaporation. Many of the hand specimens show morphological characteristics of both types, providing evidence of a fluctuating water table during calcite precipitation.

The palaeohydrological setting in which radial calcites were formed provides a valuable tool to support palaeoenvironmental reconstruction.

2.2 Introduction

Carbonate deposits are abundant in the sediments at Olduvai Gorge, and they exhibit a wide range of crystal textures, with multiple carbonate phases occurring during their growth. Terrestrial calcite deposits have previously been identified as ‘coarsely crystalline nodules’ and ‘finely crystalline nodules’ (Hay, 1973). In previous studies they have typically been described as pedogenic where they are small, <2cm, irregular, fine grained and structureless and associated with root-marked and fluvial claystones. Nodules described as non-pedogenic tend to be larger, coarse grained and concentrically layered, forming clusters like bunches of grapes (Hay, 1976). More recently, investigations into the carbonates at Olduvai have identified and classified them as rootmat horizons, micritic nodules, spherulitic and pisolitic carbonates, sparry calcite nodules and sulphate rose pseudomorphs and rhizocretions (Bennett et al., 2012), and rhizoliths (Bennett et al., 2012; Liutkus et al., 2005).

Formation of carbonates in shallow terrestrial sedimentary environments can occur though biotic and abiotic processes in shallow phreatic and vadose conditions (Chafetz and Guidry, 1999; Chafetz et al., 1991; Henderson et al., 1987; Pedley et al., 2009; Wright, 2008). The processes controlling the mineralogy and crystal habit of carbonates are driven by; the state of supersaturation of the groundwater; rate of evaporation, evapotranspiration and degassing; biological activity; and trace elements affecting potential nucleation sites (Andreassen et al., 2010; Beck and Andreassen, 2010a, b; Beck et al., 2011; Chafetz et al., 1991; Fernández-Díaz et al., 2006; García Carmona et al., 2003; Wright, 2008). Because similar textures can be produced by different processes, it is important to use multiple textural methods and geochemical analyses to avoid erroneous categorisation (Alonso-Zarza and Wright, 2010b; Retallack, 2001; Sheldon and Tabor; Wright, 2008). Consequently, the crystal texture, and trace element and stable isotope analyses of carbonates in terrestrial sedimentary environments, can be used to interpret the processes of deposition and so infer their depositional setting (Cerling and Hay, 1986; Mount and Cohen, 1984; Wright, 2008).

In this study, textural characteristics have been used to identify two types of radial calcite, sparry nodules and spherulitic clusters. Their geochemistry has then been used to interpret the processes, and so palaeohydrological conditions, operating during their deposition.

2.3 Geological setting

The exposed sediments at Olduvai comprise a ~100m thick stratigraphic sequence, and this study concentrates on the older part of the sequence, which includes Bed I and Lower Bed II between ~2Ma and ~1.72Ma (Figure 2-1).

Bed I sediments are bounded by the basal Naabi ignimbrite and the top of Tuff IF, and those of Lower Bed II are bounded by the top of Tuff IF and a major disconformity which has locally eroded Tuff IIA (Figure 2-1). Carbonates investigated in this study were taken from the clay beds, composed of smectite, illite and interlayered illite/smectite, which are primarily derived from weathered volcaniclastic material and subsequently diagenetically altered by either lake or fresh water (Deocampo, 2004; Deocampo et al., 2002; Hay and Kyser, 2001; McHenry, 2009). Stevensite-rich, neoformed clays are also present in some central basin and eastern lake margin clays at the top of Bed I and the base of bed II (Hay and Kyser, 2001; Stanistreet, 2011). A few carbonates and a dolomite were sampled from clays with a 'Butter claystone' texture (Stanistreet, 2011) inferred to be Mg-rich smectite. A few specimens were taken from siliceous, earthy claystones, interpreted as wetland sediments deposited in a fresher water setting (Deocampo et al., 2002; Mees et al., 2007).

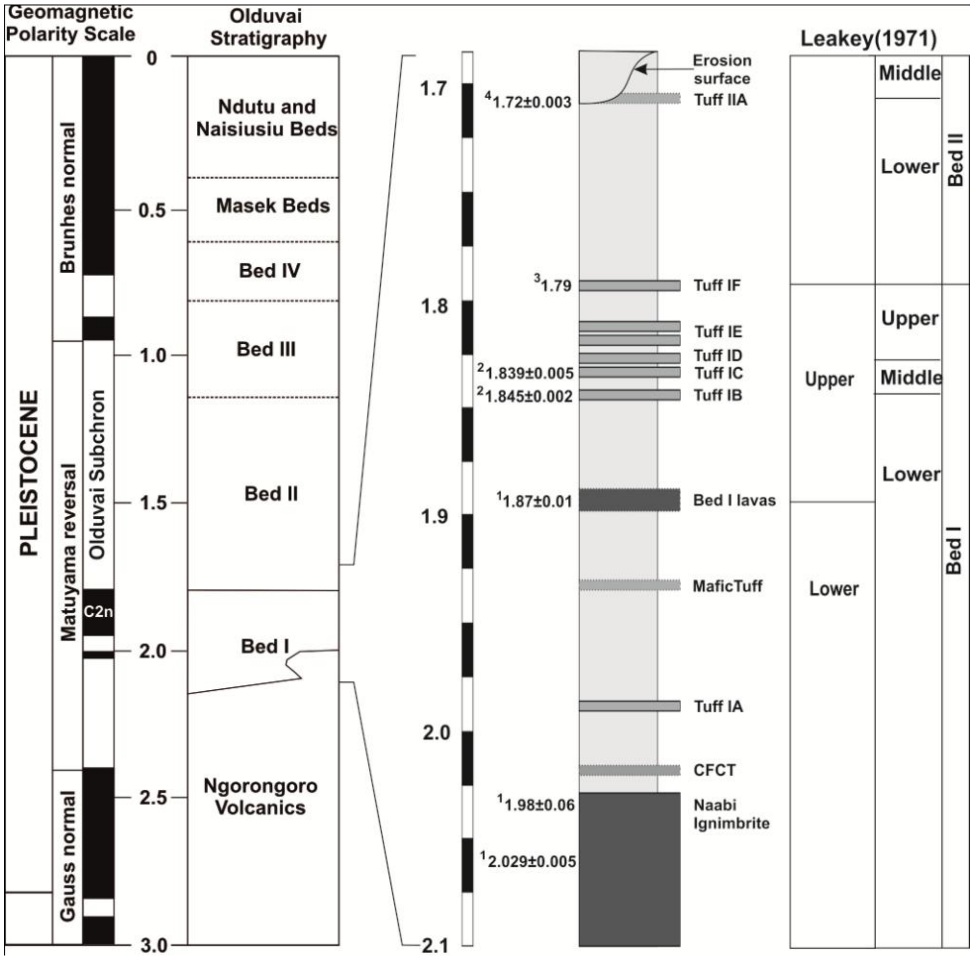

Figure 2-1: Generalised stratigraphy of the Olduvai beds (Stollhofen et al., 2008), including archaeological bed divisions for Bed I and Lower Bed II (Leakey, 1971) and the geological bed divisions (Hay, 1976). This study is focussed on the stratigraphy between ~2.0Ma and ~1.72Ma. The generalised stratigraphic succession comprises interbedded clays, sandstones and volcanic sediments. Published dates were determined using $^{40}Ar/^{39}Ar$ single crystal analyses of tuffs 1) (Walter et al., 1992), 2) (Blumenschine et al., 2003), 4) (Manega, 1993), and the date of Tuff IF defined by the base of the Olduvai Subchron 3) (Hay and Kyser, 2001). The Augitic Sandstone overlies the erosion surface at the top of the stratigraphic column.

2.4 Sampling strategy and analytical methods

Carbonate specimens were collected from archaeological trenches and exposure sites at multiple locations and stratigraphic levels (Appendix 1). The emphasis was to collect from places and levels associated with key hominin finds and to obtain as extensive a spread of specimens as possible both geographically and throughout the stratigraphy of Bed I and Lower Bed II. The samples were initially cut open using a rock saw and one of the cut faces polished using a flat lap polisher. The samples were initially grouped based on their textural similarities visible in the polished faces in hand specimen. Samples that represented a range of textures at different stratigraphic levels and geographical locations were then chosen for thin section.

Standard polished 30μm thin sections impregnated with blue resin were prepared of 110 specimens and examined using transmitted light microscopy, cathode-luminescence and where appropriate UV fluorescence microscopy.

Scanning electron microscope investigations using Secondary Electron (SEM-SE) and Backscatter (SEM-BS) detectors were performed on carbon-coated thin sections and on gold coated fresh rock chips using a Phillips XL30 Scanning Electron Microscope fitted with Oxford Instruments Energy Dispersive X-Ray analysis (EDX).

Samples that are representative of the different textural groups determined using hand specimen and thin section were chosen for geochemical analysis. Where multiple analyses were possible samples from different stratigraphic levels and geographical locations were initially chosen to identify potential variations. A second or third group of samples were chosen for analysis to examine patterns produced by the first dataset.

Carbonate mineralogy was determined by X-ray diffraction (XRD) using a Siemens Kristaloflex instrument with a scanning speed of 5 seconds per $0.2^{o}2\theta$ between 24 and 33 $^{o}2\theta$. Samples for XRD were sampled using a 1mm nickel carbide drill bit and hand-held modelling drill rather than using bulk mineralogy of the carbonate bodies, to avoid sampling any inclusions of clay or detrital siliciclastic grains where possible. Samples were carefully crushed using an agate mortar and pestle to reduce lattice strain during preparation. Sample sizes of a few mg were analysed using a specially made small sample holder.

Specimens for isotope analysis were sampled differently according to the specimen types and the accuracy required, using either 0.5mm and 1mm nickel carbide bit and hand-held modelling drill or with 0.1mm and 1mm nickel carbide bits in a Sherline Model 2010-DROCE vertical milling machine with XYZ control set up for this study. Carbon and oxygen stable isotope values were determined on 3mg samples either using a VG Sira mass spectrometer by reaction in an online phosphoric acid in Isocarb unit at 90°C or by reaction of individual aliquots with 2ml of anhydrous 100% orthophosphoric acid under high vacuum (<$5x10^{-5}$ Torr) at 25°C. Data were corrected using standard procedures and reported in δ ‰ (VPDB) with a reproducibility of better than ± 0.1‰ for $\delta^{18}O$ and $\delta^{13}C$.

Solution ICP-AES analyses were performed on a Perkin-Elmer Optima 5300 dual view ICP-AES at the University of Manchester. 10mg powered samples were dissolved in 10mg of 2% Nitric acid prepared from 6N Analytical Grade nitric acid and distilled water. Samples were centrifuged and the supernatant decanted off for analysis for Mg, Fe, Sr, Mn, and Ba. Detection limits for these elements are between 10 and 100ppb and are well below the concentrations present in the specimens. Laser ablation ICP of polished blocks of sparry nodules was performed at the University of Aberystwyth using a Thermofinnigan Elements2 ICP-MS with a Lambdaphysik complex pro MicroLAS 193 Ar-F Excima gas laser. Laser ablation circular spot sizes were 10µm diameter ablated using a fluence of 5J/cm^2 and a 5Hz rep rate. The standard used was NIST SRM 612 so the data have not been calibrated to 100% calcium carbonate. Rare earth element data was normalised to North American Shale (Gromet et al., 1984).

2.5 Description of carbonates

2.5.1 Spherulitic clusters

A common feature in the Pleistocene lake margin sediments at Olduvai are clusters of small, low-Mg calcite spherulites consisting of radial, micron-scale crystallites (Figure 2-2). The component spherulites vary in size but tend to occur in either of two modal sizes; large spherulites between ~1mm and ~4mm diameter or small spherulites between ¼mm and ½mm diameter.

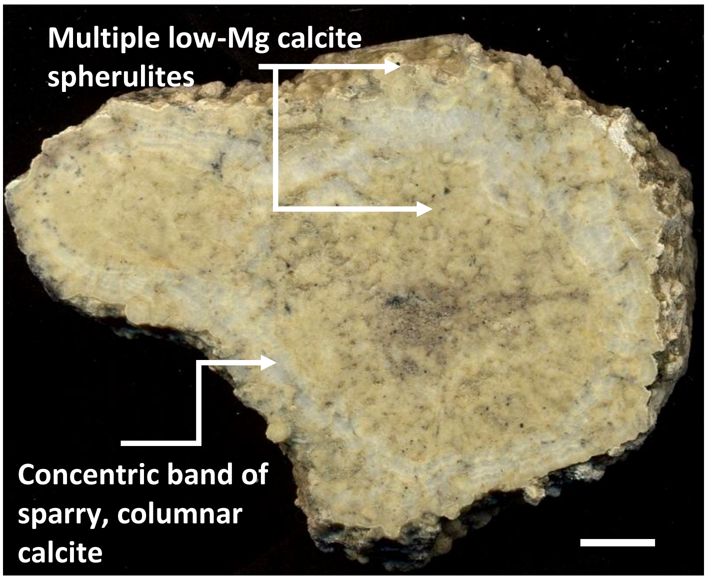

Figure 2-2: Polished cross section of a spherulitic cluster. (2008 Tr147 CA5) Scale bar 1cm. Spherulitic clusters are composed of multiple, low-Mg calcite spherulites. Partway through the cluster is a concentric band of sparry columnar calcite, which has textures similar to those found in the sparry nodules (Section 2.5.2). Detrital clay particle are usually trapped between the individual spherulites.

The clusters occur in beds of olive-green, waxy claystone at multiple locations and stratigraphic levels on the eastern lake margin and the western part of the alluvial fan. Within the clay beds there were no diagnostic pedogenic features such as mottling, stratification and horizonation. In one case there is unequivocal bioturbation directly associated with the spherulites (Tr47; Figure 2-3), although many specimens have rhizocretions directly above them in the same bed (eg Tr120; Figure 2-4, Tr144, Tr147).

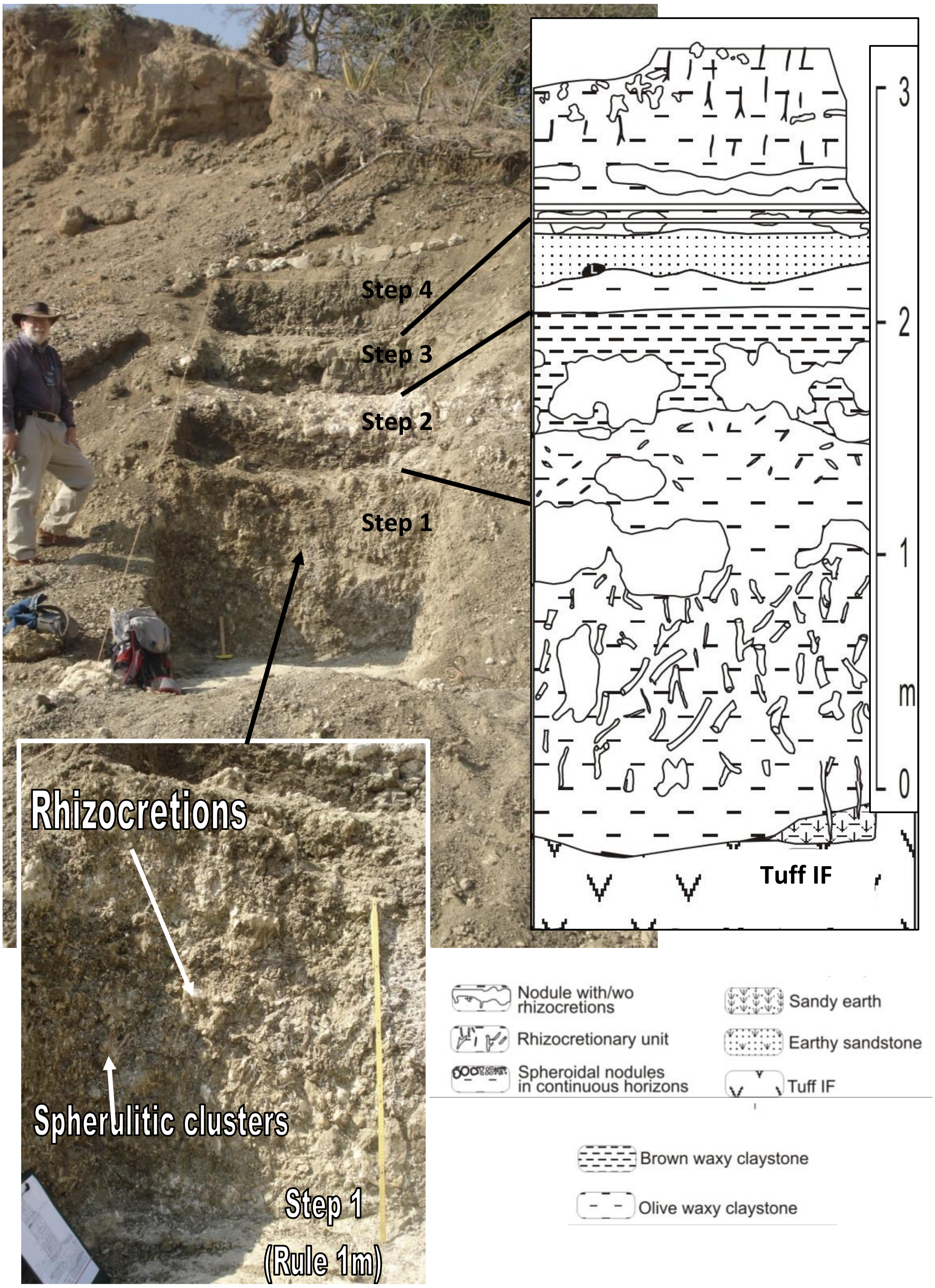

Figure 2-3: Tr 47 at the Eastern Lake Margin, Olduvai Gorge.
Trench 47 (Lower Bed II) contains spherulitic clusters in olive waxy claystone, associated with unequivocal bioturbation demonstrated by abundant rhizocretions. Trench map by Ian Stanistreet.

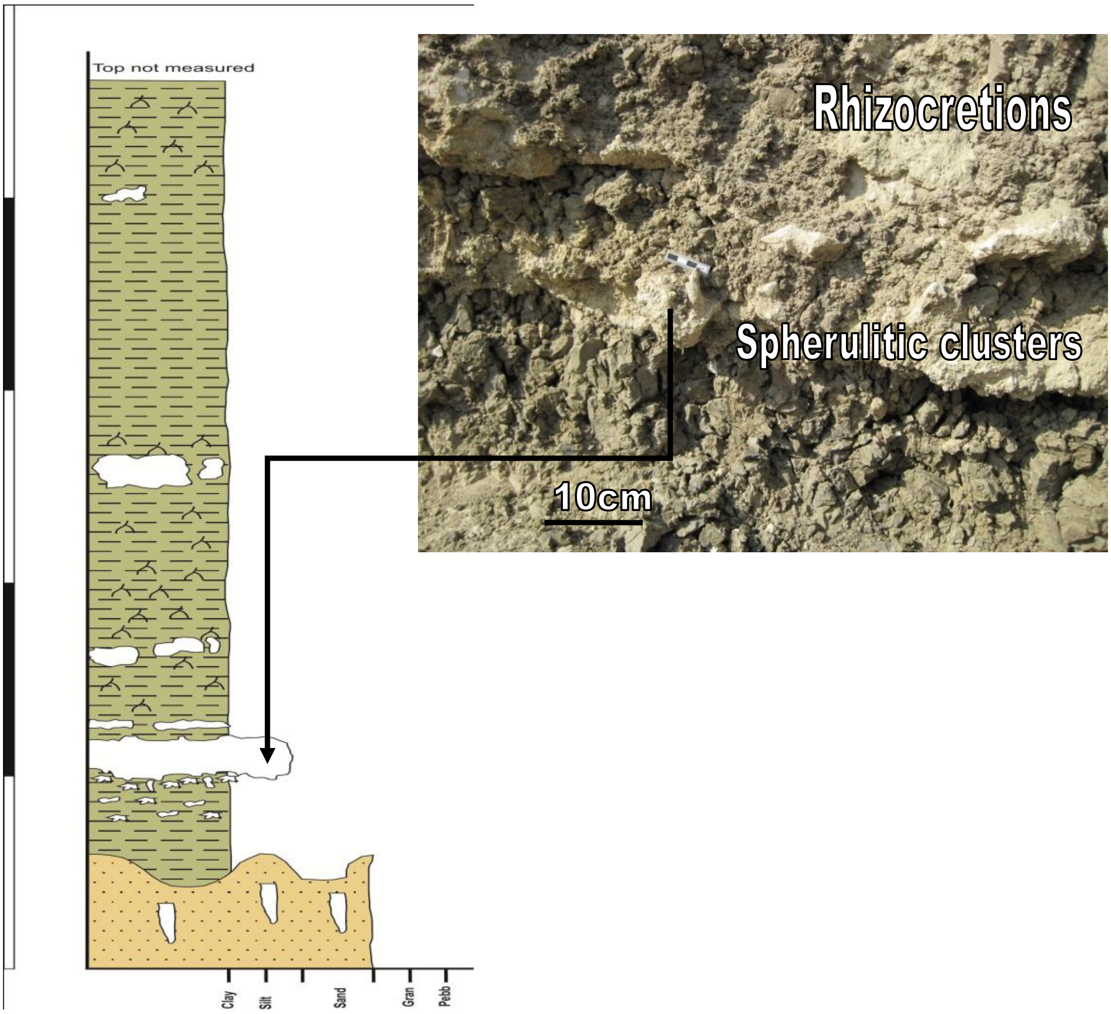

Figure 2-4: Tr120 at the Eastern Lake Margin, Olduvai Gorge. Trench of Bed I contains spherulitic clusters with roots ( ) in the overlying olive waxy claystones (Green) (Scale bar 0.5m). The coarse volcaniclastic sandstone (yellow) is part of Tuff IF so the sediments are part of Lower bed II.

The clusters of spherulites usually range in size between about 4 and 20cm, except for the one occurrence, at the eastern lake margin (Tr47), in the heavily bioturbated bed (Figure 2-3), where they occur as part of a larger cluster ~1m long and ~0.5m high. The clusters are interpreted to have formed *in situ,* and there is no indication of reworking or redistribution in their host sediments. The spherulites are sometimes formed around larger, concentrically developed, spherical, sparry nuclei similar to those described in section 2.5.2. Many of the clusters have columnar calcite crystals patchily developed in the cavities between spherulites. In others, columnar calcite is developed as a concentric band, up to 3 or 4mm thick, around which more spherulites have grown (Figure 2-2). The columnar calcite has macro morphological and micromorphological characteristics similar to those seen in the sparry nodules, and the significance of these is described later (section 2.5.2). Often the clusters contain one or more generations of cracks, which in some cases have caused the individual spherulites to fracture. The cracks are usually cemented with multiple generations of low-Mg calcite, but dolomite, strontianite and barite also occur. Three types of spherulitic growth have been defined using their micromorphological characteristics (Table 2). Some spherulitic clusters contain more than one type of spherulite.

	Type 1 **1-4mm**	**Type 2** **1-4mm & 0.25-0.5mm**	**Type 3** **0.5-2mm**
Shape of spherulites	Spherical to ovoid	Spherical to ovoid	Ovoid
Pattern of spherulites	Flower-like pattern of crystallites radiating from nucleus	Flower-like pattern of crystallites radiating from nucleus	Polygonal pattern formed by the intersection of crystal boundaries
Radial structure	Feather-like lines of inclusions forming each crystallite	Each crystallite formed of sub-parallel fibrous bundles Inclusion lines radiate from concentric micritic band partway between nucleus and edge of spherulite	Radial lines of inclusions
Concentric structures in spherulites	Multiple growth bands Concentric inclusion-rich and inclusion-poor bands Changing thicknesses of concentric bands from centre to edge of spherulite	Concentric microsparite bands partway between nucleus and edge of spherulite	Concentric lines of inclusions
Cross-section and Terminations of fibres in crystallites	Sub-hexagonal cross section Pointed and lobate terminations	Sub-hexagonal cross section	Sharply pointed terminations of individual radial fibres
Other features	Cuspate and smooth outer surface	Two forms radial calcite seen using SEM – euhedral and nodular	Inclusion free calcite rim
Nucleus	Micrite Bundles of fibrous calcite	Small, sub-spherical, micrite or inclusion poor	No nucleus
Extinction pattern in crossed-Nichols	Non-undulose extinction Undulose extinction – fascicular optic	Patchy extinction, Pseudo-uniaxial cross, Undulose extinction - fascicular-optic	Individual spheres composed of a single crystal of calcite

Table 2: Textural characteristics of the spherulites. Three types of spherulite have been identified based on their micromorphology.

Spherulite type 1

Type 1 spherulites are 1-4mm diameter and composed of multiple, radially orientated, feather-like, low-Mg calcite crystallites (Figure 2-5). Each feather-like crystallite is composed of individual fibres diverging from a central vein.

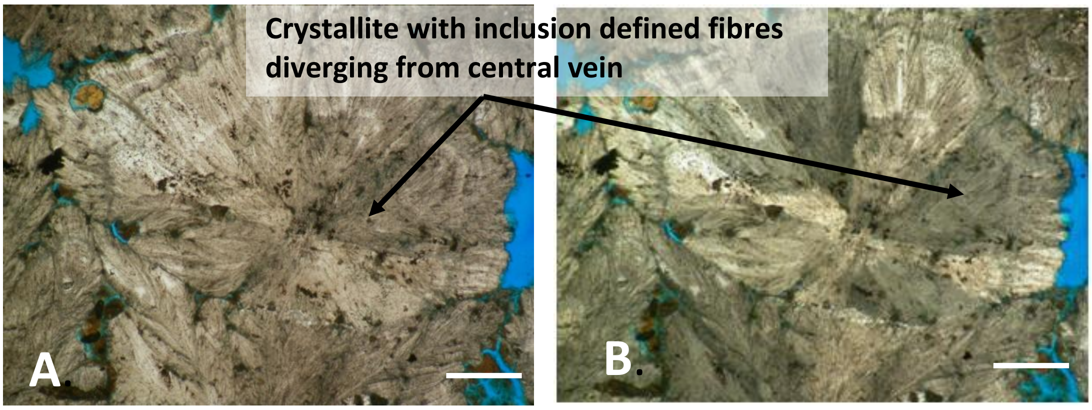

Figure 2-5: Type 1 spherulite shown in thin section. (2009 HWKE CA8) A) plain polarised light (PPL) and B) crossed polarised light (XPL). Scale bar 1mm. Spherulites are composed of radially orientated, feather-like, low-Mg calcite crystallites diverging from a central nucleus and producing a flower-like pattern. Each feather-like crystallite is composed of individual fibres diverging from a central vein. Growth bands can be identified by concentric zones which are either inclusion-rich or inclusion poor. Extinction under crossed Nichols is usually non-undulose.

The texture of the crystallites is defined by radiating lines of inclusions which are usually sub-microscopic, although some are identifiable by SEM as clay particles or voids. The crystallites initiate either from a single point or from a nucleus composed of micrite or bundles of fibrous calcite. The micritic nuclei are small, < 0.25mm, and tend to be either oblate or with a non-uniform morphology, whereas the nuclei formed from bundles of fibrous calcite tend to be larger, up to 2mm diameter and sub-spherical. The crystallites fan radially outwards, producing spherulites with a flower-like pattern. In some cases a patchwork pattern results from the intergrowth of adjacent crystallites. Crystal terminations, seen in thin section, are usually sharply pointed, but occasionally lobate. The outer surface of the spherulites is usually smooth and spherical. Occasionally the spherulites have a cuspate morphology to the outer surface, and these specimens have multiple, alternating inclusion-rich and inclusion-poor concentric zones, which become closer together from the centre to the edge of the spherulite. The spherulites are pseudopleochroic, and each crystallite has either an individual, non-undulose extinction pattern under crossed-Nichols, or an undulose radial extinction pattern under crossed-Nichols with divergent fascicular-optic orientation (Richter et al., 2003). There are some detrital siliciclastic grains trapped between the individual spherulites but few grains are entrained within the individual spherulites.

Spherulite type 2

Type 2 spherulites are composed of radially orientated crystallites composed of fans of sub-parallel fibres (Figure 2-6).

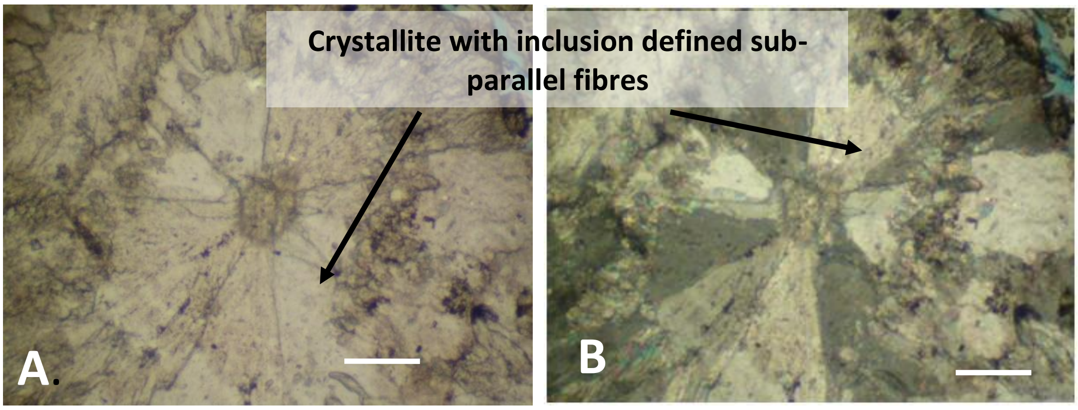

Figure 2-6: Type 2 spherulites shown in thin section. (2003 Tr120 KK 20) A) PPL and B) XPL. Scale bar 1mm. Spherulites are composed of radially orientated, low-Mg calcite crystallites with inclusion defined sub-parallel fibres. Each crystallite is composed of individual fibres diverging from a central vein. Concentric growth bands are composed of calcite microspar.

Clusters of the both the larger, and smaller, diameter spherulites exhibit type 2 micromorphological characteristics. The crystallites initiate from a central point which in some cases has a small, 0.5-1mm sized nucleus. SEM analysis shows that the nucleus is composed of multiple, sub-hexagonal, calcite grains <5μm diameter, and trapped clay particles (Figure 2-7). Often there are one, or two, concentric bands of calcite microspar partway between the centre and the edge of the spherulite.

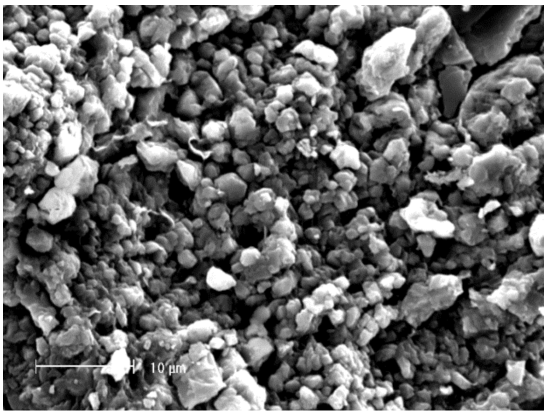

Figure 2-7: SEM-SE image of the nucleus of a type 2 Spherulite , composed of <5μm sized crystals of low-Mg calcite and trapped clay particles. (2003 Tr120 KK 7) Scale bar 10μm. Clay particles are partially intergrown with the calcite.

Using SEM-SE imaging, the radial calcite has two morphological forms. One of the forms has fibres which have straight edges from the interface with the nucleus to the edge of the spherulite. These have a sub-hexagonal cross section showing a core and rim separated by a more porous zone (Figure 2-8).

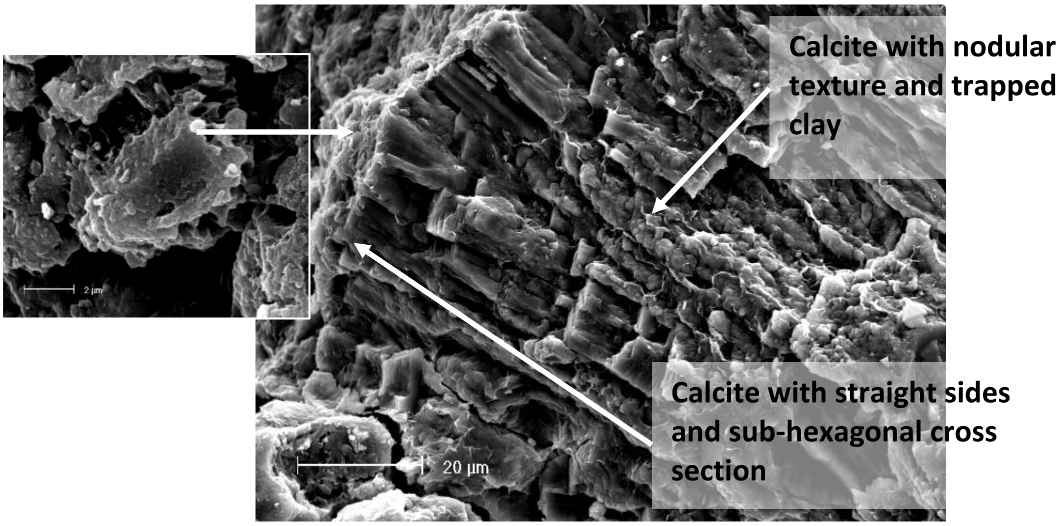

Figure 2-8: SEM-SE image of crystallites from Type 2 spherulites composed of two morphological forms of radial calcite fibres. (2003 Tr120 KK 7) The two forms can be present in a single spherulite. Form one can be seen on the left of the photograph, where the calcite fibres have straight sides and a sub-hexagonal cross section. Form two can be seen on the right hand side, where the calcite has a nodular texture and trapped lines of clay particles. Scale bar 20µm.

The other form consists of thin clay particles trapped between agglomerated <1µm calcite grains forming a nodular texture (Figure 2-8). It occurs in patches and is more common at the nucleus interface. Type 2 spherulites are pseudopleochroic and exhibit a cross-like extinction pattern under crossed-Nichols, which rotates around the spherulites as the microscope stage is turned. One specimen has a spherulitic texture composed of radiating needles of low magnesium calcite and a well defined pseudo-uniaxial cross extinction pattern (Wright and Tucker, 1991). Individual crystallites of calcite often exhibit fascicular-optic undulose extinction. The pattern of brightness under cathode-luminescence alternates between bright and dull orange luminescence throughout a single spherulite. The microsparite growth bands, and nucleus where present, are dully luminescent, whereas the crystallite fibres vary between bright and dull orange luminescence, with non-luminescent outer growth. The columnar calcite which formed after the spherulites is dully luminescent (Figure 2-9).

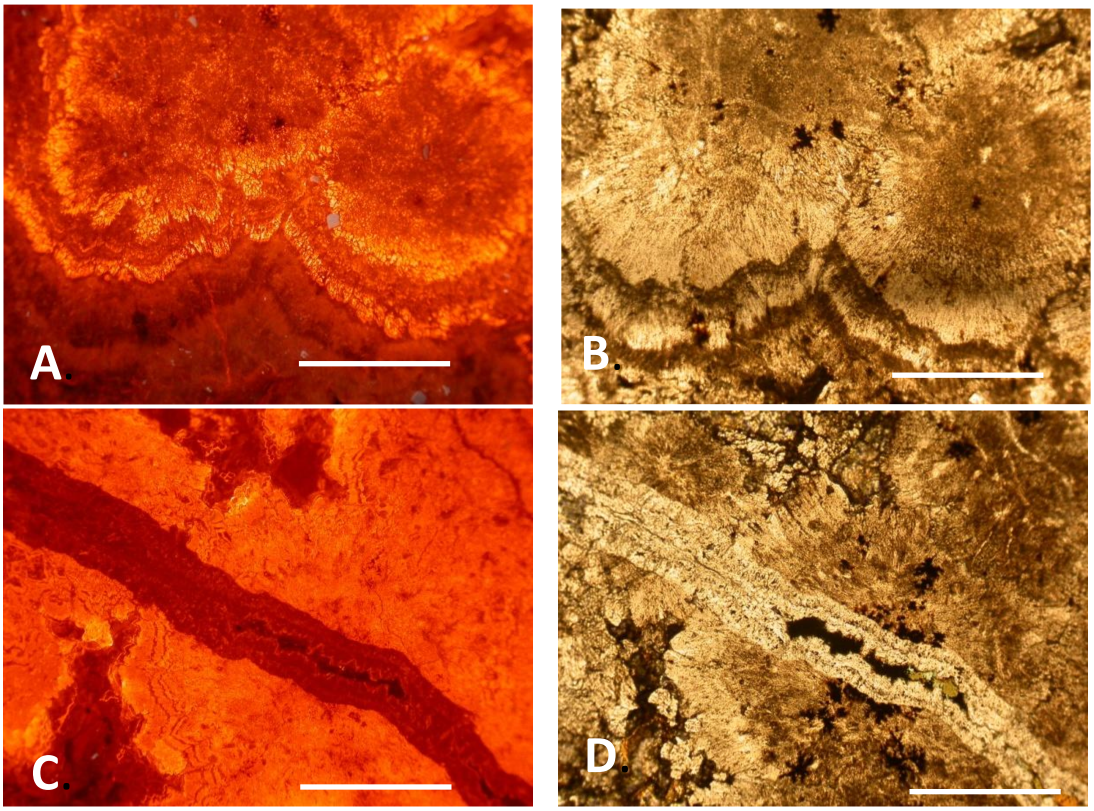

Figure 2-9: CL and corresponding PPL images of a thin section of a type 2 spherulitic cluster. (2008 Tr148 CA3) A,B) the sparry fibres that comprise the crystallites have an alternating pattern of dull orange, bright orange and no luminescence. Bands which are composed of micrite are dully luminescent. C,D) A calcite cement filled fractures which has dissected a spherulite. The cement has bands of varying luminescence which are sub-parallel to the fracture wall. Scale bar 0.5mm.

Spherulite type 3

Type 3 spherulites are sub-spherical to ovoid, low-Mg calcite, ranging in size between 0.5mm and 2mm. Inter-crystalline boundaries define a polygonal pattern (Figure 2-10). Each crystal has a small inclusion-rich spherical area in the centre and may exhibit one or two concentric layers of sub-microscopic inclusions.

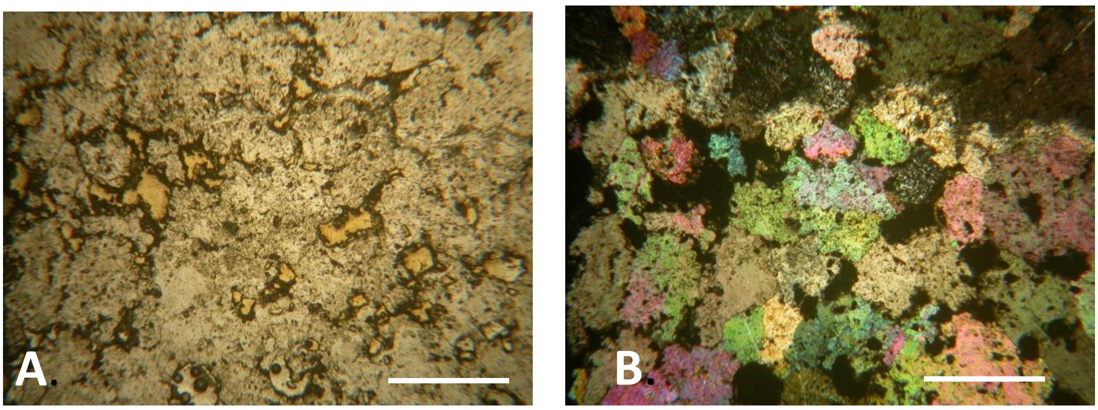

Figure 2-10: PPL and corresponding XPL images of a thin section of a type 3 spherulitic cluster. (2008 Tr144 NL3) Scale bar 1mm. The inter-crystalline boundaries of the spherulites form a polygonal pattern

Some of the spherulites also have radial lines of inclusions from the centre to the edge defining individual elongate fibres with sharply pointed terminations, which form a spiky surface to the crystal (Figure 2-10). In many cases the spherulites have a thin outer rim of calcite in the same optical orientation as the rest of the spherulite. The spherulites are dull orange to non-luminescent under cathode-luminescence, apart from the outer rim which is bright orange luminescent. (Figure 2-11).

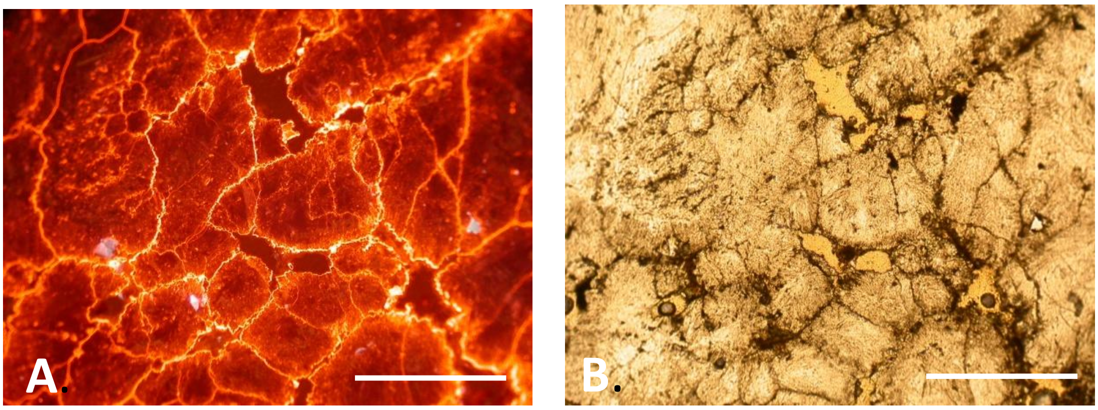

Figure 2-11: CL and corresponding PPL images of a thin section of a type 3 spherulitic cluster. (2008 Tr144 NL3) Scale bar is 0.5mm. The spherulites are dull orange to non-luminescent and the outer rim has a bright orange luminescence. Each spherulite also has spots and thin bands of high brightness orange luminescence with no apparent spherical or radial pattern.

Sparry concentric bands

Many of the spherulitic clusters have a concentric sparry band of columnar calcite present partway through the precipitate. The characteristics of these are identical to those described in detail in section 2.5.2 except that many more of them have a fascicular-optic extinction pattern compared to the non-undulose extinction pattern common in other columnar calcite specimens from Bed I and Lower Bed II at Olduvai Gorge.

Trace element analysis

Trace element analysis, by solution ICP-AES, was carried out on six spherulitic clusters, and in four cases the sparry bands associated with them (Table 3). Levels of magnesium ranged from 1.37 to 3.83 Mol% $MgCO_3$, which is consistent with low-magnesium calcite (Flügel, 2010). The abundance of iron is generally much higher than that of manganese with Fe/Mn ratios up to 48. The samples also contain strontium values between ~200ppm and ~1750ppm and barium values between ~20ppm and ~330ppm. Overall, the abundance of the trace elements in the spherulites is higher than in the sparry bands, which have similar values to those seen in the sparry nodules (Section 2.5.2).

	Fe	Mn	Fe/Mn	Sr	Ba	Mg	Mol% $MgCO_3$
2010 DK3 small spherulite	3302	1771	1.9	1750	335	8658	3.56
2010 DK3 sparry	1407	2202	0.6	998	161	9323	3.83
HWKE CA8 sperulites	2387	49	48.5	581	35	5842	2.40
HWKE CA8 Sparry	1483	334	4.4	205	70	3326	1.37
HWKE CA6 Spherulites	1353	120	11.3	1003	54	5638	2.32
HWKE CA6 Sparry	900	243	3.7	455	105	3554	1.46
147 CA5 Spherulite	1642	116	14.2	330	45	6709	2.76
147 CA5 Sparry	927	77	12.0	249	21	6477	2.66
143 CA5	681	991	0.7	1285	46	5416	2.23
120 CA106 all	1391	60	23.1	746	50	7169	2.95

Table 3: Table of trace element analyses for spherulitic clusters. Concentration data is in ppm.

Stable isotope results

Twenty-two specimens of spherulitic clusters were selected for analysis (Appendix 2). Larger individual spherulites were sampled from both their centre and their edge, in order to identify variations within an individual spherulite. In addition, multiple samples of whole spherulites were taken from several positions in a cluster, in order to identify any variation within the cluster. When all the data is plotted together they are covariant and the values range from $\delta^{18}O_{VPDB}$ -6.9‰ to -0.9‰ and $\delta^{13}C_{VPDB}$ -6.8‰ to 0.5‰ with an r^2 value of 0.85, $r(73) = 0.92$, $p < 0.0001$ (Figure 2-12).

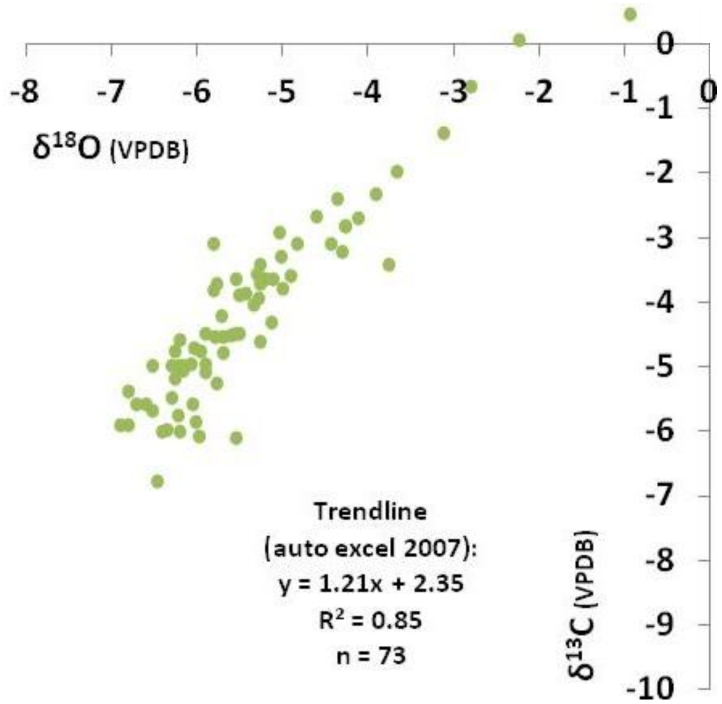

Figure 2-12: Stable isotope data for all spherulitic cluster samples. The $\delta^{18}O_{VPDB}$ and $\delta^{13}C_{VPDB}$ isotope ratios are covariant with an $r = 0.92$, t-test = 20.04 and $p < 0.0001$. This is considered to be a highly statistically significant correlation

The isotope ratios of both the centres and the edges of the individual spherulites share a very similar range of values and show no grouping which would indicate consistent changes in isotopic ratios as the spherulites form. The data from the centre points varies between $\delta^{18}O_{VPDB}$ -6.8‰ to -3.1‰ and $\delta^{13}C_{VPDB}$ -6.9‰ to -4.3‰ and those from the edges between $\delta^{18}O_{VPDB}$ -5.9‰ to -2.7‰ and $\delta^{13}C_{VPDB}$ -6.8‰ to -4.1‰ (Figure 2-13).

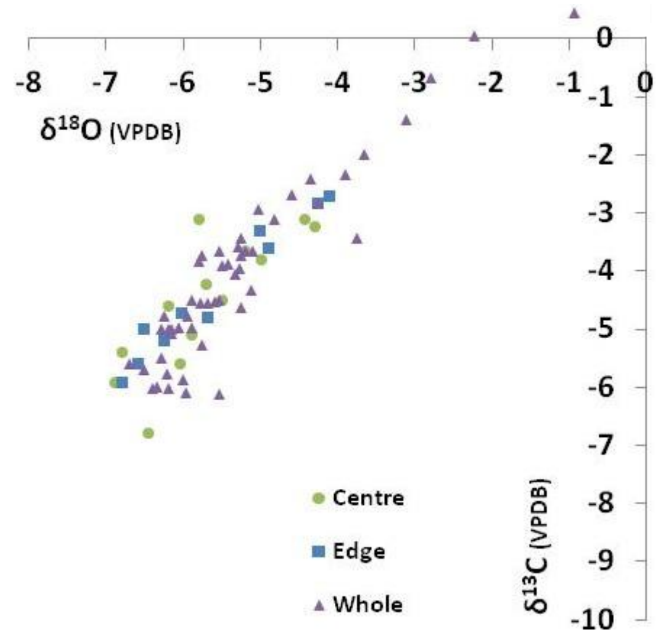

Figure 2-13: Stable isotope data grouped by spherulite sampling positions the edge of individual spherulites (Blue squares), the centre of individual spherulites (Green circles), and whole spherulites (Purple triangles). There is considerable overlap of the different sampling groups, and no apparent separation of the different groups.

The data from the whole spherulites, sampled at several positions from centre to edge of a spherulitic cluster, shows no covariance, and has values ranging between $\delta^{18}O_{VPDB}$ 6.1‰ to 0.5‰ and $\delta^{13}C_{VPDB}$ 6.7‰ to -0.9‰ (Figure 2-13). Finally the data was grouped by stratigraphic level. The same range of data was found in each set of samples and there is no apparent grouping at specific time horizons (Figure 2-14).

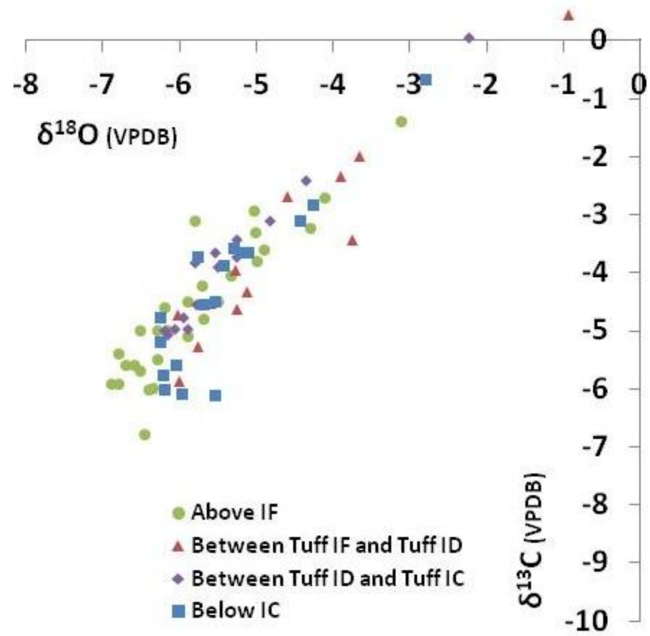

Figure 2-14: Stable isotope data for spherulitic clusters grouped by stratigraphic level. The stratigraphic levels are shown as: above Tuff IF (Green circles), between Tuff IF and Tuff ID (Red triangles), between Tuff ID and Tuff IC (Grey diamonds), and below Tuff IC (Blue squares). There is considerable overlap between the different levels and no apparent pattern of change between them.

2.5.2 Sparry nodules

A distinctive feature of the sediments at Olduvai Gorge is the presence of sub-spherical, low-Mg calcite nodules with multiple concentric sparry radial growth bands developed around a central nucleus. They are always found in massive, olive green, waxy lacustrine claystone in six locations of the eastern lake margin and one location in the alluvial fan sediments. They occur singly and as cemented clusters of multiple nodules and individual examples vary in size between ~1cm and ~18cm diameter (Figure 2-15).


Figure 2-15: A distinctive feature of the sediments at Olduvai Gorge is sub-spherical sparry nodules. Scale bar 1cm. (Left: 2008 Tr111 CA3, right: 2008 Tr111 CA1) The photograph on the left shows two sparry nodules, each with a small nucleus, which have been cemented together by spherulites and have a subsequent growth of plates of micritic calcite. The photograph on the right shows a single nodule with a large nucleus. Both have multiple, concentric bands of sparry calcite.

On the eastern lake margin they are found in Bed I below Tuff IC at Tr150 (Figure 2-16) and in Lower Bed II above Tuff IF in Tr 111 (Figure 2-17). The sparry nodules in the more eastern parts of the Gorge, at site DK, are found above Tuff IF, partially where the lower part of the clay bed is mixed with the underlying tuff (Figure 2-18). Calcite cemented ovoid tubes identified as insect burrows are preserved winding between the sparry nodules at site DK. These are interpreted to have formed after the sparry nodules as they are not intersected by the nodules. They are not recorded at the Eastern Lake Margin sites.

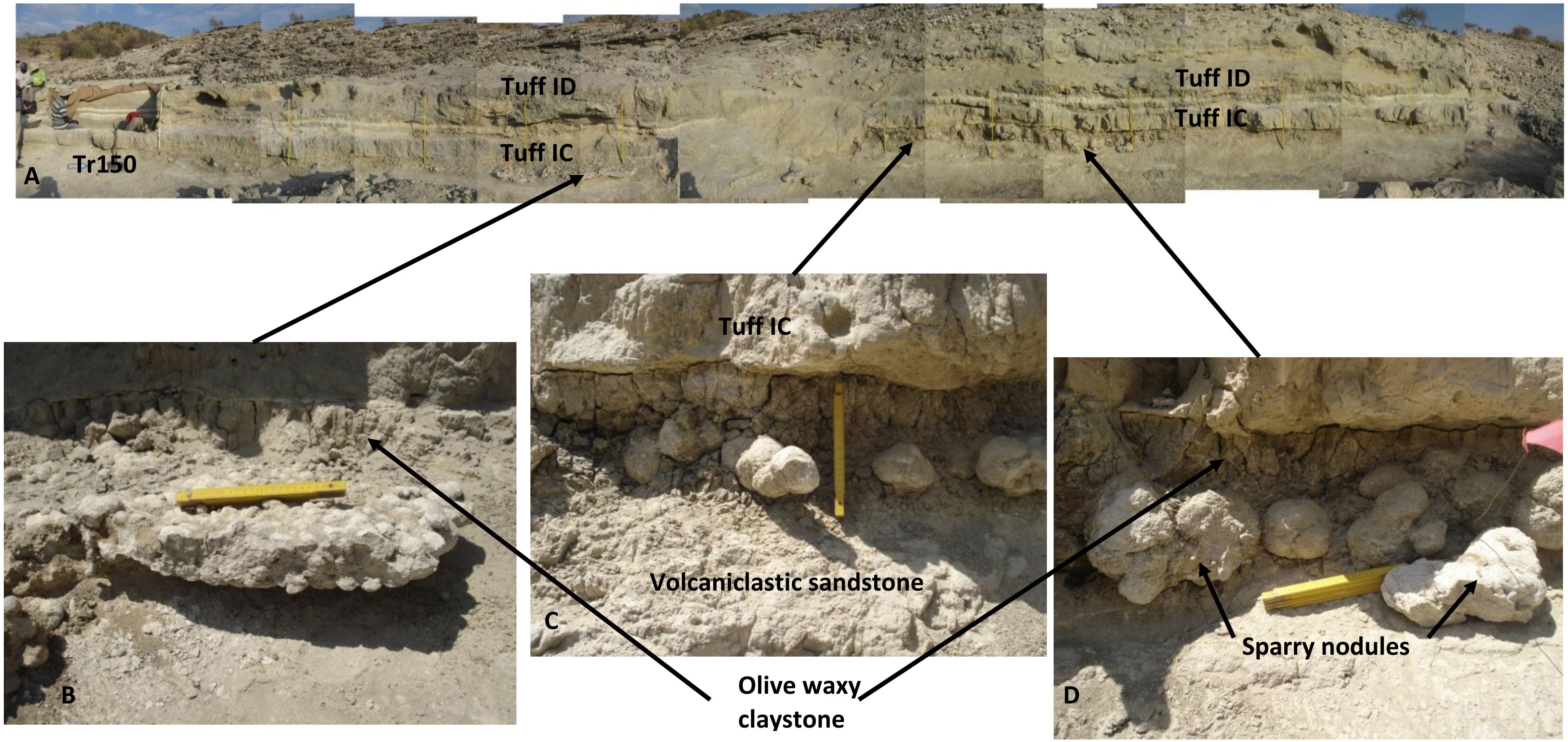

Figure 2-16: Prepared exposure at VEK (adjacent to Tr150) on the eastern lake margin, showing sparry nodules below tuff IC(A: The yellow rule is 1m). B: C: D: Sparry nodules are found in massive olive green waxy claystone (yellow rule 30cm) between Tuff IC and a volcaniclastic sandstone. The lower surface of Tuff IC and the upper surface of the volcaniclastic sandstone are erosional surfaces.

Figure 2-17: Sparry nodules with fossil remains of Elephantid at Tr111, Eastern Lake Margin. The nodules in Lower Bed II and are interpreted to have formed *in situ* with no indication of reworking or redistribution (Photograph Ian Stanistreet).

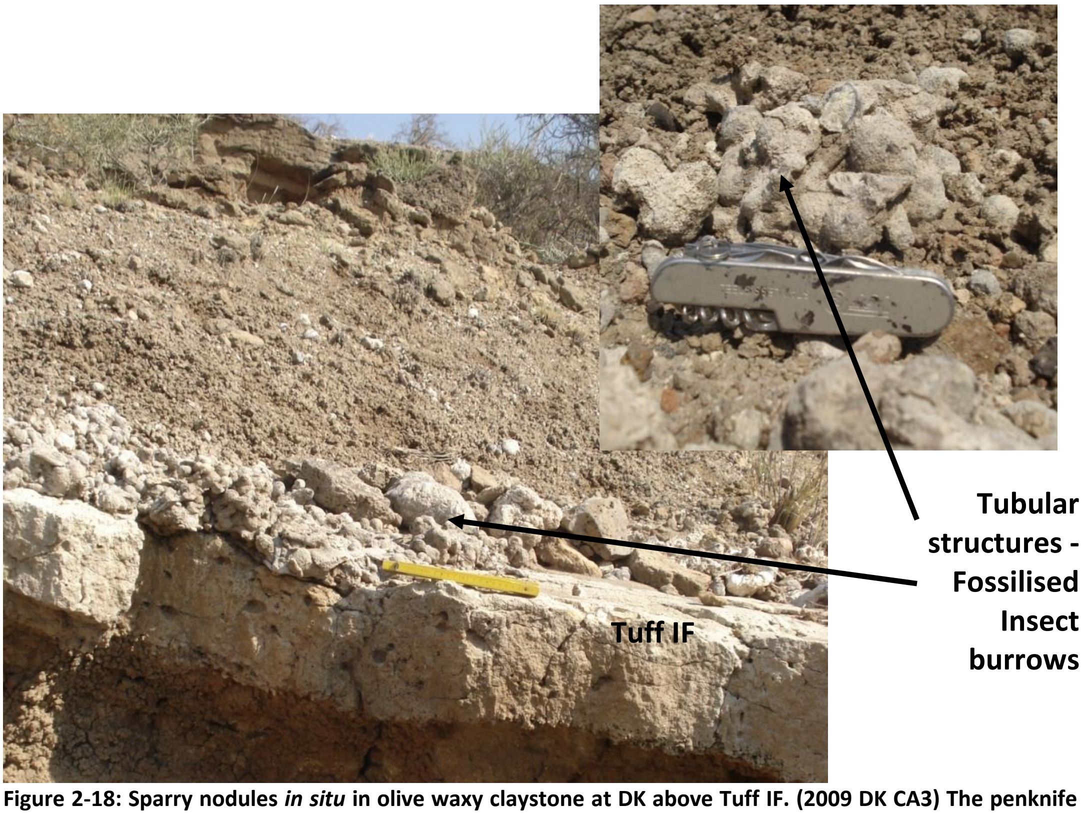

Figure 2-18: Sparry nodules *in situ* in olive waxy claystone at DK above Tuff IF. (2009 DK CA3) The penknife is 6cm long, the yellow rule is 30cm long. The nodule on the top of the group is broken showing the radial calcite and the outer manganese rich coating. The tubular structures are fossilised insect burrows which were formed after the concentric bands of the sparry nodules and during the formation of the cortex.

The lower boundary Tuff IC is deposited on an erosion surface and in some cases the overlying tuff is separated from the sparry nodules by as little as 1cm of clay. The nodules are interpreted to have formed *in situ* with no indication of reworking or redistribution. The nodules comprise four distinct morphological zones; the nucleus, the sparry bands, the transition zone (between the nuclei and the sparry bands), and the cortex.

Nucleus

The nuclei are usually sub-spherical, and vary in size between ~ 0.5cm and 4cm diameter. They consist of pseudopleochroic, equant, interlocking low-Mg calcite crystals, which vary in size between 0.1mm and 5mm, and have patterns defined by sub-microscopic inclusions. These patterns are usually intersected by the boundaries of the equant calcite crystals showing them to be neomorphic. The nuclei have been grouped into three types based on their inclusion patterns.

Type 1

The fabric of Type 1 nuclei is by far the most abundant. It comprises multiple bundles of sub-parallel, elongate fibres, with pointed terminations, which initiate from a single point and fan outwards. An increased inclusion density defines the boundaries of each bundle. The bundles range in size between 0.1mm and 2mm (Figure 2-19), and those in an individual specimen are a similar size.

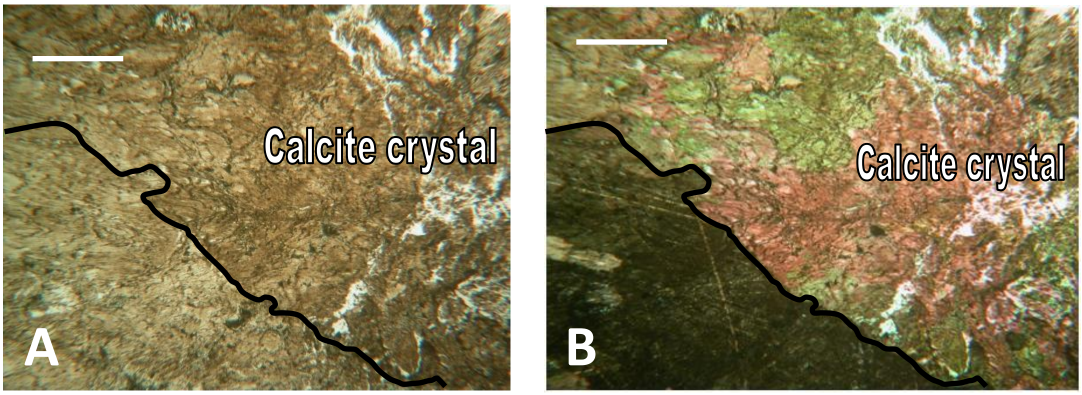

Figure 2-19: PPL and XPL photograph of nucleus type 1, composed of multiple bundles of fibrous crystals defined by lines of inclusions. (2008 Tr111 CA5) The extinction pattern under crossed-Nichols (XPL) (B) can be

used to identify individual calcite crystal boundaries, one of which is shown on the PPL image (A) by a black line. In (A), the brown colouration is darker on one side of the line compared to the other, possibly indicating concentration of organic material during recrystallisation. Towards the bottom right of the photographs the nucleus has a clotted texture with calcite filled cracks. Scale bar 1mm.

Rarely bundles exhibit growth lines shown by inclusion-poor bands normal to the crystal growth direction. The bundles in the centre of the nucleus tend to have no preferred orientation, and they interdigitate with no apparent pattern. Often a new bundle initiates at the termination of the previous bundle. Crystal bundles become more radially orientated towards the outer part of the core.

Some bundles have a feather-like texture, where individual fibres diverge from a central vein (Figure 2-20). Occasionally, adjacent feather-like features converge at the outer part of the nuclei, and where this occurs the outer surfaces of the nuclei have traces of cuspate terminations produced by competitive growth.

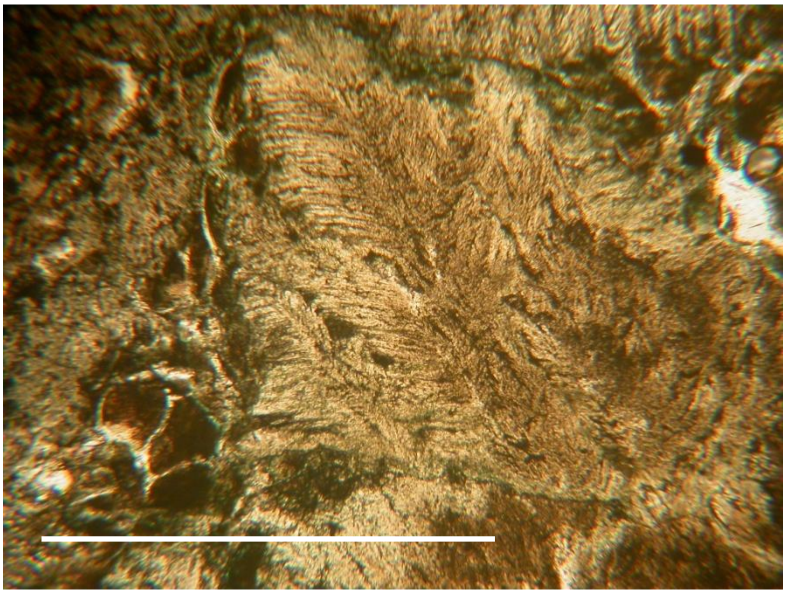

Figure 2-20: Feather-like crystal from nucleus type 1, with crystal fibres diverging from a central vein defined by lines of inclusions. (2008 Tr111 CA5) Small pieces of a cracked detrital clay pellet are cemented adjacent to the crystal. Scale bar 1mm.

Some areas in the centre of the nucleus have a clotted texture, and trapped detrital silicate grains usually have either circumgranular or stellate cracks cemented with low Mg calcite (Figure 2-19). The calcite crystals that form the nucleus have a dull orange luminescence (Figure 2-21).

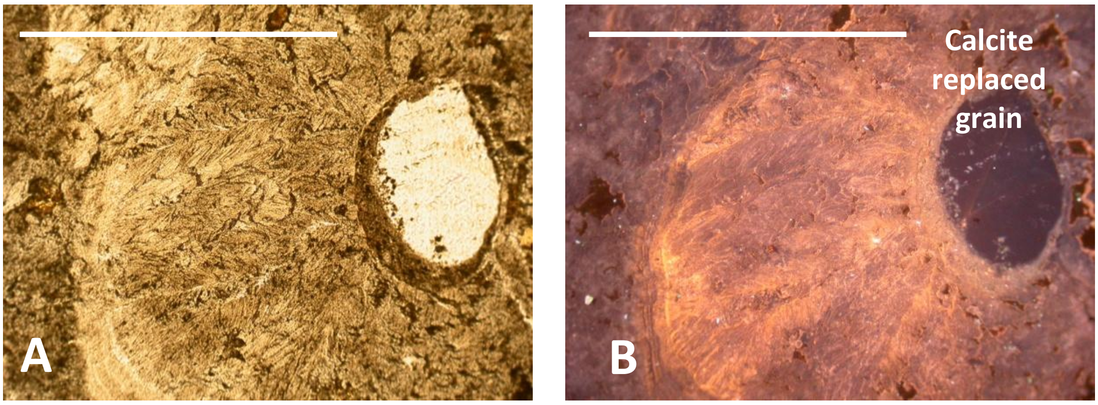

Figure 2-21: PPL and CL image of nucleus type 1(2008 Tr111 CA5).Scale bar 1mm. The entire area in the photographs is one crystal of calcite (A) with an inclusion-defined neomorphic fabric. The CL image of the calcite (B) shows a dull orange luminescence, with some bright orange luminescence at a concentric growth band radiating away from a calcite replaced grain. Although the area is a single crystal, there are bands of fine lines within it with different CL responses, possibly indicating that the replacement or recrystallisation has not completely overwritten the original trace elements.

Type 2

Type 2 fabric is composed of multiple, ovoid crystals, defined by inclusion-rich crystal boundaries, which range in size between 0.5mm and 2mm along the long axis (Figure 2-22). In the centre of each crystal is a small, spherical area composed of sub-microscopic inclusions, and often one or two concentric lines of inclusions between this area and an the crystal boundary. Some crystals have radially arranged lines of inclusions which define individual elongate fibres. The concentric lines of inclusions tend to be more spherical in the crystal centre and increasingly ovoid towards the edge, showing elongation along a single axis during growth.

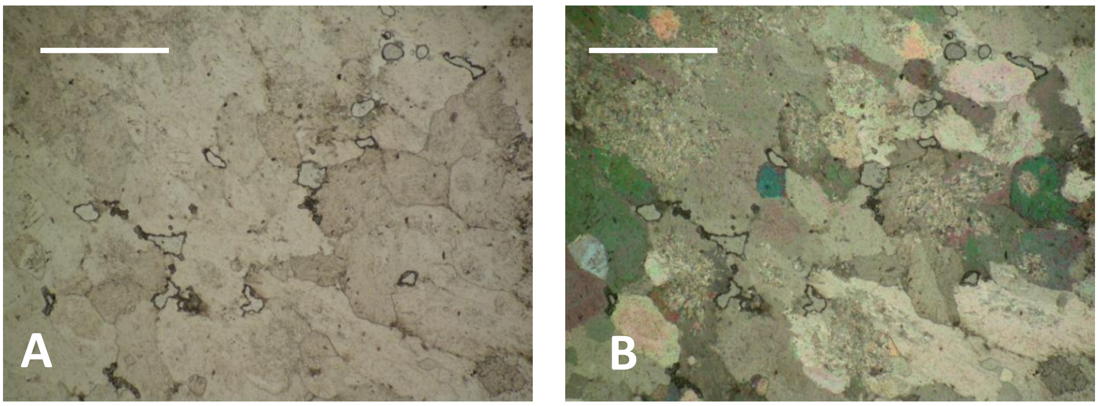

Figure 2-22: PPL and XPL photograph of nucleus type 2(2009 Zinj GA), composed of multiple ovoid crystals defined by lines of sub-microscopic inclusions. The crystals are packed closely together in the centre of the nuclei and where crystal boundaries are in the contact the intersection is undulating. Scale bar 1mm.

The crystals are packed closely together in the centre of the nucleus and form a polygonal pattern where crystal boundaries come into contact. There is increasing space between crystals in the outer part of the nucleus, and an increasing density of siliciclastic particles trapped between them. Where the boundaries of adjacent crystals are in contact they are undulating, and where they are not in contact they are smoothly rounded.

Type 3

The type 3 nuclei are very dark brown, and have a mottled appearance caused by abundant trapped, detrital, siliciclastic, grains and clay particles, and sub-microscopic inclusions (Figure 2-23). The nucleus has a clotted texture with circumgranular cracks, root traces, and ribbon-like cracks, cemented with low-magnesium calcite in optical continuity with that of the equant calcite crystals.

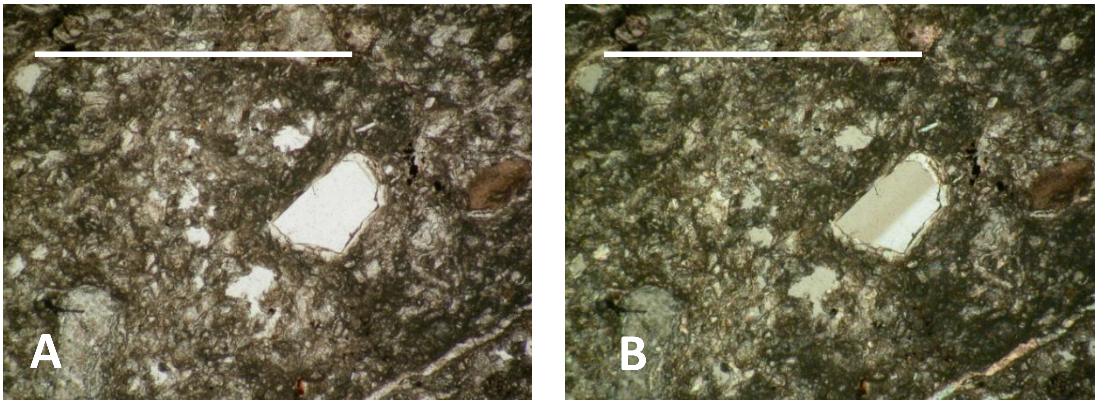

Figure 2-23: PPL and XPL photograph of nucleus type 3(2008 Tr143 NL6) composed of very dark brown low-Mg calcite which is inclusion-rich, mottled and has calcite filled circumgranular cracks. Scale bar 1mm.

Concentric sparry bands

The concentric bands of sparry calcite exhibit a radiating, competitive, columnar growth pattern (Dickson, 1978). Apart from a single specimen, the development of each of the different textural zones has no preferred growth orientation, indicating no restriction to radial growth. The calcite is colourless to grey/brown, transparent, weakly pseudopleochroic, and with very few trapped, detrital, siliciclastic grains. The sparry bands are developed radially, and although they thin in places, individual bands do not completely pinch out. The varying thickness of a band bears no relationship to the field orientation of a specimen; for example, there is no evidence of a specimen growing away from a surface on which it rests. Individual sparry bands are up to 4mm thick and are typically thickest towards the nucleus and become increasingly thin toward the cortex. Where two or more specimens have grown close together, the sparry bands have sometimes formed concentrically around both of them (Figure 2-24).

The sparry bands are defined by repeated, inclusion-rich zones, inclusion-poor zones, or microcrystalline calcite. In addition scalenodehral calcite or spherulite growth is sometimes present along the growth bands. Generally, samples show a combination of the different growth forms.

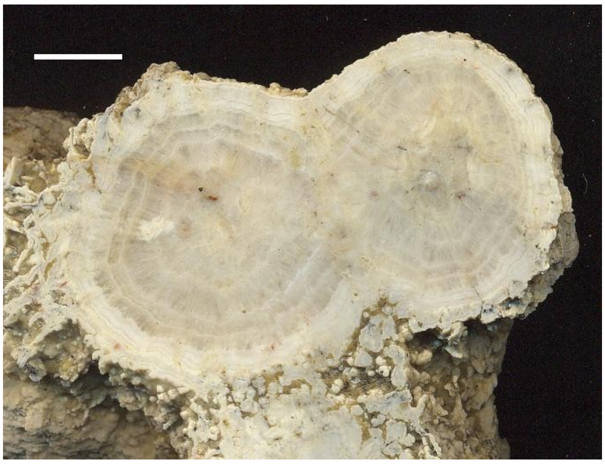

Figure 2-24: A polished face of two, intergrown, sparry nodules.(2008 Tr111 CA4) The outer concentric bands of calcite have grown around both of the samples showing that radial growth must occur without the need for specimen agitation or rolling. Scale bar 1cm.

Sparry bands comprise individual columnar crystals which are between 1 and 4mm long, up to 1.5 mm at their widest point and can span multiple growth bands. The individual crystals have a hexagonal cross section and non-planar crystal boundaries. Using a gypsum filter in the petrographic microscope (Kendall, 1978), the columnar calcite at Olduvai has been identified as length fast, so has the long axis parallel to the c-axis. They have long-axis sub-parallel lines of inclusions, which initiate from a single point, fan outwards, and then become sub-parallel. These are most apparent in the outer part of crystals with the centres often almost inclusion-free. The boundaries of individual crystals are usually inclusion-free, but can be seen by their extinction pattern using crossed-Nichols. Many of the inclusions are sub-microscopic, and in some cases cannot be identified even using SEM analysis but, where identifiable, they are clay particles or voids.

The columnar crystals usually display a euhedral growth front indicated by the sparry band inclusions. A euhedral growth pattern for the columnar calcite is also visible in cathode-luminescence as a repeated pattern of dull orange and non-luminescence, and occasionally a bright orange luminescent band, which is coincident with the sparry band growth face (Figure 2-25).

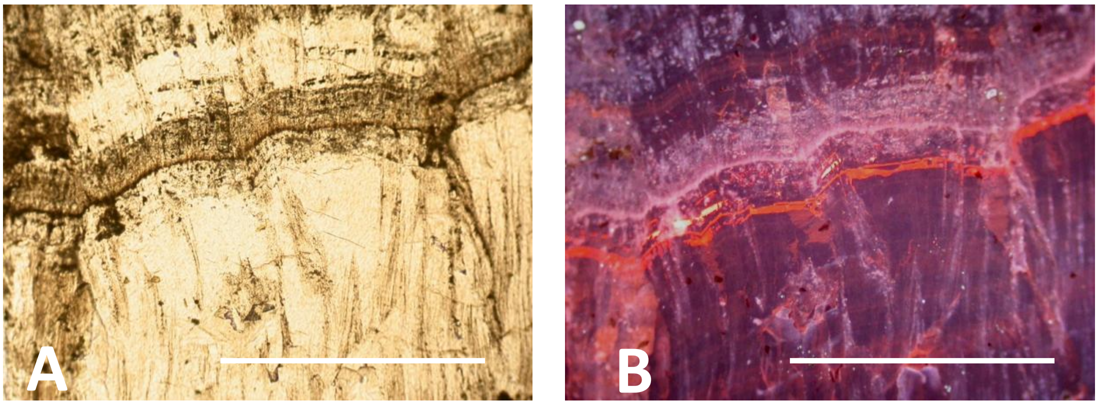

Figure 2-25: The PPL (A) and CL (B) image of the sparry bands and a series of inclusion bands (2008 TR111 CA5) show that the sparry calcite has multiple variations between dull and non-luminescent calcite, with an orange high brightness band just underneath the start of the inclusion rich calcite. Scale bar 1mm. The pink and blue luminescence is likely due to clay particle inclusions, although it may also be intrinsic luminescence caused by crystal imperfections in calcite with low concentrations of trace elements (Habermann et al., 1998).

In addition to the features described above, the sparry nodules from the alluvial fan have a discontinuous, concentric, band of strongly pleochroic dark brown to very dark brown patches in the sparry bands partway through the development of the specimen (Figure 2-26). The feature has dominant peaks of fluorine and calcium using the EDX during SEM-BS analysis, and both fluorite and low-Mg calcite are detected using XRD analysis. However, they do not fluoresce using ultraviolet florescence microscopy, and the band is not isotropic.

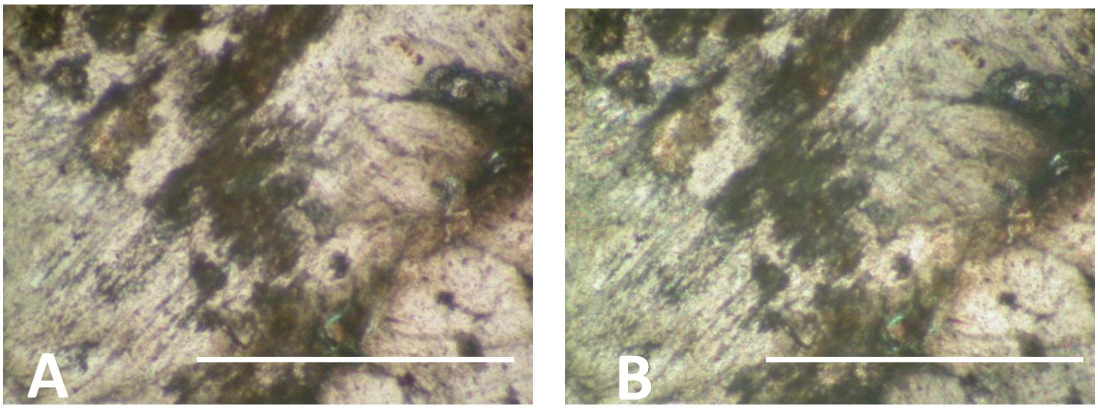

Figure 2-26: A discontinuous band of brown patches of fluorite. The PPL (A) and XPL (B) images show brown patches which form a discontinuous band in the outer layers of concentric sparry calcite (2009 DK CA1). These are identified as fluorite using EDX and XRD. However their brown colour is pleochroic and they are not isotropic, possibly as the result of incomplete replacement of a calcite precursor. Scale bar 1mm.

Transition zone

Between the nucleus and the sparry concentric calcite is a transition zone with mixed characteristics of the two. The transition zone is pseudopleochroic, usually inclusion-rich compared to the sparry bands, and contains a high abundance of detrital grains. Calcite growth commonly initiates on the surface of the nucleus via spherulites described in section 2.5.1. Elongate, length-fast, columnar crystals then initiate from the surface of the spherulites, and finally develop into concentric sparry bands (Figure 2-27). The sparry, columnar, calcite may restart more than once, either from spherulites or, rarely, a band of microspar. Feather-like crystals, similar to those described in nucleus type 1, are also present in the transition zone. The columnar calcite usually has straight extinction, although one site, unusually, displays fascicular-optic fibrous calcite.

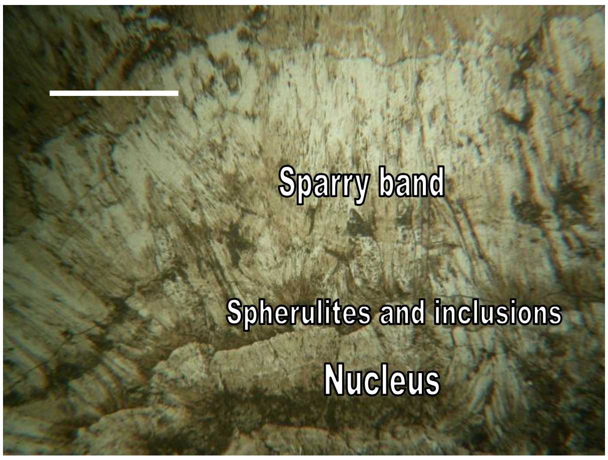

Figure 2-27: The PPL image of the transition zone in the sparry nodules(2008 Tr111 CA4), where the nucleus is at the bottom of the picture and the cortex is beyond the top of the picture. The sparry bands are seen to initiate on inclusion rich zones with a less well defined concentric behaviour and more interruptions in growth. Following this first sparry band there is a highly inclusion-rich band with some spherulites. This pattern repeats twice towards the cortex with the sparry bands becoming more dominant and the inclusion-rich bands less so. Scale bar 1mm

In many of the specimens the first development of columnar calcite on top of the nucleus is brightly luminescent under cathode-luminescence analysis (Figure 2-28).

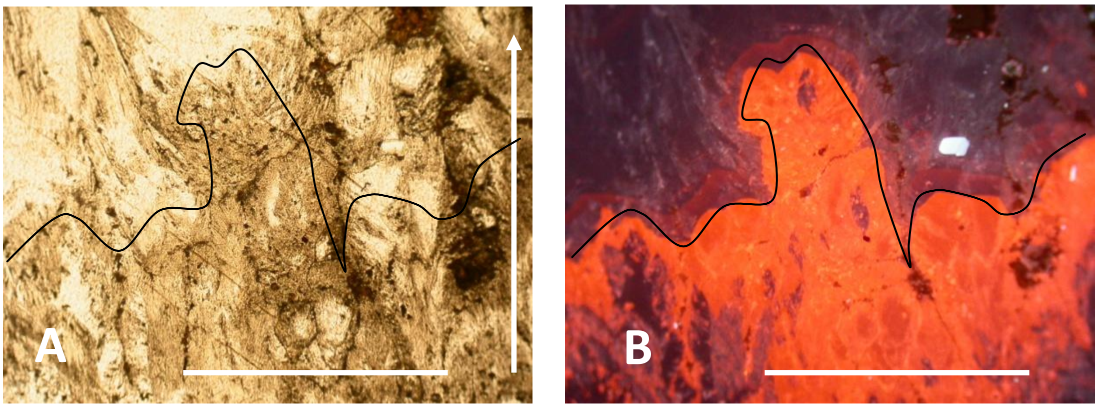

Figure 2-28: Cathode-luminescence image of the first sparry columnar growth. The TL (A) and CL (B) images of the first sparry columnar calcite growth band on top of the nucleus often has bright orange luminescence under CL. (2008 Tr111 CA5) The arrow points in the direction of growth from nucleus to cortex. Scale bar 1mm.

Cortex

The outer part of the specimen, termed the cortex, is knobbly, and comprises spherulites and thin, interlocking walls of calcite <1mm thick (Figure 2-29). The spherulites vary in size between 0.2mm and 2mm.

Figure 2-29: The cortex of the sparry nodules with spherulites and intersecting plates of micritic calcite with clay trapped between them. (2002 Tr111 5) The clay plates are probably where the surrounding clay has desiccated causing shrinking and cracking, then calcite has precipitated filling the voids. Scale bar 1cm.

The crystal textures are described in section 2.5.1. They are abundant on the surface of individual sparry nodules, and also form as clusters in the voids between adjacent, joined sparry nodules (Figure 2-30). They are cemented into, and developed on top of, walls of calcite composed of micrite.

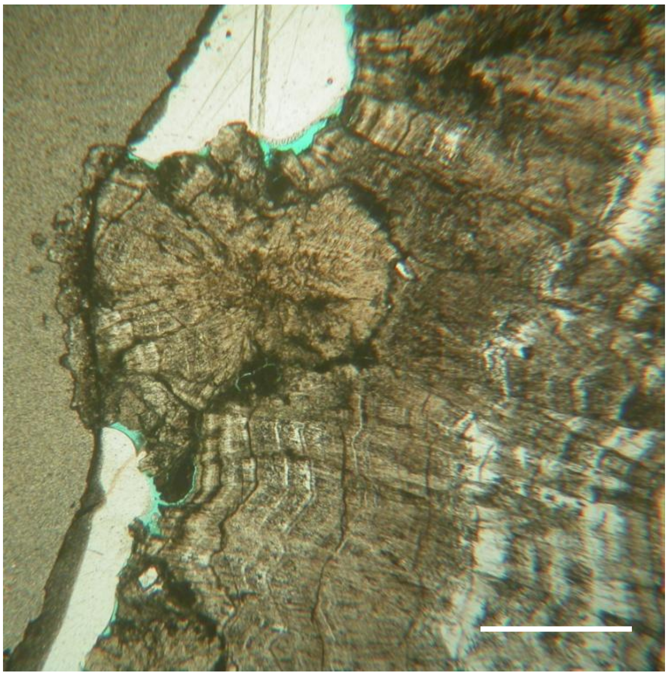

Figure 2-30: Spherulites, commonly formed on and within the cortex of the sparry nodules. (2008 Tr111 CA5) They have a similar structure to that seen in the type 2 spherulitic clusters with radiating sub-parallel lines of inclusions. Scale bar 1mm.

Trace element analysis

Trace element analysis was carried out on three sparry calcite nodules (Appendix 3). Solution ICP-AES analysis was performed at the University of Manchester to identify barium, strontium, iron, manganese and magnesium values at between 7 and 9 different locations between the centre and edge of two of the nodules. The large amount of drilled material required for these analyses (~10-13mg) reduce the number of sampling locations possible per specimen. Laser ablation ICP-MS analysis was performed at the University of Aberystwyth to identify some trace elements and REE at 18 different locations between the centre and the edge of two of the nodules. One of the samples was used in both methods, and in all cases material was sampled from both the nucleus and the sparry bands.

The magnesium concentrations ranged from just over 3800ppm (1.56 Mol%$MgCO_3$) to over 9000ppm (3.76 Mol% $MgCO_3$) which are consistent with low-magnesium calcite. There are significantly higher values of iron compared to manganese in all the samples, with Fe values ranging from ~80ppm to ~1400ppm and the Mn values only from ~10ppm to ~90ppm, they have very similar Fe/Mn ratios to each other. Sample CA5 has an Fe/Mn ratio between 10 and 20 with an *r(7DoF) = 0.84,* and sample CA0 has an Fe/Mn ratio between 3 and 20 with an *r(5DoF) = 0.9.* These are both statistically significant correlations of $p < 0.005$, indicating that the changing values of Fe and Mn occur by the same process and are likely to be related to changing redox conditions. The samples also contain strontium values which range from ~220ppm to ~1400ppm and barium values between ~120ppm to ~180ppm. Trace element abundance varied between sampling positions. Sr, Fe and Mn are highest at the centre and the edge of the sample and lowest in the sparry bands, whereas Mg and Ba are similar throughout the saple (Figure 2-31,Figure 2-32).

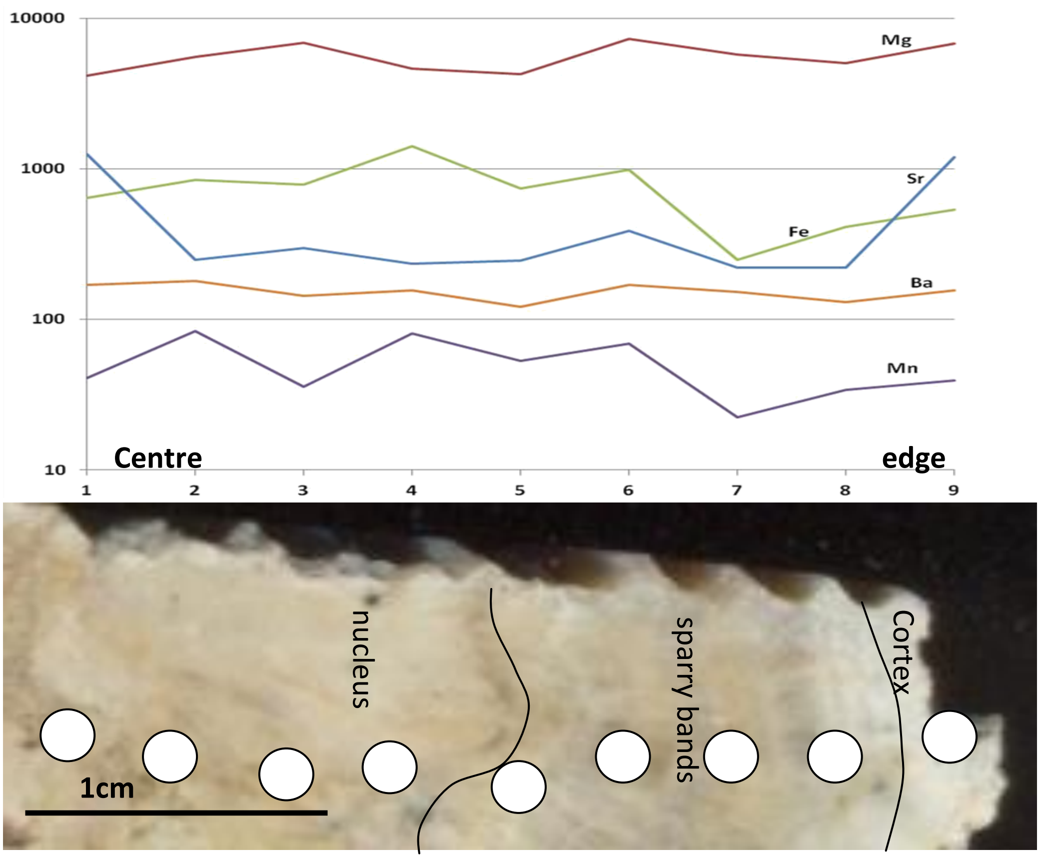

Figure 2-31: Trace element data of a sparry nodule sampled at 9 positions from centre to edge approximately 2mm apart. Specimen number 2009 Tr111 CA5. The trace element abundances vary between sampling points and are generally least abundant in the sparry bands. Fe/Mn ratios are always much greater than 1. White circle identifies sampling points.

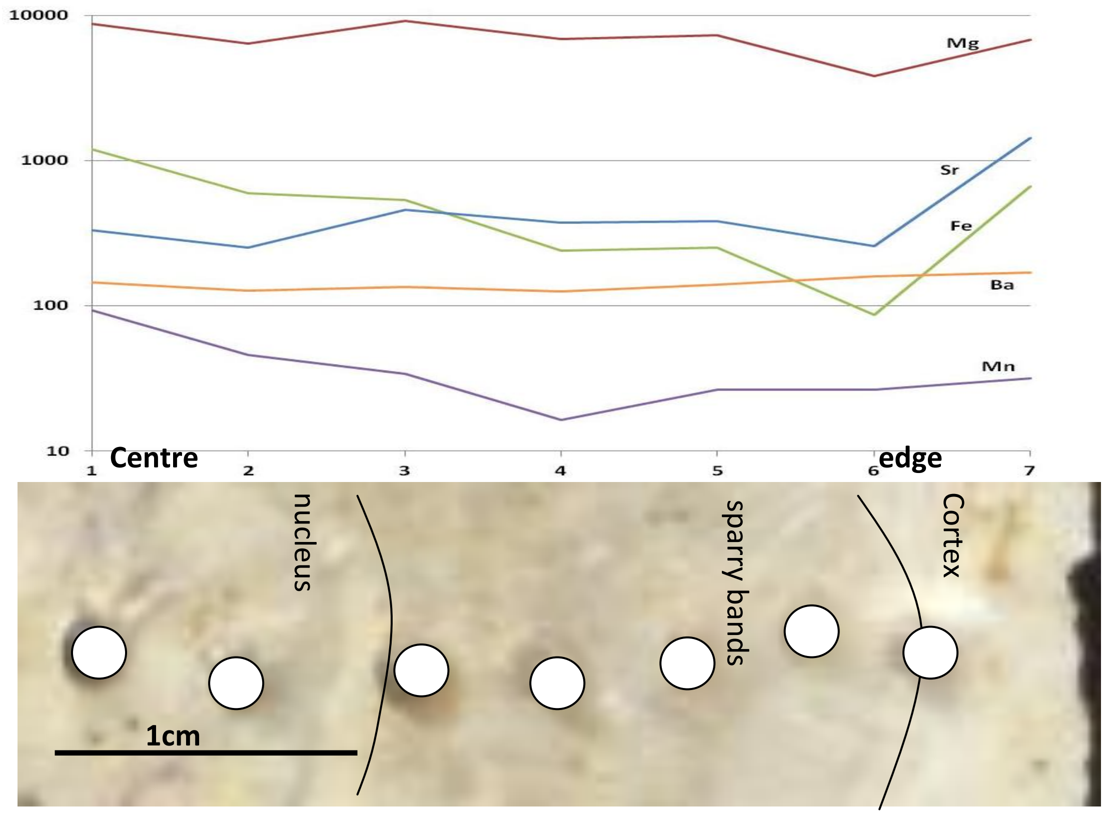

Figure 2-32: Trace element data of a sparry nodule sampled at 7 positions from centre to edge approximately 3mm apart. Specimen number 2009 Tr111 CA0. The trace element abundances vary between sampling points and are generally least abundant in the sparry bands. Fe/Mn ratios are always much greater than 1. White circle identifies sampling points.

Lighter rare earth elements (LREE), La to Nd, are present in quantities up to 160ppm, up to an order of magnitude greater than the heavier rare earth elements (HREE), Sm to Lu, which are present up to about 12ppm. There is no detectable europium or terbium in any of the samples.

Trace element abundance varies between the sampling positions (Figure 2-33), and comparison of the two specimens shows a similar pattern of change associated with the different textural areas of the sparry nodules. The samples from the nucleus tend to have more consistent element abundance between sampling positions compared to the results from the sparry bands, which vary much more between sampling positions. Both specimens show the same large increase in the abundance of the lanthanides at the cortex of the samples. Eu, Tb and Ho are all below detection limits

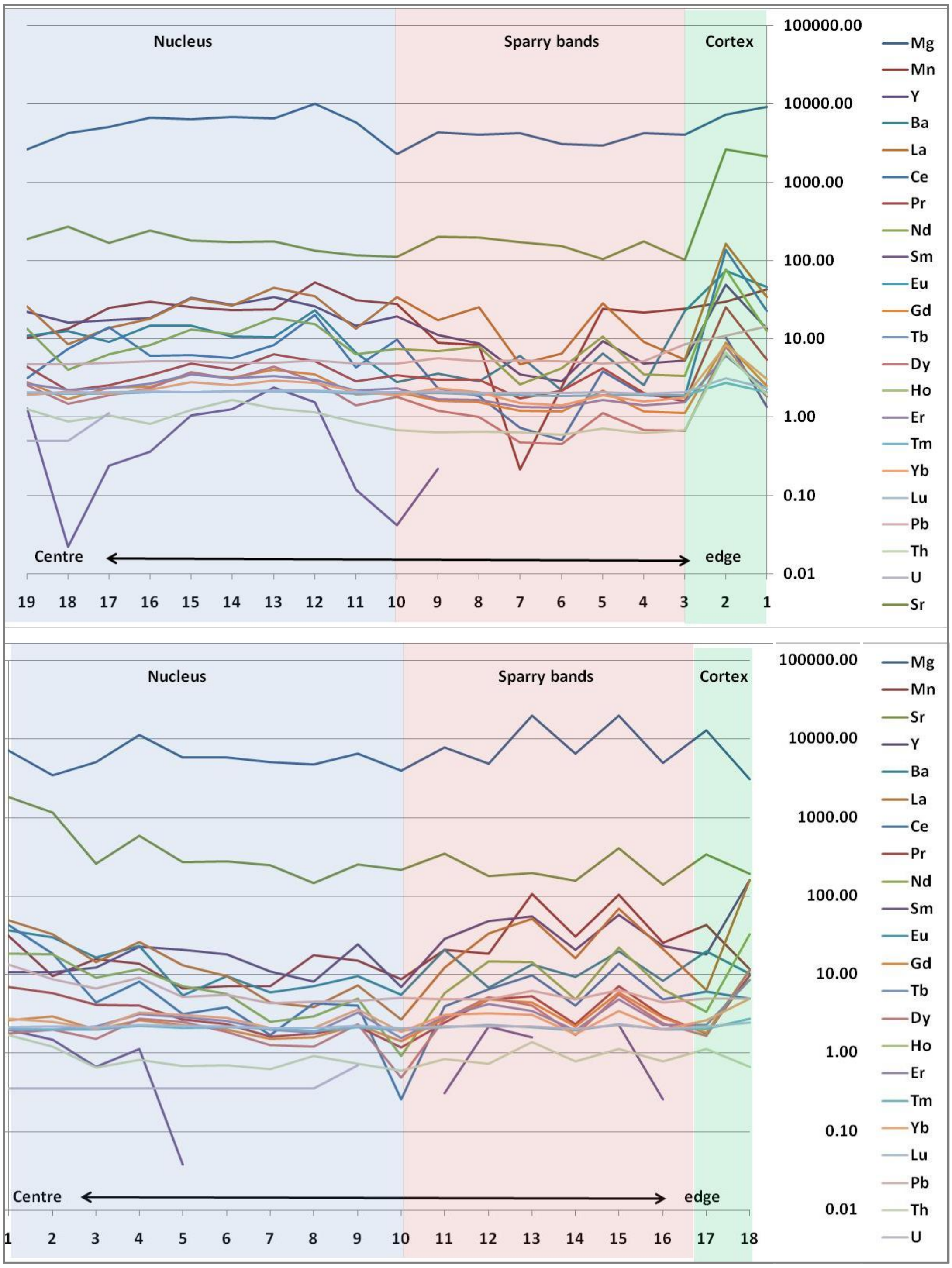

Figure 2-33: The variation in trace element abundance between different sampling positions in two sparry nodules. The analytical samples were taken from multiple sampling positions from approximately the centre of the sparry nodule to the cortex. Sampling positions were spaced 1-2mm apart. Abundances are in ppm. The top graph is of specimen 2008 Tr111 CA1 and the bottom graph is of specimen 2008 Tr111 CA0. The sampling positions in the nucleus (taken from approximately the centre of the nucleus to the edge of the nucleus) are in the blue zone, those in the sparry bands (Taken from the first sparry band occurrence to the final sparry band occurrence) are in the pink zone, and those from the cortex are in the green zone. Discontinuous traces represent elements where the abundances of some elements are below the detection limits.

The data was normalised to North American Shale Composite (NASC) (Gromet et al., 1984) to compare environmental influences to REE supply. Normalised data shows a negative cerium anomaly in both specimens which varies in magnitude at different sampling positions (Figure 2-34). Eu and Tb are below detection limits in both samples and the Sm concentration is also below the detection limits at some of the sampling positions.

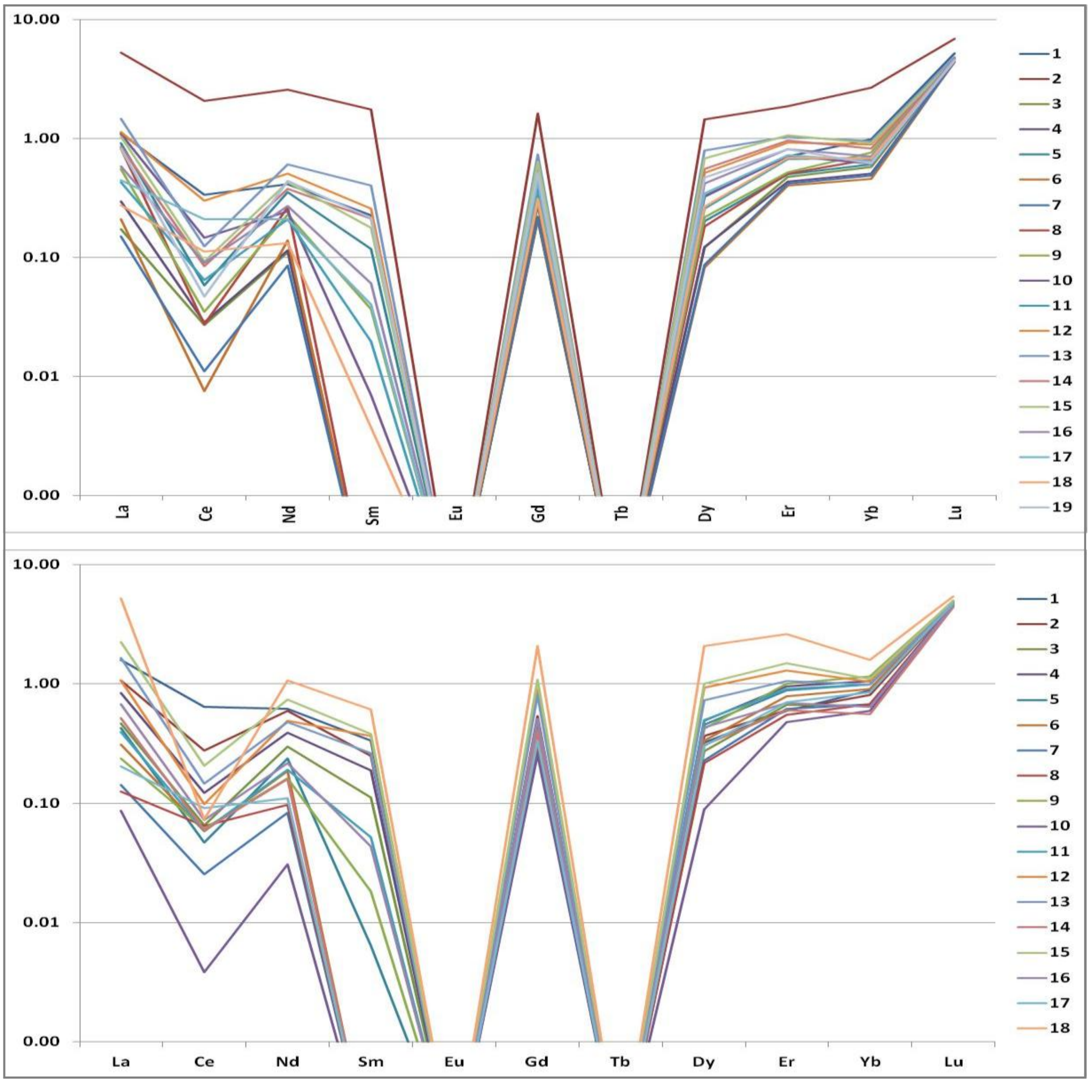

Figure 2-34: REE data for two sparry nodules normalised to NASC. The top graph is of specimen 2008 Tr111 CA1 and the bottom graph is of specimen 2008 Tr111 CA0. Each coloured line represents the data from a different sampling position, and the samples and sampling positions are the same as those in Figure 2-31. The data have been normalised to a NASC standard (Gromet et al., 1984). There is no detectable europium or terbium. There is a small cerium anomaly at all the sampling positions and a variable Sm concentration.

Stable isotope results

Twenty-five specimens were selected for analysis from various sites (Appendix 4). Each specimen was sampled at multiple points along a transect from centre to edge which produced between 3 and 8 samples depending upon the size of the individual nodule. In addition, 6 of the specimens were sequentially sampled using a micromill at 1mm intervals which produced between 7 and 29 samples per specimen to identify a more detailed record of any variations in stable isotope values. The pattern of data for the sparry nodules is relatively consistent between samples, and shows a covariant change from lower to higher $\delta^{18}O_{VPDB}$ and $\delta^{13}C_{VPDB}$ isotope ratios from the centre to the edge of the sample. The combined data ranges from $\delta^{18}O_{VPDB}$ -7.1‰ to -0.2‰ and $\delta^{13}C_{VPDB}$ -8.8‰ to -0.1‰ with an r^2 value of 0.67, $r(184) = 0.82$, $p < 0.0001$ (Figure 2-35). The dotted line on the graph (Figure 2-35) represents a possible second trend line within the data set comparable to that identified in the nuclei of the sparry nodules (Bennett et al., 2012).

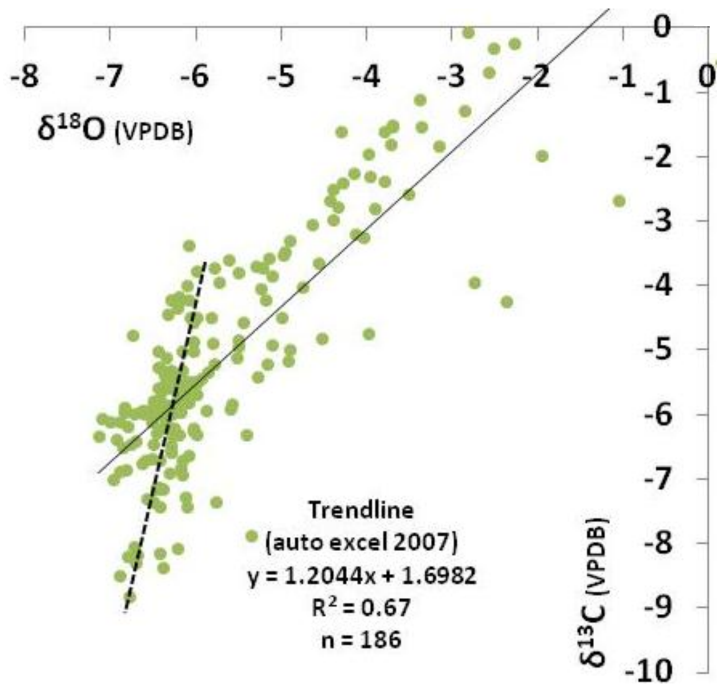

Figure 2-35: Combined stable isotope data for sparry nodules. The trendline produced by Excel 2007 has an *r* = 0.82, *t*-test = 19.38 and *p* < 0.0001. This is considered to be a highly statistically significant correlation. Although Excel has fitted the trendline to the group of points, those with the lower $\delta^{18}O_{VPDB}$ and $\delta^{13}C_{VPDB}$ isotope ratios possibly represent a second trend line within the data set comparable to that identified in the centres of the sparry nodules (Bennett et al., 2012).

The data have been grouped by the different petrographic textural zones identified earlier in this chapter; the nucleus and the transitional zone, the sparry bands and the cortex (Figure 2-36). The transitional and nuclei zone data are grouped together because the petrographic characteristics are most similar. This graph highlights the different ranges of stable isotope values between the textural zones. Data from the nuclei, in general, tend to group closely at low values, apart from a few anomalous data points. There is only a small amount of overlap between the data from the nucleus and that from the cortex which form a more dispersed and covariant group at higher values. The samples taken from the sparry bands overlap the data from both nucleus and cortex.

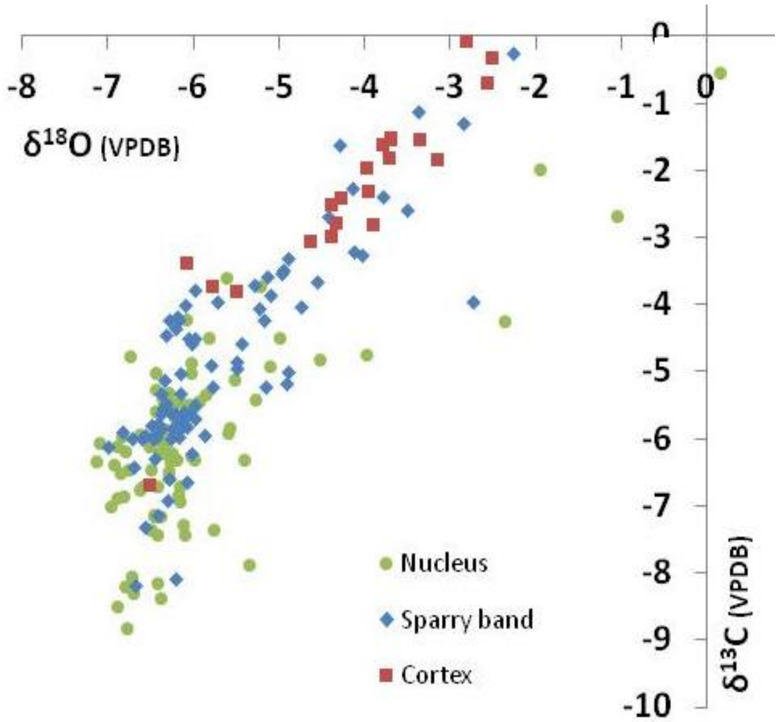

Figure 2-36: The stable isotope data grouped according to their textural zones ; the nucleus(green spots) , the sparry bands (blue diamonds) and the cortex (red squares). The transition zone was incorporated with the nucleus because the textures were most similar. Although there is some overlap, the nuclei tend to have lower isotopic values and the cortex the higher values with the sparry bands in between these two extremes.

Within this overall covariant trend are two specific groups of data, those from the nucleus and those from the sparry bands and cortex. The highest resolution sampling in this study involved samples, taken sequentially at 1mm intervals along a transect from centre to edge of the sparry bands and cortex. Overall they vary from lower to higher stable isotope values along the transect. However, samples with multiple analyses within a nucleus do not show any covariance, and the variation from sample point to sample point along the transect is much less predictable (Figure 2-37).

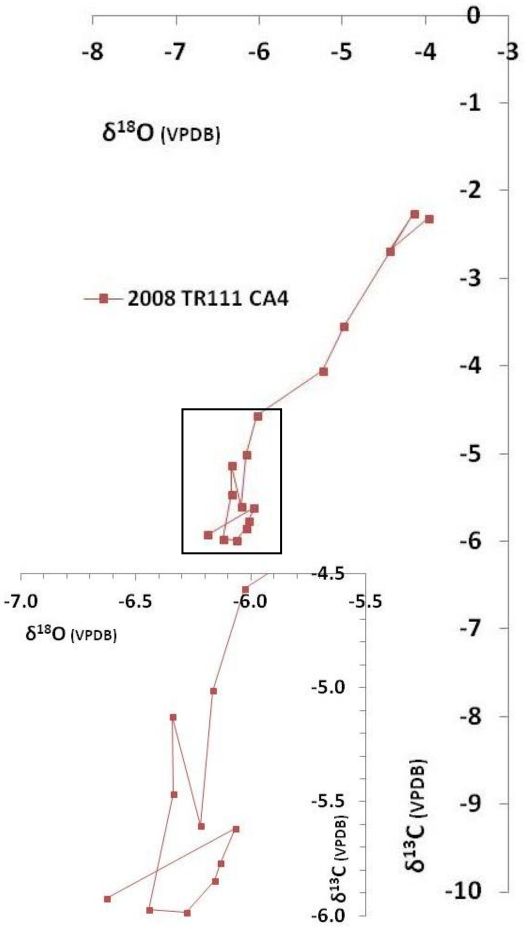

Figure 2-37: Stable isotope data taken along a transect from centre to edge of a sparry nodule. Specimen 2008 Tr111 CA4. The data are plotted sequentially. The data points from the nuclei are highlighted in the box, and do not show any covariance. From the transition zone to the cortex, however, the data along the transect are covariant and trend towards higher values.

The data from samples from both sites above Tuff IF, Tr111 and DK, follow a similar covariant trend, although the range of values differs (Figure 2-38). Specimens from the ELM above Tuff IF vary between $\delta^{18}O_{VPDB}$ -7.0‰ to -0.1‰ and $\delta^{13}C_{VPDB}$ -8.8‰ to -0.5‰ with an r^2 value of 0.67, $r(126) = 0.81$, $p < 0.0001$. This sub-set of data contains the largest number of specimens and samples and dominates the overall trend. Specimens from the AF above Tuff IF vary between $\delta^{18}O_{VPDB}$ -6.2‰ to -2.5‰ and $\delta^{13}C_{VPDB}$ -5.4‰ to -0.1‰ with an r^2 value of 0.77, $r(12) = 0.88$, $p < 0.0002$. This data sub-set has stable isotope values which group towards the higher range of values, albeit with a much smaller number of samples.

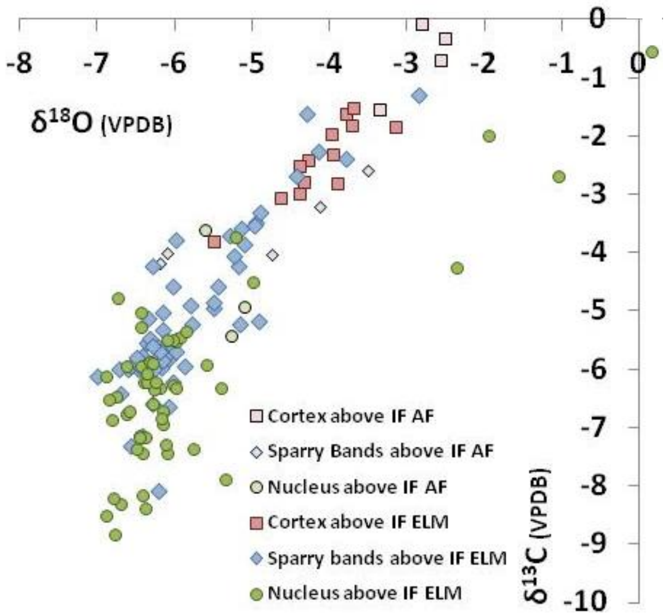

Figure 2-38: The stable isotope data from both sites above Tuff IF have a similar trend. The samples from the ELM (dark pink square, blue diamond and green spot) and AF (pale pink square, blue diamond and green spot) have the same variations in their stable isotope values when the data is categorised by texture. That is, the samples from the nucleus (green spots) plot at lower values than those from the cortex (pink squares). However, the values of the specimens from the AF (paler colours) plot at overall higher values than those from the ELM (darker colours).

The expected covariant trend of three sparry nodules from the lowest of four sampling levels above Tuff IF within the ELM is interrupted by a reversal to low values, which in each case occurs partway through the sparry bands. Two of the samples have a reversal to lower values of both the oxygen and carbon isotopes (Figure 2-39), whereas the third has a change to lower carbon values but higher oxygen values. This characteristic is absent in other samples at either different levels or other locations.

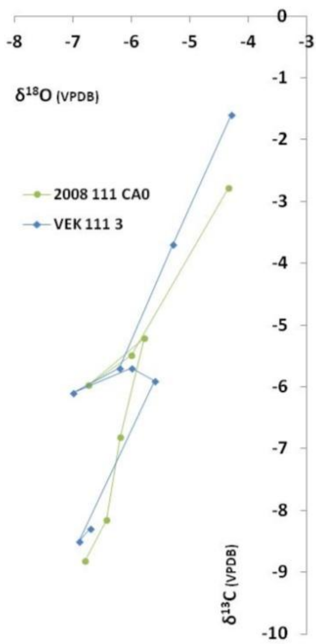

Figure 2-39: Samples from the first bed overlying Tuff IF show a reversal in the stable isotope trend partway through the sparry band growth.

2.6 Formation of carbonate textures

2.6.1 Spherulitic cluster textures

Spherulites, comprising radial crystals of calcite, are abundant in the terrestrial rock record (Alonso-Zarza et al., 1998; Alonso-Zarza and Wright, 2010a; Arenas-Abad et al., 2010; Chafetz et al., 1991; Freytet and Verrecchia, 2002; Jones and Renaut, 2010; Kostecka, 1993; Mees, 1999; Rossi and Canaveras, 1999; Wright, 2008). They are usually small, ranging in size from 1 or 2 µm up to approximately 100 or 200µm in diameter, with only one reported occurrence of more than 1mm (Alonso-Zarza and Wright, 2010a; Chafetz and Butler, 1980). Spherulitic textures are often associated with aragonite (Alonso-Zarza and Wright, 2010a; Chafetz et al., 1991; Kostecka, 1993), but are also reported in terrestrial carbonates formed from vaterite (Braissant et al., 2003), siderite (Browne and Kingston, 1993), low-Mg calcite (Alonso-Zarza and Wright, 2010a; Arenas-Abad et al., 2010; Braissant et al., 2003; Freytet and Verrecchia, 1999; Freytet and Verrecchia, 2002; Wright, 2008; Wright and Tucker, 1991), and dolomite (Rossi and Canaveras, 1999; Wanas, 2002).

Their formation has been interpreted as rapid precipitation from carbonate supersaturated pore fluids or recrystallisation within a calcrete (Alonso-Zarza and Wright, 2010a; Chafetz and Butler, 1980; Chafetz et al., 1991; Jones and Renaut, 2010; Kostecka, 1993; Wright, 2008). Trace element incorporation in the calcite lattice (Fernández-Díaz et al., 2006), and heterotrophic bacteria within or just below root mats (Arenas-Abad et al., 2010; Calvet, 1983), have been linked to spherulite formation. They have also been identified as fracture fills with no relationship to either bacterial or root activity (Mees, 1999).

The Pleistocene spherulitic clusters from Olduvai Gorge do not have any specific characteristics indicating formation from pedogenic processes. Although spherulites have been associated with soil horizons (Freytet and Verrecchia, 2002), the absence of other pedogenic features in the clusters makes this interpretation difficult to support for specimens from Olduvai. However, palaeosol profiles under a semi-arid climate may be very thin (Retallack, 2001) and easily lost through erosion. Consequently it is likely that the spherulites were deposited beneath an exposure surface with a thin palaeosol but not necessarily by pedogenic processes.

During spherulite growth, clay particles were trapped between calcite fibres, resulting in the long-axis parallel inclusion lines. Concentric bands of inclusions probably represent hiatal surfaces where clay particles become trapped when calcite growth re-started. Fluctuations in the growth pattern may be caused by changes in the supply of groundwater; either by an increase in meteoric input lowering its supersaturation to a point where it could not deposit calcite, or conversely by an influx of ground water providing Ca^{2+} ions to Ca^{2+}-poor but carbonate-enriched water prompting calcite formation (Warren, 2006). Where calcite fibres are in optical continuity through inclusion bands, the restart of growth was probably syntaxial.

Type 1 clusters

Fascicular-optic and non-undulose extinction patterns seen in Type 1 spherulites can be produced in calcite precipitated by both inorganic and biologically induced means (Richter et al., 2003). Consequently process interpretation is difficult. It seems that although the likely depositional processes for these two are very similar, some differences in growth conditions must occur. The more lobate textures identified in the Type 1 spherulites bear some morphological similarities to the bacterial shrubs identified as the result of biologically mediated precipitation of calcite in hot water travertines. Here the bacteria cause precipitation of calcite and the bacterial clumps influence the morphology of the calcite as it precipitates (Chafetz and Guidry, 1999). However, the feather-like crystal texture in the Olduvai spherulites is generally more regularly developed than the bacterial shrubs and similar textural differences have been identified as a competing abiotic control of crystal development (Chafetz and Guidry, 1999). The crystal textures are also similar to calcite dendrites reported in hot spring travertines in Kenya (Jones and Renaut, 1996), in Iceland (Jones et al., 2005) and from travertines in Canada (Jones and

Renaut, 2008), although the radial growth fabric implies precipitation from still rather than flowing water.

Type 2 clusters

The radiating calcite structure has little indication of a competitive growth fabric, suggesting that the individual calcite fibres nucleated and grew rapidly and simultaneously from highly carbonate supersaturated water. Spherulite growth experiments under laboratory conditions have been investigated extensively and show the importance of the extent of supersaturation of water in the transition from deposition of monocrystalline calcite to polycrystalline calcite. Formation of calcite structures similar to type 2 spherulites, albeit much smaller – a few micrometers in diameter, is strongly dependent upon the level of supersaturation of the water and temperature, with the most spherulitic morphology produced from highly carbonate supersaturated fluids at temperatures below 30^{o}C (Andreassen et al., 2010; Beck and Andreassen, 2010a, b; Beck et al., 2011). However, unlike the laboratory-produced spherulites, those from the sediments at Olduvai tend to be present in fan-shaped clusters rather than individual radiating needles. During formation of type 2 spherulites, their initial growth may have had fewer nucleation sites than seen in laboratory experiments and trapped very small, mostly clay, particles as the crystals grew.

Changes in the calcite texture between sparry calcite and micritic calcite represents a change in the crystallisation processes operating during spherulite formation. Where nucleation is very rapid, this may have resulted in bands of microspar prior to a second stage of spherulite fibre growth. This alternating pattern of calcite textures has also been identified in tufa deposits (Pedley, 2009). Microbial extracellular polymeric substances (EPS) can be important in both micrite and sparry calcite precipitation, particularly in alkaline settings (Pedley et al., 2009) and is associated with the precipitation of spherulites (Fernandez-Diaz et al., 1996; Pedley et al., 2009). Sparry calcite deposits abiotically whilst the biofilm is active, and micrite forms as a response to the bacterial filaments of the cyanobacteria in

EPS deposits drying out (Pedley et al., 2009). So the alternating texture of elongate radial fibres and microspar in the spherulites may be the result of alternating abiotic and biotic calcite formation processes. Although no bacterial material is found in the spherulites from Olduvai, this does not necessarily mean that it can be ruled out because of its poor preservation potential.

Type 3 clusters

Type 3 spherulites occur as single crystals, yet they have a radiating pattern of inclusions which look similar to the structure of type 2 spherulites. Similar examples have been interpreted as the neomorphic replacement of an original radiating fabric (Alonso-Zarza and Wright, 2010a, b; Arenas-Abad et al., 2010; Rossi and Canaveras, 1999) although it has been suggested that they may represent an original split-crystals fabric rather than a recrystallised texture (Kendall, 1985; Rossi and Canaveras, 1999).

2.6.2 Sparry nodule textures

The range of different petrographic textures, and combinations of textures, implies that the sparry nodules were not formed by any simple, single, process, but by a combination of processes whose dominance varied during their formation. The specimens are inferred to have grown displacively as they entrain very little sedimentary matter. This may be a function of the rate of formation, where the sparry nodules form very slowly from only slightly carbonate supersaturated pore waters. Indeed, displacive morphologies are reported to be indicative of growth below the water table (Deocampo, 2010). Texturally similar calcite nodules of comparable size, with radial, concentric, growth bands are found in cave pools (Kendall, 1978), and shallow, evaporative pools in Bolivia (Jones and Manning, 1994). However, with no evidence of either caves or shallow, sub-aerial pools in the host sediments, it is proposed that these specimens grew displacively in the shallow phreatic zone, in waxy, claystone beds which would support a concentric radial growth. Bands of columnar calcite, around two or more individual spheres, are also consistent with specimens grown in soft sediment rather than in agitated water. The sediments and water at Olduvai are likely to be rich in organic matter and humic substances from the vegetation and animal debris derived from the overlying exposure surface. The organic matter may act to entrain sediments in a colloidal mass and restrict its mobility in the sediment pore water, effectively reducing the likelihood of the clay being entrained in the calcite lattice.

The euhedral, interlocking calcite crystals of the nucleus, with inclusion-defined fibrous bundles, are typical of a neomorphic recrystallisation fabric (Armenteros, 2010; Marshall, 1981). This is supported by the euhedral crystal boundaries which cross-cut the fibrous bundles, and the change in intensity of the brown colouration of the calcite across euhedral crystal boundaries, caused by mobilisation of organic matter during recrystallisation. The inclusion defined fabric represents an original growth morphology, however, the lack of evidence of different minerals prior to the calcite, suggests that the original was low-Mg calcite or a more soluble mineral such as high-Mg calcite or aragonite.

The fibrous bundles of Type 1 nuclei have similar textures to those seen in carbonates and other evaporite minerals such as gypsum (Chaftez and Butler, 1980; Marshall, 1982), precipitated from supersaturated water in the vadose zone. Problematically similar textures have been reported by both inorganic and biologically mediated processes. The elongate fibres with long-axis parallel inclusion bands may be the result of rapid growth trapping sediments and producing the linear inclusion bands. The feathery textures, and occasional cuspate terminations, are similar to those seen in bacterial shrubs, where the calcite grows rapidly in supersaturated water which requires sulphur oxidation and lack of light (Chafetz and Guidry, 1999).

Type 2 nuclei are texturally similar to Type 3 spherulites and are interpreted to have originally formed by the same processes. Textures seen in Type 3 nuclei are similar to micritic nodules type 1 (chapter 3) which are interpreted to have formed by pedogenic processes.

Columnar crystals of the sparry bands are commonly found in terrestrial depositional settings including speleothems (Kostecka, 1993), in septarian crack-fill cements (Kendall, 1978; Lindholm, 1974), and in the pedogenic phreatic zone (Searl, 1989). They have been interpreted to form by the lateral coalescence of individual crystallites during growth, and the ubiquitous linear inclusions defined by former inter-crystallite faces (Kendall, 1978). This interpretation is supported by long-axis parallel inclusion lines seen in thin section. In fascicular-optic and radiaxial fibrous calcite, undulose extinction is due to progressive lattice offset during crystallite coalescence (Kostecka, 1993), so the lack of undulose extinction suggests that the adjacent crystallites are incorporated without any lattice mismatch. The inclusion-rich, and microcrystalline calcite, bands that are perpendicular to the long crystal axes are considered hiatal stages of columnar growth. The inclusions define the position of former crystal terminations and subsequent initiation of syntaxial crystal growth. Where there are bands of microcrystalline and scalenohedral calcite growth is, at least in part, non-syntaxial.

Although fluorite is reported to be present in some of the lake deposits and ELM sediments at Olduvai (Hay, 1976; Hay and Kyser, 2001), it has not previously been reported in the terrestrial carbonates. It can occur by replacement of calcite with fluorite through reaction with fluorine rich brines (Jones et al., 1977; Surdam and Eugster, 1976). It can also form as an early diagenetic product in evaporitic systems on volcanic terrain, where the source water is both alkaline and highly concentrated with a suitable source of F^- (Jones, 1978; Verrecchia, 2007). That they occur only in the sparry nodules at DK, indicates a slightly different, more evaporative, water source than found at other sites.

The transition zone has elements of both the nucleus and the sparry bands, and represents the changes between the formation processes. The alternation between the two sets of processes in all specimens implies that that the mechanisms of formation were the same regardless of the stratigraphic level, and points towards periodic variations in hydrology. Spherulite growth during formation of sparry nodules indicates a rapid increase in the supersaturation of water supply.

The formation of the cortex is interpreted to be due to increasing levels of evaporation and drying out of the sediments. The micrite and spherulites represent rapid nucleation from very highly carbonate supersaturated water. The morphology of the plates of micrite is interpreted to be controlled by desiccation cracks in the waxy claystone, which form voids in which the final stage of calcite precipitation occurs.

2.7 Geochemistry and palaeohydrology

2.7.1 Trace element analysis

The variation in luminescence between none, dull orange, and bright orange, in the spherulites and sparry nodules, indicates fluctuating redox conditions during their deposition. The abundances of Fe and Mn identified by ICP analyses are within the range expected to produce the luminescence observed (Figure 2-40; Figure 2-41).

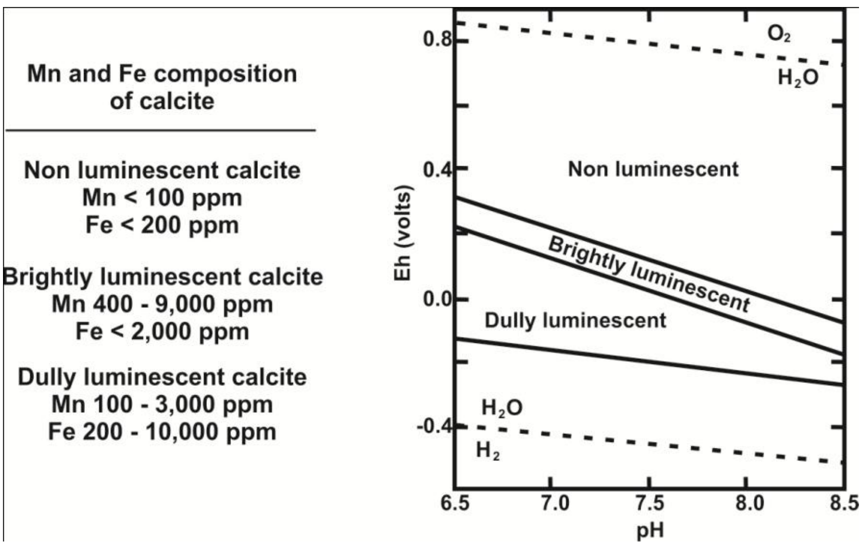

Figure 2-40: The ranges of concentrations of Fe and Mn, and proposed redox and pH values, for calcite formation with bright, dull and no luminescence. Redrawn from Barnaby and Rimstidt (1989). The luminescence range expressed as dull luminescence is considered to be anoxic, that of bright luminescence is sub-oxic, and that of non-luminescent is oxic conditions. The spherulitic clusters and sparry nodules have alternating zones of bright, dull, and no luminescence indicating alternating redox conditions in the supply fluid.

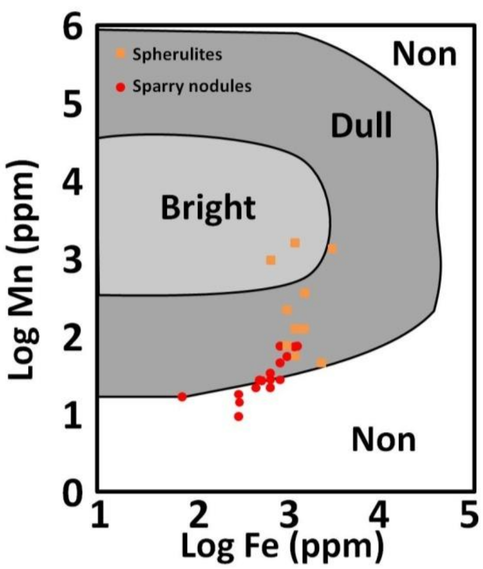

Figure 2-41: The Log Fe and Mn values (ppm) for sparry nodules and spherulitic clusters compared to the luminescence predicted by Machel (2000). The data from the spherulitic clusters plots in the range between anoxic (Dull luminescence) and sub-oxic (Bright luminescence), whereas that from the sparry nodules plots in the range between anoxic and oxic (Non luminescence). Although concentric zones of bright luminescence are seen in the sparry nodules, they are thin and may not be fully represented.

The spherulites are interpreted to have formed in an anoxic to sub-oxic environment (Barnaby and Rimstidt, 1989), compatible with formation in the capillary zone. The sparry nodules are interpreted to have formed in an environment in which the groundwater fluctuates between anoxic, suboxic and oxic, compatible with formation in the shallow phreatic and capillary zones.

In both the spherulitic clusters and the sparry nodules, the concentration of trace elements Fe and Sr are higher, and Mn is lower, in the spherulites compared to the columnar sparry bands. The distribution coefficients of Fe and Mn > 1, and Sr < 1 will affect the incorporation of the elements in the calcite lattice. However, the pattern shown in the spherulites and sparry nodules indicates that the differences between the sparry bands and the spherulites may be influenced by other factors. The concentration of the elements in solution may vary during the precipitation of the specimen. The spherulites are interpreted to have formed from water with a much higher concentration of trace elements, compatible with formation from much more evaporative fluids than the sparry bands. The response of Mn and Sr also varies with rates of calcite formation (Brand and Veizer, 1980; Lorens, 1981). Mn is incorporated less abundantly in the calcite lattice with increasing growth rate and Sr incorporates more abundantly, which supports the suggested rapid growth rate for spherulites compared to the sparry bands.

The mineralogical composition of parent materials in a sedimentary setting is reported to be the principal control on availability of trace elements (Laveuf and Cornu, 2009). However, the volcanic sources of tuffs in Bed I and Lower Bed II, when normalised, have LREE that are enriched compared to HREE (Mollel et al., 2008; Mollel et al., 2009), and the carbonates do not. The pH levels of the supply fluid affects how clay particles adsorb LREE and HREE; smectitic clays at high pH levels tend to be enriched in HREE and have a positive cerium anomaly, whereas illite will be enriched in LREE and have a negative cerium anomaly (Laveuf and Cornu, 2009). Thus the REE available for incorporation into the calcite lattice will be correspondingly altered. The clays of Lower Bed II at Olduvai in which the carbonates were found are interlayered illite-smectite (Deocampo, 2004), which varies across the field area through differential diagenesis (Deocampo and Tactikos). The amount of LREE and HREE in the carbonates is likely to be influenced by REE fractionation in the original composition of the clays in which the calcite was precipitated.

By comparison to the margins of contemporary lakes in East Africa, clay sediments at Olduvai are very likely to have been rich in organic matter. Organic ligands generally form more stable complexes with HREEs, which include Sm, Eu, and Tb, than with LREEs, which include Ce (Laveuf and Cornu, 2009). Sm, Eu and Tb are present in the volcanic sources of the tuffs in Bed I and Lower Bed II (Mollel et al., 2008; Mollel et al., 2009), so their absence in the carbonates may be related to the presence of organic ligands fractionating the REE in the groundwater.

The carbonates have a negative cerium anomaly, which can indicate the redox conditions of the water source and imply formation in an oxic setting. This occurs where Ce^{3+} is oxidised to Ce^{4+}, possibly via Mn-oxides, and subsequently forms insoluble minerals (Vaniman and Chipera, 1996) and reduces the availability of Ce in the supply fluid. The Fe/Mn ratios indicate carbonate formation in an environment with fluctuating redox conditions so that the abundance of Ce may be controlled by the competing influences described above, rather than simply by the redox conditions of the supply fluid. At sampling positions within a sparry nodule where there is a strong negative Ce anomaly, the Sm becomes non-detectable. As Sm is not considered to be redox sensitive, this may imply that this fractionation is the result of reactions with organic ligands.

2.7.2 Stable isotopes

The comparable gradient, and strong covariance between the $\delta^{18}O$ and $\delta^{13}C$, seen in both the spherulitic clusters and the sparry nodules indicates that the fluid evolution is controlled by the same processes. The pattern of change of both $\delta^{18}O$ and $\delta^{13}C$ within a single specimen can be as large as several permil (Bennett et al., 2012; Liutkus et al., 2005), which is on the same order of magnitude as is found throughout the stratigraphy (Cerling and Hay, 1986; Cerling et al., 1977). Most previous studies have used spot samples of various carbonates and interpreted the variations in oxygen values as exclusively produced by changes in the climate. The covariant carbon values of pedogenic carbonates are interpreted to be the result of changes in the dominance of C3 and C4 vegetation, driven by climate change (Ashley, 2000; Cerling and Hay, 1986; Cerling et al., 1977; Hay, 1976; Hay and Reeder, 1978; Sikes, 1994; Sikes and Ashley, 2007). A study involving more detailed sampling of individual rhizoliths (Liutkus et al., 2005) interpreted a similar range of stable isotope values as changes as climate driven variations in dominance of lake water and meteoric water at the margins of Palaeolake Olduvai. The pilot study to this project (Bennett et al., 2012) concluded that a covariant change in the oxygen and carbon isotopes throughout the development of the specimens was the result of an increasing lake water influence in the originally meteoric groundwater. This has highlighted the importance of linking the stable isotope analysis sampling strategy to the petrography, and emphasises the need to consider the palaeohydrology in any interpretations.

Spherulitic clusters

The similarity between the range of values in spherulites found at different stratigraphic levels, and at different sampling positions within each spherulite, indicates that the groundwater evolution was similar for all specimens. As the values found at different sampling positions within individual clusters are also similar, it shows that the spherulites in a cluster probably nucleated and grew at the same time. The overall range of values is likely due to the evolution of the groundwater and may reflect either a mixing between different water sources or a water source with varying levels of evaporation and dilution.

Sparry nodules

The lowest $\delta^{18}O$ and $\delta^{13}C$ values, seen in the nucleus of the sparry nodules, are absent in the spherulites. These are indicative of meteoric water, which is consistent with the original constituent of the nucleus being replaced by, or recrystallised to low-Mg calcite following a fresh water input, producing a non-covariant change when sampled from the centre to the edge of the nucleus. The covariant change from lower to higher $\delta^{18}O$ and $\delta^{13}C$ values, through the sparry bands to the cortex, shows a gradual change in the source water caused either by an increasing contribution of the more evolved lake water with the groundwater, or an increasing evaporation of the groundwater itself. This is consistent with the findings of the pilot study (Bennett et al., 2012). A similar trend is seen in Lake Bosumtwi, Ghana, where lacustrine carbonates lie on a covariant trend of lake water evolution between fresher and more evaporative water (Talbot, 1990). The cortex and the spherulites have a similar range of $\delta^{18}O$ and $\delta^{13}C$ values and represent the most evaporative part of the fluid evolution.

Although the $\delta^{18}O$ and $\delta^{13}C$ values of sparry nodules from the lacustrine sediments on the alluvial fan at DK have a similar covariant trend in to $\delta^{18}O$ and $\delta^{13}C$ values as the sparry nodules from the lacustrine sediments at the eastern lake margin, they are generally higher. Freshwater sources are known at the eastern lake margin, because of the presence of diatomaceous earth in Lower Bed II (Hay, 1976). This source, or the proximity of fluvial input, may be responsible for the overall lower values seen in these specimens. Therefore the sparry nodules from DK presumably formed from a more evaporative fluid as was deduced by the presence of fluorite (Section 2.7.1).

Oxygen isotopes

The $\delta^{18}O$ of lake water is principally affected by the local and regional climate, influencing both input and loss through evaporation; the drainage basin size and lithology; and by the residence time of the water in the lake (Casanova and Hillaire-Marcel, 1992; Hillaire-Marcel and Casanova, 1987; Levin et al., 2009). Whereas the most important influence on the $\delta^{18}O$ of water in a shallow sub-surface terrestrial setting is probably the composition of the meteoric precipitation because of the volume of delivery. However, the evolution of the groundwater is also affected by the soil temperature and input of water other than rainfall, such as lake water (Liutkus et al., 2005; PiPujol and Buurman, 1997). The $\delta^{18}O$ of the carbonates formed at the lake margin will likely reflect the balance between these competing factors.

The $\delta^{18}O$ of meteoric water in East Africa is reported to be very variable, both in the modern day and in the geological record, and varies as a function of temperature, source, rainfall pattern, and latitude due to seasonal and longer term climate changes. Seasonal changes at individual locations have been reported to change by several permil over the course of a single year, and delivery mechanisms, such as the Indian monsoon, are reported to alter the oxygen isotopic ratio of meteoric water in East Africa by 6 permil compared to terrestrial water (Cerling, 1984; Levin et al., 2009; McKenzie, 2001; PiPujol and Buurman, 1997). Probably as a consequence of this, river and spring water in Kenya and Ethiopia may vary by several permil over a single year and between years (Levin et al., 2009; PiPujol and Buurman, 1997). The variations of $\delta^{18}O$ in carbonates are also strongly influenced by the temperature of the sediments. At shallower depths, closer to the ground-air interface, the temperature is both warmer and more prone to fluctuations than deeper in the sub-surface sediment. This can result in pore waters becoming more evaporated, resulting in higher isotopic ratios. At depths of 30cm or below, the soil temperature is equilibrated with mean annual ambient temperature and is not subject to the fluctuating temperatures found nearer to the surface (PiPujol and Buurman, 1997).

Carbon isotopes

Carbonates formed in the terrestrial environment can be broadly divided into formation above the water table and formation below the water table. $\delta^{13}C$ of non-pedogenic carbonates formed above the water table will be affected by the soil CO_2 and the atmospheric CO_2. As with the relationship seen in $\delta^{18}O$, the $\delta^{13}C$ will reflect the depth of formation. Direct exchange with atmospheric CO_2 is limited to the top few cm of the sediment surface so at greater depth the most important influence is biogenic CO_2 (Cerling, 1984). Consequently, the $\delta^{13}C$ of pedogenic and sub-surface carbonates will be strongly influenced by the proportion of C3 and C4 vegetation (Cerling, 1984; Cerling and Hay, 1986; Cerling et al., 1977; Sikes, 1994; Sikes and Ashley, 2007). C3 vegetation is understood to produce much lower $\delta^{13}C$ isotopic ratios than C4 vegetation (Sikes, 1994; Sikes and Ashley, 2007). In contrast the $\delta^{13}C$ of carbonates formed below the water table, especially in a lake marginal setting, may be significantly affected by the influence of lake water in the groundwater system.

Saline, alkaline lakes

Covariance between $\delta^{18}O$ and $\delta^{13}C$ has been reported in many hydrologically closed modern lakes in East Africa, while open systems tend not to be covariant, with different lakes having a different trend determined by their individual hydrological regime (Talbot, 1990). The covariance is likely to be determined by the balance between vapour exchange, evaporation and productivity (Li and Ku, 1997). There are challenges to understanding the fractionation between the stable isotope composition of lake water and carbonates in highly saline and alkaline lakes. Dissolved salts such as trona have been reported to significantly affect the fractionation of stable isotopes in saline lakes (Horita, 1989; Horita et al., 1993; Matsuo et al., 1972; Talbot, 1990). Potentially this could result in uncertainty in correlating the results of carbonates formed from such a water supply with the evolution of the water body itself.

The stable isotopic composition of the palaeolake water is inferred from the composition of lacustrine calcite crystals which have high $\delta^{13}C$ and $\delta^{18}O$ values (See Chapter 5). The high $\delta^{13}C$ values have been interpreted to be due to methanogenesis (Hay, 1976), and evaporation and algal growth (Bennett et al., 2012; Cerling and Hay, 1986). The high $\delta^{18}O$ values are interpreted to be due to evaporation (Bennett et al., 2012; Cerling and Hay, 1986). Studies of other saline alkaline lakes in east Africa have interpreted the high values of $\delta^{13}C$ to be due to either high alkalinity and pH (Abell et al., 1982) or fractionation by algal growth (Hillaire-Marcel and Casanova, 1987). Lake carbonates are interpreted to have consistent values through time because of the long residence time of the lake water. This has been shown where the $\delta^{13}C$ and $\delta^{18}O$ in lake water has been inferred from the stable isotopic ratios of carbon in stromatolites from Lakes Magadi and Lake Natron. Sequential analyses of three generations of stromatolites deposited over 200ka from both of these lakes has shown covariant trends with $\delta^{13}C$ from ~3‰ to ~ 6‰ and $\delta^{18}O$ from ~0‰ to ~4‰ (Hillaire-Marcel et al., 1986; Hillaire-Marcel and Casanova, 1987). Each generation has a similar isotopic range which is considered to be due to the long residence time of the water in the lake, even though the input to the lakes from springs and rivers has a significantly lower isotopic range. Similar studies on stromatolites and oncolites in Lake Turkana produced a lower range of values but still showed consistency between specimens of different ages (Abell et al., 1982).

2.8 Formation and palaeohydrology of spherulitic clusters

The textures and geochemistry of the spherulites are compatible with a hypothesis of rapid precipitation in the capillary zone above the water table. Figure 2-42 shows the suggested positions within the sediment where spherulites would form, with the source fluid supplied primarily by capillary action from ground water, driven by either evaporation or evapotranspiration, or a combination of both mechanisms. Although the spherulites are found in a range of crystal sizes, their adoption one of two specific modal sizes in a particular cluster indicates; i) that all the spherulites in a single cluster nucleate and grow at the same time and ii) that a specific set of depositional processes, source of ions or growth period was operating for each modal size.

The involvement of biological activity, including the presence of extra-cellular polymeric substances (EPS), bacteria and plant growth, causing either direct precipitation of the spherulites or a change in the potential for abiotic calcite precipitation from groundwater, cannot be either disregarded or confirmed. However, for carbonates growing in the shallow sub-surface just above the water table, and the reported presence of vegetation on exposure surfaces with micro and macrofauna (Albert et al., 2009; Ashley et al., 2010a, b; Bamford, 2005; Bamford et al., 2006; Bamford et al., 2008; Blumenschine et al., 2011a; Peters and Blumenschine, 1995; van der Merwe, 2008), significant bacterial activity is very likely.

The spherulitic clusters usually form as discrete bodies which implies that there are certain times and places when they are likely to form. This may be a function of groundwater being directed by lithological variations or faults causing groundwater pooling, but it also may be caused by overlying groups of plant growth causing groundwater to move up through the sediments by capillary rise forced by evapotranspiration. The spherulite formation may also be located in areas where bacterial colonies are associated with overlying vegetation.

The same range of stable isotope values is seen in the spherulites regardless of location or stratigraphic position which indicates that deposition does not appear to be due to change in the vegetation. Instead it more likely to have been controlled by the level of supersaturation of the water, and so is primarily an abiotic depositional process.

The concentric bands of columnar calcite partway through the spherulitic clusters suggest that, during formation, the specimen must have been in a shallow phreatic setting. This indicates a change in the position of the water table. However, where the columnar calcite is developed in patches in the cavities between the spherulites it was more likely to have been in the vadose zone, probably in the capillary fringe close to the water table.

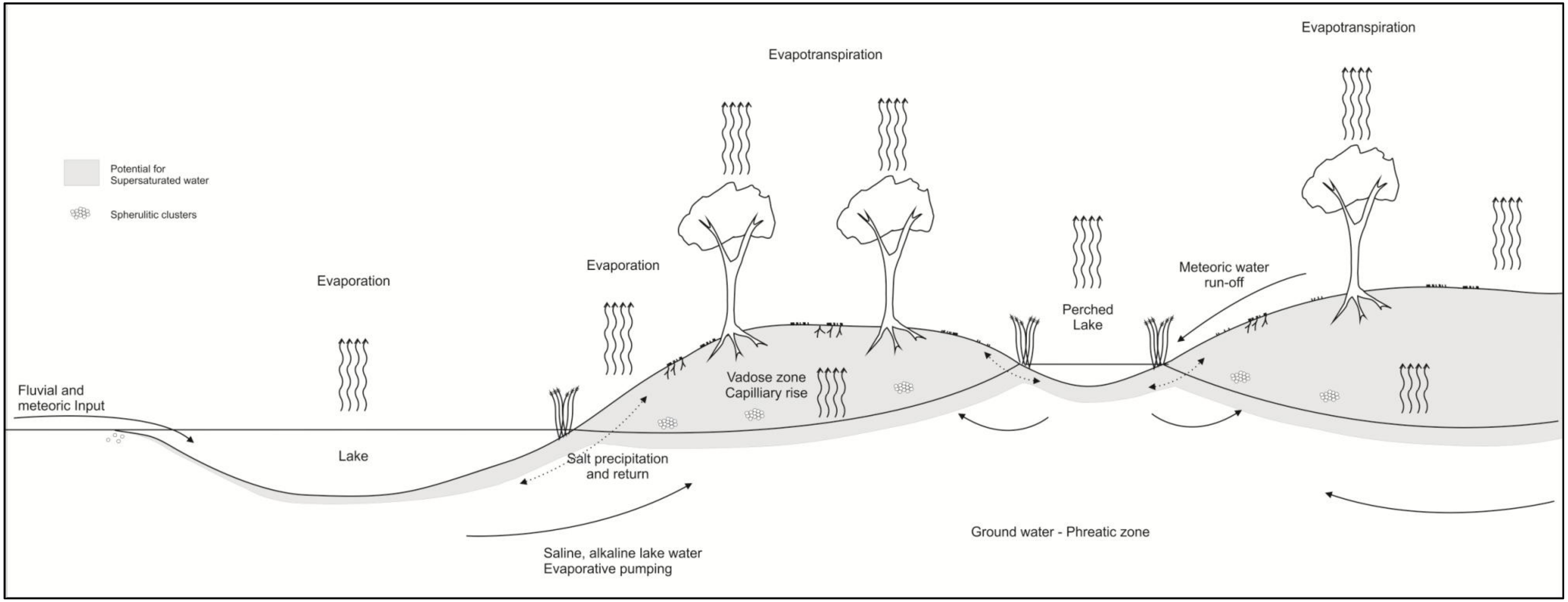

Figure 2-42: The spherulitic clusters are interpreted to form in carbonate supersaturated fluid just above the water table, possibly in the capillary fringe. The supersaturation may be due to evaporation from an overlying exposure surface which is poorly vegetated or alternatively overlying vegetation may cause supersaturation due to evapotranspiration. Evaporation and evapotranspiration will cause capillary rise of groundwater and, in the absence of meteoric or fluvial input, lake water may be pumped into the groundwater. The state of supersaturation will be a combination of the effects of evaporation and evapotranspiration, consequent salt precipitation, and recharge from meteoric and fluvial sources. In order to make the different carbonate settings clear, the diagram exaggerates the vertical scale of the terrestrial setting which is likely to have been only ~1m of relief compared to the lake of <10m depth.

2.9 Formation and palaeohydrology of sparry nodules

Sparry nodules are interpreted to be formed by non-pedogenic processes, primarily in phreatic conditions just below the water table, perhaps 0.5m to 1m below the ground surface (Figure 2-43). Initial deposition of the fibrous bundles (type 1 nucleus) shown by the neomorphic inclusion-defined fabric is interpreted to occur in vadose conditions in a highly evaporative setting. However it is not possible to identify the original mineralogy. The spherulitic (type 2), and the pedogenic (type 3), nuclei can both be products of formation above the water table. The low stable isotope ratios of the interlocking, equant calcite crystals that comprise the nucleus, and the lack of systematic change in samples taken from centre to edge of the nucleus, are indicative of recrystallisation or replacement of the original mineral by water with meteoric isotope values.

The sparry bands are interpreted to form by displacive growth just below the water table in clay sediments. The covariant change from negative to low positive isotope values throughout the development of a single nodule is most easily explained as an increasing influence of lake water in the groundwater, as the lighter isotopic ratios of meteorically dominated groundwater is contaminated by heavier isotopic ratios from the evaporative lake (Bennett et al., 2012).

Spherulite formation both partway through the sparry growth and as a final stage of calcite precipitation would require the nodules to form very close to the water table. Each time the water table dropped below that of the sparry nodules spherulites could form in the capillary zone.

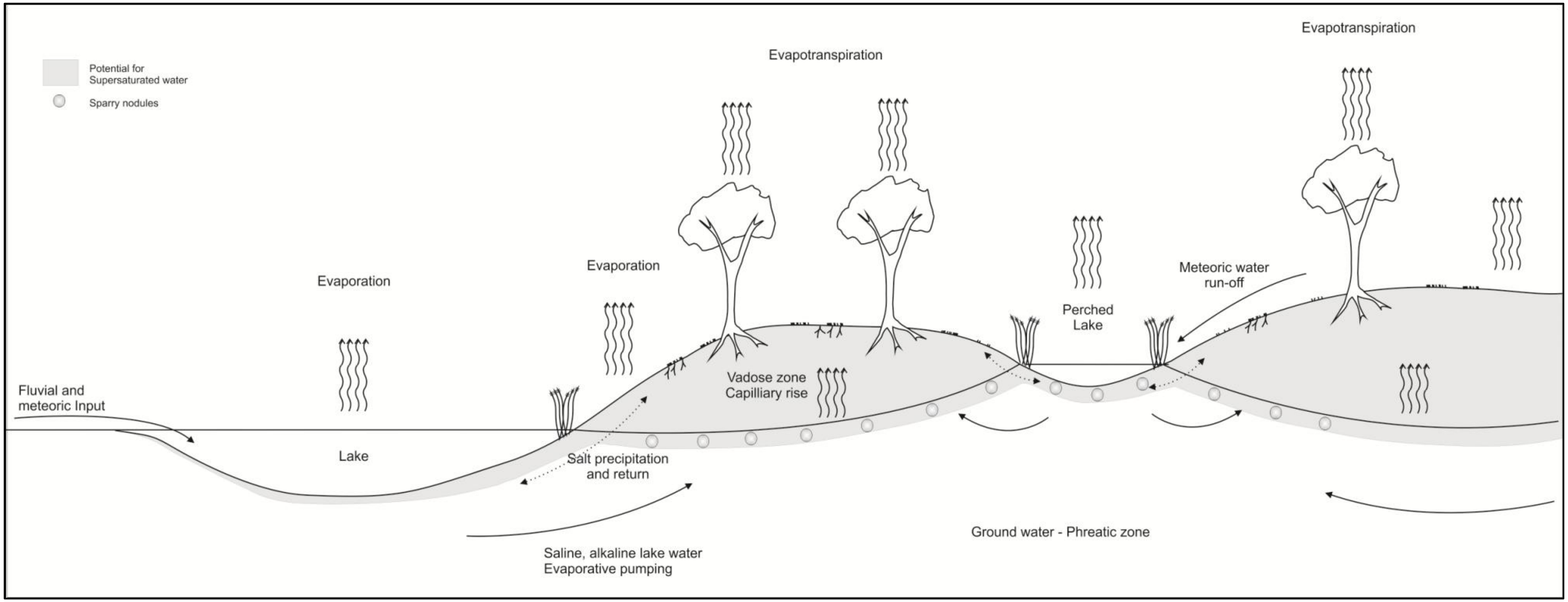

Figure 2-43: The sparry nodules are interpreted to form from carbonate supersaturated fluid just below the water table in wet clay to support the concentric sparry bands during growth. As with the spherulitic clusters, supersaturation is likely to be due to evaporation and evapotranspiration. In order to make the different carbonate setting clear, the diagram exaggerates the vertical scale of the terrestrial setting which is likely to have been only ~1m of relief compared to the lake of <10m depth.

In all cases, the nucleus, spherulites, and cortex are interpreted to form in similar ways, however, two possible mechanisms for the formation of the sparry bands are proposed, which require different changes in climate driven hydrology (Figure 2-44).

In the first, the formation of the sparry bands initiates as meteoric input causes the water table to rise above the nuclei, so their initial development has low isotope ratios (Figure 2-44 (3)). During dry spells, where the evaporation rate is high and the lake level is lowering, lake water is then delivered into the groundwater by evaporative pumping (Figure 2-44 (4a)). That is, the continuing evaporation and evapotranspiration cause capillary rise of groundwater to the exposure surface, forcing the lake water to be drawn landwards (Tooth and McCarthy, 2007). This process was proposed to explain the pattern of isotope ratios in rhizoliths from the ELM at Olduvai (Liutkus et al., 2005). This model describes a setting where the groundwater evolution is influenced by an increasingly dry environment.

The second mechanism requires sparry nodules to begin formation in meteoric water again as the water table rises. In this case, however, the water input into the lake continues, causing lake level rise, flooding and transgression of the lake (Figure 2-44 (4b)). This would cause lake water to enter the groundwater by infiltration because of the increased hydrostatic head. This model, proposed for sparry nodule formation (Bennett et al., 2012), would occur during wet spells where the delivery of water to the lake is greater and the evaporation rate is likely to be lower.

Both models would result in the groundwater becoming increasingly influenced by lake water, and consequently having increasingly heavy stable isotope values and trace element concentrations through time. However, although the stable isotope values become increasingly higher from the centre to the edge of the sparry bands, a similar pattern of change is not seen in the trace elements. This may be because the availability of trace elements during calcite precipitation is controlled by the clay minerals and humic substances in the system rather than the abundance of the elements in the water.

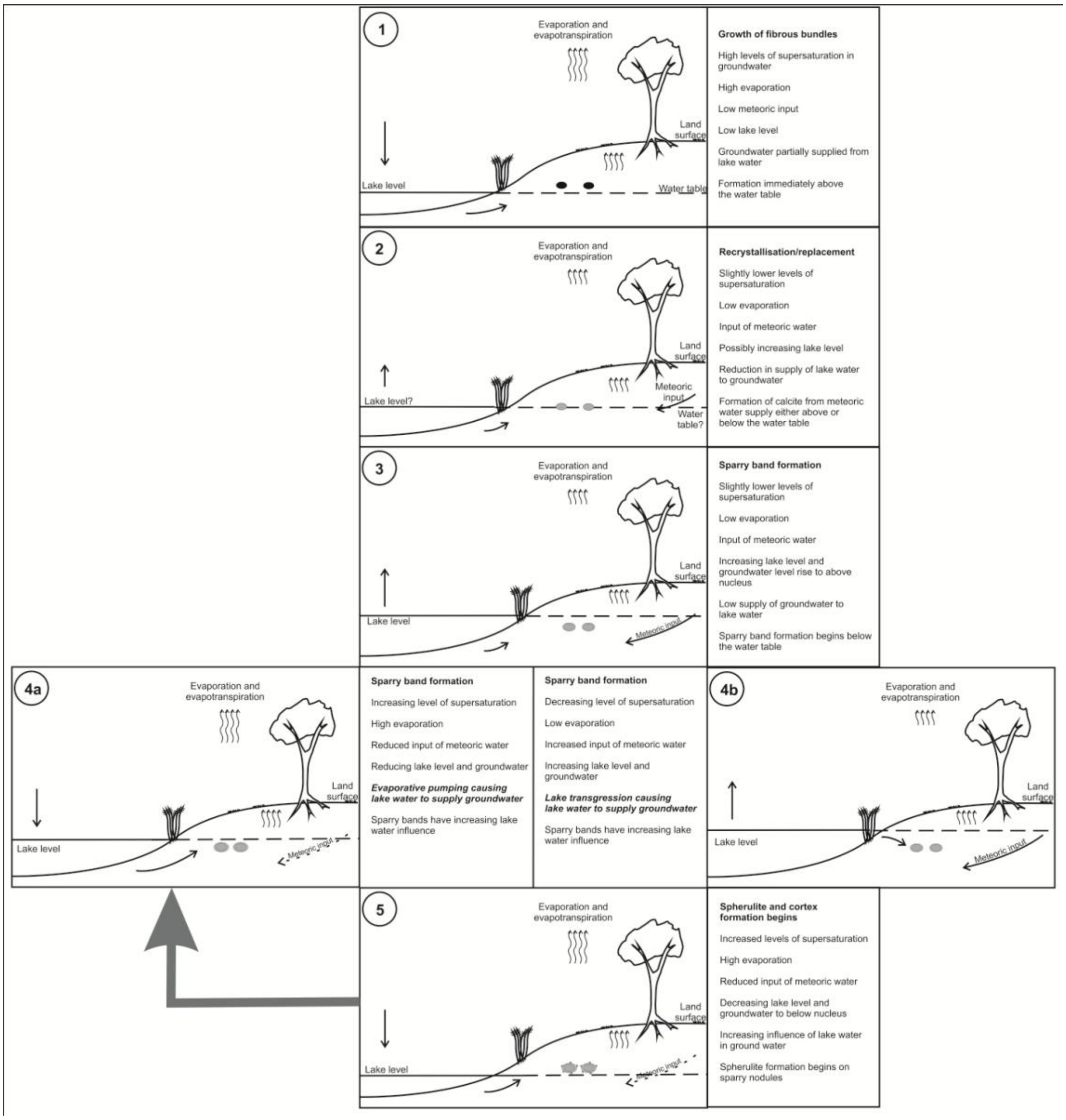

Figure 2-44: Models for sparry nodule formation. Two models are proposed which differ in the ways that the groundwater is enriched in highly concentrated lake water. Because of their complexity, formation of the sparry nodules must occur through a series of processes. The processes proposed follow 5 steps to produce a nucleus, sparry bands and cortex/spherulites. To produce a sparry nodule with spherulites developed within the sparry bands the arrow returns the depositional process from step 5 to step 4. Within the sparry bands produced in step 4 the multiple inclusion bands are interpreted to be formed by changes in the height of the water table.

The pattern of change of the stable isotopes in the sparry bands indicates that throughout this process of repeated changes in the height of the water table, the input of meteoric water in not sufficient to cause a reversal in the overall trend, apart from the nodules at the single horizon at the base of Lower Bed II (Figure 2-39). This situation could occur in either model, but does indicate that in both models, apart from the one exception, large inputs of meteoric water sufficient to significantly alter the stable isotope values of the groundwater do not occur during the carbonate formation.

There are repeated hiatuses in calcite growth during the sparry band formation shown by the growth bands, and these are sometimes sufficient for spherulite growth. This shows that during their formation, the sparry nodules must be close to the air-water interface of the water table as mentioned earlier, and the height of the water table must repeatedly fluctuate over at least the size of the nodule which is a few centimetres.

In model 4a, the delivery of lake water to the groundwater occurs through evaporative pumping at a time of high evaporation and low meteoric input. During events where evaporation and evapotranspiration reduce there will then be a reduction in the supply of lake water into the groundwater and cause a lowering in the height of the water table. In model 4b, however, a reduction in the lake level is required in order to lower the water table sufficiently for the air-water interface of the groundwater to be lowered below the sparry nodule. The timescales for these two models may be very different, with model 4a potentially occurring more frequently than 4b. The clays from which the sparry nodules are sampled are lake parasequences which form over 4000-5000 years (Stanistreet, 2011). Consequently, as sparry nodules are formed within this timeframe, multiple fluctuations in the height of the water table must also have happened. This may make model 4a more likely.

2.10 Conclusions

- Two types of radial calcite deposits have been identified based on their macromorphology and micromorphology; spherulitic clusters and sparry nodules.
- The carbonate textures, and their trace element and stable isotope geochemistry, have been used to interpret the processes of precipitation involved in their formation.
- The relative brightness and colour of the CL of specimens, plus their Fe/Mn ratio identified by ICP analyses, indicate that both forms of radial carbonates were formed in reducing conditions, varying between anoxic, sub-oxic, and oxic.
- The stable isotope ratios of carbon and oxygen for the radial calcites have a consistently covariant pattern over a very similar range of values. It is proposed that the dominant calcite depositional processes operating at Olduvai Gorge were abiotic, so that the stable isotope values were determined by the source water and evaporation.
- A model for the growth of spherulitic clusters is proposed where they are deposited rapidly from highly super-saturated, evaporitic, pore fluids in the vadose zone.
- The growth of sparry nodules is more complex, and several stages of calcite formation have been identified;
    - Nuclei are formed in the vadose zone, and subsequently replaced or recrystallised by meteoric water
    - The unusual concentric sparry bands are hypothesised to have precipitated in soft sediment in the shallow phreatic zone
    - The final carbonate growth occurs as the sediments become increasingly dry and carbonate growth ceases
    - The groundwater evolution is the result of mixing of the lake water and meteorically supplied groundwater, and two potential hydrological models have been proposed

- Many of the specimens contain more than one type of radial calcite, indicating fluctuations in the processes operating during their precipitation.
- The carbonate specimens can potentially be used in the field as a useful rough guide to the palaeohydrology of the system during archaeological excavation.
- By using a suite of analyses, this method can be used as a tool both at Olduvai Gorge and elsewhere to predict vegetation distribution, water supplies and so potential hominin land use.
- Because of the likelihood of diagenetic alteration of carbonates, and the potential alteration of the stable isotope values of a specimen, carbonate textures offer a valuable tool to support palaeoenvironmental reconstruction over different timescales and geographic areas.

Chapter 3: The origins of non-radial calcites, Bed I and Lower Bed II, Olduvai Gorge, Tanzania

3.1 Overview

Several forms of carbonates with a non-radial structure have been identified using their macromorphology and micromorphology: two types of micritic nodules; rhizocretions, insect burrows, fossilised rootmats and evaporite pseudomorphs.

Micritic nodules occur either individually; with an irregular to sub-spherical shape varying in size from 1cm to 20cm in diameter; or in beds up to 1m thick and 10s of m long. All are composed of low-Mg calcite micrite to microsparite. Micritic nodules have been separated into two types based on their textural characteristics in thin section. Type 1 nodules are composed of brown calcite with pedogenic features including root traces and alveolar textures, and are interpreted as forming in the vadose zone. Whereas type 2 micritic nodules are composed of white micrite with no pedogenic features, and are interpreted to have formed either in the vadose zone or in a palustrine setting. The calcite formation is interpreted to be primarily abiotic and groundwater evolution is inferred to be driven by evaporation.

Rhizocretions, insect burrows, and rootmats are likely to have formed close to the exposure surface, in the vadose zone. Evaporite pseudomorphs are likely to have formed in a highly evaporative setting from super-saturated water such as the shallow sub-surface at the lake margin, with subsequent replacement by meteoric water.

The palaeohydrological setting in which these carbonates were formed can provide a valuable tool to support palaeoenvironmental reconstruction.

3.2 Introduction

Using crystal textures recognisable in hand specimen, the carbonates investigated in this study have been divided into three groups: micritic nodules; rhizocretions, insect burrows, fossilised rootmats and evaporite pseudomorphs. Each carbonate group represents a specific set of processes operating during their formation, although a single specimen may have characteristics from more than one set of processes indicating fluctuating conditions during formation.

The geology of the settings from which the carbonate specimens were recovered, and the analytical methodology, is detailed in Chapter 2.

3.3 Carbonate description

3.3.1 Micritic nodules

Micritic nodules are a common feature of the clay beds, and occur either as individual nodules, or laterally more extensive horizons. They occur at many of the stratigraphic levels and sampling locations investigated in this study, and have previously been documented in the literature (Hay, 1976; Leakey, 1971). The individual nodules vary in size from 1cm to 20cm in diameter and the laterally extensive horizons can be up to 1m thick and several 10s of metres long; they are irregularly shaped with a smooth surface texture. The nodules are grouped into two types based on their textural characteristics in thin section.

Type 1 textures

Type 1 specimens are found as nodules between 1 cm and 20cm in diameter. For example at MNK (side gorge at the ELM; Figure 1-5) multiple bands of Type 1 micritic nodules are present in olive waxy claystone beds between Tuff IF and the Augitic Sandstone (Figure 3-1).

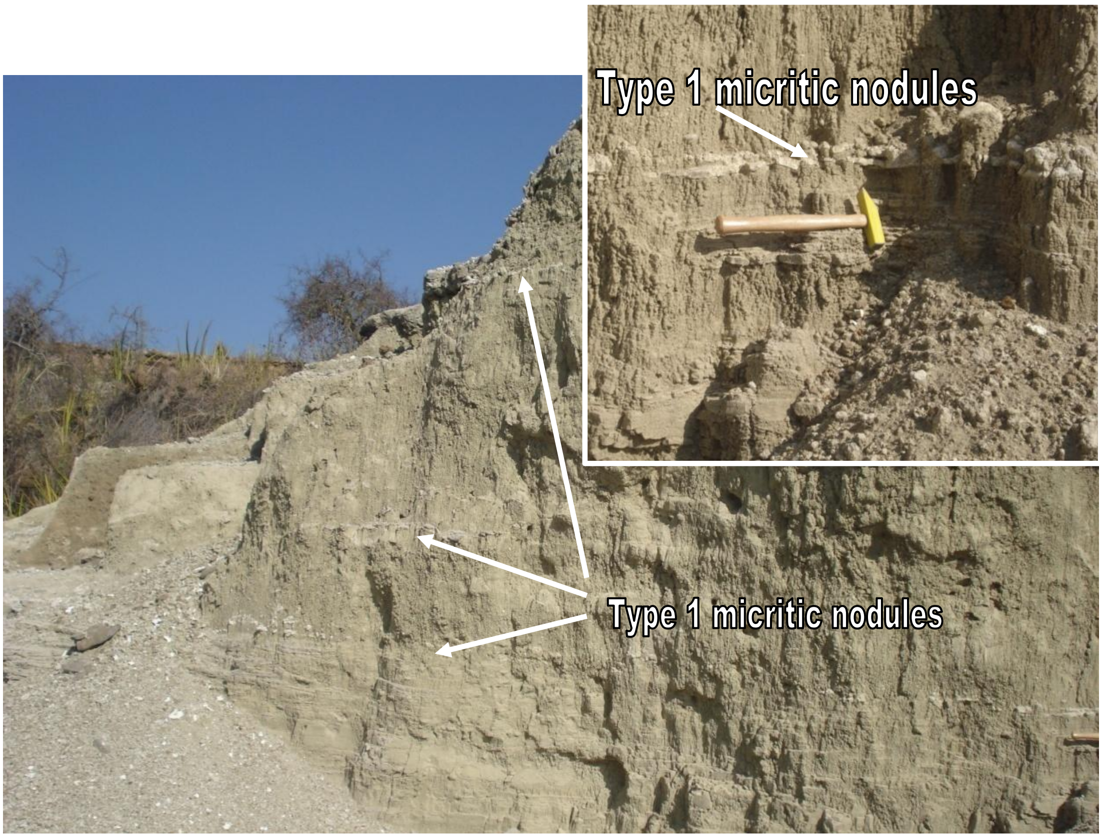

Figure 3-1: Site MNK (Lower Bed II) at the ELM. The beds of olive waxy claystones contain Type 1 micritic nodules at several horizons between Tuff IF and the Augitic Sandstone (Hammer 30cm).

They are either massive or have a concentric structure (Figure 3-2). The specimens often have multiple, radiating and/or circumgranular, cracks, similar to septarian features.

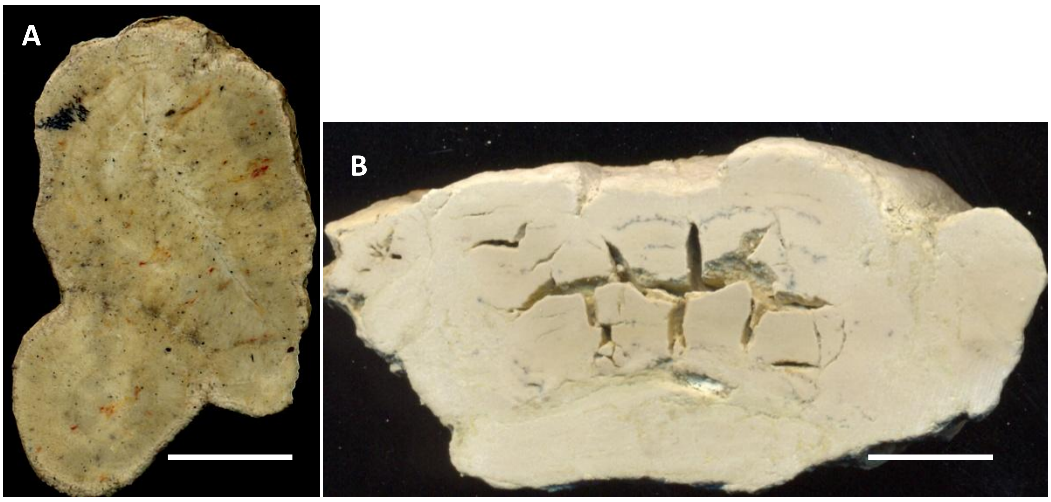

Figure 3-2: Type 1 micritic nodules occur with either A) a concentric structure (2007 TR135 NL2) or B) are massive (2009 SHK CA2) (Scale bar 1cm). They both have multiple, intersecting cracks, usually filled with a carbonate cement.

In thin section they have a clotted texture, a network of fine, intersecting veins, and abundant detrital siliciclastic grains (Figure 3-3). The detrital grains have clay cutans and calcite cemented circumgranular cracks. Often they have a dark, mottled, brown colour.

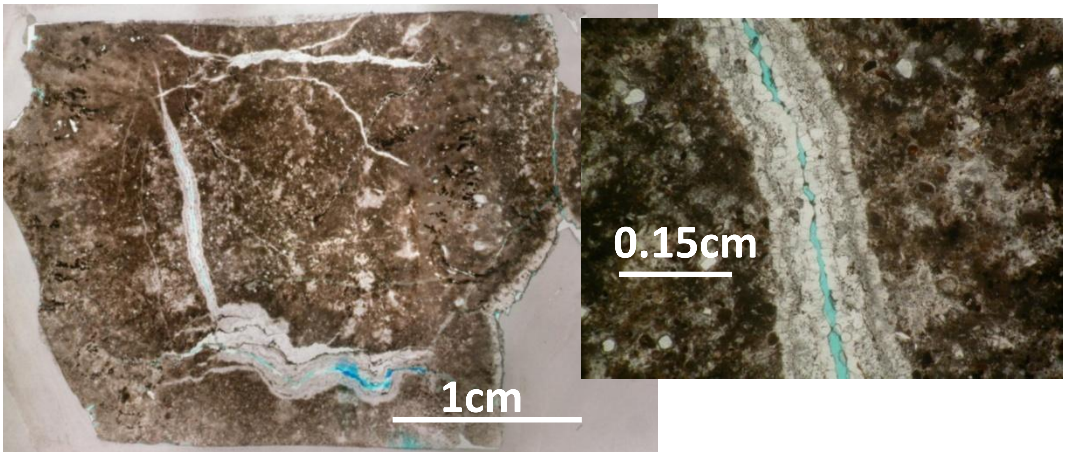

Figure 3-3: Thin section of micritic nodule type 1 in PPL (2009 DK CA11), showing abundant detrital material and mottled brown appearance with multiple calcite veins. Scale bar is 1cm.

The specimens are composed of micritic calcite and calcite microspar, although the actual crystal size and shape is difficult to confirm in all specimens in thin section because of the very dark brown colour which obscures the grain boundaries. These textures are similar to those which form the type 3 nuclei of sparry nodules (Chapter 2) and fossilised rootmat specimens (This chapter), and are consistent with a Beta calcrete fabric (Wright, 2008). There are usually multiple generations of cracks. Crack fill cements tend to have multiple zones of cement seen by variations in brightness using CL (Figure 3-4).

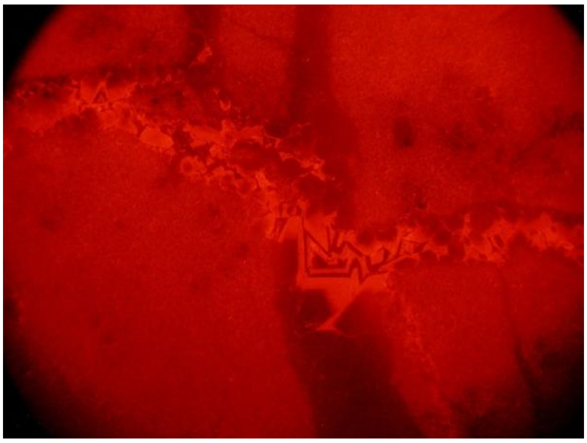

Figure 3-4: CL image of a carbonate cemented vein in a Type 1 micritic nodule (2007 Tr134 NL0). The veins show two generations of cracking and subsequent cementation. The massive micrite has high brightness luminescence. The CL brightness of the vein repeats between non- luminescent and high brightness luminescence. (Scale bar 0.5mm)

The crack fill cements are usually calcite, and often have additional phases of dolomite and strontianite (Figure 3-7).

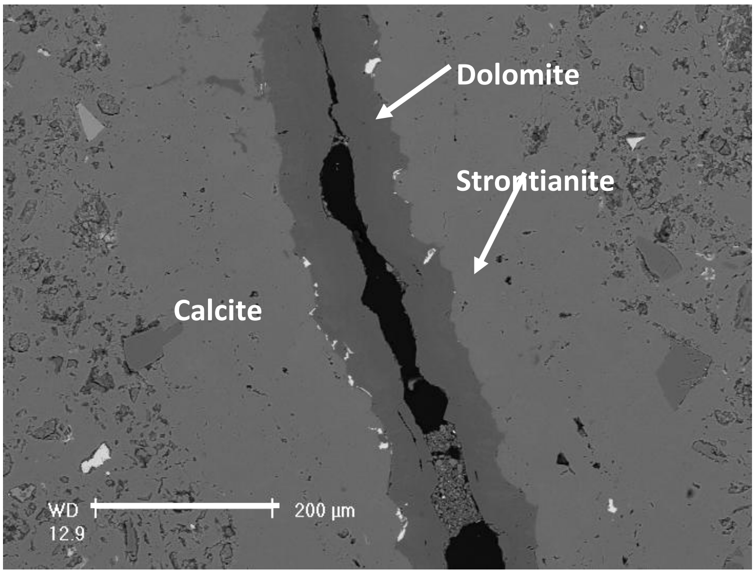

Figure 3-5: SEM image of a type 1 Micritic Nodule (2009 DK CA11). The crack -fill cement comprises three different carbonates, identified using SEM-EDX analyses, which show a paragenetic order. First is the calcite seen in pale grey. The next mineral to form is strontianite seen as the very high brightness phase, which formed between the calcite and the subsequent dolomite growth, seen as the dark grey phase, which is developed on top of the calcite growing into the void space.

Type 2 textures

Type 2 specimens are found as nodules between 1 cm and 20cm in diameter and as larger, more continuous horizons of calcite in beds of waxy claystone. For example at DK on the alluvial fan between Tuff IF and Tuff IIA.

Figure 3-6: Site DK (Lower Bed II) at the alluvial fan. The beds of olive waxy claystones contain Type 2 micritic nodule at a single horizon between Tuff IF and the Augitic Sandstone (Hammer 30cm).

Type 2 micritic nodules are massive and have more than one generation of intersecting cracks with multiple generations of cement (Figure 3-7; Figure 3-8).

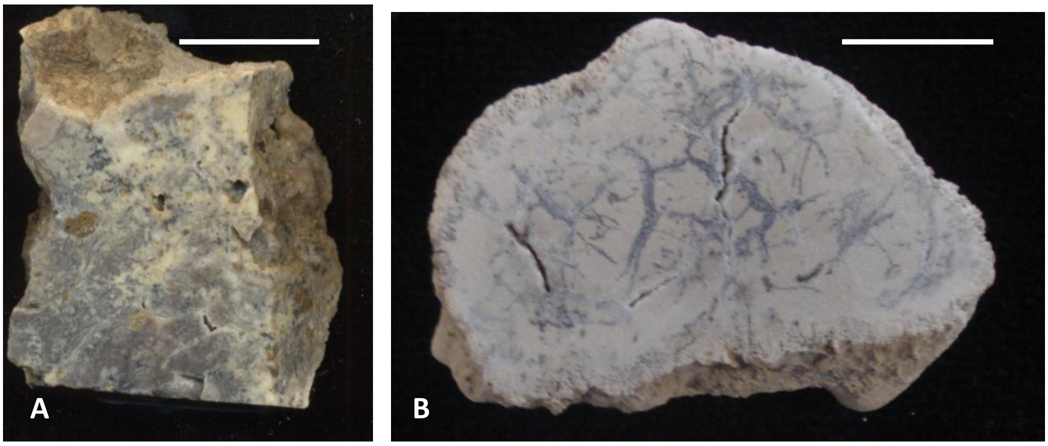

Figure 3-7: Type 2 micritic nodules occur either A) as part of a laterally extensive horizon (2009 DK CA17) or B) individual nodules (2001 TR47 22B) (Scale bar 1cm). They are both composed of massive micrite with multiple, intersecting cracks, usually filled with a carbonate cement.

They are composed of massive, white, micritic calcite, often with a nodular texture. Some patches of calcite are composed of microsparite whose grain size is up to four times as large as the majority of the crystals. There are few or no inclusions of clay particles or other grains, and the texture is consistent with an alpha calcrete fabric (Wright, 2008).

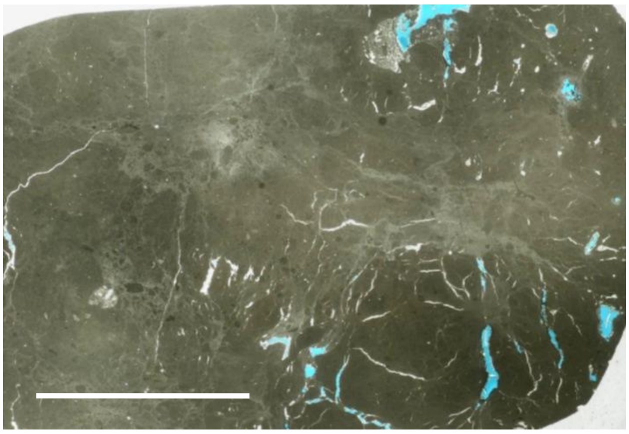

Figure 3-8: Thin section of micritic nodule type 2 (2003 Tr47 13) in plain polarised light. It is composed of white micrite with patches of microsparry calcite, few detrital grains, and fine, thread-like, calcite cemented cracks, often with a nodular texture. (Scale bar 1cm).

In both types of micritic nodule the calcite that forms the main body of the specimen has high brightness luminescence, and the cements in the cracks vary between orange, high brightness to non-luminescent.

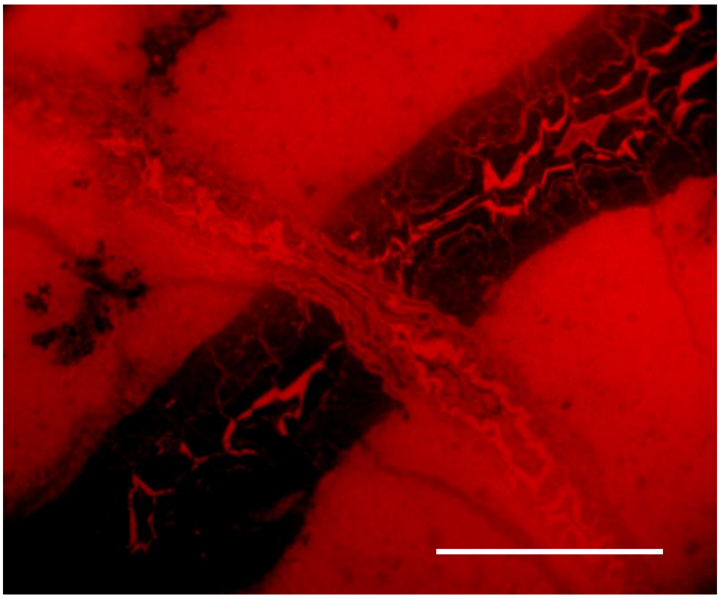

Figure 3-9: CL image of two intersecting carbonate cemented veins in a Type 2 micritic nodule (2001 TR47 22B). The veins show two generations of cracking and subsequent cementation. The massive micrite has high brightness luminescence. The CL brightness of the veins repeats between non- luminescent and high brightness luminescence. (Scale bar 0.5mm)

Trace element data

Four type 1 micritic nodules were sequentially sampled at 4 to 7 positions from centre to edge for ICP-AES analyses (Method in Chapter 2; data Appendix 5). The magnesium concentrations ranged from just over 80ppm (0.04 Mol% $MgCO_3$) to almost 1600ppm (0.65 Mol% $MgCO_3$), which are both consistent with their being 'low-magnesium' calcite. The iron and manganese concentrations are between from 1ppm to ~1800ppm, and have a mean Fe/Mn ratio of 4.4 (SD 1.7) (not including one outlier of Fe/Mn 31). The samples also contain widely varying strontium values which range from ~2ppm to ~1900ppm and barium values between 1ppm and ~1200ppm.

Using a standard staining technique (Dickson, 1965), only one specimen, from the western lake margin below Tuff IC (2009 Loc 60 CA7), is identified as being composed of ferroan calcite. All of the others are composed of low-Mg, non-ferroan calcite.

Stable isotope data

Forty-six specimens from several locations and stratigraphic levels were analysed for their stable isotope ratios (Method Chapter 2; data Appendix 6). Specimens with a concentric structure were sampled at between 3 and 6 positions along a transect from centre to edge. Very small nodular specimens, and those with no concentric structure, were sampled in only one or two positions within the nodule. The isotope ratios range from $\delta^{18}O_{VPDB}$ -6.8‰ to -2.0‰ and $\delta^{13}C_{VPDB}$ -6.7‰ to 2.1‰ with an r^2 value of 0.62, $r(107) = 0.79$, $p < 0.0001$ and show a covariant pattern of change (Figure 3-10).

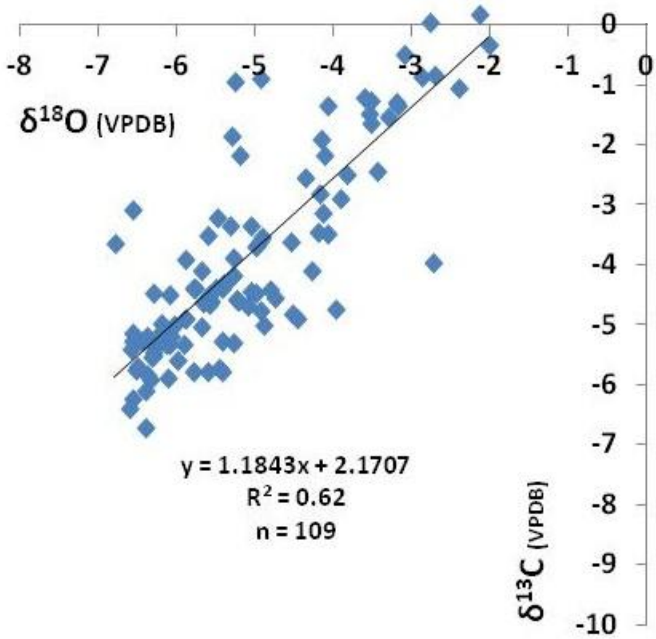

Figure 3-10: Combined stable isotope data for micritic nodules. The combined data from forty-six specimens have an r^2 value of 0.62, $r(107) = 0.79$, $p < 0.0001$ and have a statistically significant covariant pattern of change.

When the data from different locations across the Gorge were compared there is considerable overlap; however the eastern lake margin data tends to plot at lower values than those from the alluvial fan or western lake margin (Figure 3-11).

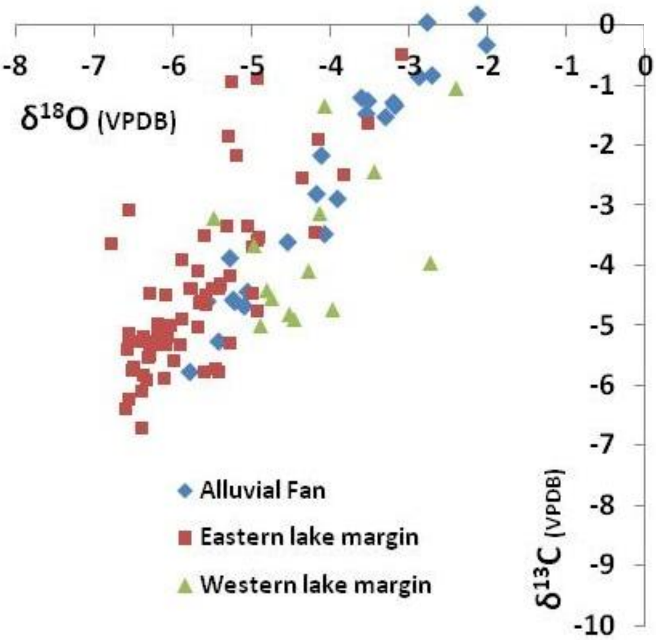

Figure 3-11: Stable isotope values for micritic nodules from different depositional settings. There is considerable overlap in the different datasets, however the eastern lake margin data (red squares) tends to plot at lower values than the alluvial fan (blue diamonds) or western lake margin (green triangles) data. This indicates carbonate formation from more dilute fluids at the eastern lake margin.

Where data from different stratigraphic levels were compared, the overlap is similarly complex (Figure 3-12). However, when this is further divided into samples from different locations as well as stratigraphic levels, a clearer pattern emerges (Figure 3-13,Figure 3-14). Above Tuff IF samples came from the AF and the ELM, and those from below IB were taken from the WLM and the ELM. All of the other samples were largely taken from the ELM. Samples taken from below Tuff IB at the WLM plot at higher values than those taken from the ELM, and similarly, samples from above Tuff IF at the AF have higher values than those taken from the ELM (Figure 3-13, Figure 3-14).

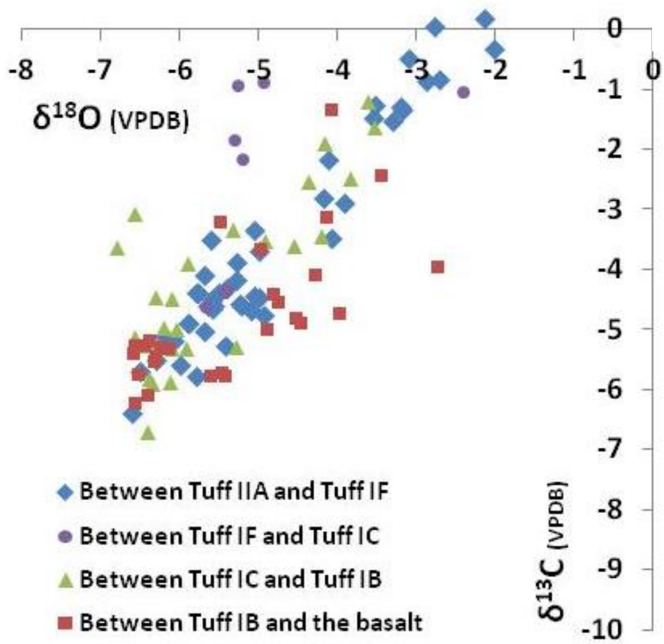

Figure 3-12: Stable isotope values for micritic nodules from different stratigraphic levels. As with the depositional setting categories seen in Figure 3-11, there is considerable overlap between the different datasets. Samples from between Tuff IIA and Tuff IF (blue diamonds) were taken from the alluvial fan and the eastern lake margin and those from Between Tuff IB and the basalt (red squares) were taken from the western lake margin and the eastern lake margin. All of the other samples (Between Tuff IC and Tuff IB: green triangles, and between Tuff IF and Tuff IC: purple spots) were largely taken from the eastern lake margin.

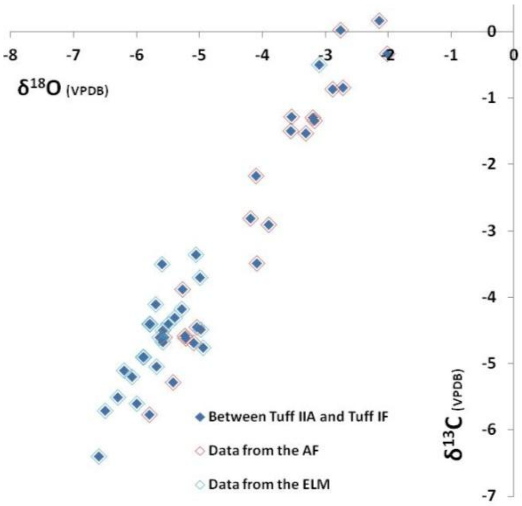

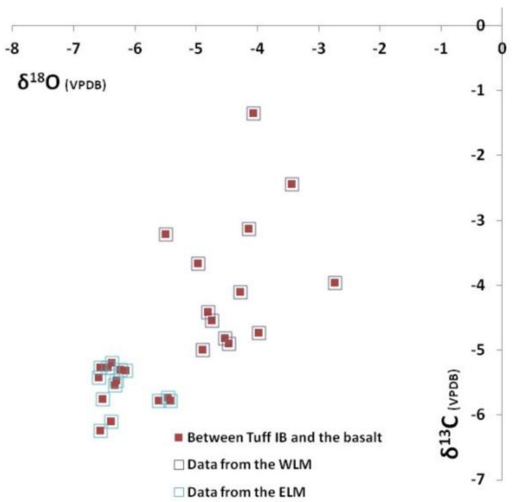

Figure 3-13: Stable isotope analyses of micritic nodules from between Tuff IIA and Tuff IF. Specimens from this stratigraphic interval on the alluvial fan (blue diamonds with red edge) plot at higher values than those at the eastern lake margin (blue diamonds with blue edge). This indicates more dilute fluids at the eastern lake margin.

Figure 3-14: Stable isotope analyses of micritic nodules from between IB and the basalt.Samples from the same stratigraphic interval on the western lake margin (red square with red edge) plot at higher values than those at the eastern lake margin (red square with blue edge). This indicates more dilute fluids found at the eastern lake margin.

Interestingly, for Type 1 micritic nodules which have a concentric structure, the results of sequential samples from centre to edge of the nodule do not have the same lower to higher $\delta^{18}O_{VPDB}$ and $\delta^{13}C_{VPDB}$ trend as shown in the concentric bands of the sparry nodules. Rather they vary unsystematically between lower and higher values (Figure 3-15) as is seen in the nuclei of the sparry nodules. The stable isotope data from Type 2 micritic nodules are much more closely clustered than those from type 1 (Figure 3-16).

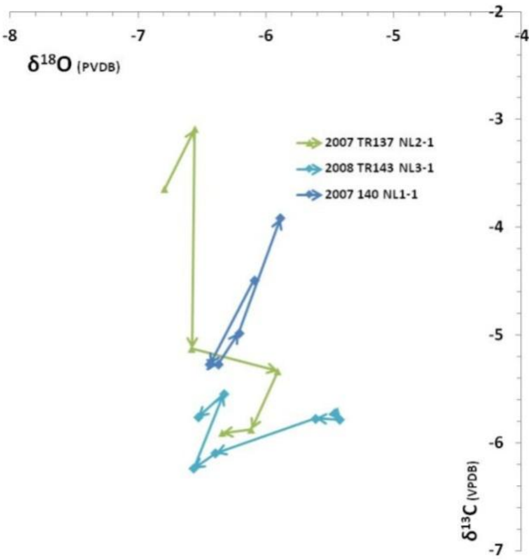

Figure 3-15: Unsystematic trend of stable isotope ratios in micritic nodules. The samples are taken sequentially from the centre to the edge of samples with a concentric structure. They do not show the same lower to higher trend seen in the sparry bands of the sparry nodules. Rather they resemble the unsystematic change found in the nuclei of the sparry nodules.

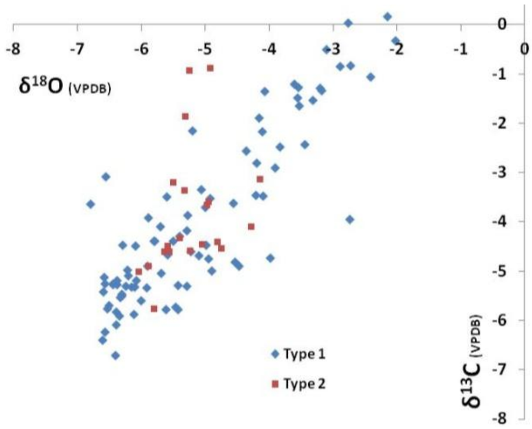

Figure 3-16: Stable isotope values from the two different types of micritic nodule. Data from Type 2 micritic nodules (red square) are much more tightly clustered than from type 1 micritic nodules (blue diamonds).

3.3.2 Rhizocretions, insect burrows, and fossilised rootmats

Tube-like carbonate bodies occur frequently throughout the stratigraphy, and can be produced by both roots and insects. Distinguishing features for rhizocretions include tapering of the tubes downwards, preserved cell structure, and branching morphology which tends to occur at acute angles to tubes pointing downwards (Retallack, 2001). Insect tubes tend not to taper, have no internal structure, and the branching tends to be either normal to tubes or have no consistent orientation (Retallack, 2001). All of the specimens from Olduvai have been grouped into either one of these two.

Rhizocretions and insect burrows

The specimens for this study were sampled from clay beds, and were generally orientated sub-vertically in the sediment. They vary in size between 2cm and 6cm long and 0.5cm to 2cm diameter. The bodies interpreted as rhizocretions tend to have a circular cross-section whilst those thought to be the insect burrows have an ovoid cross-section (Figure 3-17). The outer surface of both types is coated with spherulites and thin, interlocking plates of calcite <1mm thick with no consistent size, shape or orientation, similar to those found on the cortices of sparry nodules (Section 2.6.2). Thin section analysis has shown that they usually exhibit brown to pale brown pseudopleochroism, and the tube walls are composed of pale brown micrite.

The centres of the rhizocretions are often filled with multiple generations of sparry cement. The first precipitates are usually scalenohedral calcite, nucleated on the internal face of the wall growing inwards towards the centre of the tube. Residual void space was subsequently filled by an equant calcite cement. Where the voids have either not been cemented, or been partially cemented, spherulites have developed on the internal face of the wall. Often geopetal clay particles are trapped in the centre of the tubes. In some cases the tubes have an outward-radiating columnar calcite cement formed on the outer surface, and have concentric lines of inclusions indicating multiple episodes of formation.

The insect burrows are most clearly differentiated fom the rhizocretions where filled with micrite. The tubes do not have sparry calcite growth either in the tube centre or radiating from the outer edge of the tube.

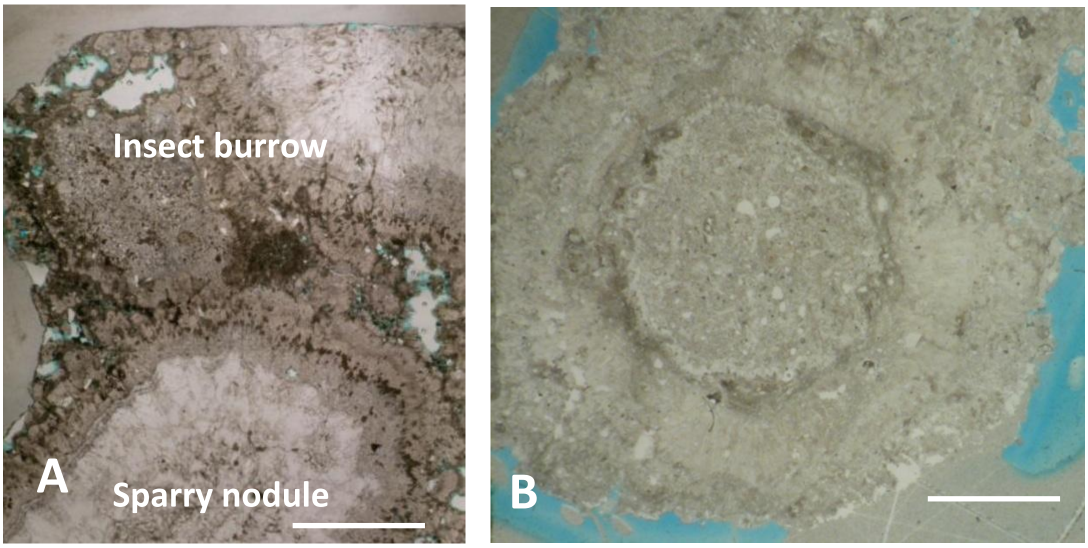

Figure 3-17: Cross sections of a fossilised insect burrow and a rhizocretion in thin section. (PPL, scale bar 1cm). A) is a fossilised insect burrow formed adjacent to a sparry nodule (2009 DK CA1). The outer part is composed of thin, brown, micritic calcite and the centre is composed of lighter brown micritic calcite. B) The rhizocretion (2001 FLKN 1b) has a thick white micritic calcite wall and the centre is composed of sparry, euhedral calcite.

Fossilised rootmats

Three specimens of preserved rootmats were found at locations in the FLK complex at the eastern lake margin. In thin section, the specimens have a mottled, dark brown colour, with a clotted texture, and trapped, angular, siliciclastic grains and clay particles. The detrital grains often have clay cutans and calcite cemented circumgranular cracks. There is an abundant network of fine veins which form elongate groups and branches, and tend to form an alveolar structure (Figure 3-18).

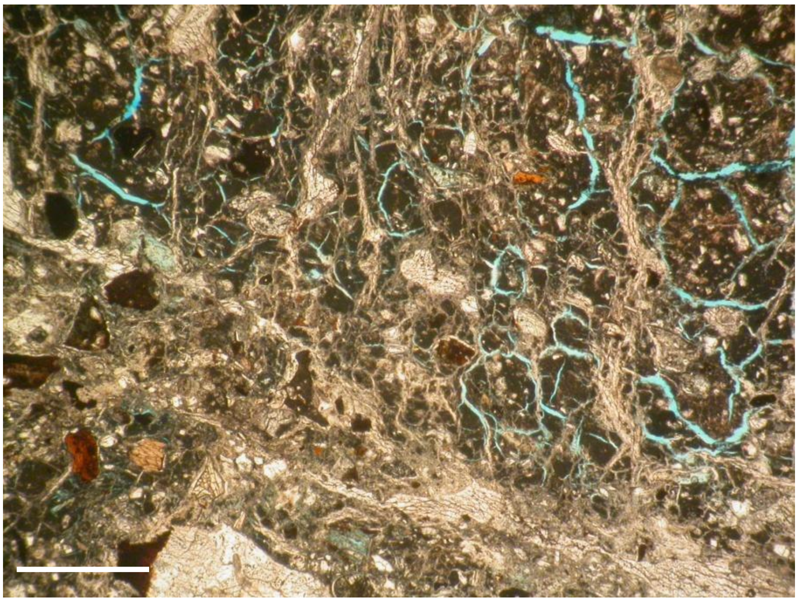

Figure 3-18: Fossilised rootmats from below Tuff IF(2009 HWKE GR1) , with a network of fine veins, circumgranular cracks and a clotted texture (Scale bar 1mm)

The whole is cemented with pseudopleochroic microspar calcite, although the extinction pattern is difficult to diagnose using standard thin sections because of the dark brown colour of the specimens in thin section.

3.3.3 Evaporite pseudomorphs

Stellate samples, composed of low-Mg calcite, have been identified in four different locations at the ELM, from clay beds just below and just above Tuff IF. They are equant, between 3cm and 5cm in diameter, and have protruding plate-like forms which intersect with one another as they radiate outwards. The outer surface has 1mm diameter spherulites attached over much of the surface. They are usually present as groups of individual specimens, although occasionally occur as multiple specimens cemented together.

Individual specimens have a radial structure with a cuspate outer surface. The specimens have between 4 and 7 lines of calcite which radiate from the centre, and from which divergent fibres produce a feather-like texture. In specimens where several are cemented together, the radiating lines are less well defined and frequently intersect. Often there are one or more sets of cracks which intersect the radial structure. The cracks are filled with multiple generations of low-Mg cement, and rarely strontianite is present as a later cement.

Figure 3-19: Cross sections of a stellate carbonate scale bar 1cm. Specimens have a radial structure and a cuspate outer surface. The specimens comprise equant calcite and feather-like crystals. Cracks are cemented by low-Mg calcite and occasionally strontianite.

The crystal texture is a mixture of approximately equant and feather-like crystals of calcite, which exhibits weak brown to pale brown pseudopleochroism. The equant crystals have an irregular boundary at crystal intersections, non-undulose extinction under crossed-Nichols, and crystal boundaries which intersect a pattern of sub-microscopic inclusion lines. The feather-like crystals have an undulose extinction pattern defined by lines of sub-microscopic inclusions. Crystal terminations are poorly defined, but where seen they are lobate.

Three specimens were selected for isotopic analysis and sampled in the centre, middle and edge. The data shows a covariant change from lower to higher $\delta^{18}O_{VPDB}$ and $\delta^{13}C_{VPDB}$ isotope ratios, and the data values range from $\delta^{18}O_{VPDB}$ -6.6‰ to -4.7‰ and $\delta^{13}C_{VPDB}$ -7.2‰ to -2.2‰ which is similar to that seen in the other carbonates.

3.4 Carbonate Formation

3.4.1 Micritic nodules

The formation of micritic nodules in sedimentary profiles, as nodular and laminar calcretes, can occur through both pedogenic (Quinn et al., 2007; Wright, 2008; Wright and Tucker, 1991) and non-pedogenic processes (Nash and McLaren, 2003; Wright, 2008). They are typically indicative of vadose conditions, where calcite growth occurs from a highly evaporated, restricted water supply. Type 1 micritic nodules with a Beta assemblage (Wright, 2008), including alveolar septal fabrics, have abundant and typical pedogenic features (Ashley, 2000; Retallack, 2001; Retallack et al., 2002). Type 2 specimens with an Alpha assemblage (Wright, 2008), including a crystalline matrix and complex cracks filled or partially filled with calcite cement, are consistent with formation as either pedogenic calcrete in a soil horizon (Wright, 2008) or non-pedogenic calcite deposition on lake marginal mud flats (Eugster and Hardie, 1975). Cracks are interpreted to be caused through one or more desiccation events. Crystal size changes are attributed to diagenesis, causing aggrading neomorphism by Ostwald ripening (Alonso-Zarza and Wright, 2010a).

The bright orange luminescence seen under CL, and the Fe and Mn concentrations and Fe/Mn ratios, are consistent with deposition in a sub-oxic setting, either through pedogenic or non-pedogenic processes (Barnaby and Rimstidt, 1989; Watson, 1985). The Sr and Ba values are much higher than seen in the radial calcites. As these are not redox sensitive elements during calcite formation, this may indicate a higher level of evaporation in fluid supplied to the micritic nodules compared to the radial calcites, however, the much lower Mg incorporation, compared to that seen in the sparry nodules and spherulitic clusters, may indicate that the water source is likely to have been dilute, suggesting that the incorporation of Sr and Ba is controlled by factors other than the evaporation. The partition coefficients of Ba and Sr are lower than 1, but can be increased by changes in the source water pH (Ichikuni, 1973; Tang et al., 2008; Yoshida et al., 2008) or replacement of Ca^{2+} by the smaller Mg^{2+} cation. In addition, the incorporation Sr and Ba in the calcite lattice can also be increased by increasing the rate of calcite precipitation and partitioning by colloidal organic matter (Curti, 1999; Elbaz-Poulichet et al., 1996; Lorens, 1981; Yoshida et al., 2008). Importantly, the trace element data may also have been influenced by subsequent diagenesis, and may not necessarily represent the initial nodule formation processes. The much lower magnesium concentrations in the micritic nodules may be the result of much less lake water influence compared to the radial calcites.

The range of $\delta^{18}O$ and $\delta^{13}C$ values, and the change in those values through a stratigraphic sequence, has previously been used to assign variations in groundwater evolution and C3 and C4 vegetation (Sikes, 2000). The covariance in the range of $\delta^{18}O$ and $\delta^{13}C$ values of the radial calcites, sparry nodules and spherulitic clusters, and the micritic nodules, is the same (Figure 3-20), although like the spherulitic clusters, the micritic nodules do not have the very lowest values seen in the nuclei of the sparry nodules. In general, the lack of spherulite growth on the outside of the micritic nodules indicates deposition away from the water table in the vadose zone.

As with the radial calcites, the higher $\delta^{18}O$ and $\delta^{13}C$ values on the alluvial fan and the western lake margin compared to the eastern lake margin suggest a much fresher water influence at the eastern lake margin possibly from springs or fluvial input to the lake.

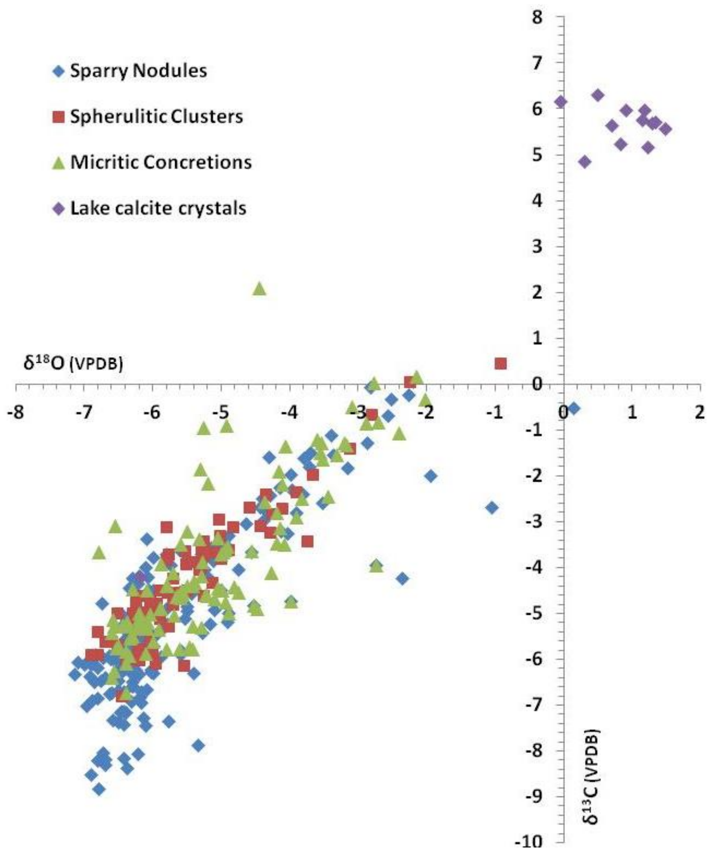

Figure 3-20: Stable isotope data of Sparry nodules, spherulitic clusters and micritic nodules. Radial calcites (sparry nodules (blue diamonds) and spherulitic clusters (red squares)) are described in chapter 2 of this thesis, and have a similar range of stable isotope values to those seen in the micritic nodules (green triangles).

Care must be taken during the interpretation of these data, as carbonate textures show that diagenetic changes cannot be ruled out, and isotopic values may not necessarily represent the primary groundwater, and so palaeoenvironmental conditions. The lack of systematic change in the stable isotope ratios of specimens sampled from centre to edge implies that either the calcite was not deposited in a gradually concentric manner, or that it may have been wholly or partially re-set by subsequent diagenesis. Similarly, recrystallisation of the type 2 nodules, interpreted by changes crystal size through the sample and attributed to Ostwald ripening, when compared to the type 1 nodules, may be the cause of closer grouping of the stable isotope values. The similarity between the covariance and gradient of all samples, regardless of their location or stratigraphic level, indicates that they are formed by similar processes. Although it is likely that vegetation will have influenced the primary stable isotopic values of pedogenic carbonates, the main processes responsible for the formation of these specimens are probably physicochemical, driven by evaporation and evapotranspiration at the overlying exposure surface.

3.4.2 Bioturbation: rhizocretions, insect burrows, and fossilised rootmats

Rhizocretions, insect burrows and rootmats are all indicative of sub-aerial exposure surfaces and pedogenic processes. Carbonate tubes were first documented at Olduvai by Hay (1976), who identified them as bioturbation by roots or burrowing organisms which extensively modified the ash beds and other sediments. Since then rhizocretions and fossilised grassland have been investigated by other authors (Albert and Bamford, 2011; Albert et al., 2009; Bamford, 2011; Bamford et al., 2006; Bamford et al., 2008; Liutkus et al., 2005). A wide variety of vegetation has been recorded at Olduvai identifying different depositional settings including grassland typical of savannah and roots of typha and reeds from lake marginal settings (Albert et al., 2009; Bamford, 2011; Bamford et al., 2006; Bamford et al., 2008; Hay, 1976; Liutkus et al., 2005).

3.4.3 Evaporite pseudomorphs

The stellate precipitates have been interpreted as calcite replacements of gypsum rosettes (Hay, 1976). Their formation indicates early mineral growth in a desiccating environment, when shallow pools evaporate to dryness (Watson, 1985). They occur in only a few locations, below Tuff IB and below Tuff IF (Hay, 1973), and above Tuff IF in the ELM sediments (this study) and their limited occurrence both stratigraphically and geographically indicate that there were very few times when the groundwater was supersaturated with respect to SO_4^{2-} rather than HCO_3^-/CO_3^{2-}. The complete replacement of gypsum by low-Mg calcite is reported to occur through meteoric diagenesis, because of the high solubility of gypsum in undersaturated, meteoric, water (Alonso-Zarza and Wright, 2010a; Sanz-Rubio et al., 2001). This supports the findings of low stable isotope values in the samples from Olduvai indicating pseudomorph formation by water dominated by a meteoric supply.

Calcitisation of gypsum can also occur by bacterial reduction of sulphate in organic rich sediments producing calcite with low $\delta^{13}C$ values. Interestingly dolomite is present in the lacustrine sediments at Olduvai at the three stratigraphically comparable levels to the gypsum rose occurrences (Chapter 6). Dolomite, gypsum, and high magnesium clays, are found to occur at the same stratigraphic level in both modern and ancient lakes, associated with sulphate reduction (Armenteros, 2010; Bustillo et al., 2002; Hay, 1976). The clay mineralogy has not been determined in this study, but the paired occurrence of the dolomite and gypsum supports the association of sulphate reduction conditions at three stratigraphic levels during the history of Palaeolake Olduvai between ~2 and 1.4 Ma.

3.5 The palaeohydrology of the non-radial carbonates

Type 1 micritic nodules, rhizocretions, insect burrows, and rootmats have unequivocal pedogenic features and are interpreted to be formed from carbonate supersaturated fluids in the vadose zone (Figure 3-21), primarily by abiotic processes, and certainly in association with roots. Type 2 micritic nodules, however, have no specific pedogenic features and their formation is more equivocal. Although they may have formed from carbonate supersaturated fluid in the vadose zone, they may also have been formed in a palustrine setting. The bioturbation found in some specimens could be post-depositional, or could also be the result of plants, such as reeds, in the lake margin during carbonate formation. The slightly lower stable isotope values of type 2 nodules indicate that they formed from fresher water, and without such a strongly evaporative trend, as seen in the type 1 nodules. They are considered for the palaeohydrological model to be formed in the vadose zone/palustrine zone (Figure 3-21). Rhizocretions, insect burrows and rootmats are all indicative of sub-aerial exposure surfaces and pedogenic processes, and evaporite pseudomorphs are interpreted to form close to the lake edge in highly carbonate supersaturated fluids (Figure 3-21).

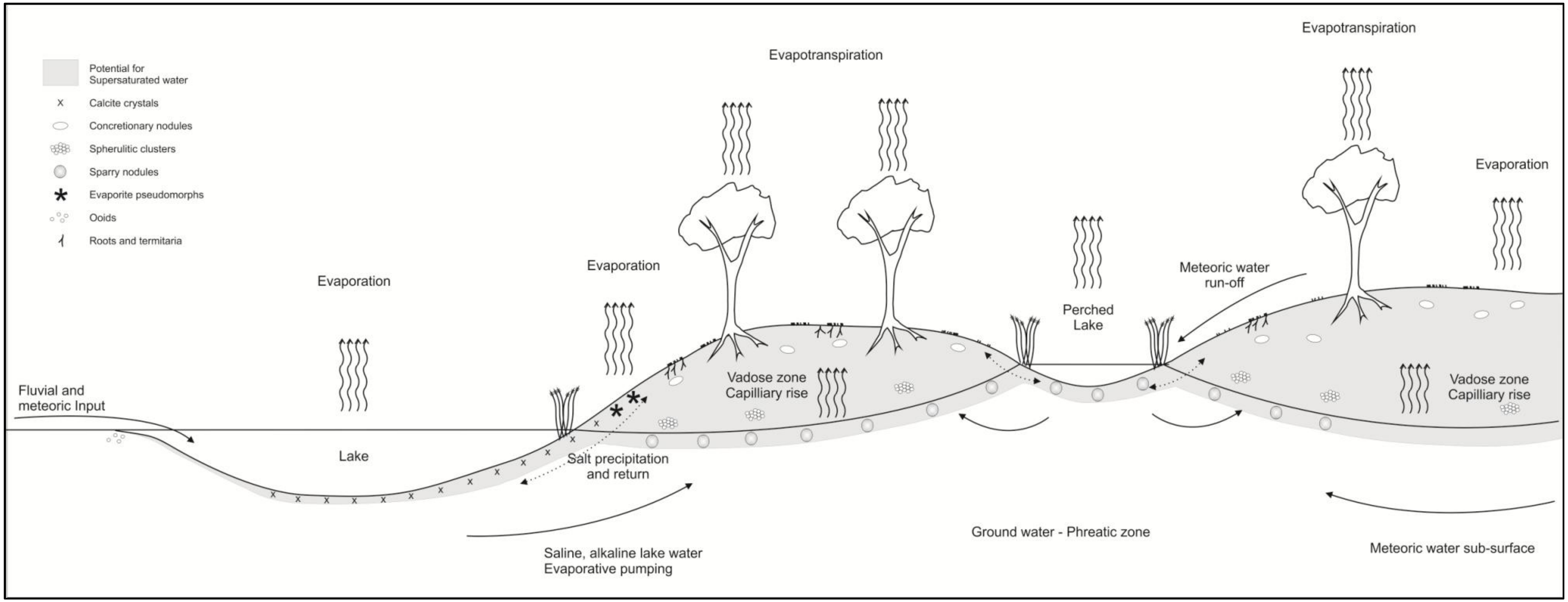

Figure 3-21: The non-radial carbonates are interpreted to form from carbonate supersaturated fluids in the vadose zone; micritic nodule rhizocretions, insect burrows and rootmats are proposed to form from carbonate supersaturated fluid in the vadose zone, above the capillary zone and evaporite pseudomorphs are interpreted to form close to the lake edge in highly carbonate supersaturated fluids. In order to make the different carbonate setting clear, the diagram exaggerates the vertical scale of the terrestrial setting which is likely to have been only ~1m of relief compared to the lake of <10m depth.

3.6 Conclusions

- Non-radial carbonates have been identified based on their macromorphology and micromorphology: Type 1 and Type 2 micritic nodules; rhizocretions, insect burrows and rootmats; and evaporite pseudomorphs.
- The carbonate textures and their stable isotope and trace element geochemistry have been used to interpret the processes of formation, and so propose hydrological models for their depositional setting.
- Micritic nodules type 1: formed in the vadose zone, likely by pedogenic processes. Occasional influences of formation in the capillary fringe or shallow phreatic, showing a fluctuating water table or evaporative pumping.
- Micritic nodules type 2: formed in the vadose zone or in a palustrine setting with episodic desiccation events, without any pedogenic influences
- Rhizocretions, insect burrows, and rootmats are formed close to the exposure surface, in the vadose zone.
- Evaporite pseudomorphs formed in an evaporative setting, in the shallow sub-surface, such as a playa-like environment, shallow pool, and lake margin.
- As the carbon and oxygen stable isotope values of the different carbonate types have a very similar range of values, their dominant depositional processes are interpreted to be abiotic, so fluctuations in the stable isotope values are inferred to be driven by the source water and the levels of evaporation.
- Because of the likelihood of diagenetic alteration of carbonates and the potential alteration of the trace elements and stable isotope values of a specimen, carbonate textures offer a valuable tool to support palaeoenvironmental reconstruction over different timescales and geographical areas.

Chapter 4: Carbonates as indicators of palaeohydrology in Bed I and Lower Bed II, at the eastern lake margin, Olduvai Gorge, Tanzania

4.1 Overview

Carbonate deposits from the Pleistocene sediments at Olduvai provide a useful resource for investigating palaeohydrology. Their crystal textures and geochemistry were determined by the processes operating both during their formation, and by subsequent diagenetic alteration. Using this information, hydrological settings for the formation of the individual types of carbonates from Olduvai Gorge have been proposed (Chapter 2 and 3). This chapter reviews the location of the carbonates in their stratigraphic and geographical settings: the carbonates are then used to identify the lateral and temporal changes in palaeohydrology operating during deposition of the sedimentary sequence. This chapter explores the possibility of using this information to provide an understanding of the wider pattern of palaeohydrology at Olduvai and throws new light on the development of some specific hominin exploitation surfaces. It also develops a technique for investigating palaeohydrology, and palaeoenvironment, that can potentially transferred to other important sites where sediments were deposited in similar settings.

The sedimentary successions of multiple locations within the FLK fault compartment have been correlated using lithology and volcanic deposits. By identifying the different carbonate types within these sedimentary successions (highlighted using using different coloured shapes to illustrate the distributions), the patterns of palaeohydrology, and how they changed through the stratigraphy, have been identified. Three groups of hydrological patterns were identified, characterising the stratigraphic ranges from below Tuff IB to Tuff ID, between Tuff ID and Tuff IF, and above Tuff IF. Each shows an overall drying trend upwards through the sequence. These are superimposed on multiple, more frequent changes in palaeohydrology. The trends are likely to have been influenced by both climate and tectonics. The carbonate distributions demonstrate the importance of synsedimentary fault activity in controlling the local hydrology at important hominin exploitation levels. The distribution of the carbonates identifies water table position and changes in it through time. They demonstrate persistent fault control over the water table through the whole section and that activity on both the FLK and KK faults was already initiated before deposition of Tuff IB.

Because the textures are often visible in hand specimen, the carbonates can potentially be used in the field as a guide to the palaeohydrology of the system during archaeological excavation. By combining hand specimen description with more detailed analyses, this method can be used as a transferable tool both at Olduvai Gorge and elsewhere to infer palaeohydrology, vegetation distribution, and so potential hominin land use.

4.2 Introduction

4.2.1 The landscape approach to evolutionary studies

Our understanding of hominin evolution has been greatly informed by investigations into their early habitats. Many different theories regarding the potential influence of environmental and climate changes on hominin adaptive evolution have been proposed (Cerling and Hay, 1986; Potts, 1998; Sikes, 1994). A detailed review (Potts, 1998) of the various theories concluded that "Further understanding of the adaptive history of hominins requires well-calibrated data on palaeoenvironments and their exact association of hominins" and called for an integrated teamwork approach. Increasingly, this landscape approach to understanding hominin evolutionary change, by concentrating on specific stratigraphic intervals over a wide spatial area, has influenced the methodology adopted by archaeological and palaeoanthropological researchers (Blumenschine et al., 2009; Blumenschine and Masao, 1991; Blumenschine et al., 2011a; Blumenschine and Peters, 1998; Bunn et al., 2010; Peters and Blumenschine, 1995; Potts, 1998; Potts et al., 1999). The potential forcing factors for change include variation in climate and the extent of its influence on seasonality, the changing topography and hydrology of the land in the tectonically and volcanically active Oldowan Basin, and the changes in other flora and fauna interacting with the environment.

4.2.2 Geology of the eastern lake margin

The fossil and geological record at Olduvai has been investigated by several teams of investigators at more than 350 sites throughout the gorge. At the eastern lake margin (ELM) multiple sites, named FLK, VEK, HWK, and KK, have been defined based on archaeological analyses(Hay, 1976; Leakey, 1971), and have been used as key study areas (Ashley, 2007; Ashley and Hay, 2002; Blumenschine et al., 2011b; Hay, 1976; Hay, 1996; Hay and Kyser, 2001; Stollhofen and Stanistreet, 2011). These areas have produced the most frequent occurrence of artefacts and as such have been investigated more extensively than any other (Leakey, 1971), which is reflected in much denser sampling of carbonates here than elsewhere.

Hydrological changes in East Africa have been identified on both Milankovitch timescales and also on much shorter timescales (Ashley, 2007; Gasse, 2000; Liutkus et al., 2005; Stanistreet, 2011; Trauth et al., 2005). These are reported to significantly affect lake levels and consequently the flora, faunal, and human activities at the lake margins (Gasse, 2000). The large scale supply of water to the area is probably controlled by climate change, but the detailed palaeohydrology at an individual time horizon is likely to have been influenced by a combination of climate and other factors, including fault-controlled topography, lithological variations, vegetation types and the pattern of plant growth (Albert and Bamford, 2011; McCarthy et al., 1991; McCarthy and Metcalfe, 1990; Tooth and McCarthy, 2007), fluvial delivery and springs (Ashley et al., 2010b; Blumenschine et al., 2011b; Deocampo and Ashley, 1999; Stollhofen and Stanistreet, 2011; Stollhofen et al., 2008).

The ELM sediments are interbedded waxy clays, siliceous, earthy clays, and tuffs, with minor sandstones (Hay, 1976). The waxy clays have been identified as smectite, illite and interlayered illite/smectite. Approximately two thirds of the waxy clay is thought to be the result of early diagenetic alteration of weathered detrital material by reaction with saline, alkaline water from Palaeolake Olduvai and approximately one third is unaltered detrital clay (Ashley and Hay, 2002; Deocampo, 2004; Deocampo et al., 2002; Hay and Kyser, 2001; Hover and Ashley, 2003; McHenry, 2009). The waxy clay beds are interpreted to be deposited during lake transgression, and variations in the clay mineralogy are caused by "differential post-depositional alteration" during lake retreat and the influence of meteoric water (Deocampo et al., 2002). Beneath Tuff IF, stevensite, a Mg-rich smectite, is present as a neoformed clay precipitating from Palaeolake Olduvai during lake transgression (Hay and Kyser, 2001; Hover and Ashley, 2003), and has been termed 'Butter claystone' due to its having the viscosity of translucent butter and a 'paper-shale' texture (Bamford et al., 2008). The earths and earthy claystones are interpreted to have formed as wetland sediments deposited in a stable fresher water setting (Ashley and Hay, 2002; Deocampo et al., 2002; Mees et al., 2007). Such wetlands exist where there is "a locally positive (near-) surface water balance for all or part of the year" and water retention occurs, for example though fault control or lithology (Tooth and McCarthy, 2007). They are fairly common in the sediments from the ELM of Palaeolake Olduvai, and are reported to have covered an area 10-20km by 1-10km, fed either by a combination of surface and groundwater discharge (Ashley, 2000; Blumenschine et al., 2011b; Cerling and Hay, 1986; Deocampo and Ashley, 1999; Hay, 1990), or by fluvial input from the alluvial fan drainage system (Blumenschine and Masao, 1991; Stanistreet, 2011; Stollhofen and Stanistreet, 2011).

The waxy clay beds were deposited during episodic transgression of the lake and the earthy clay beds during lake regression and sub-aerial exposure (Deocampo, 2002). Overall, the palaeoenvironment between ~2Ma and 1.7MA is understood to have been freshest against the eastern lake margin, near stream drainage and springs from the volcanic highland, which may account for the high density of artefacts, as animals and hominins are more likely to be attracted to more potable sources of water (Deocampo, 2002; Peters and Blumenschine, 1995). Similar lake systems and wetlands are found in modern lakes in East Africa, for example at Big Marsh near Lake Ndutu on the Serengeti Plain (Figure 4-1), Lake Makat in the Ngorongoro caldera (Figure 4-2), and Lake Natron in northern Tanzania (Figure 4-3).

Figure 4-1: Big Swamp at Lake Ndutu on the Serengeti Plain. The wetlands are supplied from springs and run-off from the Serengeti Plain to the west, and the constant source of freshwater provides a location for large numbers of animal populations. The marsh is heavily vegetated and drains into Lake Ndutu to the east, which is the primary source for the present day Olduvai River.

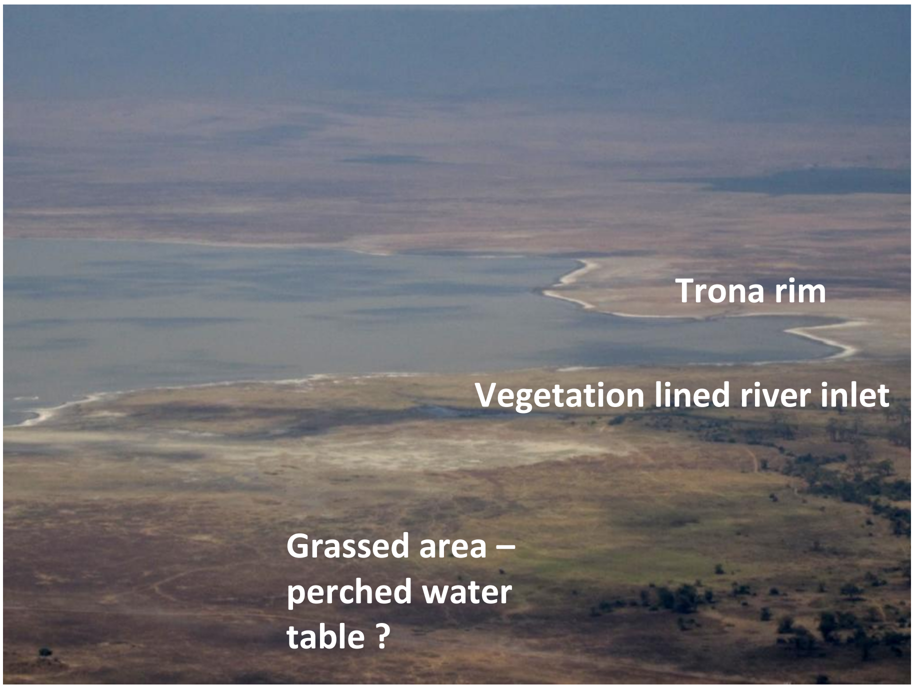

Figure 4-2: Lake Makat within the Ngorongoro caldera. The photograph is taken looking down at the lake from the Serena Safari Lodge on the southern edge of the crater rim. It is a saline, alkaline lake fed by the Munge River via the wetlands at the Hippo Pools, and the white rim is caused mostly by trona precipitation. A vegetated narrow river inlet can be seen running from the bottom right hand of the photograph north-west into the lake. A greener patch is from denser grassland where the water table is closer to the surface, either though a spring or perched water table. The overall relief is no more than two or three metres.

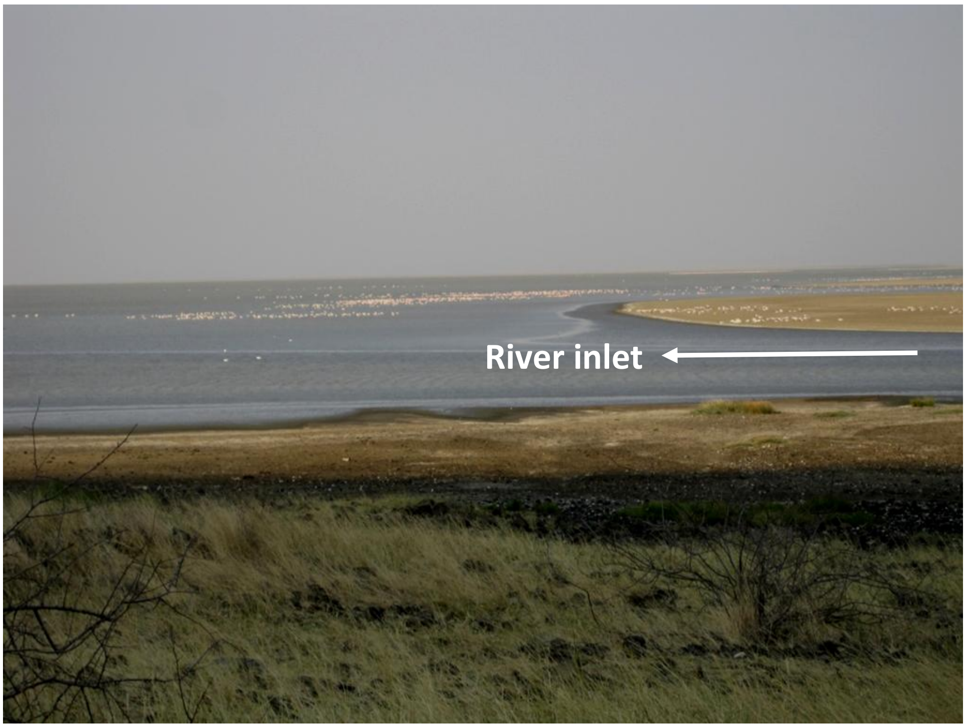

Figure 4-3: Lake Natron near river inlet. Lake Natron is the largest of these three lakes fed by springs and rivers. A large river inlet can be seen flowing into the main lake from the right hand side of the photograph. The lake is highly saline and alkaline and although a trona crust is found around much of the edge of the lake, it is less visible by the river inlet. Grassy areas and low shrub vegetation are developed several metres away from the shoreline with a relief of approximately 1m.

4.2.3 Stratigraphy and important hominin fossil horizons

Certain stratigraphic levels have been associated with important hominin and archaeological finds. The famous hominin fossil "*Zinjanthropus", (*now *Paranthropus boisei),* is associated with the basal surface of Tuff IC (also called the *Zinj* level (Leakey, 1971)) and below Tuff IB at DK. The beds above Tuff IF at HWK, and above Tuff IB at FLKNN, are associated with *Homo habilis* fossils and artefacts (Leakey, 1971). Previous work has identified a complex palaeohydrology with climate and tectonic influences. These studies have largely interpreted climate to be the driving force of change throughout the stratigraphy and, apart from Hay (1976) and Ashley and Hay (2002), most have not found evidence of any active faulting during Bed I or Lower Bed II. However, Stollhofen and Stanistreet (2011) have used changes in facies and bed thicknesses to demonstrate that the FLK and KK faults were active during latest Bed I after Tuff IE and through Lower Bed II. In addition, the archaeological lithic localities are reported to be concentrated on the footwall areas of the fault compartments (Blumenschine et al., 2011b; Stollhofen and Stanistreet, 2011), and evidence presented by Blumenschine (2011) suggests that the FLK fault, at least, was operating earlier in Bed I.

Stratigraphic packages of sediments at Olduvai Gorge were initially defined by the distribution of Tuffs which define sedimentary packages of about 10ka and 50Ka duration (Hay, 1976). Analysis of the sedimentary lithologies and carbonates has documented multiple superimposed timescales for the sedimentary and hydrological changes at Olduvai that are interpreted as cycles of lake advance and retreat (Liutkus et al., 2005; Stanistreet, 2011). The recognition of different numbers of cycles of lake expansion and retreat in any given package of beds will clearly influence any interpretation of the palaeohydrological change and the potential forcing factors involved. Two separate studies have suggested very different timescales of lake advance and retreat due to differences in the recognition of the number of individual lake transgression events between Tuffs. An earlier study (Ashley, 2007) recognised 5 cycles of lake expansion and retreat from the sedimentary sequence between Tuff IB and Tuff IIA, including the alternations between waxy and earthy claystones described above. Using the tuff dates and inferred sedimentation rates, these cycles are each interpreted to be ~21Ka and caused by Milankovitch timescale climate changes (Ashley, 2007). In the most recent study of Bed I between Tuff IB and Tuff IC, and Lower Bed II between Tuff IF and Tuff IIA, a minimum of 13 “lake-parasequences” have been recognised (Stanistreet, 2011). Using the Tuff dates as an overall depositional period, these have been estimated as cycles of ~ 4000Ka on average (Stanistreet, 2011), and so significantly sub-Milankovitch in recurrence. As the carbonates associated with each cycle are interpreted to form prior to the deposition of the overlying bed, this is thus inferred to occur at periods of 21Ka or 4.2Ka depending on the sedimentological interpretation. Understanding the timescales involved is crucial to providing an understanding of the forcing factors involved and provides a framework for interpreting the frequency and duration of the palaeohydrological change.

4.2.4 Carbonates in palaeoenvironmental studies

The textural and geochemical characteristics of terrestrial and lake-margin carbonates have often been used to interpret the processes involved in their formation, and so provide an insight into the palaeoenvironmental hydrology operating at that time (Arenas-Abad et al., 2010; Bennett et al., 2012; Cerling and Hay, 1986; Liutkus, 2009; Liutkus et al., 2005; Mount and Cohen, 1984; Sikes, 1994, 2000; Sikes and Ashley, 2007; Wright, 2008). Each carbonate group represents a specific group of processes which operated during their formation, and so can be used to interpret the palaeohydrology. Often a single specimen will have characteristics from more than one group of processes, providing evidence of fluctuating conditions during formation. To illustrate the distribution of different carbonate types, the specimens investigated in Chapters 2 and 3 have been assigned various coloured shapes according to which carbonate group they belong (Table 4). These have been used to identify the locations of specific carbonate groups at different stratigraphic levels on trench maps and logs, and at different geographical locations on the plan view of the eastern lake margin. The emergent pattern of carbonate distribution provides an overview of the spatial and temporal variation in palaeohydrology.

Most of the carbonate specimens sampled for this study were from waxy claystone beds which were deposited during lake transgression. The carbonates themselves have meteoric isotopic compositions that suggest the carbonate precipitation took place after lake regression and perhaps during subsequent transgression. Many of the clay beds have an upper erosional contact with the overlying sediment (Figure 4-4), which is sometimes directly on top of the carbonates, indicating that they were formed prior to the erosive event. In addition, some of the carbonates are pedogenic in origin, or associated with deposition at a sediment surface, and so their formation is also interpreted to be prior to deposition of the overlying sediments. Consequently, the carbonates are interpreted to have formed in the clay sediments following lake regression and prior to the deposition of the overlying bed or prior to an erosive surface, and so represent the local hydrological conditions operating during that time period. Formation of carbonates in sedimentary sequences is reported to occur on timescales from a few years to several thousand years (Wright, 2008; Wright and Tucker, 1991). Although it is not possible to ascribe exact timing to the formation of the carbonates, it is reasonable to assume that they deposited within the few thousand years suggested for the timing of each parasequence (Stanistreet, 2011).

Carbonate group	Palaeohydrological setting	Coloured shape identification
Spherulitic clusters	Vadose zone. In, or just above, the capillary fringe, close to the water table	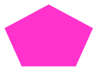
Sparry nodules	In the shallow phreatic zone, with repeated lake level changes resulting in episodic spherulite formation in the capillary fringe	X
Micritic nodules Type 1	In the pedogenic vadose zone, often with pedogenic modification	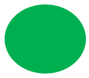
Micritic nodules Type 2	Either in the non-pedogenic vadose zone, or in a palustrine setting	
Rhizocretions/Insect burrows	In the vadose zone	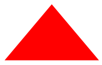
Fossilised rootmats	In the vadose zone at the sediment surface	
Evaporite pseudomorphs	At the lake margin in a highly evaporative setting	

Table 4: The palaeohydrological setting has been interpreted for each carbonate group and assigned a coloured shape to locate specific carbonates within a stratigraphic succession. Pink pentagons represent spherulitic clusters formed in the vadose zone much closer to the water table and probably in the capillary fringe. Purple crosses represent the sparry nodules formed by a complex set of processes including deposition below the water table in the shallow phreatic zone. Green spots represent micritic nodules type 1 formed in the sediment sub-surface vadose zone though pedogenic processes. Blue squares represent micritic nodules type 2 which may have a non-pedogenic or palustrine origin. Red triangles represent rhizocretions and insect burrows, and orange diamonds fossilised rootmats, both formed through pedogenic processes at or near the sediment surface. Grey stars represent evaporite pseudomorphs formed in the shallow sub-surface under highly evaporative conditions.

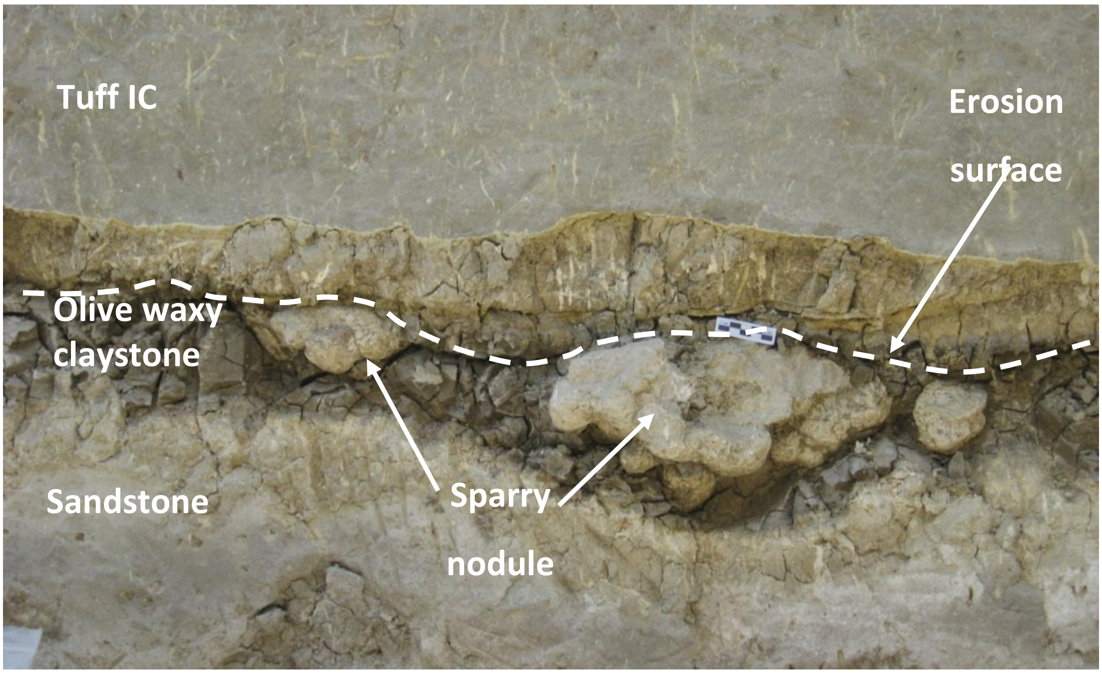

Figure 4-4: Erosion surface immediately above the sparry nodule samples adjacent to Tr150, with Tuff IC above indicating that the carbonates were formed prior to the erosive event. Scale bar in cm's.

4.2.5 Palaeoenvironmental interpretation

This chapter focuses on the potential to use the distribution of carbonate types to interpret the palaeoenvironment at the ELM, principally in the fault compartment between the FLK and KK faults (Figure 4-5; Figure 4-6).

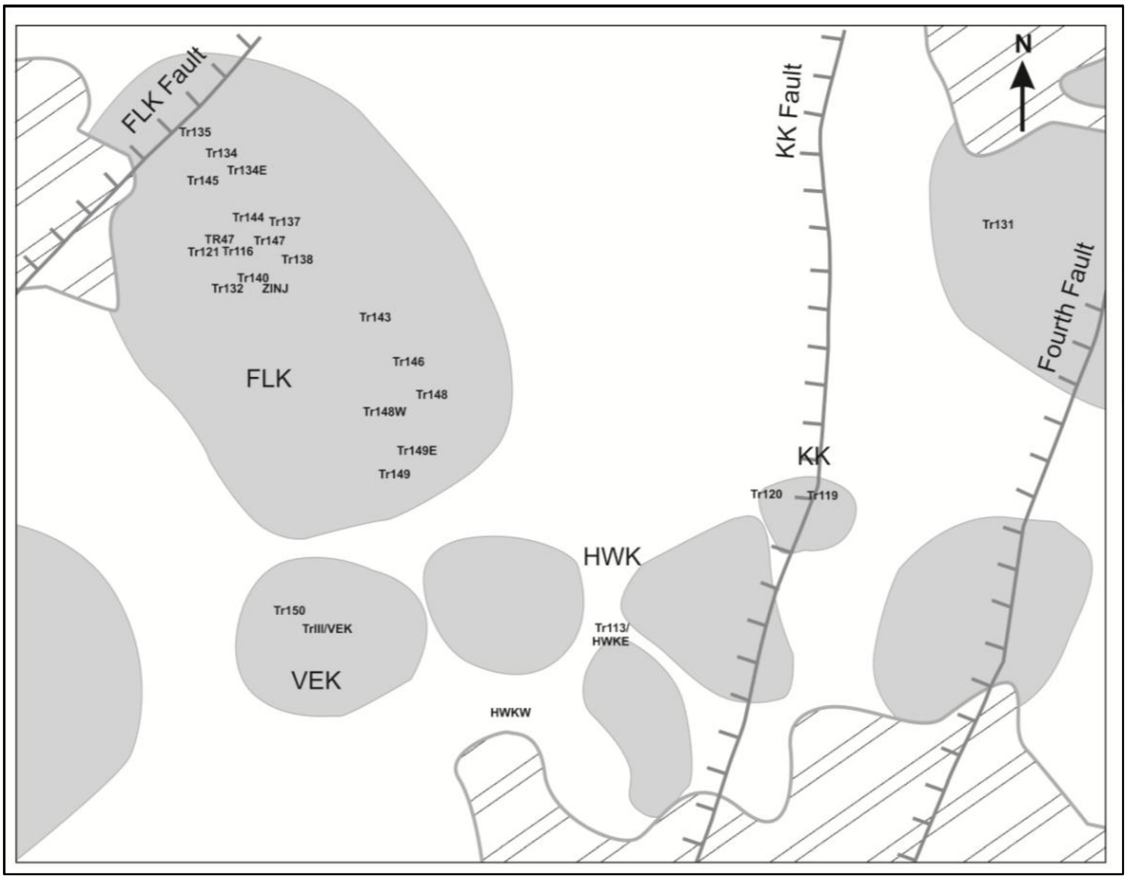

Figure 4-5: Plan view of the archaeological complexes FLK, VEK, HWK and KK at the eastern lake margin between the FLK and KK faults. Twenty-six sampling locations are identified by their trench numbers. The zinj site is located approximately in the centre of the FLK complex. Fourth fault was not active during Bed I and Lower Bed II but is included here for identification of the present day fault positions.

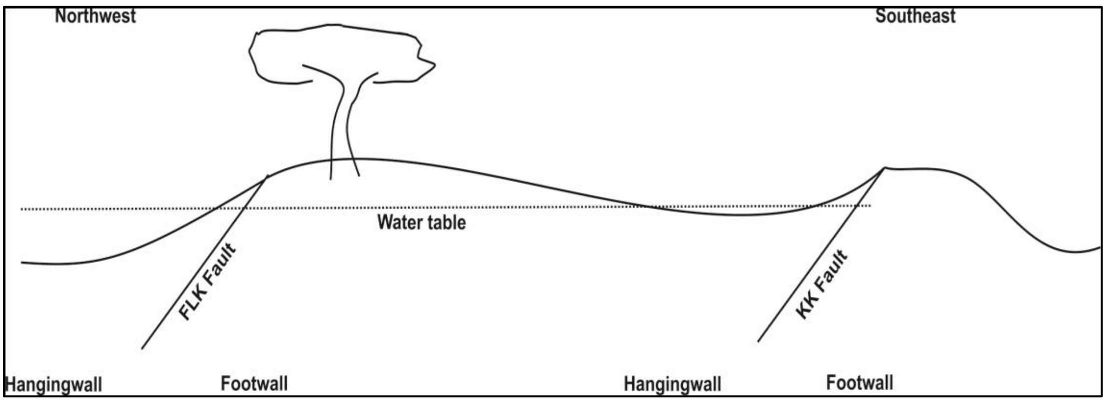

Figure 4-6: Cartoon of the approximate cross section of the fault compartment between the FLK and KK faults

This study has concentrated on two important time horizons associated with the most extensive records of hominin fossils and artefacts; Bed I between Tuff IB and Tuff IC, and Lower Bed II between Tuff IF and a major disconformity, the Crocodile valley incision (Blumenschine and Masao, 1991; Stanistreet, 2011). A high resolution stratigraphy of the Bed I and Lower Bed II sequence in this study has been recorded using the detailed sedimentary logs of multiple locations of trenches excavated for joint archaeological and geological purposes between 2000 and 2010.

The carbonates have first been used to illustrate the palaeohydrological interpretations that can be made, using two trenches from the FLK complex, Tr 144 and Tr147. This concept has then been extended by placing each specimen within a high resolution stratigraphy of multiple, correlated locations within the FLK fault compartment, to form a geographical picture of the changing palaeoenvironment through time.

4.3 Small scale analysis: palaeohydrological analyses of individual specimens from two closely-spaced sampling trenches

The sedimentological association of different carbonates are illustrated by the distribution of coloured shapes representing carbonate types positioned on the sedimentary logs of two OLAPP trenches from the FLK complex, Tr 144 and Tr147 (Figure 4-7), and the lithofacies and tuff beds have been used to correlate the two trenches. The carbonates in Level NN1 and Level NN3 (Leakey, 1971) which are in two clay beds, identified as the transgressive parts of lake-parasequences caused by major lake expansion and retreat between Tuff IB and Tuff IC (Blumenschine et al., 2011b; Stanistreet, 2011). They are interpreted to represent parasequential periods averaging about 4000a determined using $^{40}Ar/^{39}Ar$ Tuff dates (Stanistreet, 2011). In addition, carbonates occur in a series of interbedded lake clays and earthy clays between Tuff IC and Tuff ID. This suite of sediments, named 'Trip', is considered to correlate to the Tripartite Unit of Leakey (1971).

Interpretation of the changes in the palaeohydrology does not necessarily provide a continuous picture of all depositional events, because of the time record lost at erosion surfaces. For example, a fourth bed is reported between Tuff IB and Tuff IC (Blumenschine et al., 2011b; Stanistreet, 2011) at the ZINJ site but is reported to have been lost at Tr144 and Tr147 due to erosion (Blumenschine et al., 2011b). However they do provide a detailed interpretation of events at a series of specific time horizons.

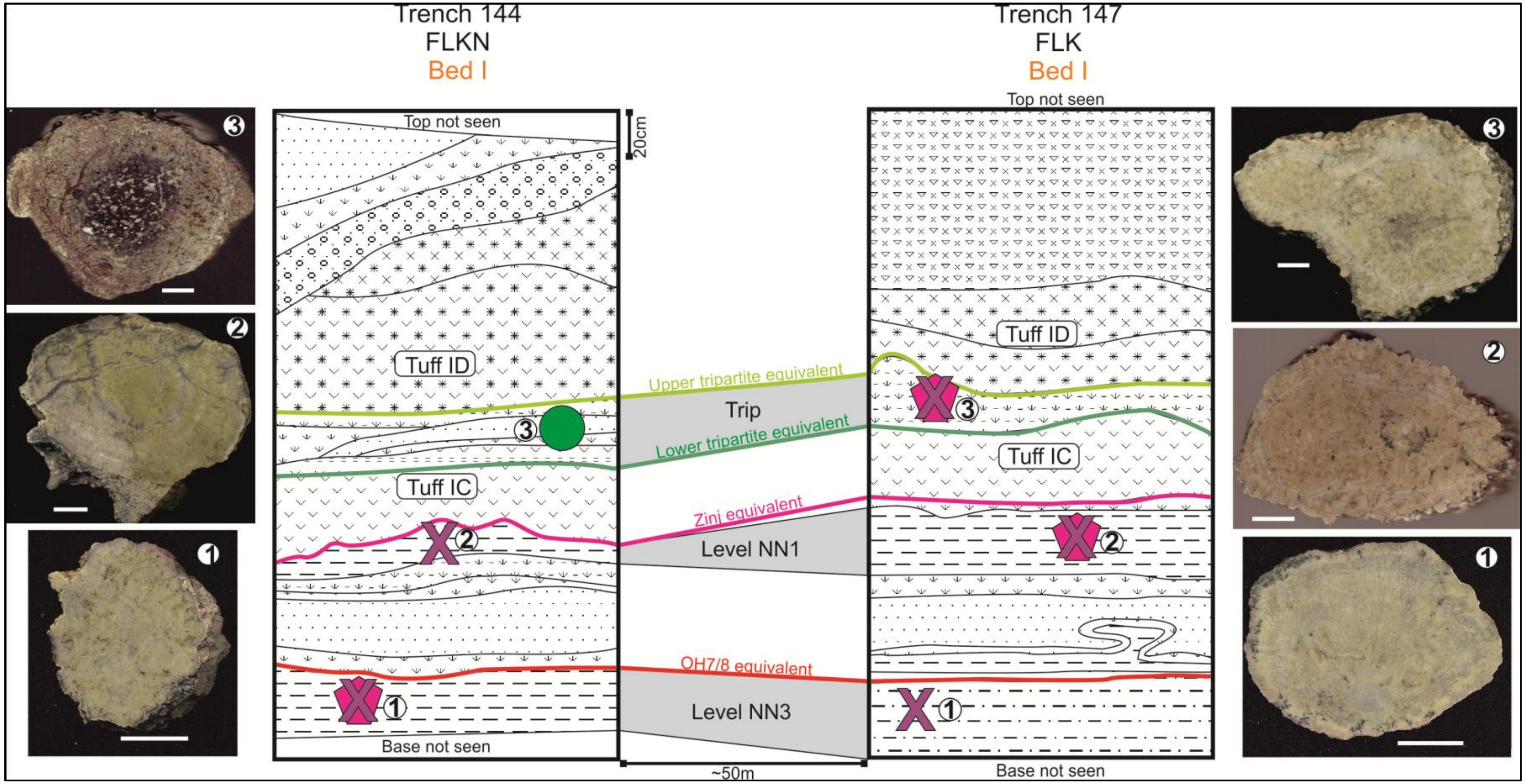

Figure 4-7: Detailed trench maps of two locations at the eastern lake margin in the FLK complex. Trench 144 is approximately 50m northwest of Trench 147. Specimens identified at three different stratigraphic levels in each trench are numbered 1-3. They are shown with their polished cut faces and located on the diagram with a coloured symbol. The pink pentagons represent spherulitic clusters, purple crosses represent sparry nodules and green circles represent micritic nodules type 1. Where two symbols are used the specimen has textural components of both of them. The equivalent stratigraphic levels are indicated on the diagram using coloured lines. Although the trenches are only 50m apart, the specimens have formed in slightly different hydrological conditions. The carbonates in trench 147 have formed in slightly wetter conditions than Trench 147 than those in trench 144. In each case the environment is tending towards drier higher in the sequence recorded here.

Distribution at Trench 144

Carbonate types differ through the stratigraphy. At the lowest sampling level, equivalent to Level NN3, the specimen is a spherulitic cluster with patches of columnar calcite forming a discontinuous sparry band. The specimen from Level NN1, is a sparry nodule and the specimen between Tuff IC and Tuff ID is a micritic nodule. The spherulitic cluster at level NN3 is interpreted to have been deposited in the vadose zone immediately above and close to the water table. The spherulites are likely to have been formed close to or within the capillary fringe so that columnar calcite could form in any cracks or voids wetted or completely immersed during a subsequent rise in groundwater level.

The formation of the sparry nodule from Level NN1 is likely to have initiated in the vadose zone, but the sparry bands are interpreted to have formed in the shallow phreatic zone, subsequently followed by spherulite formation in the vadose zone again, showing fluctuations in the water table. Between Tuff IC and ID the micritic nodule would have formed in the vadose zone, above the capillary fringe where the sediments are not permanently wet.

Distribution at trench 147

At this site the change in specimen types contrasts with those at Tr144. The lowest sampling level, equivalent to Level NN3, is a sparry nodule and those from Levels NN1 and between Tuff IC and Tuff ID are spherulitic clusters with well formed, concentric sparry bands partway through the nodule. The sparry nodule from Level NN3 is unusual in the radial carbonate specimens identified at Olduvai Gorge. It developed non-concentrically with the sparry bands developed upwards and outwards away from a nucleus (type 1). As there was nothing in the surrounding sediments to indicate a physical impediment to growth, this suggests that the growth direction was restricted by the availability of water, possibly with a local lithological control. The spherulitic clusters in Level NN1 and between Tuff IC and Tuff ID have well-developed concentric sparry bands which would require the specimen to form initially in the vadose zone, followed by precipitation in the shallow phreatic zone and finally growth in the vadose zone again.

Discussion of carbonate distribution at trenches 144 and 147

At the lowest level in the stratigraphy, NN3, although during their formation there are slight fluctuations in their positions relative to the water table, the specimen at Tr147 was primarily formed in the phreatic zone, and that from Tr144 in the capillary zone and partially in the phreatic zone. This implies a lateral variation in groundwater hydrology between the two trenches, with carbonates from Tr147 forming more consistently below the water table than at Tr144.

This may be the result of either; an increase in the level of an adjacent water body resulting in flooding of the overlying ground surface; an increase in the water table through capillary rise, potentially driven by an increased evaporation at the overlying ground surface because of variations in the vegetation type or density; or it may have been affected by a slight topographic high at Tr144 compared to Tr147. Lateral changes in vegetation caused by adjacent wet and dry zones have been identified in contemporary settings such as the Okavango Swamp, caused by only a few 10’s cm topographic relief (McCarthy et al., 1991). Such small variations have also been proposed to influence vegetation type and abundance and the potential for hominin use at Olduvai Gorge (Blumenschine et al., 2011b).

Specimens from Level NN1 show a similar series of slight fluctuations in groundwater during their formation, but in this case carbonates from Tr144 formed more consistently below the water table than at Tr147. The reasons for this may be due to a slight shift in the depth of the water table caused by a spring, river or perched lake, or potentially a change in the overlying vegetation impacting on the extent and locations of capillary rise.

Specimens from Tr144 at the Trip Level are indicate formation in the vadose zone, away from the capillary fringe, and likely influenced by pedogenic processes, whereas those in Tr147 are spherulitic clusters with sparry bands. This suggests that carbonates in Tr147 are formed much closer to the top of the water table compared to those in Tr144 at this level, and overlying vegetation and soil development is dominant nearer to Tr144.

Throughout the sedimentary sequence, although the two locations were subject to slight lateral variations in hydrology, and an overall lowering of the water table through time, and so a drying trend between Tuff IB and ID, the subtle differences in topography persist over several lake transgressive-regressive cycles. So each time the meteoric system re-established itself the groundwater table was in a similar position with respect to the new layer of sediment.

The differences described above highlight the importance of understanding the sedimentary succession of the carbonate locations to properly interpret the changing palaeohydrology.

4.4 Broad scale analysis of carbonate distribution: the hydrological pattern between the FLK and KK faults

Twenty-six trenches investigated by OLAPP from the FLK and KK complexes have been used to provide a case study of longer term influences over the hydrology at the ELM across a fault compartment. For this study the FLK complex has been divided into three areas; western FLK, central FLK and eastern FLK (Figure 4-8). Specific trenches in these sectors correspond to previous designations FLKNN, FLKN, FLK, Maikao Gully, and FLKS (Appendix 1). The different locations are correlated using the Tuff beds and the lithologies and lithofacies between the tuffs (Blumenschine et al., 2011b; Stanistreet, 2011).

This study utilises the carbonates from ten different stratigraphic levels to identify patterns of change; six levels below Tuff IF and four levels above Tuff IF (Figure 4-8). Each level has been designated as a lake-parasequence (Stanistreet, 2011). Some of the locations were sampled at several sub-levels a few centimetres apart vertically.

For the purposes of this study the different levels have been interpolated to all the locations to identify time equivalent sampled carbonate horizons. The emergent geographical pattern of the carbonate types at each stratigraphic level, identified by coloured shapes, can be used as a proxy for the palaeohydrological conditions and is shown also in Figure 4-9 and Figure 4-10. The variation in the pattern between different stratigraphic levels will show how the palaeohydrology of exposure surfaces changed through time.

Three patterns of carbonate variation can be seen (Figure 4-8); from below Tuff IB to Tuff ID; between Tuff ID and Tuff IF; and from Tuff IF to parasequence 4 of Lower Bed II. The ranges are interpreted to represent different hydrological systems and are discussed separately.

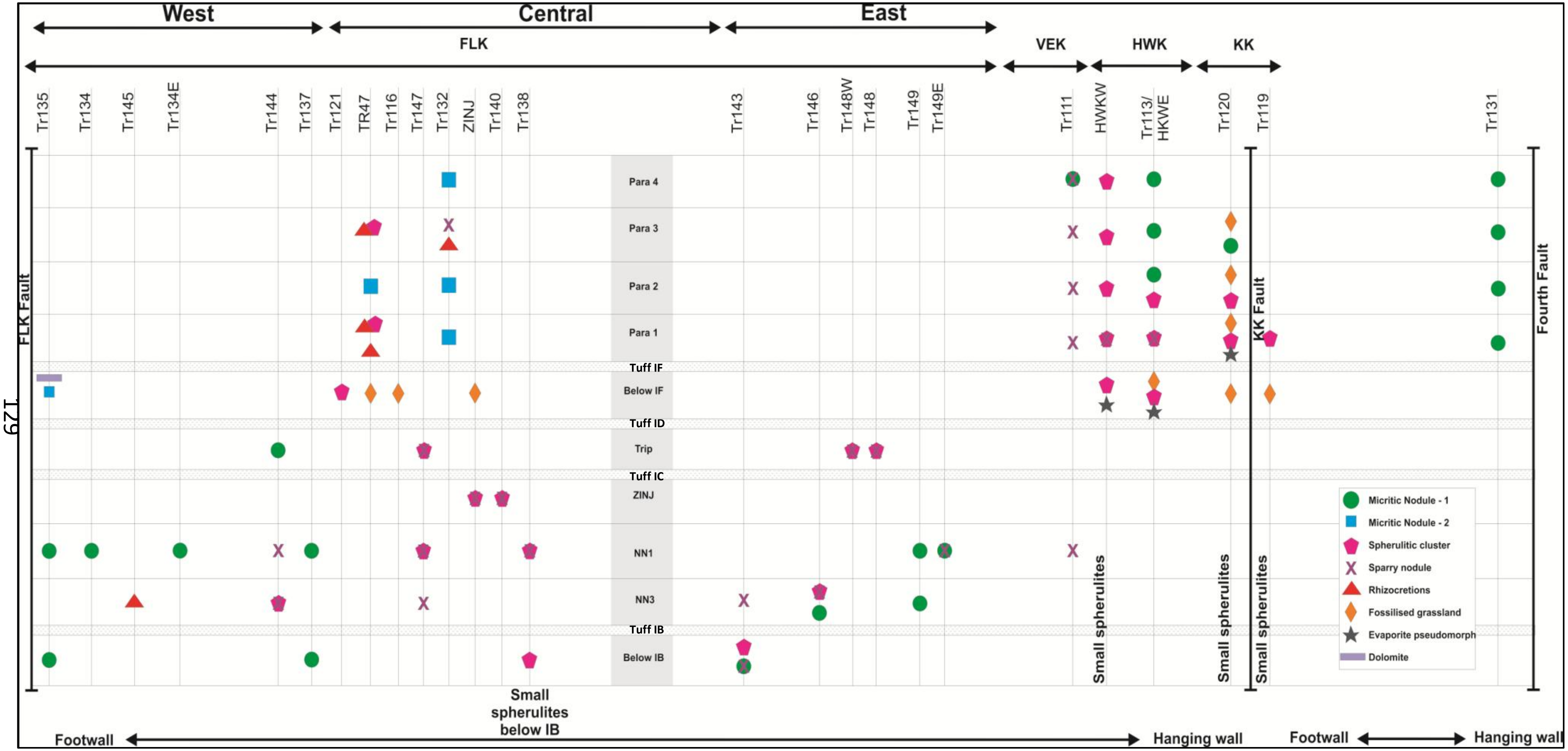

Figure 4-8: The different carbonate types at each of the ten different stratigraphic levels at twenty-six trenches from between the FLK and KK complexes at the eastern lake margin. The emergent pattern of colours and shapes identify the hydrological pattern at each level and how that might have changed through time. Although there is a variation in the pattern through time, three different groups can be seen; from below Tuff IB to Tuff ID; from Tuff ID to Tuff IF; and above Tuff IF. Para 1-4 are four lake parasequences defined by (Stanistreet, 2011). The persistence of carbonates formed in the capillary and phreatic zones in the centre and slightly east of centre in the FLK fault compartment demonstrates the repeated re-establishment of palaeohydrological conditions following lake transgression-regression cycles.

4.4.1 Carbonates below Tuff ID

The western and eastern parts of the FLK complex are dominated by Type 1 micritic nodules (green spots) representing vadose settings associated with vegetation (Figure 4-8,

Figure 4-9). Whereas, the central part of FLK is dominated by spherulitic clusters (pink pentagons) and sparry nodules (purple crosses) representing carbonate growth close to or below the water table, and not necessarily associated with vegetation (Figure 4-8;

Figure 4-9). The presence of phreatic and capillary zone carbonates at two levels (NN3 and NN1; Figure 4-7) of Tr 144 differs from this pattern. It indicates that the specimens from Tr144 are formed slightly closer to the water table compared to the adjacent trenches. This may be the result of local control of the water supply to the area by lithological variations, the presence of springs or fluvial channels, or variations in vegetation causing a localised elevation in the water table by capillary rise.

The overall geographical pattern of carbonate types in the western part of the FLK fault compartment below Tuff ID, other than at Tr144, are those formed in persistent vadose conditions. Conversely, that in the central part of the fault compartment is persistently wet, forming carbonates in the phreatic or capillary zone through several lake transgressive-regressive cycles. In the eastern part of the fault compartment vadose conditions give way to phreatic and capillary zone conditions upwards through the stratigraphy.

A key hominin level in this stratigraphic range is below Tuff IC at the particular location where the partial skeletal remains of ‘*Zinjanthropus*’ *Paranthropus boisei* were recovered, and so named the Zinj site (Leakey, 1971). Because of the importance of the fossil record at this level, this has probably been the most investigated site and level at Olduvai Gorge, and several different palaeoenvironmental mosaics have been proposed. The western part of the ELM at FLK has been identified as a composite setting where the Zinj site (Carbonate samples Figure 4-9D) itself is a low relief wooded peninsula bounded by a wetland to the west and a river channel to the east (Blumenschine et al., 2011b).

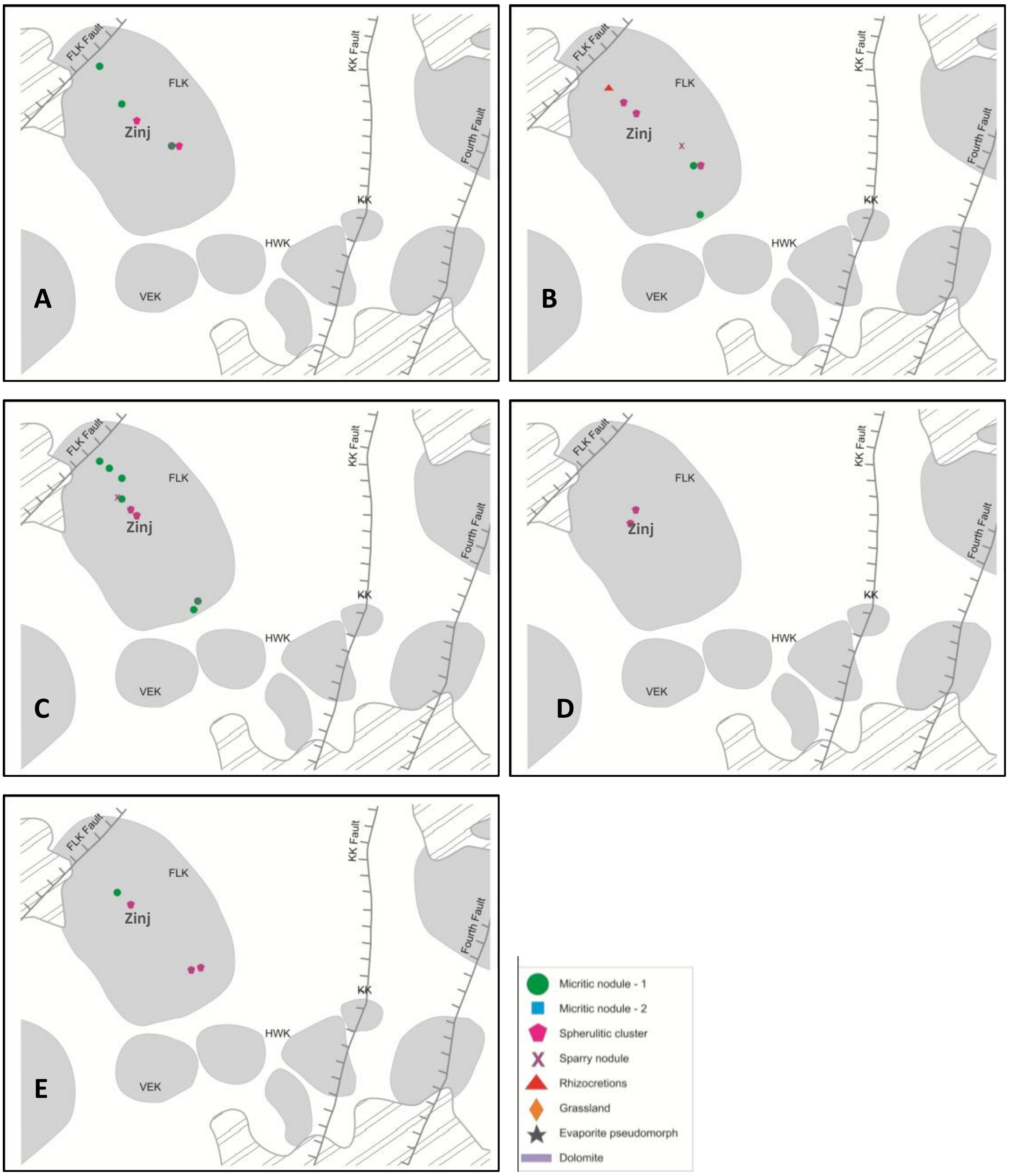

Figure 4-9: The variation of carbonate types at five different horizons below Tuff ID shown in plan view as described in Figure 4-8. A) is below Tuff IB, B) Level NN3, C) Level NN1, D) Level Zinj, and E) Between Tuff IC and Tuff ID. The green circles that represent the vadose condition persistently occur close to the FLK fault, with episodic occurrences on the western boundary of the FLK complex. Whereas the Sparry nodules and the

spherulitic clusters that represent the phreatic and vadose/phreatic conditions occur in the middle of the FLK complex.

Similarly, the Zinj level has been interpreted as a dryland in the middle of a marsh (Diez-Martin et al., 2010). Springs producing wet ground and standing water have also been reported below Tuff IC at several places within the FLK locality adjacent to low relief sites which are densely wooded (Ashley et al., 2010b). These are reported to be delivered along fault lines interpreted to migrate eastwards across the fault compartment, from Middle Bed I to Lower Bed II, due to rift related tectonics (Ashley et al., 2010a; Ashley et al., 2009; Domínguez-Rodrigo et al., 2010). In a recent study of macroplant fossils, preserved marshland vegetation is recorded beneath Tuff IB, Tuff IC and Tuff ID close to the western part of the FLK complex (Bamford, 2011). These repeated occurrences of vegetated surfaces are interpreted to support a cyclicity of hominin use (Bamford, 2011).

The overall pattern of carbonate specimens from this study below Tuff ID is consistent with previous interpretations of the relative positioning of wetter and drier terrains within FLK. This supports the concept that carbonate textures offer an additional, valuable, proxy to refine palaeoenvironmental studies, especially where other data is not available.

4.4.2 Carbonates between Tuff ID and Tuff IF

The terrestrial sediments between Tuff ID and Tuff IF are unusual compared to the other levels, as they are the only ones with dolomite (Chapter 6) (Purple rectangle). The dolomite is found on the footwall in a unit of claystone with a ‘paper-shale’ oily and translucent Stevensite-like texture termed “Butter Claystone” (Bamford et al., 2008), a Mg-rich smectitic neoformed clay deposited during lake transgression. This overlies an ~2m thick series of beds of micritic nodules type 2 (blue squares) found in olive waxy claystone. Although spring tufas have been identified on the western most point of FLK, close to the FLK fault (Ashley et al., 2010b), the micritic nodules from Tr135 do not have the characteristic biogenic features of tufas such as plant fragments or diatoms, and they are not laminated. Consequently they are interpreted here to have formed either in a palustrine setting or in the vadose zone during lake regression. The dolomite is interpreted to have formed in shallow water (Chapter6) and so represents growth during lake transgression following deposition of the stevensitic clay.

The stratigraphy between Tuff ID and Tuff IF commonly has fossilised rootmats (orange diamonds). These are immediately overlain by Tuff IF, and are dominant in both the FLK complex and the eastern HWK and KK complexes. They represent the driest locations at the sediment surface. They overlie the same unit of Butter Claystone in which dolomite is present. Spherulitic clusters (pink hexagons) and evaporite pseudomorphs (grey stars) are present in the eastern part of the fault compartment at the HWK and KK complexes in a unit of olive waxy claystone which is below the butter claystone horizon, and are interpreted to have formed close to a highly carbonate supersaturated water source.

The carbonates on the hanging wall of the fault compartment show a general drying trend upwards through the sequence. The dolomite on the footwall indicates a lake transgression over the micrite, and is stratigraphically overlain by the fossilised rootmats. Overall, the carbonates demonstrate a drying trend upwards through the sequence, punctuated by a lake transgression producing the stevensitic clay and dolomite and is consistent with previously reported data indicating an overall drying out of the lake prior to the deposition of Tuff IF (Bamford, 2011; Bamford et al., 2008; Hay, 1976; Hay and Kyser, 2001).

4.4.3 Carbonates above Tuff IF

Above Tuff IF in Lower Bed II fossilised rootmats are present (Bennett et al., 2012); however, unlike the carbonates immediately below Tuff IF, spherulitic clusters, sparry nodules, and micritic nodules type 1 and 2 are the dominant forms of carbonate (Figure 4-8; Figure 4-10).

The western trenches at FLK, Tr47 and Tr132, have a combination of micritic nodules type 2, rhizocretions which are sometimes developed with abundant spherulitic clusters, and one specimen of a sparry nodule. As with trenches 144 and 147 discussed earlier they are only about 50m apart, yet they have produced significantly different carbonate types at each of the four different parasequences. Overall Tr47 tends to have rhizocretions and Tr132 has micritic nodules type 2. The rhizocretions in Tr47 have formed in conjunction with spherulitic clusters at parasequences 1 and 3 indicating formation in the vadose/capillary zone. The specimens from 50m east at Tr132 are more difficult to interpret. They are massive white micrite with no evidence of pedogenic processes. The massive micrites can form as a mature calcrete in the vadose zone, or as palustrine deposits (Ford and Pedley, 1996).

The palaeohydrological interpretation derived from carbonates in the eastern trenches above Tuff IF at VEK, HWK and KK show a predicative pattern throughout the four parasequences in the stratigraphy, with an overall drying trend upwards through the sequence. At VEK and HWK the carbonates are more dominantly sparry nodules and spherulitic clusters in the lower parasequences and are present as micritic nodules type 1 in the upper part of the stratigraphy. This indicates that the carbonates are forming in increasingly vadose conditions from older to younger levels.

Tr111 is the only location in the eastern part of the fault compartment with specimens both above and below Tuff IF. It has only sparry nodule carbonates in both stratigraphic ranges at multiple levels, apart from parasequence 4 which is a composite specimen of sparry nodule and micritic nodule. The repeated occurrence of sparry nodules at VEK through both Bed I and Lower Bed II implies that the position of the water table at this point was long-lived. This may be due to the persistence of the depocentre of the fault compartment supplied by water from springs (Ashley et al., 2009) or fluvial channels (Stollhofen and Stanistreet, 2011). The adjacent trenches at HWK also have a very similar pattern with spherulitic clusters present throughout the four parasequence levels, likely to be due to the proximity of the persistent water source at VEK. Parasequences 1, 2, and 3, at Tr120, the easternmost trench in the fault compartment, was sampled at two sub-levels within each parasequence. The lower sub-level contains either, an evaporite pseudomorph, a spherulitic cluster or a micritic nodule type 1, and the upper sub-level is a fossilised rootmat. This demonstrates a drying upwards trend within each parasequence, superimposed on a larger scale drying upwards trend through the four parasequences.

The similarity in the carbonate profile at the four parasequence levels shows that the palaeohydrology was comparatively stable, and returned to a similar state following each lake transgression/regression cycle. This suggests that the controls influencing the palaeohydrology at each level are similarly consistent.

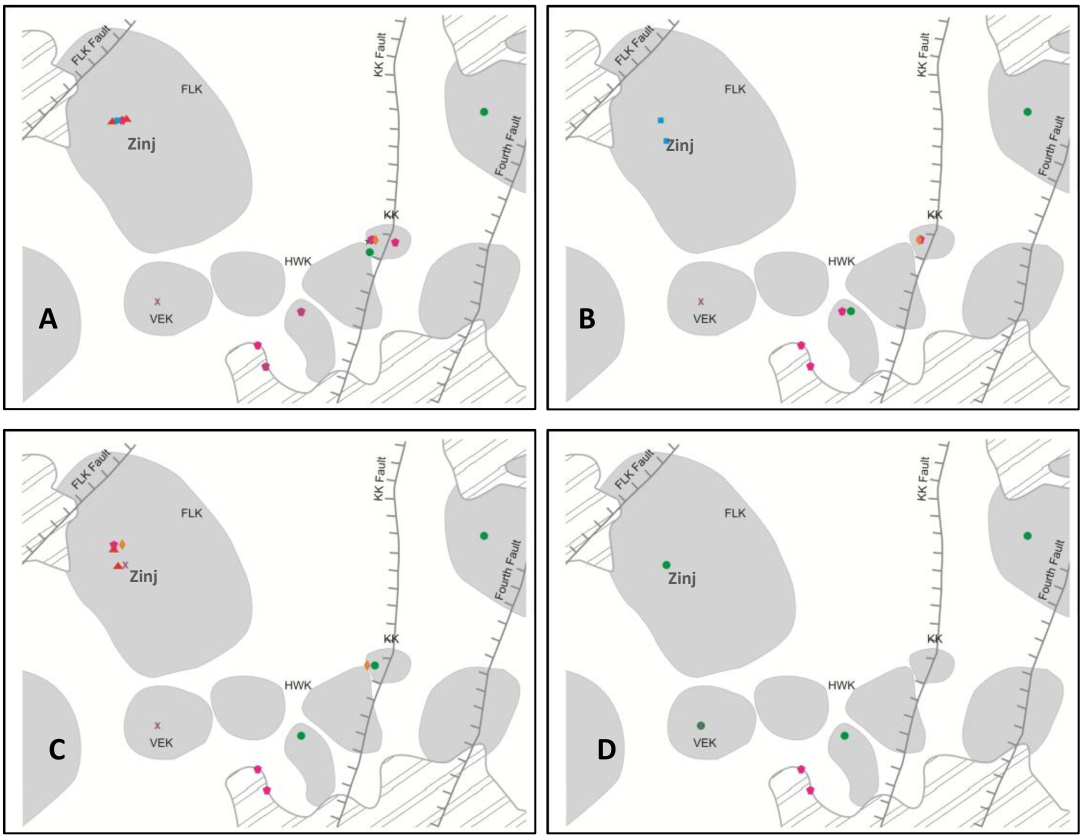

Figure 4-10: The variation of carbonate types at four different horizons above Tuff IF showing a plan view of the levels in Figure 4-8. A) is Parasequence 1, B) Parasequence 2, C) Parasequence 3, D) Parasequence 4. The Blue squares that represent the vadose or palustrine conditions persistently occur on the footwall close to the FLK fault. Whereas the Sparry nodules and the spherulitic clusters that represent the phreatic and vadose/phreatic conditions occur on the hangingwall of the fault block at the VEK, HWK and KK complexes.

A significant change in climate and palaeohydrology above Tuff IF compared to below Tuff IF has been inferred using multiple proxies. The carbon isotope values of pedogenic carbonates have previously been used to interpret a change in vegetation between Bed I and Lower Bed II, changing from closed woodland to grassy woodland at the FLK and HWK (Sikes, 1994). Phytolith analyses of the sediments from lower Bed II at the ELM have identified a pattern of grasses and low shrubs at FLKN, open woodland at HWKE and HWKEE, and a slightly more open grassland at VEK compared to the HWK locations (Bamford et al., 2008). Sparse fossil wood has been reported at HWKE from lowermost Bed II sediments confirming the presence of evergreen fine shady trees and palms recorded at HWKEE indicating a freshwater source (Albert et al., 2009; Bamford et al., 2008).

The pilot study to this project identified a change in carbonate morphology across the ELM using three trenches from FLK, VEK and KK above Tuff IF. This change was interpreted to be due to fault controlled variations in the hydrology of the ELM (Bennett et al., 2012).

4.4.4 Fault control of palaeohydrology and hominin activity

The overall pattern of carbonates indicates that the drier parts of the fault compartment are closest to the footwall and the hangingwall boundaries. Conversely, the water table is closest to the surface in the centre of the fault compartment below Tuff ID, extending towards the eastern part of the fault compartment above Tuff IF. Several factors may affect the location of water in the fault compartment, and so carbonate formation: surface topography, lithological control, and fault control.

The topography of the exposure surface may have influenced the observed hydrological variations. Variations in the availability and the supersaturation of water can be very localised, for example near shallow water bodies subject to evaporation, or near low lying vegetated islands with high rates of evapotranspiration (McCarthy and Metcalfe, 1990; Tooth and McCarthy, 2007). This can potentially cause significant changes to the types of carbonates formed a very short distance apart. However it is unlikely to control long term trends in palaeohydrology.

Basement geology is not reported to greatly control the surface topography at the eastern lake margin post Tuff IB, but the basalt topography is considered to have had some effect up to Tuff ID (Hay, 1976; Stollhofen and Stanistreet, 2011). This is likely to have had an impact on the groundwater hydrology. Where found, the basalt has a highly undulating surface, but because of poor exposure the actual topographic profile is not known beyond the stratigraphic profile of Hay (1976), and so cannot yet be directly related to the palaeohydrological pattern identified using carbonates.

The thickness of Tuff IF varies across the ELM between the FLK and KK faults and has been attributed to synsedimentary fault activity (Hay, 1976; Stollhofen and Stanistreet, 2011). This filling of a faulted topography indicates the size and shape of the accommodation space provided, and so the pre-sedimentation topographic relief (Figure 4-11).

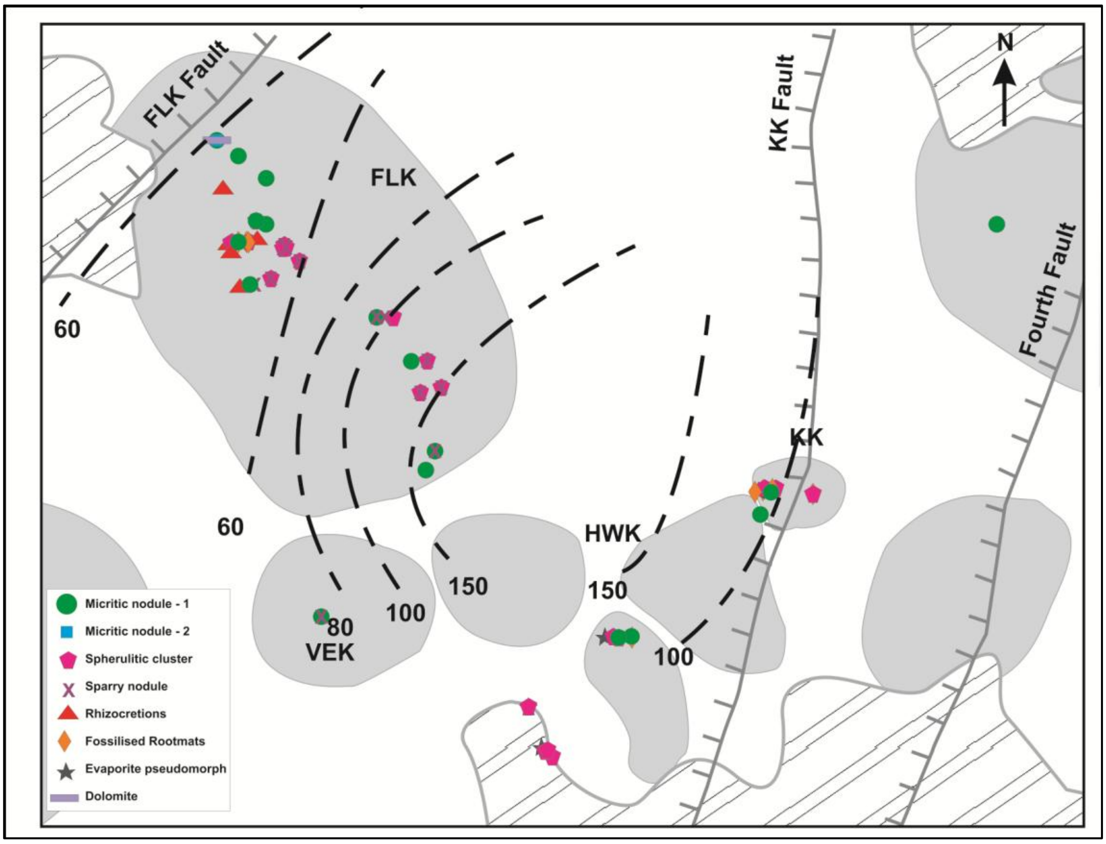

Figure 4-11: Inferred isopachs of Tuff IF at the ELM. Based on Hay (1976) with tuff thickness in cm. The carbonates are from all stratigraphic levels are seen to form clusters of similar types; those representative of vadose conditions (Green, blue, red, orange) close to the FLK and KK fault, where tuff thickness is smallest; and those representative of capillary zone and phreatic conditions (purple and pink) at intermediate tuff thicknesses.

Tuff IF is thinnest at the western most part of the FLK complex, close to the FLK fault, and the depocentre of the fault compartment is at HWK (Figure 4-11) (Hay, 1976; Stollhofen and Stanistreet, 2011). Recent research has shown that the FLK and KK faults were likely to have been active throughout much of the stratigraphic range, possibly as early as Tuff ID (Stollhofen and Stanistreet, 2011). Fault throws were consistently down to the northwest, so during the formation of the carbonates the eastern part of the fault compartment would have been lower, and potentially wetter, than the western part. The pattern of data derived from the carbonates is consistent with this hypothesis, apart from at the very easternmost trenches, next to the KK fault, where the specimens show a change to drier conditions. This indicates a local high not identified using the Tuff IF thicknesses. However, recent work has also identified a topographical high at this point understood to have formed by drag during KK fault displacement (Stanistreet, 2011; Stollhofen and Stanistreet, 2011).

The palaeohydrological pattern shows an increasing dominance in carbonates that formed in the capillary and phreatic zones in the eastern part of the FLK complex upwards through the stratigraphy. This suggests that continuing synsedimentary faulting caused increased uplift of the footwall, moving the depocentre of the fault compartment eastwards through time. The palaeohydrological profile below Tuff IB is comparable to that above Tuff IF, indicating that the fault activity for both the FLK and KK faults were active earlier than documented so far and as early as before Tuff IB.

Hominins are likely to have chosen sites for their activities where there is a good source of food and water, for example lake and river margins, as is seen in contemporary lakes in East Africa (Figure 4-1; Figure 4-2; Figure 4-3). The presence of artefacts and fossils at the same stratigraphic horizon as the carbonates suggests that the carbonates formed in locations compatible with animal activity, as is clearly seen in Lower Bed II where the elephant skeleton and sparry nodules are found together (Figure 2-17). The carbonates will form in the lake system but also in the lake margins and perched lakes and wetlands adjacent to the main lake as seen in the Ngorongoro crater (Figure 4-12), and similar settings may have provided appropriate places for hominin activity during the Pleistocene at Olduvai. The hominins are also expected to have chosen areas with the possibility of refuge, such as in wooded settings (Blumenschine et al., 2011a; Blumenschine and Peters, 1998), to reduce predation risk to themselves and provide them with the greatest opportunity for success. Consequently, the distribution of the artefacts should indicate areas within the palaeolandscape preferred by the hominins, and this in turn is likely to have been driven by the palaeoecology.

Figure 4-12: Lake Makat within the Ngorongoro caldera. The photograph is taken looking down at the lake from the southern side of the crater rim looking north. A vegetated narrow river inlet can be seen running into the lake and a greener patch is from denser grassland where the water table is closer to the surface, either though a spring or perched water table. There is a smaller body of water on the eastern side connected to the main lake by a narrow channel with a small woodland close by. The overall relief is no more than two or three metres.

Hominin fossils and evidence of Oldowan activity from stone tools at Olduvai are most abundant on the footwall of the FLK fault compartment (Blumenschine et al., 2011a). This is seen at Olduvai, where there are stone tools and evidence of flaking debris from their manufacture around the skeleton of a rhinoceros that appeared to have become trapped in mud (Blumenschine et al., 2011a). One of the most famous artefacts at Olduvai, the fossil skull of *'Zinjanthropus boisei',* is found in an area which from sedimentological and palaeobotanical data has been interpreted as an area of dryland adjacent to marshland on one side and a river or spring on the other (Ashley et al., 2010b; Blumenschine et al., 2011b). Lithic artefacts are found with the highest densities on the footwall and the hangingwall, and a reduction in density where the carbonates predict the wettest terrain. The carbonates predict a comparable palaeoenvironmental mosaic to that already understood.

This method provides a new opportunity to contribute to the landscape approach of understanding hominin evolutionary development through an improved knowledge of the palaeoenvironmental drivers to landscape usage.

The carbonates have been shown to provide a valuable proxy for understanding the palaeohydrological conditions at Olduvai Gorge over a range of time and spatial scales. They offer us a very detailed understanding of formation processes at specific locations and stratigraphic horizons. In addition, where multiple locations are robustly correlated, they also provide a larger scale overview of palaeohydrological and palaeoenvironmental development over 100s of metres.

Specifically, they offer us a valuable insight into the evolving palaeohydrology of the FLK fault compartment following each regression of the lake. Superimposed cycles of change in the palaeohydrology have been identified, allowing interpretation of the relative influence of climate and tectonics on the palaeoenvironmental development. The extent of delivery of water to the Olduvai Basin and the extent of lake withdrawal in dry periods is likely to have been largely climate controlled. However this study has shown that the palaeohydrological pattern at exposure surfaces (including hominin exploitation horizons) was strongly influenced by subtle differences in topography controlled largely by synsedimentary tectonic development. This study has shown that faults active before Tuff IB continued to control the hydrology of regressive surfaces for a considerable period of time and at least until after deposition of Tuff IF.

This method offers the opportunity to use carbonates in a new way, to support palaeoenvironmental reconstruction, and to better understand, interpret and predict animal and hominin land use at the overlying land surface. It offers a useful tool for a crude overview of local palaeohydrological conditions during excavation works, which can be supported and enhanced by a detailed examination of specimens to provide a high resolution understanding of palaeoenvironmental conditions.

Carbonates are abundant in semi-arid settings worldwide, and are also found in the sediments of other hominin-bearing archaeological sites in East Africa. This method can potentially be transferred to other sites, and provide a proxy for investigating palaeoenvironment and the influences of climate and tectonics. It also has the potential to be used as a predictive tool, where an understanding of the carbonates in well constrained sedimentary successions, can indicate the most plausible locations for hominin exploitation.

4.5 Conclusions

- The textures and geochemistry of carbonates have been used to interpret the processes of deposition involved in their formation, and so suggest hydrological models for the setting in which they grew.
- Many of the specimens have characteristics of more than one type of carbonate, indicating fluctuations in the dominant processes operating during their precipitation.
- By locating the carbonate types in a sedimentary succession, they can be used to identify subtle details of the palaeohydrology in particular locations, at specific time intervals, and variations in the palaeohydrology through the stratigraphy.
- By correlating multiple sedimentary successions, they can also be used to investigate palaeohydrological trends over larger geographical areas, and how it varies throughout a stratigraphic sequence.
- Because of the likelihood of diagenetic alteration of carbonates, and so the potential alteration of the stable isotope values of a specimen, carbonate textures offer a valuable tool to support palaeoenvironmental reconstruction over different timescales and geographical areas.
- Synsedimentary tectonic development controlled the groundwater hydrology within the FLK fault block, and so strongly influenced the palaeoenvironmental development between the FLK and KK faults.
- The palaeohydrological pattern indicates that the tectonic development of the FLK fault compartment was active below Tuff IB.
- This can potentially be used in the field as a rough guide to the palaeohydrology of the system during archaeological excavation.
- With more detailed analyses, this method could be used as a tool, both at Olduvai Gorge and elsewhere, to infer palaeohydrology, vegetation distribution, and so potential hominin land use.

Chapter 5: The genesis and significance of early diagenetic lacustrine calcite crystals from Olduvai Gorge, Tanzania

5.1 Overview

Euhedral, sand-sized, low-Mg calcite crystals are found almost ubiquitously in the lake-centre clay sediments at Olduvai Gorge. This work investigates the potential for these crystals to be used as dating tools using U-Pb geochronology. The sedimentary succession has been extensively dated using $^{40}Ar/^{39}Ar$ dates on tuffs, and so provides a test bed suitable for development of this technique. Petrographic and geochemical analyse shows the calcite crystals to have formed in anoxic to sub-oxic, shallow sub-surface, lake basin sediments, either by recrystallisation of micritic grains, from an evaporite mineral precursor or by direct precipitation of calcite. The crystals have unusually high concentrations of uranium, up to ~120ppm, and very low concentrations of common lead. The crystals display cathode-luminescence sector zoning, and elemental concentrations are strongly partitioned in discreet sectors. The preferential incorporation of uranium in the prismatic sectors of crystals rather than the rhombohedral equivalent means that individual crystals have a wide range of elemental concentrations and U/Pb values. Individually the crystals therefore have the potential to be used to generate isochrons and provide a novel tool for dating Pleistocene-age sediments.

5.2 Introduction

Palaeolake Olduvai (Figure 5-1) was saline, alkaline and hydrologically closed (Hay, 1976), and euhedral calcite crystals, ~0.5mm to 2mm long, are present almost ubiquitously in the lake-centre sediments.

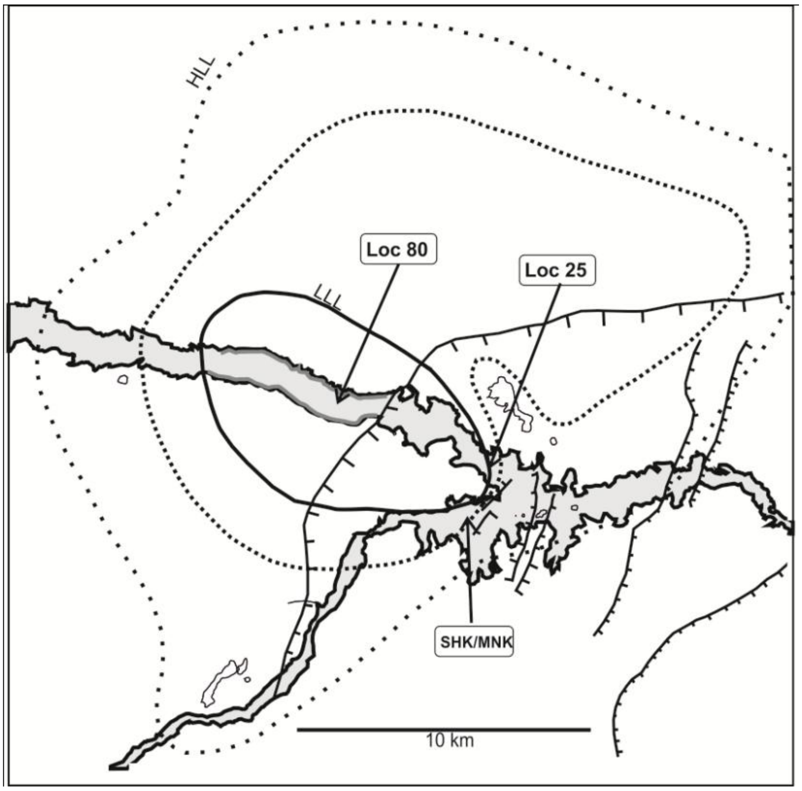

Figure 5-1: Olduvai Gorge, Tanzania, East Africa, showing calcite crystal sample locations Olduvai Gorge, is identified in grey. The positions of major faults are indicated by lines with ticks on the downthrow side. The outcrop of the central lake basin sediments are identified as the darker grey area. The variable extent of Palaeolake Olduvai is identified as LLL (Low lake level) and HLL (High Lake level) using the palaeogeographical reconstruction immediately above Tuff IF (Hay, 1976). The calcite crystals sampled for this study were taken from Loc 80 (also known as 'Richard Hay Cliff' – or RHC) and Loc 25. Site SHK/MNK identifies the westernmost location of Tuff IIA prior to loss through erosion by the overlying Augitic Sandstone.

In the course of this study similar crystals have also been discovered in the sub-surface shoreline sediments of contemporary Lakes Ndutu, Makat and Natron, Tanzania (Figure 5-2). The purpose of this study is to use the mineralogy, crystal texture, trace elements, and the carbon and oxygen stable isotope compositions of the calcite crystals in Bed I and Bed II, between 2Ma and 1.4ma, to investigate the genesis of these enigmatic crystals and the potential for dating them using U-Pb analyses.

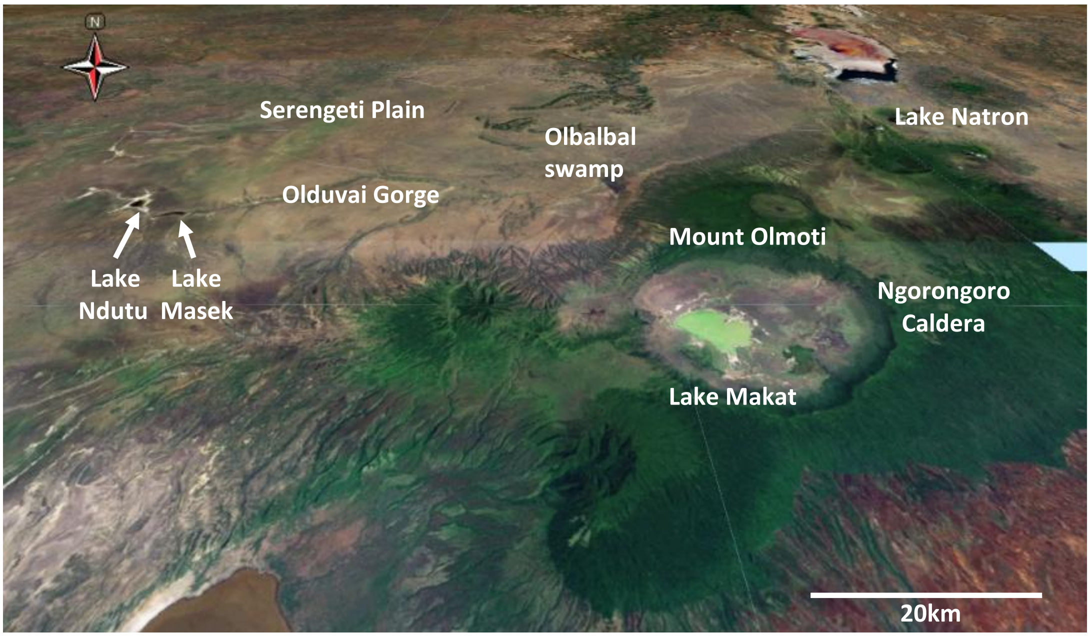

Figure 5-2: Satellite image of the modern lakes sampled for water and shoreline sub-surface sediments (Google Earth 2010). Lake Ndutu and Lake Masek are hydrologically open and the catchment area is from the Serengeti Plain. The Olbalbal Swamp, Lake Makat and Lake Natron are all hydrologically closed, but with different catchments. Lake Makat. is within the Ngorongoro Caldera, the Olbalbal Swamp is on the western edge of the caldera, and Lake Natron is within the East African Rift system.

5.3 Geology

Palaeolake Olduvai formed in a shallow, rift shoulder basin on the edge of what is now the Serengeti Plain, supplied by fluvial delivery draining from the alluvial fan to the east and from the craton in the west (Hay, 1976). Similar to many lakes in the region today palaeolake Olduvai has been interpreted to have been saline with a high pH of ~9.5-10 (Hay and Kyser, 2001). The lake appears to have been persistent and from stratigraphic considerations likely no more than a few metres deep, perhaps up to 10 metres at highstands (Hay, 1976). The lacustrine sediments are primarily olive-green, waxy, Mg-rich smectite and interlayered illite/smectite clays derived largely by alteration of volcaniclastic material by reaction with the saline, alkaline lake water, and partially from unaltered detrital material (Deocampo et al., 2002; Hay and Kyser, 2001; Mees et al., 2007). In addition, the lake basin trapped episodic influxes of the volcaniclastic deposits are used to correlate the stratigraphy across the gorge. This depositional complex produced a unique stratigraphy of interbedded lake sediments, sandstones and tuffs, and provided host sediments for the authigenic precipitation of carbonates (Figure 5-3).

The modern lakes selected for this study represent potential analogues to Palaeolake Olduvai. Lake Natron, Lake Makat and the Olbalbal swamp are hydrologically closed. Lake Ndutu and Lake Masek are partially closed, as they supply the Olduvai River during the rainy season. They are all saline and alkaline but have differing bedrock geologies and catchment areas.

Lake Ndutu and Lake Masek are on the Serengeti Plain and are supplied by springs and river water sourced from the Tanzanian Craton. The Tanzanian Craton is Achaean and comprises a complex set of terranes of metasediments intruded by granites and subsequently migmatised (Dawson, 2008). The eastern Rift Valley developed along the western edge of the Mozambique Fold Belt, an elongate north-south orientated orogen of Achaean to Palaeoproterozoic age (Dawson, 2008). Lake Natron is located in northern Tanzania within the eastern rift valley and is supplied from springs and several small rivers with the main input from the Ewaso Ng'iro. To the south of Lake Natron is the volcano Oldoinyo Lengai which episodically deposits carbonatitic ash across the lake and across the Serengeti Plain (Hay, 1976). Lake Makat in the Ngorongoro Caldera is supplied by springs through the volcanic complex and by the River Munge draining from the Mount Olmoti crater to the north. The Olbalbal Swamp is on the western flank of the Ngorongoro Caldera and is supplied seasonally by the Olduvai River draining from western Lake Masek and Lake Ndutu across the Serengeti Plain. It is an ephemeral wetland and was unusually host to a standing water body when sampled in summer 2010.

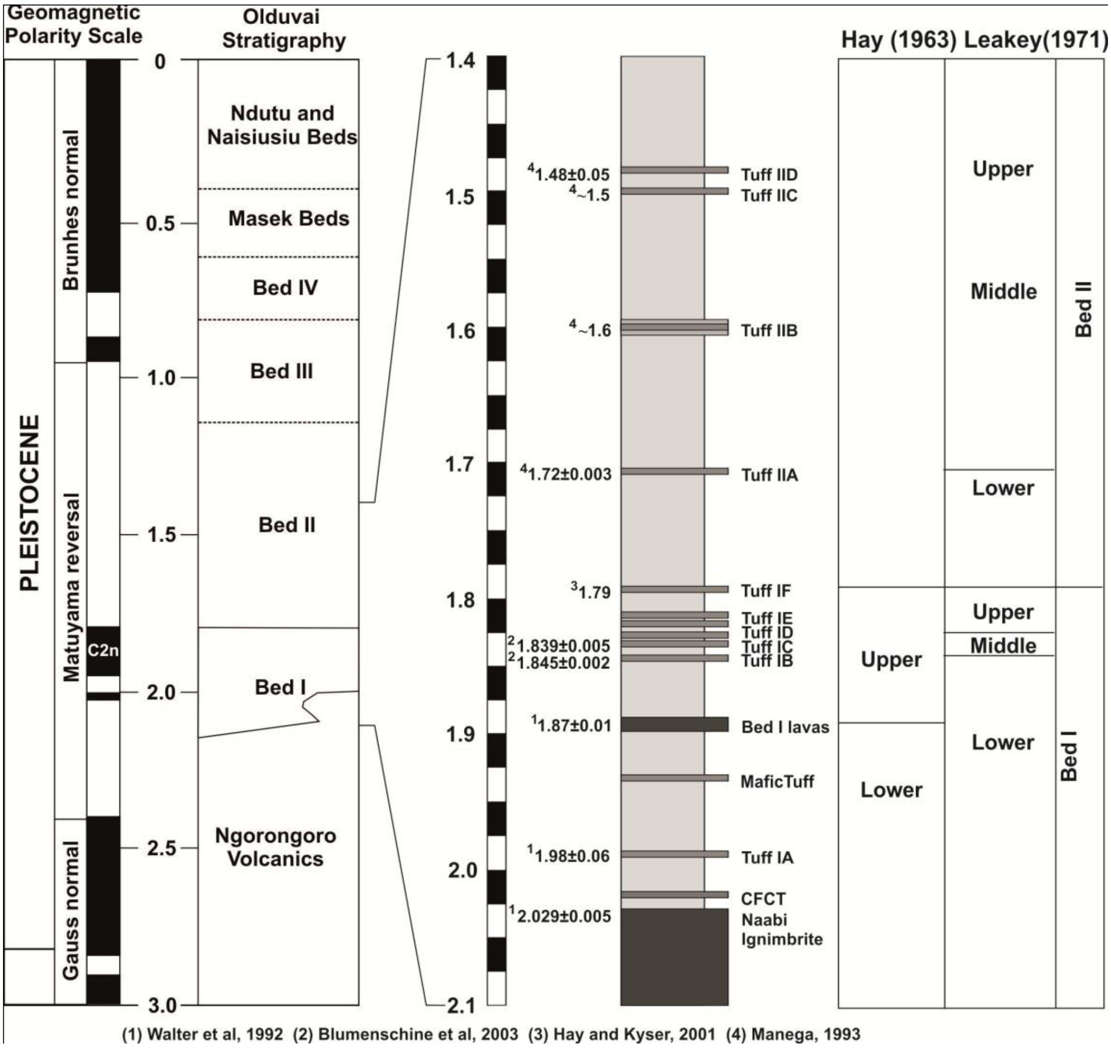

Figure 5-3: Generalised stratigraphy of the Olduvai beds (Stollhofen et al., 2008) including archaeological and geological bed divisions for Bed I and Lower Bed II (Hay, 1976; Leakey, 1971; Stollhofen et al., 2008). The present study is focussed on the stratigraphy between ~2.0Ma and 1.4Ma. The generalised stratigraphic succession comprises interbedded clays, sandstones and volcanic sediments. Published dates were all determined using $^{40}Ar/^{39}Ar$ single crystals analyses of tuffs apart from Tuff IF which is defined by the base of the Olduvai Subchron. 1) (Walter et al., 1992), 2) (Blumenschine et al., 2003), 3) (Hay and Kyser, 2001), 4) (Manega, 1993).

5.4 Materials and methods

5.4.1 Sampling and analysis of calcite crystals

Clay containing calcite crystals at Olduvai Gorge was collected at eight levels in the Bed I and Bed II sediments from two locations in the palaeolake basin, Loc 25 and Loc 80. Because the lake level is understood to have repeatedly fluctuated on a variety of frequencies, the aim was to collect an extensive spread of samples throughout the stratigraphy of Bed I and Bed II to assess any potential morphological, textural and geochemical variations. Samples of modern lake shoreline sediments were taken from five contemporary lakes during August 2010 to identify the presence of calcite crystals and assess their similarity to the Early Pleistocene specimens. A volume of sediment approximately 10cm x 10cm x 10cm was taken from ~10cm below the surface and within 2m of the shoreline (on the day of sampling).

Where the (dried) sediments containing the crystals were friable and crystals large enough to clearly see with the naked eye, tweezers were used to separate them. Where the clay sediments were more indurated or the crystals were too small to easily see with the naked eye, the clay sediments were washed with distilled water and the grains filtered through a 0.25mm sieve. After air drying, the individual crystals were separated from other mineral grains using a binocular microscope and tweezers. The individual crystal batches were cleaned in de-ionised water for 15 minutes in an ultrasonic bath at room temperature; dried, separated from any remaining clay and washed and dried again.

Standard polished 30µm thin sections, impregnated with blue resin, of calcite crystals in their clay matrix were prepared (University of Birmingham). Whole crystals were set in resin (Buehler Epxoicure Resin (20-8130-128) and Hardener (20-8132-032)) and each mount was ground using wet SiC paper from 800 to 2400 and finally 2micron alumina suspension. Crystals were examined using transmitted light microscopy and cathode-luminescence.

Scanning electron microscope investigations, using Secondary Electron (SEM-SE) and Backscatter (SEM-BS) detectors, were performed on carbon-coated thin sections and polished mounts and on gold coated whole crystals using a Phillips XL30 Scanning Electron Microscope fitted with Oxford Instruments Energy Dispersive X-Ray analysis (EDX).

XRD analysis was performed on samples from each of the different stratigraphic levels to identify their mineralogy and any change through the sequence. Multiple, whole crystals were carefully crushed using an agate mortar and pestle to produce enough material for analysis. Samples sizes of a few mg were analysed using a specially made small sample holder. Carbonate mineralogy was determined by X-ray diffraction (XRD) using a Siemens Kristaloflex with a scanning speed of 5 seconds per $0.2^{o}2\theta$ between 24 and 55 $^{o}2\theta$ (CuKα).

Specimens selected for stable isotope analysis were washed in deionised water and air-dried. Multiple crystals from each level were combined to produce a sufficient quantity of sample for analysis. They were ground in an agate mortar and pestle to produce a fine powder. Carbon and oxygen stable isotopes values of calcites were determined on 3mg samples using a VG Sira mass spectrometer by reaction in an online phosphoric acid in Isocarb unit at 90^{o}C. Data were corrected using standard procedures and reported in δ ‰ (VPDB) with a reproducibility of better than ± 0.1‰ for $\delta^{18}O$ and $\delta^{13}C$. Five analytical samples, each composed of several crystals from a single level (RHCII CA7) were analysed to investigate variation at a single level. Because the variation between the samples was low, single analytical samples composed of several crystals, were analysed from each of the other stratigraphic levels.

Laser ablation ICP-MS of calcite crystals in polished mounts was performed at the University of Aberystwyth using a Thermofinnigan Elements2 ICP-MS with a Lambdaphysik complex pro MicroLAS 193 Ar-F Excima gas laser. 10µm diameter circular spot sizes were ablated using a fluence of 5J/cm^2 and a 5Hz rep rate. Rare earth element data was normalised to North American Shale (NASC) (Gromet et al., 1984). Solution ICP-MS of whole calcite crystals was performed at the University of Aberystwyth using a Thermofinnigan Elements2 ICP-MS. The samples chosen were those previously analysed in chapter 7. Individual crystals were chosen because they are representative of the size, shape and colour of all of the isolated specimens from each level. Four from each level were chosen to investigate the age and geochemical variation between samples. Four horizons within Level 3 (resulting in sixteen crystals at this level) were chosen to investigate the variation within a level and so the potential age resolution.

5.4.2 Sampling and analysis of modern lake water

Samples of the lake water were taken at the same time as the modern lake calcite crystals were sampled. Conductivity, temperature and pH were measured at the time of sampling, and then ~2000mls of water was transferred to the laboratory using a water bottle previously flushed out twice with lake water. The water was filtered on the same day as collection to remove particulates and bacterial and organic matter, before storage and transfer to the UK. The water was filtered through a 0.2µm Sartobran© 300 filter and stored in a HDPE screw top bottle that had previously been prepared at Liverpool by washing with Reagent Grade nitric acid and de-ionised water and rinsed twice using the filtered lake water. It was not possible to refrigerate the samples until return to the UK approximately 1 month after sampling, although the filtration should have removed both bacterial and algal material. Following return to Liverpool the water was refrigerated, and up to 12 months later no algal growth was apparent on visual inspection. The cation, anion and trace element analyses of modern lake water were performed at the University of Aberystwyth. Trace elements were determined using Solution ICP-MS using a Thermofinnigan Elements2 ICP-MS. Analysis of the $\delta^{18}O$ of the lake water was not successful due to the high concentrations of salts.

5.5 Early Pleistocene calcite crystals

Samples for this study have been selected from clay beds at four different stratigraphic levels, three at Loc 80 and one at Loc25 (Table 5):

- Lower Bed I (Loc 80) from one sampling level between Tuff IA and Tuff IB(Figure 5-4);
- Upper Bed I from two sampling levels between Tuff IE and Tuff IF (Figure 5-4);
- Lower Bed II, from four sampling levels between Tuff IF and the erosion surface at the base of the augitic sandstone unit (Figure 5-4);
- Upper Bed II (Loc 25), at one sampling level between Tuff IIC and Tuff IID. The sample from Loc 25 was in a clay bed immediately below Tuff ID, located on the sedimentary log published in Hay (1976).

Sample identification	Location	Stratigraphic level
2010 LOC25	Loc 25	Upper Bed II
2009 RHCII CA7	Loc 80	Lower Bed II
2009 RHCII CA6	Loc 80	
2009 RHCII CA5	Loc 80	
2009 RHCII CA3	Loc 80	
2009 RHCI CA10	Loc 80	Upper Bed I
2009 RHCI CA7	Loc 80	
2010 RHC I CA104	Loc 80	Lower Bed I

Table 5: Calcite crystal sample locations. sample identification codes for each sample level, and their corresponding stratigraphic level named after the geological and archaeological sites (Figure 5-3). Four crystals were sampled from each sampling level. Two sampling levels were used within Upper Bed I and four within Lower Bed II. One sample level was used in Lower Bed I and One in Upper Bed II.

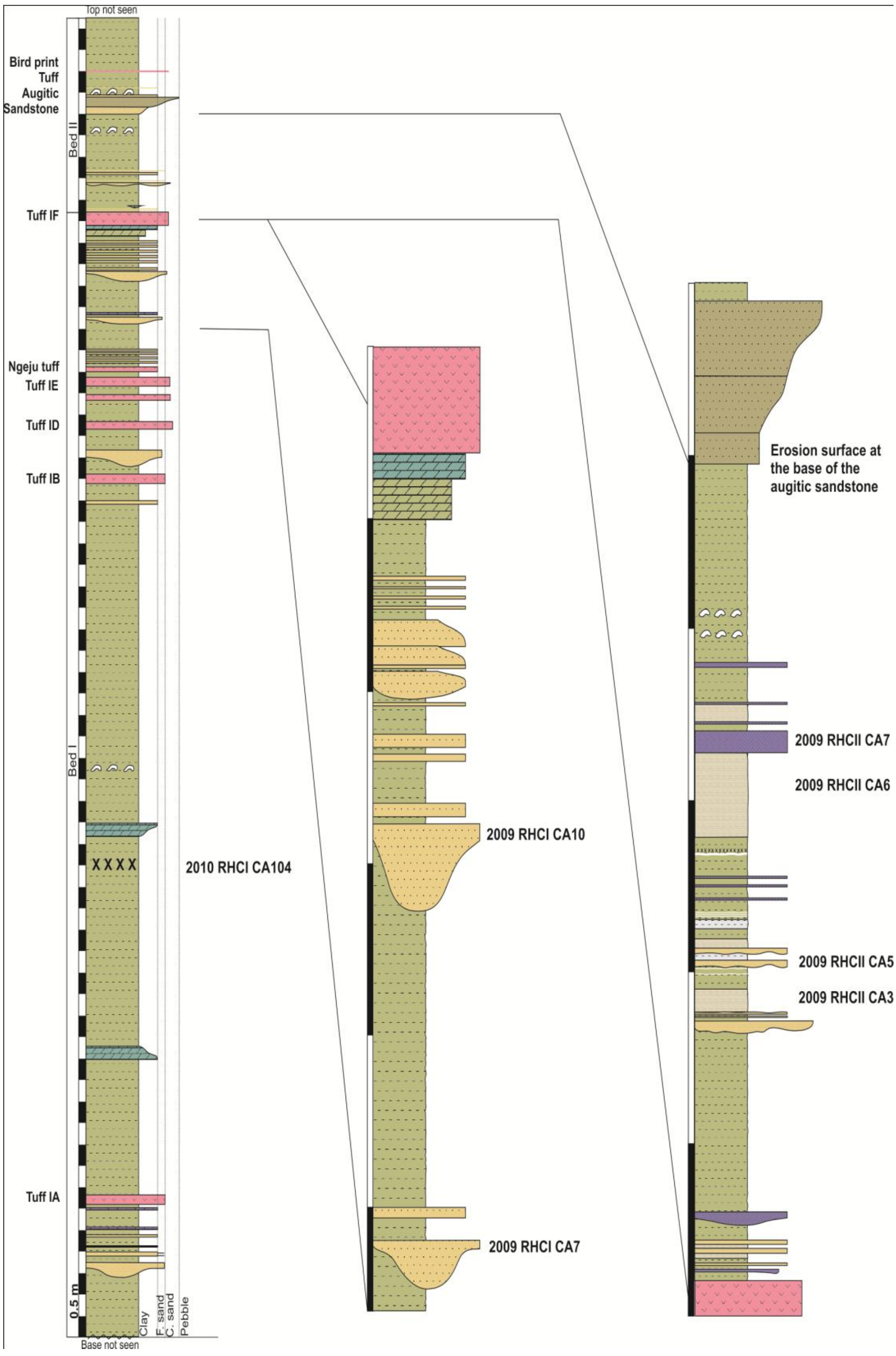

Figure 5-4: Sedimentary log of Loc 80 with calcite crystal sampling locations identified by specimen numbers. The scale bars are 0.5m. Olive green waxy clay (green), Volcanic deposits (pink), Augitic sandstone (brown), Sandstone (yellow), Dolomite (blue), Calcite (purple), Pale buff waxy clay (buff).

The sedimentological setting of the calcite crystals varies with sampling level and location. They occur either; a) dispersed through the clay with no apparent preferred orientation or consistent distance between crystals, b) as concentrations of crystals in thin beds which often have shallow erosional bases and laminae of crystal rich and poor clay (Figure 5-5a,b) forming groups of arching sprays ~ 6cm high originating from the base of the clay (Figure 5-5c,d).

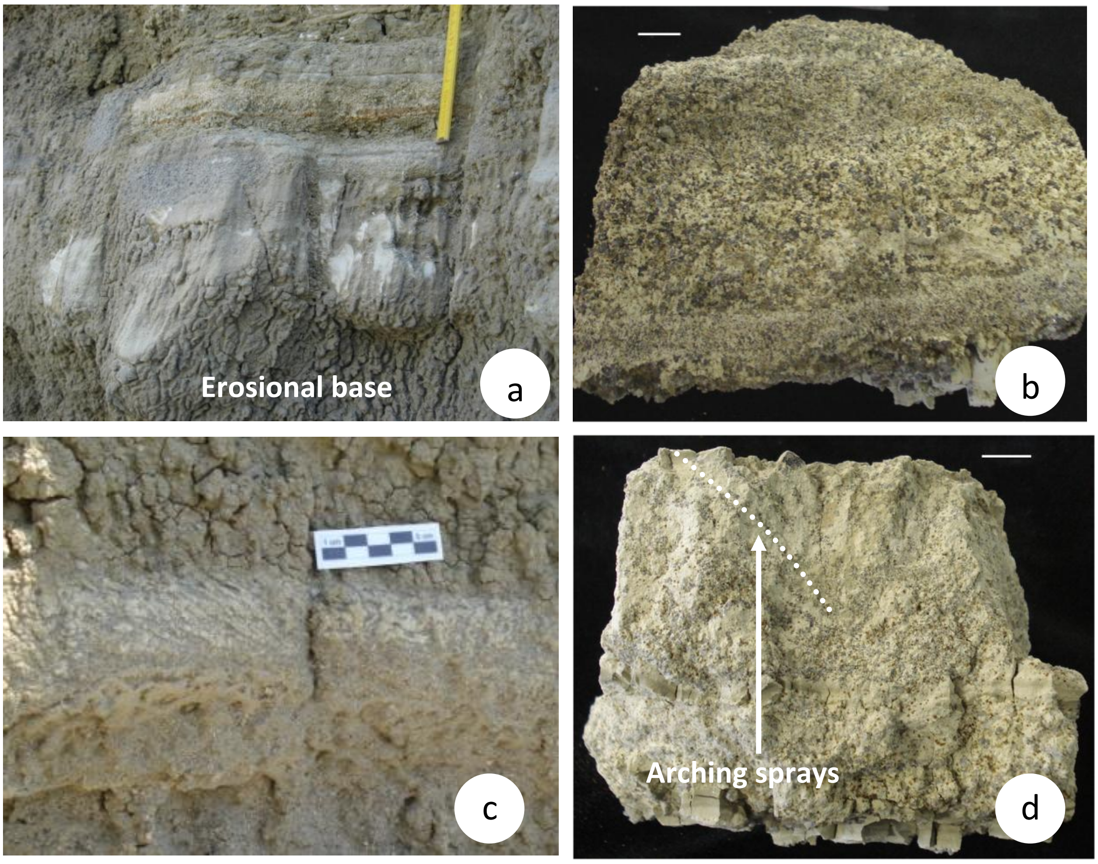

Figure 5-5: Photographs of calcite crystals occurring in different ways in the sediments : a) shows the field scale view of concentrations of calcite crystals in beds with an erosional base (Rule is 20cm long) (RHCII CA7) and b) a hand specimen of the calcite crystal bed in (a) showing clay rich and poor laminations of calcite crystals (scale bar 1cm). c) shows the field scale view of groups of arching sprays formed by calcite crystals originating from the base of the clay bed (Scale in cm)(RHCII CA3) and d) is a hand specimen showing the crystals (darker grey) forming radial linear arrays (scale bar 1cm).

5.5.1 Morphology and Petrography

Crystals lowest in the sequence (RHCI CA104) vary in size between ~1mm – 2mm long; they are euhedral, scalenohedral, opaque white, and are dispersed in the clay (Figure 5-6a). The crystals are composed of multiple rhombic calcite sub-crystals arranged with a step-like fabric producing an irregular external morphology. Unlike the calcite crystals from all other levels there are no enveloping euhedral calcite overgrowths. The pattern of brightness in cathode-luminescence differs from all the other levels. The centres of the crystals are orange and high brightness and have a diffuse boundary with the outer crystal which is dull to non-luminescent. The very outer edges of the crystals sometimes have a very thin zone of orange high brightness luminescence (Figure 5-6b).

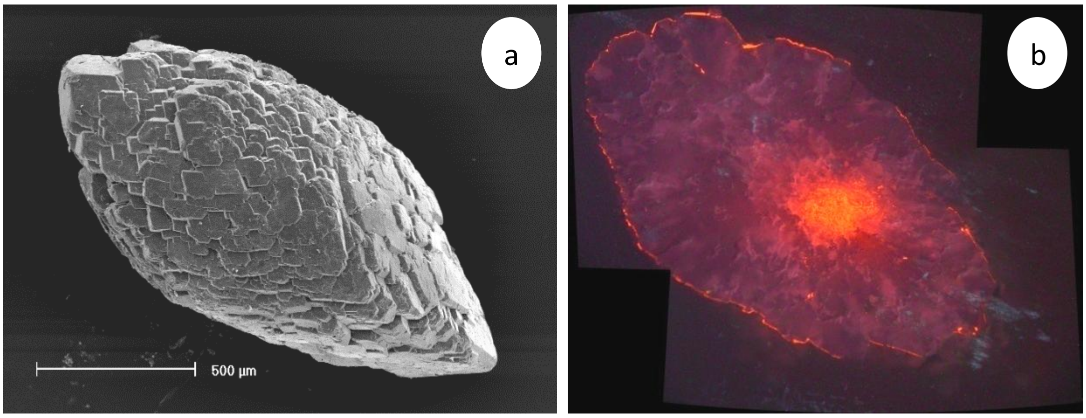

Figure 5-6: SEM-SE and CL photographs of calcite crystals from sampling level RHCI CA104 ; a) SEM-SE photograph shows crystals are scalenohedral are composed of multiple rhombic calcite crystals arranged with a step-like fabric arranged producing an irregular external morphology and no euhedral calcite overgrowth. b) using cathode-luminescence. Crystals are ~2mm long.

Crystals from higher in Bed I (RHCI CA7, RHCI CA10), and Bed II at both locations (RHCII CA3, RHCII CA5, RHCII CA6, RHCII CA7 and Loc 25), are euhedral and translucent grey/green to colourless ranging from approximately 2mm to 0.25mm long or smaller (Figure 5-7). Crystals from RHCI CA7, RHCI CA10, and RHCII CA7 are found in laminated, calcite crystal rich beds, with an erosional base. Those from RHCII CA3 and RHCII CA5 are found in arching sprays; and those from RHCII CA6 and Loc 25 are found dispersed in the sediment. The crystals have previously been described as having scalenohedral side faces of the form [8.4.12.1], and end faces of unit rhombohedra of the form [1011] (Hay, 1976). The crystals examined for this study show no convergence to the c-axis either in the whole crystal SEM-SE image or in the CL zoning pattern, and have prismatic side faces with rhombohedral terminations. In a few cases the centres of the crystals are hollow with the outer, euhedral part intact (Figure 5-7), although these form the minority of samples. The crystals are found individually or as clusters of multiple, intergrown, crystals.

Individual crystals often have several, smaller, non-epitaxial crystals intergrown with them. All but one sampling level have both clusters and individual crystals. Level RHCII CA6, however, only has individual crystals commonly 1-2mm long dispersed in the clay sediments.

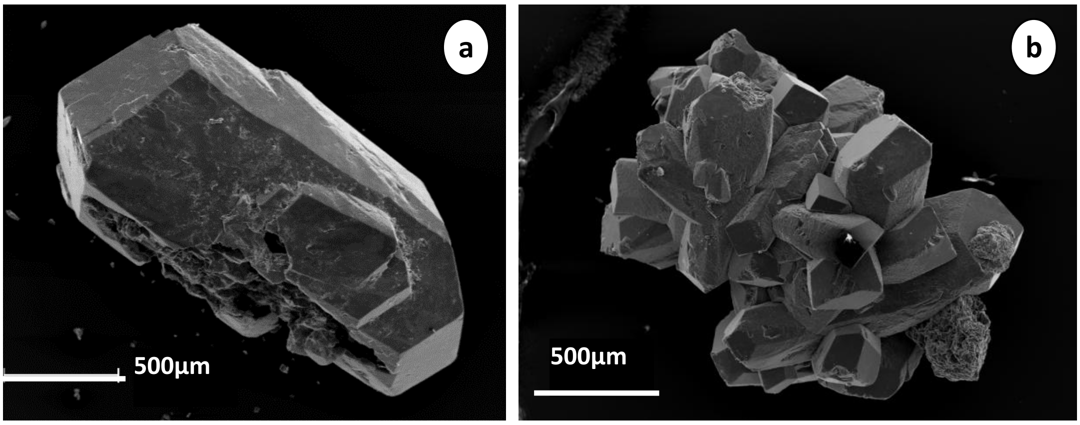

Figure 5-7: SEM-SE photograph of calcite crystals from upper Bed I and Bed II showing external morphology ; a) Individual calcite crystals with smaller crystals developed along a prismatic side face (2009 RHCII CA7, Loc 80). The centre of the crystal is hollow. b) Cluster of intergrown crystals (2009 RHCI CA7, Loc 80).

In thin section, the calcite is colourless, transparent, and non-pleochroic, and has non-undulose extinction under crossed-Nichols. The crystals have patches of inclusions which are often, but not always, concentrated in their centres (Figure 5-8a). In some cases there are discontinuous concentric bands of inclusions part way between the nucleus and the edge of the specimen defining two growth bands. Inclusions that are visible using SEM-BS were analysed using EDX and have high Al, Si, Mg and K peaks consistent with clay particles.

The CL images show a complex pattern of concentric, sector and intra-sector zoning (Figure 5-8b,c). In many of the individual crystals, the CL defines two pairs of non-equivalent sectors, one with bright to dull luminescence and one with dull to no luminescence (Figure 5-8b). A comparable morphology of calcite crystal growth and pattern of zoning under cathode-luminescence has been identified in sparry calcite cements (Hendry and Marshall, 1991a; Hendry and Marshall, 1991b) (Figure 5-9). The two brighter CL sectors are opposite to one another and form the prismatic faces of the crystal, and the two less bright areas form the terminal or rhombohedral faces of the crystal (Figure 5-9).

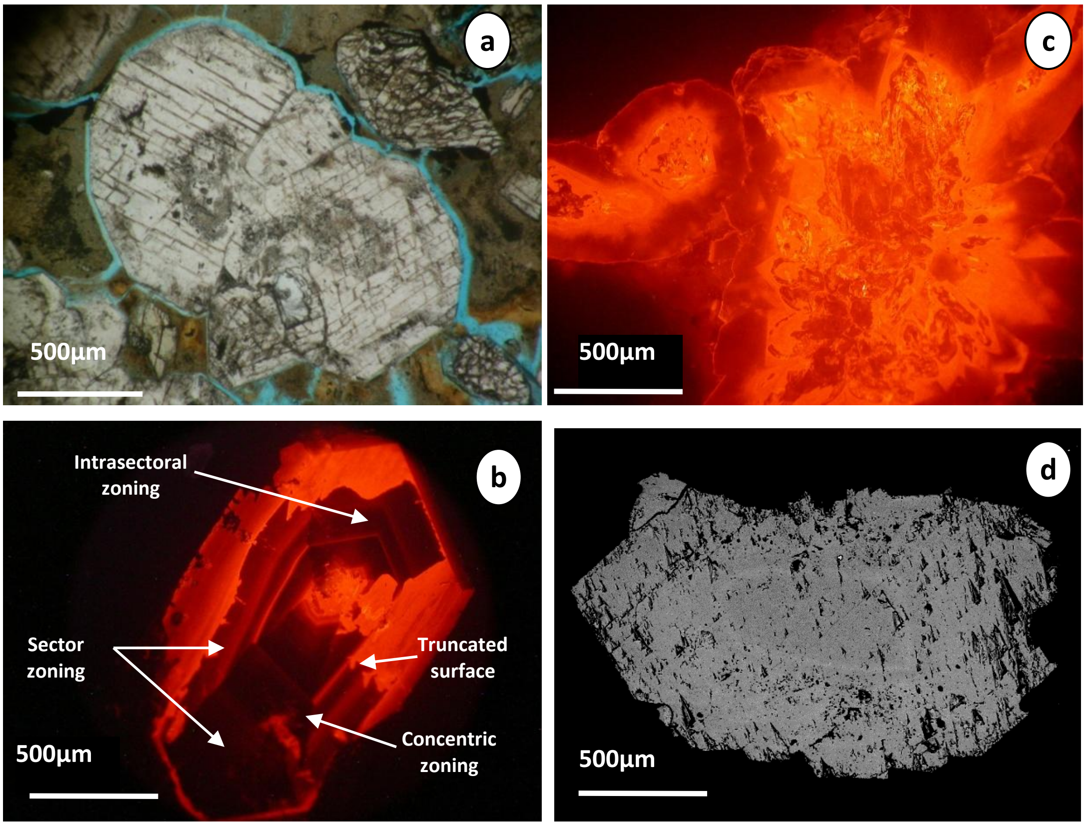

Figure 5-8: Photomicrographs of calcite crystals from Loc 80 and Loc 25 ; a) a thin section of multiple, intergrown, calcite crystals in clay matrix. Inclusions are concentrated in the centres of the crystals and there are discontinuous bands of inclusions partway between the centre and the edge of the crystals; b) a CL photograph of a single calcite crystal from sampling level RHCI CA5 showing concentric, sector and intra-sector zoning and truncated surfaces; c) a CL photograph of a cluster of intergrown crystals showing complex zoning defined by multiple intergrown crystal faces and truncated growth surfaces; d) an SEM-BS photograph image of a single crystal showing contrasting back-scatter intensity attributed to element zoning. The lighter grey bands have detectable Mn using EDX and the darker bands have Mn below detection limits of the instrument.

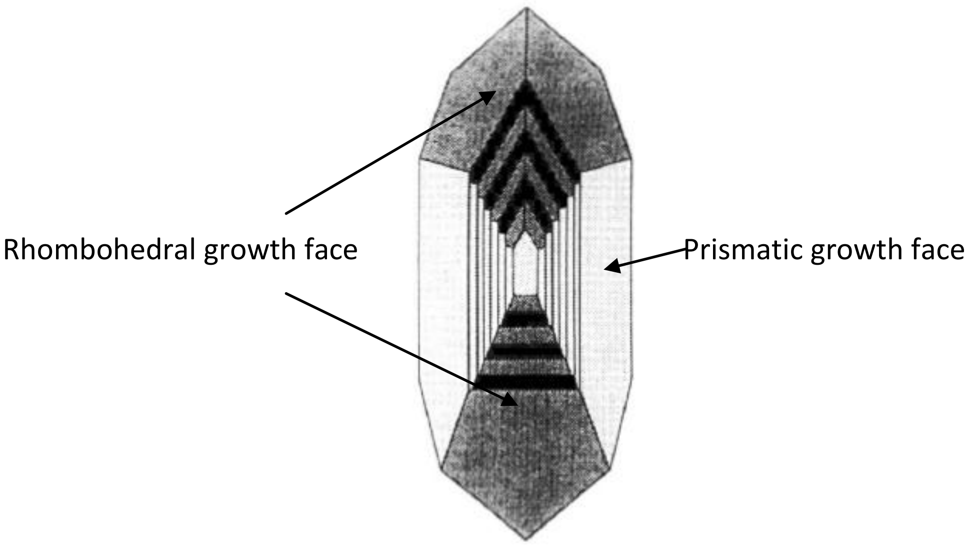

Figure 5-9: crystallographic interpretation of non-concentric zoning pattern (Hendry and Marshall, 1991b). The calcite crystals are interpreted to have grown on two compositionally different faces, one rhombohedral and one prismatic. The calcite crystals from Olduvai have a similar structure, and the prismatic faces exhibit brighter luminescence than the rhombohedral faces.

In some cases, intrasectoral zoning is seen in the concentric bands of the rhombohedral sectors. The calcite crystal clusters have a series of alternating bright orange and dull luminescent bands which are often truncated or discontinuous (Figure 5-8c). The bands are most truncated in the centre of the crystal and become increasingly more euhedral towards the outer part of the crystal cluster. The outermost band of calcite is often continuous and envelopes multiple crystals in the cluster. The zonation pattern formed in the clusters of intergrown crystals (Figure 5-8c), is often found in the centres of each of the single crystals, where it is subsequently overgrown by concentrically zoned euhedral calcite (Figure 5-8b), potentially demonstrating a two stage process of crystal formation.

The concentric zonation is also identifiable in some samples using SEM-BS (Figure 5-8d), and EDX analysis shows trace variations in Mn levels between zones of different brightness. Thin sections of the clay beds containing calcite crystals also contain a cubic phase which appears to have formed later than the calcite, shown where its euhedral shape is compromised when it meets a calcite crystal. The mineral has dominant iron and oxygen peaks using SEM-EDX which is consistent with haematite replacing original pyrite.

5.5.2 Trace element analysis of whole crystals using ICP-MS

Trace element analysis was carried out on four samples of whole crystals from a single sampling level In Bed II, RHCII CA6, using solution ICP-MS (Appendix 7) Levels of magnesium ranged from just over 850ppm (0.35 mol% $MgCO_3$) to over 4500ppm (1.87 mol% $MgCO_3$) which is consistent with it being 'low-magnesium' calcite. There are significantly higher values of manganese compared to iron in all the samples, with Fe values ranging from ~400ppm to ~680ppm and the Mn values from ~570ppm to ~3600ppm with Fe/Mn ratios ranging from 0.11 to 0.74. The samples also have strontium values which range from ~730ppm to ~1100ppm and barium values between ~200ppm to ~260ppm (Figure 5-10).

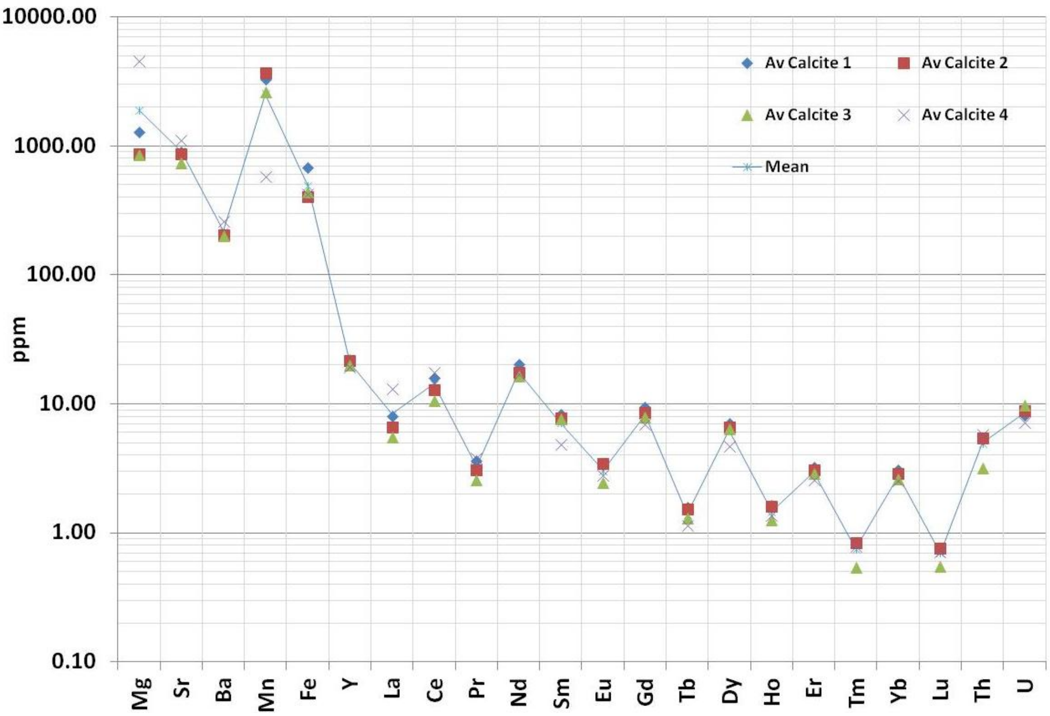

Figure 5-10: Trace element concentrations (ppm) for four crystals from 2009 RHCII CA6, Loc 80, determined by solution ICP-MS. The mean abundances of the four crystals is shown by the blue line. LREE (La - Nd) are more abundant than HREE (Sm - Lu). Non-lanthanide trace elements are most abundant. Mn is greater than Fe in all crystals. Uranium concentrations in the crystals are high, up to nearly 10ppm.

The lighter rare earth elements (LREE), La to Nd, are present in quantities up to 20ppm and are always greater than the heavier rare earth elements (HREE), Sm to Lu, which are each present only to about 9ppm (Figure 5-10). The higher abundance of the LREE's compared to the HREE, and the zig-zag pattern of higher abundance of elements with an even atomic number, is consistent with other natural samples (Rollinson, 1993).

When the REE data was normalised to NASC, however, the pattern of data appears to show relative enrichment in HREE compared to the LREE and, significantly, no major excursion of the redox sensitive elements, Ce and Eu (Figure 5-11). However, because the line has a zig-zag shape, this interpretation is not unequivocal, and the same pattern of data could be interpreted as having a small negative Ce anomaly and a small positive Eu anomaly.

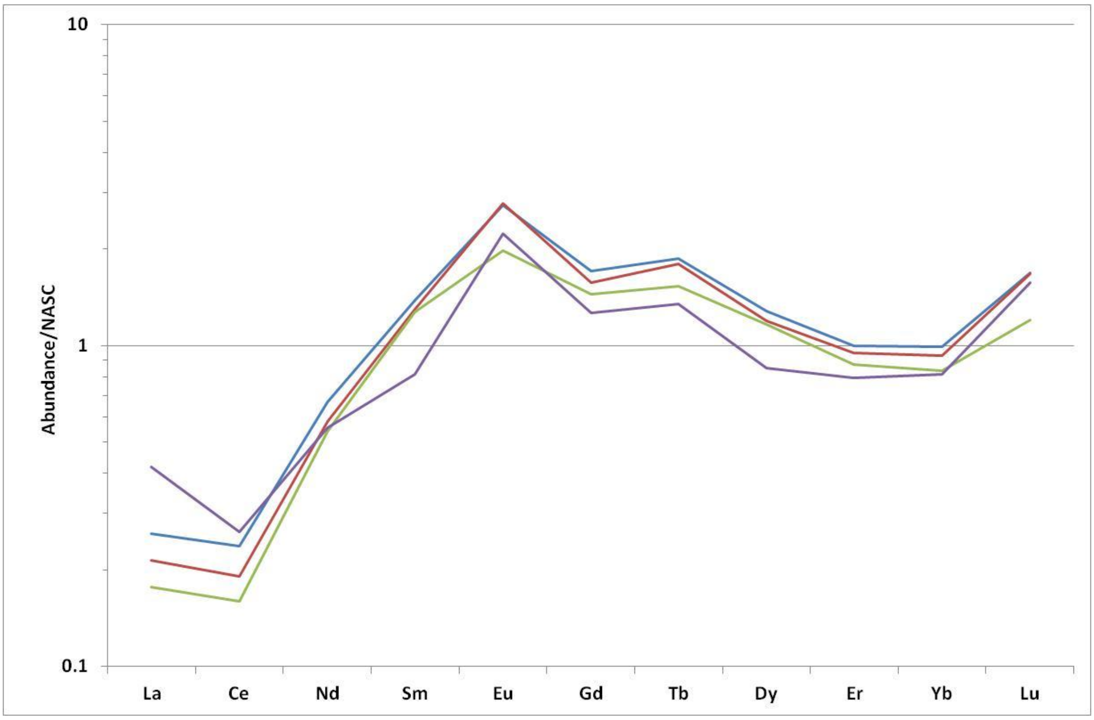

Figure 5-11: REE concentrations of whole calcite crystals (2009 RHCII CA6, Loc80) normalised to NASC (Gromet et al., 1984). In all cases, HREE (Sm - Lu) are enriched relative to LREE (La - Nd). However, the slightly zig-zag shape of the lines may indicate a small positive Eu anomaly and a small negative Ce anomaly.

5.5.3 Trace element analysis using laser ablation ICP-MS

Four crystals, set in polished mounts, from each of the eight sampling horizons, were used for U-Pb geochronology analyses at the NERC Isotope Geosciences Laboratory (NIGL), BGS, Keyworth (results in Chapter 7) before trace element analysis at Aberystwyth. The locations for trace element laser ablation analyses at the University of Aberystwyth (Appendix 8) were targeted on the ablation pits from the geochronology analyses to provide a direct correlation between the two data sets. The laser ablation spots were located on the CL images for each crystal, and the trace element concentrations for each spot were characterised by CL brightness, positions in the sector zoning where this was clearly defined, and stratigraphic level, to investigate patterns of trace element incorporation in the crystal.

The concentrations of magnesium in all crystals ranged from just over 30ppm (0.01 mol% $MgCO_3$) to just over 10,000ppm (4.26 mol% $MgCO_3$) with an overall mean of 2100ppm (0.86 mol% $MgCO_3$). This is consistent with them being low-magnesium calcite. However, the mean abundance of magnesium in crystals from RHCI CA104, the lowest stratigraphic level in Lower Bed I, is significantly higher than those crystals higher up in the stratigraphy, with a value of ~5900ppm (2.44 mol% $MgCO_3$). This is still consistent with a 'low-Mg' calcite but shows a variation in the composition, and potentially lacustrine Mg/Ca ratios during formation, compared to crystals from the three other stratigraphic levels. Conversely, the amount of Mn was much less in the lowest stratigraphic level than seen in the three upper levels, with a mean concentration of ~80ppm compared to the mean concentrations of the other three levels of between ~1900ppm to ~5500ppm. The crystals also have strontium values which range from ~220ppm to ~6000ppm and barium values between ~12ppm to ~2200ppm which have similar mean values at all stratigraphic levels.

Fe/Mn ratios

The Fe/Mn ratios are affected by element availability and by the redox state of the pore waters during calcite precipitation. Only three of the sampling levels (2009 RHCII CA3, RHCII CA5, RHCII CA6), from the lower part of bed II, provide information about concentrations of Fe, due to poor detection limits for the minor iron isotopes measured on the LA ICP-MS instrument. The range of Mn and Fe concentrations varies between the different crystals and also between the three sampling levels and show a trend towards increased concentrations of both Fe and Mn from lower to higher in the stratigraphy (Figure 5-12). In the lowest level (2009 RHCII CA3), there are significantly higher values of iron compared to manganese, with Fe values ranging between ~230ppm and ~2200ppm and the Mn values from ~40ppm to ~1100ppm. This produces an average Fe/Mn ratio of 6.44. In the next stratigraphic level up (2009 RHCII CA5), the range of values of Fe is from ~330ppm to ~2400ppm and the Mn values range between non-detected and ~2000ppm, which produces an average Fe/Mn ratio of 2.96. The upper level of the three, 2009 RHCII CA6, has Fe values between ~270ppm and ~5500ppm, Mn values between ~220ppm and ~6800ppm and an Fe/Mn ratio of 0.54. Although overall Fe and Mn abundances increase, the increase in Mn is much greater than that of the Fe, which is also shown also by the decreasing Fe/Mn ratios through the succession. This indicates a general increase in availability of the elements, particularly Mn in the source fluid, or a change in the redox conditions from anoxic to sub-oxic conditions.

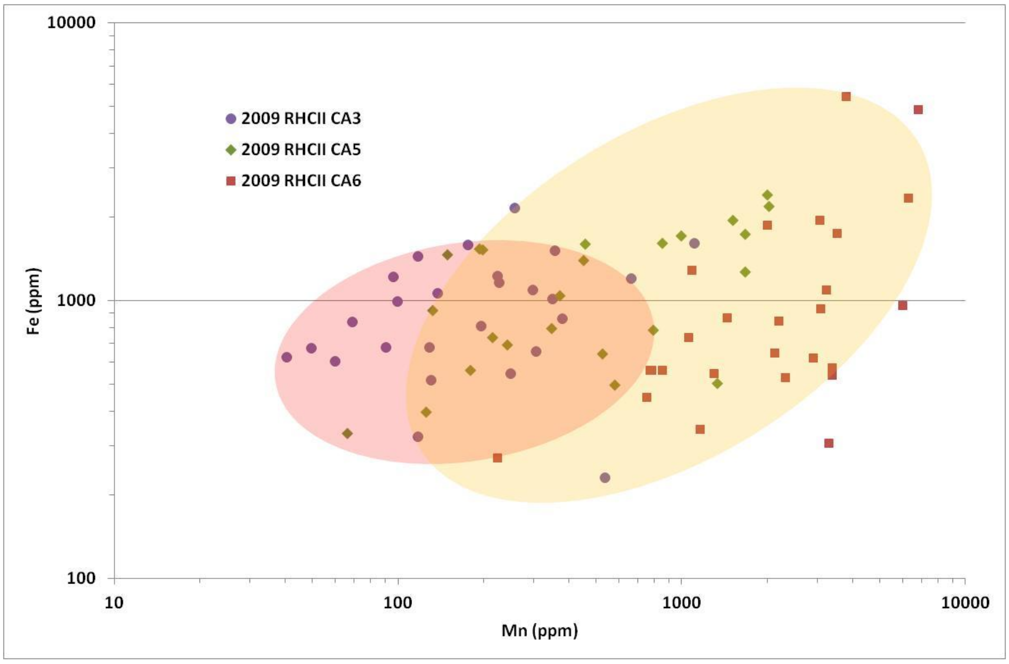

Figure 5-12: The Fe and Mn concentrations of multiple LA-ICP-MS spot analyses of calcite crystals (ppm). Four crystals were analysed from each of three different stratigraphic levels in Lower Bed II, RHCII CA3,5,6. Fe and Mn concentrations for each laser ablation analysis (RHCII CA3 - purple circle, RHCII CA5 - green diamond, RHCII CA6 - red square) show an overall increase in both, but with a reduction in the Fe/Mn ratio from lower to higher stratigraphic levels. This indicates a general increase in availability of the elements in the source fluid, or a change in the redox conditions from anoxic to sub-oxic as the concentrations of Mn increase. The spots which fall within the pale pink ellipse are laser ablation spots which are primarily in dully luminescent crystal zones. Those in the pale orange ellipse are laser ablation spots which are primarily in brightly luminescent.

Patterns of REE element abundance

The abundance of LREEs (La - Nd) in the calcite crystals is generally higher than their abundance of HREEs (Sm - Lu) (Appendix 8). The mean values of multiple analyses of the crystals from each stratigraphic level were used to compare general trends in the REE abundances (Figure 5-13). Calcite crystals from the uppermost stratigraphic level, Upper Bed II, are much more abundant in LREEs, and least abundant in HREEs, compared to calcite crystals from Lower Bed II and Upper Bed I. The crystals from the lowest part of the stratigraphy, Lower Bed I, generally have the least abundance of REE compared to the upper stratigraphic levels.

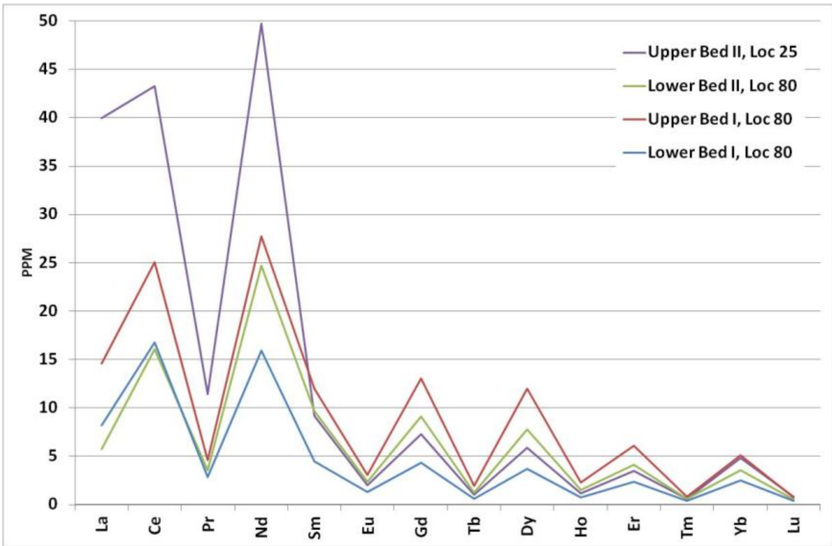

Figure 5-13: Mean REE concentrations of multiple calcite crystals from four stratigraphic levels (ppm) using laser ablation ICP-MS. The HREE (La - Nd) are present in higher concentrations than the LREE (Sm- Lu). The uppermost stratigraphic level (purple line) is much more enriched in the LREE compared to all the lower stratigraphic levels, whereas it is depleted in the HREE compared to Lower Bed II (green line) and Upper Bed I (red line). The crystals from Lower Bed I (blue line) generally have the least amount of REE compared to the upper stratigraphic levels.

The pattern of REE data of the mean values of multiple crystals from each stratigraphic level, when normalised to NASC, shows enrichment in HREE compared to LREE (Figure 5-14), apart from the data from Upper Bed II, Loc 25, which shows no enrichment. There is a negative Ce anomaly, often seen under oxidising conditions, which is most pronounced in Upper Bed II. The small positive Eu anomaly seen in the normalised data of the whole calcite crystals (Figure 5-11) is less apparent in this data set.

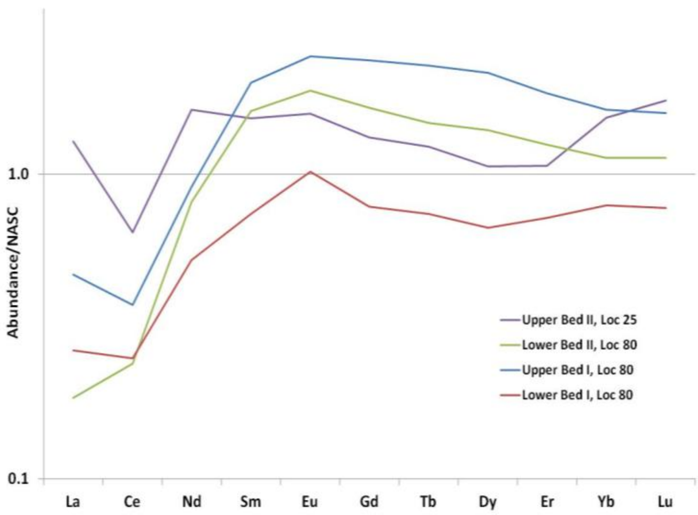

Figure 5-14: The mean REE abundances of calcite crystals from four stratigraphic levels, normalised to NASC. (Gromet et al., 1984) The data from the stratigraphic levels Upper bed I (purple line), Lower bed II (green line), Upper Bed I (blue line), and Lower Bed I (red line), are the mean values of multiple laser ablation sampling points on four crystals from one or more sampling levels (Table 5). They each show an enrichment in the HREE compared to the LREE. There is a small negative Ce anomaly at all levels, which is most pronounced in the Upper Bed II samples at Loc 25.

Trace elements and CL zoning

The relative brightness of the CL zones, for each calcite crystal that exhibits zoning, was categorised as bright, dull, and no luminescence (Figure 5-9; Figure 5-15), and, in general, the prismatic sectors tend to have bright or dull luminescence and the rhombohedral sectors have dull or no luminescence (Hendry and Marshall, 1991a; Hendry and Marshall, 1991b). The concentrations of trace elements at each of the laser ablation spots within zones of relative CL brightness were compared (Figure 5-16, Figure 5-17).

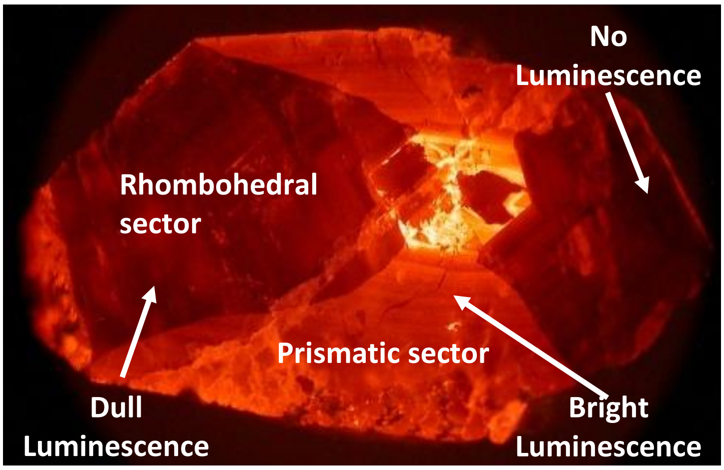

Figure 5-15: Calcite crystal sectors shown by the pattern of luminescence and the approximate range of luminescence seen in the calcite crystals.

Overall, the concentrations of Mn and Fe tend to be highest in the sectors with high luminescence, which tend to be the prismatic sectors, compared to the sectors with dull and no luminescence which tend to be the rhombohedral sectors (Figure 5-16). The mean amount of Mn in the sectors with high luminescence is significantly greater than the mean amount of iron, whereas in the sectors with dull and no luminescence the mean concentrations are more comparable in magnitude. Although the mean Fe/Mn ratios of between 6.44 and 0.54, from crystals at three sampling levels, show that Fe concentrations are higher than the Mn concentrations, the high level of Mn seen in Figure 5-16 is the result of high levels of Mn present where Fe concentrations were below the detection limits. These data are consistent with Mn being an activator of luminescence and Fe being a quencher, and high Fe/Mn ratios and cathode luminescence brightness dependent not only on the total amount of Fe and Mn but also the Fe/Mn ratio (Bruhn et al., 1995; Machel, 2000). The mean concentrations of Sr and Ba, however, tend to be lowest in the high brightness sectors, which tend to be the prismatic sectors, which is the opposite pattern to that seen with the Fe and Mn (Figure 5-16). Sr is not an activator or a quencher of luminescence and will preferentially incorporate onto the rhombohedral sector rather than the prismatic sector, whereas Mn and Fe will preferentially incorporate into the calcite lattice in the prismatic sector (Paquette and Reeder, 1990, 1995). This indicates that incorporation of the trace elements is influenced by element partitioning during crystal growth, as well as source water chemistry.

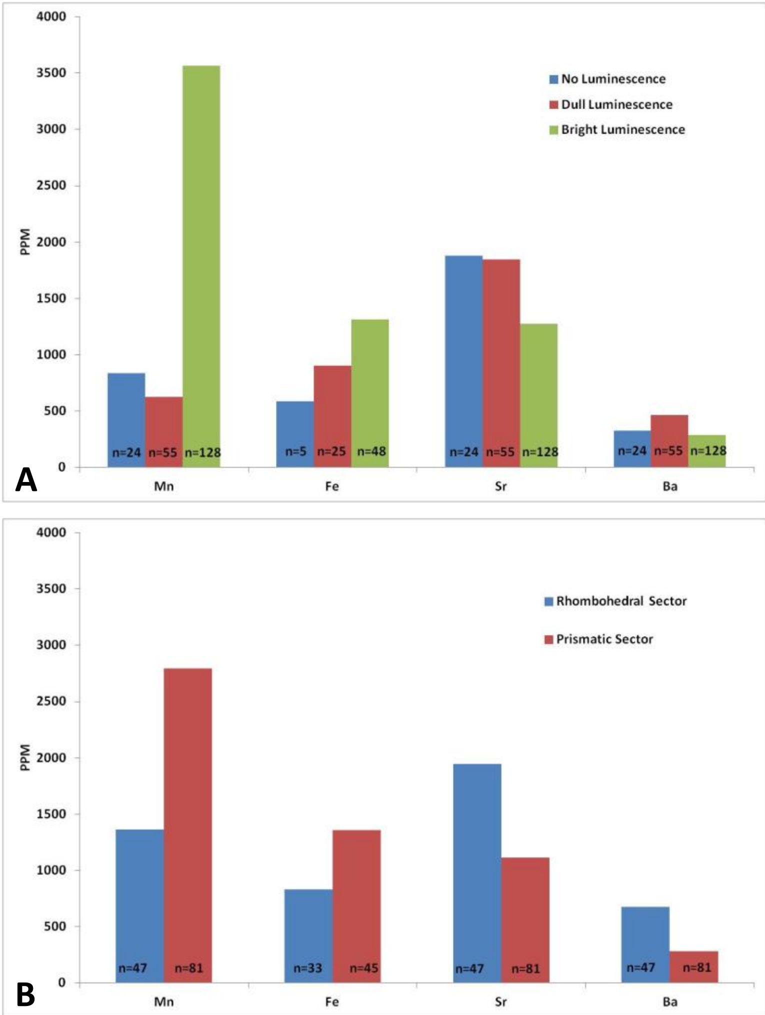

Figure 5-16: The mean trace element concentrations (Mn, Fe, Sr, Ba) (ppm) in the different zones of CL brightness and crystal sectors defined by brightness. A) The concentrations of Mn and Fe tend to be highest in the high brightness sectors, whereas the concentrations of Sr and Ba tend to be highest in the sectors with dull or no luminescence. B) Similarly, the concentrations of Mn and Fe tend to be highest in the prismatic sectors, whereas the concentrations of Sr and Ba tend to be highest in the rhombohedral sectors.

Similarly, the concentrations of the REE which act as sensitizers and activators to luminescence (Machel, 2000), are highest in the high brightness sectors. Although the REEs are likely to contribute to the luminescence, the dominant influence is probably the Mn (Machel, 2000). The LREEs (La – Nd) show a trend where there is increasing concentration with increasing brightness. However in the HREE's (Sm – Lu) the sectors with none and bright luminescence have higher concentrations than the sectors with dull luminescence.

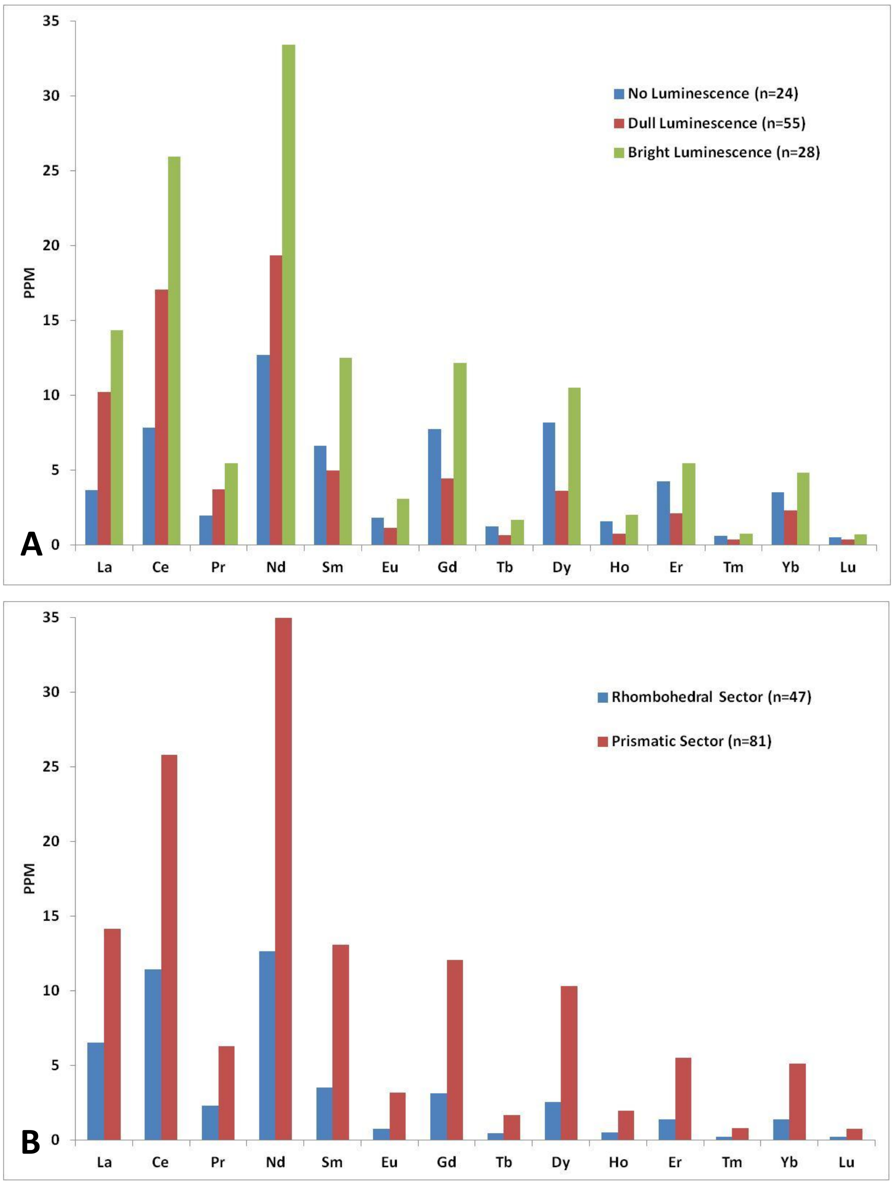

Figure 5-17: The mean trace element concentrations (REE) (ppm) in the different zones of CL brightness. A) The concentrations of the REE are highest in the high brightness sectors. The LREE's (La – Nd) show a trend where there is increasing concentrations with increasing brightness. However in the HREE's (Sm – Lu) the sectors with bright and no luminescence are higher than the dull luminescence sectors. B) The concentrations of REE tend to be highest in the prismatic sectors, compared to the rhombohedral sectors..

Stratigraphic change in U and Pb abundances

In general the mean abundance and pattern of the trace elements in the calcite crystals from different stratigraphic levels is very similar. However, the uranium and lead abundances at different levels varies significantly (Figure 5-18). At the lowest stratigraphic level, RHCI CA104, crystals contain between 32 ppm and 110 ppm of uranium, which is up to four times as much uranium as in the upper levels. The lead abundances range from non-detected to ~11 ppm, but are an order of magnitude higher in upper Bed I and Loc 25 compared to the other two sampling horizons.

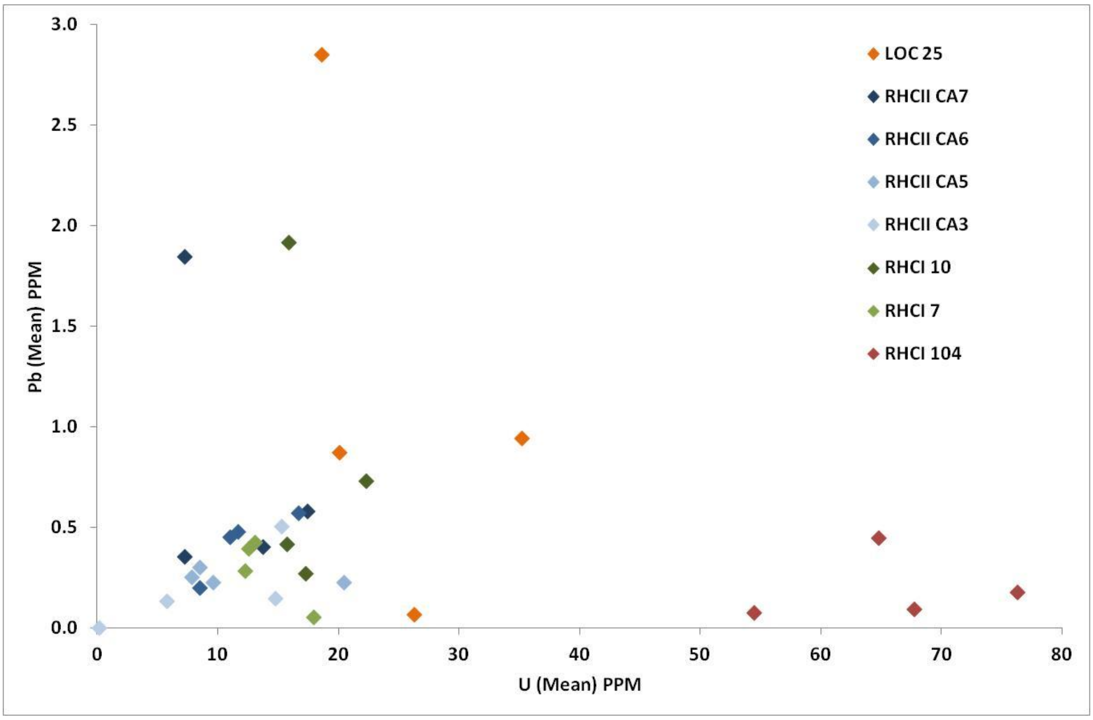

Figure 5-18: The mean uranium and lead concentrations of crystals through the stratigraphy. Crystals are from Lower bed I (RHCI 104, red diamonds, one sampling level), Upper Bed I (RHCI CA7, 10, green diamonds, two sampling levels), Lower Bed II (RHCII CA3,5,6,7, blue diamonds, four sampling levels), and Upper Bed II (LOC25, orange diamonds, one sampling g level). The lowest level in the stratigraphy, RHCI CA104, has four times as much U as Upper Bed I and Lower Bed II crystals. The crystals from Upper Bed II at Loc 25 have approximately twice as much U as those in lower Bed II. Conversely, the lowest level in the stratigraphy, RHCI CA104, has less Pb compared to Upper Bed I, Lower Bed II, and Upper Bed II crystals.

Twelve samples from the different stratigraphic levels were selected for stable isotope analysis (Table 6). Whole crystal analysis was performed, as it was not possible to separate calcite from separate CL zones or sectors using the facilities available. Several crystals were powdered in order to give enough calcite for acid digestion. Future studies might use laser technology or ion probe to investigate isotopic inhomogeneity within crystals.

Sample Name	**δ^{13}C (VPDB)**	**δ^{18}O (VPDB)**
Loc25	5.2	1.2
RHCIICA7	6.0	1.2
RHCIICA75	5.2	0.8
RHCIICA74	5.7	1.3
RHCIICA73	5.6	1.5
RHCIICA72	5.8	1.1
RHCIICA71	5.7	1.3
RHCIICA6	6.0	0.9
RHCIICA3	6.3	0.5
RHCICA7A	5.6	0.7
RHCICA10	6.2	-0.1
RHCI104	4.9	0.3

Table 6: Stable isotope data from Pleistocene calcite crystals from Palaeolake Olduvai. Multiple calcite crystals were powdered for each sample.

The carbon and oxygen stable isotope values form a cluster, generally with low positive δ^{18}O, whose values range from $\delta^{18}O_{VPDB}$ -0.1‰ to 1.5‰ and positive $\delta^{13}C_{VPDB}$ 4.9‰ to 6.3‰, apart from one atypical sample which has values $\delta^{18}O_{VPDB}$ -6.2‰ and $\delta^{13}C_{VPDB}$ -4.2‰ (Lower Bed II RHCII CA5, not shown on chart) (Figure 5-19). There is no obvious trend between the different stratigraphic levels, which is consistent with previously reported stable isotope analyses of the lake crystals (Hay and Kyser, 2001). The consistency between all the samples from Lower bed II apart from the single sample RHCII CA5 suggests that the latter is not representative of the interval.

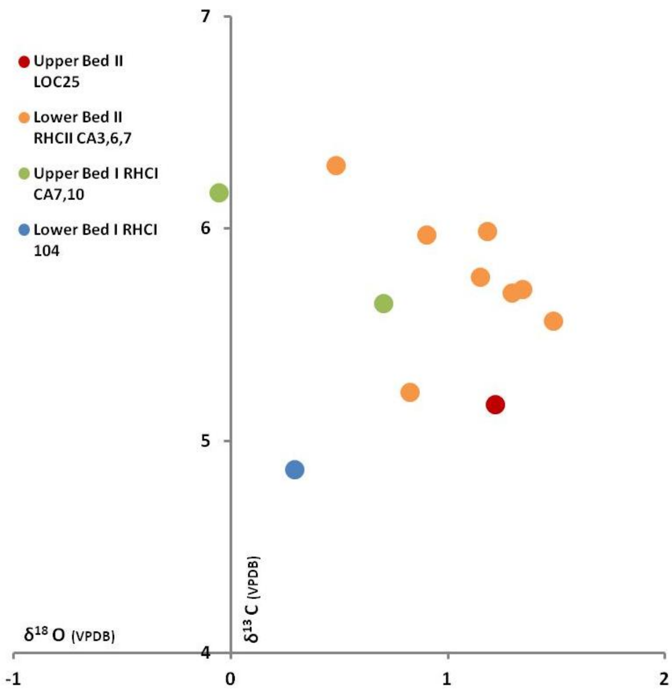

Figure 5-19: Stable isotope data of whole calcite crystals from different stratigraphic levels. Multiple calcite crystals were powdered for each sample. Samples were from four different stratigraphic levels; from lower to higher in the stratigraphy - Lower Bed I (RHCI 104, blue spot), Upper Bed I (RHCI CA7,10, green spot), Lower Bed II (RHCII CA3,6,7, orange spot), and Upper Bed II (LOC25, red spot). Generally the crystals have low positive δ^{18}O values and positive δ^{13}C values, and there is no clear trend in the variation between crystals at different stratigraphic levels.

5.6 Contemporary crystals

5.6.1 Calcite crystal textures

The occurrence of calcite crystals similar to the Pleistocene crystals from Olduvai Gorge have previously been reported in contemporary Lake Ndutu on the Serengeti Plain and in the Ngorongoro Crater lake (Hay, 1976), however there are no reports of any detailed petrography or analytical investigations. In the current study calcite crystals were found in very shallow sub-surface shoreline sediments, approximately 10-20 cm below the surface, in three out of the five modern lakes investigated; Lake Ndutu, Lake Makat and Lake Natron. Carbonates were also identified in the Lake Masek sediments but these took the form of small, ~1mm and 4mm in diameter, sub-spherical to ovoid grains composed of micrite; these were not investigated any further in this study. No calcite crystals were found in the sub-surface sediments from the margins of Olbalbal Swamp which is a much more ephemeral water body than the others.

At all sites where crystals were found, the top surface of the lake margin sediments was covered in a white or dark grey mineral crust. XRD analyses were compared to data from the RRUFF Project (Downs, 2006) to identify the mineralogy, and showed this crust to be principally composed of trona ($Na_3(CO_3)(HCO_3)\bullet2(H_2O)$) and halite (NaCl). The sample from Lake Natron also contained natron ($Na_2CO_3\bullet10(H_2O)$).

The contemporary carbonates consist of clusters of euhedral to anhedral crystals between ~0.5mm and 3mm in diameter. Calcite specimens from the shallow sub-surface shoreline sediments at Lake Makat are composed of multiple euhedral to subhedral intergrown crystals with pitted surfaces, those from Lake Natron are composed of multiple euhedral intergrown crystals with no pitting, and those from Lake Ndutu are composed of multiple anhedral intergrown crystals with very pitted surfaces (Figure 5-20). Where they are euhedral, the individual crystals generally have a similar morphology to the Pleistocene crystals, with prismatic side faces and unit rhombohedral terminations, although, unlike the crystals from Olduvai, the surfaces are often pitted (Figure 5-20). There is no sedimentological evidence of reworking and transport or broken faces on the crystals, and the pitted surface is developed consistently over the crystals surface, so is typical of chemical corrosion rather than physical abrasion.

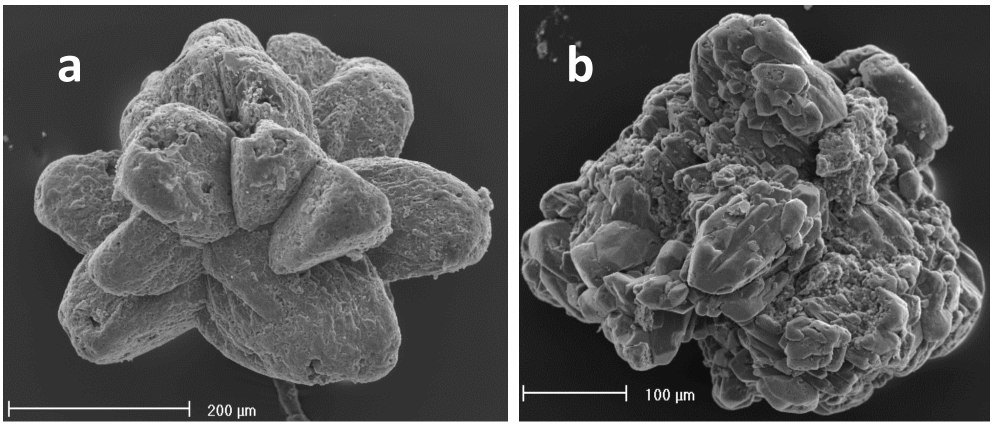

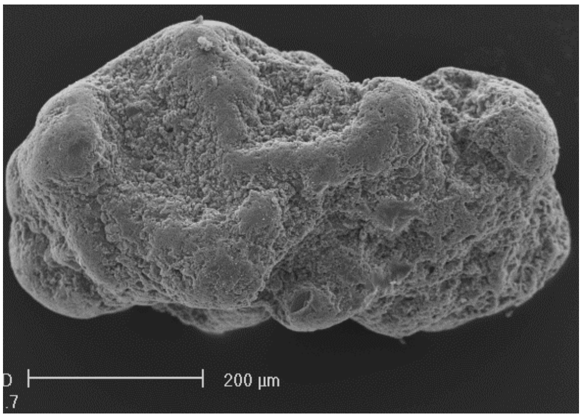

Figure 5-20: SEM images of external morphology of calcite crystals from very shallow sub-surface shoreline sediments of contemporary lakes in Tanzania. a) Calcite specimens from Lake Makat, comprising multiple euhedral to subhedral intergrown crystals with pitted surfaces (Scale bar 200µm), b) Calcite specimens Lake Natron comprising multiple euhedral intergrown crystals (Scale bar 100µm), c) Calcite specimens from Lake Ndutu comprising multiple anhedral intergrown crystals with very pitted surfaces (Scale bar 200µ).

Internal crystal textures were investigated using polished resin mounts. The crystal clusters from Lake Makat are clear and colourless, with dark patches of inclusions visible using SEM. SEM-BS-EDX analyses shows them to have high Al, Si, Mg and K peaks consistent with clay particles. These specimens are most comparable to crystal clusters from Early Pleistocene crystals in Upper Bed I and Bed II, but do not resemble those from Lower Bed I (RHC CA104). Carbonates from Lake Natron are clear and colourless clusters of intergrown euhedral crystals with clay particle inclusions. Specimens from Lake Ndutu are composed of clusters of very small, subhedral to anhedral, clear and buff coloured crystals. As with the specimens from Lake Makat, these also have dark patches of clay particle inclusions. The central parts of the specimens are often non-transparent and appear to have a micritic texture which is overgrown by individual euhedral crystals.

The CL images of polished crystals from Lakes Ndutu, Natron and Makat show a complex pattern of both sector and concentric zonation which is comparable to that seen in Pleistocene crystals at Olduvai above Tuff IB (Figure 5-21). Carbonates from Lake Makat and Lake Natron both have alternating bands of bright, dull, and non orange luminescence, which in some cases are truncated. Although the resolution is poorer than in the Pleistocene crystals because of their small size, sector and concentric zoning of intergrown crystals can be identified. Carbonates from Lake Ndutu have bright orange luminescence with a mottled pattern but without zoning, showing crystal sizes much smaller than the resolution of the CL analytical equipment.

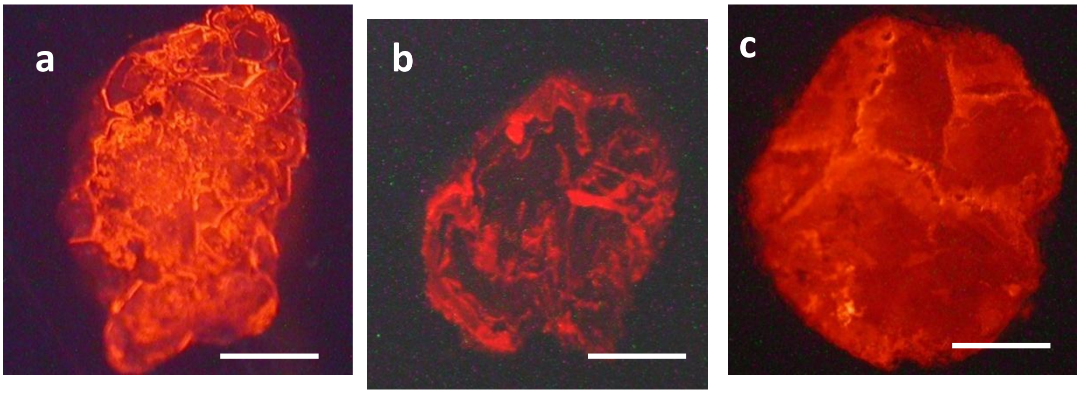

Figure 5-21: CL images of cut and polished contemporary lake calcite crystals. (Scale bar 0.25mm) a) Lake Makat, and b) Lake Natron, showing alternating orange bright, dull and none luminescent bands with sector and concentric zoning of intergrown crystals, and c) Lake Ndutu showing bright orange luminescence but without zoning

In contrast to the Pleistocene crystals from Olduvai Gorge, zoning in the calcite is not identifiable in SEM-BS. Small patches of magnesium rich calcite, or possibly dolomite, have been identified using SEM-BS in crystals from Lake Natron, and patches of fluorite with strontium have been identified in crystals from Lake Ndutu (Figure 5-22), and these show multiple stages of mineral growth.

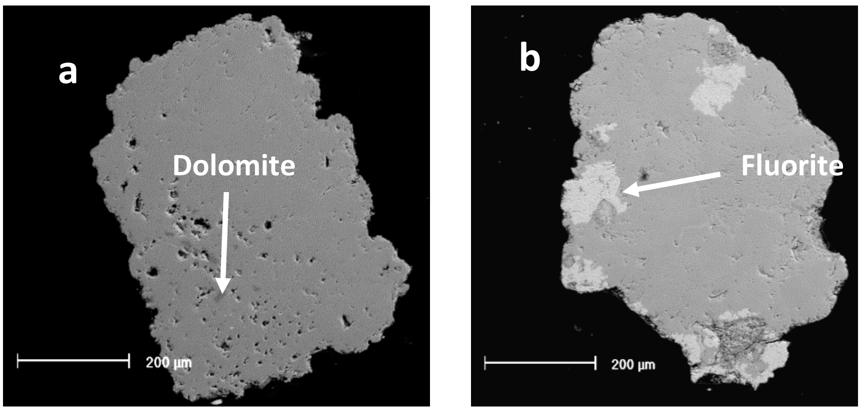

Figure 5-22: SEM-BS image of cut and polished crystals from contemporary lakes in Tanzania. (Scale bar 200µm) a) Crystals from Lake Natron. Small darker patches have a high Mg peak using EDX, and b) crystals from Lake Ndutu. Patches of Fluorite with trace Sr have a higher backscatter coefficient than the calcite..

5.6.2 Trace element analysis using LA ICP-MS

Modern calcite crystals were not analysed for U-Pb at NIGL so separate mounts were prepared for trace element analysis. Laser ablation sampling points were targeted over a range of CL brightnesses where this was possible, and where the resolution between CL brightness was not clear, several spots were analysed from a transect along the crystal (Appendix 10).

Lake Natron:

Levels of magnesium range from just over 100ppm (0.04 mol%) to over 1800ppm (0.77 mol%) which is consistent with it being 'low-magnesium' calcite. There are on average higher values of iron compared to manganese in all the samples, with Fe values ranging from ~270ppm to ~1500ppm and the Mn values from ~160ppm to ~3000ppm, and Fe/Mn ratios between 0.35 and 4.16. The samples also have strontium values which range from ~370ppm to ~3000ppm and barium values between non-detected and ~600ppm. The uranium values are on average ~ 3.6ppm but can be as high as 12 ppm and Pb values are very low and range from 0.01ppm to 0.39ppm. The LREE are present in quantities up to 210ppm which are slightly greater than the HREE which are present up to about 140ppm. When the REE data was normalised to NASC the pattern of data shows enrichment in HREE compared to the LREE (Figure 5-23). The mean values of three crystals show a small negative Eu anomaly and one crystal shows a positive Eu anomaly. The zig-zag shape of the lines makes it difficult to assess if there is a small negative Ce anomaly.

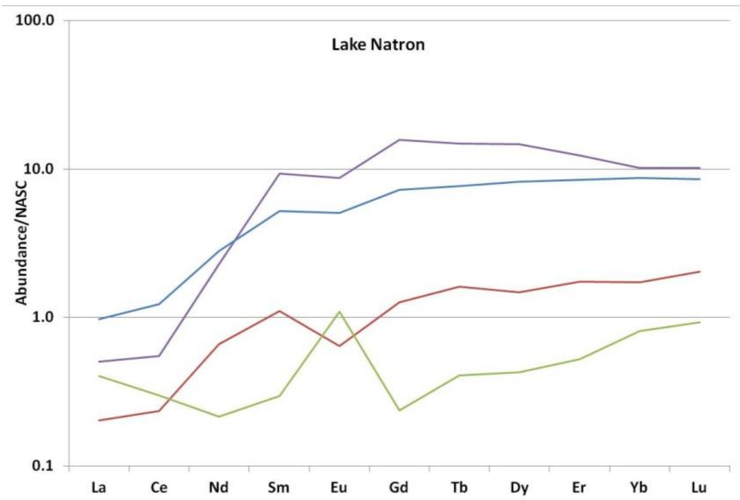

Figure 5-23: Laser ablation ICP-MS data four crystals from contemporary Lake Natron, Tanzania. Each line is the mean abundance of multiple laser ablation spots for each crystal, normalised to NASC. In genral there is an enrichment in HREE compared to LREE. Three crystals show a small negative Eu anomaly and one shows a positive Eu anomaly. It is unclear if there is a small negative Ce anomaly.

Lake Ndutu:

Levels of magnesium in the specimens from Ndutu are significantly higher than those at Natron and range from just over 310ppm (0.13 mol%) to over 6200ppm (2.56 mol%) which is consistent with 'low-magnesium' calcite. There are on average higher values of iron compared to manganese in all the samples, with Fe values ranging from ~90ppm to ~11000ppm and the Mn values from ~40ppm to ~2100ppm, and Fe/Mn ratios between 0.46 and 21.91. This is a much higher ratio than found in the Natron samples. The samples also have strontium values which range from ~1200ppm to ~8300ppm and barium values between non-detected to ~2100ppm. The uranium values are on average ~ 2ppm but can be up to 6ppm and Pb values are much higher and range from 0.15ppm to 37ppm. The LREE are present in quantities up to 330ppm, which are slightly greater than the HREE present up to about 10ppm. When the REE data was normalised to NASC the pattern of data shows no enrichment in HREE compared to the LREE. The zig-zag pattern of data makes identification of specific Ce or Eu anomalies equivocal (Figure 5-24).

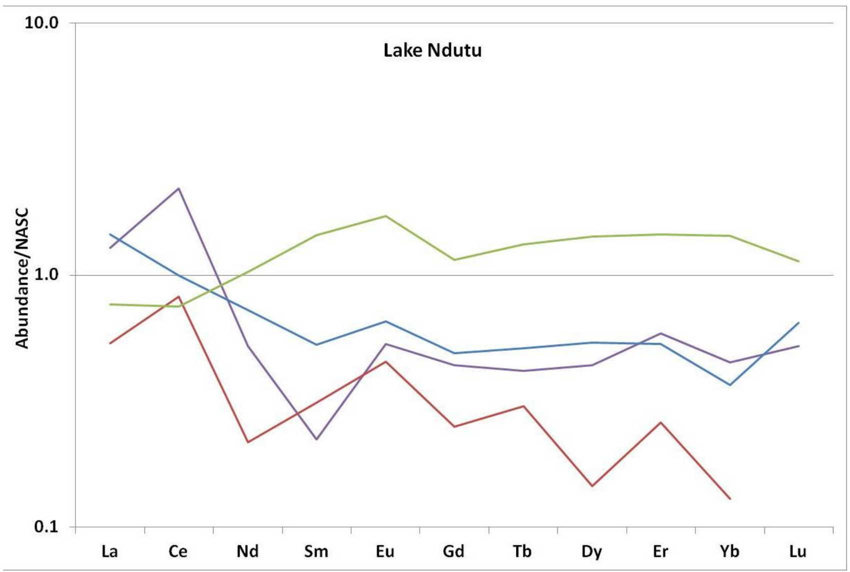

Figure 5-24: Laser ablation ICP-MS data four crystals from contemporary Lake Ndutu, Tanzania. Each line is the mean abundance of multiple laser ablation spots for each crystal, normalised to NASC. There is no enrichment in HREE compared to LREE. The zig-zag pattern of data makes identification of specific Ce or Eu anomalies difficult.

Lake Makat:

Levels of magnesium in the specimens from Makat are between those at Natron and Ndutu and range from just over 100ppm (0.04 mol%) to over 3700ppm (1.53 mol%) which is consistent with 'low-magnesium' calcite. There are on average higher values of iron compared to manganese in all the samples, with Fe values ranging from n.d. to ~3600ppm and the Mn values from non-detected to ~720ppm, and Fe/Mn ratios between 0.22 and 16.41. This is a much higher ratio than found in the Natron samples and slightly lower than found in the Ndutu samples. Similarly, the Sr and Ba concentrations lie between those found at Natron and Ndutu, as samples have strontium values which range from ~1600ppm to ~5400ppm and barium values between ~200ppm to ~920ppm. The uranium values are on average ~ 2ppm but can be up to 8.6ppm which is comparable to the Natron and Ndutu samples. The Pb values are also in a range between those found in Natron and Ndutu, from ~8ppm to ~18ppm. The LREE are present in much larger quantities than the other two lakes, up to 850ppm, and are slightly greater than the HREE present up to about 14ppm. When the REE data was normalised to NASC the pattern of data shows no enrichment in HREE compared to the LREE. (Figure 5-25). Two crystals have a negative Ce anomaly and one has a positive Ce anomaly.

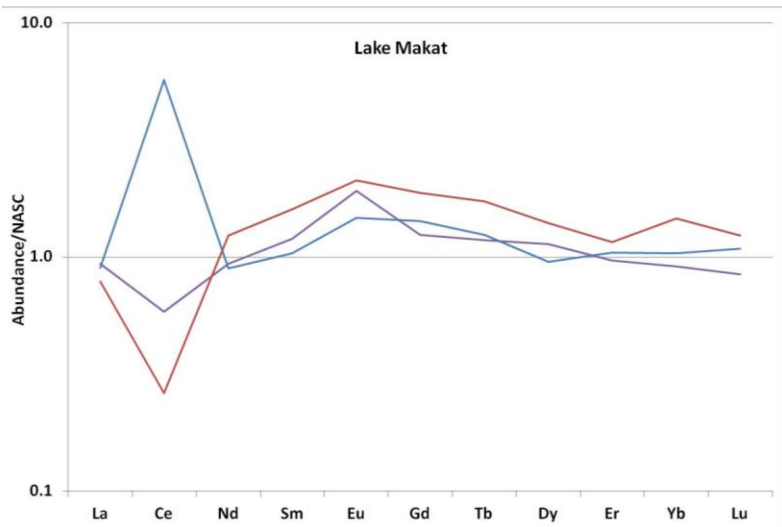

Figure 5-25: Laser ablation ICP-MS data three crystals from contemporary Lake Ndutu, Tanzania. Each line is the mean abundance of multiple laser ablation spots for each crystal, normalised to NASC. In genral there is no enrichment in HREE compared to LREE. The mean values for each of the three crystals have either a negative or positive Ce anomaly showing changing depositional conditions.

5.6.3 Stable isotope analysis

The $\delta^{18}O_{(VPDB)}$ and $\delta^{13}C_{(VPDB)}$ of crystals from each of the three lakes was compared to the data from the Pleistocene crystals. The sample from Lake Natron plots with the Pleistocene calcite crystals from Olduvai Gorge, whereas the sample from Lake Makat in the Ngorongoro caldera has higher $\delta^{18}O$ and $\delta^{13}C$ values and the sample from Lake Ndutu on the Serengeti Plain has much lower $\delta^{18}O$ and $\delta^{13}C$ values (Figure 5-26).

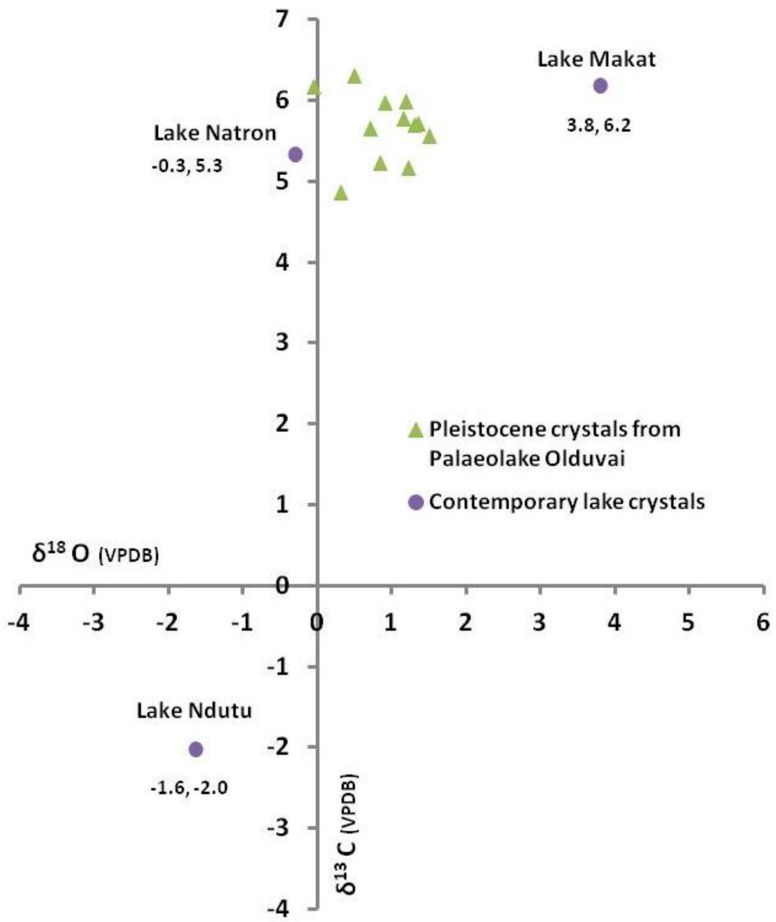

Figure 5-26: Stable isotope data for calcite crystals from the contemporary lake margin sediments of Lake Ndutu, Lake Makat and Lake Natron. The crystals from Lake Natron have similar values to those of the Pleistocene sediments at Olduvai. Crystals from Lake Ndutu have much lower values and those from Lake Makat higher values

5.6.4 Lake water

Lakes Natron, Makat and the Olbalbal swamp are hydrologically closed, Lake Masek and Lake Ndutu are the source water for the Olduvai River which only flows during the rainy season, and all are subject to frequent, climate driven, changes in lake level. Consequently the lake level during this sampling exercise does not necessarily represent either maximum or minimum lake fill conditions. All water samples were collected during August 2010, approximately three months after the main rainy season. Olbalbal swamp is ephemeral and only occasionally filled with water, but following a very wet winter there was a large standing body of water to be sampled for this study. Although Lakes Ndutu and Masek are not completely hydrologically closed, they supply the Olduvai River only during the rainy season, and so are subject to high levels of evaporation at other times. During the 2009 August field season Lake Masek was almost completely dried out - in part due to water abstraction - and the remaining water body surrounded by glutinous mud flats was inaccessible, but lake level was much higher for the 2010 August field season and so could be sampled for this study. The lake water chemistry varied significantly between the five different sites (Table 7).

Olbalbal, as expected, had a much lower concentration of dissolved ions, and a lower pH and conductivity, compared the other four. However, the concentrations of Ca and Mg were much higher, and no calcite crystals were found in the shoreline subsurface sediments, showing that the water had low levels of CO_3^{2-}/HCO_3^{-} ions, or other possibly inhibitors to calcite growth (Reddy and Hoch, 2012). Although the other four lakes have dissimilar chemistry, in general, they have high concentrations of dissolved ions and trace elements, deposit calcite and evaporite minerals in their shoreline sediments, and are more likely to operate similar processes to Palaeolake Olduvai.

	Lake Ndutu	Lake Masek	Lake Natron	Lake Makat	Olbalbal
UTM/UPS WGS 84	0723750 9666422	0726310 9665488	0822105 973470	0782225 9649054	0775043 9672486
Ph	9.72	9.67	10.01	9.77	9.00
Conductivity (mS/cm)	69.3	23.7	9.95	30.1	1.33
Temperature (^{o}C)	27.2	27.1	28.2	28.5	26.1
Na (µg/mL)	25280	4060	2460	9180	318
K (µg/mL)	397	30.60	46.60	1195	16.80
Ca (µg/mL)	1.27	2.88	0.27	0.53	10.11
Mg (µg/mL)	0.16	0.30	0.08	0.12	1.60
F (µg/mL)	1660	222	54.20	163	16.20
Cl (µg/mL)	7628	1597	1090	2758	38.30
SO4 (µg/mL)	3818	248	123	1846	15.30
Mn (mg/ml)	0.025	0.055	0.046	0.050	0.101
Fe (mg/ml)	0.003	0.086	0.010	0.011	0.00001
Pb (mg/ml)	0.004	0.00006	0.00001	0.00001	0.00001
U (mg/ml)	1.198	0.191	0.016	0.229	0.006
Molar Mg:Ca ratios	0.2	0.2	0.5	0.4	0.3
Ca/Mg	7.9	9.6	3.4	4.4	6.3
Fe/Mn	0.11	1.58	0.23	0.21	0.0001
Calcite crystal U (ppm)	Max 6.13 (n=18)		Max 12.33 (n=14)	Max 8.62 (n=14)	
	Mean 2.02 (n=18)		Mean 4.67 (n=14)	Mean 1.72 (n=14)	

Table 7: Chemistry of five contemporary lakes, Tanzania. The pH, conductivity and temperature were determined at the time of sampling. The cations, anions and trace elements were determined in the UK (University of Aberystwyth).The maximum and mean concentrations of uranium(ppm) from multiple laser ablation spots from four crystals from each lake in the calcite crystals from the lake margin sediments (minimum concentrations were below detection limits). Molar Mg:Ca ratios <2 indicate low magnesium calcite formation (Müller et al., 1972).

5.7 Discussion

5.7.1 Calcite crystal formation

Occurrence and genesis

Calcite crystals from the very shallow, sub-surface, shoreline sediments of contemporary Lake Natron, Ndutu, and Makat have similar textural and geochemical characteristics to the Pleistocene crystals from Olduvai. It is likely that they are formed by similar processes and in a comparable depositional setting.

Pleistocene crystals

At Olduvai, the concentration of crystals in shallow scours with erosional bases, and the high density of calcite crystals in laminated or thinly bedded layers, indicate reworking, and demonstrate that the crystals must have a synsedimentary origin. Crystals formed in the shallow sub-surface could be easily mobilised during agitation by wind waves in shallow water, or more easily by fluvial action. Consequently, the bedded crystal beds, and crystal rich lag deposits in shallow scours, are likely to have been sourced from shallow sub-aerial sediments at the lake margins or sub-aqueous sediments in the lake itself. Where the calcite crystals are dispersed through the clay beds, or found in arching sprays, the sediments show no evidence of reworking or remobilisation, and are likely to represent the original formational context. Crystals found in these settings are likely to have been preserved in slightly deeper water, or in more cohesive sediments. The arching sprays in the clay sediments at Olduvai have a similar morphology to those found in fine-grained sandstone beds, both in the Eocene Green River Formation, Wyoming (Eugster and Hardie, 1975), and on the western lake margin at Olduvai Gorge (Hay, 1976), which are both interpreted to be pseudomorphs after trona.

Overall, Palaeolake Olduvai is understood to have become shallower through Bed I, and following a lake expansion above Tuff IF, again became shallower through Bed II (Hay, 1976; Hay and Kyser, 2001). However, erosion surfaces and reworked sediments are commonly found throughout the lacustrine sedimentary sequence at Olduvai (Figure 5-4), and the presence of beds with reworked calcite crystals both above and below beds of calcite crystals found in arching sprays, show repeated changes in lake depth superimposed on this overall trend.

Contemporary crystals

Contemporary specimens from Lake Ndutu have a micritic centre overgrown by sparry calcite, and so it is possible that the crystals from Lake Ndutu were formed by partial recrystallisation of, or formation of an anhedral overgrowth on, sand-sized carbonate grains composed of micrite. The sub-surface shoreline sediments of Lake Masek, which is a secondary lake down-river from Lake Ndutu, contain sand-sized carbonate grains which are also composed of micrite, although in this case there is no evidence of recrystallisation to sparry calcite as they break-up easily into micrite powder. Both of these lakes are west of Palaeolake Olduvai on the Serengeti Plain, and have a common source, and higher Ca^{2+} abundances and Ca/Mg ratios than either Lake Makat or Lake Natron. Because they are hydrologically linked they are likely to have similar lake chemistry and calcite depositional conditions.

Calcite crystals from Lakes Natron and Makat, to the east of Palaeolake Olduvai in the Rift system, do not have the micritic centre to the crystals. They are more euhedral and transparent, and texturally they are most similar to the Pleistocene crystals from Olduvai. In this case it is more likely that the calcite crystal formation occurred by recrystallisation of an evaporite mineral, or by direct growth. The Ca^{2+} abundance, and Ca/Mg ratios, are much lower than those found at Lakes Ndutu and Masek, and although they are chemically more similar to one another than to the lakes on the Serengeti Plain, the lakes are not hydrologically linked.

In general the concentrations of anions in Lakes Ndutu and Masek are higher than in Lakes Natron and Makat. Lakes Ndutu and Masek are smaller water bodies than Lakes Natron and Makat, and the difference in anion concentrations may be the result of less precipitation on the Serengeti Plain compared to the higher levels of rainfall found in the Rift (Norton-Griffiths et al., 1975).

Crystal genesis

The Pleistocene crystals from Upper Bed I (RHCI CA7,10) and Bed II (RHCII CA3,5,6,7 and Loc 25) at Olduvai do not have a micritic texture as seen in the specimens from Lake Ndutu. Rather their inclusion-rich nuclei are texturally similar to the contemporary crystals from Lakes Natron and Masek. This implies that the Pleistocene crystals grew in conditions similar to the contemporary crystals from the two Rift lakes. Lacustrine calcite crystals from Olduvai have previously been interpreted to be secondary, formed by pseudomorphic replacement of an evaporite mineral precursor such as trona ($Na_3(CO_3)(HCO_3)\cdot 2(H_2O)$) or gaylussite ($Na_2Ca(CO_3)_2\cdot 5H_2O$), or by recrystallisation of primary micrite (Hay and Kyser, 2001). Calcite pseudomorphs after trona are commonly described in the literature (Eugster and Hardie, 1975; Larsen, 2008; Southgate et al., 1989; Warren, 2006), however, crystals from Olduvai are probably not true pseudomorphs as they do not mimic the trona or gaylussite morphology. It is possible that the evaporite minerals provided a nucleation point and a suitable source of ions for the calcite precipitation to initiate. Primary micrite may also act as a nucleation point for sparry calcite growth, and so calcite may also be able to precipitate independently of an evaporite precursor. The lack of a micritic centre, no evidence of partially recrystallised evaporite minerals, and complex geochemical zoning in both the nucleus and the euhedral overgrowth, indicates that these crystals are likely to have formed by direct precipitation in the sediments, possibly by utilization of ions from highly soluble evaporite minerals.

In contrast, the morphology and petrographic textures of calcite crystals from Lower Bed I (RHCI CA104) differ significantly from those crystals found at other Pleistocene sampling horizons in this study and from contemporary crystals. Their scalenohedral shape and milky colour, and absence of nuclei and euhedral zoning, suggest that they formed from significantly different fluid compositions, or a different precursor mineral, compared to calcite crystals from other levels. Indeed, the higher concentration of magnesium in crystals from this stratigraphic level indicates that the supply fluid potentially had a much higher Mg/Ca ratio compared to that at all other stratigraphic levels sampled. There are no specific criteria to infer that they are synsedimentary as all specimens from this level are dispersed in the clay. However, as crystals from Lower Bed II are also found dispersed in clay beds that occur between beds of reworked crystals, it is possible that they are synsedimentary. As there is no evidence of a previous evaporite mineral, or of a micritic precursor, in the specimens examined, it is possible that these crystals formed by direct precipitation of calcite.

Many of the Pleistocene calcite crystals, apart from those from Lower Bed II (RHCI CA104), have a nucleus with a complex CL zoning pattern. This pattern is comparable to that seen in crystal clusters produced by multiple intergrown crystals. It is hypothesised that the nuclei may have originally been small crystal clusters, distinguishable by bright luminescence (Figure 5-8c), on which euhedral overgrowths, with often dull luminescence, have formed (Figure 5-8c). Where the CL images of the calcite crystals show truncation of the zoning pattern, this is interpreted to be due to dissolution and re-precipitation events, and which is also likely to be the cause of the more complex zoned areas identified in crystal clusters. An example of this is seen in the contemporary calcite crystals from Lake Ndutu and Lake Makat, which have pitted surfaces, likely to be due to chemical corrosion. This is consistent with a previous study which identified the euhedral coatings as diagenetic overgrowths on abraded crystals (Hay and Kyser, 2001), although corrosion rather than abrasion is considered here to be the most likely mechanism for the pitting.

Hollow centres of some crystals shown in SEM photographs may be caused by preferential dissolution of the nucleus. Increasing the magnesium content in calcite can increase its solubility (Folk, 1975; Wright, 2008). However, although the laser ablation ICP-MS analyses identified variations in the magnesium content at different locations on the crystals, there was no indication of higher magnesium content preferentially associated with the CL zoning pattern interpreted as the crystal nucleus. So the dissolution may be caused by undersaturated pore fluids acting in areas of the crystal that are damaged, rather than a systematic feature.

Significance of zoning and trace element abundance

The morphology of calcite crystals may be influenced by chemical, physical or biological processes during crystal growth (Wright, 2008). Where calcite deposition is promoted by biological processes the resulting crystal morphology tends to be complex, and so euhedral calcite crystals are more likely to be deposited by abiotic processes. During calcite growth, trace elements will fractionate and incorporate selectively on different faces of the crystal (Fernández-Díaz et al., 2006; Paquette and Reeder, 1990). Elements larger than the Ca ion, such as Pb, Ba and Sr, promote the growth of calcite with rhombohedral habits, whereas calcite grown in the presence of cations smaller than the Ca ion, such as Mg, Mn and Co, produce a variety of morphologies including peanut, spheres, and spherulites (Paquette and Reeder, 1990). Their morphology may also be influenced by the conductivity of the water. A change from rhombohedral to scalenohedral calcite can be observed due to an increase in the supersaturation and an increase in the $[Ca]_{ch}/[CO_3]_{ch}$ ratio, as the conductivity is increased from 1 to $7mScm^{-1}$ (García Carmona et al., 2003). As all the contemporary lakes investigated here have conductivities greater than $7mScm^{-1}$, the dominant control over the calcite morphology is likely to be due to incorporation of trace elements.

The brightness of carbonates under cathode-luminescence microscopy is primarily a function of the balance between Mn and Fe, although REEs can contribute as either activators, sensitizers, and quenchers to luminescence (Barnaby and Rimstidt, 1989; Habermann, 2002; Habermann et al., 1998; Machel, 2000). The intensity of luminescence is related to the concentrations of Mn and Fe in calcite and the Fe/Mn ratios, which in turn are determined by the redox conditions and pH of the supply fluid (Figure 5-27).

Consequently, although this is only a qualitative technique, the brightness of the CL has been used to indicate the redox conditions of the water supply during carbonate precipitation and so the hydrology of the depositional setting (Barnaby and Rimstidt, 1989). Where the actual Fe and Mn data are available (2009 RHCII CA3,5,6), their high abundances in the calcite crystals, and the range of CL brightness, show that calcite crystals were formed in reducing conditions which varied between anoxic and sub-oxic states. Where the Fe concentration data is not known (RHCI CA7,10 and LOC25), the bright luminescence and Mn concentrations indicate sub-oxic to anoxic conditions comparable to those from Lower Bed II. However, the dull luminescence and very low Mn concentrations in Lower Bed I (RHCI 104) may indicate oxic conditions. The variation in luminescence that defines the concentric zoning may indicate fluctuating redox conditions during crystal growth which is compatible with formation in the shallow sub-surface.

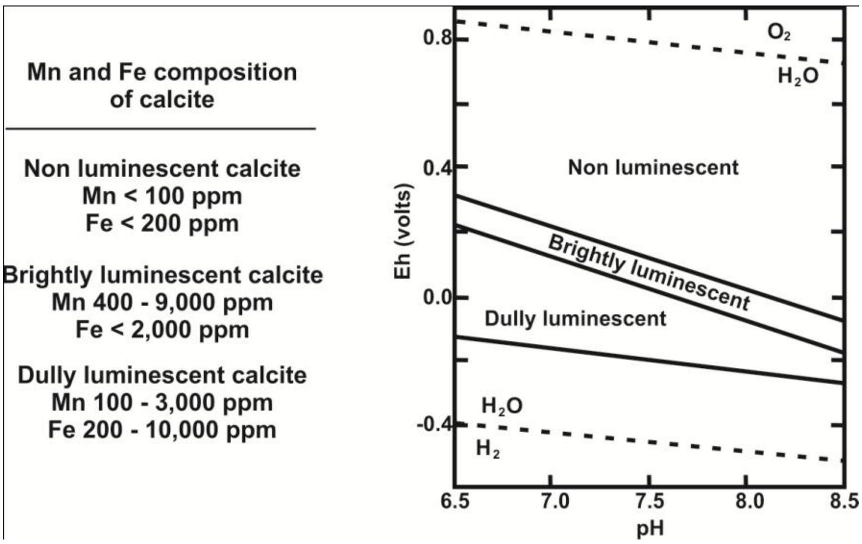

Figure 5-27: The ranges of concentrations of Fe and Mn, and proposed redox and pH values, for calcite formation with bright, dull and no luminescence. Taken from Barnaby and Rimstidt (1989). The luminescence range expressed as dull luminescence is considered to be anoxic, that of bright luminescence is sub-oxic, and that of non-luminescent is oxic conditions. The calcite crystals often have alternating zones of bright, dull, and no luminescence indicating alternating redox conditions in the supply fluid, with dominantly sub-oxic conditions.

The trace elements in the calcite crystals, Sr and Ba, are not redox sensitive, and have similar mean concentrations at all levels. The partition coefficients for Ba and Sr into calcite are less than 1, and as the concentrations of Sr and Ba in the calcite crystals is high, it indicates that the supply fluid was highly evaporative. Both Ba and

Sr also exhibit a strong structural control over the calcite growth, and Ba and Sr incorporation can be high regardless of partition coefficients (Astilleros et al., 2000, 2003; Brand and Veizer, 1980; Lorens, 1981). This mechanism can permit high levels of Sr and Ba incorporation into the calcite where those elements are readily available, such as in highly evaporative water. In addition, in those crystals with clearly defined sector zoning, prismatic sectors have higher concentrations of most of the trace elements and REE, apart from Sr and Ba which are most concentrated on the rhombohedral sectors. This shows the link between trace element partitioning and crystal structure.

Interestingly, Sr and Ba are abundant in the calcite crystals, at almost an order of magnitude higher than values found in the terrestrial lake margin sparry nodules and spherulitic clusters (Chapter 2). This shows that they are likely to have formed from highly evolved lake water, subject to high levels of evaporation compared to the source for the terrestrial samples. However, the cortex of the terrestrial samples has higher levels of Sr and Ba compared to the sparry bands, showing that this final stage of carbonate deposition took place in a highly evaporative setting, from water with a lacustrine influence.

Although the mineralogical composition of parent materials in a sedimentary setting is reported to be the principal control on availability of trace elements (Laveuf and Cornu, 2009), the calcite crystals are generally slightly enriched in the HREE. At high pH levels ~10, source water affects how clay particles adsorb LREE and HREE. Smectite clays at high pH levels tend to be enriched in HREE with a positive cerium anomaly, whereas illite will be enriched in LREE with a negative cerium anomaly (Laveuf and Cornu, 2009). When normalised to NASC, the majority of crystals have a negative Ce anomaly indicating the redox conditions of the water source, and implying formation in an oxic setting where Ce^{3+} is oxidised to Ce^{4+}, possibly via Mn-oxides, and which subsequently forms insoluble minerals (Vaniman and Chipera, 1996). The variation in the magnitude of the Ce anomaly and HREE enrichment in both the Pleistocene and contemporary crystals may be the result of variations in the mineralogy of the clay, pH of the supply fluid, and redox conditions.

Interpretation of the isotopic data

The Pleistocene calcite crystals have low positive $\delta^{18}O$ and $\delta^{13}C$ values which is consistent with previously reported data (Hay and Kyser, 2001), where the high $\delta^{18}O$ values are interpreted to have been produced by evaporative effects of the lake and inflow water, and the high $\delta^{13}C$ values caused either by methanogenesis (Hay and Kyser, 2001) or by evaporation (Bennett et al., 2012; Liutkus et al., 2005). As the calcite crystals are interpreted in this study to be contemporary with the sediments, and so representative of the original lacustrine setting, potentially they can be used as an indicator of the original lake water composition. However caution must be exercised, as investigations into the $\delta^{18}O$ and $\delta^{13}C$ values of carbonates from similar, contemporary lakes has highlighted the difficulty in relating those values directly to the lake water, because of the complex exchange of ions between the water body and the evaporite minerals (Horita, 1989; Horita et al., 1993; Talbot, 1990). Direct comparisons of lake water and calcite crystals from Lakes Makat, Ndutu and Natron are not possible because isotopic analyses of lake water were not successful due to the high concentrations of dissolved salts.

The calcite crystal data do not have a covariant trend. Studies of hydrologically closed lakes have shown that covariant trends in the $\delta^{18}O$ and $\delta^{13}C$ values of lake water are primarily influenced by the evaporation, productivity, and residence times of the lake, where hydrological closure is dominant over a long time scale of more than 5000 years (Li and Ku, 1997; Talbot, 1990). However over shorter time scales of a few hundred years, the lack of covariance in the $\delta^{18}O$ and $\delta^{13}C$ values of lake water is not necessarily an indicator of open system behaviour, and has been interpreted to be due to high levels of alkalinity reducing the impact of freshwater input and productivity (Li and Ku, 1997).

More importantly, when the calcite crystal data is plotted with the terrestrial carbonate data (Figure 5-28), the covariant trend in $\delta^{18}O$ and $\delta^{13}C$ values tends towards those of the calcite crystals. This has been interpreted as a mixing trend between lake and meteoric waters (Bennett et al., 2012) as seen in chapters 2 and 3.

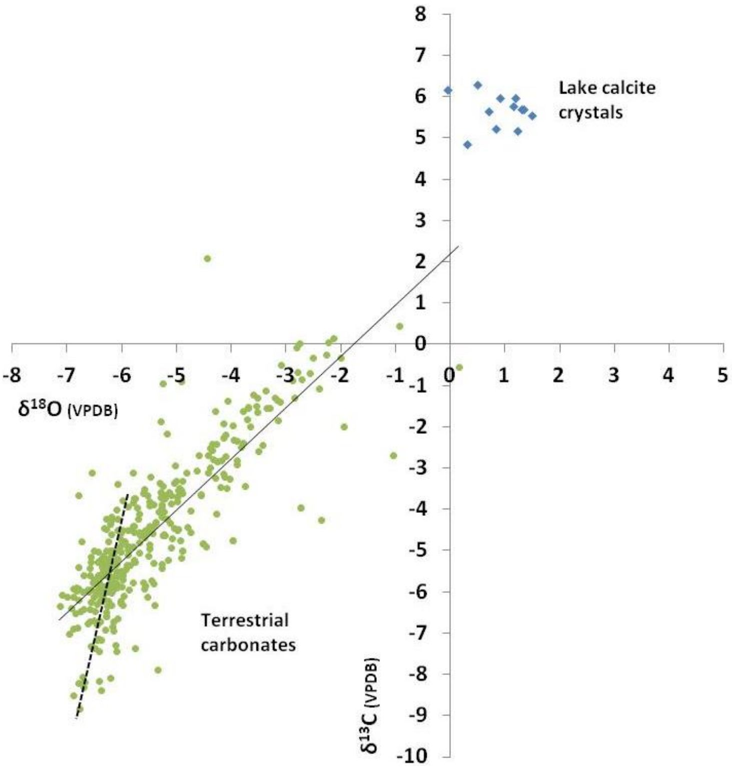

Figure 5-28: Calcite crystal and terrestrial carbonate stable isotope data.. The data from this study (Terrestrial carbonates - Green spots; Lake calcite crystals – blue diamonds) is plotted with the calcite crystal data from Hay and Kyser (2001) (Red squares). The dashed black line indicates the meteoric influence in the nuclei of the sparry nodules, and the continuous black line represents the mixing trend between meteoric and lake water.

Crystal formation- interim conclusions

- Crystal formed in the shallow sub-surface of the lake sediments and the lake margin sediments
- Crystals are frequently reworked in shallow scours (Figure 5-29)
- Crystals are found individually and as intergrown clusters
- The calcite crystals initiate by either utilising an original evaporate mineral precursor, or by direct precipitation of calcite
- Many of the euhedral calcite crystals have a nucleus that is morphologically similar to the crystal clusters

- Corrosion surfaces show multiple episodes of growth and dissolution during their formation
- There are repeated changes in the redox conditions during their formation
- Calcite crystals form fairly rapidly, within the timescales of the erosion surfaces at Olduvai

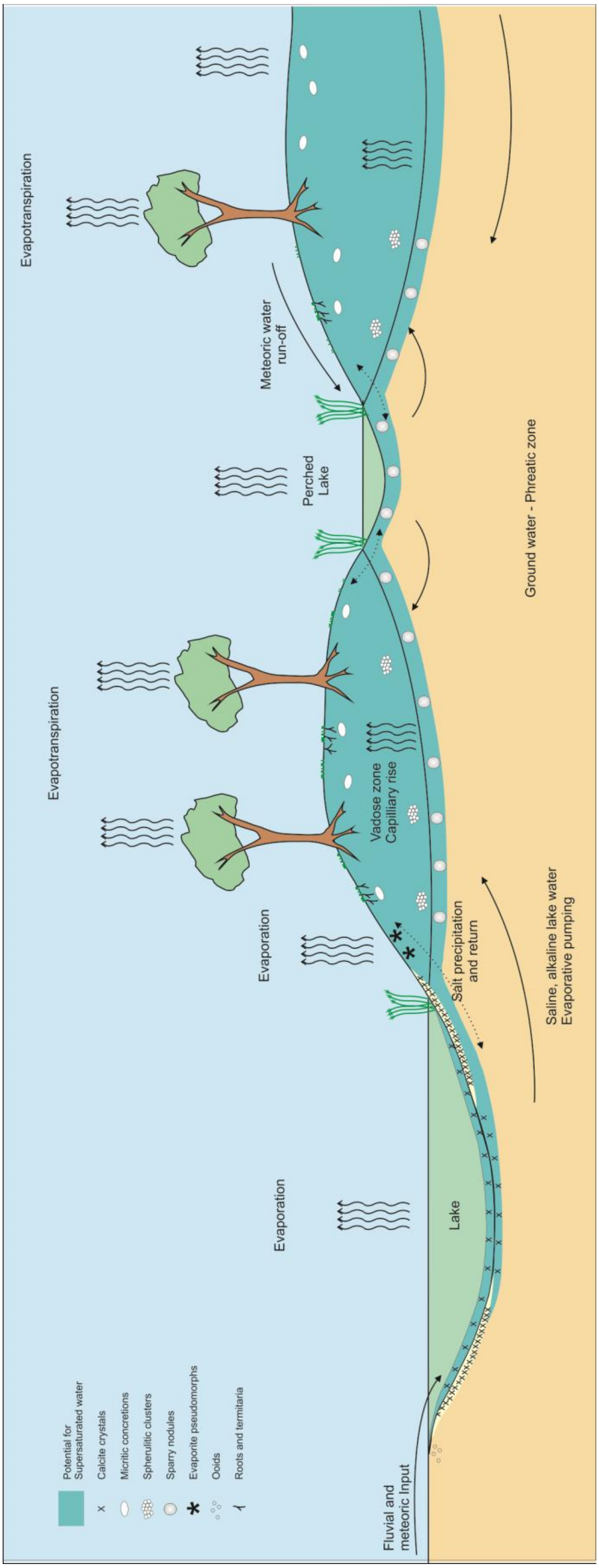

Figure 5-29: The calcite crystals are interpreted to form in the shallow sub-surface sediments on the lake floor or lake margins under anoxic to sub-oxic conditions (Crystals shown as x). At times of lower lake level these were reworked in shallow scours in the lake basin producing thinly bedded crystals rich sediments, confirming that they are geologically contemporaneous with their stratigraphic level. In order to make the different carbonate setting clear, the diagram exaggerates the vertical scale of the terrestrial setting which is likely to have been only ~1m of relief compared to the lake of <10m depth.

5.7.2 Uranium and lead in lacustrine calcite crystals

The potential to use calcite crystals for uranium-lead geochronology is of particular interest in this study (Chapter 7). The U^{238} - Pb^{206} decay series has a very long half life of 4.47 x 10^9y (Bourdon et al., 2003) and so very little radiogenic lead is likely to have been produced from uranium in the ~2Ma to 1.4Ma since the calcites from Olduvai formed. In order for the U-Pb method to be applied successfully to produce dates with useful precisions (comparable, say, to K/Ar) from such young carbonates it is necessary to identify material with high initial uranium and low common lead abundances. In addition, in order to adequately constrain an isochron, a wide range of $^{238}U/^{206}Pb$ values is required. Consequently, it is important to understand the factors controlling the incorporation of uranium and lead into the calcite lattice.

Uranium sources

Hydrologically closed and evaporative lakes can become enriched in uranium, and total uranium values can reach 15ppm (Linhoff et al., 2011). The supply of uranium to Palaeolake Olduvai was likely to have been by dissolution of source minerals, via fluvial delivery, from the volcanic complex in the east and from the Tanzanian Craton in the west, and by direct delivery of volcanic detritus susceptible to dissolution to the lake itself (Hay, 1976). If uranium availability in the supply fluid was the driving influence behind the uranium incorporation into lacustrine calcite crystals, the variation in total uranium abundance found in the Pleistocene crystals at different stratigraphic levels (Figure 5-18) would imply either different uranium sources, or rates of delivery, through time. Potentially the two different terrains associated with drainage from the west and east into Palaeolake Olduvai may have caused variation in the uranium abundance through time. Although there is no reported evidence for changes in the predominant direction of water delivery into the Olduvai basin, the climate at Olduvai is known to have varied through the stratigraphic sequence (Hay and Kyser, 2001). Different uranium source minerals will respond differently to weathering and dissolution (Goetz and Hillaire-Marcel, 1992; Jahn and Cuvellier, 1994; Kronfeld and Vogel, 1991), resulting in variations in the uranium concentrations in the water source.

Trace element data is not available for the craton. However, fluvial sources would have been in contact with granitic terrain and the Bukoban Shales, both of which are reported at the headwaters of Olduvai Gorge (Hay, 1976), and potentially provide a source of uranium. From the eastern volcanic complex, the end of the Ngorongoro, and entire Olmoti, volcanic histories are understood to provide the sources of the tuff and volcaniclastic deposits of Bed I and Lowermost Bed II. Uranium abundances from samples of the crater walls of these volcanoes are equivalent to the volcanic deposits found in the Olduvai stratigraphic succession. They contain uranium levels between 1 and 6ppm (McHenry et al., 2008; Mollel et al., 2008; Mollel et al., 2009). No data is available for tuffs associated with Upper Bed II between Tuff IIC and Tuff IID.

Tuffs associated with the Lower bed I (RHCI CA104) crystals, which have the highest uranium concentration, are reported to be derived from the Ngorongoro volcano which yields uranium values of between 0.86 and 2.97ppm (Mollel et al., 2008). Whereas those from Upper Bed I (RHCI CA7,10), which have the lowest uranium concentrations, are from the Olmoti volcano which yield uranium values between 0.5ppm and 5.7ppm (Mollel et al., 2008). Overall, calcite crystals associated with the Ngorongoro volcanics have higher uranium concentrations than those associated with the Olmoti volcanics, which is the opposite of the concentrations in the volcanics themselves. This suggests that the volcanic sources deposited in Palaeolake Olduvai are not the main influence on the amounts of uranium in the calcite.

Interestingly, contemporary lake crystals do not show a positive covariance between their uranium abundance and that of their associated lake water (Table 7). Although Lake Natron has the lowest uranium concentration in the water, its calcite crystals have the overall highest amounts of uranium. Conversely although the concentration of uranium in the water from Lake Ndutu is the highest of the three lakes, the calcite crystals have the lowest overall concentrations.

Consequently, the amount of uranium available in the water source is probably not the control over the abundance of uranium in calcite crystals.

Uranium incorporation into the calcite lattice

Uranium abundance of up to 120ppm in the Pleistocene crystals from Olduvai is unusually high for calcite formed by earth surface processes. The partition coefficient of U into calcite is less than 1 (Curti, 1999; Jahn and Cuvellier, 1994; Reeder et al., 2001), and typically uranium is present in calcite at less than 10ppm, unless it has been recrystallised from a more uranium-rich precursor such as aragonite which can have much higher concentrations of uranium (Kelly et al., 2006; Kitano and Oomori, 1971; Reeder et al., 2001). There is no textural or geochemical evidence of an aragonite precursor for the calcite crystals that would explain the high uranium values, and any potential precursor minerals, trona or gaylussite, are reported to have only low concentrations up to 2ppm (Henderson et al., 1987; Hillaire-Marcel et al., 1986). As neither the supply of uranium, nor the crystal mineralogy, is considered here to be a major factor in its incorporation in calcite, the high levels of uranium in the lacustrine calcite crystals are inferred to be primarily controlled by the mechanism with which it incorporates in the calcite lattice.

Incorporation of uranium in the calcite lattice under oxic or mildly reducing conditions is reported to occur in high pH, carbonate rich water, with uranium in the U(VI) oxidation state as the $UO_2(CO_3)_3^{4-}$ ion (Kelly et al., 2006; Langmuir, 1978; Reeder et al., 2001). If the water source is highly reducing, uranium incorporation into the lattice at high pH may occur via the U(IV) moiety the $(UO_2)_3(OH)_5^{+}$ ion (Langmuir, 1978; Sturchio et al., 1998). The smaller size of the U(IV) compared to the U(VI) ion would indicate that it would preferentially fit into the calcite lattice, but it has a much lower solubility and requires highly reducing conditions, whereas the U(VI) ion is much more soluble and much more abundant. The presence of organic matter and bio-reducing conditions has also been associated with uranium incorporation in the calcite lattice (Kelly et al., 2006; Rasbury et al., 2000).

Palaeolake Olduvai is understood to have been saline, alkaline, and organic-rich, similar to contemporary Lakes Makat, Ndutu and Natron. The generally high Fe/Mn ratios of the Pleistocene crystals from RHCII CA3, 5, and 6, and the contemporary calcite crystals from Lakes Makat, Ndutu and Natron, indicate formation in a reducing environment. The cubic morphology of the haematite, present in the clays with the calcite crystals, indicates that it may have originally been pyrite, previously recorded in the lake sediments at Olduvai (Hay, 1976). This too identifies a reducing environment, and sulphate reduction of organic matter during calcite crystal formation.

It is likely that the very high pH, high alkalinity, presence of organic matter, and the reducing environment, contributed towards the incorporation of unusually high levels of uranium in the lake calcite crystals. It is not possible to distinguish from these data whether this occurred via the U(VI) moiety through highly alkaline conditions, or the U(IV) moiety due to highly reducing conditions, and further detailed spectroscopic work, comparable to that completed by Sturchio (1998), would be required to identify the uranium species involved.

Lead incorporation into the calcite lattice

Lead is poorly soluble in aqueous systems with pH higher than ~3 (Aspinall, 2001; Bourdon et al., 2003; Jahn and Cuvellier, 1994), and so only very low amounts of lead might be expected to be incorporated into a calcite lattice. However it can be adsorbed onto clay particles which can subsequently become trapped in the calcite structure during crystallization (Jahn and Cuvellier, 1994). Terrestrial lake margin carbonates, interpreted to have formed immediately below the water table at Olduvai, contain up to ~15ppm of lead, interpreted to be from clay particle inclusions (Chapter 2). As the lake and the terrestrial sediments are linked one would not expect the lacustrine system to be free of lead. Yet importantly, although the Pleistocene lacustrine crystals analysed in this study contain clay inclusions, they have exceptionally low values of common lead compared to the lake margin carbonates (Figure 5-30).

Although petrographic screening did not identify any obvious differences in the density of clay particle inclusions between Pleistocene and contemporary crystals, crystals from Lake Natron have similar Pb and U concentrations as the Pleistocene specimens, whereas contemporary crystals from Lake Makat and Lake Ndutu have U and Pb abundances more comparable to the sparry nodules (Figure 5-30).

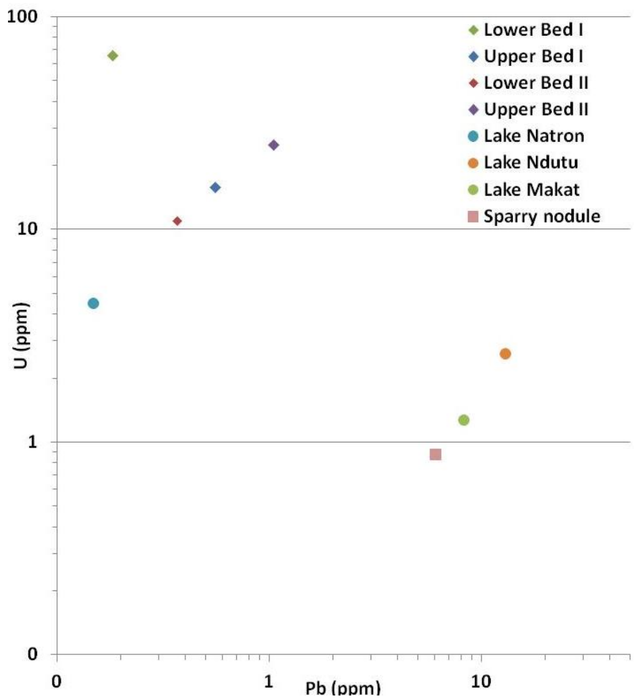

Figure 5-30: U and Pb abundance in Pleistocene and contemporary calcite crystals and a terrestrial sparry nodule. The lead and uranium abundance (ppm) in calcite crystals at four different stratigraphic levels from Olduvai Gorge compared to that of calcite crystals from contemporary Lakes Natron, Ndutu and Makat, and a lake margin carbonate from the equivalent of Lower Bed II at Olduvai Gorge.

It is reasonable to assume that calcite crystals formed at Olduvai were precipitated in lakes rich in humic substances, similar to the modern lakes examined in this study. Primary productivity in these environments is high, and a thick algal growth is common on the lake floor. The abundant algae, plus the waste products of lake fauna, produce sediments rich in decaying organic matter. At the high pH values encountered in contemporary saline, alkaline lakes (Table 7), lead is complexed by organic molecules such as humic and fulvic acids, and these will preferentially remove lead which otherwise would be adsorbed onto clay particles and desorb Pb already adsorbed onto clay (Erel and Morgan, 1992; Jackson and Skippen, 1978). This may be a mechanism whereby the clay inclusions in the calcite crystals can have such very low concentrations of lead.

5.8 Conclusions

- Small, euhedral, calcite crystals are interpreted to have formed in the shallow sub-surface sediments on the lake floor or lake margins under anoxic to sub-oxic conditions
- At times of lower lake level these were reworked in shallow scours in the lake basin producing thinly bedded crystals rich sediments, confirming that they are geologically contemporaneous with their stratigraphic level.
- Two forms of crystal have been identified, those from Olduvai Gorge in Lower Bed II (RHCI CA104) which are scalenohedral, and those from other stratigraphic levels at Olduvai, and contemporary lake crystals, which have prismatic side faces and unit rhombohedral terminations
- Pleistocene crystals from Lower Bed I at Olduvai Gorge are opaque, milky-white, and not zoned. They are interpreted to have formed from fluids which are richer in Mg^{2+} ions than at other levels, and in sediments not subject to reworking.
- Pleistocene crystal from Upper Bed I, Lower Bed II and Upper Bed II at Olduvai, and contemporary crystals from Lakes Natron, Ndutu, and Makat, are transparent, grey-green, yellow or colourless with sub-microscopic inclusions. They are interpreted to have formed in sediments which often reworked by wind driven waves or fluvial activity.
- The crystals or crystal aggregates are interpreted to have formed by two stages:
- The first stage is either by direct calcite precipitation or by utilisation of an evaporite mineral precursor, apart from contemporary crystals at Lake Ndutu which formed by recrystallisation of grains composed of micrite.
- This stage is followed by a later stage of calcite overgrowth which is usually euhedral.
- Sector, concentric and intrasectoral zoning seen in cathode-luminescence identifies a partitioning of trace elements on particular crystal faces.
- Intermediate stages of chemical corrosion are seen by truncation of zones in cathode-luminescence, identifying a multi-stage process of deposition.

- Prismatic sectors have higher concentrations of uranium than the rhombohedral sectors, potentially providing a range of U/Pb values
- The calcite crystals from all levels have exceptionally low lead values and high uranium concentrations, hypothesised to be due to the interaction of humic substances with lake sediments in water with high pH and high alkalinity.
- The favourable combination of uranium and lead concentrations and so the potential range of U/Pb values within crystals, make these lacustrine calcite crystals potential targets for U-Pb geochronology.

Chapter 6: Lacustrine dolomite of Bed I, Olduvai Gorge, Tanzania

6.1 Overview

Two types of early authigenic, lacustrine, dolomite have been identified in the lake centre sediments of Palaeolake Olduvai, Tanzania. They are interpreted to represent two types of dolomite formation processes that were operating in the saline, alkaline, lake environment. Lower Bed I dolomite is interpreted to have formed in deeper water settings, from more evaporative, saline fluids, compared to the Upper Bed I dolomite which is interpreted to have formed during a lowstand in a shallow lake margin setting, in less concentrated brines. The Upper Bed I dolomite is contemporary with a newly identified dolomite occurrence at the eastern lake margin, found as blocks of dolomite rather than laterally persistent beds. The lake water evolution is inferred to be driven primarily by evaporation and mixing with meteoric water at the lake margins.

6.2 Introduction to lacustrine dolomite occurrences

Olduvai Gorge, Tanzania, is a modern fluvial incision exposing Pleistocene sediments that were deposited in a saline, alkaline lake (Hay, 1976). Carbonate minerals are found throughout the stratigraphic sequence, and although these are dominantly low-Mg calcite (Chapter 2, 3, 5), there are several, episodic occurrences of synsedimentary dolomite (Hay and Kyser, 2001). Understanding the processes which may have been involved during the dolomite formation can provide an insight into the lacustrine conditions operating at the time.

Ideal dolomite, $CaMg(CO_3)_2$, has a Ca:Mg ratio of 1:1 and is composed of alternating Ca and Mg sites through the crystal structure. Authigenic lacustrine dolomites are usually non-stoichiometric and calcium-rich with Ca:[Ca,Mg] ratio >0.5, although near-stoichiometric dolomite can be formed in Mg^{2+} rich water such as found in evaporitic, arid settings, or as the result of increasing textural alteration (Armenteros, 2010). The degree of disorder of Ca-Mg, and the likely consequent disorder of layers within the crystal lattice is often pronounced in lacustrine samples compared to an ideal dolomite. These variations from the ideal stoichiometry and lattice disorder may be the result of environmental conditions controlling dolomite formation (Armenteros, 2010; Wright, 2008), and in conjunction with the crystal textures, can help identify the origin of the dolomite.

Authigenic lacustrine dolomite has been described as having a ‘primary’, an ‘early diagenetic’ or a ‘secondary’ origin; where ‘primary’ dolomite requires precipitation directly out of the water column, ‘early diagenetic’ dolomite is formed within the lake sediments, and ‘secondary’ describes dolomite formed by alteration of an earlier mineral, particularly calcite (Armenteros, 2010). Primary and early diagenetic dolomite is reported to form by abiotic precipitation in the water column or within the lake sediments (Rosen et al., 1989). It is associated with source water with a high Mg^{2+}/Ca^{2+} ratio, a high ionic strength, high alkalinity, high CO_3^{2-}/Ca^{2+} ratio, and low SO_4^{2-} concentration (Armenteros, 2010). It can also occur through microbial mediation (De Deckker and Last, 1989; De Deckker, 1988; Folk, 1975; García Del

Cura et al., 2001; Last, 1990; Wacey et al., 2007). As a secondary mineral it is reported to form through replacement of gypsum by microbial activity, replacement of authigenic or allogenic micrite in brines, and by recrystallisation of high-Mg calcite (Armenteros, 2010; Eugster and Hardie, 1975; Rosen and Coshell, 1992).

The $\delta^{18}O$ values of dolomites are controlled by both equilibrium and kinetic isotope fractionation. The ambient temperature, isotopic composition of the pore fluid, and the stoichiometry of the dolomite, are the principal influences over equilibrium $\delta^{18}O$ values, and the rate of dolomite precipitation is the main cause of kinetic fractionation (Humphrey, 2000; Schmidt et al., 2005; Wacey et al., 2007; Wheeler et al., 1999). The $\delta^{13}C$ values of lacustrine dolomites are influenced by both organic processes and inorganic processes. High rates of primary productivity and methanogenic processes will preferentially enrich the dissolved inorganic carbon in pore fluids in ^{13}C (Aharon et al., 1977; Armenteros, 2010; Talbot, 1990; Talbot, 1991), whereas bacterial decomposition via sulphate reduction or methane oxidation will preferentially deplete the pore fluid in ^{13}C (Armenteros, 2010). In addition, ^{13}C enrichment of pore fluid by inorganic processes is reported to occur through high rates of evaporation and degassing of CO_2 to the atmosphere (Mees et al., 1998; Rosen et al., 1989).

A textural and geochemical investigation of the dolomites from Olduvai has been undertaken to provide an insight into the processes operating during their formation. This study uses detailed XRD analyses to determine the stoichiometry and relative lattice ordering of the dolomites, in conjunction with $\delta^{13}C$ and $\delta^{18}O$ values and textural investigations to interpret the dolomite depositional processes at two different stratigraphic levels in Palaeolake Olduvai.

6.3 Materials and methods used in dolomite investigation

Dolomite for this study was sampled from two beds in the central lake basin, Upper Bed I and Lower Bed I, to investigate potential variation in the dolomite mineralogy at different points in the stratigraphy (Figure 6-1, Table 8). Lower Bed I dolomite is located in the wholly lacustrine lake basin succession between Tuff IA and Tuff IB and the Upper Bed I dolomite is in the lake basin sediments directly beneath Tuff IF. Three units of Lower Bed I dolomite were sampled at three location over a distance of about 100m to investigate any variation laterally on this scale. A newly-discovered dolomite from the lake margin (Tr135) was also sampled to identify, if possible, a link between the lake basin and lake marginal dolomite at the same stratigraphic level (Upper Bed I dolomite). The lacustrine sediments and general geology of the area are described in Chapter 5.

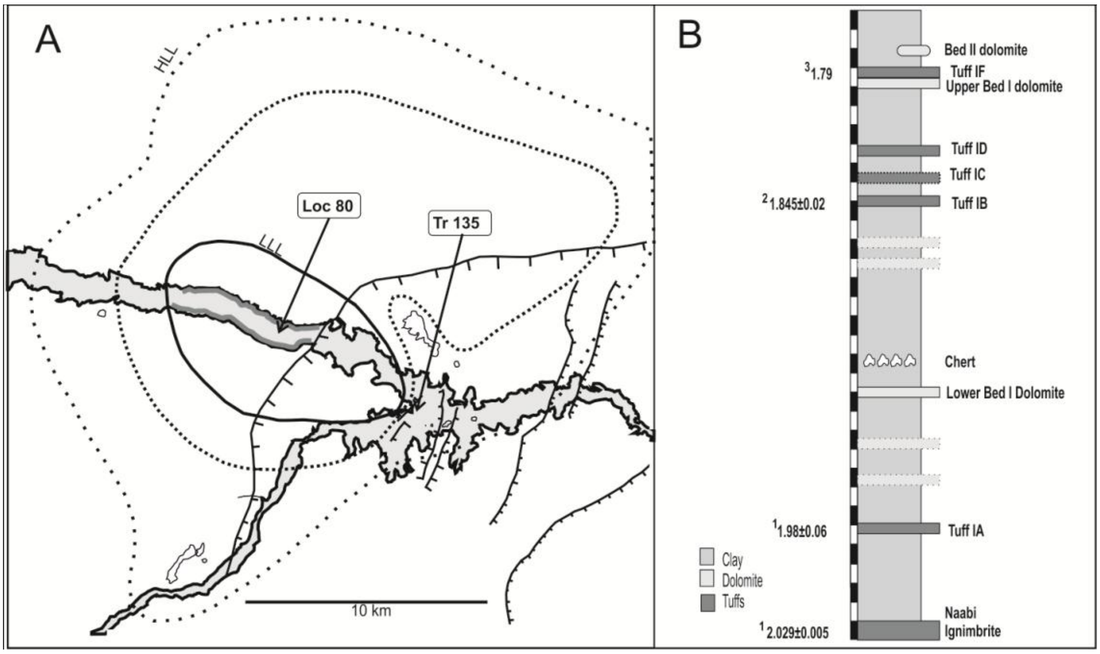

Figure 6-1: Olduvai Gorge and dolomite sample positions in a generalised lacustrine stratigraphy. A) Olduvai Gorge, Tanzania, East Africa, a modern fluvial incision into Pleistocene sediments is identified in grey. The positions of major faults are indicated by lines with ticks on the downthrow side. The outcrop of the central lake basin sediments are identified as the darker grey area. The variable extent of Palaeolake Olduvai is identified as LLL (Low lake level) and HLL (High Lake level) using the palaeogeographical reconstruction immediately above Tuff IF (Hay, 1976). The dolomites sampled for this study were taken from Loc 80 (Richard Hay Cliff - RHC) and Tr 135. B) Generalised Bed I and Lower Bed II stratigraphy at Loc 80 comprises interbedded clays, tuffs and dolomites (Scale bar 1m). Bed I dolomites previously identified in Hay (1976) but not investigated here have a dashed edge. Lower Bed I dolomite here is referred to as the 'middle dolomite' in Hay (1976). A Lower Bed II dolomite was identified at Loc 80 during this research although not analysed for this chapter. Published dates were all determined using $^{40}Ar/^{39}Ar$ single crystal analyses of tuffs apart from Tuff IF which is defined by the base of the Olduvai Subchron. 1) (Walter et al., 1992), 2) (Blumenschine et al., 2003), 3) (Hay and Kyser, 2001).

Dolomite specimens	Sampling Location
Lake margin dolomite	
Tr135 CA8 1	Tr135 eastern lake margin, overlain by Tuff IF
Tr135 CA8 2	
Upper Bed I dolomite	
RHCI CA9U - upper unit	Loc 80 lake basin, two samples from the upper unit at sampling site1
CA9-2 - upper unit	
RHCI CA9L - lower unit	Loc 80 lake basin, two samples from the lower unit at sampling site1
CA9-1 - lower unit	
Lower Bed I dolomite top unit	
CA6	Loc 80 lake basin, two samples from the top unit at sampling site1
RHCI CA6	
RHCI Gul CA1	Loc 80 lake basin, one sample from the top unit 50m east of sampling site1
RHCI CA116	Loc 80 lake basin, two samples from the top unit unit 50m west of sampling site1
116	
Lower Bed I dolomite middle unit	
CA5	Loc 80 lake basin, two samples from the middle unit at sampling site1
RHCI CA5	
RHCI CA117	Loc 80 lake basin, two samples from the middle unit 50m west of sampling site1
117	
Lower Bed I dolomite bottom unit	
RHCI CA118	Loc 80 lake basin, two samples from the bottom unit 50m west of sampling site1
118	

Table 8: Dolomite samples from Olduvai Gorge analysed for this chapter. The Lake margin dolomite was taken from Tr135 and the Upper Bed I dolomite and Lower Bed I dolomites were taken from Loc 80. The Lower Bed I dolomite was composed of three units, the top, middle and bottom units. Samples from Tr135 were selected from a single sampling site. Samples from Loc 80 were taken from three sampling sites at RHC; a principal sampling site where the complete stratigraphic succession was most completely exposed, a sampling site ~50m east of the main site and a sampling site ~50m west of the main sampling site where the Lower Bed I dolomite was exposed in gullies.

Standard polished 30µm thick thin sections impregnated with blue resin were prepared and examined using transmitted light microscopy and cathode-luminescence. Scanning electron microscope investigations using secondary electron (SEM-SE) and backscatter (SEM-BS) detectors were performed on carbon-coated thin sections and on gold coated fresh rock chips using a Phillips XL30 Scanning Electron Microscope fitted with an Oxford Instruments Energy Dispersive X-Ray analyser (EDX).

A standard staining technique was used to identify if the dolomite is ferroan or non-ferroan using alizarin red and potassium ferricyanide in weak hydrochloric acid. Non-ferroan dolomite does not change colour whereas ferroan dolomite stains pale blue to turquoise (Dickson, 1965).

The X-ray diffraction (XRD) analysis of carbonates was initially performed to confirm their mineralogy. The powdered samples for XRD were produced from each of the six dolomite specimens using a hand-held modelling drill with a 1mm nickel carbide bit, avoiding contamination of samples by inclusions of clay or detrital siliciclastic grains where possible. Samples were gently crushed using an agate mortar and pestle to reduce lattice strain during preparation (Gavish and Friedman, 1973). Sample sizes of a few mg were analysed using a specially made small sample holder, and carbonate mineralogy was identified using a Siemens 0-500 x-ray diffractometer (Method 1) with a scanning speed of 5 seconds per $0.2^{o}2\theta$ between 24 and 55 $^{o}2\theta$ (CuKα).

Following initial screening, more diffraction measurements were made in order to determine (Method 2a – detailed below) the lattice ordering, unit cell parameters, excess Ca and (Method 2b) the possibility of more than one dolomite phase per sample. A sample of recent Coorong dolomite, as an example of poorly ordered dolomite, and a well crystallised, ordered, near-stoichiometric dolomite were also analysed for comparison. Approximately 4g of sample were required for each analysis. In each case small chips of dolomite were selected to be as free from clay and any external weathering as possible. The samples were coarsely crushed for ~30 seconds using a mechanical Tema mill and an agate mortar and pestle, again taking care to avoid lattice damage. The samples were passed through a 1.25ϕ sieve. 2.7g of sieved dolomite and 0.3g silicon standard were mixed using a McCrone® micronising mill with ~10ml distilled water. The samples were then freeze-dried to produce an homogenous powder.

Method 2a: Some of the samples were initially run with a divergence and antiscatter slit of 0.3^{o}, a detector slit of 0.05^{o}, and a scanning speed of 4 seconds per $0.02^{o}2\theta$ between 20 and $62^{o}2\theta$ (CuKα). The dolomite standard and the sample of Coorong dolomite were also run using these parameters.

Method 2b: Further dolomite analyses were run to achieve a more highly resolved trace using a divergence and antiscatter slit of 0.3^{o}, a detector slit of 0.05^{o}, and a scanning speed of 30 seconds per $0.01^{o}2\theta$ between 20 and $62^{o}2\theta$ and between 68 and $76^{o}2\theta$ (CuKα).

$CuK\alpha_2$ contributions were removed from the raw diffraction data using an algorithm available in the PowderX computer code (Dong et al., 1999), selected on the basis of a visual inspection of each diffraction pattern. Peak fitting was processed using the TRACES X-ray diffraction screen processing software and accessories programme (Diffraction Technology Pty. Ltd.). The background was removed and the peak heights and intensities were derived using a pseudo-Voight function. Dolomite peak positions were identified by their *hkl* reflections and corrected for instrumental errors using the silicon standard peak positions. The degree of ordering of the dolomite lattice compared to a well ordered dolomite is derived by using the linear relationship between the relative order of the dolomite specimens from Olduvai, normalised to a near-stoichiometric dolomite (Equation 1), and the ratio of ordering and non-ordering reflections in the samples (Equation 2) (Wheeler et al., 1999). This assumes that the degree of ordering is proportional to the intensity of the ordering reflection (Aharon et al., 1977), and other trace elements are not present in sufficient quantities to affect the intensity and peak position of the ordering reflections.

$$relative\ order\ (\%) = 100\ x\ \frac{\left(\frac{I_{015}}{I_{110}}\right) sample}{\left(\frac{I_{015}}{I_{110}}\right) OD}$$

Equation 1: The degree of ordering of dolomite. I is peak intensity of the 015 and 110 reflections of the sample and the well ordered dolomite (OD) (Wheeler et al., 1999). The 015 reflections are sensitive to dolomite ordering, and are normalised to the 110 reflections, which are insensitive to dolomite ordering (Aharon et al., 1977), to offset the potential effects of different abundances of more than one phase of dolomite.

$$reflection\, ratio = \frac{(I_{113}) sample}{(I_{113} + I_{015}) sample}$$

Equation 2: Comparison of ordered and non-ordered reflections. I is peak intensity of the 015 and 113 reflections of the sample (Wheeler et al., 1999). The 015 reflections are sensitive to dolomite ordering and the 113 reflection is insensitive (Aharon et al., 1977).

The unit cell parameters were calculated from the corrected $^{o}2\theta$ values using the UNIT CELL program (Holland and Redfern, 1997) with $CuK\alpha_1$ values 1.540593λ (Hölzer et al., 1997). These data were then used to calculate the average amount of Ca per structural unit (n_{Ca}) (Equation 3) (McCarty et al., 2006), and from that the mol%$CaCO_3$.

$$c\ axis\ = 0.8632n_{Ca} + 15.14$$
$$a\ axis\ = 0.1168n_{Ca} + 4.6903$$
$$d(104) = 0.119n_{Ca} + 2.7658$$
$$a_{eff}\ = 0.11967n_{Ca} + 4.6872$$
$$c_{eff}\ = 0.8852n_{Ca} + 15.1146$$
$$a_{eff}\ = 1.0251d(104) +\ 1.8499$$
$$a_{eff}\ = 1.0251d(104) +\ 1.8499$$
$$a_{eff}\ = 1.8215d(113) + 0.8157$$
$$c_{eff}\ = 7.5244d(104) -\ 5.7065$$

Equation 3: Calculation of the average amount of Ca per structural unit (n_{Ca}) in the dolomite samples using the unit cell parameters and lattice hkl spacings (McCarty et al., 2006). c_{eff} and a_{eff} are calculated from the 104 and 113 reflections. The average of these values were used to calculate the mol%$CaCO_3$.

Carbon and oxygen stable isotopes values of powdered dolomite were determined on 5mg samples by reaction of individual aliquots with 2ml of 100% orthophosphoric acid under high vacuum ($<5x10^{-5}$ Torr) at 25°C. Data were corrected using standard procedures and reported in δ ‰ (VPDB) with a reproducibility of better than ± 0.1‰ for $\delta^{18}O$ and $\delta^{13}C$.

6.4 Results of dolomite analysis

6.4.1 Field relationships and Textural analysis

Lower Bed I dolomite

The Lower Bed I dolomite is composed of three tabular, stacked, massive beds, with varying clay content, within a thick clay sequence. Staining showed that it is non-ferroan. The top unit is massive, tabular well indurated, and ~30cm thick. It has sharp upper and lower contacts and displays no visible vertical variation. The middle and bottom units are each similarly ~30cm thick, they have sharp tops but are increasingly green in colour, increasingly friable, and have an increasing clay abundance downwards. The top unit is composed of euhedral to subhedral rhombic crystals <5µm in size with clay particles partially cemented by the dolomite crystals. The dolomite crystal size in the lower two units is smaller than the top unit, <3µm, and typically <1µm (Figure 6-2).

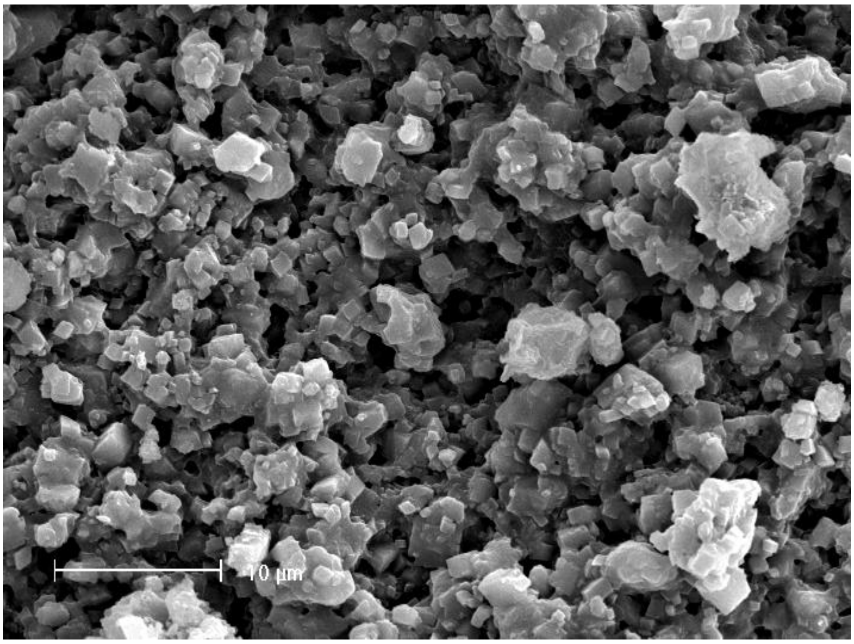

Figure 6-2: SEM-SE images of Lower Bed I dolomite (RHCI CA6). Dolomite crystals are <3µm with clay particles partially cemented in the dolomite (Scale bar 10µm).

Upper Bed I dolomite

The upper dolomite forms a tabular bed ~10cm thick composed of approximately equal upper and lower units separated by a thin layer of green silt. The dolomite caps a succession of upward-thinning clay beds with multiple erosion surfaces interpreted to have formed during gradual shallowing of the lake. It is overlain by Tuff IF. Staining indicates the dolomite to be non-ferroan. Both units have the same macromorphological and micromorphological features in hand specimen. They are well indurated and produce sub-conchoidal fractures, and the upper surfaces of each unit display wave ripples and cross-lamination (Figure 6-3).

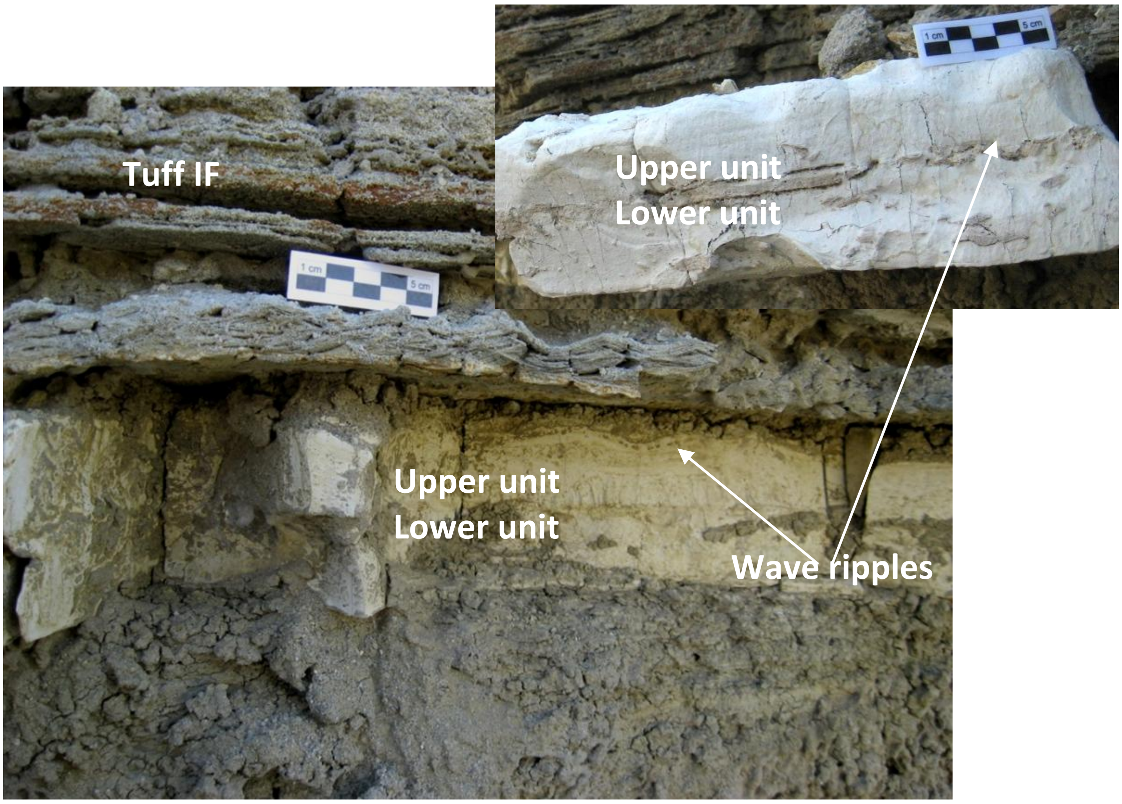

Figure 6-3: The Upper Bed I dolomite (Loc 80) is overlain by Tuff IF. Wave ripples and cross-lamination are present on the upper surface of each the two dolomite units, which are separated by a thin layer of green silt

The dolomite bed contains a few fine sand-sized, detrital grains of siliciclastic minerals, including mica and quartz. The dolomite is largely composed of euhedral rhombic crystals <5µm in size with clay particles partially cemented into the dolomite crystals (Figure 6-4a). Some broken faces exhibit a raised polygonal network of dolomite cemented clay (Figure 6-4b). There is no evidence of roots or bacterial fibres, although bacterial fibres have poor preservation potential. Often this dolomite has subvertical mm-scale cracks which are lined with dolomite cement crystals which are ~10µm.

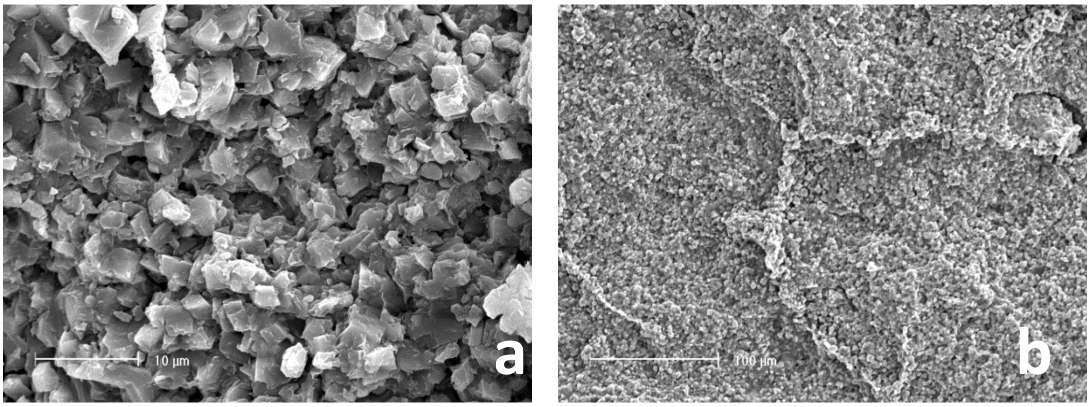

Figure 6-4: SEM-SE images of Upper Bed I dolomite (RHCI CA9U); a) Dolomite crystals from the Upper Bed I dolomite are <5µm with clay particles partially cemented in the dolomite (Scale bar 10µm) b) some broken faces have a polygonal network of clay rich dolomite crystals (Scale bar 100µm).

Both units have sub-spherical voids ~10µm to 100µm in diameter, not seen in the Lower Bed I dolomite samples. Thin section analyses reveal they are surrounded by a dark brown halo of sub-microscopic inclusions. The voids are lined by euhedral, rhombic, dolomite crystals ~ 10µm in size, which do not have clay particles trapped in them as the main mass of dolomite crystals does (Figure 6-5a). Usually the small crystals at the edge of the void are cemented by the larger crystals, showing the larger crystal to be a later dolomite growth. The pore lining dolomite crystals contains strontium detectable using SEM-EDX analysis. SEM-BS analyses reveals zoning in the pore lining dolomites, and EDX analyses show variable Mn concentrations, with the brighter zones characterised by increased Mn (Figure 6-5b).

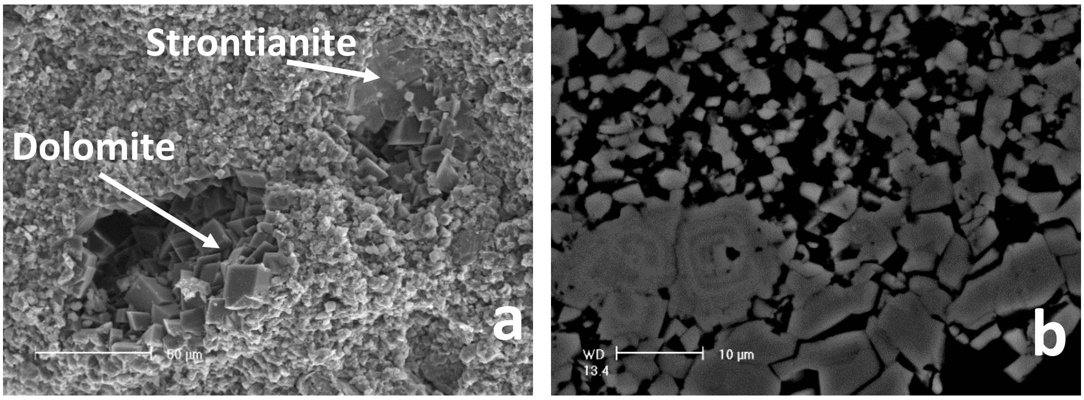

Figure 6-5: SEM-SE identification of textures and geochemical zoning in the Upper Bed I dolomite (Loc 80, RHCI CA9L). a) SEM-SE image of sub-spherical voids in the dolomite are lined by euhedral, rhombic, dolomite crystals, partially cementing the walls of the void, and contain no visible clay. Some of these voids contain strontianite which succeeds the void lining dolomite (Scale bar µm) b) SEM-BS image of larger dolomite crystals. These are concentrically zoned and the brighter bands contain trace Mn (Scale bar 10µm).

Strontianite ($SrCO_3$), identified by EDX, succeeds the larger dolomite crystals which form the pore lining, and also occurs as patches cementing the smaller dolomicrite mass, and is revealed as a radiating structure using SEM-BS (Figure 6-5a, Figure 6-6).

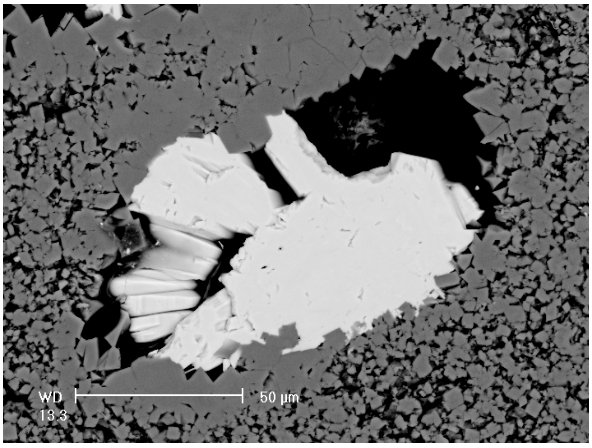

Figure 6-6: SEM-BS image of strontianite showing a radiating structure (Loc 80, RHCI CA9L). The strontianite is precipitated on top of the pore lining dolomite (Scale bar 50µm)

Tr 135 dolomite

This study reports for the first time dolomite on the westernmost location of the eastern lake margin at Tr135. It is found immediately below Tuff IF and is in the same stratigraphic position, and has the same micromorphological characteristics, as the Upper Bed I dolomite of the lake basin sediments. The macromorphological characteristics differ however, as it does not form a thin and tabular bed but is found as undulating and broken blocks up to ~30cm thick, in translucent green/yellow waxy claystones with a Stevensite-like texture (Figure 6-7).

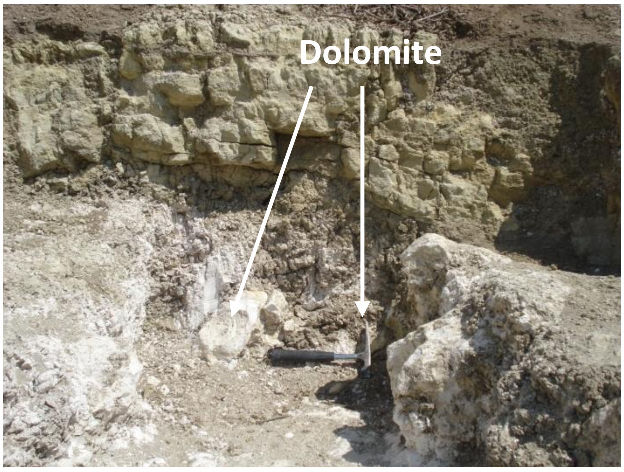

Figure 6-7: Dolomite at Tr 135, western lake margin, in Upper Bed I. The dolomite is found in thick and broken blocks, with a rounded and undulating surface. Beds of micritic calcite underlie the dolomite blocks.

Cathode-luminescence

Most of the dolomite has bright red luminescence under CL. In the upper dolomite the larger dolomite crystals developed in the voids, and the strontianite, have only dull red luminescence. This indicates at least two phases of dolomite prior to strontianite formation.

6.4.2 Stable isotope results

Seventeen samples from the three dolomites were selected for stable isotope analysis (Table 9).

Dolomite	$\delta^{13}C$ (VPDB)	$\delta^{18}O$ (VPDB)
Lake margin dolomite		
Tr135 CA8 1	-1.09	-2.15
Tr135 CA8 2	-1.02	-1.98
Upper Bed I dolomite		
RHCI CA9U - upper unit	-2.21	-1.53
CA9-2 - upper unit	-2.10	-1.88
RHCI CA9L - lower unit	-2.22	-1.74
CA9-1 - lower unit	-2.16	-1.77
Lower Bed I dolomite top unit		
CA6	1.95	1.74
RHCI CA6	1.61	1.37
RHCI Gul CA1	1.82	2.11
RHCI CA116	1.88	1.83
116	1.87	1.26
Lower Bed I dolomite middle unit		
CA5	4.64	4.27
RHCI CA5	4.79	4.56
RHCI CA117	3.11	3.17
117	2.90	3.09
Lower Bed I dolomite bottom unit		
RHCI CA118	1.39	1.37
118	1.40	1.48

Table 9: $\delta^{18}O_{VPDB}$ and $\delta^{13}C_{VPDB}$ ratios for the dolomite units.

Bulk dolomite was sampled, avoiding any weathered edges or patches obviously heavily contaminated by clay. Overall a covariant change from lower to higher $\delta^{18}O_{VPDB}$ and $\delta^{13}C_{VPDB}$ isotope ratios is seen (Figure 6-8). The values range from $\delta^{18}O_{VPDB}$ -2.2‰ to 4.6‰ and $\delta^{13}C_{VPDB}$ -2.2‰ to 4.8‰ with an r^2 value of 0.96, $r(17) = 0.98$, $p < 0.0001$, and the data from each of the individual beds is tightly clustered (Figure 6-8). The $\delta^{18}O$ and $\delta^{13}C$ values of the Upper Bed I dolomite and trench 135 dolomite, which are at comparable stratigraphic levels, are much lower than those in the Lower bed I dolomite. The Upper Bed I dolomite and Tr135 have a narrow range which varies between $\delta^{18}O_{VPDB}$ -2.2‰ to -1.5‰ and $\delta^{13}C_{VPDB}$ -2.2‰ to -1.0‰. The top unit of the Lower Bed I dolomite varies between $\delta^{18}O_{VPDB}$ 1.3‰ to 2.1‰ and $\delta^{13}C_{VPDB}$ 1.6‰ to 2.0‰, the middle unit of the Lower Bed I dolomite varies between $\delta^{18}O_{VPDB}$ 3.1‰ to 4.6‰ and $\delta^{13}C_{VPDB}$ 2.9‰ to 4.8‰, and finally the bottom unit of the Lower Bed I dolomite varies between $\delta^{18}O_{VPDB}$ 1.4‰ to 1.5‰ and $\delta^{13}C_{VPDB}$ is 1.4‰ in both cases.

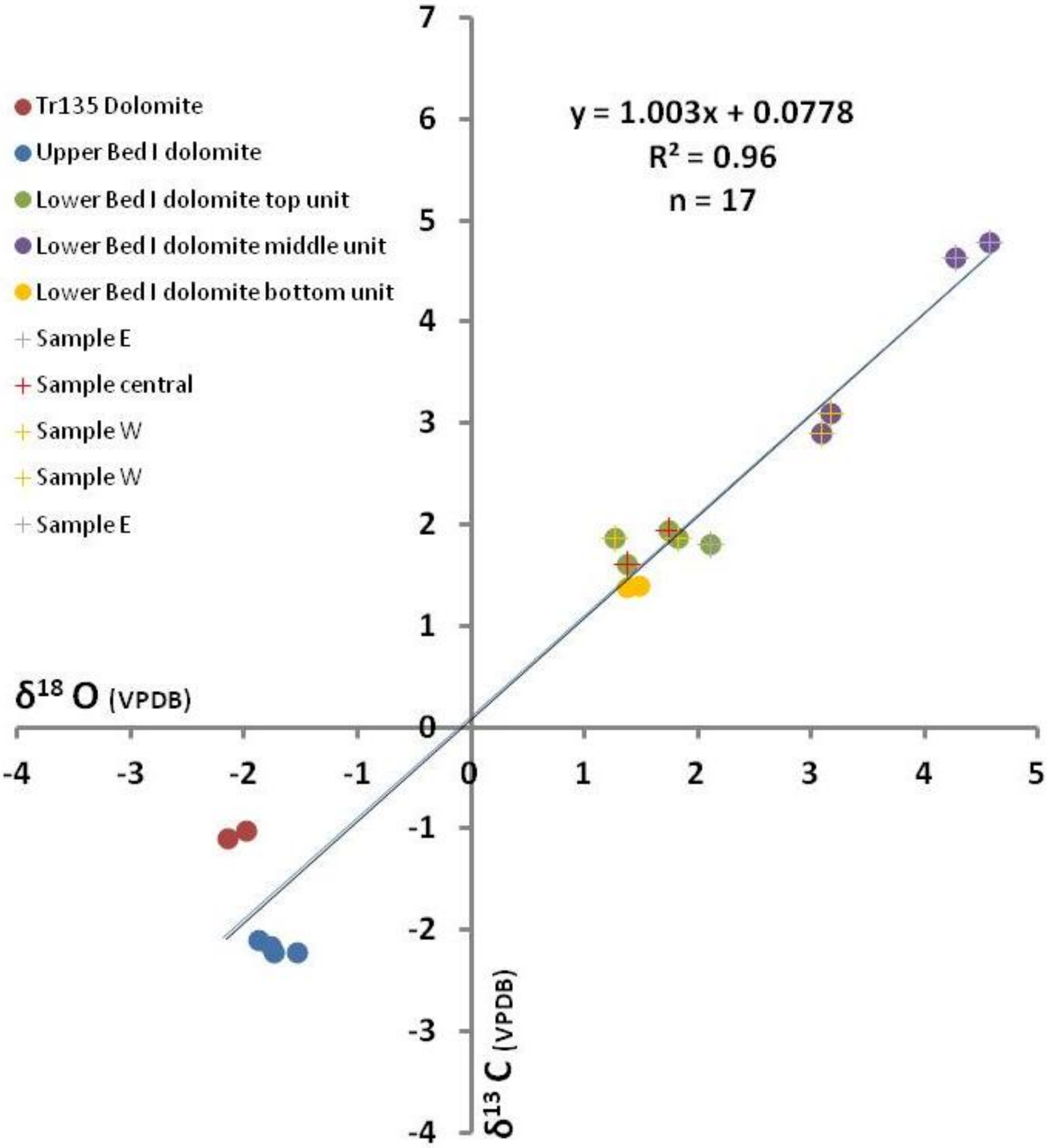

Figure 6-8: Stable isotope data for all dolomite samples through the stratigraphy plot on a covariant trend. Dolomite from the Lower Bed I dolomite (green, purple and yellow spots) has low positive $\delta^{13}C$ and $\delta^{18}O$ values. Dolomite from Upper Bed I (blue spots) has low negative $\delta^{13}C$ and $\delta^{18}O$ values, and dolomite from Tr135 (red spots) has low negative $\delta^{13}C$ and $\delta^{18}O$ values. The middle unit of the Lower bed I dolomite (purple spots) has higher values than the top unit (Green spots) and bottom unit (yellow spot). Samples of the top bed of Lower Bed I dolomite from the three different sampling sites (red- central, yellow-west, and lilac-east, crosses) are closely grouped, whereas samples of the middle bed of Lower Bed I dolomite from the two sampling sites (yellow-west, and lilac-east, crosses) plot in different areas.

6.4.3 XRD results

Dolomite specimens from all three sampling locations were investigated (Table 10).

Sample	Description	XRD method(s)
RHCI CA9 upper	Upper Bed I dolomite - upper unit	Method 1 Method 2a Method 2b
RHCI CA9 lower	Upper Bed I dolomite - lower unit	Method 1 Method 2a Method 2b
TR135	Dolomite eastern lake margin	Method 1 Method 2b
RHCI CA1,6	Lower Bed I dolomite - top unit	Method 1 Method 2a Method 2b
RHCI CA118	Lower Bed I dolomite - top unit	Method 2b
RHCI CA5	Lower Bed I dolomite middle unit	Method 1
Standard dolomite		Method 2a Method 2b
Coorong dolomite		Method 2a

Table 10: XRD methods used for the dolomite samples.

Method 1 was initially used to confirm the mineralogy as dolomite, then the diffraction peaks of both units of the Upper Bed I dolomite, Tr135 and the top and middle unit of the Lower Bed I dolomite were compared. The diffraction peaks produced by the Upper Bed I dolomite and Tr135 dolomite are not coincident with those from the Lower Bed I dolomite, and are shifted by up to $1^{o}2\theta$ relative to one another, possibly as the result of a non-stoichiometric Mg:Ca ratio or non-ideal lattice ordering. The sample RHCI CA5, representing the middle unit of the Lower Bed I dolomite which contains the most clay of the samples analysed here, has several broad, low intensity peaks at low angles, and much greater peak broadening interpreted to be produced by the clay minerals. An expanded view of the diffraction pattern corresponding to the *hkl* reflections *024, 018* and *116,* shows peak broadening with a shoulder on the high angle side (Figure 6-9), caused either by overlapping peaks, a non-stoichiometric chemical composition, or crystallographic factors such as variations in the crystal size, lattice strain or lattice defects.

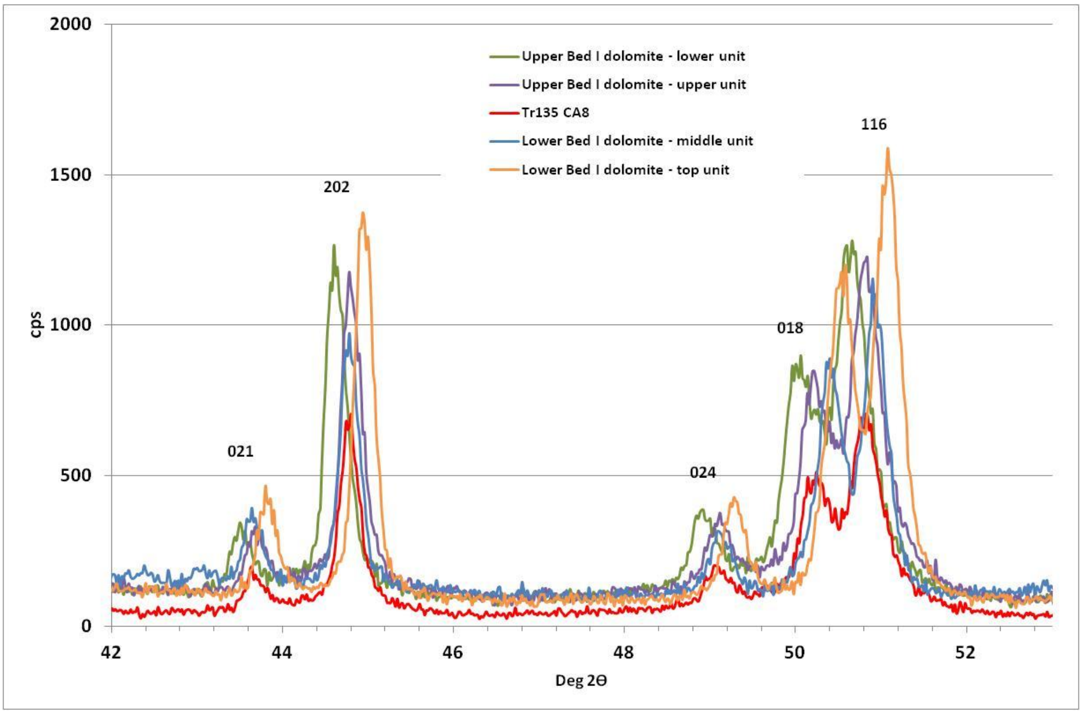

Figure 6-9: A comparison of the XRD traces for the dolomite samples using Method 1 showing attenuation and relative peak shift variations. The top unit of the Lower Bed I dolomite (orange line) is shifted to higher angles by ~1^{o}2 θ, and the lower unit of the Upper Bed I dolomite (green line) is shifted to lower angles by ~1^{o}2θ, compared to the other dolomite samples. The peaks are broadened, and a shoulder is present on the high angle side of the peak.

Because of the peak broadening in the sample from the middle unit of Lower Bed I dolomite (blue line), likely to be caused by incorporation of clay particles in the samples, neither this sample nor ones from the bottom unit of the Lower Bed I dolomite were used for detailed XRD analyses.

Using method 2a, more detailed XRD analyses were run for samples representing the two units of the Upper Bed I dolomite, the top unit of the Lower Bed I dolomite, a sample of the Coorong dolomite and the standard dolomite in order to identify the unit cell size, relative lattice ordering, and Mg/Ca ratios in the lake dolomites compared to examples of well ordered and disordered dolomite. The standard dolomite, representing a fully ordered dolomite, provides a baseline for identifying any shift to higher or lower ranges, or attenuation, of the reflection peaks from the Olduvai Gorge or Coorong specimens caused by disorder in the dolomite lattice. All specimens are shifted to lower angles by between 0.5^{o}2θ and 1.0^{o}2θ from the standard dolomite, and they are all attenuated (Figure 6-10).

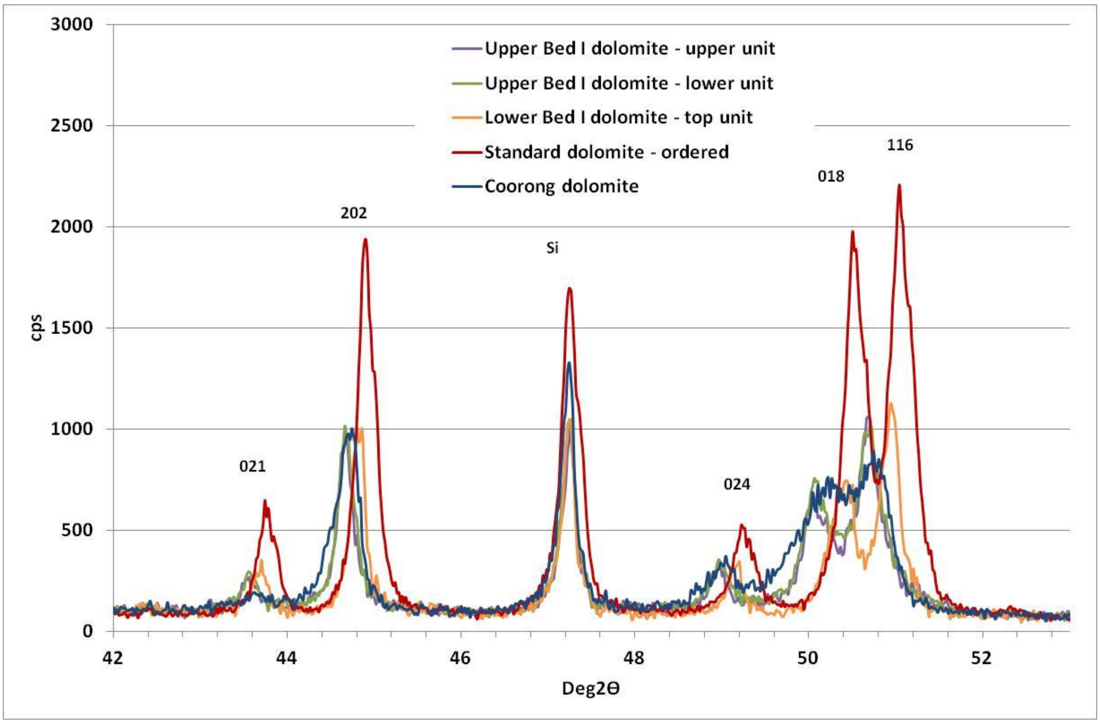

Figure 6-10: A comparison of the XRD traces obtained using Method 2a for the dolomite sample. XRD traces of the upper (purple line) and lower (green line) units of the Upper Bed I dolomite, the Lower Bed I dolomite (yellow line), and the Coorong (blue line) and near stoichiometric dolomite (red line) samples. All samples are attenuated compared to the near-stoichiometric dolomite and diffraction peaks are shifted to lower angles by up to 1°2θ.

The Lower Bed I dolomite is most similar to the standard dolomite; the peaks are the least attenuated and shifted only ~ 0.5°2θ. The Upper Bed I dolomite is most similar to the Coorong sample and they have a similar peak shift and attenuation compared to the standard dolomite, although the peak broadening in the Coorong dolomite is the most pronounced of all (Figure 6-10).

The XRD scans were calibrated using the silicon internal standard and the unit cell dimensions, reflection ratio, relative lattice ordering, the average amount of calcium per structural unit, and Mol% Ca were calculated (Appendix 10). The unit cell dimensions for the Olduvai Gorge samples are between 4.81 Å and 4.83 Å for *a* and 16.04 Å and 16.16 Å for *c* with a cell volume of 322 Å^3 to 326 Å^3. In comparison the unit cell dimensions for the Coorong dolomite are 4.82 Å for *a* and 16.11 Å for *c* with a cell volume of 324 Å^3 and the unit cell dimensions for the near stoichiometric dolomite are 4.81 Å for *a* and 16.00 Å for *c* with a cell volume of 320 Å^3. This shows an increasingly larger unit cell size as the samples get younger in the stratigraphy.

The relative ordering of the samples from Olduvai Gorge varies between 51.45% and 62.63% and was calculated assuming that the near stoichiometric dolomite is 100% ordered, and also shows the Coorong dolomite is least well ordered (Appendix 10) (Figure 6-11).

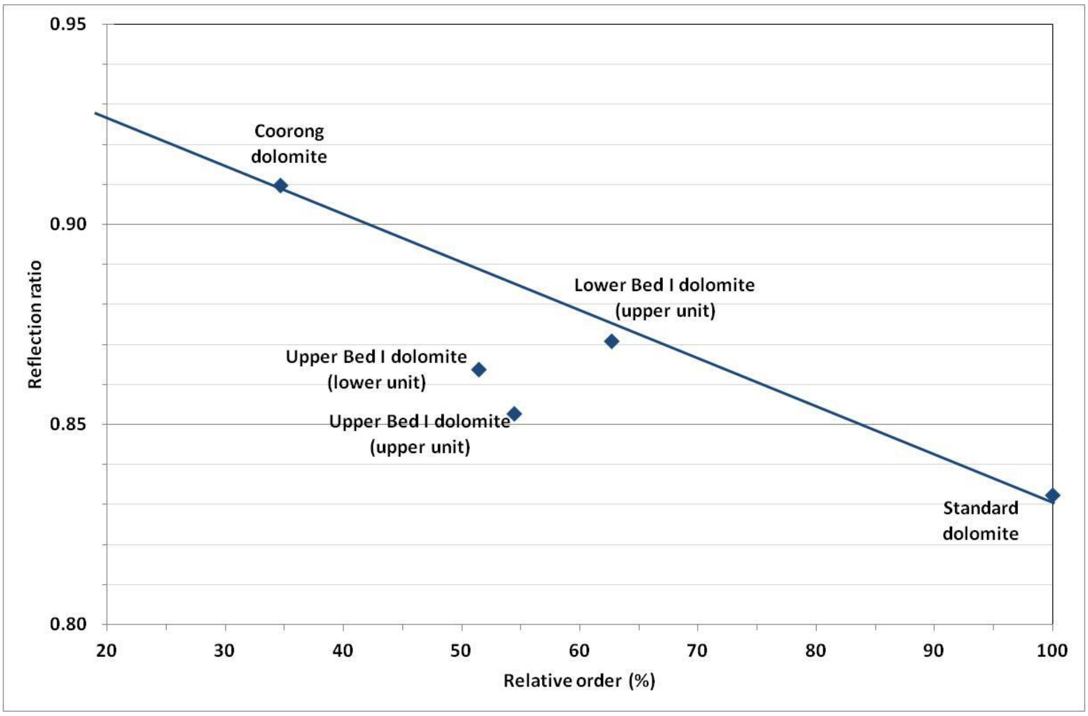

Figure 6-11: Relative ordering of the dolomite samples compared to the near stoichiometric dolomite. The relative ordering of the samples from Olduvai Gorge are grouped between the near stoichiometric and the Coorong dolomite. Lower Bed I dolomite is slightly better ordered, that is it is slightly closer to the near stoichiometric dolomite, than the Upper Bed I dolomites.

The Lower Bed I dolomite and the two Upper Bed I dolomite samples are closely grouped and lie partway along the linear change between the lattice ordering of well ordered dolomite and the poorly ordered Coorong dolomite. However, the Lower Bed I dolomite has a slightly more ordered lattice compared to the Upper Bed I dolomites.

The stoichiometry is calculated using the *hkl* reflectors *104* and *113* and the unit cell dimensions via the average amount of calcium per structural unit, n_{Ca} (Appendix 10) (McCarty et al., 2006). The Average amount of Ca per structural unit and the corresponding mol% Ca values of the Olduvai Gorge samples varies; the Upper Bed I dolomite upper unit is n_{Ca} 1.18 (59.2 Mol% Ca), the Upper Bed I dolomite lower unit is is n_{Ca} 1.17 (58.5 Mol% Ca), and the Lower Bed I dolomite top unit is n_{Ca} 1.05 (52.7 Mol% Ca). The near stoichiometric dolomite has an n_{Ca} 1.01 (50.3 Mol% Ca) and the Coorong dolomite n_{Ca} 1.14 (57.2 Mol% Ca) (Figure 6-12).

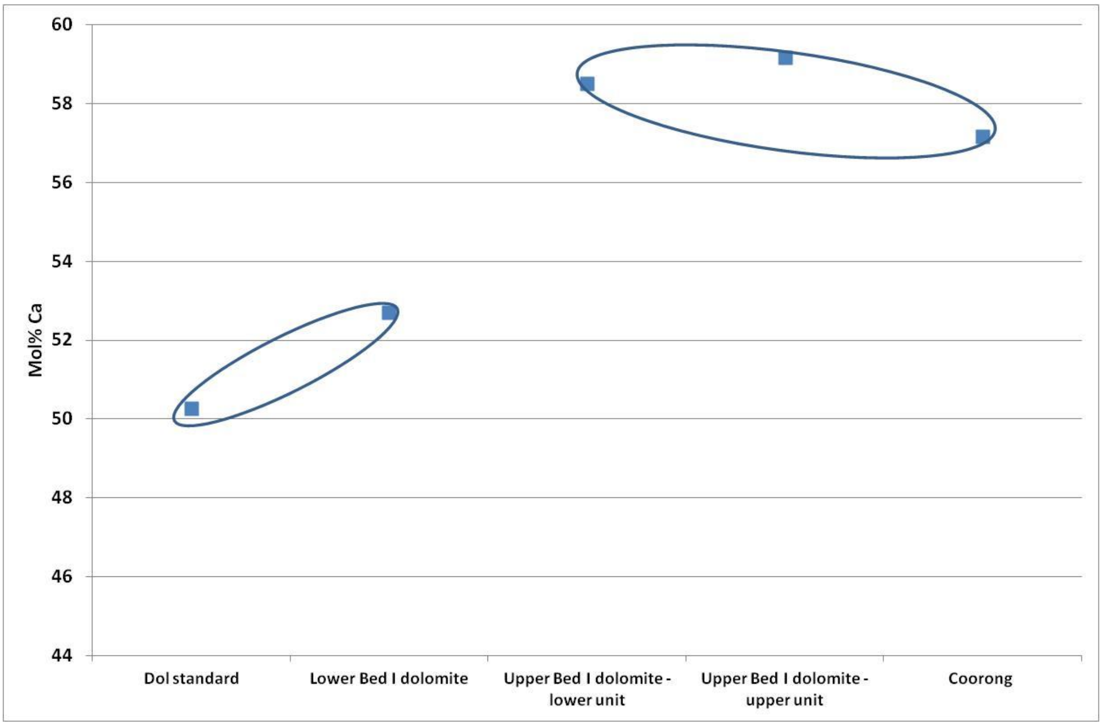

Figure 6-12: The calculated mol%Ca values of the different dolomites. Ideal dolomite would be 50 Mol%Ca. The Lower Bed I dolomite is similar to the ideal stoichiometric values seen in the near stoichiometric dolomite, whereas the Upper Bed I dolomite is closer to the more disordered Coorong dolomite.

This analysis shows that the stoichiometry of the Lower bed I dolomite is closer to the most stoichiometric near ideal dolomite compared to the Upper Bed I dolomite, whose values are closer to that of the less well ordered Coorong dolomite.

The shoulder on the high angle side of the diffraction peaks (Figure 6-10) and the high n_{Ca} values >1.07 may indicate two phases of dolomite in most of the samples apart from the near ideal dolomite. In order to investigate the possibility that the dolomite samples from Olduvai are composed of two phases, and so the potential to extract the unit cell data, composition and Mol%Ca values of each of the separate phases, the samples were analysed in more detail using method 2b. Particular emphasis was placed on the high angle peaks *0012, 217* and *0210* between 68^{o}2θ and 76^{o}2θ, where resolution of the two phases of dolomite is significantly improved compared to those at lower angles (Drits et al., 2005). Tr 135 dolomite was also included in the investigation to compare with the lacustrine samples. The pattern of shifts of reflections seen at lower angles is also seen with the same magnitude at these higher angle reflections (Figure 6-13).

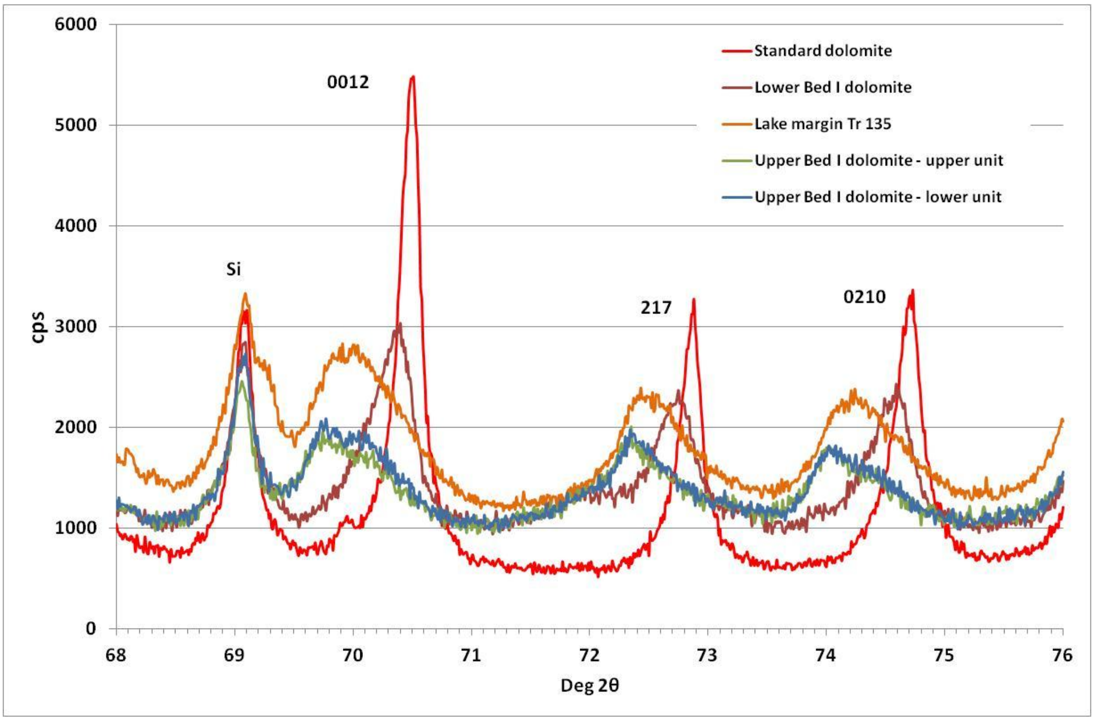

Figure 6-13: A comparison of the high angle detailed XRD traces of the dolomite samples showing attenuation and relative peak shift variations. Comparison of the upper and lower units of the Upper Bed I dolomite (Green and blue lines), the Lower Bed I dolomite (brown line), Tr135 dolomite (orange line), and the near stoichiometric dolomite (red line). All samples are attenuated compared to the near stoichiometric dolomite standard and diffraction peaks are shifted to lower angles by up to 1°2θ. Although the peaks from the Olduvai samples are broadened compared to the near stoichiometric dolomite, only the 0012 peak shows potential splitting, and so there is no evidence of two phases of dolomite.

The two units from the upper dolomite are shifted to lower angles by approximately 0.5 - 1°2θ compared to the near stoichiometric dolomite. Only the *0012* peak has a shoulder at the high angle side and the *217* and *0210* reflectors do not. Accurate resolution of the reflections representing the two potential different dolomite phases is difficult because of the peak broadening and attenuation, possibly as a result of clay contamination, resulting in high levels of uncertainty in correctly assigning peak positions. From these data these is no evidence of overlapping reflectors, and so no evidence of multiple dolomite phases.

6.5 Discussion

The dolomites investigated in this study are likely to be authigenic, because no potential allogenic sources have been identified in the lake catchment (Hay, 1976). Palaeolake Olduvai was predominantly a calcite depositional system, and the increase in the Mg^{2+}/Ca^{2+} ratios required for dolomite precipitation may have occurred due to Ca^{2+} removal by either calcite or gypsum precipitation (Eugster and Hardie, 1975; Hardie, 1986), or though input of Mg-rich water from the volcanic terrain, such as occurred at Amboseli, Kenya (Hay, 1995).

The three stacked, massive, beds of the Lower Bed I dolomite, with varying clay incorporation, indicate deposition in a clay rich environment. This is suggested to have been within the lake floor sediments, at sufficient depth to reduce the possibility of sediment re-working. The varying amount of clay incorporated in the three stacked dolomite beds indicates a changing rate or period of dolomite production. The two units, with a lower clay abundance, of the Upper Bed I dolomite, indicate two separate dolomite depositional events controlled by similar processes. These may have formed in the water column rather than within the sediment. Especially as the reworked surfaces of the two units, and the silt layer between the two units, suggest formation in shallow waters subject to wind-induced waves, and deposition of sediment during a hiatus in the dolomite formation. Formation of authigenic dolomite at Olduvai by direct precipitation was proposed by Hay and Kyser (2001), although dolomitisation of micrite was not ruled out.

Although the crystal fabrics identified in this study suggest that the dolomite formed by direct precipitation either in the water column or within the lake basin sediments, as textural analyses have not identified any features which may indicate replacement of an earlier carbonate precursor, such as partially replaced grains. However, this is not an unequivocal interpretation where micrite is completely dolomitised. A further consideration is that sulphate reducing bacteria are inferred to have been present in the clay sediments at the time of dolomite precipitation because of the presence of pyrite. Dark centres to dolomite crystals in some Coorong dolomites, similar to those seen in the Olduvai dolomites, have been interpreted to be an earlier stage of bacterially deposited dolomite formed by sulphate reducing bacteria (Wacey et al., 2007). However, without evidence of recrystallisation, this cloudy texture may be due to incorporated clay particles rather than recrystallisation of either micrite or bacterially deposited dolomite, and consequently the dolomites are interpreted to be primary.

The voids, lined by dolomite and strontianite, in the Upper Bed I dolomite may be the result of preferential dissolution of a less stable mineral such as high-Mg calcite, or possibly organic material. The consistently sub-spherical shape of the voids may indicate loss of small shells or algal matter, and although none of the samples examined had relict material, the dark brown inclusions around the voids may indicate organic inclusions. Similar textures have been identified in other authigenic playa-lake and lacustrine primary or early diagenetic dolomites and are interpreted as loss of previous plant fragments (Armenteros, 2010).

The larger, void lining, dolomite crystals represent a later stage of deposition, and the lack of clay particle inclusions in these crystals, compared to the earlier stage dolomite, indicates that it occurred after the formation of the dolomicrite, growing into clay-free space. The presence of Mn in the pore lining dolomite may be the result of a changing Mn supply to the lake or sediment pore water, or as a result of a change in the balance of ions available for the dolomite through precipitation of less soluble minerals. The alternating Mn-richer and poorer bands seen in SEM-BS may be the result of fluctuating redox conditions during growth, or due to evolution of the pore fluid at the crystal surface are growth occurs, as seen in Liesegang rings (Barge et al., 2011; Steefel, 2008). The latest stage of cementation in the voids, by strontianite, may be the result of increasing evaporation in the lake water or pore fluid (Busenberg et al., 1984; Witherow, 2009), or a change in the rate of crystal growth (Brand and Veizer, 1980; Curti, 1999; Lorens, 1981).

Covariance between $\delta^{18}O$ and $\delta^{13}C$ is indicative of hydrologically closed basins, and has been suggested to indicate that deposits of dolomite are primary (Talbot, 1990). Although stable isotope fractionation in the Olduvai samples is likely to be influenced by a complex set of factors, the highly significant covariant change in $\delta^{18}O$ and $\delta^{13}C$ values indicates that the variation between dolomites is primarily controlled by abiotic processes. The low $\delta^{13}C$ values of the lacustrine dolomites, compared to the lacustrine calcite crystals (Chapter 5), have been interpreted to indicate dolomite formation in a non-methanogenic environment (Hay and Kyser, 2001). However, even dolomites precipitated through microbial mediation can incorporate carbon abiotically from the lake water (Wacey et al., 2007).

The variation of carbon and oxygen isotope values in dolomites at different stratigraphic levels in this study are thus interpreted to be from differing fluid compositions caused by evaporation or dilution of lake water, although this does not necessarily imply that the dolomite formed exclusively by abiotic processes. The lower values for $\delta^{18}O$ and $\delta^{13}C$ in the Upper Bed I dolomite may be due to formation through inorganic precipitation, where fresher, possibly Mg-rich waters are delivered to the basin via fluvial input. Whereas the higher values in the Lower Bed I dolomite may be due to either inorganic or biologically mediated processes from deeper, more evaporative water.

Calcium enrichment in the Olduvai dolomites and the Coorong dolomite, when compared to the near-stoichiometric dolomite, is accompanied by; a) an increase in the unit cell parameters, b) a shift of the reflection peaks to lower angles, c) attenuation of the peaks, and d) peak broadening. The effect is most marked in the Upper Bed I dolomite compared to the Lower Bed I dolomite and is consistent with other studies of calcium enrichment in dolomite (Drits et al., 2005; Goldsmith, 1958). The unit cell dimensions, and thus the calculated relative ordering of the lattice and Mol% Ca values of the different dolomite samples (Figure 6-11, Figure 6-12) show a consistent pattern between the two stratigraphic levels. They indicate that the sample from the Lower Bed I dolomite is more ordered and most similar to the near stoichiometric dolomite, compared to the samples from the Upper Bed I dolomite and Tr 135, which are less well ordered and most similar to the Coorong dolomite. Similar changes, through a stratigraphic sequence with multiple dolomite beds, have been identified in the Coorong lakes where two types of dolomite, Type A and Type B, were differentiated using Mg and Ca content, unit cell dimensions, sedimentology, and stable isotope values (Warren, 1990, 2000). In these studies, Type A dolomite has higher $\delta^{13}C$ than Type B by 3-6‰ and also has higher $\delta^{18}O$ values, a more heterogeneous microstructure, and a more stoichiometric Mol% Ca. Type A dolomites are interpreted as basinal precipitates formed in the centres of evaporative lakes under highly saline conditions. Type B dolomites are interpreted to form in the margins of lakes under less saline conditions, or at the early stages of lake fill (Warren, 1988, 1990). Two forms of dolomite from a Jurassic lagoon in Scotland have also shown comparable differences and are interpreted to have formed either during a dry, arid period or a wetter period (Andrews et al., 1987). Extending these criteria to the dolomites at Olduvai Gorge would imply that the Lower Bed I dolomite deposition took place in deeper water and from more saline and evaporated fluid compared to the Upper Bed I dolomite which was deposited in shallower, fresher, water on the lake margin.

6.6 Conclusions

- Two types of authigenic dolomite have been identified at the two stratigraphic levels investigated, based on their textural and chemical differences. These are either precipitated directly in the water column or passively within the sediment, but are not considered to be replacements as they contain no apparent features that would be consistent with recrystallisation of a pre-existing carbonate.
- The dolomite is most likely to have been precipitated inorganically.
- Lower bed I dolomite was probably formed in the lake basin sediments; whereas the Upper bed I dolomite, with its wave rippled surfaces, may have precipitated from the water column.
- The positive correlation between the $\delta^{18}O$ and $\delta^{13}C$ values of both types of dolomites are likely to be primarily controlled by source water and evaporation driven changes.
- XRD analyses indicate that each dolomite type is composed of a single phase. All the dolomites have excess Ca, although the Lower Bed I dolomite is nearer to a stoichiometric Ca:Mg ratio of 1:1 than the Upper Bed I dolomite and Tr135 dolomite.
- The Lower Bed I dolomite is more ordered than the Upper Bed I dolomite, which is likely to be a consequence of growth conditions.
- Two depositional settings are proposed;
    - Lower Bed I dolomite formed passively in a basinal setting in the sediment sub-surface, primarily by inorganic precipitation, from evaporative and saline interstitial water with a high Mg/Ca ratio.
    - Upper bed I dolomite, and Tr135 dolomite, formed in a marginal setting, possibly in the water column, from less evaporative lake water subject to freshwater, possibly Mg-rich, input.

Chapter 7: ^{238}U-^{206}Pb dating of lacustrine calcite crystals by laser ablation MC-ICP-MS

7.1 Overview

Obtaining accurate dates of hominin bearing sedimentary successions is essential for our understanding of human evolution. Bed I and Lower Bed II of Olduvai Gorge, Tanzania contain one of the world's most important Pleistocene records of our early ancestors. This research reports for the first time the significant potential for using the U-Pb decay series to date uranium-rich, early diagenetic, lacustrine calcite crystals, and so directly constrain the time of sedimentation. Calcite crystals found in the saline, alkaline lake sediments contain a range of total uranium concentrations, between ~5 and 120ppm, and unusually low amounts of common lead, which permit accurate determination of $^{238}U/^{206}Pb$ and $^{207}Pb/^{206}Pb$ ratios. Calcite crystals are sector zoned and differential partitioning of uranium into different growth sectors allows isochrons to be constructed using single crystals. The clay sediments in which the lacustrine calcite crystals are found are interstratified with tuffs that have been dated using $^{40}Ar/^{39}Ar$ (biotite, anorthoclase and sanidine) geochronology and by equivalence to the top of the Olduvai sub-chron, which can be used to correlate sediments in the lake basin with those at the lake margins and provide information about absolute ages. This provides an ideal test bed for investigating the potential of directly dating important fossils-bearing horizons at the lake margins using the U-Pb systematics of the lacustrine calcite crystals. The combined laser ablation data from multiple crystals at the same sampling level produced carbonate ages that have 3- 5% uncertainties and are on average 100 ka older than the tuff age. Individual crystals ages are either within error of the tuff ages or are up to 200 ka older. Laser ablation MC-ICP-MS has an advantage over isotope dilution methods as a greater spread in U-Pb ratios can be determined permitting a better assessment of initial Pb composition and heterogeneity. $^{234}U/^{238}U$ activity ratios of the Pleistocene crystals indicate that different levels are more affected by open system behaviour than others. Early-diagenetic calcite crystals show exciting promise for directly dating saline, alkaline lake sediments, which would have particular potential for sites that do not contain datable tuff units.

7.2 Introduction

Olduvai Gorge, Tanzania is a World Heritage Site which has, and continues to, provide an important contribution to the study of human origins since the pioneering work by the Leakey family (Leakey, 1959, 1967; Leakey, 1971) (Figure 7-1). An extensive range of hominin fossils and artefacts have been recovered from Bed I and Bed II sediments deposited in and around saline, alkaline, Palaeolake Olduvai between ~2Ma and 1.4Ma (Blumenschine and Masao, 1991; Blumenschine et al., 2003; Blumenschine et al., 2011b; Leakey, 1971). Accurate dating of Early and Middle Pleistocene hominin archaeological sites is usually dependent upon the presence of volcanic deposits and radio-isotopic dating ($^{40}Ar/^{39}Ar$) in the stratigraphic succession. Where these have been chemically altered, reworked, or are not present, there are few options for direct dating of fossil-bearing sediments and so the development of a hominin chronology.

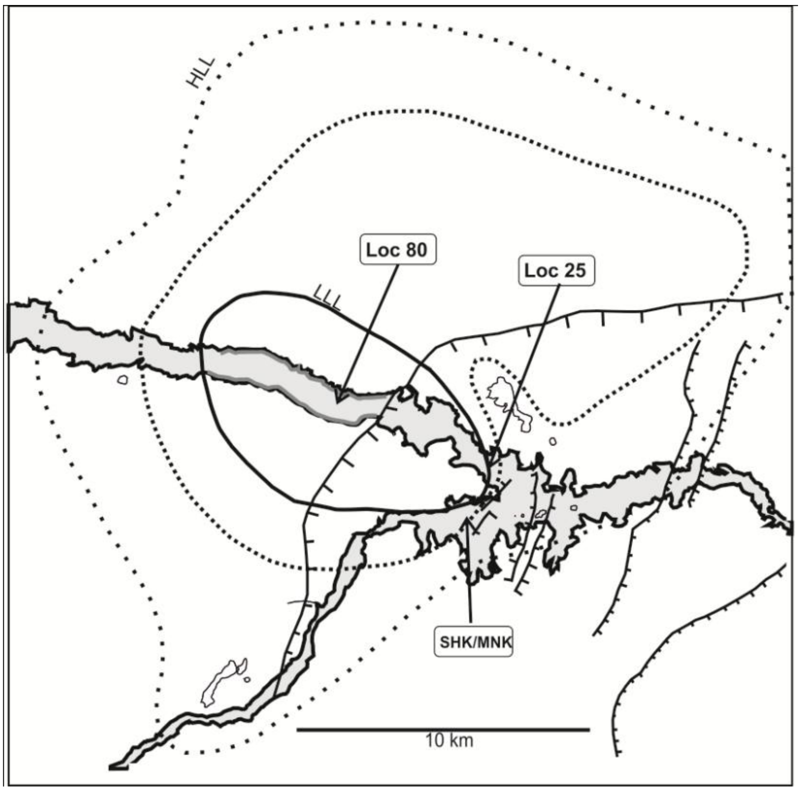

Figure 7-1: Olduvai Gorge, Tanzania, East Africa. The variable extent of Palaeolake Olduvai is identified as LLL (Low lake level) and HLL (High Lake level) using the palaeogeographic reconstruction immediately above Tuff IF (Hay, 1976). Calcite crystal sampling points, Loc 80 and Loc 25, are located on the northern side of the Main Gorge. Site SHK/MNK identifies the westernmost location of Tuff IIA prior to loss through erosion by the overlying Augitic Sandstone.

Euhedral to subhedral calcite crystals, ~0.25 – 2mm long, are abundant in the lake basin sediments and have been demonstrated to be geologically contemporaneous with the deposition of the lacustrine clays (Chapter 5).

When dating young calcites in terrestrial and lacustrine settings, uncertainties can be introduced through initial heterogeneous system behaviour; a) contamination by common lead; b) initial uranium disequilibrium; (c) post-crystallisation open-system behaviour. Although Pb is usually insoluble in water, it can be adsorbed onto the surface of clay particles which can become trapped in calcite as it forms. Young calcite deposits which often have low uranium, consequently have very low concentrations of in-grown radiogenic lead, resulting in large uncertainties in the abundance of radiogenic Pb after correction for the initial common lead (Rasbury and Cole, 2009). A pilot study to this project investigated the potential for U-Pb dating of sparry calcite nodules which are the terrestrial equivalent to Lower Bed II (Figure 7-2, Section 7.4) (Appendix 12). These samples have low concentrations of uranium and high levels of contamination by common lead resulting in a narrow range of $^{238}U/^{206}Pb$ ratios (between 1 and 6), significant scatter of the data (shown by high mean square weighted deviation (MSWD) values), and resulting age uncertainties of more than 6 Ma. By contrast, the lacustrine calcite crystals generally have higher concentrations of uranium with low values of common lead, and offer a potentially more suitable dating material (Chapter 5).

Uranium/Lead geochronology relies on the assumption that Uranium trapped in the crystal lattice is in secular equilibrium (see Chapter 1), or that corrections can be made for initial disequilibrium (see below). Many natural aqueous systems, however, have initial isotopic disequilibrium where the $^{234}U/^{238}U$ ratio is greater than 1, i.e. an excess of disequilibrium product, and calcite formed under these conditions would give a ^{238}U-^{206}Pb dates that is too old. Uranium disequilibrium in water sources is reported to occur by preferential leaching of ^{234}U relative to ^{238}U from source minerals, largely because of lattice damage caused by α-recoil during radioactive decay of the ^{238}U isotope (Chabaux et al., 2003; Chen et al., 1986;

Kigoshi, 1971). This may exert a strong influence on the accuracy of U-Pb series age determination (Casanova and Hillaire-Marcel, 1992; Goetz and Hillaire-Marcel, 1992; Hillaire-Marcel et al., 1986; Reynolds et al., 2003; Richards et al., 1998; van Calsteren and Thomas, 2006; Woodhead et al., 2006). Unfortunately there are very little published data on uranium disequilibrium in East African lakes with which to estimate its potential impact on the ages determined from calcite crystals in this study.

Late Quaternary (10 ka – 40 ka) stromatolites from Lake Manyara, Lake Magadi, and Lake Natron, which are possible analogues to Palaeolake Olduvai, have a $^{234}U/^{238}U$ activity ratio of between 1.1 and 1.6, and water from Lake Magadi, Kenya, has a $^{234}U/^{238}U$ ratio of between 1.44 and 1.62 (Casanova and Hillaire-Marcel, 1992; Goetz and Hillaire-Marcel, 1992; Hillaire-Marcel et al., 1986). $^{234}U/^{238}U$ activity ratios up to 2.6 have been reported in rivers in South Africa, attributed to weathering of different source minerals (Kronfeld and Vogel, 1991). As the Olduvai lacustrine calcite crystals are interpreted to form over a few years (Chapter 5), the $^{234}U/^{238}U$ activity ratios of calcite crystals from contemporary lakes can be considered as examples of the potential initial uranium disequilibrium in Pleistocene precursors. These data may offer an insight into the impact initial uranium disequilibrium may have had on the U-Pb ages of the crystals from Olduvai.

Uncertainties may also be introduced where calcites are subject to diagenetic alteration and open-system behaviour, and parent-daughter ratios can be significantly altered through loss of daughter products, producing an artificially young age. Careful selection of specimens and screening for recrystallisation or later mineral precipitation can reduce the potential for these sources of open-system behaviour but are not fully diagnostic.

In previous studies Laser Ablation MC-ICP-MS of carbonate minerals has been used primarily for screening specimens for suitability for subsequent dating by isotope dilution methods, because its sensitivities and precision are reduced when compared to isotope dilution methods (Chen, 1999; Košler, 2007). However for certain materials laser ablation offers considerable advantages because of the much simpler and shorter preparation and analytical time involved (Eggins et al., 2005), and recently it has been successfully used for dating fossil corals and speleothems using U-series (Eggins et al., 2005; McGregor et al., 2011), albeit with increased uncertainties when compared to isotope dilution analyses. Analytical challenges are introduced through a complex set of isotope fractionation within the instrument; Laser Induced Elemental Fractionation causes change in the elemental ratio during the course of the analysis (Horstwood et al., 2006) and mass bias (or mass discrimination) produces changes in molar sensitivity with changing mass (Košler, 2007). Uncertainties caused by these fractionation effects have been reduced by using a short wavelength 193nm laser, keeping the pit aspect ratio (depth:width) very low and using a calcite standard (Chen, 1999; Horstwood et al., 2006; Košler, 2007; Ludwig, 2001; Mattinson, 1987). Although previously not available at NIGL, this study has been able to use a calcite standard to reduce the potential for uncertainties caused by differences in matrix between the standard and the specimen (reference provided by Professor T. Rasbury, Stony Brook University and U-Pb systematics determined at NIGL by isotope dilution). Comparative analyses between dates produced using the Laser ablation MC-ICP-MS method, and isotope dilution MC-ICP-MS analyses of whole crystals, can be used to investigate the accuracy of the results and to interpret the potential impact of analytical and systematic uncertainties.

Saline, alkaline, lake deposits have been associated with the geological record at important hominin sites (Hay, 1995; Issac, 1967), and euhedral calcite crystals have been reported in both. Where the lacustrine calcite deposits can be reliably correlated with ancient land surfaces associated with fossils and artefacts, dating synsedimentary calcite crystals therefore offers a potentially important method for constraining the timescales of hominin evolution where other methods are unavailable. The lacustrine sedimentary succession at Olduvai comprises interbedded lacustrine clay, sandstones and volcanic deposits with rare dolomites (Figure 7-2), and calcite crystals are present in the clay sediments at multiple levels.

The published geochronology of the volcanic deposits at Olduvai Gorge (Blumenschine et al., 2003; Hay and Kyser, 2001; Manega, 1993; Walter et al., 1992) provides us with depositional time constraints for the clay beds, and so a unique test-bed for the development of alternative dating methods using the carbonates. This study, assesses the accuracy, reproducibility and precision of using laser ablation MC-ICP-MS to date Pleistocene age lacustrine calcite crystals using U/Pb isotopes.

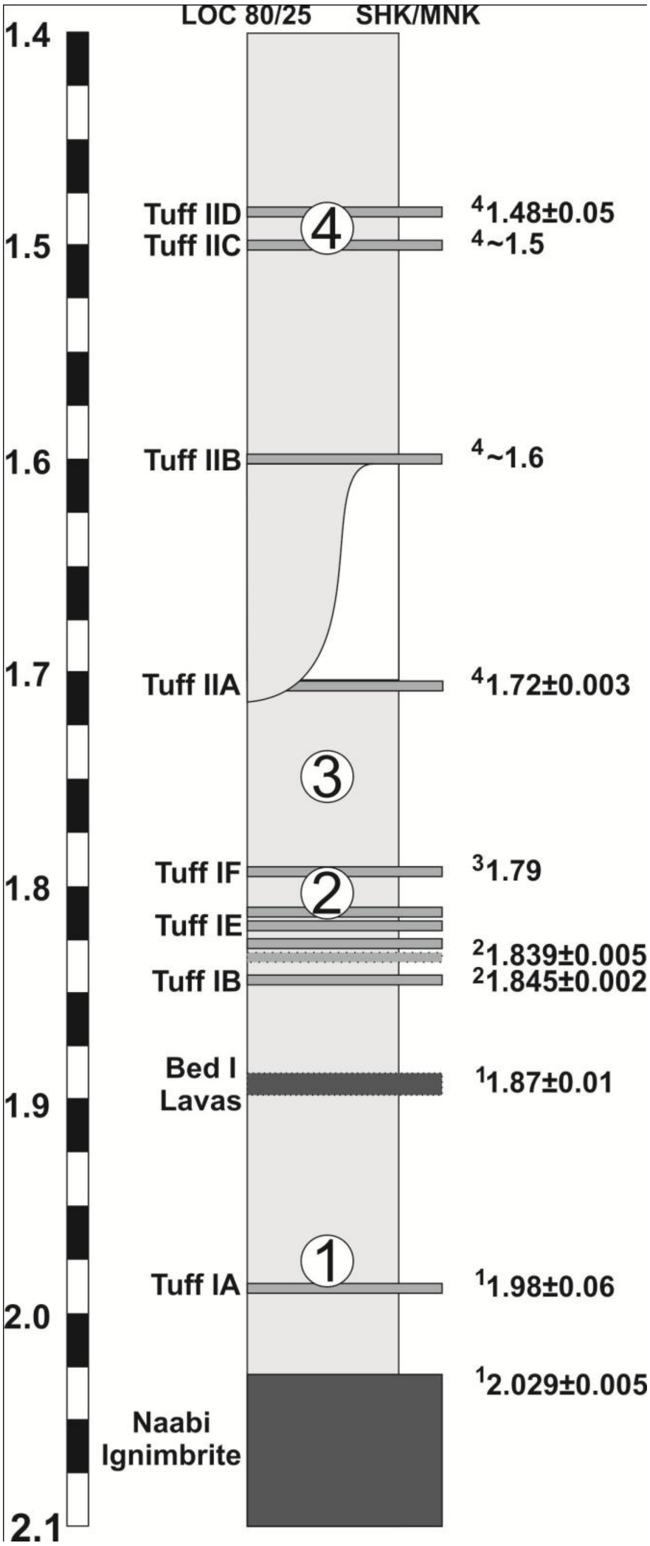

Figure 7-2: The generalised stratigraphic succession comprises interbedded clays, sandstones and volcanic sediments. The data collection in this test-bed study is focussed on the stratigraphy between ~2Ma and 1.4Ma. Published dates were determined using $^{40}Ar/^{39}Ar$ single crystals analyses of tuffs apart from Tuff IF, whose date is defined by the top of the Olduvai Subchron. (1) (Walter et al., 1992), (2) (Blumenschine et al., 2003), (3) (Hay and Kyser, 2001), (4) (Manega, 1993). Calcite crystals were sampled from four different stratigraphic levels, 1, 2, 3, 4. Dashed layers indicate the position of volcanic sediments which are only present outside the lake. Level 1, 2, and 3 were sampled from LOC80, and Level 4 was sample from LOC25. Level 3 is interpreted to be below Tuff IIA, as it overlies Tuff IF and underlies the erosion surface which is inferred to erode out Tuff IIA west of the SHK/MNK archaeological complexes.

7.3 Geological setting

Olduvai Gorge, Tanzania, is a rift related fluvial incision exposing Early and Middle Pleistocene sediments that were deposited in and around a now extinct lake formed within a rift-shoulder basin. Palaeolake Olduvai was a hydrologically closed, shallow (maximum~10m) (Hay, 1976), saline, alkaline lake, supplied by rivers from the western Tanzanian craton, and via springs, rivers, and meteorically fed groundwater from the eastern volcanic highlands of the Gregory Rift (Hay, 1976). The lake is deduced to have varied in size, from up to 40 km across to only a few km, and fluctuated multiple times during the deposition of the Bed I and Bed II sediments (Blumenschine et al., 2011a; Hay, 1976; Stanistreet, 2011). At times it almost dried out leaving small, localised playas (Stollhofen et al., 2008). The lacustrine clay is largely the result of early diagenetic alteration of weathered detrital and volcaniclastic material by reaction with saline alkaline water from Palaeolake Olduvai, although neoformed clays were also precipitated (Deocampo, 2004; Deocampo et al., 2002; Hay and Kyser, 2001). The clays are interbedded with episodic influxes of volcaniclastic deposits from the eastern volcanic complex. The geochronology of the tuffs has been determined using $^{40}Ar/^{39}Ar$ analyses, apart from Tuff IF which was constrained by correlation with the top of the Olduvai Subchron, and so maximum and minimum ages of the clay sediments are known. Calcite crystals are most abundant in the clays of the central lake basin where they are present either: disseminated through the clay; forming beds of arching sprays of multiple crystals; or in inter-laminated crystal rich and poor clay beds with erosive bases (Chapter 5). These are interpreted to have formed under anoxic to sub-oxic conditions in the shallow sub-surface sediments of the lake floor and lake margins, and grew by early diagenetic precipitation, possibly as replacements after evaporite minerals such as trona and gaylussite, or as primary precipitates (Hay and Kyser, 2001) (Chapter 5). Specimens from all but one stratigraphic horizon exhibit complex zoning when viewed by cathode-luminescence (Figure 7-3a, b) and the crystals have a range of trace element concentrations across the different areas of brightness. Specimens from level 1, however, are not zoned (Figure 7-3 c,d) and the trace element variation at different positions on the crystals in general do not vary as much (Appendix 11).

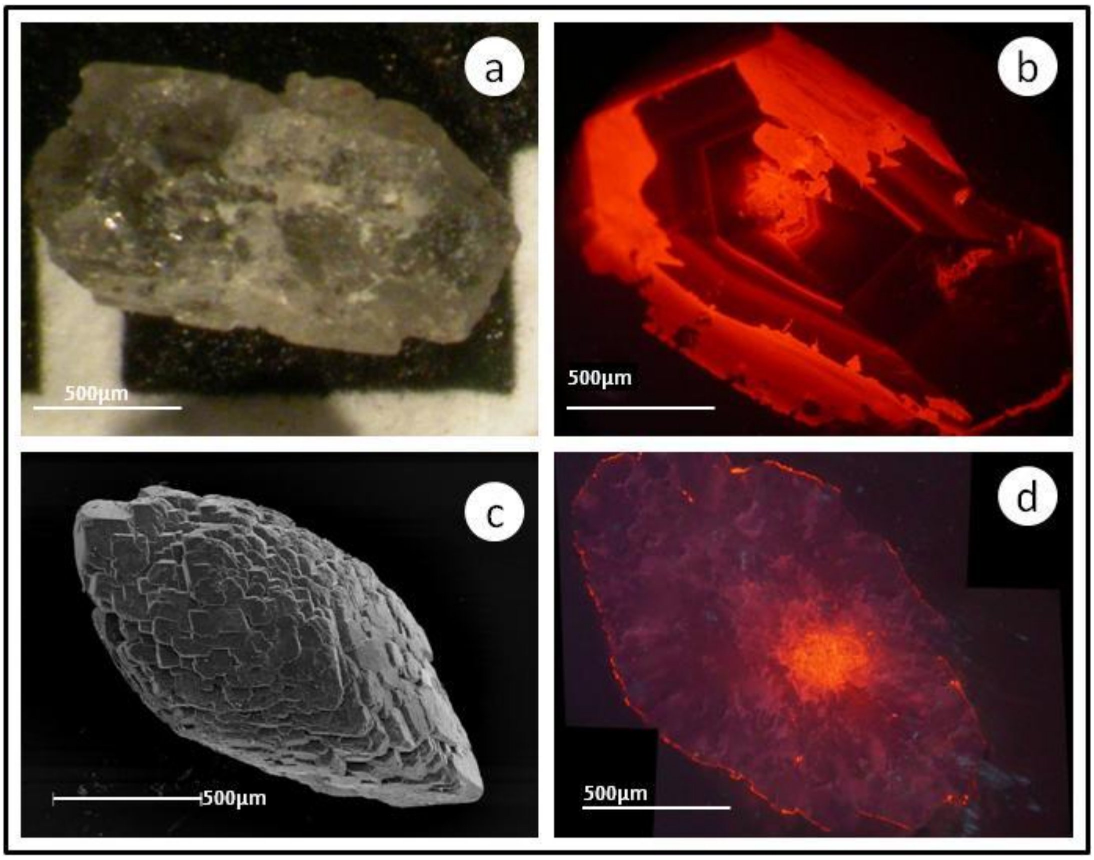

Figure 7-3: Authigenic calcite crystals from lacustrine clays, Olduvai Gorge, Tanzania. (Scale bar 500µm). a) Calcite crystal after washing (2009 RHCII CA5) - representative of crystals from Levels 2, 3 and 4 b) Cathode luminescence photograph of polished crystal from (a) showing high and low brightness concentric, sector and intrasectoral zoning c) calcite crystal from Level 1 (2010 RHCI 104) d) cathode luminescence photograph of polished crystal from (c) with no concentric zonation.

Modern saline, alkaline lakes in East Africa, which may be compared to Palaeolake Olduvai, also have calcite crystals in their shoreline sediments, however Lake Makat, Lake Natron, and Lake Ndutu, have different bedrock and water catchment characteristics (Figure 7-4). Lake Makat in the Ngorongoro caldera is supplied by springs within the volcanic complex and by fluvial delivery via the River Munge from the Mount Olmoti crater to the north. Lake Natron is within the Rift Valley and is supplied via the Peninj and Moinik Rivers, and from springs and several small rivers with the main input from the Ewaso Ng'iro River which drains through the Rift valley. Lake Natron also has ash delivered from the nearby active carbonatitic volcano Oldoinyo Lengai. Lake Ndutu is situated on the Serengeti Plain and is supplied by rivers draining from the Tanzanian craton.

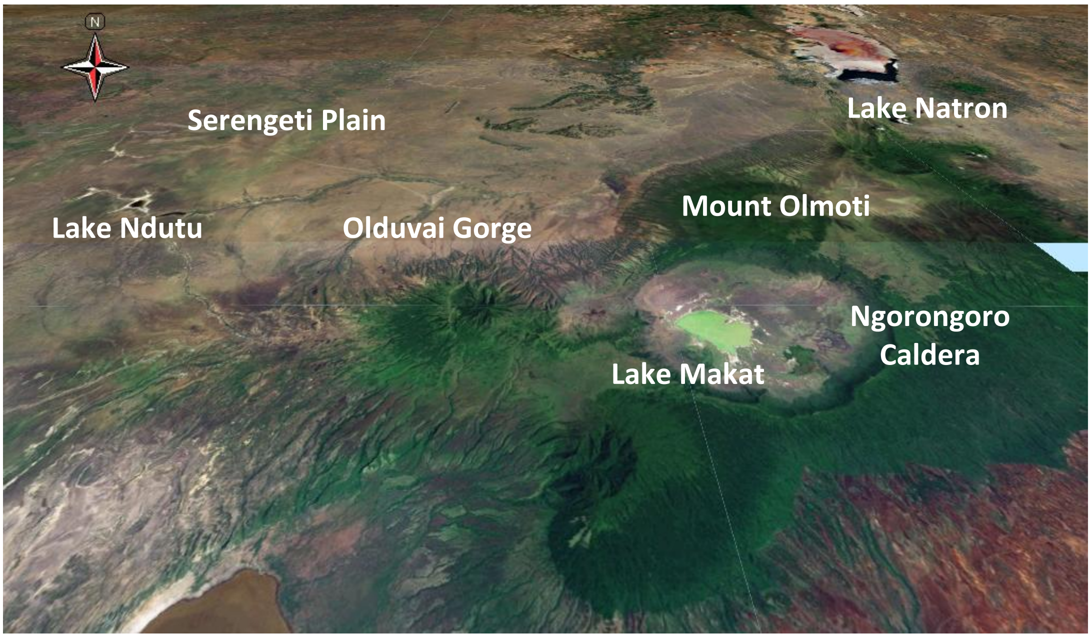

Figure 7-4: Locations of the three modern lakes sampled for calcite crystals (Google Earth 2010). Lake Ndutu on the Serengeti Plain, Lake Makat within the Ngorongoro Caldera, and Lake Natron within the Rift system.

7.4 Methods

Calcite crystals were recovered from two sampling locations at Olduvai Gorge, Loc 80 (also named RHC – Richard Hay Cliff (Hay, 1976; Leakey, 1971)) and Loc 25. Specimens were chosen from four different levels through the stratigraphy to test the resolution of the dating method (Figure 7-2). These are the same levels used for the investigation into calcite crystal genesis in Chapter 5 of this thesis. (Table 11):

- Level 1: Lower Bed I (Loc 80) from one sampling level between Tuff IA and Tuff IB (Figure 7-2);
- Level 2: Upper Bed I from two sampling levels between Tuff IE and Tuff IF (Figure 7-2);
- Level 3: Lower Bed II, from four sampling levels between Tuff IF and the erosion surface at the base of the Augitic Sandstone units (Figure 7-2);

- Level 4: Upper Bed II (Loc 25), at one sampling level between Tuff IIC and Tuff IID. The sample from Loc 25 was in a clay bed immediately below Tuff ID, located on the sedimentary log published in Hay (1976).

Sample identification	Location	Stratigraphic level
2010 LOC25	Loc 25	Upper Bed II
2009 RHCII CA7	Loc 80	Lower Bed II
2009 RHCII CA6	Loc 80	
2009 RHCII CA5	Loc 80	
2009 RHCII CA3	Loc 80	
2009 RHCI CA10	Loc 80	Upper Bed I
2009 RHCI CA7	Loc 80	
2010 RHC I CA104	Loc 80	Lower Bed I

Table 11: Calcite crystal sample locations. Sample identification codes for each sample level, and their corresponding stratigraphic level named after the geological and archaeological bed definitions (Figure 7-2). Four crystals were sampled from each sampling level. Two sampling levels were used within Upper Bed I and four within Lower Bed II. One sample level was in Lower Bed I and one in Upper Bed II.

Loc 80 is a well exposed section of the lake basin sedimentary succession and provided specimens from Levels 1, 2, and 3. A single horizon was sampled at Level 1; at Level 2 two horizons 1m apart in the stratigraphy were sampled; and at Level 3 four horizons were sampled in a 1m section within the stratigraphy. It was not possible to reach the upper part of the stratigraphy at Loc 80 and specimens from one horizon at Level 4 were recovered from Loc25. Four specimens from each sampling horizon were chosen to test the reproducibility of the analyses. In addition, specimens of calcite crystals from three modern lakes were sampled to identify potential uranium disequilibrium and to use them as modern analogues to the Pleistocene crystals; 1) Lake Ndutu, on the Serengeti Plain, 2) Lake Natron, in the Rift Valley in Northern Tanzania, and 3) Lake Makat in the Ngorongoro caldera. The crystals were selected from the shoreline during August 2010 from approximately 10cm below the surface and within 2m of the water's edge (on the day of sampling).

Where the dried sediments were friable, and the crystals large enough to see clearly with the naked eye, tweezers were used to separate them. Where the clay sediments were more indurated or the crystals were too small to see easily with the naked eye, the clay sediments were washed with distilled water and the grains filtered through a 0.25mm sieve. After air drying, the individual crystals were separated from other mineral grains using a binocular microscope and tweezers. The individual crystal batches were cleaned in de-ionised water for 15 minutes in an ultrasonic bath at room temperature; dried, separated from any remaining clay with tweezers, and washed and dried again.

Individual crystals were chosen because they are representative of the size, shape and colour of all of the isolated specimens from each level. Four from each level were chosen to investigate the age variation between samples. Four horizons within Level 3 (resulting in sixteen crystals at this level) were chosen to investigate the variation within a level and so the potential age resolution.

The geochemistry and petrography of the crystal specimens were described using XRD, stable isotopes of carbon and oxygen, trace elements including rare earth elements, transmitted light microscopy, and cathode-luminescence in chapter 5 of this thesis.

7.4.1 Laser ablation analysis of crystals from Olduvai Gorge

Four specimens of crystals from each stratigraphic horizon were selected for LA MC-ICP-MS. The crystals were set in resin (Buehler Epoxicure Resin (20-8130-128) and Hardener (20-8132-032)). Each mount contained samples from up to four different stratigraphic horizons to reduce sample change-over time during analysis. Polished cross-sections through the crystals were obtained by grinding the mounts using wet silicon carbide paper from 800 to 2400 grade, finally using 2micron alumina suspension to produce a polished surface suitable for laser ablation. Each crystal was photographed using transmitted light and cathode-luminescence.

The specimens were analysed using a Nu Plasma HR Inductively Coupled Plasma Multi-collector Mass Spectrometer with a Nu Instruments DSN-100 dry aerosol nebuliser. The laser ablation system was a New Wave Research UP-193 with solid state Nd/YAG laser. Between 5 and 9 100µm diameter circular spots were ablated on each crystal, targeting a range of cathode-luminescence brightness areas. The data was collected simultaneously in two Faraday Cups (^{238}U and ^{235}U) and six ion counters (^{207}Pb, ^{206}Pb, ^{205}Tl, ^{204}Pb+^{204}Hg, ^{203}Tl, and ^{202}Hg). The Faraday collector and ion counter array was set up with ion counters used for the lower abundance isotopes. The ablation chamber had a volume of approximately 30cc and the specimen was fitted in the chamber with a small block of calcite standard material attached to its top surface. Care was taken to ensure that the specimen and standard were fitted closely to ensure an even flow of the helium carrier gas. The chamber was flushed to remove atmospheric oxygen introduced during specimen loading, during which time the mass spectrometer was tuned to maximise a steady response in the gain between the Faraday cups and the ion counters. The gas flow was 0.8 l/min and a 20 second washout delay was used between individual spot analyses to avoid overlapping data (Table 12). The data were collected continuously during ablation in three analytical runs (Table 13). The calcite standard was ablated 3 times at the beginning and end of each set of data collection, and 2 or 3 times between each crystal. The scans were reviewed following collection. No significant drift was observed during the analyses. In all cases, for both specimens and standards, there was an initial spike of lead from surface contamination of the sample which was discarded during the data selection process as it is not representative of the calcite. Between 1 and 3 different sections of the data for each ablation were selected. The data is normalised to a calcite standard dated at 251Ma (Professor T. Rasbury and NIGL) to correct for uncertainties produced by mass and inter-element fractionation during analyses.

MS	Parameters	Samples
Rep rate	10 Hz	All
Fluence	~ 3.7 joules/cm^2 ~ 3.8 Joules/cm^2	2009 RHC II CA3, CA5, CA6, CA7 2010 RHCI 104, 2009 RHCI CA7, CA10, 2010 Loc 25
Power	80%	All
Carrier gas	He@ 0.8 l/min	All
Aspiration	0.5ppb ^{205}Tl-^{203}Tl-^{235}U in 2% nitric Dry plasma	All apart from 2009 RHCII CA7 2009 RHCII CA7
Spot size	Round, 100µm diameter	All

Table 12: LA MC ICP MS - Individual sample analysis parameters.

1	2	3	4
Sample name	**Stratigraphic position on sedimentary log**	**Analysis run**	**Maximum and minimum tuff dates (Ma)**
2010 LOC25 CA1	4	3	Min: 1.48±0.05 Max: ~1.5
2009 RHCII CA3 2009 RHCII CA5 2009 RHCII CA6 2009 RHCII CA7	3	1 (2) 1 (2) 1 (2) 2	Min: 1.72±0.003 Max: 1.79
2009 RHCI CA7 2009 RHCI CA10	2	3	Min: 1.79 Max: 1.839±0.005
2010 RHCI 104	1	3	Min: 1.845±0.002 Max: 1.98±0.06

Table 13: Analytical run information : column 1 is the unique sample collection code identifying the year of collection, the sampling location and the sample number; column 2 identifies the stratigraphic location for each set of samples which is cross-referenced on the sedimentary log (Figure 7-2); column 3 identifies the analytical run for each set of samples; column 4 identifies the maximum and minimum tuff dates that constrain the sedimentary horizon for each sampling level.

7.4.2 Isotope dilution analysis

Specimens of crystals from three levels at Olduvai Gorge, 1, 3, and 4, were selected from the previously washed material for isotope dilution analysis using Thermal Ionisation Mass Spectrometry (TIMS) and MC-ICP-MS to compare the results with those produced using the laser ablation MC-ICP-MS method. For isotope dilution analyses the whole crystals need to be dissolved. Common lead and other isotopes of the U-Pb series, which were not produced by the radiogenic decay of uranium in the calcite crystal, may have been adsorbed onto clay particles trapped in the calcite. In order to reduce potential inaccuracies caused by leaching of these isotopes during sample preparation, specimens were selected to have as few visible contaminants as possible. They were then broken and re-washed using the same method as before and the parts of the broken crystals separated using tweezers and a binocular microscope to select pieces that were as free from clay inclusions as possible. The small size of the broken crystals made this process difficult and many of the specimens had to be prepared and subsequently analysed with visible contaminants.

Samples were spiked with a mixed ^{205}Pb-^{233}U-^{235}U tracer and dissolved using established protocols for the dissolution of carbonate. Following chemical purification, U was measured by multi-collector ICP-MS using a Nu Plasma HR at NIGL using a static faraday cup array. Mass fractionation was monitored externally using IRMM-184 as a reference material to correct for mass bias as it has a $^{235}U/^{238}U$ ratio similar to that of the spiked samples. Washout and background contributions between samples and standards were therefore minimised. Any residual mass bias was resolved using the corrected $^{233}U/^{235}U$ double spike ratio.

Pb was measured by thermal ionisation mass spectrometry (TIMS) using a ThermoScientific Triton and a static faraday cup array. Mass bias was determined by measurement of NBS 981 and NBS 982 on similar sized loads over an extended period of time. Total procedural blanks were determined to be <10 pg for Pb and <0.1 pg for U. The algorithms of Schmitz and Schoene (2007) were used for U-Pb data reduction (isotope dilution, spike and blank subtraction and correction for mass bias).

7.4.3 $^{234}U/^{238}U$ analysis

The $^{234}U/^{238}U$ uranium ratios were investigated in specimens of crystals from the same three levels at Olduvai Gorge, 1, 3, and 4, selected for isotope ratio analysis. In addition, specimens of modern calcite crystals from Lake, Ndutu, Lake Makat and Lake Natron, were analysed to identify potential initial uranium disequilibrium in contemporary systems.

Calcite samples for $^{234}U/^{238}U$ determinations were processed using the same methods outlined above for the U-Pb isotope dilution analyses (see above) except that samples were not spiked with any tracer isotopes and only U was collected. $^{234}U/^{238}U$ ratios were determined using the Neptune plus MC-ICP-MS at NIGL. ^{234}U was measured using a discrete dynode secondary electron multiplier (SEM) and ^{238}U on a faraday cup with a 10^{11} Ω resistor, SEM yield and mass bias were monitored by analyses of CRM 112a natural uranium standard using the value of $^{234}U/^{238}U$ = 54.887×10^{-6} (Cheng et al., 2000).

7.4.4 Data presentation using the Tera-Wasserburg diagrams

For very young carbonate specimens the amount of radiogenic lead produced is very small because of the very long half-lives of the parent uranium species. Compounding this is variable initial common Pb incorporated into the crystals at the time of formation. Accurate quantification of very small amounts of radiogenic Pb, requires quantification of the amount and composition of the initial Pb component. This can be achieved by using a Tera-Wasserburg (T-W) $^{238}U/^{206}Pb$ - $^{207}Pb/^{206}Pb$ concordia plot where a mixture between initial Pb (i.e. Pb not contributed by the radioactive decay of the uranium in the calcite crystals), and the system's radiogenic Pb (Ludwig, 1998, 2001) will plot as a linear array. The slope of the array (isochron) produces the date, its intersection with the y-axis produces the initial isotopic composition, and the uncertainties are determined by the intersection with the concordia (Rasbury and Cole, 2009). The data are plotted and an age produced using Isoplot 3.00 and reported with 2σ analytical uncertainties (Ludwig, 2003). In order to assess confidence in the results there is a need to quantify the uncertainties at each step. The mean square weighted derivative (MSWD) is used as an indicator of the resolvable scatter within a given dataset (i.e., isochron). Ideally this will be equal to 1 where all scatter can be accounted for by analytical uncertainties. Where the MSWD is <<1 then it indicates an overestimation of data point uncertainties and analytical errors. Where the MSWD >>1 then not all of the uncertainties can be accounted for through analysis and are likely to be due to other causes such as heterogeneity in the initial system (Rasbury and Cole, 2009) or reflect post-crystallisation open system behaviour. As outlined above, the T-W U-Pb dates produced will require correction for initial $^{234}U/^{238}U$ disequilibrium. Where initial $^{234}U/^{238}U$ activity ratios are >1 the non-correct T-W will be maximum ages, and for initial $^{234}U/^{238}U$ activity ratios are <1 the non-correct T-W will be minimum ages.

7.5 Results

7.5.1 Laser ablation U-Pb dates

Linear arrays were produced from the combined results of multiple spot analyses of each of four calcite crystals from each sampling horizon (Appendix 13). The regression calculation in Isoplot does not propagate for excess scatter where the MSWD >1. As the MSWD is >> 1 (and up to 13) the uncertainty has been propagated using the square root of the MSWD value, and the expanded uncertainty is shown in square brackets. Although the error ellipses are large, the spread of $^{238}U/^{206}Pb$ ratios has produced isochrons with 3-5% uncertainties. These data will need to be corrected for any initial ^{234}U disequilibrium.

The crystals from the oldest part of the stratigraphy, Level 1 (RHCI 104), are found dispersed throughout the waxy clay bed with no indication of preferential orientation or reworking. Unlike crystals from other parts of the stratigraphy, these specimens have neither sector nor concentric zonation revealed under cathode-luminescence (Figure 7-3 c,d). The combined analyses of multiple laser ablation spots on four of these crystals (2010 RHCI 104) produced a range of total uranium concentrations (U*) between ~40 ppm and ~125ppm and $^{238}U/^{206}Pb$ values from 1600 to 3200. This produced a date of 1.98 ± 0.034 [± 0.067] Ma (Figure 7-5 a).

At Level 2 four specimens were analysed from each of two horizons 1m apart in the stratigraphy (2009 RHCI CA7 - lower sampling horizon and 2009 RHCI CA10 - upper sampling horizon). Each horizon has a high concentration of calcite crystals and an erosional base, and they are interpreted to be shallow scours formed through reworking of the sediments. The crystals exhibit complex sector, concentric, and intrasectoral zoning in cathode-luminescence (Figure 7-3). The U* range between ~3ppm and ~40ppm, and $^{238}U/^{206}Pb$ values range from 12 to 3400, which is much wider than seen in the specimens from Level 1, and includes much lower values. The combined analyses of multiple laser ablation spots on four crystals from sampling horizon 2009 RHCI CA7 produced an age of 1.915 ± 0.04 [± 0.063] Ma

(Figure 7-5 c), and those from sampling horizon 2009 RHCI CA10 produced an age of 1.934 ± 0.038 [± 0.062]Ma (Figure 7-5 d).

Crystals from each of four sampling horizons 1m apart in the stratigraphy at Level 3 (2009 RHCII CA3, 2009 RHCII CA5, 2009 RHCII CA6, and 2009 RHCII CA7 - lowest to highest in the stratigraphy) had U* between ~2ppm and ~45ppm and gave a similarly wide range of $^{238}U/^{206}Pb$ values from ~10 to ~3000. Crystals were found differently in the sediments at the four sampling horizons; in a concentrated crystal bed interpreted as a lag deposit in a shallow scour (CA7), dispersed throughout the clay matrix (CA6), in an arching spray (CA3), and in clay matrix interpreted to be a partially collapsed arching feature (CA5). The crystals exhibit complex sector, concentric, and intrasectoral zoning in cathode-luminescence. The combined analyses of multiple laser ablation spots on four crystals from sampling horizon 2009 RHCII CA3 produced an age of 1.95 ± 0.083 [± 0.114] Ma (Figure 7-5 e), those from sampling horizon 2009 RHCII CA5 produced an age of 2.02 ± 0.10 [± 0.36] Ma (Figure 7-5 f), those from 2009 RHCII CA6 produced an age of 1.897 ± 0.06 [± 0.1] Ma (Figure 7-5 g), and those from sampling horizon 2009 RHCII CA7 produced an age of 1.847 ± 0.047 [± 0.129] Ma (Figure 7-5 h).

Finally, the analyses of four crystals from horizon Level 4 (2010 LOC25) with similar physical characteristics to those at Levels 2 and 3, had U* between ~4ppm and ~84ppm and produced a wide range of $^{238}U/^{206}Pb$ values, between ~23 and ~4000. The combined analyses of multiple laser ablation spots on four crystals from sampling horizon 2009 LOC25 produced an T-W date of 1.601 ± 0.032 [± 0.088] Ma (Figure 7-5 b).

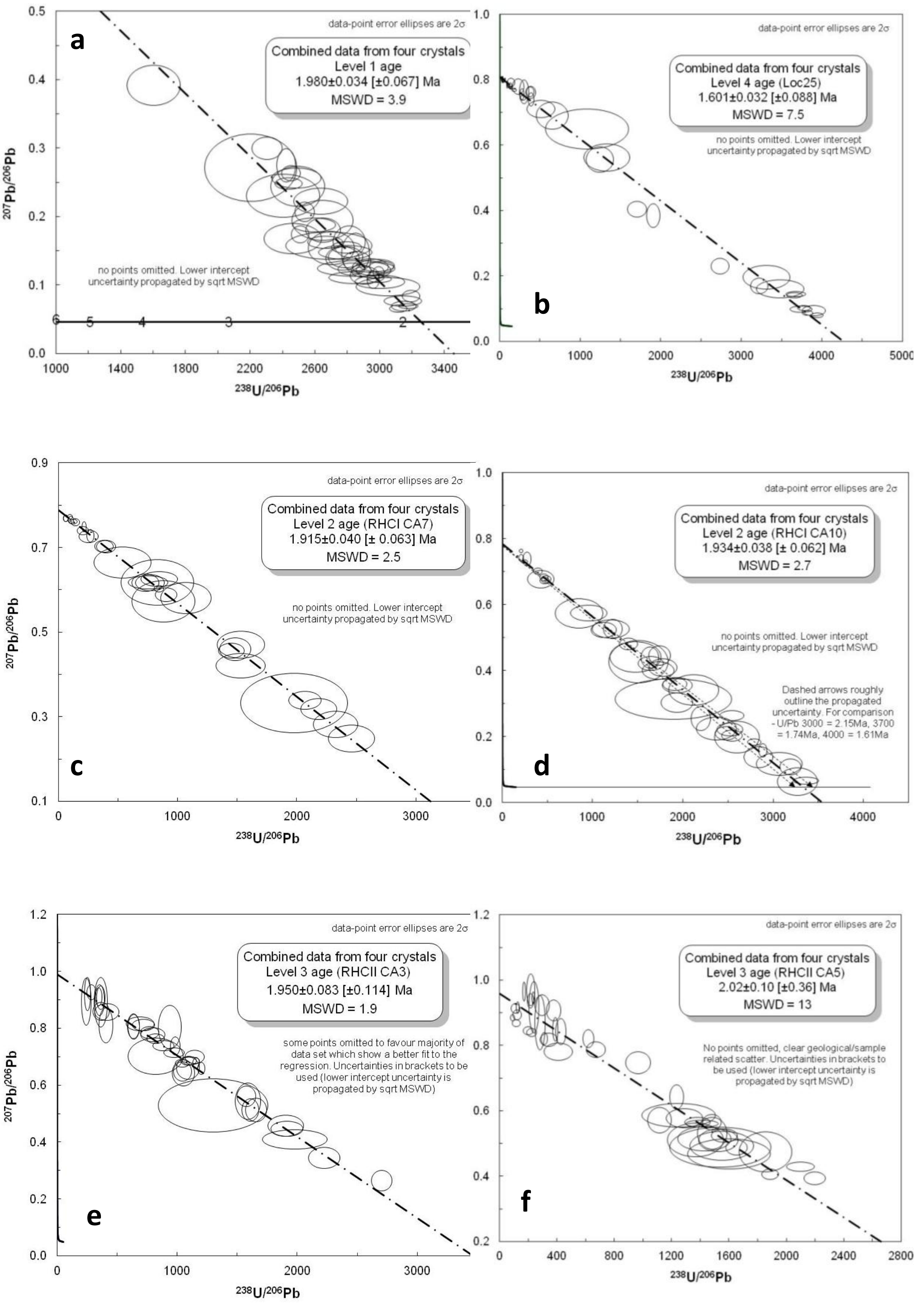
a
data-point error ellipses are 2σ
Combined data from four crystals
Level 1 age
1.980±0.034 [±0.067] Ma
MSWD = 3.9
no points omitted. Lower intercept uncertainty propagated by sqrt MSWD
207Pb/206Pb
238U/206Pb
b
data-point error ellipses are 2σ
Combined data from four crystals
Level 4 age (Loc25)
1.601±0.032 [±0.088] Ma
MSWD = 7.5
no points omitted. Lower intercept uncertainty propagated by sqrt MSWD
238U/206Pb
c
data-point error ellipses are 2σ
Combined data from four crystals
Level 2 age (RHCI CA7)
1.915±0.040 [± 0.063] Ma
MSWD = 2.5
no points omitted. Lower intercept uncertainty propagated by sqrt MSWD
207Pb/206Pb
238U/206Pb
d
data-point error ellipses are 2σ
Combined data from four crystals
Level 2 age (RHCI CA10)
1.934±0.038 [± 0.062] Ma
MSWD = 2.7
no points omitted. Lower intercept uncertainty propagated by sqrt MSWD
Dashed arrows roughly outline the propagated uncertainty. For comparison - U/Pb 3000 = 2.15Ma, 3700 = 1.74Ma, 4000 = 1.61Ma
238U/206Pb
e
data-point error ellipses are 2σ
Combined data from four crystals
Level 3 age (RHCII CA3)
1.950±0.083 [±0.114] Ma
MSWD = 1.9
some points omitted to favour majority of data set which show a better fit to the regression. Uncertainties in brackets to be used (lower intercept uncertainty is propagated by sqrt MSWD)
207Pb/206Pb
238U/206Pb
f
data-point error ellipses are 2σ
Combined data from four crystals
Level 3 age (RHCII CA5)
2.02±0.10 [±0.36] Ma
MSWD = 13
No points omitted, clear geological/sample related scatter. Uncertainties in brackets to be used (lower intercept uncertainty is propagated by sqrt MSWD)
238U/206Pb

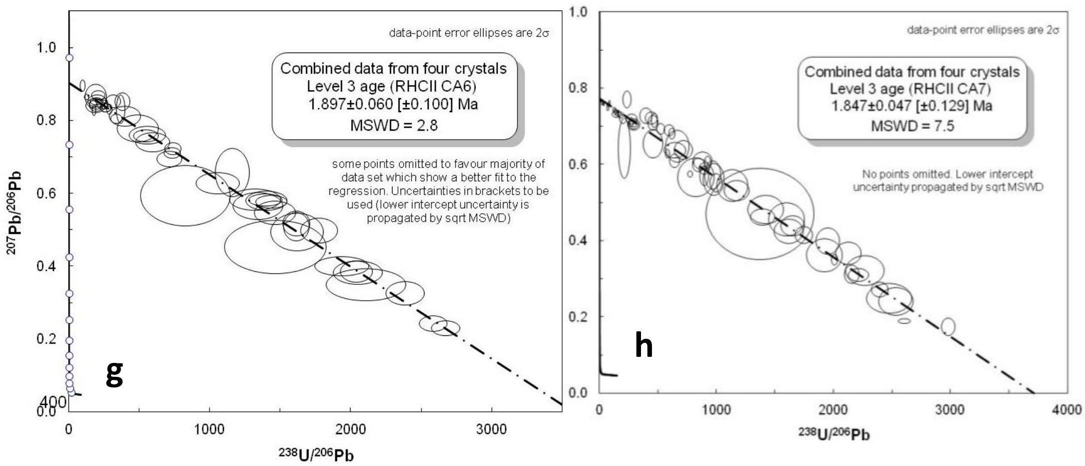

Figure 7-5: U-Pb data for calcite crystals. The isochrons were produced from the combined results of multiple spot analyses of each of four calcite crystals. Isoplot regression calculation does not propagate for excess scatter where the MSWD >1. As the MSWD is >> 1 the uncertainty has been propagated using the square root of the MSWD value. The expanded uncertainty is shown in square brackets. Although the error ellipses are large the excellent spread of $^{238}U/^{206}Pb$ ratios has produced isochrons with 2-5% uncertainties

The uncertainties of the calcite crystal ages determined using laser ablation analysis are significantly smaller than those of the sparry nodules from the terrestrial lake margin carbonates from the pilot study (Appendix 12). This is due in part to the greater spread of $^{238}U/^{206}Pb$ values and the high uranium and low lead concentrations in the lacustrine crystals compared to the terrestrial specimens. In addition the use of the calcite standard, rather than the NIST glass standard used in a pilot study, contributed to an improvement in the accuracy (Appendix 12).

7.5.2 Isotope dilution

Calcite crystals were investigated by isotope dilution analysis in order to compare the ages and uncertainties with those produced using laser ablation analyses (Appendix 14). Calcite crystals were chosen from the lowest level, Level 1 (RHCI 104), a single sampling horizon at Level 3 (RHCII CA5), and from the highest sampling horizon, Level 4 (LOC25).

The data produced by isotope dilution analysis of samples from Level 1 and Level 3 show significant scatter, and the isochrons at both levels have a low statistical probability of fit so were not constructed. However, when the data from both the isotope dilution analyses and the laser ablation analyses are plotted together, the much smaller isotope dilution error ellipses are seen to fit within the larger error ellipses of the laser ablation data (Figure 7-6).

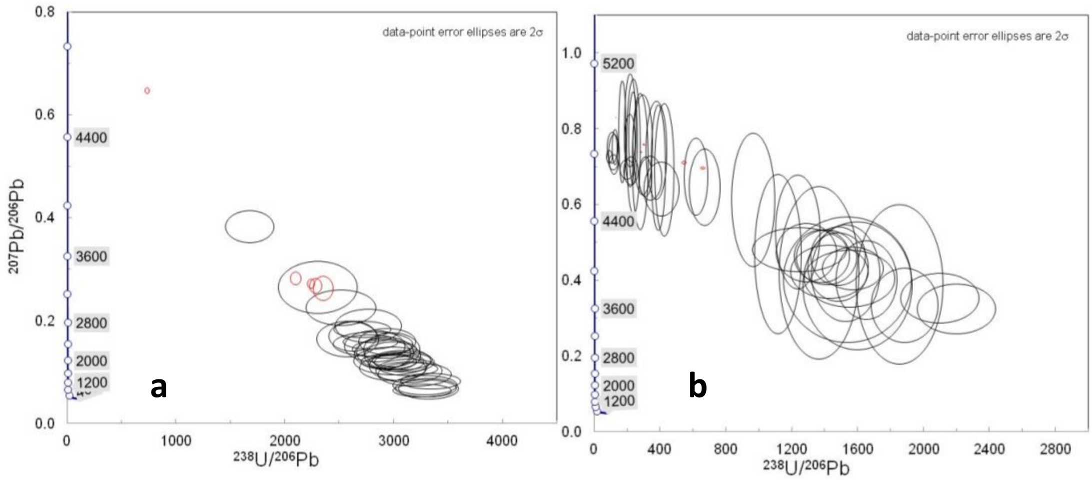

Figure 7-6: Comparison of Isotope dilution data and laser ablation data of crystals from Level 1 and Level 3. An isochron cannot be constructed for the data points produced using the isotope dilution method of multiple crystals from Level 1 (a: RHCI 104) and Level 3 (b: RHCII CA5). However, the isotope dilution ellipses (red ellipses) fall within the error of the laser ablation data (black ellipses).

Isotope dilution analyses of crystals from Level 4 (Loc 25) produced a well constrained $^{238}U/^{206}Pb$ - $^{207}Pb/^{206}Pb$ isochron with an age of 1.46 ± 0.19 Ma, but with an MSWD of 264 showing high non-analytical scatter (Figure 7-7a). A $^{235}U/^{204}Pb$ - $^{207}Pb/^{204}Pb$ isochron could also be plotted and produced an isochron age of 1.13 ± 0.15 Ma (MSWD = 0.23) (Figure 7-7b) indicating a discordance between the $^{206}Pb/^{238}U$ and $^{207}Pb/^{235}U$ systems. As with data from Levels 1 and 3, the error ellipses produced from isotope dilution data are significantly smaller than those produced from laser ablation data. However the spread in U-Pb space is reduced resulting in large uncertainties in the T-W regression (Figure 7-7c).

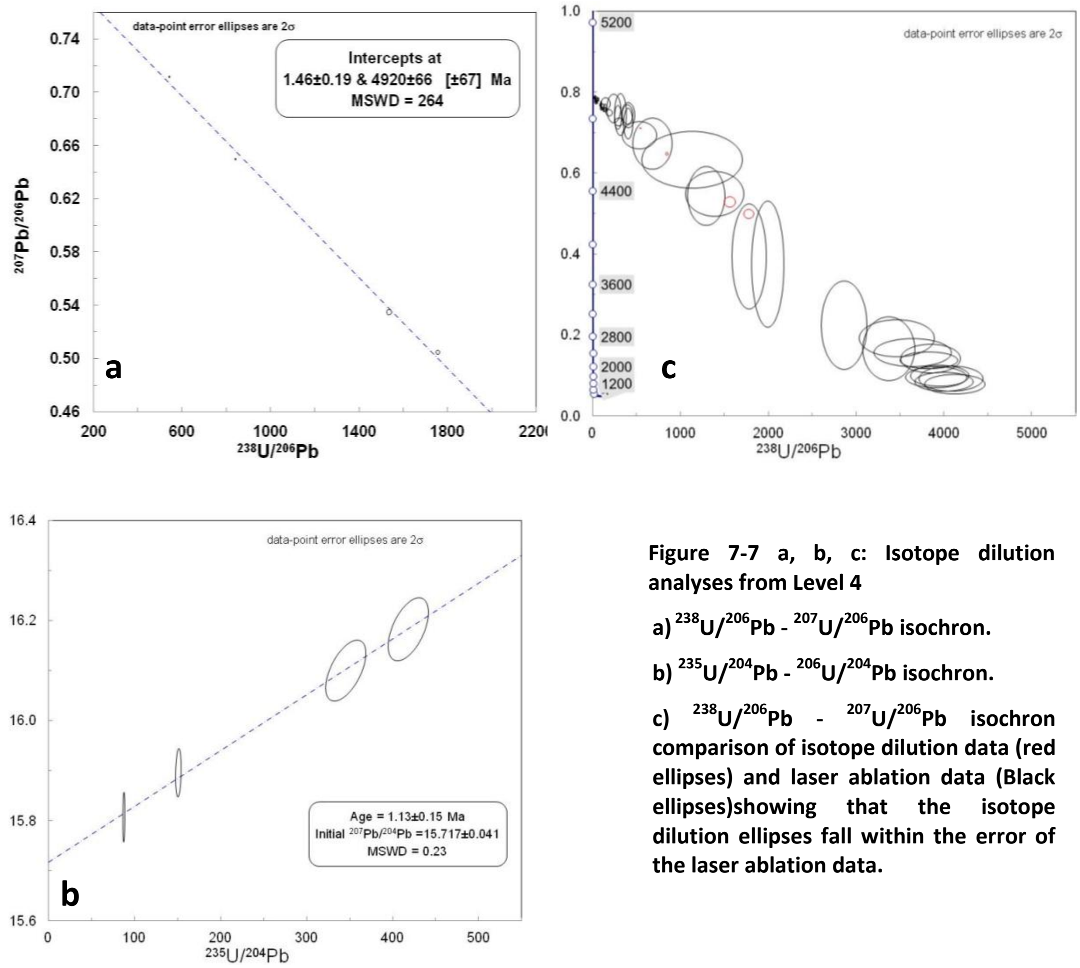

Figure 7-7 a, b, c: Isotope dilution analyses from Level 4

a) ^{238}U/^{206}Pb - ^{207}U/^{206}Pb isochron.

b) ^{235}U/^{204}Pb - ^{206}U/^{204}Pb isochron.

c) ^{238}U/^{206}Pb - ^{207}U/^{206}Pb isochron comparison of isotope dilution data (red ellipses) and laser ablation data (Black ellipses)showing that the isotope dilution ellipses fall within the error of the laser ablation data.

7.5.3 Initial uranium disequilibrium

Pleistocene calcite crystals, from the same sampling horizons at Olduvai Gorge as those used in the isotope dilution analyses, were chosen to investigate their current ^{234}U/^{238}U activity ratios, and so to calculate their initial uranium disequilibrium by extrapolation, assuming they remained as closed systems (Appendix 15). In addition, the ^{234}U/^{238}U activity ratios of calcite crystals from three contemporary lakes, considered to be geochemically comparable to Olduvai (Chapter 5), were also investigated as indicators of the potential initial uranium disequilibrium that may be expected in the Pleistocene crystals (Appendix 15).

The ^{234}U/^{238}U activity ratio of samples from Lake Natron is 1.035, from Lake Ndutu 1.292, and from Lake Makat 1.473. There is very little published data on the uranium activity ratios of contemporary lakes in East Africa, however, the data from this study are comparable to values calculated from stromatolites in Lake Magadi and Lake Natron, which were in the region of ~1.3-~1.6 (Goetz and Hillaire-Marcel, 1992; Hillaire-Marcel et al., 1986), the inflow water for Lakes Magadi and Lakes Natron of 1.62 (Goetz and Hillaire-Marcel, 1992), and water from Lake Malawi of 1.25 (Kronfeld and Vogel, 1991).

The $^{234}U/^{238}U$ ratio of each of two crystals from Level 1 (RHCI 104) is 1.010. The calculated (Equation 4) initial $^{234}U/^{238}U$ activity ratio of crystals in a closed system with an expected age of 1.9Ma (from Tuff dates) would be 3.149. This is significantly higher than the $^{234}U/^{238}U$ activity ratios found in the contemporary crystals. The residual $^{234}U/^{238}U$ combined with the U-Pb data results in a disequilibrium corrected U-Pb date of 1.675 Ma ± 0.018 Ma and an initial $^{234}U/^{238}U$ activity ratio of 2.132 ± 0.06 (Table 14).

$$[^{234}U/^{238}U]_{initial} = 1 + \left([^{234}U/^{238}U]_{system} - 1\right)e^{\lambda_{234}t}$$

Equation 4: Calculation of the initial uranium activity ratios, $[^{234}U/^{238}U]_{system}$ is the calculated activity ratio from the measured $^{234}U/^{235}U$ values (Cheng et al., 2000; Cowan and Adler, 1976; Jaffey et al., 1971), t =s the time in years and $\lambda^{234}U$ = 2.83xe^{-6} (Cheng et al., 2000) (Appendix 15).

Similarly for Level 3 (RHCII CA5), the $^{234}U/^{238}U$ ratio is 1.0021, i.e. it is effectively at secular equilibrium. The calculated (Equation 4) initial $^{234}U/^{238}U$ activity ratio of these crystals in a closed system with an expected age of 1.8 Ma (from Tuff dates) would be 1.340. This is comparable to crystals from Lake Makat at 1.473 and Lake Ndutu at 1.292. The residual $^{234}U/^{238}U$ combined with the U-Pb data results in a disequilibrium corrected U-Pb date of 1.938 Ma ± 0.076 Ma and an initial $^{234}U/^{238}U$ activity ratio of 1.489 ± 0.12 (Table 14).

Finally, the $^{234}U/^{238}U$ ratio of crystals from Level 4 (LOC25) is 1.0262 ± 0.00051 and the calculated (Equation 4) initial $^{234}U/^{238}U$ activity ratio of these crystals in a closed system with an expected age of 1.5 Ma would be 2.817. This is higher than the $^{234}U/^{238}U$ activity ratios found in the contemporary crystals. The residual $^{234}U/^{238}U$ combined with the U-Pb data results in a disequilibrium corrected U-Pb date for the laser ablation data of 1.319 Ma ± 0.019 Ma and an initial $^{234}U/^{238}U$ activity ratio of 2.089 ± 0.06. The residual $^{234}U/^{238}U$ combined with the U-Pb data results in a disequilibrium corrected U-Pb date for the isotope dilution data of 1.284 Ma ± 0.055 Ma and an initial $^{234}U/^{238}U$ activity ratio of 1.893 ± 0.14 (Table 14).

Sample ID	T-W age (Ma)	2σ (abs)	MSWD	235-207-204 age (Ma)	2σ (abs)	MSWD	$[234/238]_m$	2σ (abs)
RHC11 CA5*	2.020	0.10	13				1.0021	0.00049
Loc-25§	1.460	0.19	264	1.12	0.15	0.24	1.0262	0.00051
Loc-25*	1.601	0.03	7.5	1.12	0.15	0.24	1.0262	0.00051
104*	1.980	0.03	3.9				1.0100	3.74E-06

Sample ID	2σ (abs)	$[234/238]_{i\ median}$	Mean corrected Age (Ma)	2σ (abs)	Median corrected Age (Ma)
RHC11 CA5*	0.12	1.487	1.938	0.076	1.938
Loc-25§	0.14	1.892	1.284	0.055	1.249
Loc-25*	0.06	2.090	1.319	0.019	1.320
104*	0.06	2.133	1.675	0.018	1.676

Table 14: Summary of uranium analyses data. The residual $^{234}U/^{238}U$ is combined with the U-Pb data results to produce a disequilibrium corrected U-Pb date for the isotope dilution data (Dr. D. Condon, NIGL). * Laser ablation T-W age, § ID T-W age, Corrected ages and initial activity ratios reflect a triangular distribution of [230/238] initial ratios, peaking at 0.5, Mean and median [AR] and age values calculated to provide a measure of the non-Gaussian nature of the monte carlo array.

7.6 Discussion

The accuracy and precision of the sample analyses are a function of the analytical method, potential open system behaviour and initial system heterogeneity.

7.6.1 Analytical method and crystal sampling strategy

On average the LA U-Pb ages (not corrected for initial $^{234}U/^{238}U$ disequilibrium) vary between 0 ka and 200 ka too old compared to the $^{40}Ar/^{39}Ar$ ages of the tuffs (Figure 7-8). Although the error ellipses are large, the spread of $^{238}U/^{206}Pb$ ratios produced by multiple LA sampling positions within individual crystals has produced isochrons with only 3-5% uncertainties. In comparison, although the isotope dilution method has the potential to produce more precise analytical uncertainties, the isotope dilution T-W age for the sample which produced an isochron (Loc25) has uncertainties much greater than the comparable LA regressions (Figure 7-8).

The crystals contain varying amounts of clay and this may provide an additional source of decay series isotopes, both through leaching of, and decay to, daughter products adsorbed on the clay minerals. These will be non-consistent between crystals. During the ID analyses whole crystals are dissolved, and so the U/Pb values are averages of the whole specimen. Consequently, the high uncertainty in the U-Pb T-W age is likely to be influenced by the averaging effect of the sampling method and varying amounts of clay contamination between crystals. However, during LA analyses, multiple sampling points over a high-spatial resolution within a single crystal produce a much wider range of values, and analyses are less likely to be contaminated by clay minerals because of the very small sample size. Thus the LA method generally produces much smaller uncertainties than the ID method.

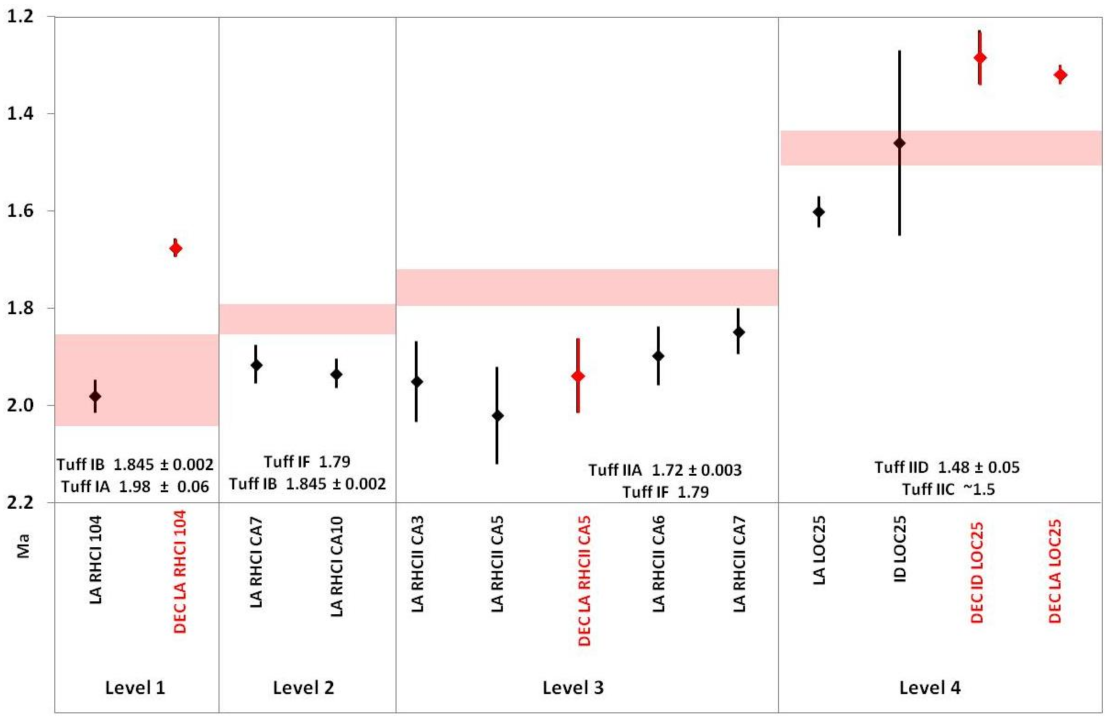

Figure 7-8: Comparison of tuff ages and calcite crystal ages at Levels 1 to 4. The pink bands represent the age range of the tuffs which form the upper and lower boundaries of the sediments in which the calcite crystals were sampled, and so represent the expected age range of the calcite crystals at each level. The black diamonds are the U-Pb Laser ablation (LA) Tera-Wasserburg (T-W) ages of the combined data from four crystals at each sampling horizon within each level, or U-Pb Isotope dilution (ID) T-W age of single crystal analyses (uncorrected for disequilibrium), and the black bar represents their uncertainties. The $^{234}U/^{238}U$ activity ratio was measured by analysis of single crystals, and the red diamonds are the LA or ID ages of the crystals corrected for disequilibrium (DEC). In general the uncorrected LA ages of the calcite crystals are older than the expected ages determined by the tuffs, apart from the lowest sampling horizon, Level 1, and the ID data from Level 4. The disequilibrium corrected ages are generally younger than the expected age, apart from the sample at Level 3 which is older than the tuff age but still younger than the uncorrected age.

Crystals are likely to have formed both in the lake basin and in the lake margin sediments (Chapter 5), and they are found differently in the sediments; dispersed, in arching sprays, and as reworked lags. Variations in crystal formation processes between locations, and their diagenetic history, may affect the crystal response to the analytical methods used. They may also produce a variation in open system behaviour and initial system heterogeneity between levels. Visually there is no obvious textural difference between the crystals from Levels 2, 3 and 4 that would indicate variations in calcite crystal formation processes. Yet the crystals at different levels have different accuracies and levels of uncertainty. In addition, crystals from Level 1 are texturally dissimilar to the those from the other levels, and have much higher concentrations of U^*, yet produce a comparable range of accuracies and levels of uncertainty. Crystals at Level 1, Level 2, and Level 4 have similar magnitudes of uncertainties, and are found either dispersed in the lacustrine clay beds or re-worked in laminated crystal rich beds. Although overall the uncertainties for the Level 3 samples are higher than for the other three levels, the highest uncertainties are for those crystals which are found in arching sprays, or slightly collapsed arching sprays. Potentially the change in the uncertainty of the crystals is caused by changes in the processes operating during and post formation.

An investigation of the Pleistocene crystals sampled more frequently through the stratigraphic succession, and a comparison of how they are found in the sediments compared to their textural and geochemical analyses, may provide an insight into the different processes controlling the changes between them, and produce a sampling strategy to identify the most suitable crystals for dating.

7.6.2 Open system behaviour

Dissolution and re-precipitation events during calcite crystal growth, revealed by the cathode-luminescence pattern at levels 2, 3, and 4, are evidence of likely open system behaviour. The cathode-luminescence images of calcite crystals from level 1 do not show the same pattern and there is no apparent visual indication of potential open system behaviour. The $^{234}U/^{238}U$ activity ratios for the Pleistocene crystals are >1 and so the uncorrected LA and ID Tera-Wasserburg ages would be expected to be a maximum. When the LA and ID analyses are corrected for the $^{234}U/^{238}U$ AR, the new ages are indeed younger than the uncorrected ones. However, those from Levels 1 and 4 are markedly younger than those from Level 3.

The projected initial activity ratio of the Pleistocene crystals (Appendix 15) for both Level 1 and Level 4 crystals would require a much higher $^{234}U/^{238}U$ activity ratio than is found in the contemporary lakes analysed in this study. Although this is possible, it may indicate open system behaviour. The discordance between the U-Pb dates derived from the $^{206}Pb/^{238}U$ and $^{207}Pb/^{235}U$ systems of the Level 4 crystals (Figure 7-7) also indicates open system behaviour. However, at level 3, the calculated initial uranium activity ratio is comparable to a modern system identified in this study, and indicates a system less influenced by open system behaviour.

The evidence of multiple dissolution and precipitation events not only shows open system behaviour, but also, potentially, multiple sources of water with different uranium activity ratios (AR) during crystal formation. The $^{234}U/^{238}U$ activity ratio of the source water is likely to have fluctuated during crystal growth; however, the AR of the crystals is determined using whole crystal dissolution producing an average AR during crystal formation. Although no fractionation of the uranium isotopes has been shown in low temperature carbonate systems (Stirling et al., 2007), redox control in both biogenic and abiotic low temperature carbonates is a target for current research (Brennecka et al., 2011; Herrmann, 2010). Changes in the incorporation of ^{234}U during the growth of the crystal due to either changes in the AR of the source water, or low temperature fractionation of uranium due to redox changes of the calcite crystals, may produce a similar result to open system behaviour.

Further work on the results of low temperature fractionation may provide an insight into the relative effect of these different influences in the future.

7.6.3 Initial system heterogeneity

Initial uranium heterogeneity

In a closed system secular equilibrium will be reached after 5 to 8 half lives of the daughter product, which for ^{234}U would be between ~1.2 Ma and ~2.0 Ma (Bourdon et al., 2003). Consequently, samples investigated at Olduvai may have formed with an initial uranium disequilibrium but be at secular equilibrium today. The $^{234}U/^{238}U$ activity ratios of the Pleistocene crystals from Olduvai Gorge are much closer to secular equilibrium than the $^{234}U/^{238}U$ activity ratios of crystals from the modern lakes (Appendix 15). There is very little reported data on the potential uranium sources for Palaeolake Olduvai, but it is likely to have been via both inflow water sources and directly from volcanic deposits. Fluvial input to the lake was from both the western Tanzanian Craton and the volcanic highland to the east (Hay, 1976), and synsedimentary springs are inferred along faults in the upper part of Bed I and Lower Bed II (Ashley et al., 2010b). Uranium concentrations between 1ppm and 6ppm are reported from the eastern volcanic sources, which are likely to have supplied uranium via fluvial systems and directly from ashfall deposits (McHenry et al., 2008; Mollel et al., 2008; Mollel et al., 2009). Although trace element data are not available for the craton, uranium mining prospects have been identified in several areas west of the Gorge, and fluvial input to the lake in contact with granitic terrain may provide a source of uranium.

Fractionation of uranium isotopes, and so generation of $^{234}U/^{238}U$ activity ratios > 1, occur where the water is delivered via fluvial systems or springs through terrain where the minerals are susceptible to weathering and dissolution (Goetz and Hillaire-Marcel, 1992; Kronfeld and Vogel, 1991). The variation in the $^{234}U/^{238}U$ activity ratios of the contemporary calcite crystals from Lakes Ndutu, Makat, and Natron may indicate how differences in uranium supply mechanisms may affect activity ratios. Crystals from Lake Natron have the lowest $^{234}U/^{238}U$ activity ratio of the three modern lakes measured for this study. Input of carbonatitic ash from nearby Oldoinyo Lengai (Dawson, 1962; Dawson and Gale, 1970) may contribute to the low values of $^{234}U/^{238}U$ activity ratio in the lake water, and so the calcite crystals. Whereas crystals from Lake Makat and Lake Ndutu have higher $^{234}U/^{238}U$ activity ratios and the lake water is primarily sourced by fluvial input. The different levels of uranium disequilibrium between crystals from Lake Makat and Lake Ndutu may simply be an indicator that the susceptibility to weathering and dissolution of the uranium source minerals. The apparent initial uranium disequilibrium in Palaeolake Olduvai may thus differ through the stratigraphy because of changes in the dominance of the fluvial source and delivery of volcanic deposits and so may represent synsedimentary changes in the impact of weathering of source minerals.

Interestingly, the $^{234}U/^{238}U$ activity ratio of the contemporary calcite crystals from Lake Natron (1.035) is somewhat lower than the $^{234}U/^{238}U$ activity ratio of the Late Quaternary stromatolites from Lake Natron (1.1-1.6). This may represent changes in the $^{234}U/^{238}U$ in the lake over a period of 10-40Ka. Significant fractionation of the ^{234}U, ^{235}U and ^{238}U isotopes during mineral formation at low temperatures is generally not expected because of their high masses (Stirling et al., 2007). However, $^{235}U/^{238}U$ and $^{234}U/^{238}U$ disequilibrium of between 4 and 9 epsilon units ($2\sigma = 1$ epsilon unit) has been measured in terrestrial carbonates (Stirling et al., 2007) due to preferential leaching of ^{234}U and ^{235}U from source minerals. Determining the $^{234}U/^{238}U$ activity ratio of the contemporary lake water may clarify if the difference is due to changes in the lake water or potentially uranium isotope fractionation during calcite precipitation.

Initial lead heterogeneity

Initial lead heterogeneity can cause large uncertainties and high MSWD values in young calcites. The LA T-W isochron of crystals from level 4 produced non-concordant results with the ID T-W isochron, and the high MSWD values shows scatter greater than non-analytical uncertainty which may be caused by initial lead heterogeneity (Figure 7-7). Crystals from Levels 2, 3, and 4 contain inclusions which in some cases have been identified as clay particles. Although the crystals have relatively low concentrations of Pb, potentially some still remains adsorbed onto the clay particles. During sample preparation for analysis by isotope dilution MC-ICP-MS any remaining Pb may be leached from them. During ablation of the crystals, however, the small amount of calcite removed from 100μm pits may sample little or none of the clay. Although the error ellipses using the laser ablation method are much larger than when using the isotope dilution method, using a large number of data points helps to reduce the uncertainties. The presence of common lead may have a less detrimental impact on age determination and uncertainties when using the laser ablation analyses of calcite crystals compared to the isotope dilution method which makes laser ablation a preferable method for dating the calcite crystals.

7.7 Conclusions

- The pattern of cathode-luminescence brightness can be used to target a range of $^{238}U/^{206}Pb$ values which produce well constrained $^{238}U/^{206}Pb$ - $^{207}Pb/^{206}Pb$ isochrons.
- The crystal dates, determined using laser ablation analyses and normalising to a calcite standard, are either accurate within error or up to 200 ka older, with a mean age 100 ka older, than the expected ages determined by the $^{40}Ar/^{39}Ar$ geochronology of the tuff beds, with uncertainties between 3 and 5%.
- Laser Ablation MC-ICP-MS analyses of calcite crystals show an advantage over isotope dilution methods because whole crystal dissolution is not required and uncertainties associated with initial system heterogeneity are reduced.
- Assuming that the calcite crystals are closed systems, the initial uranium disequilibrium of Palaeolake Olduvai was different at various stratigraphic levels, possibly as a result of changes in the delivery of uranium.
- Open system behaviour is more dominant at different stratigraphic levels. Further investigation of crystal textures, geochemistry, and differences in formation and diagenetic processes may help to identify the most promising crystals for U-Pb age determination.
- Although open system behaviour, initial uranium disequilibrium, and initial Pb heterogeneity, are factors to consider, the consistent close agreement of the calcite ages with the tuff dates suggest that the method potentially offers an alternative dating tool for Pleistocene lacustrine sediments from saline alkaline lakes, especially where other radiometric dating techniques are unsuitable.

Chapter 8: Conclusions and further work

The research aim for this thesis was to evaluate the terrestrial and lacustrine carbonates found at Olduvai Gorge, Tanzania, to help us to understand palaeoenvironmental conditions operating during their formation, and the potential for their dating using U-Pb geochronology. This was addressed using the four key questions outlined in the introduction:

- Using their textures and geochemistry, is it possible to use the carbonates from the terrestrial sediments as palaeohydrological indictors?
- Can the terrestrial carbonates then be used as predictive tools for palaeohydrological and palaeoenvironmental investigations at Olduvai Gorge, and potentially elsewhere?
- What is the genesis of the lacustrine carbonates and what information can they offer us in terms of palaeoenvironmental reconstruction?
- Can the lacustrine and terrestrial carbonates be accurately dated using the uranium-lead decay series, and so potentially provide a novel dating tool both at Olduvai and also at other, similar, hominin locations?

Using their textures and geochemistry, is it possible to use the carbonates from the terrestrial sediments as palaeohydrological indictors?

Chapters 2 and 3 specifically address this question. The terrestrial carbonates have a wide variety of textures, and a simple visual analysis of the carbonate macromorphology combined with thin section analysis of a representative sample of the specimens meant that they could confidently be placed in one of five groups: sparry nodules; spherulitic clusters; micritic nodules type 1 and type 2; bioturbation in the forms of rhizocretions, insect burrows, and rootmats; and early diagenetic evaporite pseudomorphs. Once the initial criteria had been decided, many of the remaining samples could be placed in their group based solely on uncut specimens, although for some of the samples a cut face was necessary to properly categorise them.

The advantage of this simple grouping process meant that the specimen types could be identified at a preliminary stage during an archaeological excavation or geological field work to aid understanding of the site at the earliest stage possible.

The detailed textural analyses using multiple microscopic techniques proved to be essential to unravel the formation history of the carbonates, in particular, providing an understanding of their diagenetic history. The stable isotope and trace element data from each of the different groups was interpreted in terms of the source water supply and groundwater conditions. The combination of textural and geochemical techniques significantly enhanced our understanding of the complexities of the carbonate formation and the presence of patterns of events during their formation. They have provided a means to interpret the palaeoenvironmental settings of each different group and the development of palaeohydrological models.

Micritic nodules are common in the sediments at Olduvai, and are both composed of massive micrite with cemented cracks, but through this process of analyses they can be divided into two types. Type 1 is interpreted to be pedogenic and they have micromorphological textures including root traces, circumgranular cracking around siliciclastic grains and alveolar features. In addition to the fossilised grassland, rhizocretions and fossilised insect burrows, these carbonates are judged to be formed in the vadose zone. The palaeoenvironment in which Type 2 nodules were formed is less clear, and they contain none of the pedogenic features described for the type 1 nodules. They are deduced to have been formed in either the vadose zone or a palustrine setting. The evaporite pseudomorphs are interpreted to have initially formed in an evaporitic setting palustrine setting – with replacement by calcite.

Two groups of carbonates with radial structures have not previously been described by other research groups. Spherulitic clusters are proposed to have formed by rapidly deposited carbonate from highly super-saturated, evaporitic, pore fluids in the vadose zone. The growth of sparry nodules is more complex, and several stages of calcite formation have been identified; nuclei likely formed in the vadose or capillary zone, and were subsequently replaced or recrystallised by calcite from a meteoric water supply; the concentric sparry bands are hypothesised to have precipitated in soft sediment in the shallow phreatic zone; the final carbonate growth occurred as the sediments became increasingly dry until carbonate growth ceased. The water supply for the formation of the sparry bands was initially meteoric and then became increasingly influenced by lake water. Two hydrological models have been proposed for their formation. The model where lake water is supplied to the ground water via evaporative pumping is favoured because of the pattern of change in the stable isotopes through the sparry bands; however the model where water is supplied during lake flooding cannot be discounted because rapid changes in lake level are known.

The sparry nodules and the spherulitic clusters are texturally complex and indicate that the water table repeatedly changed in height. Yet even the stable isotope analyses every 1mm showed very little variation along the covariant trend from lower to higher values. It may be possible to identify more frequent fluctuations in the pattern of both stable isotope ratios and trace elements using ion probe or laser techniques and so identify any subtle variations and their possible relationship to cyclical or episodic changes in climate. Because of the unusual nature of these radial carbonates, it would also be of value to investigate the sub-surface of contemporary lake margin sites to try to identify if these carbonate are forming in the modern day.

Importantly, this combination of analytical techniques has identified that only two of the groups of carbonates found at Olduvai are unequivocally pedogenic, and that the range of stable isotope values previously documented through the stratigraphic sequence at Olduvai are similar to the range of values within individual carbonates. Consequently variations in stable isotope ratios in carbonates at Olduvai through the stratigraphic sequence are not necessarily driven primarily by climate driven changes in vegetation, but by evaporation and mixing of meteoric and lake water in the groundwater system.

Other East African sites of archaeological interest have carbonates in the sedimentary sequence. The next step would be to repeat the combination of textural and geochemical techniques at these sites, to test if the methodology works elsewhere.

This study has shown that the palaeohydrology of carbonates in terrestrial sediments can be identified using a combination of detailed textural and geochemical analyses. They in turn can then be used as palaeohydrological indicators in subsequent geological and archaeological fieldwork.

Can the terrestrial carbonates then be used as predictive tools for palaeohydrological and palaeoenvironmental investigations at Olduvai Gorge, and potentially elsewhere?

Chapter 4 describes how the carbonate types within a sedimentary log can be used to interpret the palaeohydrology at a specific geographical position and stratigraphic level. When each of the different carbonate groups is identified by a coloured symbol located on a sedimentary log, they provide an indication of the palaeohydrological change at that specific location and sedimentary unit. This study also shows that where multiple stratigraphic logs across the FLK fault compartment are correlated, the overall pattern of symbols that represent the different carbonate groups show the geographical palaeohydrology at specific sedimentary horizons, and how that varies throughout a stratigraphic sequence.

In particular, this highlighted that the carbonates were persistently forming in either vadose or phreatic conditions in specific areas within the fault compartment over a period of ~100ka. This tells us that the controls over the groundwater hydrology at specific sedimentary horizons are likely to be controlled by fault activity as well as climate. Specifically, the palaeohydrological pattern indicates that the tectonic development of the FLK fault compartment was active below Tuff IB, which is earlier than has previously been recorded.

Fossil hominin and stone tool artefact finds at Olduvai are concentrated at the Eastern lake margin in the footwall of the FLK fault compartment. In contemporary lake systems, the lake margins are favourable habitats for animal and human use. The most famous find at Olduvai, the fossil skull of *'Zinjanthropus boisei',* is found in an area which, from sedimentological and palaeobotanical data, has been interpreted as an area of dryland adjacent to marshland on one side and a river or spring on the other. It is exciting to find that the carbonates predict the same pattern of palaeohydrology within the fault compartment at particular horizons as the other indicators.

This data may also indicate that the onset of faulting and the development of the palaeoenvironmental mosaic identified in this and previous studies was the driver for differences in hominin exploitation. Knowing the palaeohydrological pattern at specific horizons may explain why concentrations of fossils are found at certain locations, and may provide us with the opportunity to predict other possible fossil sites. The next step would be to test this hypothesis at the adjacent KK fault compartment at Olduvai and possibly a similar site at other Pleistocene archaeological sites.

The carbonate groups have proved they offer an effective method for understanding the wider palaeohydrology at exposure surface and the factors influencing hominin exploitation at particular locations. This in turn has the potential to provide a predictive tool for future archaeological investigations.

What is the genesis of the lacustrine carbonates and what information can they offer us in terms of palaeoenvironmental reconstruction?

Chapters 5 and 6 investigates two types of lacustrine carbonates, sand-sized calcite crystals and dolomite beds, using a combination of textural and geochemical techniques. Small, euhedral, calcite crystals are abundant in the lake basin sediments at Olduvai. The investigation of the crystals in Chapter 5 has shown that they are found in arching sprays, dispersed in the clay sediments, and are often found reworked in shallow scours in the lake basin, producing thinly bedded crystal rich sediments. This latter information confirms that they are geologically contemporaneous with their stratigraphic level, and so representative of the lacustrine conditions operating at the time. The use of cathode-luminescence microscopy proved to be of great value, and complex sector, concentric and intrasectoral zoning was seen, identifying partitioning of trace elements on particular crystal faces. Chemical corrosion was identified by the truncation of zones in the cathode-luminescence image, and so used to detect a multi-stage process of crystal formation. The ability to target ICP analysis on a range of sectors, identified by ranges of brightness seen in cathode luminescence images, provided very specific data about the range of trace elements. This allowed interpretation about the genesis of the crystals and their potential usefulness in dating. The data have indicated that the crystals are formed in the shallow sub-surface sediments on the lake floor or lake margins under anoxic to sub-oxic conditions. They are interpreted to have formed in two stages; by direct calcite precipitation or by utilisation of an evaporite mineral precursor, followed by a later stage of calcite overgrowth.

The crystals have been used to indicate the lake conditions during their formation, and to provide information about the groundwater evolution during the formation of the sparry nodules in chapter 2. The crystals are ≤ 2mm long, and it was not possible to identify potential variations in the values of stable isotopes at different stages of the crystal growth. Further analysis using laser or ion probe techniques may reveal additional patterns of change that will provide information on the crystal genesis and original lacustrine conditions.

It would be useful to conduct a similar study to this one, comparing the Pleistocene crystals from Olduvai Gorge with those of similar ages reported in other similar sites in East Africa to identify the variations between different lake systems. As crystals are found in contemporary lakes, it would be additionally useful to obtain and study a core from their lake centres. This could be used to investigate any similarities or differences in size, morphology, mineralogy, stable isotope values or trace element concentrations of crystals found in the contemporary lake margins and the Pleistocene crystals. This may also yield information about how they are found in the sediments - if they are in found in beds of concentrated crystals showing reworking and if they are in arching sprays.

The calcite crystals from all levels have exceptionally low lead values and high uranium concentrations, hypothesised to be due to the interaction of humic substances with lake sediments in water with high pH and high alkalinity. This feature, combined with the range of U/Pb values within crystals, make these lacustrine calcite crystals potential targets for U-Pb geochronology. Chapter 7 reports the radiogenic isotope investigation of the crystals

The investigation of dolomites at two different stratigraphic levels in Chapter 6 identified two different types based on their textural and chemical differences. The analyses showed that the beds at different stratigraphic levels have different macromorphological and micromorphological textures and different stable isotope values. XRD analyses were able to provide information about the differences in the mineralogy of the dolomites. They indicated that each dolomite type is composed of a single phase, and all the dolomites have excess Ca, although the amount of excess differs between the dolomites from different stratigraphic levels. From XRD data the difference in the ordering of the dolomites was also identified. These differences are likely to be a consequence of growth conditions. The textural data, mineralogical data, and the stable isotope values of both types of dolomites, indicated that the dolomite is most likely to have been precipitated inorganically with stable isotope values primarily controlled by source water and evaporation.

Using these data it is inferred that the two types of dolomite were probably formed under different conditions. The first in a basinal setting in the sediment sub-surface, primarily by inorganic precipitation, from evaporated and saline interstitial water with a high Mg/Ca ratio, and the second in a marginal setting, possibly in the water column, from less evaporated lake water possibly influenced by the input of , possibly Mg-rich, freshwater input.

The analyses of two very different types of lacustrine carbonate have thus provided information about their genesis and they both provide useful indicators of palaeolake conditions.

Can the lacustrine and terrestrial carbonates be accurately dated using the uranium-lead decay series, and so potentially provide a novel dating tool both at Olduvai and also at other, similar, hominin locations?

Chapter 7 documents the results of dating the lacustrine calcite crystals using the uranium-lead decay series, and the exciting potential for using this method at other, similar, but less well-dated sites. As discussed in chapter 5, trace element and U/Pb values vary between different cathode-luminescence zones within the calcite crystals. The zones have a range $^{238}U/^{206}Pb$ values, and enable well constrained $^{238}U/^{206}Pb$ - $^{207}Pb/^{206}Pb$ isochrons on a Tera-Wasserburg plot to be produced. The data acquired using laser ablation MC-ICP-MS was normalised to a calcite standard. The dates produced with uncertainties between 2 and 5%, are either within error, or up to 200ka older, than the expected ages determined by the $^{40}Ar/^{39}Ar$ geochronology of the adjacent tuff beds in the succession.

The crystals are found differently in the sediments; in reworked beds, dispersed, or in arching sprays; and are either found singly or as clusters. At some levels multiple horizons with these differing characteristics were investigated, and they produced slightly differing ages and uncertainties. Further work is necessary to evaluate the reasons behind this difference. This should include investigating if the textural detail, or trace element analyses, of different horizons or crystals can be related to open system behaviour and increased uncertainties. It may be possible by investigating the ages for individual crystals with respect to the trace element data and the zoning patterns to identify crystals with characteristics that are likely to produce the least errors.

This study has identified that the sedimentary sequence in the lake is much more complex that previously recorded, with multiple erosion surfaces and variations in clay colour and texture. An understanding of the variations in sedimentation and calcite precipitation may provide the necessary information to assess why certain crystal horizons produce better ages than others. This could be undertaken by detailed field mapping and analysis of a much more comprehensive set of crystals and the clay sediments in which they are found.

This study has identified that Laser Ablation MC-ICP-MS analyses of calcite crystals show an advantage over isotope dilution methods because whole crystal dissolution is not required, and uncertainties associated with initial Pb heterogeneity are reduced. Lacustrine calcite crystals offer an alternative method for dating Pleistocene saline, alkaline, lake sediments, especially where other radiometric dating techniques are unsuitable.

Summary

Overall, the results have confirmed the exciting possibilities offered by the carbonates to answer these questions, the value of the techniques employed, and the likelihood of these methods being transferred to other, similar sites of archaeological interest. Several future directions for research have been identified that can continue this research and develop its potential for contributing to our understanding of past environments and hominin evolution.

References

Abell, P. I., Awramik, S. M., Osborne, R. H., and Tomellini, S., 1982, Plio-pleistocene lacustrine stromatolites from lake Turkana, Kenya: Morphology, stratigraphy and stable isotopes: Sedimentary Geology, v. 32, no. 1-2, p. 1-26.

Aharon, P., Kolodny, Y., and Sass, E., 1977, Recent Hot Brine Dolomitization in the "Solar Lake," Gulf of Elat, Isotopici, Chemical, and Mineralogical Study: The Journal of Geology, v. 85, no. 1, p. 27-48.

Albert, R. M., and Bamford, M. K., 2011, Vegetation during UMBI and deposition of Tuff IF at Olduvai Gorge, Tanzania (ca. 1.8 Ma) based on phytoliths and plant remains: Quaternary International, v. In Press, p. 1-9.

Albert, R. M., Bamford, M. K., and Cabanes, D., 2009, Palaeoecological significance of palms at Olduvai Gorge, Tanzania, based on phytolith remains: Quaternary International, v. 193, no. 1-2, p. 41-48.

Alonso-Zarza, A. M., Sanz, M. E., Calvo, J. P., and Estévez, P., 1998, Calcified root cells in Miocene pedogenic carbonates of the Madrid Basin: evidence for the origin of Microcodium b: Sedimentary Geology, v. 116, no. 1-2, p. 81-97.

Alonso-Zarza, A. M., and Wright, V. P., 2010a, Chapter 2 Palustrine Carbonates, *in* Alonso-Zarza, A. M., and Tanner, L. H., eds., Developments in Sedimentology, Volume Volume 61, Elsevier, p. 103-131.

-, 2010b, Chapter 5 Calcretes, *in* Alonso-Zarza, A. M., and Tanner, L. H., eds., Developments in Sedimentology, Volume Volume 61, Elsevier, p. 225-267.

Andreassen, J.-P., Flaten, E. M., Beck, R., and Lewis, A. E., 2010, Investigations of spherulitic growth in industrial crystallization: Chemical Engineering Research and Design, v. 88, no. 9, p. 1163-1168.

Andrews, J. E., Hamilton, P. J., and Fallick, A. E., 1987, The geochemistry of early diagenetic dolostones from a low-salinity Jurassic lagoon: Journal of the Geological Society, v. 144, no. 5, p. 687-698.

Arenas-Abad, C., Vázquez-Urbez, M., Pardo-Tirapu, G., and Sancho-Marcén, C., 2010, Chapter 3 Fluvial and Associated Carbonate Deposits, *in* Alonso-Zarza, A. M., and Tanner, L. H., eds., Developments in Sedimentology, Volume Volume 61, Elsevier, p. 133-175.

Armenteros, I., 2010, Chapter 2 Diagenesis of Carbonates in Continental Settings, *in* Alonso-Zarza, A. M., and Tanner, L. H., eds., Developments in Sedimentology, Volume Volume 62, Elsevier, p. 61-151.

Ashley, G. M., 2007, Orbital rhythms, monsoons, and playa lake response, Olduvai Basin, equatorial East Africa (ca. 1.85 Ma &1.74 Ma): Geology, v. 35, no. 12, p. 1091-1094.

Ashley, G. M., Barboni, D., Dominguez-Rodrigo, M., Bunn, H. T., Mabulla, A. Z. P., Diez-Martin, F., Barba, R., and Baquedano, E., 2010a, Paleoenvironmental and paleoecological reconstruction of a freshwater oasis in savannah grassland at FLK North, Olduvai Gorge, Tanzania: Quaternary Research, v. 74, no. 3, p. 333-343.

-, 2010b, A spring and wooded habitat at FLK Zinj and their relevance to origins of human behavior: Quaternary Research, v. 74, no. 3, p. 304-314.

Ashley, G. M., and Hay, R. L., 2002, Sedimentation patterns in a Plio-Pleistocene volcaniclastic rift-platform basin, Olduvai gorge, Tanzania., *in* Renaut, R. W., and Ashley, G. M., eds., Sedimentation in Continental Rifts, SEPM, Tulsa, p. 107-122.

Ashley, G. M., Tactikos, J. C., and Owen, R. B., 2009, Hominin use of springs and wetlands: Paleoclimate and archaeological records from Olduvai Gorge (~ 1.79-1.74 Ma): Palaeogeography, Palaeoclimatology, Palaeoecology, v. 272, no. 1-2, p. 1-16.

Ashley, G. M. a. D., Steven G., 2000, Paleopedology and Paleohydrology of a Volcaniclastic Paleosol Interval: Implications for Early Pleistocene Stratigraphy and Paleoclimate Record, Olduvai Gorge, Tanzania: Journal of Sedimentary Research, v. 70, no. 5, p. 1065-1080.

Aspinall, H., 2001, Chemistry of the f-Block Elements Taylor and Francis.

Astilleros, J. M., Pina, C. M., Fernández-Díaz, L., and Putnis, A., 2000, The effect of barium on calcite {1014} surfaces during growth: Geochimica et Cosmochimica Acta, v. 64, no. 17, p. 2965-2972.

-, 2003, Metastable phenomena on calcite {10$\bar{1}$4} surfaces growing from Sr^{2+}–Ca^{2+}–CO^{32}– aqueous solutions: Chemical Geology, v. 193, no. 1–2, p. 93-107.

Bamford, M. K., 2005, Early Pleistocene fossil wood from Olduvai Gorge, Tanzania: Quaternary International, v. 129, no. 1, p. 15-22.

Bamford, M. K., 2011, Fossil sedges, macroplants, and roots from Olduvai Gorge, Tanzania: Journal of Human Evolution, v. In Press, Corrected proof.

Bamford, M. K., Albert, R. M., and Cabanes, D., 2006, Plio-Pleistocene macroplant fossil remains and phytoliths from Lowermost Bed II in the eastern palaeolake margin of Olduvai Gorge, Tanzania: Quaternary International, v. 148, no. 1, p. 95-112.

Bamford, M. K., Stanistreet, I. G., Stollhofen, H., and Albert, R. M., 2008, Late Pliocene grassland from Olduvai Gorge, Tanzania: Palaeogeography, Palaeoclimatology, Palaeoecology, v. 257, no. 3, p. 280-293.

Barge, L. M., Hammond, D. E., Chan, M. A., Potter, S., Petruska, J., and Nealson, K. H., 2011, Precipitation patterns formed by self-organizing processes in porous media: Geofluids, v. 11, no. 2, p. 124-133.

Barnaby, R. J., and Rimstidt, J. D., 1989, Redox conditions of calcite cementation interpreted from Mn and Fe contents of authigenic calcites: Geological Society of America Bulletin, v. 101, no. 6, p. 795-804.

Beck, R., and Andreassen, J.-P., 2010a, The onset of spherulitic growth in crystallization of calcium carbonate: Journal of Crystal Growth, v. 312, no. 15, p. 2226-2238.

-, 2010b, Spherulitic Growth of Calcium Carbonate: Crystal Growth & Design, v. 10, no. 7, p. 2934-2947.

Beck, R., Flaten, E., and Andreassen, J. P., 2011, Influence of Crystallization Conditions on the Growth of Polycrystalline Particles: Chemical Engineering & Technology, v. 34, no. 4, p. 631-638.

Bennett, C. E., Marshall, J. D., and Stanistreet, I. G., 2012, Carbonate horizons, paleosols and lake flooding cycles: Beds I and II of Olduvai Gorge, Tanzania.: Journal of Human Evolution, v. In Press.

Bjørlykke, K., and Bjørlykke, K., 2010, Sedimentary Geochemistry, Petroleum Geoscience, Springer Berlin Heidelberg, p. 87-111.

Blumenschine, R., Masao, F., and Stanistreet, I. G., 2009, Changes in hominin transport of stone for Oldowan tools across the eastern Olduvai Basin during lowermost bed II times, *in* Schick, K., and Trauth, M. H., eds., The Cutting Edge: new approaches to the archaeology of human origins, Stone Age institue Press, p. 344.

Blumenschine, R. J., and Masao, F. T., 1991, Living sites at Olduvai Gorge, Tanzania? Preliminary landscape archaeology results in the basal Bed II lake margin zone: Journal of Human Evolution, v. 21, no. 6, p. 451-462.

Blumenschine, R. J., Masao, F. T., Stollhofen, H., Stanistreet, I. G., Bamford, M. K., Albert, R. M., Njau, J. K., and Prassack, K. A., 2011a, Landscape distribution of Oldowan stone artifact assemblages across the fault compartments of the eastern Olduvai Lake Basin during early lowermost Bed II times: Journal of Human Evolution, v. In Press, Corrected proof.

Blumenschine, R. J., Masao, F. T., Tactikos, J. C., and Ebert, J. I., 2008, Effects of distance from stone source on landscape-scale variation in Oldowan artifact assemblages in the Paleo-Olduvai Basin, Tanzania: Journal of Archaeological Science, v. 35, no. 1, p. 76-86.

Blumenschine, R. J., and Peters, C. R., 1998, Archaeological predictions for hominid land use in the paleo-Olduvai Basin, Tanzania, during lowermost Bed II times: Journal of Human Evolution, v. 34, no. 6, p. 565-607.

Blumenschine, R. J., Peters, C. R., Masao, F. T., Clarke, R. J., Deino, A. L., Hay, R. L., Swisher, C. C., Stanistreet, I. G., Ashley, G. M., McHenry, L. J., Sikes, N. E., van der Merwe, N. J., Tactikos, J. C., Cushing, A. E., Deocampo, D. M., Njau, J. K., and Ebert, J. I., 2003, Late Pliocene Homo and Hominid Land Use from Western Olduvai Gorge, Tanzania: Science, v. 299, no. 5610, p. 1217-1221.

Blumenschine, R. J., Stanistreet, I. G., Njau, J. K., Bamford, M. K., Masao, F. T., Stollhofen, H., Andrews, P., Fernández-Jalvo, Y., Prassack, K. A., Albert, R. M., McHenry, L. J., E.L, C., and J.I, E., 2011b, Environments and activity traces of Oldowan hominins across the FLK Peninsula during *Zinjanthropus* times (1.84 Ma), Olduvai Gorge, Tanzania.: Journal of Human Evolution, v. In Press, Corrected proof.

Bourdon, B., Turner, S., Henderson, G. M., and Lundstrom, C. C., 2003, Introduction to U-series geochemistry, Reviews in Mineralogy and Geochemistry, Volume 52.

Braissant, O., Cailleau, G., Dupraz, C., and Verrecchia, E. P., 2003, Bacterially Induced Mineralization of Calcium Carbonate in Terrestrial Environments: The Role of Exopolysaccharides and Amino Acids: Journal of Sedimentary Research, v. 73, no. 3, p. 485-490.

Brand, U., and Veizer, J., 1980, Chemical diagenesis of a multicomponent carbonate system - 1: trace elements: Journal of Sedimentary Petrology, v. 50, no. 4, p. 1219-1236.

Brennecka, G. A., Wasylenki, L. E., Bargar, J. R., Weyer, S., and Anbar, A. D., 2011, Uranium Isotope Fractionation during Adsorption to Mn-Oxyhydroxides: Environmental Science & Technology, v. 45, no. 4, p. 1370-1375.

Browne, G. H., and Kingston, D. M., 1993, Early diagenetic spherulitic siderites from Pennsylvanian palaeosols in the Boss Point Formation, Maritime Canada: Sedimentology, v. 40, no. 3, p. 467-474.

Bruhn, F., Bruckschen, P., Richter, D. K., Meijer, J., Stephan, A., and Veizer, J., 1995, Diagenetic history of sedimentary carbonates: Constraints from combined cathodoluminescence and trace element analyses by micro-PIXE: Nuclear Instruments and Methods in Physics Research Section B: Beam Interactions with Materials and Atoms, v. 104, no. 1–4, p. 409-414.

Bunn, H. T., Mabulla, A. Z. P., Domínguez-Rodrigo, M., Ashley, G. M., Barba, R., Diez-Martín, F., Remer, K., Yravedra, J., and Baquedano, E., 2010, Was FLK North levels 1-2 a classic "living floor" of Oldowan hominins or a taphonomically complex palimpsest dominated by large carnivore feeding behavior?: Quaternary Research, v. 74, no. 3, p. 355-362.

Busenberg, E., Plummer, L. N., and Parker, V. B., 1984, The solubility of strontianite (SrCO3) in CO2-H2O solutions between 2 and 91°C, the association constants of SrHCO+3(aq) and SrCO03(aq) between 5 and 80°C, and an evaluation of the thermodynamic properties of Sr2+(aq) and SrCO3(cr) at 25°C and 1 atm total pressure: Geochimica et Cosmochimica Acta, v. 48, no. 10, p. 2021-2035.

Bustillo, M. A., Arribas, M. E., and Bustillo, M., 2002, Dolomitization and silicification in low-energy lacustrine carbonates (Paleogene, Madrid Basin, Spain): Sedimentary Geology, v. 151, no. 1-2, p. 107-126.

Calvet, F., 1983, Pisoids in the caliche profiles of Tarragona (NE Spain), *in* Peryet, T. M., ed., Coated Grains: Berlin, Springer Verlag, p. 655.

Casanova, J., and Hillaire-Marcel, C., 1992, Chronology and paleohydrology of late Quaternary high lake levels in the Manyara basin (Tanzania) from isotopic data (^{18}O, ^{13}C, ^{14}C, Th/U) on fossil stromatolites: Quaternary Research, v. 38, no. 2, p. 205-226.

Cerling, T. E., 1984, The stable isotopic composition of modern soil carbonate and its relationship to climate: Earth and Planetary Science Letters, v. 71, no. 2, p. 229-240.

Cerling, T. E., and Hay, R. L., 1986, An isotopic study of paleosol carbonates from Olduvai Gorge: Quaternary Research, v. 25, no. 1, p. 63-78.

Cerling, T. E., Hay, R. L., and O'Neil, J. R., 1977, Isotopic evidence for dramatic climatic changes in East Africa during the Pleistocene: Nature, v. 267, no. 5607, p. 137-138.

Chabaux, F., Riotte, J., and Dequincey, O., 2003, U-Th-Ra Fractionation during weathering and river transport.: Reviews in Mineralogy and Geochemistry, v. 52, no. 1, p. 533-576.

Chafetz, H. S., and Butler, J. C., 1980, Petrology of recent caliche pisolites, spherulites, and speleothem deposits from central Texas: Sedimentology, v. 27, no. 5, p. 497-518.

Chafetz, H. S., and Guidry, S. A., 1999, Bacterial shrubs, crystal shrubs, and ray-crystal shrubs: bacterial vs. abiotic precipitation: Sedimentary Geology, v. 126, no. 1-4, p. 57-74.

Chafetz, H. S., Rush, P. F., and Utech, N. M., 1991, Microenvironmental controls on mineralogy and habit of $CaCO_3$ precipitates: an example from an active travertine system: Sedimentology, v. 38, no. 1, p. 107-126.

Chaftez, H. S., and Butler, J. C., 1980, Petrology of recent caliche pisolites, spherulites, and speleothem deposits from central Texas: Sedimentology, v. 27, no. 5, p. 497-518.

Chen, J. H., Lawrence Edwards, R., and Wasserburg, G. J., 1986, ^{238}U, ^{234}U and ^{232}Th in seawater: Earth and Planetary Science Letters, v. 80, no. 3-4, p. 241-251.

Chen, Z., 1999, Inter-element fractionation and correction in laser ablation inductively coupled plasma mass spectrometry: Journal of Analytical Atomic Spectrometry, v. 14, no. 12, p. 1823-1828.

Cheng, H., Edwards, R. L., Hoff, J., Gallup, C. D., Richards, D. A., and Asmerom, Y., 2000, The half-lives of uranium-234 and thorium-230: Chemical Geology, v. 169, no. 1–2, p. 17-33.

Copeland, S. R., 2007, Vegetation and plant food reconstruction of lowermost Bed II, Olduvai Gorge, using modern analogs: Journal of Human Evolution, v. 53, no. 2, p. 146-175.

Cowan, G. A., and Adler, H. H., 1976, The variability of the natural abundance of ^{235}U: Geochimica et Cosmochimica Acta, v. 40, no. 12, p. 1487-1490.

Curti, E., 1999, Coprecipitation of radionuclides with calcite: estimation of partition coefficients based on a review of laboratory investigations and geochemical data: Applied Geochemistry, v. 14, no. 4, p. 433-445.

Dawson, J., 1962, The geology of Oldoinyo Lengai: Bulletin of Volcanology, v. 24, no. 1, p. 349-387.

Dawson, J. B., 1992, Neogene tectonics and volcanicity in the North Tanzania sector of the Gregory Rift Valley: contrasts with the Kenya sector: Tectonophysics, v. 204, no. 1-2, p. 81-83, 87-92.

-, 2008, The Gregory Rift Valley and Neogene-Recent Volcanoes of Northern Tanzania, The Geological Society of London, Geological Society Memoir No.33.

Dawson, J. B., and Gale, N. H., 1970, Uranium and thorium in alkalic rocks from the active carbonatite volcano Oldoinyo Lengai (Tanzania): Chemical Geology, v. 6, p. 221-231.

De Deckker, P., and Last, W. M., 1989, Modern, non-marine dolomite in evaporitic playas of western Victoria, Australia: Sedimentary Geology, v. 64, no. 4, p. 223-238.

De Deckker, P. a. L., W. M., 1988, Modern dolomite deposition in continental, saline lakes, western Victoria, Australia: Geology, v. 16, p. 29-32.

Deocampo, D., M., 2002, Sedimentary Processes and Lithofacies in lake-margin groundwater-fed wetlands in East Africa, Sedimentation in Continental Rifts, SEPM Special Publication no 73, p. 295-308.

Deocampo, D. M., 2004, Authigenic clays in East Africa: Regional trends and paleolimnology at the Plio–Pleistocene boundary, Olduvai Gorge, Tanzania: Journal of Paleolimnology, v. 31, no. 1, p. 1-9.

Deocampo, D. M., 2010, Chapter 1 The Geochemistry of Continental Carbonates, *in* Alonso-Zarza, A. M., and Tanner, L. H., eds., Developments in Sedimentology, Volume Volume 62, Elsevier, p. 1-59.

Deocampo, D. M., and Ashley, G. M., 1999, Siliceous islands in a carbonate sea; modern and Pleistocene spring-fed wetlands in Ngorongoro Crater and Oldupai Gorge, Tanzania: Journal of Sedimentary Research, v. 69, no. 5, p. 974-979.

Deocampo, D. M., Blumenschine, R. J., and Ashley, G. M., 2002, Wetland Diagenesis and Traces of Early Hominids, Olduvai Gorge, Tanzania: Quaternary Research, v. 57, no. 2, p. 271-281.

Deocampo, D. M., and Tactikos, J. C., 2010, Geochemical gradients and artifact mass densities on the lowermost Bed II eastern lake margin (~ 1.8 Ma), Olduvai Gorge, Tanzania: Quaternary Research, v. 74, no. 3, p. 411-423.

Dickson, J. A. D., 1965, A Modified Staining Technique for Carbonates in Thin Section: Nature, v. 205, no. 4971, p. 587-587.

Dickson, J. A. D., 1978, Length-slow and length-fast calcite: A tale of two elongations: Geology, v. 6, no. 9, p. 560-561.

Diez-Martin, F., Sanchez Yustos, P., Domínguez-Rodrigo, M., Mabulla, A. Z. P., Bunn, H. T., Ashley, G. M., Barba, R., and Baquedano, E., 2010, New insights into hominin lithic activities at FLK North Bed I, Olduvai Gorge, Tanzania: Quaternary Research, v. 74, no. 3, p. 376-387.

Domínguez-Rodrigo, M., Bunn, H. T., Mabulla, A. Z. P., Ashley, G. M., Diez-Martin, F., Barboni, D., Prendergast, M. E., Yravedra, J., Barba, R., Sánchez, A., Baquedano, E., and Pickering, T. R., 2010, New excavations at the FLK Zinjanthropus site and its surrounding landscape and their behavioral implications: Quaternary Research, v. 74, no. 3, p. 315-332.

Dong, C., Chen, H., and Wu, F., 1999, A new Cu Kα2-elimination algorithm: Journal of Applied Crystallography, v. 32, no. 2, p. 168-173.

Downs, R. T., 2006, The RRUFF Project: an integrated study of the chemistry, crysallography, Raman and infrared spectroscopy of minerals: Programme and abstracts of the 19th General meeting of the International Mineralogical Association in Kobe, Japan. O03-13.

Drits, V. A., McCarty, D. K., Sakharov, B., and Milliken, K. L., 2005, New insight into structural and compositional variability in some ancient excess-Ca dolomite: Can Mineral, v. 43, no. 4, p. 1255-1290.

Eggins, S. M., Grün, R., McCulloch, M. T., Pike, A. W. G., Chappell, J., Kinsley, L., Mortimer, G., Shelley, M., Murray-Wallace, C. V., Spötl, C., and Taylor, L., 2005, In situ U-series dating by laser-ablation multi-collector ICPMS: new prospects for Quaternary geochronology: Quaternary Science Reviews, v. 24, no. 23-24, p. 2523-2538.

Elbaz-Poulichet, F., Nagy, A., Cserny, T., and Pomogyi, P., 1996, Biogeochemistry of trace metals (Mn, Sr, Rb, Ba, Cu, Zn, Pb and Cd) in a river-wetland-lake system (Balaton Region, Hungary): Aquatic Geochemistry, v. 2, no. 4, p. 379-402.

Erel, Y., and Morgan, J. J., 1992, The relationships between rock-derived lead and iron in natural waters: Geochimica et Cosmochimica Acta, v. 56, no. 12, p. 4157-4167.

Eugster, H. P., and Hardie, L. A., 1975, Sedimentation in an Ancient Playa-Lake Complex: The Wilkins Peak Member of the Green River Formation of Wyoming: Geological Society of America Bulletin, v. 86, no. 3, p. 319-334.

Farquhar, G. D., Ehleringer, J. R., and Hubick, K. T., 1989, Carbon Isotope Discrimination and Photosynthesis: Annual Review of Plant Physiology and Plant Molecular Biology, v. 40, no. 1, p. 503-537.

Fernández-Díaz, L., Astilleros, J. M., and Pina, C. M., 2006, The morphology of calcite crystals grown in a porous medium doped with divalent cations: Chemical Geology, v. 225, no. 3-4, p. 314-321.

Fernandez-Diaz, L., Putnis, A., Prieto, M., and Putnis, C. V., 1996, The role of magnesium in the crystallization of calcite and aragonite in a porous medium: Journal of Sedimentary Research, v. 66, no. 3, p. 482-491.

Fernández-Jalvo, Y., Denys, C., Andrews, P., Williams, T., Dauphin, Y., and Humphrey, L., 1998, Taphonomy and palaeoecology of Olduvai Bed-I (Pleistocene, Tanzania): Journal of Human Evolution, v. 34, no. 2, p. 137-172.

Flügel, E., 2010, Microfacies of Carbonate Rocks. Analysis, Interpretation and Application, Springer.

Folk, R. L. a. L., L. S., 1975, Mg/Ca Ratio and salinity: two controls over crystallisation of dolomite: AAPG Bulletin, v. 59, p. 60-68.

Ford, T. D., and Pedley, H. M., 1996, A review of tufa and travertine deposits of the world: Earth-Science Reviews, v. 41, no. 3-4, p. 117-175.

Freytet, P., and Verrecchia, E. P., 1999, Calcitic radial palisadic fabric in freshwater stromatolites: diagenetic and recrystallized feature or physicochemical sinter crust?: Sedimentary Geology, v. 126, no. 1-4, p. 97-102.

Freytet, P., and Verrecchia, E. P., 2002, Lacustrine and palustrine carbonate petrography: an overview: Journal of Paleolimnology, v. 27, no. 2, p. 221-237.

García Carmona, J., Gómez Morales, J., and Rodríguez Clemente, R., 2003, Rhombohedral-scalenohedral calcite transition produced by adjusting the solution electrical conductivity in the system $Ca(OH)_2$-CO_2-H_2O: Journal of Colloid and Interface Science, v. 261, no. 2, p. 434-440.

García Del Cura, M. A., Calvo, J. P., Ordóñez, S., Jones, B. F., and Cañaveras, J. C., 2001, Petrographic and geochemical evidence for the formation of primary, bacterially induced lacustrine dolomite: La Roda 'white earth' (Pliocene, central Spain): Sedimentology, v. 48, no. 4, p. 897-915.

Gasse, F., 2000, Hydrological changes in the African tropics since the Last Glacial Maximum: Quaternary Science Reviews, v. 19, no. 1-5, p. 189-211.

Gavish, E., and Friedman, G. M., 1973, Quantitative analysis of calcite and Mg-calcite by X-ray diffraction: effect of grinding on peak height and peak area: Sedimentology, v. 20, no. 3, p. 437-444.

Goetz, C., and Hillaire-Marcel, C., 1992, U-series disequilibria in early diagenetic minerals from Lake Magadi sediments, Kenya: Dating potential: Geochimica et Cosmochimica Acta, v. 56, no. 3, p. 1331-1341.

Goldsmith, J. R. a. G., D. L., 1958, Relation between the lattice constants and composition of the Ca-Mg carbonates: The American Mineralogist, v. 43, p. 84-101.

Gromet, L. P., Haskin, L. A., Korotev, R. L., and Dymek, R. F., 1984, The "North American shale composite": Its compilation, major and trace element characteristics: Geochimica et Cosmochimica Acta, v. 48, no. 12, p. 2469-2482.

Habermann, D., 2002, Quantitative cathodoluminescence (CL) spectroscopy of minerals: possibilities and limitations: Mineralogy and Petrology, v. 76, no. 3, p. 247-259.

Habermann, D., Neuser, R. D., and Richter, D. K., 1998, Low limit of Mn2+-activated cathodoluminescence of calcite: state of the art: Sedimentary Geology, v. 116, no. 1-2, p. 13-24.

Hardie, L. A., 1986, Perspectives. Dolomitization: A critical view of some current views: Journal of Sedimentary Petrology, v. 57, no. 1, p. 166-183.

Hay, R. L., 1973, Lithofacies and environments of Bed I, Olduvai Gorge, Tanzania: Quaternary Research, v. 3, no. 4, p. 541-560.

Hay, R. L., 1976, Geology of the Olduvai Gorge, University of California Press.

-, 1990, Olduvai Gorge; a case history in the interpretation of hominid palaeoenvironments in East Africa *in* F., L. L., ed., Establishment of a Geologic Framework for Palaeoanthropology: Boulder, Colorado, Geological Society of America Special Paper 242.

-, 1995, Magnesium-rich clays of the Meerschaum mines in the Amboseli Basin, Tanania and Kenya: Clays and Clay Minerals, v. 43, no. 4, p. 455-466.

Hay, R. L., 1996, Stratigraphy and lake-margin environments of lowermost Bed II in Olduvai Gorge.: Kaupia Darmstadter Beitrage zur Naturgeschichte., v. 6, p. 223-230.

Hay, R. L., and Kyser, T. K., 2001, Chemical sedimentology and paleoenvironmental history of Lake Olduvai, a Pliocene lake in northern Tanzania: Geological Society of America Bulletin, v. 113, no. 12, p. 1505-1521.

Hay, R. L., and Reeder, R. J., 1978, Calcretes of Olduvai Gorge and the Ndolanya Beds of northern Tanzania: Sedimentology, v. 25, no. 5, p. 649-673.

Henderson, P., Pickford, M., and Williams, C. T., 1987, A geochemical study of rocks and spring waters at Kanam and Kanjera, Kenya, and the implications concerning element mobility and uptake: Journal of African Earth Sciences, v. 6, no. 2, p. 221-227.

Hendry, J. P., and Marshall, J. D., 1991a, Disequilibrium trace element partitioning in Jurassic sparry calcite cements: implications for crystal growth mechanisms during diagenesis: Journal of the Geological Society, v. 148, no. 5, p. 835-848.

Hendry, J. P., and Marshall, J. D., 1991b, Interpretation of complex non-concentric zoning fabrics in sparry calcite cements: Middle Jurassic limestones, central England: Sedimentary Geology, v. 75, no. 1–2, p. 39-55.

Herrmann, A. D., 2010, Uranium isotopic compositions of carbonate sediments as a potential redox proxy: Geological Society of America Annual Denver Meeting (31 october - 3 November), v. Paper number 216-8.

Hillaire-Marcel, C., Carro, O., and Casanova, J., 1986, 14C and Th/U dating of Pleistocene and Holocene stromatolites from East African paleolakes: Quaternary Research, v. 25, no. 3, p. 312-329.

Hillaire-Marcel, C., and Casanova, J., 1987, Isotopic hydrology and paleohydrology of the Madagi (Kenya)-Natron (Tanzania) basin during the late quaternary: Palaeogeography, Palaeoclimatology, Palaeoecology, v. 58, no. 3-4, p. 155-181.

Holland, T. J. B., and Redfern, S. A. T., 1997, Unit cell refinement from powder diffraction data; the use of regression diagnostics: Mineral Mag, v. 61, no. 1, p. 65-77.

Hölzer, G., Fritsch, M., Deutsch, M., Härtwig, J., and Förster, E., 1997, Kα_{1,2} and Kβ_{1,3} x-ray emission lines of the 3d transition metals: Physical Review A, v. 56, no. 6, p. 4554-4568.

Horita, J., 1989, Analytical aspects of stable isotopes in brines: Chemical Geology: Isotope Geoscience section, v. 79, no. 2, p. 107-112.

Horita, J., Cole, D. R., and Wesolowski, D. J., 1993, The activity-composition relationship of oxygen and hydrogen isotopes in aqueous salt solutions: II. Vapor-liquid water equilibration of mixed salt solutions from 50 to 100°C and geochemical implications: Geochimica et Cosmochimica Acta, v. 57, no. 19, p. 4703-4711.

Horstwood, M. S. A., Parrish, R. R., Condon, D. J., and Pashley, V., 2006, Laser ablation acquisition protocols and non-matrix matched standardisation of U–Pb data: Geochimica et Cosmochimica Acta, v. 70, no. 18, Supplement, p. A264.

Hover, V. C., and Ashley, G. M., 2003, Geochemical signatures of paleodepositional and diagenetic environments: a STEM/AEM study of authigenic clay minerals from an arid rift basin, Olduvai Gorge, Tanzania: Clays and Clay Minerals, v. 51, p. 231-251.

Humphrey, J. D., 2000, New Geochemical Support for Mixing-Zone Dolomitization at Golden Grove, Barbados: Journal of Sedimentary Research, v. 70, no. 5, p. 1160-1170.

Ichikuni, M., 1973, Partition of strontium between calcite and solution: Effect of substitution by manganese: Chemical Geology, v. 11, no. 4, p. 315-319.

Issac, G. L., 1967, The stratigraph of the Peninj Group, *in* Bishop, W. W., and Clark, J. D., eds., Background to evolution in Africa, University of Chicago Press, p. 229-257.

Jackson, K. S., and Skippen, G. B., 1978, Geochemical dispersion of heavy metals via organic complexing: A laboratory study of copper, lead, zinc, and nickel behaviour at a simulated sediment-water boundary: Journal of Geochemical Exploration, v. 10, no. 2, p. 117-138.

Jaffey, A. H., Flynn, K. F., Glendenin, L. E., Bentley, W. C., and Essling, A. M., 1971, Precision Measurement of Half-Lives and Specific Activities of ^{235}U and ^{238}U: Physical Review C, v. 4, no. 5, p. 1889-1906.

Jahn, B.-m., and Cuvellier, H., 1994, Pb---Pb and U---Pb geochronology of carbonate rocks: an assessment: Chemical Geology, v. 115, no. 1-2, p. 125-151.

Jones, B., and Manning, D. A. C., 1994, Comparison of geochemical indices used for the interpretation of palaeoredox conditions in ancient mudstones: Chemical Geology, v. 111, no. 1-4, p. 111-129.

Jones, B., and Renaut, R. W., 1996, Skeletal crystals of calcite and trona from hot-spring deposits in Kenya and New Zealand: Journal of Sedimentary Research, v. 66, no. 1, p. 265-274.

-, 2008, Cyclic development of large, complex, calcite dendrite crystals in the Clinton travertine, Interior British Columbia, Canada: Sedimentary Geology, v. 203, no. 1-2, p. 17-35.

-, 2010, Chapter 4 Calcareous Spring Deposits in Continental Settings, *in* Alonso-Zarza, A. M., and Tanner, L. H., eds., Developments in Sedimentology, Volume Volume 61, Elsevier, p. 177-224.

Jones, B., Renaut, R. W., Owen, R. B., and Torfason, H., 2005, Growth patterns and implications of complex dendrites in calcite travertines from Lýsuhóll, Snæfellsnes, Iceland: Sedimentology, v. 52, no. 6, p. 1277-1301.

Jones, B. F., Eugster, H. P., and Rettig, S. L., 1977, Hydrochemistry of the Lake Magadi basin, Kenya: Geochimica et Cosmochimica Acta, v. 41, no. 1, p. 53-72.

Jones, B. F. a. B., C. J., 1978, The mineralogy and related chemistry of lake sediments, *in* Lernam, A., ed., Lakes: Chemistry, Geology, Physics: Berlin, Springer, p. 179-235.

Kelly, S. D., Rasbury, E. T., Chattopadhyay, S., Kropf, A. J., and Kemner, K. M., 2006, Evidence of a Stable Uranyl Site in Ancient Organic-Rich Calcite: Environmental Science & Technology, v. 40, no. 7, p. 2262-2268.

Kendall, A. C., 1985, Radiaxial fibrous calcite: a reappraisal: The Society of Economic Paleontologists and Mineralogists.

Kendall, A. C. a. B., P. L., 1978, Origin of fabrics in speleothems composed of columnar calcite crystals: Journal of Sedimentary Petrology, v. 48, p. 519-538.

Kigoshi, K., 1971, Alpha-Recoil Thorium-234: Dissolution into water and the Uranium-234/Uranium-238 Disequilibrium in Nature: Science, v. 173, no. 3991, p. 47-48.

Kingston, J. D., Deino, A. L., Edgar, R. K., and Hill, A., 2007, Astronomically forced climate change in the Kenyan Rift Valley 2.7-2.55 Ma: implications for the evolution of early hominin ecosystems: Journal of Human Evolution, v. 53, no. 5, p. 487-503.

Kitano, Y., and Oomori, T., 1971, The coprecipitation of uranium with calcium carbonate: Journal of Oceanography, v. 27, no. 1, p. 34-42.

Košler, J., 2007, Laser ablation ICP—MS — a new dating tool in Earth science: Proceedings of the Geologists' Association, v. 118, no. 1, p. 19-24.

Kostecka, A., 1993, Calcite from the Quaternary spring waters at Tylicz, Krynica, Polish Carpathians: Sedimentology, v. 40, no. 1, p. 27-39.

Kronfeld, J., and Vogel, J. C., 1991, Uranium isotopes in surface waters from southern Africa: Earth and Planetary Science Letters, v. 105, no. 1–3, p. 191-195.

Langmuir, D., 1978, Uranium solution-mineral equilibria at low temperatures with applications to sedimentary ore deposits: Geochimica et Cosmochimica Acta, v. 42, no. 6, Part A, p. 547-569.

Larsen, D., 2008, Revisiting silicate authigenesis in the Pliocene-Pleistocene Lake Tecopa beds, southeastern California: Depositional and hydrological controls: Geosphere, v. 4, no. 3, p. 612-639.

Last, W. M., 1990, Lacustrine dolomite--an overview of modern, Holocene, and Pleistocene occurrences: Earth-Science Reviews, v. 27, no. 3, p. 221-263.

Laveuf, C., and Cornu, S., 2009, A review on the potentiality of Rare Earth Elements to trace pedogenetic processes: Geoderma, v. 154, no. 1-2, p. 1-12.

Leakey, L. S. B., 1959, New Fossil Skull from Olduvai.: Nature, v. 184(4685), p. 491-493.

-, 1967, Olduvai Gorge, Cambridge University Press.

Leakey, M. D., 1971, Olduvai Gorge 3. Excavations in Beds I and II, Cambridge University Press.

Leeder, M. R., Mack, G. H., Brasier, A. T., Parrish, R. R., McIntosh, W. C., Andrews, J. E., and Duermeijer, C. E., 2008, Late-Pliocene timing of Corinth (Greece) rift-margin fault migration: Earth and Planetary Science Letters, v. 274, no. 1–2, p. 132-141.

Levin, N. E., Brown, F. H., Behrensmeyer, A. K., Bobe, R., and Cerling, T. E., 2011, Paleosol carbonates from the Omo Group: Isotopic records of local and regional environmental change in East Africa: Palaeogeography Palaeoclimatology Palaeoecology, v. 307, no. 1-4, p. 75-89.

Levin, N. E., Zipser, E. J., and Cerling, T. E., 2009, Isotopic composition of waters from Ethiopia and Kenya: Insights into moisture sources for eastern Africa: J. Geophys. Res., v. 114, no. D23, p. D23306.

Li, H. C., and Ku, T. L., 1997, $\delta^{13}C$-$\delta^{18}C$ covariance as a paleohydrological indicator for closed-basin lakes: Palaeogeography, Palaeoclimatology, Palaeoecology, v. 133, no. 1-2, p. 69-80.

Lindholm, R. C., 1974, Fabric and chemistry of pore filling calcite in spetarian veins: models for limestone cementation: Journal of Sedimentary Petrology, v. 44, no. 2, p. 428-440.

Linhoff, B., Bennett, P., Puntsag, T., and Gerel, O., 2011, Geochemical evolution of uraniferous soda lakes in Eastern Mongolia: Environmental Earth Sciences, v. 62, no. 1, p. 171-183.

Liutkus, C. M., 2009, Using Petrography and Geochemistry to Determine the Origin and Formation Mechanism of Calcitic Plant Molds; Rhizolith or Tufa?: Journal of Sedimentary Research, v. 79, no. 12, p. 906-917.

Liutkus, C. M., and Ashley, G. M., 2003, Facies Model of a Semiarid Freshwater Wetland, Olduvai Gorge, Tanzania: Journal of Sedimentary Research, v. 73, no. 5, p. 691-705.

Liutkus, C. M., Wright, J. D., Ashley, G. M., and Sikes, N. E., 2005, Paleoenvironmental interpretation of lake-margin deposits using δ13C and δ18O results from early Pleistocene carbonate rhizoliths, Olduvai Gorge, Tanzania: Geology, v. 33, no. 5, p. 377-380.

Lorens, R. B., 1981, Sr, Cd, Mn and Co distribution coefficients in calcite as a function of calcite precipitation rate: Geochimica et Cosmochimica Acta, v. 45, no. 4, p. 553-561.

Ludwig, K. R., 1998, On the Treatment of Concordant Uranium-Lead Ages: Geochimica et Cosmochimica Acta, v. 62, no. 4, p. 665-676.

-, 2001, Eliminating mass-fractionation effects on U-Pb isochron ages without double spiking: Geochimica et Cosmochimica Acta, v. 65, no. 18, p. 3139-3145.

Ludwig, K. R., 2003, User's manual for Isoplot 3.00: A geochronological toolkit for Microsoft Excel: Special Publication: Berkeley Geochronology Centre, Berkeley, California, v. 4.

Machel, H. G., 2000, Application of Cathodoluminescence to Carbonate Diagenesis, *in* Pagel, M., Barbin, V.,Blanc., Ohnensteller, D., ed., Cathodoluminescence in Geosciences: Berlin, Springer.

Manega, P. C., 1993, Geochronology, geochemistry and isotopic study of the Plio-Pleistocene hominid sites and the Ngorongoro Volcanic Highland in northern Tanzania [PhD: University of Colorado, 382 p.

Marshall, J. D., 1981, Zoned calcites in Jurassic ammonite chambers: trace elements, isotopes and neomorphic origin: Sedimentology, v. 28, no. 6, p. 867-887.

Marshall, J. D., 1982, Isotopic composition of displacive fibrous calcite veins: reversals in pore-water composition trends during burial diagenesis: Journal of Sedimentary Petrology, v. 52, no. 2, p. 615-630.

Matsuo, S., Friedman, I., and Smith, G. I., 1972, Studies of quaternary saline lakes--I. Hydrogen isotope fractionation in saline minerals: Geochimica et Cosmochimica Acta, v. 36, no. 4, p. 427-435.

Mattinson, J. M., 1987, U---Pb ages of zircons: A basic examination of error propagation: Chemical Geology: Isotope Geoscience section, v. 66, no. 1-2, p. 151-162.

McCarthy, T. S., McIver, J. R., and Verhagen, B. T., 1991, Groundwater evolution, chemical sedimentation and carbonate brine formation on an island in the Okavango Delta swamp, Botswana: Applied Geochemistry, v. 6, no. 6, p. 577-595.

McCarthy, T. S., and Metcalfe, J., 1990, Chemical sedimentation in the semi-arid environment of the Okavango Delta, Botswana: Chemical Geology, v. 89, no. 1-2, p. 157-178.

McCarty, D. K., Drits, V. A., and Sakharov, B., 2006, Relationship between composition and lattice parameters of some sedimentary dolomite varieties: Eur J Mineral, v. 18, no. 5, p. 611-627.

McGregor, H. V., Hellstrom, J., Fink, D., Hua, Q., and Woodroffe, C. D., 2011, Rapid U-series dating of young fossil corals by laser ablation MC-ICPMS: Quaternary Geochronology, v. 6, no. 2, p. 195-206.

McHenry, L. J., 2009, Element mobility during zeolitic and argillic alteration of volcanic ash in a closed-basin lacustrine environment: Case study Olduvai Gorge, Tanzania: Chemical Geology, v. 265, no. 3-4, p. 540-552.

McHenry, L. J., Mollel, G. F., and Swisher Iii, C. C., 2008, Compositional and textural correlations between Olduvai Gorge Bed I tephra and volcanic sources in the Ngorongoro Volcanic Highlands, Tanzania: Quaternary International, v. 178, no. 1, p. 306-319.

McKenzie, J. M., Siegel, D. I., Patterson, W. and McKenzie, D. J., 2001, A geochemical survey of spring water from the main Ethiopian rift valley, southern Ethiopia: implications for well-head protection: Hydrogeology Journal, v. 9, p. 265-272.

Mees, F., 1999, The unsuitability of calcite spherulites as indicators of subaerial exposure: Journal of Arid Environments, v. 42, no. 2, p. 149-154.

Mees, F., Reyes, E., and Keppens, E., 1998, Stable isotope chemistry of gaylussite and nahcolite from the deposits of the crater lake at Malha, northern Sudan: Chemical Geology, v. 146, no. 1–2, p. 87-98.

Mees, F., Segers, S., and Ranst, E. V., 2007, Palaeoenvironmental significance of the clay mineral composition of Olduvai basin deposits, northern Tanzania: Journal of African Earth Sciences, v. 47, no. 1, p. 39-48.

Mollel, G. F., 2007, Petrochemistry and Geochronology of Nogorongoro Volcanic Highland Complex (NVHC) and it's relationship to Laetoli and Olduvai Gorge, Tanzania [PhD: Rutgers, The State University of New Jersey, 233 p.

Mollel, G. F., Swisher III, C. C., Feigenson, M. D., and Carr, M. J., 2008, Geochemical evolution of Ngorongoro Caldera, Northern Tanzania: Implications for crust-magma interaction: Earth and Planetary Science Letters, v. 271, no. 1-4, p. 337-347.

Mollel, G. F., Swisher Iii, C. C., McHenry, L. J., Feigenson, M. D., and Carr, M. J., 2009, Petrogenesis of basalt-trachyte lavas from Olmoti Crater, Tanzania: Journal of African Earth Sciences, v. 54, no. 5, p. 127-143.

Mount, J. F., and Cohen, A. S., 1984, Petrology and geochemistry of rhizoliths from Plio-Pleistocene fluvial and marginal lacustrine deposits, east Lake Turkana, Kenya: Journal of Sedimentary Research, v. 54, no. 1, p. 263-275.

Müller, G., Irion, G., and Förstner, U., 1972, Formation and diagenesis of inorganic Ca−Mg carbonates in the lacustrine environment: Naturwissenschaften, v. 59, no. 4, p. 158-164.

Nash, D. J., and McLaren, S. J., 2003, Kalahari valley calcretes: their nature, origins, and environmental significance: Quaternary International, v. 111, no. 1, p. 3-22.

Norton-Griffiths, M., Herlocker, D., and Pennycuick, L., 1975, The patterns of rainfall in the Serengeti Ecosystem, Tanzania: African Journal of Ecology, v. 13, no. 3-4, p. 347-374.

Paquette, J., and Reeder, R. J., 1990, New type of compositional zoning in calcite: Insights into crystal-growth mechanisms: Geology, v. 18, no. 12, p. 1244-1247.

-, 1995, Relationship between surface structure, growth mechanism, and trace element incorporation in calcite: Geochimica et Cosmochimica Acta, v. 59, no. 4, p. 735-749.

Pedley, M., 2009, Tufas and travertines of the Mediterranean region: a testing ground for freshwater carbonate concepts and developments, Sedimentology Special Volume 56, Blackwell Publishing Ltd, p. 221-246.

Pedley, M., Rogerson, M., and Middleton, R., 2009, Freshwater calcite precipitates from in vitro mesocosm flume experiments: a case for biomediation of tufas, Sedimentology Special, Volume 56, Blackwell Publishing Ltd, p. 511-527.

Peters, C. R., and Blumenschine, R. J., 1995, Landscape perspectives on possible land use patterns for Early Pleistocene hominids in the Olduvai Basin, Tanzania: Journal of Human Evolution, v. 29, no. 4, p. 321-362.

PiPujol, M. D., and Buurman, P., 1997, Dynamics of iron and calcium carbonate redistribution and palaeohydrology in middle Eocene alluvial paleosols of the southeast Ebro Basin margin (Catalonia, northeast Spain): Palaeogeography, Palaeoclimatology, Palaeoecology, v. 134, no. 1–4, p. 87-107.

Potts, R., 1998, Environmental hypotheses of hominin evolution: Yearbook of Physical Anthropology, v. 41, p. 93-136.

Potts, R., Behrensmeyer, A. K., and Ditchfield, P., 1999, Paleolandscape variation and Early Pleistocene hominid activities: Members 1 and 7, Olorgesailie Formation, Kenya: Journal of Human Evolution, v. 37, no. 5, p. 747-788.

Quinn, R. L., Lepre, C. J., Wright, J. D., and Feibel, C. S., 2007, Paleogeographic variations of pedogenic carbonate [delta]13C values from Koobi Fora, Kenya: implications for floral compositions of Plio-Pleistocene hominin environments: Journal of Human Evolution, v. 53, no. 5, p. 560-573.

Rasbury, E. T., and Cole, J. M., 2009, Directly dating geologic events: U-Pb dating of carbonates: Rev. Geophys., v. 47, no. 3, p. RG3001.

Rasbury, E. T., Meyers, W. J., Hanson, G. N., Goldstein, R. H., and Saller, A. H., 2000, Relationship of Uranium to Petrography of Caliche Paleosols with Application to Precisely Dating the Time of Sedimentation: Journal of Sedimentary Research, v. 70, no. 3, p. 604-618.

Reddy, M., and Hoch, A., 2012, Calcium Carbonate Nucleation in an Alkaline Lake Surface Water, Pyramid Lake, Nevada, USA: Aquatic Geochemistry, v. 18, no. 2, p. 95-113.

Reeder, R. J., Nugent, M., Tait, C. D., Morris, D. E., Heald, S. M., Beck, K. M., Hess, W. P., and Lanzirotti, A., 2001, Coprecipitation of Uranium(VI) with Calcite: XAFS, micro-XAS, and luminescence characterization: Geochimica et Cosmochimica Acta, v. 65, no. 20, p. 3491-3503.

Retallack, G. J., 2001, Soils of the past: an introduction to palaeopedology, Blackwell Publications.

Retallack, G. J., Wynn, J. G., Benefit, B. R., and McCrossin, M. L., 2002, Paleosols and paleoenvironments of the middle Miocene, Maboko Formation, Kenya: Journal of Human Evolution, v. 42, no. 6, p. 659-703.

Reynolds, B. C., Wasserburg, G. J., and Baskaran, M., 2003, The transport of U- and Th-series nuclides in sandy confined aquifers: Geochimica et Cosmochimica Acta, v. 67, no. 11, p. 1955-1972.

Richards, D. A., Bottrell, S. H., Cliff, R. A., Ströhle, K., and Rowe, P. J., 1998, U-Pb dating of a speleothem of Quaternary age: Geochimica et Cosmochimica Acta, v. 62, no. 23-24, p. 3683-3688.

Richter, D. K., Götte, T., Götze, J., and Neuser, R. D., 2003, Progress in application of cathodoluminescence (CL) in sedimentary petrology: Mineralogy and Petrology, v. 79, no. 3, p. 127-166.

Rollinson, H. R., 1993, Using geochemical data: Evaluation, Presentation, Interpretation, Longman, UK, 352 p.:

Rosen, M. R., and Coshell, L. E. E., 1992, A new location of Holocene dolomite formation, Lake Hayward, Western Australia: Sedimentology, v. 39, no. 1, p. 161-166.

Rosen, M. R., Miser, D. E., Starcher, M. A., and Warren, J. K., 1989, Formation of dolomite in the Coorong region, South Australia: Geochimica et Cosmochimica Acta, v. 53, no. 3, p. 661-669.

Rossi, C., and Canaveras, J. C., 1999, Pseudospherulitic fibrous calcite in paleo-groundwater, unconformity-related diagenetic carbonates (Paleocene of the Ager Basin and Miocene of the Madrid Basin, Spain): Journal of Sedimentary Research, v. 69, no. 1, p. 224-238.

Sanz-Rubio, E., Sánchez-Moral, S., Cañaveras, J. C., Calvo, J. P., and Rouchy, J. M., 2001, Calcitization of Mg-Ca carbonate and Ca sulphate deposits in a continental Tertiary basin (Calatayud Basin, NE Spain): Sedimentary Geology, v. 140, no. 1-2, p. 123-142.

Schmidt, M., Xeflide, S., Botz, R., and Mann, S., 2005, Oxygen isotope fractionation during synthesis of CaMg-carbonate and implications for sedimentary dolomite formation: Geochimica et Cosmochimica Acta, v. 69, no. 19, p. 4665-4674.

Schmitz, M. D. a. S., B., 2007, Derivation of isotope ratios, errors, and correlations for U-Pb geochronology using ^{205}Pb-^{235}U-(^{233}U)-spiked isotope dilution thermal ionisation mass spectrometric data: Geochemistry, Geophysics, Geosystems, v. 8, p. 1-20.

Searl, A., 1989, Podogenic columnar calcite from the Oolite Group (Lower Carboniferous), South Wales: Sedimentary Geology, v. 62, no. 1, p. 47-58.

Sheldon, N. D., and Tabor, N. J., Quantitative Paleoenvironmental and Paleoclimatic Reconstruction Using Paleosols: Earth-Science Reviews, v. In Press, Accepted Manuscript.

Sikes, N. E., 1994, Early hominid habitat preferences in East Africa: Paleosol carbon isotopic evidence: Journal of Human Evolution, v. 27, no. 1-3, p. 25-45.

-, 2000, Using plaeosol stable isotopes to reconstruct Olduvai basin landscapes.: Journal of Human Evolution, v. 38(3), p. A28-A28.

Sikes, N. E., and Ashley, G. M., 2007, Stable isotopes of pedogenic carbonates as indicators of paleoecology in the Plio-Pleistocene (upper Bed I), western margin of the Olduvai Basin, Tanzania: Journal of Human Evolution, v. 53, no. 5, p. 574-594.

Southgate, P. N., Lambert, I. B., Donnelly, T. H., Henry, R., Etminan, H., and Weste, G., 1989, Depositional environments and diagenesis in Lake Parakeelya: a Cambrian alkaline playa from the Officer Basin, South Australia: Sedimentology, v. 36, no. 6, p. 1091-1112.

Stanistreet, I. G., 2011, Fine resolution of early hominin time, Beds I & II, Olduvai Gorge, Tanzania: Journal of Human Evolution., v. In Press, Corrected proof.

Steefel, C. I., 2008, Geochemical kinetics and transport, *in* Brantley, S. L., Kubicki, J. D., and White, A.F., ed., Kinetics of water-rock interactions, Springer.

Stirling, C. H., Andersen, M. B., Potter, E.-K., and Halliday, A. N., 2007, Low-temperature isotopic fractionation of uranium: Earth and Planetary Science Letters, v. 264, no. 1-2, p. 208-225.

Stollhofen, H., and Stanistreet, I. G., 2011, Plio-Pleistocene synsedimentary fault compartments, foundation for the eastern Olduvai Basin paleoenvironmental mosaic, Tanzania: Journal of Human Evolution, v. In press, p. 1-19.

Stollhofen, H., Stanistreet, I. G., McHenry, L. J., Mollel, G. F., Blumenschine, R. J., and Masao, F. T., 2008, Fingerprinting facies of the Tuff IF marker, with implications for early hominin palaeoecology, Olduvai Gorge, Tanzania:

Palaeogeography, Palaeoclimatology, Palaeoecology, v. 259, no. 4, p. 382-409.

Sturchio, N. C., Antonio, M. R., Soderholm, L., Sutton, S. R., and Brannon, J. C., 1998, Tetravalent Uranium in Calcite: Science, v. 281, no. 5379, p. 971-973.

Surdam, R. C., and Eugster, H. P., 1976, Mineral reactions in the sedimentary deposits of the Lake Magadi region, Kenya: Geological Society of America Bulletin, v. 87, no. 12, p. 1739-1752.

Talbot, M. R., 1990, A review of the palaeohydrological interpretation of carbon and oxygen isotopic ratios in primary lacustrine carbonates: Chemical Geology: Isotope Geoscience section, v. 80, no. 4, p. 261-279.

Talbot, M. R. a. K., K., 1991, Paleolimnological signatures from carbon and oxygen isotopoc ratios in carbonates from organic carbon-rich lacustrine sediments, *in* Katz, B. J., ed., Lacustrine Basin Exploration, Volume 50, Menoirs of the American Assoociation of Petroleum Geology, p. 99-112.

Tang, J., Köhler, S. J., and Dietzel, M., 2008, Sr^{2+}/Ca^{2+} and $^{44}Ca/^{40}Ca$ fractionation during inorganic calcite formation: I. Sr incorporation: Geochimica et Cosmochimica Acta, v. 72, no. 15, p. 3718-3732.

Tanner, L. H., 2010, Chapter 4 Continental Carbonates as Indicators of Paleoclimate, *in* Alonso-Zarza, A. M., and Tanner, L. H., eds., Developments in Sedimentology, Volume Volume 62, Elsevier, p. 179-214.

Tooth, S., and McCarthy, T. S., 2007, Wetlands in drylands: geomorphological and sedimentological characteristics, with emphasis on examples from southern Africa: Progress in Physical Geography, v. 31, no. 1, p. 3-41.

Trauth, M. H., Maslin, M. A., Deino, A., and Strecker, M. R., 2005, Late Cenozoic Moisture History of East Africa: Science, v. 309, no. 5743, p. 2051-2053.

van Calsteren, P., and Thomas, L., 2006, Uranium-series dating applications in natural environmental science: Earth-Science Reviews, v. 75, no. 1-4, p. 155-175.

van der Merwe, N. J., Masao, Fidelis T. and Bamford, Marion K., 2008, Isotopic Evidence for Contrasting Diets of Early Hominins *Homo habilis* and *Australopithecus boisei* of Tanzania: South African Journal of Science, v. 104, p. 153-155.

Vaniman, D. T., and Chipera, S. J., 1996, Paleotransport of lanthanides and strontium recorded in calcite compositions from tuffs at Yucca Mountain, Nevada, USA: Geochimica et Cosmochimica Acta, v. 60, no. 22, p. 4417-4433.

Verrecchia, E. P., 2007, Lacustrine and palustrine geochemical sediments, *in* Nash, D. J. a. M., S. J., ed., Geochemical sediments and landscapes: Malden, USA, Blackwell Publishing, p. 298-329.

Wacey, D., Wright, D. T., and Boyce, A. J., 2007, A stable isotope study of microbial dolomite formation in the Coorong Region, South Australia: Chemical Geology, v. 244, no. 1-2, p. 155-174.

Walker, J., Cliff, R. A., and Latham, A. G., 2006, U-Pb Isotopic Age of the StW 573 Hominid from Sterkfontein, South Africa: Science, v. 314, no. 5805, p. 1592-1594.

Walter, R. C., Manega, P. C., and Hay, R. L., 1992, Tephrochronology of Bed I, Olduvai Gorge: An application of laser-fusion dating to calibrating biological and climatic change: Quaternary International, v. 13-14, p. 37-46.

Wanas, H. A., 2002, Petrography, geochemistry and primary origin of spheroidal dolomte from the Upper Cretaceous/Lower tertiary Maghra El-Bahari Formation at Gabal Ataqa. Northwest Gulf of Suez, Egypt: Sedimentary Geology, v. 151, p. 211-224.

Warren, J. K., 1988, Sedimentology of Coorong dolomite in the Salt Creek region, South Australia: Carbonates and Evaporites, v. 3, no. 2, p. 175-199.

-, 1990, Sedimentology and mineralogy of dolomitic Coorong lakes, South Australia: Journal of Sedimentary Research, v. 60, no. 6, p. 843-858.

-, 2000, Dolomite: occurrence, evolution and economically important associations: Earth-Science Reviews, v. 52, no. 1–3, p. 1-81.

-, 2006, Evaporites: Sediments, Resources and Hydrocarbons, Springer.

Watson, A., 1985, Structure, chemistry and origins of gypsum crusts in southern Tunisia and the central Namib Desert: Sedimentology, v. 32, no. 6, p. 855-875.

Wheeler, C. W., Aharon, P., and Ferrell, R. E., 1999, Successions of late Cenozoic platform dolomites distinguished by texture, geochemistry, and crystal chemistry; Niue, South Pacific: Journal of Sedimentary Research, v. 69, no. 1, p. 239-255.

Witherow, R. A., 2009, Minor Alkaline Earth Element and Alkali Metal Behaviour in Closed Basin Lakes [PhD: The Ohio State University.

Woodhead, J., Hellstrom, J., Maas, R., Drysdale, R., Zanchetta, G., Devine, P., and Taylor, E., 2006, U-Pb geochronology of speleothems by MC-ICPMS: Quaternary Geochronology, v. 1, no. 3, p. 208-221.

Wright, V. P., 2008, Calcrete, *in* Nash, D. J., and McLaren, S. J., eds., Geochemical Sediments and Landscapes, Blackwell Publishing, p. 10-45.

Wright, V. P., and Tucker, M. E., 1991, Calcretes, Blackwells Science Publications, Reprint series Volume 2 of the International Association of Sedimentologists.

Yoshida, Y., Yoshikawa, H., and Nakanishi, T., 2008, Partition coefficients of Ra and Ba in calcite: Geochemical Journal, v. 42, p. 295-304.

Appendices

Appendix 1: Master sample list for non-lacustrine carbonate specimens

Sample identification	OLAPP Trench	Hay Loc	Archaeological Complex	Sample Type	Depositional setting	Bed
2001 TR47 FLKN 10	47	45A	FLKN	Micritic nodule type 2	ELM	II
2001 TR47 FLKN 11	47	45A	FLKN	Micritic nodule type 2	ELM	II
2001 TR47 FLKN 17	47	45A	FLKN	Micritic nodule type 2	ELM	II
2001 TR47 FLKN 1B	47	45A	FLKN	Rhizocretion	ELM	II
2001 TR47 FLKN 20B	47	45A	FLKN	Micritic nodule type 2	ELM	II
2001 TR47 FLKN 22B	47	45A	FLKN	Micritic nodule type 2	ELM	II
2001 TR47 FLKN 25B	47	45A	FLKN	Micritic nodule type 2	ELM	II
2001 TR47 FLKN 27	47	45A	FLKN	Micritic nodule type 2	ELM	II
2001 TR47 FLKN 28	47	45A	FLKN	Micritic nodule type 2	ELM	II
2001 TR47 FLKN 29	47	45A	FLKN	Micritic nodule type 2	ELM	II
2001 TR47 FLKN 2B	47	45A	FLKN	Rhizocretion	ELM	II
2001 TR47 FLKN 35	47	45A	FLKN	Micritic nodule type 2	ELM	II
2001 TR47 FLKN 36	47	45A	FLKN	Micritic nodule type 2	ELM	II
2001 TR47 FLKN 37	47	45A	FLKN	Micritic nodule type 2	ELM	II
2001 TR47 FLKN 3B	47	45A	FLKN	Rhizocretion	ELM	II
2001 TR47 FLKN 44	47	45A	FLKN	Micritic nodule type 2	ELM	II
2001 TR47 FLKN 45	47	45A	FLKN	Micritic nodule type 2	ELM	II
2001 TR47 FLKN 46	47	45A	FLKN	Micritic nodule type 2	ELM	II
2001 TR47 FLKN 47	47	45A	FLKN	Micritic nodule type 2	ELM	II
2001 TR47 FLKN 49	47	45A	FLKN	Fossilised rootmat	ELM	II
2001 TR47 FLKN 4B	47	45A	FLKN	Spherulite with rhizocretion	ELM	II
2001 TR47 FLKN 5	47	45A	FLKN	Spherulite with rhizocretion	ELM	II
2001 TR47 FLKN 6	47	45A	FLKN	Spherulite with rhizocretion	ELM	II
2001 TR47 FLKN 7	47	45A	FLKN	Spherulite with rhizocretion	ELM	II
2001 TR47 FLKN 9	47	45A	FLKN	Micritic nodule type 2	ELM	II
2002 TR111 VEK 3	111		VEK	Sparry nodule	ELM	II
2002 TR111 VEK 5	111		VEK	Sparry nodule	ELM	II
2002 TR111 VEK 7	111		VEK	Sparry nodule	ELM	II
2002 TR111 VEK 9	111		VEK	Sparry nodule	ELM	II
2003 TR113 HWKE 6	113		HWKE	Fossilised rootmat	ELM	I
2003 TR113 HWKE 7	113		HWKE	Evaporite pseudomorph	ELM	I
2003 TR116 FLKN 10	116		FLKN	Fossilised rootmat	ELM	II
2003 TR119 KK 3	119		KK	Fossilised rootmat	ELM	I
2003 TR119 KK 303	119		KK	Fossilised rootmat	ELM	II
2003 TR119 KK 7	119		KK	Fossilised rootmat	ELM	II
2003 TR120 KK 19	120		KK	Small Spherulite with veins	ELM	II
2003 TR120 KK 20	120		KK	Small Spherulite with veins	ELM	II
2003 TR120 KK 25	120		KK	Small Spherulite with veins	ELM	II
2003 TR120 KK 7	120		KK	Spherulite with veins	ELM	II
2003 TR121 FLKN 12	121		FLKN	Spherulite with veins	ELM	I
2003 TR122 TK 12	122		TK	Micritic nodule type 1	ELM	II
2003 TR122 TK 16	122		TK	Micritic nodule type 1	ELM	II
2003 TR122 TK 4	122		TK	Micritic nodule type 1	ELM	II
2003 TR124A TK 5	124A		TK	Fossilised rootmat?	ELM	II
2003 TR124A TK 8	124A		TK	Small spherulite	ELM	II
2003 TR124B TK 14	124B		TK	Small spherulite	ELM	II
2003 TR124B TK 18	124B		TK	Small spherulite	ELM	II
2003 TR124B TK 19	124B		TK	Small spherulite	ELM	II

Sample identification	OLAPP Trench	Hay Loc	Archaeological Complex	Sample Type	Depositional setting	Bed
2003 TR124B TK 21	124B		TK	Small spherulite	ELM	II
2003 TR124C TK G	124C		TK	Small spherulite	ELM	II
2003 TR124C TK I	124C		TK	Small spherulite	ELM	II
2003 TR124C TK K	124C		TK	Small spherulite	ELM	II
2003 TR124C TK O	124C		TK	Small spherulite	ELM	II
2003 TR124C TK P	124C		TK	Small spherulite	ELM	II
2003 TR124C TK R	124C		TK	Small spherulite	ELM	II
2003 TR124D TK 4	124D		TK	Spherulite	ELM	II
2003 TR47 FLKN 12	47		FLKN	Spherulite with Rhizocretion	ELM	II
2003 TR47 FLKN 13	47		FLKN	Micritic nodule Type 2	ELM	II
2005 TR129 Long KE 4	129		Long K E	Spherulite	ELM	II
2006 TR130 KK NL3	130		KK	Spherulite	ELM	II
2006 TR130 KK NL4	130		KK	Spherulites with rhizocretions	ELM	II
2006 TR131 20 NL1	131		20	Micritic nodule type 1	ELM	II
2006 TR131 20 NL2	131		20	Micritic nodule type 1	ELM	II
2006 TR131 20 NL3A	131		20	Micritic nodule type 1	ELM	II
2006 TR131 20 NL3B	131		20	Micritic nodule type 1	ELM	II
2006 TR132 NL1	132		FLK	Micritic nodule type 2	ELM	II
2006 TR132 NL2	132		FLK	Micritic nodule type 2	ELM	II
2006 TR132 NL3	132		FLK	Rhizocretion	ELM	II
2006 TR132 NL4	132		FLK	Sparry nodule	ELM	II
2006 TR132 NL5	132		FLK	Micritic nodule type 2	ELM	II
2006 TR132 NL6	132		FLK	Micritic nodule type 2	ELM	II
2007 FLK cannon ball nodule			FLK	Sparry nodule	ELM	I
2007 FLK musket ball nodules			FLK	Sparry nodule	ELM	I
2007 FLK sulphate rosettes			FLK	Sparry nodule	ELM	I
2007 TR134 FLK NL0	134		FLK	Micritic nodule type 1	ELM	I
2007 TR135 FLKNN NL1	135		FLKNN	Micritic nodule type 1	ELM	I
2007 TR135 FLKNN NL2	135		FLKNN	Micritic nodule type 1	ELM	I
2007 TR135 FLKNN NL3	135		FLKNN	Micritic nodule type 1	ELM	I
2007 TR135 FLKNN NL4	135		FLKNN	Micritic nodule type 1	ELM	I
2007 TR137 Croc trench NL1	137		FLKN	Micritic nodule type 1	ELM	I
2007 TR137 Croc trench NL2	137		FLKN	Micritic nodule type 1	ELM	I
2007 TR138 FLK	138		FLK	Small Spherulite	ELM	I
2007 TR138 FLK LMST	138		FLK	Micritic nodule type 1 with sparry band	ELM	I
2007 TR140 FLK NL1	140		FLK	Spherulite with Sparry bands	ELM	I
2008 TR111 VEK CA0	111		VEK	Sparry nodule	ELM	II
2008 TR111 VEK CA1	111		VEK	Sparry nodule	ELM	II
2008 TR111 VEK CA10	111		VEK	Micritic nodule type 1	ELM	II
2008 TR111 VEK CA11	111		VEK	Micritic nodule type 1	ELM	II
2008 TR111 VEK CA2	111		VEK	Sparry nodule	ELM	II
2008 TR111 VEK CA3	111		VEK	Sparry nodule	ELM	II

Sample identification	OLAPP Trench	Hay Loc	Archaeological Complex	Sample Type	Depositional setting	Bed
2008 TR111 VEK CA4	111		VEK	Sparry nodule	ELM	II
2008 TR111 VEK CA5	111		VEK	Sparry nodule	ELM	II
2008 TR111 VEK CA6	111		VEK	Sparry nodule	ELM	II
2008 TR111 VEK CA7	111		VEK	Sparry nodule	ELM	II
2008 TR111 VEK CA8	111		VEK	Sparry nodule	ELM	II
2008 TR111 VEK CA9	111		VEK	Sparry nodule	ELM	II
2008 TR138 FLK CA1	138		FLK	Spherulite with Sparry bands	ELM	I
2008 TR143 MG NL1	143		FLK	Micritic nodule type 1 with sparry band	ELM	I
2008 TR143 MG NL2	143		FLK	Micritic nodule type 1 with sparry band	ELM	I
2008 TR143 MG NL3	143		FLK	Micritic nodule type 1 with sparry band	ELM	I
2008 TR143 MG NL4	143		FLK	Micritic nodule type 1 with sparry band	ELM	I
2008 TR143 MG NL5	143		FLK	Spherulite	ELM	I
2008 TR143 MG NL6	143		FLK	Sparry nodule	ELM	I
2008 TR143 MG NL7	143		FLK	Sparry nodule	ELM	I
2008 TR143 MG NL8	143		FLK	Sparry nodule	ELM	I
2008 TR144 FLKN CROC CA2	144		FLKN	Micritic nodule type 1	ELM	I
2008 TR144 FLKN CROC CA5	144		FLKN	Micritic nodule type 1	ELM	I
2008 TR144 FLKN NL1	144		FLKN	Micritic nodule type 1	ELM	I
2008 TR144 FLKN NL2	144		FLKN	Spherulite with Sparry bands	ELM	I
2008 TR144 FLKN NL3	144		FLKN	Sparry nodule with spherulites	ELM	I
2008 TR144 FLKN NL4	144		FLKN	Spherulite with Sparry bands	ELM	I
2008 TR146 MGS CA1	146		FLK	Micritic nodule type 1	ELM	I
2008 TR146 MGS CA2	146		FLK	Spherulite with Sparry bands	ELM	I
2008 TR147 FLK CA1	147		FLK	Spherulite with Sparry bands	ELM	I
2008 TR147 FLK CA2	147		FLK	Spherulite with Sparry bands	ELM	I
2008 TR147 FLK CA3	147		FLK	Spherulite with Sparry bands	ELM	I
2008 TR147 FLK CA4	147		FLK	Spherulite with Sparry bands	ELM	I
2008 TR147 FLK CA5	147		FLK	Spherulite with Sparry bands	ELM	I
2008 TR147 FLK CA6	147		FLK	Spherulite with Sparry bands	ELM	I
2008 TR148 FLK CA1	148		FLK	Spherulite with Sparry bands	ELM	I
2008 TR148 FLK CA2	148		FLK	Spherulite with Sparry bands	ELM	I
2008 TR148 FLK CA3	148		FLK	Spherulite with Sparry bands	ELM	I
2008 TR148 FLK CA4	148		FLK	Spherulite with Sparry bands	ELM	I
2008 TR148 FLK NL1	148		FLK	Spherulite with Sparry bands	ELM	I
2008 TR148 FLK NL2	148		FLK	Spherulite with Sparry bands	ELM	I
2008 TR148 FLK NL3A	148		FLK	Spherulite with Sparry bands	ELM	I
2008 TR148 FLK NL3B	148		FLK	Spherulite with Sparry bands	ELM	I
2009 DK CA1			DK	Sparry nodule with insect burrows	AF	II
2009 DK CA10			DK	Micritic nodule type 1	AF	II
2009 DK CA11			DK	Micritic nodule type 1	AF	II
2009 DK CA12			DK	Micritic nodule type 1	AF	II
2009 DK CA13			DK	Micritic nodule type 1	AF	II

Sample identification	OLAPP Trench	Hay Loc	Archaeological Complex	Sample Type	Depositional setting	Bed
2009 DK CA14			DK	Micritic nodule type 1	AF	II
2009 DK CA15			DK	Micritic nodule type 1	AF	II
2009 DK CA16			DK	Micritic nodule type 1	AF	II
2009 DK CA17			DK	Micritic nodule type 2	AF	II
2009 DK CA18			DK	Micritic nodule type 2	AF	II
2009 DK CA2			DK	Sparry nodule with insect burrows	AF	II
2009 DK CA3			DK	Sparry nodule with insect burrows	AF	II
2009 DK CA4			DK	Sparry nodule with insect burrows	AF	II
2009 DK CA5			DK	Sparry nodule with insect burrows	AF	II
2009 DK CA6			DK	Micritic nodule type 1	AF	II
2009 DK CA7			DK	Micritic nodule type 1	AF	II
2009 DK CA8a			DK	Micritic nodule type 1	AF	II
2009 DK CA8b			DK	Micritic nodule type 1	AF	II
2009 DK CA9a			DK	Micritic nodule type 1	AF	II
2009 DK CA9b			DK	Micritic nodule type 1	AF	II
2009 HWKE CA1			HWKE	Spherulites with sparry bands	ELM	I
2009 HWKE CA10			HWKE	Micritic nodule type 1	ELM	II
2009 HWKE CA11			HWKE	Micritic nodule type 1	ELM	II
2009 HWKE CA12			HWKE	Large Spherulite	ELM	I
2009 HWKE CA13			HWKE	Large Spherulite	ELM	I
2009 HWKE CA2			HWKE	Evaporite pseudomorph	ELM	I
2009 HWKE CA3			HWKE	Spherulites with veins	ELM	I
2009 HWKE CA4			HWKE	Micritic nodule type 1 with spherulites	ELM	I
2009 HWKE CA5			HWKE	Sparry nodule with spherulites	ELM	I
2009 HWKE CA6			HWKE	Micritic nodule type 1	ELM	II
2009 HWKE CA8			HWKE	Spherulites with veins	ELM	II
2009 HWKE CA9			HWKE	Spherulites	ELM	II
2009 HWKE GR1			HWKE	Fossilised rootmat	ELM	I
2009 HWKEE GS1			HWKEE	Fossilised rootmat	ELM	I
2009 HWKEE GS2			HWKEE	Fossilised rootmat	ELM	I
2009 Loc 5 CA1		5		Micritic nodule type 1	AF	I
2009 LOC 60 CA1		60	Naisiusiu	Micritic nodule type 1	WLM	I
2009 LOC 60 CA10		60	Naisiusiu	Micritic nodule type 1	WLM	I
2009 LOC 60 CA11		60	Naisiusiu	Micritic nodule type 1	WLM	I
2009 LOC 60 CA12		60	Naisiusiu	Spherulite	WLM	I
2009 LOC 60 CA2		60	Naisiusiu	Spherulite	WLM	I
2009 LOC 60 CA3		60	Naisiusiu	Spherulite with sparry bands	WLM	I
2009 LOC 60 CA4		60	Naisiusiu	Micritic nodule type 1	WLM	I
2009 LOC 60 CA5		60	Naisiusiu	Micritic nodule type 1	WLM	I
2009 LOC 60 CA6		60	Naisiusiu	Micritic nodule type 1	WLM	I
2009 LOC 60 CA7		60	Naisiusiu	Micritic nodule type 1	WLM	I
2009 LOC 60 CA8		60	Naisiusiu	Micritic nodule type 1	WLM	I
2009 LOC 60 CA9		60	Naisiusiu	Micritic nodule type 1	WLM	I
2009 LOC 60 CH1		60	Naisiusiu	Micritic nodule type 1	WLM	I
2009 Loc 65 1		65	Naisiusiu	Micritic nodule type 1	WLM	I
2009 Loc 65 2		65	Naisiusiu	Micritic nodule type 1	WLM	I
2009 Loc 65 3		65	Naisiusiu	Micritic nodule type 1	WLM	I

Sample identification	OLAPP Trench	Hay Loc	Archaeological Complex	Sample Type	Depositional setting	Bed
2009 MK west CA1			MK west	Micritic nodule type 1	AF	II
2009 MNK CA1			MNK	Micritic nodule type 1	ELM	II
2009 MNK CA2			MNK	Micritic nodule type 1	ELM	II
2009 MNK CA3			MNK	Micritic nodule type 1	ELM	II
2009 MNK CA4			MNK	Micritic nodule type 1	ELM	II
2009 MNK CA5			MNK	Micritic nodule type 1	ELM	II
2009 MNK CA6			MNK	Micritic nodule type 1	ELM	II
2009 MNK CA7			MNK	Micritic nodule type 1	ELM	II
2009 MNK CA9			MNK	Micritic nodule type 1	ELM	II
2009 SHK CA1			SHK	Micritic nodule type 1	ELM	II
2009 SHK CA2			SHK	Micritic nodule type 1	ELM	II
2009 SHK CA3			SHK	Micritic nodule type 1	ELM	II
2009 SHK CA4			SHK	Micritic nodule type 1	ELM	II
2009 SSE TR149 CA1	SSE TR149		FLKNN	Micritic nodule type 1 with sparry band and spherulites	ELM	I
2009 SSE TR149 CA2	SSE TR149		FLKNN	Micritic nodule type 1 with sparry band and spherulites	ELM	I
2009 TR134 E CA1	TR134East ext		FLKNN	Micritic nodule type 1	ELM	I
2009 TR135 CA1	135		FLKNN	Micritic nodule type 2	ELM	I
2009 TR135 CA2	135		FLKNN	Micritic nodule type 2	ELM	I
2009 TR135 CA3	135		FLKNN	Micritic nodule type 2	ELM	I
2009 TR135 CA4	135		FLKNN	Micritic nodule type 2	ELM	I
2009 TR135 CA5	135		FLKNN	Micritic nodule type 2	ELM	I
2009 TR135 CA6	135		FLKNN	Micritic nodule type 2	ELM	I
2009 TR135 CA7	135		FLKNN	Micritic nodule type 2	ELM	I
2009 TR135 CA8	135		FLKNN	Dolomite	ELM	I
2009 TR149 CA1	149		FLKS	Micritic nodule type 1	ELM	I
2009 TR149 CA1a	149		FLKNN	Micritic nodule type 1	ELM	I
2009 TR149 CA1b	149		FLKNN	Micritic nodule type 1	ELM	I
2009 TR149 CA1c	149		FLKNN	Micritic nodule type 1	ELM	I
2009 TR149 CA2	149		FLKS	Micritic nodule type 1	ELM	I
2009 TR149 CA3	149		FLKS	Micritic nodule type 1	ELM	I
2009 TR149 CA4	149		FLKS	Micritic nodule type 1	ELM	I
2009 TR149 CA5	149		FLKS	Micritic nodule type 1	ELM	I
2009 TR149 CA6	149		FLKS	Micritic nodule type 1	ELM	I
2009 TR149 CA7	149		FLKS	Micritic nodule type 1	ELM	I
2009 TR150 CA1	150		VEK	Sparry nodule	ELM	I
2009 TR150 CA2	150		VEK	Sparry nodule	ELM	I
2009 TR150 CA3	150		VEK	Sparry nodule	ELM	I
2009 TR150 CA4	150		VEK	Sparry nodule	ELM	I
2009 TR150 CA5	150		VEK	Sparry nodule	ELM	I
2009 TR47 101	47		FLKN	Micritic nodule type 1	ELM	II
2009 TR47 102	47		FLKN	Rhizocretion	ELM	II
2009 TR47 103	47		FLKN	Rhizocretion	ELM	II
2009 TR47 104	47		FLKN	Rhizocretion	ELM	II
2009 TR47 105	47		FLKN	Spherulite with rhizocretion	ELM	II
2009 TR47 106	47		FLKN	Spherulite with rhizocretion	ELM	II
2009 TR47 107	47		FLKN	Spherulite with rhizocretion	ELM	II
2009 TR47 108	47		FLKN	Micritic nodule type 2	ELM	II
2009 TR47 109	47		FLKN	Micritic nodule type 2	ELM	II
2009 TR47 110	47		FLKN	Micritic nodule type 2	ELM	II

Sample identification	OLAPP Trench	Hay Loc	Archaeological Complex	Sample Type	Depositional setting	Bed
2009 TR47 111	47		FLKN	Micritic nodule type 2	ELM	II
2009 TR47 112	47		FLKN	Micritic nodule type 2	ELM	II
2009 TR47 113	47		FLKN	Micritic nodule type 2	ELM	II
2009 TR47 114	47		FLKN	Micritic nodule type 2	ELM	II
2009 TR47 116	47		FLKN	Fossilised rootmat	ELM	II
2009 TR47 120	47		FLKN	Micritic nodule type 2	ELM	II
2009 TR47 121	47		FLKN	Micritic nodule type 2	ELM	II
2009 TR47 122	47		FLKN	Micritic nodule type 2	ELM	II
2009 TR47 123	47		FLKN	Micritic nodule type 2	ELM	II
2009 TR47 124	47		FLKN	Micritic nodule type 2	ELM	II
2009 TR47 125	47		FLKN	Micritic nodule type 2	ELM	II
2009 TR47 126	47		FLKN	Micritic nodule type 2	ELM	II
2009 TR47 127	47		FLKN	Micritic nodule type 2	ELM	II
2009 VEK 150-152 CA1	150-152		VEK 150-152	Sparry nodule	ELM	I
2009 VEK 150-152 CA2	150-152		VEK 150-152	Sparry nodule	ELM	I
2009 VEK 150-152 CA3	150-152		VEK 150-152	Sparry nodule	ELM	I
2009 VEK 150-152 CA4	150-152		VEK 150-153	Sparry nodule	ELM	I
2009 VEK 150-152 CA5	150-152		VEK 150-152	Sparry nodule	ELM	I
2009 WTR148 CA1	West of Tr 148		FLK	Spherulite with Sparry bands	ELM	I
2009 WTR148 CA2a	West of Tr 148		FLK	Spherulite with Sparry bands	ELM	I
2009 WTR148 CA2b	West of Tr 148		FLK	Spherulite with Sparry bands	ELM	I
2009 ZINJ GR2		45	FLK	Fossilised rootmat	ELM	I
2009 ZINJ CA1		45	FLK	Sparry nodule	ELM	I
2009 ZINJ carbonate GA		45	FLK	Sparry nodule	ELM	I
2009 Zinj E 1	Zinj East	45	FLK	Fossilised rootmat	ELM	I
2010 DK1 CA1			DK	Spherulite	AF	I
2010 DK1 CA2			DK	Spherulite	AF	I
2010 DK2 CA1			DK	Micritic nodule type 1	AF	I
2010 DK2 CA2			DK	Micritic nodule type 1	AF	I
2010 DK2 CA3			DK	Micritic nodule type 1 with sparry bands	AF	I
2010 DK2 CA4			DK	Spherulite with veins	AF	I
2010 DK2 CA5			DK	Spherulite	AF	I
2010 DK2 CA6			DK	Small Spherulite with veins	AF	I
2010 DK3 CA1			DK	Spherulite with Sparry nodules	AF	I
2010 HWHW SW CA10			HWKW	Small Spherulite with veins	ELM	II
2010 HWHW SW CA11			HWKW	Small Spherulite with veins	ELM	II
2010 HWHW SW CA12			HWKW	Small Spherulite with Sparry band	ELM	II
2010 HWHW SW CA13			HWKW	Small Spherulite with Sparry band	ELM	II
2010 HWHW SW CA2			HWKW	Evaporite pseudomorph	ELM	I
2010 HWHW SW CA3			HWKW	Small Spherulite with Sparry band	ELM	I
2010 HWHW SW CA4			HWKW	Small Spherulite with veins	ELM	I

Sample identification	OLAPP Trench	Hay Loc	Archaeological Complex	Sample Type	Depositional setting	Bed
2010 HWHW SW CA5			HWKW	Small Spherulite with Sparry band	ELM	I
2010 HWHW SW CA6			HWKW	Small Spherulite with veins	ELM	II
2010 HWHW SW CA7			HWKW	Small Spherulite with Sparry band	ELM	II
2010 HWHW SW CA8			HWKW	Small Spherulite with veins	ELM	II
2010 HWHW SW CA9			HWKW	Small Spherulite	ELM	II
2010 HWKE 2010			HWKE	Rhizocretion	ELM	I
2010 HWKWNE CA1			HWKW - NE face	Evaporite pseudomorph	ELM	I
2010 HWKWNE CA11			HWKW - NE face	Small Spherulite with veins	ELM	II
2010 HWKWNE CA2			HWKW - NE face	Spherulite with Sparry bands	ELM	II
2010 HWKWNE CA4			HWKW - NE face	Small Spherulite with veins	ELM	II
2010 HWKWNE CA5			HWKW - NE face	Small Spherulite with veins	ELM	II
2010 HWKWNE CA6			HWKW - NE face	Small Spherulite with veins	ELM	II
2010 HWKWNE CA7			HWKW - NE face	Small Spherulite with veins	ELM	II
2010 HWKWNE CA8			HWKW - NE face	Small Spherulite with veins	ELM	II
2010 HWKWNE CA9			HWKW - NE face	Small Spherulite with veins	ELM	II
2010 Loc 6 CA1		6		Micritic nodule type 1	AF	I
2010 Loc 6 CA2		6		Micritic nodule type 1	AF	I
2010 Loc23 CA1		23		Micritic nodule type 1	ELM	I
2010 Loc23 CA2		23		Micritic nodule type 1	ELM	I
2010 Loc23 CA3a		23		Micritic nodule type 1	ELM	I
2010 Loc23 CA3b		23		Micritic nodule type 1	ELM	I
2010 Loc23 CA3c		23		Micritic nodule type 1	ELM	I
2010 Loc66 CA1		65	Naisiusiu	Micritic nodule type 1	WLM	I
2010 Loc66 CA10		65	Naisiusiu	Micritic nodule type 1	WLM	I
2010 Loc66 CA11		65	Naisiusiu	Micritic nodule type 1	WLM	I
2010 Loc66 CA12		65	Naisiusiu	Micritic nodule type 1	WLM	I
2010 Loc66 CA13		65	Naisiusiu	Micritic nodule type 1	WLM	I
2010 Loc66 CA14		65	Naisiusiu	Micritic nodule type 1	WLM	I
2010 Loc66 CA2		65	Naisiusiu	Micritic nodule type 1	WLM	I
2010 Loc66 CA3		65	Naisiusiu	Micritic nodule type 1	WLM	I
2010 Loc66 CA4		65	Naisiusiu	Micritic nodule type 1	WLM	I
2010 Loc66 CA5		65	Naisiusiu	Micritic nodule type 1	WLM	I
2010 Loc66 CA6		65	Naisiusiu	Micritic nodule type 1	WLM	I
2010 Loc66 CA7		65	Naisiusiu	Micritic nodule type 1	WLM	I
2010 Loc66 CA8		65	Naisiusiu	Micritic nodule type 1	WLM	I
2010 Loc66 CA9		65	Naisiusiu	Micritic nodule type 1	WLM	I
2010 Tr120 101	120		KK	Spherulite with veins	ELM	II
2010 Tr120 102	120		KK	Small Spherulite with veins	ELM	II
2010 Tr120 103	120		KK	Small Spherulite with veins	ELM	II
2010 Tr120 105	120		KK	Evaporite pseudomorph	ELM	II
2010 Tr120 106	120		KK	Small Spherulite with veins	ELM	II
2010 Tr120 107	120		KK	Spherulite with veins	ELM	II
2010 Tr120 108	120		KK	Micritic nodule type 1	ELM	II

Appendix 2: Stable isotope ratios for Spherulitic clusters

Analyses	Specimen	Sampling point	$\delta^{13}C$ (VPDB)	$\delta^{18}O$ (VPDB)
1	FLK-N TR121 12	centre	-5.1	-5.9
2	FLK-N TR47 12-1	Whole	-6.0	-6.4
3	FLK-N TR47 12-2	Whole	-5.0	-6.3
4	FLK-N TR47 12-3	Whole	-4.5	-5.9
5	FLK-N TR47 12-4	Whole	-5.5	-6.3
6	FLK-N TR47 12-5	Whole	-5.6	-6.7
7	FLK-N TR47 5a	Edge	-5.9	-6.8
8	FLK-N TR47 5b	Edge	-5.6	-6.6
9	FLK-N TR47 5c	centre	-4.6	-6.2
10	FLK-N TR47 7	centre	-5.9	-6.9
11	KK TR120 19a	centre	-3.1	-5.8
12	KK TR120 19b	outer	-3.6	-4.9
13	KK TR120 20	centre	-4.5	-5.5
14	KK TR120 7a	centre	-5.4	-6.8
15	KK TR120 7b	edge	-4.8	-5.7
16	TK TR122 4	centre	-3.8	-5.0
17	2008 138CA11	Centre	-5.6	-6.0
18	2008 138CA12	Edge	-5.2	-6.3
19	2008 138CA13	Whole	-3.7	-5.8
20	2008 138CA14	Centre	-3.1	-4.4
21	2008 144NL21	Whole	-4.8	-6.3
22	2008 144NL22	Whole	-5.8	-6.2
23	2008 144NL23	Whole	-6.1	-6.0
24	2008 144NL24	Whole	-6.0	-6.2
25	2008 147CA61	Whole	-3.4	-5.3
26	2008 147CA611	Whole	-3.8	-5.8
27	2008 147CA63	Whole	-4.5	-5.8
28	2008 147CA65	Whole	-5.0	-5.9
29	2008 147CA67	Whole	-5.1	-6.2
30	2008 147CA69	Whole	-5.0	-6.2
31	2008 148NL21	Whole	-4.8	-6.0
32	2008 148NL22	Whole	-5.0	-6.1
33	2008 148NL23	Whole	-3.9	-5.5
34	2008 148NL24	Whole	-3.6	-5.5
35	2008 148NL25	Whole	-3.7	-5.3
36	2008 148NL26	Whole	-3.1	-4.8
37	2008 148NL27	Whole	-2.4	-4.4
38	2008 148NL28	Whole	0.0	-2.2
39	2008 Tr147 CA3-1	Whole	-4.6	-5.7
40	2008 Tr147 CA3-2	Whole	-3.9	-5.4
41	2008 Tr147 CA3-3	Whole	-3.6	-5.3
42	2008 Tr147 CA3-4	Whole	-0.7	-2.8
43	2008 Tr147 CA3-5	Whole	-3.7	-5.2
44	2008 Tr147 CA3-6	Whole	-2.8	-4.3
45	2009 471071	Whole	-6.0	-6.3
46	2009 471072	Whole	-5.7	-6.5
47	2009 471073	Whole	-5.0	-6.2
48	2009 E149CA11	Whole	-6.1	-5.5
49	2009 E149CA13	Whole	-4.5	-5.5
50	2009 E149CA15	Whole	-3.7	-5.1
51	2009 HWKECA11	Whole	-2.7	-4.6
52	2009 HWKECA12	Whole	-3.4	-3.8
53	2009 HWKECA13	Whole	-5.3	-5.8
54	2009 HWKECA14	Whole	-5.9	-6.0
55	2009 HWKECA15	Whole	-4.3	-5.1

Analyses	Specimen	Sampling point	$\delta^{13}C$ (VPDB)	$\delta^{18}O$ (VPDB)
56	2009 HWKECA16	Whole	-2.3	-3.9
57	2009 HWKECA17	Whole	-2.0	-3.7
58	2009 HWKECA18	Whole	-4.6	-5.3
59	2009 HWKECA19	Whole	0.5	-0.9
60	2009 HWKECA31	Whole	-4.0	-5.3
61	2009 HWKECA32	Edge	-4.7	-6.0
62	2009 HWKECA33	Whole	-4.5	-5.6
63	2009 HWKECA81	Centre	-6.8	-6.5
64	2009 HWKECA82	Edge	-5.0	-6.5
65	2009 HWKECA83	Whole	-2.9	-5.0
66	2010 Tr120 CA101-1	Centre	-4.2	-5.7
67	2010 Tr120 CA101-2	Edge	-3.3	-5.0
68	2010 Tr120 CA101-3	Whole	-4.0	-5.3
69	2010 Tr120 CA102-1	Centre	-3.7	-5.2
70	2010 Tr120 CA102-2	Edge	-2.8	-4.3
71	2010 TR120 CA7 1	Centre	-3.2	-4.3
72	2010 TR120 CA7 2	Edge	-2.7	-4.1
73	2010 TR120 CA7 3	Whole	-1.4	-3.1

Analyses 1-16: data from Bennett et al, 2011

Analyses 17-73: data from this study

Appendix 3: ICP analyses for Sparry Nodules

2008 TR111 CA5									
	1	2	3	4	5	6	7	8	9
Fe	640	843	788	1419	738	992	250	412	533
Mn	41	83	36	81	53	69	22	34	39
Sr	1256	248	298	233	246	390	222	221	1200
Ba	170	181	143	157	122	170	151	131	157
Mg	4145	5543	6897	4626	4251	7247	5745	4998	6773
Mol%Mg	1.70	2.28	2.84	1.90	1.75	2.98	2.36	2.06	2.79
2008 TR111 CA0									
	1	2	3	4	5	6	7		
Fe	1189	594	534	241	252	86	664		
Mn	93	46	34	16	27	27	32		
Sr	333	251	459	372	384	259	1434		
Ba	144	127	135	127	140	159	170		
Mg	8715	6364	9129	6879	7321	3804	6787		
Mol%Mg	3.58	2.62	3.76	2.83	3.01	1.56	2.79		

Solution ICP-AES. Data in ppm. Analyses numbers represent sampling 1-7(9) from centre to edge of a sparry nodule.

2008 TR111 CA1	Mg	Mn	Sr	Y	Ba	La	Ce	Pr	Nd	Sm	Eu	Gd	Tb	Dy	Ho	Er	Tm	Yb	Lu	Pb	Th	U
1	9230	43	2129	13	46	35	23	5	13	1	0	3	0	2	0	2	2	3	2	14	2	0
2	7376	30	2660	50	75	164	138	26	78	10	0	9	0	8	1	6	3	8	3	11	7	0
3	4052	24	102	5	23	5	2	2	3	0	0	1	0	1	0	2	2	2	2	9	1	0
4	4253	22	177	5	3	9	2	2	4	0	0	1	0	1	0	1	2	2	2	5	1	0
5	2964	24	103	9	6	29	4	4	11	0	0	2	0	1	0	2	2	2	2	5	1	0
6	3105	2	153	3	2	7	1	2	4	0	0	1	0	0	0	1	2	1	2	5	1	0
7	4211	0	172	4	6	5	1	2	3	0	0	1	0	0	0	1	2	2	2	5	1	0
8	4072	8	198	9	3	26	2	3	8	0	0	2	0	1	0	2	2	2	2	5	1	0
9	4370	9	202	11	4	17	2	3	7	0	0	2	0	1	0	2	2	2	2	6	1	0
10	2302	28	112	20	3	34	10	3	7	0	0	2	0	2	0	2	2	2	2	5	1	0
11	5813	32	117	15	7	13	4	3	6	0	0	2	0	1	0	2	2	2	2	5	1	1
12	10067	53	134	26	23	35	20	5	15	2	0	4	0	3	0	3	2	3	2	5	1	0
13	6528	24	175	34	10	45	8	6	18	2	0	4	0	4	0	3	2	3	2	5	1	0
14	6871	23	173	27	11	27	6	4	11	1	0	3	0	3	0	3	2	3	2	5	2	0
15	6401	25	179	34	15	32	6	5	13	1	0	4	0	4	0	3	2	3	2	5	1	0
16	6757	30	244	19	15	18	6	3	8	0	0	2	0	2	0	3	2	2	2	5	1	0
17	5092	25	169	17	9	14	14	3	6	0	0	2	0	2	0	2	2	2	2	5	1	1
18	4276	14	270	16	13	9	8	2	4	0	0	2	0	1	0	2	2	2	2	5	1	0
19	2621	10	188	22	11	26	3	4	13	1	0	3	0	3	0	3	2	2	2	5	1	0
2008 TR111 CA0																						
1	7164	32	1829	11	37	50	43	7	19	2	0	3	0	2	0	2	2	3	2	14	2	0
2	3467	10	1155	11	30	33	19	6	18	1	0	3	0	2	0	2	2	3	2	9	1	0
3	5105	16	262	12	17	15	4	4	9	1	0	2	0	2	0	2	2	2	2	7	1	0
4	11241	14	586	23	23	26	8	4	12	1	0	3	0	3	0	3	2	3	2	9	1	0
5	5809	7	272	21	5	13	3	3	7	0	0	2	0	3	0	3	2	3	2	5	1	0
6	5828	7	277	18	10	10	4	2	6	0	0	2	0	2	0	3	2	3	2	6	1	0
7	5086	7	247	11	6	4	2	2	3	0	0	2	0	1	0	2	2	2	2	4	1	0
8	4757	18	148	8	7	4	4	2	3	0	0	2	0	1	0	2	2	2	2	5	1	0
9	6510	15	254	24	10	7	4	2	5	0	0	2	0	2	0	3	2	4	2	5	1	1
10	3943	9	217	7	6	3	0	1	1	0	0	1	0	0	0	2	2	2	2	5	1	0
11	7926	21	352	29	21	12	4	2	6	0	0	3	0	3	0	3	2	3	2	5	1	2
12	4875	19	179	48	7	33	7	5	15	2	0	5	0	5	0	4	2	3	2	5	1	0
13	19778	108	197	56	13	51	10	5	15	2	0	4	0	4	0	3	2	3	2	6	1	0
14	6602	30	157	21	9	16	4	2	5	0	0	2	0	2	0	2	2	2	2	5	1	0
15	19897	104	410	58	20	70	14	7	22	2	0	6	0	6	0	5	2	3	2	6	1	0
16	4980	26	141	23	8	21	5	3	7	0	0	3	0	2	0	2	2	2	2	4	1	0
17	13003	43	344	18	20	6	6	2	3	0	0	2	0	2	0	2	2	3	2	5	1	0
18	3084	12	195	160	10	162	5	10	33	4	0	11	0	12	2	9	3	5	2	5	1	0

Laser ICP-MS. Data in ppm. Analyses numbers represent sampling from edge to centre (1-19) of sparry nodule 2008 Tr111 CA0 and 1, and 1-18 from centre to edge of sparry nodules 2008 Tr111 CA0

2008 Tr 111 CA1	La	Ce	Nd	Sm	Eu	Gd	Tb	Dy	Er	Yb	Lu
1	1.11	0.34	0.42	0.23	0.00	0.46	0.00	0.33	0.70	0.99	5.18
2	5.29	2.07	2.58	1.75	0.00	1.63	0.00	1.45	1.86	2.68	6.88
3	0.17	0.03	0.11	0.00	0.00	0.21	0.00	0.12	0.47	0.58	4.59
4	0.30	0.03	0.12	0.00	0.00	0.22	0.00	0.12	0.43	0.51	4.42
5	0.92	0.06	0.35	0.12	0.00	0.40	0.00	0.20	0.50	0.61	4.55
6	0.21	0.01	0.14	0.00	0.00	0.22	0.00	0.08	0.40	0.46	4.46
7	0.15	0.01	0.09	0.00	0.00	0.22	0.00	0.09	0.42	0.49	4.47
8	0.82	0.03	0.26	0.00	0.00	0.28	0.00	0.18	0.51	0.67	4.53
9	0.56	0.03	0.23	0.04	0.00	0.30	0.00	0.22	0.52	0.76	4.67
10	1.09	0.15	0.25	0.01	0.00	0.38	0.00	0.33	0.72	0.62	4.54
11	0.43	0.06	0.21	0.02	0.00	0.36	0.00	0.26	0.67	0.69	4.62
12	1.14	0.30	0.51	0.26	0.00	0.65	0.00	0.52	0.92	0.89	4.77
13	1.46	0.12	0.60	0.41	0.00	0.73	0.00	0.80	1.04	0.95	4.82
14	0.86	0.08	0.38	0.21	0.00	0.59	0.00	0.55	0.96	0.83	4.64
15	1.04	0.09	0.43	0.18	0.00	0.64	0.00	0.68	1.07	0.91	4.63
16	0.58	0.09	0.27	0.06	0.00	0.45	0.00	0.42	0.81	0.71	4.71
17	0.45	0.21	0.21	0.04	0.00	0.44	0.00	0.35	0.72	0.65	4.55
18	0.28	0.11	0.13	0.00	0.00	0.31	0.00	0.27	0.69	0.68	4.52
19	0.83	0.05	0.44	0.22	0.00	0.51	0.00	0.47	0.81	0.62	4.57

Laser ICP-MS. Data normalised to NASC (Gromet et al., 1984). Sampling 1-19 from edge to centre of sparry nodule 2008 Tr111 CA1.

.

2008 Tr 111 CA0	La	Ce	Nd	Sm	Eu	Gd	Tb	Dy	Er	Yb	Lu
1	1.59	0.65	0.62	0.34	0.00	0.48	0.00	0.32	0.59	0.89	4.70
2	1.07	0.28	0.59	0.25	0.00	0.54	0.00	0.36	0.61	0.80	4.77
3	0.47	0.07	0.30	0.11	0.00	0.36	0.00	0.27	0.67	0.66	4.71
4	0.84	0.12	0.39	0.19	0.00	0.47	0.00	0.49	0.96	1.06	4.97
5	0.43	0.05	0.24	0.01	0.00	0.42	0.00	0.45	0.89	0.99	4.96
6	0.31	0.06	0.19	0.00	0.00	0.36	0.00	0.34	0.79	0.90	4.85
7	0.14	0.03	0.08	0.00	0.00	0.28	0.00	0.23	0.62	0.67	4.63
8	0.12	0.06	0.10	0.00	0.00	0.29	0.00	0.22	0.55	0.68	4.61
9	0.24	0.06	0.16	0.02	0.00	0.41	0.00	0.42	1.01	1.16	4.96
10	0.09	0.00	0.03	0.00	0.00	0.26	0.00	0.09	0.48	0.60	4.57
11	0.40	0.06	0.19	0.05	0.00	0.50	0.00	0.50	0.91	1.00	4.77
12	1.07	0.10	0.49	0.37	0.00	0.89	0.00	0.93	1.29	1.04	4.79
13	1.65	0.15	0.48	0.26	0.00	0.81	0.00	0.73	1.05	1.00	4.76
14	0.52	0.06	0.16	0.00	0.00	0.40	0.00	0.31	0.60	0.56	4.44
15	2.24	0.21	0.74	0.38	0.00	1.08	0.00	1.01	1.49	1.10	5.02
16	0.68	0.07	0.22	0.04	0.00	0.51	0.00	0.43	0.69	0.64	4.54
17	0.20	0.09	0.11	0.00	0.00	0.33	0.00	0.30	0.70	0.85	4.79
18	5.19	0.07	1.08	0.61	0.00	2.08	0.00	2.09	2.60	1.59	5.42

	La139	Ce140	Pr141	Nd143	Sm147	Eu151	Gd158	Tb159	Dy163	Ho165	Er166	Tm169
NASC	31.1	67	N/A	30.4	5.98	1.25	5.5	0.85	5.54	N/A	3.28	N/A

Laser ICP-MS. Data normalised to NASC (Gromet et al., 1984). Sampling 1-18 from centre to edge of sparry nodule 2008 Tr111 CA0.

Normalisation data in ppm. North American Shale Composite (Gromet et al., 1984)

Appendix 4: Stable isotope ratios for sparry nodules

	Detailed sampling		
	Specimen	$\delta^{13}C$ (PDB)	$\delta^{18}O$ (PDB)
1	11181	-2.68	-1.05
2	11182	-4.24	-2.37
3	11183	-7.87	-5.35
4	11184	-7.35	-5.77
5	11185	-6.30	-5.41
6	11186	-6.65	-6.08
7	11187	-5.81	-6.09
8	11188	-5.84	-6.25
9	11189	-4.95	-5.50
10	111810	-4.23	-5.18
11	111811	-2.39	-3.80
12	111812	-1.82	-3.16
13	2008 TR111 CA4 10	-5.62	-6.07
14	2008 TR111 CA4 13	-5.77	-6.13
15	2008 TR111 CA4 14	-5.85	-6.16
16	2008 TR111 CA4 15	-5.99	-6.28
17	2008 TR111 CA4 16	-5.97	-6.44
18	2008 TR111 CA4 17	-5.47	-6.34
19	2008 TR111 CA4 18	-5.13	-6.34
20	2008 TR111 CA4 19	-5.61	-6.22
21	2008 TR111 CA4 20	-5.01	-6.17
22	2008 TR111 CA4 21	-4.57	-6.03
23	2008 TR111 CA4 22	-4.05	-5.24
24	2008 TR111 CA4 23	-3.54	-4.98
25	2008 TR111 CA4 24	-2.25	-4.15
26	2008 TR111 CA4 25	-2.68	-4.44
27	2008 TR111 CA4 26	-2.31	-3.97
28	2008 TR111 CA4 5	-5.93	-6.63
29	111A11	-6.21	-6.41
30	111A12	-6.13	-6.35
31	111A13	-6.31	-6.21
32	111A14	-6.35	-6.28
33	111A15	-5.86	-6.34
34	111A16	-5.94	-6.45
35	111A17	-6.21	-6.37
36	111A18	-6.70	-6.16
37	111A19	-7.27	-6.13
38	111A110	-7.44	-6.10
39	111A111	-6.94	-6.17
40	111A112	-6.27	-6.02
41	111A113	-6.22	-6.25
42	111A114	-6.59	-6.29
43	111A115	-7.42	-6.43
44	111A116	-8.38	-6.38
45	111A117	-8.07	-6.22
46	111A118	-7.31	-6.58
47	111A119	-7.12	-6.43
48	111A120	-5.93	-5.88
49	111A121	-5.98	-6.48
50	111A122	-5.98	-6.62
51	111A123	-5.95	-6.17
52	111A124	-5.84	-6.38

	Detailed sampling		
	Specimen	$\delta^{13}C$ (PDB)	$\delta^{18}O$ (PDB)
53	111A125	-5.31	-6.17
54	111A126	-4.56	-5.44
55	111A127	-3.86	-5.12
56	111A128	-2.41	-4.29
57	111A129	-1.62	-3.80
58	2008 111 CA0-1	-8.82	-6.79
59	2008 111 CA0-2	-8.16	-6.42
60	2008 111 CA0-3	-6.82	-6.18
61	2008 111 CA0-4	-5.22	-5.78
62	2008 111 CA0-5	-5.98	-6.73
63	2008 111 CA0-6	-5.49	-6.00
64	2008 111 CA0-7	-2.78	-4.34
65	2008 111 CA5-1	-7.15	-6.39
66	2008 111 CA5-2	-6.75	-6.63
67	2008 111 CA5-3	-5.90	-6.29
68	2008 111 CA5-4	-6.72	-6.60
69	2008 111 CA5-5	-7.15	-6.47
70	2008 111 CA5-6	-6.22	-6.02
71	2008 111 CA5-7	-5.93	-6.57
72	2008 111 CA5-8	-5.54	-6.37
73	2008 111 CA5-9	-3.05	-4.64
74	2008 111 CA7-1	-1.98	-1.95
75	2008 111 CA7-2	-0.53	0.15
76	2008 111 CA7-3	-5.18	-4.91
77	2008 111 CA7-4	-5.60	-6.12
78	2008 111 CA7-5	-5.22	-5.17
79	2008 111 CA7-6	-4.85	-5.50
80	2008 111 CA7-7	-2.97	-4.39

	Coarse sampling		
	Specimen	$\delta^{13}C$ (PDB)	$\delta^{18}O$ (PDB)
81	111CA91	-7.14	-6.45
82	111CA92	-6.07	-6.37
83	111CA93	-3.57	-5.15
84	111CA94	-1.28	-2.86
85	143NL61	-5.12	-5.53
86	143NL62	-5.40	-6.37
87	143NL63	-4.34	-6.22
88	143NL81	-5.83	-5.57
89	143NL83	-6.12	-6.51
90	143NL85	-1.12	-3.39
91	146CA21	-5.01	-6.02
92	146CA23	-4.86	-6.03
93	146CA25	-4.21	-6.08
94	146CA27	-3.94	-5.74
95	146CA29	-1.53	-3.71
96	150CA41	-6.18	-6.81
97	150CA42	-5.95	-6.83
98	150CA43	-4.50	-5.83
99	2008 111 CA1-1	-6.47	-6.76

	Coarse sampling		
	Specimen	$\delta^{13}C$ (PDB)	$\delta^{18}O$ (PDB)
100	2008 111 CA1-2	-6.50	-6.85
101	2008 111 CA1-3	-6.85	-6.81
102	2008 111 CA1-4	-7.36	-6.50
103	2008 111 CA1-5	-6.59	-6.30
104	2008 111 CA1-6	-5.76	-6.43
105	2008 111 CA1-7	-3.47	-4.96
106	2008 111 CA1-8	-1.80	-3.72
107	2008 111 CA4-1	-5.51	-6.00
108	2008 111 CA4-2	-5.43	-5.94
109	2008 111 CA4-3	-5.34	-5.86
110	2008 111 CA4-4	-5.49	-6.04
111	2008 111 CA4-5	-5.87	-6.33
112	2008 111 CA4-6	-5.26	-6.44
113	2008 111 CA4-7	-3.73	-5.22
114	2008 Tr147 CA1-1	-4.82	-4.53
115	2008 Tr147 CA1-2	-4.74	-3.98
116	2008 Tr147 CA1-3	-3.96	-2.74
117	2008 Tr147 CA1-3	-5.00	-4.90
118	2008 Tr147 CA1-5	-6.27	-6.46
119	2008 Tr147 CA1-6	-5.63	-6.39
120	2008 Tr147 CA1-7	-4.21	-6.18
121	2008 Tr147 CA1-8	-3.72	-5.80
122	2009 Tr150 CA4-4	-3.65	-4.56
123	2009 Tr150 CA4-5	-3.26	-4.04
124	2009 Tr150 CA4-6	-0.24	-2.26
125	DKCA11	-4.91	-5.11
126	DKCA12	-5.43	-5.27
127	DKCA13	-4.17	-6.21
128	DKCA14	-3.20	-4.13
129	DKCA15	-1.53	-3.37
130	DKCA16	-0.07	-2.83
131	DKCA31	-3.60	-5.61
132	DKCA32	-3.99	-6.11
133	DKCA33	-4.03	-4.75
134	DKCA34	-2.58	-3.52
135	DKCA35	-0.32	-2.52
136	DKCA36	-0.69	-2.57
137	HWKECA51	-5.01	-6.45
138	HWKECA52	-4.78	-6.74
139	HWKECA53	-4.23	-6.30
140	HWKECA54	-3.79	-6.00
141	HWKECA55	-1.96	-3.98
142	VEKCA11	-6.06	-7.10
143	VEKCA14	-5.44	-6.34
144	VEKCA15	-5.60	-6.44
145	VEKCA17	-4.50	-5.99
146	VEKCA31	-6.33	-7.14
147	VEKCA32	-5.89	-6.83
148	VEKCA33	-4.50	-6.06
149	VEKCA41	-6.47	-6.51
150	VEKCA45	-5.31	-6.30
151	VEKCA47	-5.32	-6.39
152	ZINJCA11	-5.68	-6.21

	Coarse sampling		
	Specimen	$\delta^{13}C$ (PDB)	$\delta^{18}O$ (PDB)
153	ZINJCA110	-6.71	-6.42
154	ZINJCA113	-4.44	-6.34
155	ZINJCA114	-3.38	-6.08
156	ZINJCA19	-6.49	-6.30
157	ZINJGA1	-5.46	-6.24
158	ZINJGA2	-6.38	-6.92
159	ZINJGA3	-6.89	-6.89
160	ZINJGA4	-7.01	-6.96
161	ZINJGA5	-8.04	-6.72
162	ZINJGA6	-8.18	-6.69
163	ZINJGA7	-6.91	-6.31
164	ZINJGA8	-6.68	-6.51
165	VEK 111 3 1	-8.30	-6.70
166	VEK 111 3 2	-8.50	-6.90
167	VEK 111 3 3	-5.90	-5.60
168	VEK 111 3 4	-5.70	-6.00
169	VEK 111 3 5	-6.10	-7.00
170	VEK 111 3 6	-5.70	-6.20
171	VEK 111 3 7	-3.70	-5.30
172	VEK 111 3 8	-1.60	-4.30
173	VEK 111 3 A	-6.10	-6.90
174	VEK 111 3 B	-5.80	-6.50
175	VEK 111 3 C	-5.60	-6.30
176	VEK 111 3 D	-2.50	-4.40
177	VEK 111 5 1	-4.50	-5.00
178	VEK 111 5 2	-5.50	-6.10
179	VEK 111 5 3	-3.30	-4.90
180	VEK 111 5 4	-1.50	-3.70
181	VEK 111 7 1	-8.20	-6.80
182	VEK 111 7 2	-6.40	-6.70
183	VEK 111 7 3	-3.80	-5.50
184	VEK 111 9 1	-6.30	-6.00
185	VEK 111 9 2	-4.90	-5.80
186	VEK 111 9 3	-2.80	-3.90

Appendix 5: Solution ICP analyses for micritic nodules

2007 Tr140 NL1	**1**	**2**	**3**	**4**	**5**		
Fe	595	1435	455	702	1813		
Mg	954	591	543	737	1338		
Mn	572	1143	424	936	1466		
Sr	719	1898	1258	1621	1492		
Ba	465	778	508	758	438		
Fe/Mn	1.04	1.26	1.08	0.75	1.24		
Mol% Mg	0.39	0.24	0.22	0.30	0.55		
2008 Tr143 NL3	**1**	**2**	**3**	**4**	**5**	**6**	**7**
Fe	23	28	1127	1574	804	438	626
Mg	99	88	1591	184	843	1176	447
Mn	3	1	1772	484	851	724	915
Sr	2	2	559	863	1349	687	989
Ba	1	1	186	268	204	363	236
Fe/Mn	6.91	31.94	0.64	3.25	0.94	0.61	0.68
Mol% Mg	0.04	0.04	0.65	0.08	0.35	0.48	0.18
2008 Tr143 CA3	**1**	**2**	**3**	**4**			
Fe	162	280	608	1732			
Mg	119	1037	331	334			
Mn	219	1203	728	367			
Sr	644	500	1155	290			
Ba	242	1054	839	1280			
Fe/Mn	0.74	0.23	0.84	4.72			
Mol% Mg	0.05	0.43	0.14	0.14			
2008 Tr148 CA2	**1**	**2**	**3**	**4**			
Fe	420	1470	1631	214			
Mg	592	1213	1291	231			
Mn	566	1520	1313	413			
Sr	1724	1083	1039	678			
Ba	698	566	862	637			
Fe/Mn	0.74	0.97	1.24	0.52			
Mol% Mg	0.24	0.50	0.53	0.09			

Appendix 6: Stable isotope analyses for micritic nodules

Analysis	Specimen	$\delta^{13}C$ (PDB)	$\delta^{18}O$ (PDB)
1	2007 138 LMST-1	-5.32	-6.10
2	2007 138 LMST-2	-5.83	-6.39
3	2007 138 LMST-3	-6.72	-6.40
4	2007 138 LMST-4	-4.48	-6.30
5	2007 140 NL1-1	-4.49	-6.09
6	2007 140 NL1-2	-5.27	-6.44
7	2007 140 NL1-3	-5.27	-6.37
8	2007 140 NL1-4	-4.98	-6.21
9	2007 140 NL1-5	-3.92	-5.89
10	2007 TR137 NL2-1	-3.65	-6.79
11	2007 TR137 NL2-2	-3.09	-6.56
12	2007 TR137 NL2-3	-5.13	-6.58
13	2007 TR137 NL2-4	-5.34	-5.91
14	2007 TR137 NL2-5	-5.88	-6.11
15	2007 TR137 NL2-6	-5.91	-6.34
16	2007 TR135 NL2-1	-5.32	-6.15
17	2007 TR135 NL2-2	-5.31	-6.24
18	2007 TR135 NL2-3	-5.47	-6.31
19	2007 TR135 NL2-4	-5.27	-6.57
20	2007 TR135 NL2-5	-5.42	-6.60
21	2007 TR135 NL2-6	-5.26	-6.44
22	2007 TR135 NL2-7	-5.19	-6.38
23	2008 TR143 NL3-1	-5.72	-5.46
24	2009 TR143 NL3-2	-5.78	-5.43
25	2010 TR143 NL3-3	-5.77	-5.61
26	2011 TR143 NL3-4	-6.09	-6.40
27	2012 TR143 NL3-5	-6.24	-6.57
28	2013 TR143 NL3-6	-5.54	-6.33
29	2014 TR143 NL3-7	-5.76	-6.53
30	DKCA81	-1.49	-3.55
31	DKCA82	-0.86	-2.88
32	DKCA83	0.03	-2.77
33	DKCA84	-0.33	-2.02
34	DKCA171	-4.45	-5.05
35	DKCA172	-4.60	-5.57
36	DKCA173	-4.58	-5.24
37	DKCA174	-5.77	-5.80
38	DKCA111	-2.90	-3.91
39	DKCA112	-3.48	-4.09
40	DKCA113	-1.34	-3.17
41	DKCA114	0.17	-2.15
42	DKCA141	-4.61	-5.22
43	DKCA144	-2.17	-4.11
44	DKCA145	-3.88	-5.28
45	DKCA91	-1.53	-3.31
46	DKCA92	-0.84	-2.72
47	DKCA93	-1.29	-3.20
48	LOC60CA71	-3.21	-5.49
49	LOC60CA72	-4.54	-4.75
50	LOC60CA73	-3.66	-4.98
51	LOC60CA74	-3.13	-4.15

Analysis	Specimen	$\delta^{13}C$ (PDB)	$\delta^{18}O$ (PDB)
52	LOC60CA75	-4.11	-4.28
53	LOC60CA76	-4.41	-4.81
54	ZINJCARB1	-2.56	-4.36
55	ZINJCARB2	-3.53	-4.92
56	DKCA131	-5.28	-5.43
57	DKCA133	-4.69	-5.10
58	DKCA135	-1.28	-3.54
59	E134CA11	-5.01	-6.04
60	E134CA12	-3.36	-5.33
61	E134CA13	-3.60	-4.95
62	TR4725B1	-5.04	-5.68
63	TR4725B2	-5.20	-6.08
64	TR4725B3	-4.67	-5.59
65	4720B1	-4.90	-5.89
66	4720B1	-4.50	-5.59
67	4720B3	-4.60	-5.64
68	HWKECA61	-4.40	-5.78
69	HWKECA62	-3.35	-5.06
70	HWKECA63	-0.50	-3.10
71	2008 Tr144 CA5-1	-2.16	-5.19
72	2009 loc 5 CA1	-3.62	-4.56
73	2010 Loc66 CA5-1	-4.82	-4.53
74	2010 Loc66 CA5-2	-4.74	-3.98
75	2010 Loc66 CA1-1	-3.96	-2.74
76	2010 Loc66 CA1-2	-5.00	-4.90
77	2010 LOC6 CA1	-1.21	-3.61
78	2009 LOC77 CA2	-1.06	-2.41
79	2010 LOC66 CA10	-1.35	-4.07
80	2010 LOC66 CA5	-2.44	-3.44
81	2010 LOC66 CA9	-4.90	-4.48
82	135CA7	2.10	-4.44
83	135CA3	-4.33	-5.40
84	DK15C1	-2.81	-4.19
85	135CA2	-4.62	-5.67
86	135CA1	-4.39	-5.43
87	135CA5	-1.86	-5.31
88	135CA4	-0.94	-5.25
89	135CA6	-0.89	-4.93
90	149CA1	-3.46	-4.20
91	149C1B	-2.49	-3.83
92	149CA7	-1.64	-3.53
93	149CA3	-5.31	-5.29
94	149C41	-1.90	-4.16
95	MNK81	-4.48	-4.99
96	MNK82	-4.75	-4.94
97	MNK83	-4.18	-5.29
98	FLK-N 47 1	-5.50	-6.30
99	FLK-N 47 3a	-6.40	-6.60
100	FLK-N 47 3b	-5.70	-6.50
101	FLK-N 47 5 1	-4.90	-5.90
102	FLK-N 47 5 2	-4.10	-5.70
103	FLK-N 47 10 1	-4.40	-5.80

Analysis	Specimen	$\delta^{13}C$ (PDB)	$\delta^{18}O$ (PDB)
104	FLK-N 47 10 2	-5.10	-6.20
105	FLK-N 47 10 3	-3.70	-5.00
106	FLK-N 47 11 a	-4.30	-5.40
107	FLK-N 47 11 b	-5.60	-6.00
108	FLK-N 47 13 a	-3.50	-5.60
109	FLK-N 47 13 b	-4.40	-5.50

Appendix 7: Solution ICP-MS analyses of whole calcite crystals (2009 RHCII CA6)

ICP-MS data for four crystals at RHCII CA6 (ppm)

	Mg	mol% Mgco3	Sr	Ba	Mn	Fe	Fe/Mn	Y								
RHCII CA6 1	1284.50	0.53	901.65	206.96	3274.17	684.47	0.21	22.12								
RHCII CA6 2	870.63	0.36	870.93	203.88	3676.57	403.21	0.11	21.71								
RHCII CA6 3	858.12	0.35	735.53	201.15	2617.76	440.61	0.17	19.83								
RHCII CA6 4	4547.43	1.87	1109.85	262.00	575.99	426.56	0.74	19.43								
Mean	**1890.17**	**0.78**	**904.49**	**218.50**	**2536.12**	**488.71**	**0.31**	**20.77**								
Max	**4547.43**	**1.87**	**1109.85**	**262.00**	**3676.57**	**684.47**	**0.74**	**22.12**								
Min	**858.12**	**0.35**	**735.53**	**201.15**	**575.99**	**403.21**	**0.11**	**19.43**								
	La	**Ce**	**Pr**	**Nd**	**Sm**	**Eu**	**Gd**	**Tb**	**Dy**	**Ho**	**Er**	**Tm**	**Yb**	**Lu**	**Th**	**U**
RHCII CA6 1	8.07	15.90	3.60	20.29	8.28	3.42	9.41	1.59	7.09	1.63	3.26	0.84	3.09	0.77	5.37	8.20
RHCII CA6 2	6.65	12.78	3.08	17.65	7.75	3.46	8.63	1.53	6.61	1.60	3.10	0.85	2.89	0.76	5.44	8.90
RHCII CA6 3	5.51	10.67	2.59	16.41	7.59	2.47	7.96	1.30	6.42	1.26	2.86	0.54	2.60	0.55	3.16	9.74
RHCII CA6 4	13.00	17.63	3.82	16.90	4.88	2.79	6.95	1.15	4.72	1.36	2.59	0.79	2.53	0.72	5.79	7.18
Mean	**8.31**	**14.24**	**3.27**	**17.81**	**7.12**	**3.04**	**8.24**	**1.39**	**6.21**	**1.46**	**2.95**	**0.75**	**2.78**	**0.70**	**4.94**	**8.51**
Max	**13.00**	**17.63**	**3.82**	**20.29**	**8.28**	**3.46**	**9.41**	**1.59**	**7.09**	**1.63**	**3.26**	**0.85**	**3.09**	**0.77**	**5.79**	**9.74**
Min	**5.51**	**10.67**	**2.59**	**16.41**	**4.88**	**2.47**	**6.95**	**1.15**	**4.72**	**1.26**	**2.59**	**0.54**	**2.53**	**0.55**	**3.16**	**7.18**
Abundances normalised to NASC (Gromet et al, 1984)																
	La	**Ce**		**Nd**	**Sm**	**Eu**	**Gd**	**Tb**	**Dy**		**Er**		**Yb**	**Lu**		
	31.10	67.03		30.40	5.98	1.25	5.50	0.85	5.54		3.28		3.11	0.46		
	La	**Ce**		**Nd**	**Sm**	**Eu**	**Gd**	**Tb**	**Dy**		**Er**		**Yb**	**Lu**		
RHCII CA6 1	0.26	0.24		0.67	1.38	2.73	1.71	1.86	1.28		0.99		0.99	1.68		
RHCII CA6 2	0.21	0.19		0.58	1.30	2.76	1.57	1.80	1.19		0.95		0.93	1.67		
RHCII CA6 3	0.18	0.16		0.54	1.27	1.97	1.45	1.53	1.16		0.87		0.84	1.20		
RHCII CA6 4	0.42	0.26		0.56	0.82	2.23	1.26	1.35	0.85		0.79		0.81	1.57		

Appendix 8: Laser ablation ICP-MS analyses of calcite crystals

ICP-MS data for crystals from Loc 80 and Loc 25 (ppm)	Mol % Mg	Mg	Mn	Fe	Fe/Mn	Sr	Y	Ba	La	Ce	Pr	Nd	Sm	Eu	Gd	Tb	Dy	Ho	Er	Tm	Yb	Lu	Pb	Th	U
RHC 104 1 1	2.78	6751.61	28.83	n.d.	-	1468.25	25.82	65.86	7.49	19.44	4.12	23.39	7.03	1.56	5.01	0.69	4.86	0.85	3.11	0.57	2.77	0.46	0.50	3.91	63.91
RHC 104 1 2	2.18	5287.87	12.79	n.d.	-	2033.03	18.04	126.94	8.54	18.24	2.93	15.56	3.90	1.17	5.07	0.40	2.80	0.60	2.10	0.32	2.06	0.27	0.10	3.05	66.64
RHC 104 1 4	2.73	6629.17	63.16	n.d.	-	1814.17	23.02	139.33	12.70	24.75	3.61	18.59	4.28	1.78	5.87	0.61	4.42	1.01	2.25	0.43	3.12	0.43	n.d.	4.84	110.94
RHC 104 1 5	2.28	5539.62	22.33	n.d.	-	1881.86	14.00	117.63	6.97	11.36	1.56	10.50	2.86	0.64	2.80	0.42	2.10	0.48	1.11	0.22	1.22	0.12	0.07	2.18	49.70
RHC 104 1 6	1.92	4658.50	13.21	n.d.	-	2311.88	14.27	133.79	6.67	11.75	2.05	10.21	3.47	0.82	2.23	0.60	2.70	0.49	1.36	0.14	1.45	0.19	1.13	2.00	32.54
RHC 104 2 1	2.47	5993.17	23.26	n.d.	-	1648.49	28.46	80.27	8.61	20.59	3.38	25.01	6.11	1.85	5.82	0.90	4.65	1.23	2.79	0.62	3.15	0.54	0.00	3.33	61.35
RHC 104 2 2	2.53	6158.39	36.16	n.d.	-	1630.89	24.52	79.94	9.66	20.35	3.68	21.54	6.37	1.39	5.21	0.76	4.70	0.98	2.54	0.45	3.16	0.37	0.12	3.42	62.35
RHC 104 2 3	2.11	5121.43	23.06	n.d.	-	1691.28	20.30	65.97	6.02	15.38	3.14	15.15	6.19	1.51	4.76	0.77	3.94	0.65	2.94	0.44	2.06	0.34	0.13	2.66	43.34
RHC 104 2 4	1.77	4298.18	16.45	n.d.	-	2132.63	20.45	99.80	4.94	12.52	2.40	12.04	2.78	0.87	3.44	0.66	3.19	0.56	2.06	0.30	1.97	0.36	0.10	2.57	33.14
RHC 104 2 5	1.61	3913.01	23.33	n.d.	-	2471.29	9.68	114.04	4.76	11.14	1.61	10.34	2.23	0.54	2.34	0.36	2.05	0.31	0.99	0.21	1.38	0.14	n.d.	1.77	38.57
RHC 104 2 6	2.64	6415.98	37.02	n.d.	-	1800.17	20.72	118.67	9.62	20.59	3.22	16.24	5.04	1.11	4.60	0.82	3.87	0.69	2.53	0.42	2.46	0.50	0.04	3.50	88.10
RHC 104 3 1	3.64	8849.72	31.15	n.d.	-	2218.76	25.77	191.68	9.65	18.84	3.66	21.12	5.57	1.53	5.21	0.68	5.36	1.21	3.42	0.38	3.80	0.44	0.07	4.84	103.68
RHC 104 3 2	1.55	3765.32	911.69	n.d.	-	1805.03	26.72	325.93	21.89	33.59	3.88	19.34	5.05	1.91	5.44	0.64	5.21	0.95	2.92	0.59	3.25	0.48	0.15	3.57	39.50
RHC 104 3 3	3.97	9651.23	71.36	n.d.	-	1631.65	32.74	242.61	8.55	18.05	4.23	22.38	4.60	1.90	5.43	0.88	6.13	1.37	4.35	0.62	4.78	0.62	n.d.	4.97	81.45
RHC 104 3 4	3.13	7611.58	186.45	n.d.	-	1860.31	21.22	292.54	9.74	17.10	3.33	19.44	4.07	1.52	3.03	0.49	4.36	0.78	2.14	0.49	2.44	0.49	0.07	4.16	63.67
RHC 104 3 5	1.92	4677.69	21.63	n.d.	-	1697.49	10.42	148.14	4.28	7.81	1.58	7.28	3.09	0.99	2.40	0.32	1.96	0.34	1.23	0.11	1.34	0.15	0.09	1.93	50.28
RHC 104 4 3	2.98	7237.34	15.22	n.d.	-	1700.42	21.80	133.22	8.16	17.21	2.47	11.46	5.83	1.94	7.60	1.02	2.95	1.19	3.60	1.11	3.80	0.45	0.31	5.32	100.37
RHC 104 4 4	1.47	3563.44	7.13	n.d.	-	1875.74	6.23	126.89	1.39	3.67	0.70	4.22	1.26	0.08	1.20	0.29	0.60	0.21	1.09	0.12	0.61	0.07	n.d.	1.17	31.55
RHC 104 4 5	2.64	6427.02	24.42	n.d.	-	1859.90	20.40	148.21	6.52	15.75	2.45	18.49	4.76	1.19	4.41	0.70	4.38	0.68	2.39	0.41	2.09	0.34	0.05	4.02	97.01
Mean	**2.44**	**5923.70**	**82.56**			**1870.17**	**20.24**	**144.81**	**8.22**	**16.74**	**2.84**	**15.91**	**4.45**	**1.28**	**4.31**	**0.63**	**3.70**	**0.77**	**2.36**	**0.42**	**2.47**	**0.35**	**0.19**	**3.33**	**64.11**
Max	**3.97**	**9651.23**	**911.69**			**2471.29**	**32.74**	**325.93**	**21.89**	**33.59**	**4.23**	**25.01**	**7.03**	**1.94**	**7.60**	**1.02**	**6.13**	**1.37**	**4.35**	**1.11**	**4.78**	**0.62**	**1.13**	**5.32**	**110.94**
Min	**1.47**	**3563.44**	**7.13**			**1468.25**	**6.23**	**65.86**	**1.39**	**3.67**	**0.70**	**4.22**	**1.26**	**0.08**	**1.20**	**0.29**	**0.60**	**0.21**	**0.99**	**0.11**	**0.61**	**0.07**	**0.00**	**1.17**	**31.55**

ICP-MS data for crystals from Loc 80 and Loc 25 (ppm)																									
	Mol % Mg	Mg	Mn	Fe	Fe/Mn	Sr	Y	Ba	La	Ce	Pr	Nd	Sm	Eu	Gd	Tb	Dy	Ho	Er	Tm	Yb	Lu	Pb	Th	U
RHCl 741	0.98	2384.31	6032.87	n.d.	-	1232.67	58.17	357.31	14.88	30.46	5.45	29.38	14.55	3.21	15.88	2.14	10.74	2.33	5.48	0.90	5.47	0.59	0.02	12.19	32.42
RHCl 742	1.40	3401.76	5612.29	n.d.	-	1207.89	61.55	352.48	11.22	28.93	5.89	35.76	17.10	3.72	15.60	1.88	12.33	2.03	5.92	0.76	5.66	0.79	0.04	16.54	15.24
RHCl 744	0.31	763.10	130.96	n.d.	-	1592.63	40.03	163.76	1.77	13.45	3.27	19.06	10.38	2.31	9.17	1.28	7.53	1.44	4.35	0.38	2.97	0.51	0.00	5.32	6.92
RHCl 745	1.97	4797.28	1855.86	n.d.	-	1189.36	108.28	266.47	8.17	28.58	7.54	57.05	21.79	6.83	25.80	3.34	19.45	3.86	10.35	1.35	8.78	1.30	0.09	30.81	31.24
RHCl 743	1.34	3248.69	7266.95	n.d.	-	1140.37	32.51	282.70	6.15	17.97	3.55	26.62	11.47	3.14	12.52	1.65	7.88	1.35	2.73	0.33	2.43	0.32	0.12	3.38	5.25
RHCl 746	1.66	4028.74	3974.74	n.d.	-	1037.17	96.55	182.37	4.53	14.90	3.45	26.65	18.39	4.83	20.85	3.02	18.35	3.72	8.37	1.18	6.98	0.85	n.d.	8.08	16.53
RHCl 731	0.70	1692.95	6156.36	n.d.	-	1568.82	24.11	249.94	6.79	15.47	2.31	15.53	6.43	1.49	6.61	0.79	5.71	1.11	2.54	0.30	2.16	0.37	0.07	2.80	3.70
RHCl 732	1.69	4110.53	6950.59	n.d.	-	1248.49	85.63	230.35	66.54	83.31	12.76	61.49	18.28	3.23	17.10	2.47	14.60	2.87	8.80	1.30	7.07	1.01	0.03	6.74	11.15
RHCl 733	2.22	5386.71	4118.80	n.d.	-	1097.58	119.17	182.12	19.39	32.77	5.61	37.56	19.91	4.86	22.73	3.65	21.30	4.31	12.67	1.50	8.42	1.05	0.10	11.23	23.63
RHCl 734	1.08	2623.01	7548.24	n.d.	-	912.88	48.48	155.21	8.65	19.27	4.05	21.29	12.38	3.35	11.94	1.77	9.70	2.11	4.09	0.77	4.96	0.49	1.49	11.90	14.90
RHCl 735	4.26	10350.19	7739.00	n.d.	-	1364.94	73.37	225.50	89.10	125.40	18.03	88.65	18.17	4.53	16.46	2.42	15.78	2.58	7.38	1.04	7.71	0.96	0.30	8.06	10.98
RHCl 736	1.12	2729.91	4488.90	n.d.	-	1175.44	57.86	227.64	11.55	32.27	7.23	40.98	16.82	4.18	17.26	2.01	11.61	2.02	5.28	0.65	4.57	0.71	0.38	7.76	10.96
RHCl 721	0.98	2374.33	8380.43	n.d.	-	822.42	34.20	153.33	7.66	17.51	2.72	15.43	7.42	1.94	9.40	1.01	6.51	1.00	2.88	0.33	2.28	0.35	0.29	4.52	4.52
RHCl 722	2.34	5679.09	9638.99	n.d.	-	1681.24	107.33	173.80	94.80	102.94	15.55	74.83	21.51	4.68	21.55	3.05	18.99	3.86	11.39	1.24	9.13	1.44	0.09	6.21	10.48
RHCl 723	2.47	5993.90	8904.65	n.d.	-	1375.24	130.81	207.74	71.98	87.37	14.46	73.23	19.60	4.68	23.58	3.46	25.18	4.27	11.50	1.59	10.13	1.65	0.20	18.11	14.23
RHCl 724	1.58	3838.92	6681.16	n.d.	-	1303.68	84.52	208.54	55.51	78.56	13.14	67.25	21.79	4.15	21.48	3.01	15.75	2.86	7.99	1.15	6.73	0.94	0.63	12.21	10.79
RHCl 725	1.47	3579.02	6314.21	n.d.	-	1294.58	88.44	246.37	49.70	72.39	11.28	63.54	21.14	4.90	20.80	2.81	16.10	3.36	8.80	1.12	6.53	0.88	0.04	12.07	15.53
RHCl 726	1.01	2445.35	2492.13	n.d.	-	982.67	60.54	218.91	4.65	17.73	3.07	26.06	14.53	3.75	15.39	2.29	13.24	2.06	4.93	0.78	4.82	0.70	1.23	14.50	12.27
RHCl 727	1.24	3004.48	6910.98	n.d.	-	1075.98	59.31	193.62	7.73	22.85	4.47	34.36	18.21	4.44	17.04	2.41	13.11	1.95	4.33	0.71	4.10	0.67	0.50	8.37	10.99
RHCl 728	1.31	3192.89	3030.48	n.d.	-	1456.17	155.32	264.62	27.83	49.12	8.47	57.29	26.91	6.42	29.10	4.54	27.90	5.53	14.54	2.19	12.18	1.86	0.43	35.87	25.88
RHCl 711	1.92	4656.47	11981.97	n.d.	-	1766.60	53.45	324.69	60.49	84.71	13.25	58.21	16.36	3.46	13.92	1.95	10.28	2.40	4.46	0.73	3.73	0.68	0.82	5.06	6.53
RHCl 712	1.74	4218.37	4260.12	n.d.	-	1000.62	54.19	249.89	41.16	58.16	9.71	44.73	13.84	3.09	11.31	1.66	9.24	1.86	5.15	0.74	5.04	0.75	0.19	9.47	9.87
RHCl 713	2.15	5236.82	10981.92	n.d.	-	1020.81	59.04	117.54	1.67	10.91	2.17	22.85	16.66	4.41	16.75	2.69	14.47	2.24	6.42	0.71	4.53	0.67	0.03	3.98	14.04
RHCl 714	1.07	2600.30	3428.79	n.d.	-	956.14	37.59	267.69	10.04	29.09	4.90	32.93	10.82	2.88	11.62	1.43	7.81	1.39	3.60	0.43	3.05	0.31	0.10	6.63	9.54
RHCl 715	1.56	3797.58	14395.92	n.d.	-	1099.40	43.29	155.21	18.19	35.00	5.27	30.83	10.45	3.06	12.12	1.69	8.38	1.40	4.05	0.60	3.55	0.46	0.65	3.46	6.88
RHCl 716	3.13	7620.34	1645.32	n.d.	-	1337.95	148.87	315.18	47.71	76.01	12.71	63.48	25.96	7.20	27.81	3.94	26.82	5.37	15.32	2.10	13.66	1.96	0.12	17.33	35.00
RHCl 717	0.76	1840.63	8943.09	n.d.	-	1042.74	32.42	139.60	6.80	18.08	3.52	28.54	12.48	3.24	12.19	1.23	7.26	1.27	3.14	0.34	2.69	0.19	0.23	5.17	7.17
RHCl 718	1.01	2456.51	7106.79	n.d.	-	994.84	38.82	228.79	6.96	18.91	3.43	23.02	11.09	2.35	9.82	1.34	8.35	1.26	3.99	0.52	2.61	0.40	0.14	8.14	8.97
Mean	**1.59**	**3859.01**	**6320.45**			**1213.55**	**71.21**	**226.48**	**27.20**	**43.65**	**7.40**	**42.02**	**16.23**	**3.94**	**16.64**	**2.32**	**13.73**	**2.56**	**6.80**	**0.92**	**5.78**	**0.82**	**0.31**	**10.57**	**13.77**
Max	**4.26**	**10350.19**	**14395.92**			**1766.60**	**155.32**	**357.31**	**94.80**	**125.40**	**18.03**	**88.65**	**26.91**	**7.20**	**29.10**	**4.54**	**27.90**	**5.53**	**15.32**	**2.19**	**13.66**	**1.96**	**1.49**	**35.87**	**35.00**
Min	**0.31**	**763.10**	**130.96**			**822.42**	**24.11**	**117.54**	**1.67**	**10.91**	**2.17**	**15.43**	**6.43**	**1.49**	**6.61**	**0.79**	**5.71**	**1.00**	**2.54**	**0.30**	**2.16**	**0.19**	**0.00**	**2.80**	**3.70**

ICP-MS data for crystals from Loc 80 and Loc 25 (ppm)

	Mol % Mg	Mg	Mn	Fe	Fe/Mn	Sr	Y	Ba	La	Ce	Pr	Nd	Sm	Eu	Gd	Tb	Dy	Ho	Er	Tm	Yb	Lu	Pb	Th	U
RHCI 10 4 1	0.59	1435.56	854.72	n.d.	-	224.76	57.35	337.51	1.77	5.03	1.63	10.60	7.76	1.87	8.97	1.64	10.35	2.05	4.52	0.51	3.49	0.45	0.10	5.02	8.95
RHCI 10 4 2	0.40	982.31	826.69	n.d.	-	2143.29	52.31	428.28	2.36	5.51	1.46	11.91	5.69	1.97	6.37	1.12	7.99	1.49	4.04	0.52	2.84	0.43	2.06	4.72	7.30
RHCI 10 4 3	1.04	2517.08	17.22	n.d.	-	741.77	96.07	34.73	1.55	5.68	2.25	18.47	10.68	3.40	17.71	3.04	17.79	3.59	8.72	1.27	8.07	1.02	0.09	13.96	32.80
RHCI 10 4 4	1.28	3121.88	4389.07	n.d.	-	1546.45	30.15	453.86	7.45	13.63	1.95	12.05	7.33	1.33	5.99	0.93	6.33	0.94	2.71	0.34	2.02	0.30	0.06	2.67	6.11
RHCI 10 4 5	0.18	436.68	5.31	n.d.	-	2179.63	19.13	219.67	1.38	4.89	1.38	7.83	5.03	1.02	4.88	0.79	3.75	0.76	1.96	0.21	0.84	0.19	0.03	4.24	11.25
RHCI 10 4 6	0.81	1970.55	14.14	n.d.	-	1272.74	93.05	94.52	2.54	8.90	2.90	22.93	13.19	3.89	17.30	2.73	17.81	3.60	9.49	1.11	7.13	1.00	0.15	11.12	27.76
RHCI 10 3 1	0.53	1277.55	526.06	n.d.	-	2121.82	66.46	231.41	6.50	13.98	2.65	19.99	9.19	2.12	11.98	1.68	11.32	2.17	5.76	0.77	4.95	0.80	0.12	9.44	25.38
RHCI 10 3 2	1.72	4172.89	2805.09	n.d.	-	2423.88	63.57	284.91	18.21	41.16	7.29	38.01	10.93	3.13	14.33	2.09	12.47	2.13	6.71	0.87	4.90	0.66	0.56	11.97	23.66
RHCI 10 3 5	1.53	3725.54	278.66	n.d.	-	968.09	72.85	54.82	1.31	5.53	1.74	18.17	12.08	3.16	13.59	2.04	14.47	2.59	7.60	1.17	5.60	1.08	0.05	8.42	29.55
RHCI 10 3 4	1.09	2644.10	2232.12	n.d.	-	1232.64	41.59	258.61	2.80	6.86	1.55	12.30	5.65	1.85	6.56	1.14	7.24	1.51	4.68	0.55	3.12	0.46	0.72	4.04	7.51
RHCI 10 3 3	1.58	3834.01	369.93	n.d.	-	1492.26	59.27	83.54	5.29	11.54	2.77	15.35	8.56	2.61	9.74	1.74	11.15	1.85	5.74	0.88	5.73	0.84	0.14	6.80	10.82
RHCI 10 3 6	0.21	499.71	19.40	n.d.	-	2279.32	16.51	220.87	0.84	2.63	0.79	5.40	3.12	0.70	3.09	0.32	3.13	0.72	0.95	0.23	1.04	0.17	0.03	3.23	6.69
RHCI 10 2 1	1.13	2745.61	39.18	n.d.	-	794.01	111.96	37.62	1.09	4.73	1.95	16.91	13.03	4.34	17.61	2.91	21.74	4.55	10.87	1.70	9.34	1.49	0.18	17.76	55.06
RHCI 10 2 2	0.93	2272.67	1990.96	n.d.	-	1823.23	122.97	222.33	2.94	9.93	3.73	29.35	19.18	4.88	20.79	3.42	21.16	4.43	11.89	1.62	9.48	1.38	5.38	29.75	21.45
RHCI 10 2 3	0.24	588.92	16.47	n.d.	-	2170.61	12.38	167.72	0.47	1.39	0.52	3.52	2.42	0.69	2.32	0.33	3.04	0.46	0.97	0.17	0.73	0.18	0.02	2.40	5.15
RHCI 10 2 4	0.97	2366.86	42.87	n.d.	-	1729.33	86.54	111.90	7.68	10.38	2.97	19.44	9.62	3.48	14.59	2.45	15.59	3.18	8.01	1.19	6.39	0.97	0.12	8.34	24.71
RHCI 10 2 5	0.24	589.47	n.d.	n.d.	-	2376.68	10.93	137.97	0.31	0.86	0.28	1.20	1.62	0.25	1.35	0.24	1.58	0.37	0.96	0.12	1.39	0.14	0.09	0.86	2.56
RHCI 10 2 6	1.24	3016.17	3254.65	n.d.	-	1281.56	65.29	152.02	1.41	5.00	1.62	14.17	9.48	2.58	12.25	1.90	12.92	2.13	5.46	0.76	5.37	0.56	0.02	4.49	9.02
RHCI 10 2 7	0.97	2349.33	24.94	n.d.	-	1096.12	106.87	28.24	2.66	4.63	1.89	18.05	12.18	3.93	14.68	2.74	16.85	3.69	11.00	1.74	9.37	1.25	0.02	13.36	46.03
RHCI 10 2 8	1.09	2642.51	2734.15	n.d.	-	1545.44	58.03	106.65	2.36	7.71	2.19	16.85	12.72	2.77	13.15	2.00	13.06	2.15	5.16	0.73	5.03	0.71	0.01	15.96	14.34
RHCI 10 1b 1	0.31	764.93	45.76	n.d.	-	2279.71	19.13	248.02	1.82	5.60	1.30	9.25	3.15	1.22	4.39	0.70	3.80	0.74	1.68	0.19	1.27	0.18	0.09	3.02	7.68
RHCI 10 1b 2	0.41	995.11	972.65	n.d.	-	6010.82	43.07	747.53	9.48	17.47	3.32	17.81	8.62	1.37	6.55	1.07	6.75	1.50	3.16	0.30	2.53	0.38	0.31	5.03	5.99
RHCI 10 1b 3	0.76	1859.46	1700.83	n.d.	-	2774.80	43.87	176.84	4.11	12.33	2.38	12.59	4.84	1.39	4.51	1.03	9.54	1.25	4.05	0.56	3.34	0.54	1.63	6.36	10.04
RHCI 10 1b 4	1.37	3335.44	6588.85	n.d.	-	1765.82	32.15	397.78	6.22	10.89	1.62	10.53	5.83	1.89	6.57	1.12	5.48	1.18	3.44	0.46	2.71	0.37	0.19	3.05	7.55
RHCI 10 1a 1	0.60	1467.73	3342.19	n.d.	-	2835.41	65.39	375.57	1.79	7.16	2.32	14.73	10.19	2.82	12.65	2.14	14.95	2.34	5.30	0.70	3.95	0.74	10.89	6.30	14.23
RHCI 10 1a 2	1.07	2609.80	2899.85	n.d.	-	1284.04	40.89	151.43	1.24	5.24	1.41	13.79	6.79	1.79	8.76	1.22	7.46	1.38	3.90	0.64	3.23	0.46	n.d.	3.00	7.00
RHCI 10 1a 3	0.84	2038.23	9.74	n.d.	-	847.32	76.99	24.10	1.55	7.37	2.22	17.85	8.44	2.61	11.25	2.01	11.11	2.91	8.28	1.07	7.00	1.03	0.02	12.98	41.37
RHCI 10 1a 4	1.08	2636.09	82.69	n.d.	-	953.45	81.42	16.81	1.46	8.50	3.09	19.07	10.21	3.20	12.35	2.22	13.83	2.83	8.77	1.34	7.54	1.12	n.d.	12.09	33.97
RHCI 10 1a 5	2.06	5001.77	596.73	n.d.	-	1641.69	55.34	92.46	8.74	16.64	3.77	22.88	8.28	2.48	8.81	1.69	10.38	2.25	5.41	0.87	4.21	0.75	0.22	7.48	14.80
RHCI 10 1a 6	1.43	3471.42	6319.91	n.d.	-	1822.04	35.19	269.55	3.12	8.69	1.97	12.59	8.63	1.61	7.45	1.02	6.39	1.33	3.46	0.40	3.05	0.35	0.19	2.45	4.56
RHCI 10 1a 7	1.04	2539.35	912.37	n.d.	-	1652.85	62.86	99.21	3.03	9.80	2.31	18.12	9.00	2.42	12.57	1.59	11.95	2.34	6.73	0.80	6.25	0.63	0.11	5.35	8.33
RHCI 10 1a 8	0.26	631.31	n.d.	n.d.	-	2858.13	10.99	78.00	1.01	2.59	0.69	3.37	1.60	0.45	2.41	0.27	2.56	0.37	0.91	0.16	0.95	0.16	0.06	1.54	2.60
Mean	**0.91**	**2204.38**	**1463.77**			**1817.80**	**56.58**	**198.26**	**3.58**	**8.82**	**2.18**	**15.16**	**8.28**	**2.29**	**9.86**	**1.60**	**10.44**	**2.02**	**5.38**	**0.75**	**4.46**	**0.65**	**0.79**	**7.73**	**16.69**
Max	**2.06**	**5001.77**	**6588.85**			**6010.82**	**122.97**	**747.53**	**18.21**	**41.16**	**7.29**	**38.01**	**19.18**	**4.88**	**20.79**	**3.42**	**21.74**	**4.55**	**11.89**	**1.74**	**9.48**	**1.49**	**10.89**	**29.75**	**55.06**
Min	**0.18**	**436.68**	**5.31**			**224.76**	**10.93**	**16.81**	**0.31**	**0.86**	**0.28**	**1.20**	**1.60**	**0.25**	**1.35**	**0.24**	**1.58**	**0.37**	**0.91**	**0.12**	**0.73**	**0.14**	**0.01**	**0.86**	**2.56**
Mean CA7 and CA10	**1.22**	**2976.54**	**3808.37**			**1535.82**	**63.41**	**211.43**	**14.60**	**25.07**	**4.62**	**27.70**	**11.99**	**3.06**	**13.02**	**1.94**	**11.97**	**2.28**	**6.05**	**0.83**	**5.08**	**0.73**	**0.56**	**9.05**	**15.33**
Max CA7 and CA10	**4.26**	**10350.19**	**14395.92**			**6010.82**	**155.32**	**747.53**	**94.80**	**125.40**	**18.03**	**88.65**	**26.91**	**7.20**	**29.10**	**4.54**	**27.90**	**5.53**	**15.32**	**2.19**	**13.66**	**1.96**	**10.89**	**35.87**	**55.06**
Min CA7 and CA10	**0.18**	**436.68**	**5.31**			**224.76**	**10.93**	**16.81**	**0.31**	**0.86**	**0.28**	**1.20**	**1.60**	**0.25**	**1.35**	**0.24**	**1.58**	**0.37**	**0.91**	**0.12**	**0.73**	**0.14**	**0.00**	**0.86**	**2.56**

ICP-MS data for crystals from Loc 80 and Loc 25 (ppm)

	Mol % Mg	Mg	Mn	Fe	Fe/Mn	Sr	Y	Ba	La	Ce	Pr	Nd	Sm	Eu	Gd	Tb	Dy	Ho	Er	Tm	Yb	Lu	Pb	Th	U
RHCII CA3 4 1	0.23	552.63	95.86	1220.47	12.73	490.10	96.16	39.13	3.39	0.12	0.04	0.03	0.02	0.02	0.04	0.03	0.04	0.03	0.03	0.01	0.02	0.01	0.00	0.04	0.21
RHCII CA3 4 2	0.08	200.12	90.70	678.60	7.48	1755.13	9.22	375.53	2.67	0.06	0.01	0.01	0.00	0.00	0.01	0.00	0.00	0.00	0.00	0.00	0.00	0.00	0.00	0.01	0.03
RHCII CA3 4 3	0.27	649.62	225.99	1166.44	5.16	689.50	104.45	81.78	8.98	0.24	0.06	0.05	0.03	0.03	0.05	0.03	0.05	0.04	0.04	0.01	0.03	0.01	0.00	0.05	0.29
RHCII CA3 4 4	0.08	203.23	49.45	675.38	13.66	1938.48	14.37	458.47	3.50	0.09	0.02	0.01	0.00	0.00	0.01	0.00	0.01	0.00	0.00	0.00	0.00	0.00	0.00	0.01	0.10
RHCII CA3 4 5	0.07	167.84	59.71	608.61	10.19	1442.77	6.30	290.21	1.27	0.03	0.01	0.00	0.00	0.00	0.00	0.00	0.00	0.00	0.00	0.00	0.00	0.00	0.00	0.00	0.01
RHCII CA3 4 6	0.06	134.10	40.35	626.64	15.53	1309.82	4.72	278.00	0.81	0.03	0.01	0.00	0.00	0.00	0.00	0.00	0.00	0.00	0.00	0.00	0.00	0.00	0.00	0.00	0.01
RHCII CA3 4 7	0.09	211.87	130.31	518.95	3.98	950.01	24.22	142.47	1.59	0.07	0.02	0.02	0.01	0.01	0.01	0.01	0.01	0.01	0.01	0.00	0.00	0.00	0.00	0.01	0.04
RHCII CA3 4 8	0.23	547.70	68.77	840.04	12.21	719.13	107.58	116.60	8.30	0.22	0.06	0.05	0.02	0.03	0.05	0.03	0.05	0.04	0.03	0.01	0.03	0.01	0.00	0.06	0.31
RHCII CA3 3 1	0.06	142.67	117.57	324.62	2.76	1289.00	7.63	206.48	1.68	0.05	0.01	0.01	0.00	0.00	0.00	0.00	0.00	0.00	0.00	0.00	0.00	0.00	0.00	0.00	0.01
RHCII CA3 3 2	0.15	359.20	117.04	1447.19	12.36	2140.61	5.60	290.25	1.93	4.55	1.00	4.69	1.79	0.31	1.29	0.20	1.38	0.19	0.42	0.13	0.46	0.05	0.20	2.08	4.07
RHCII CA3 3 3	0.19	468.57	664.06	1208.53	1.82	479.06	52.35	17.06	1.47	7.09	2.10	18.03	10.70	3.08	11.07	1.67	10.07	1.83	5.40	0.78	3.63	0.55	0.12	4.58	11.73
RHCII CA3 3 4	0.05	129.53	99.18	995.23	10.03	1268.49	17.24	204.03	4.56	12.69	2.30	13.35	4.32	1.10	4.43	0.45	3.60	0.54	1.73	0.37	1.18	0.21	0.16	1.35	5.97
RHCII CA3 3 5	0.06	135.00	128.62	680.33	5.29	1275.03	7.05	254.19	1.70	4.74	0.82	5.00	2.17	0.27	1.84	0.24	1.61	0.25	0.56	0.06	0.76	0.07	0.18	0.47	0.92
RHCII CA3 3 6	0.13	325.27	306.77	659.40	2.15	814.77	48.25	100.45	4.24	14.19	3.09	21.83	11.16	2.84	10.52	1.43	10.69	2.10	3.80	0.84	2.86	0.56	0.16	3.08	11.92
RHCII CA3 2 1	0.06	157.16	195.54	811.02	4.15	1486.88	15.19	309.92	4.90	12.42	1.36	9.32	4.09	0.60	2.82	0.36	3.40	0.48	1.78	0.20	1.09	0.12	0.01	0.76	3.48
RHCII CA3 2 2	0.26	627.73	222.95	1232.19	5.53	550.92	76.85	59.78	6.62	17.45	3.84	25.71	11.20	3.15	15.83	2.32	14.33	3.26	8.11	1.17	6.94	1.18	0.03	7.79	32.69
RHCII CA3 2 3	0.35	859.76	256.65	2168.19	8.45	552.20	77.24	81.47	11.10	25.82	4.57	30.45	12.38	3.35	12.64	2.27	14.08	2.35	8.15	1.16	5.64	0.71	0.16	5.31	25.22
RHCII CA3 2 4	0.06	137.34	533.93	231.43	0.43	1458.18	10.40	265.63	3.23	8.01	1.32	8.08	1.83	0.72	3.16	0.50	2.48	0.45	1.08	0.11	0.82	0.12	0.26	0.47	1.00
RHCII CA3 2 5	0.43	1037.18	1105.75	1609.59	1.46	1085.82	87.63	76.49	9.52	32.03	10.13	49.75	15.75	4.26	17.29	2.61	16.63	3.41	9.36	1.26	8.50	1.28	0.22	9.78	25.08
RHCII CA3 2 6	0.06	155.82	137.76	1067.01	7.75	1497.79	8.28	331.87	2.05	5.60	0.77	4.55	2.16	0.36	1.90	0.33	2.45	0.45	0.75	0.11	0.54	0.14	0.20	0.36	1.05
RHCII CA3 1 1	0.26	633.96	175.61	1590.41	9.06	1546.29	10.28	331.82	5.24	9.76	1.32	6.21	2.29	0.49	2.86	0.19	2.35	0.51	0.88	0.15	1.19	0.14	0.49	1.38	2.55
RHCII CA3 1 2	0.12	301.29	248.37	547.90	2.21	1511.47	7.97	327.37	3.27	6.19	1.08	7.15	2.03	0.34	2.10	0.27	1.59	0.41	0.53	0.23	0.75	0.15	1.48	0.48	1.85
RHCII CA3 1 3	0.25	613.99	357.19	1518.76	4.25	468.57	82.04	34.75	8.54	26.08	5.10	36.69	14.16	4.00	15.58	2.13	15.88	3.04	7.96	1.27	7.16	0.88	0.17	3.68	17.85
RHCII CA3 1 4	0.29	693.50	379.55	863.55	2.28	693.76	103.53	73.16	11.87	32.58	5.92	51.07	20.49	6.12	27.16	3.39	22.91	5.31	10.92	1.39	8.87	1.20	0.14	7.46	22.08
RHCII CA3 1 5	0.25	595.70	296.93	1092.68	3.68	598.91	79.50	80.11	9.81	25.67	5.29	37.49	16.91	4.63	19.02	2.67	17.97	3.14	8.42	1.20	6.97	0.82	0.45	5.91	24.02
RHCII CA3 1 6	0.28	671.76	350.34	1015.83	2.90	617.13	91.79	74.85	12.69	32.60	8.01	46.86	17.92	5.05	21.52	3.25	18.75	4.11	10.77	1.25	7.41	1.29	0.30	4.95	23.39
Mean	**0.17**	**412.02**	**248.27**	**976.88**	**6.44**	**1101.15**	**44.45**	**188.53**	**5.19**	**10.71**	**2.24**	**14.48**	**5.82**	**1.57**	**6.58**	**0.94**	**6.17**	**1.23**	**3.11**	**0.45**	**2.49**	**0.37**	**0.18**	**2.31**	**8.30**
Max	**0.43**	**1037.18**	**1105.75**	**2168.19**	**15.53**	**2140.61**	**107.58**	**458.47**	**12.69**	**32.60**	**10.13**	**51.07**	**20.49**	**6.12**	**27.16**	**3.39**	**22.91**	**5.31**	**10.92**	**1.39**	**8.87**	**1.29**	**1.48**	**9.78**	**32.69**
Min	**0.05**	**129.53**	**40.35**	**231.43**	**0.43**	**468.57**	**4.72**	**17.06**	**0.81**	**0.03**	**0.01**	**0.00**	**0.00**	**0.00**	**0.00**	**0.00**	**0.00**	**0.00**	**0.00**	**0.00**	**0.00**	**0.00**	**0.00**	**0.00**	**0.01**

ICP-MS data for crystals from Loc 80 and Loc 25 (ppm)

	Mol % Mg	Mg	Mn	Fe	Fe/Mn	Sr	Y	Ba	La	Ce	Pr	Nd	Sm	Eu	Gd	Tb	Dy	Ho	Er	Tm	Yb	Lu	Pb	Th	U
RHCII CA5 4 1	0.07	174.99	131.81	923.67	7.01	1437.11	12.26	534.09	5.19	10.03	1.94	11.19	4.31	0.81	3.18	0.49	2.27	0.53	0.96	0.13	1.34	0.10	0.03	2.07	13.08
RHCII CA5 4 2	0.33	790.88	2023.04	2185.86	1.08	694.97	86.65	164.05	16.38	43.49	10.14	63.21	28.40	5.77	22.66	2.83	19.62	3.48	11.45	1.54	8.71	1.04	0.26	6.80	26.97
RHCII CA5 4 3	0.09	223.26	371.80	1042.55	2.80	1324.08	9.19	460.39	3.19	8.23	1.21	5.65	4.60	0.41	2.51	0.33	1.87	0.42	1.09	0.21	1.01	0.14	0.35	1.25	5.04
RHCII CA5 4 4	0.11	255.30	149.49	1471.63	9.84	1291.27	8.10	487.78	2.04	5.00	0.97	5.81	2.27	0.24	1.94	0.27	1.84	0.47	0.88	0.17	0.68	0.16	0.34	0.99	5.12
RHCII CA5 4 5	0.31	748.20	850.48	1619.32	1.90	546.46	80.81	109.91	12.50	34.48	7.30	61.30	18.91	5.18	20.87	2.53	19.91	3.26	10.23	1.32	8.48	1.07	0.14	7.84	40.01
RHCII CA5 4 6	0.06	136.59	346.52	795.72	2.30	1355.45	14.08	459.21	5.82	14.36	2.41	20.98	4.18	1.23	4.40	0.59	3.01	0.49	1.35	0.19	0.86	0.26	0.18	2.14	10.50
RHCII CA5 4 7	0.28	674.58	449.92	1399.43	3.11	717.18	100.83	159.94	12.30	36.92	7.46	52.14	20.85	7.42	23.13	3.04	21.46	3.72	10.71	1.45	8.51	1.14	0.33	8.75	36.01
RHCII CA5 4 8	0.27	668.45	1667.63	1737.21	1.04	621.07	111.62	118.84	16.78	44.85	13.62	71.90	23.40	7.57	25.99	3.52	20.59	4.00	11.89	1.69	10.54	1.46	0.19	7.52	26.58
RHCII CA5 3 1	0.07	172.65	66.16	333.05	5.03	2769.61	10.38	299.92	7.45	24.45	3.51	14.07	4.31	0.72	3.08	0.38	2.15	0.51	0.96	0.27	0.57	0.09	n.d.	6.00	5.21
RHCII CA5 3 2	0.13	312.80	1335.41	505.25	0.38	1746.97	29.30	155.76	10.03	23.17	4.27	26.96	8.79	1.73	8.75	1.00	5.67	1.59	3.03	0.39	2.29	0.34	0.29	6.06	5.74
RHCII CA5 3 3	0.54	1303.74	193.70	1535.30	7.93	1127.35	80.53	66.51	14.04	49.94	10.10	79.57	22.75	5.68	21.37	2.71	16.65	3.61	10.13	1.22	7.55	0.99	0.46	18.23	20.66
RHCII CA5 3 4	0.07	178.12	125.03	399.23	3.19	2845.82	7.34	408.58	4.58	14.02	2.03	9.89	1.88	0.26	2.07	0.29	1.50	0.27	0.98	0.11	0.63	0.13	0.18	2.20	4.40
RHCII CA5 3 5	0.51	1251.09	198.89	1527.72	7.68	1136.76	80.19	45.89	15.52	58.61	10.92	71.66	24.60	5.34	20.32	2.55	15.85	3.33	8.87	1.35	7.60	1.18	0.06	18.23	20.50
RHCII CA5 3 6	0.08	196.64	179.78	564.73	3.14	3209.50	3.32	340.42	3.45	11.60	1.61	7.64	1.56	0.00	1.23	0.25	1.14	0.15	0.37	0.09	0.21	0.06	0.14	0.96	1.17
RHCII CA5 2 1	0.25	605.46	455.46	1600.55	3.51	1634.83	19.24	288.36	5.14	14.18	3.00	14.83	5.11	0.77	3.96	0.58	3.89	0.87	2.31	0.30	2.08	0.33	0.17	2.24	7.41
RHCII CA5 2 2	0.13	305.24	581.23	499.71	0.86	2874.88	3.54	282.78	1.85	6.77	1.08	5.73	1.85	0.07	1.24	0.14	0.89	0.26	0.63	0.09	0.34	0.10	0.08	1.15	1.15
RHCII CA5 2 3	0.55	1327.33	1670.95	1273.75	0.76	922.48	76.00	63.29	11.61	40.98	8.73	68.62	22.17	4.47	20.20	2.52	15.48	3.27	8.81	1.13	7.76	1.59	0.75	6.81	17.10
RHCII CA5 2 4	0.60	1446.53	1515.39	1948.94	1.29	1117.24	64.96	42.11	8.06	35.17	9.60	54.15	17.61	3.36	16.96	1.96	16.12	2.50	7.30	1.06	5.51	0.72	0.15	16.62	19.28
RHCII CA5 2 5	0.15	369.27	214.54	738.00	3.44	2645.46	6.40	290.20	2.17	7.85	1.55	5.84	1.22	0.26	2.14	0.21	1.50	0.18	0.98	0.20	0.86	0.13	0.27	2.23	2.28
RHCII CA5 2 6	0.01	31.18	241.94	696.88	2.88	1457.25	5.53	259.77	3.24	14.73	2.11	11.33	3.04	1.11	3.06	0.34	0.54	0.24	0.50	0.13	0.62	0.04	0.11	0.44	n.d.
RHCII CA5 1 1	0.28	682.27	n.d.	1916.32	-	1803.20	4.54	337.32	1.22	3.69	0.75	3.49	0.29	0.29	1.20	0.37	0.92	0.14	0.51	0.11	0.86	0.14	0.56	0.70	1.66
RHCII CA5 1 2	0.10	242.92	523.23	646.26	1.24	3080.99	3.39	289.56	2.58	9.46	1.64	8.63	2.43	0.00	1.30	0.22	0.47	0.22	0.67	0.07	0.34	0.07	n.d.	3.07	1.47
RHCII CA5 1 3	0.34	819.42	n.d.	1227.90	-	1121.27	97.48	75.61	6.63	28.40	8.52	64.21	22.43	4.72	23.13	4.66	17.62	3.30	9.24	1.13	7.35	0.88	0.28	10.39	22.63
RHCII CA5 1 4	0.57	1376.70	1997.57	2410.51	1.21	1069.86	64.40	56.26	8.74	32.60	6.95	46.88	14.19	3.80	14.78	2.55	13.33	2.31	6.72	0.95	5.11	0.72	0.16	12.78	12.47
RHCII CA5 1 5	0.14	340.48	793.29	782.71	0.99	1921.82	6.49	179.86	5.99	14.42	2.02	9.81	2.72	0.71	2.10	0.38	0.95	0.35	0.87	0.01	0.84	0.17	n.d.	2.59	2.81
RHCII CA5 1 6	0.37	888.35	990.77	1713.38	1.73	801.28	52.70	71.46	10.39	24.87	5.07	39.98	15.72	4.61	16.50	1.98	12.15	2.23	5.58	0.75	3.58	0.55	0.21	3.00	10.11
Mean	**0.25**	**597.02**	**711.42**	**1211.37**	**3.10**	**1587.47**	**39.97**	**232.61**	**7.57**	**23.55**	**4.94**	**32.13**	**10.75**	**2.56**	**10.31**	**1.41**	**8.36**	**1.60**	**4.50**	**0.62**	**3.62**	**0.52**	**0.25**	**5.81**	**12.77**
Max	**0.60**	**1446.53**	**2023.04**	**2410.51**	**9.84**	**3209.50**	**111.62**	**534.09**	**16.78**	**58.61**	**13.62**	**79.57**	**28.40**	**7.57**	**25.99**	**4.66**	**21.46**	**4.00**	**11.89**	**1.69**	**10.54**	**1.59**	**0.75**	**18.23**	**40.01**
Min	**0.01**	**31.18**	**66.16**	**333.05**	**0.38**	**546.46**	**3.32**	**42.11**	**1.22**	**3.69**	**0.75**	**3.49**	**0.29**	**0.00**	**1.20**	**0.14**	**0.47**	**0.14**	**0.37**	**0.01**	**0.21**	**0.04**	**0.03**	**0.44**	**1.15**

ICP-MS data for crystals from Loc 80 and Loc 25 (ppm)

	Mol % Mg	Mg	Mn	Fe	Fe/Mn	Sr	Y	Ba	La	Ce	Pr	Nd	Sm	Eu	Gd	Tb	Dy	Ho	Er	Tm	Yb	Lu	Pb	Th	U
RHCII CA6 4 1	0.38	920.00	6805.18	4889.69	0.72	534.95	42.88	68.20	7.79	20.06	4.13	36.23	14.33	4.03	13.57	1.59	9.93	2.03	6.04	0.83	5.33	0.77	0.67	3.13	13.33
RHCII CA6 4 2	0.22	541.73	5998.13	965.37	0.16	403.48	27.22	22.67	1.30	5.12	1.30	14.06	8.09	1.86	8.01	1.18	8.08	1.09	3.99	0.63	3.95	0.66	n.d.	2.95	25.04
RHCII CA6 4 3	0.23	567.07	2119.74	647.20	0.31	705.82	56.92	109.17	7.57	25.56	5.70	34.14	9.12	2.68	11.70	1.79	10.98	2.24	5.59	0.90	5.55	0.84	0.58	6.73	21.47
RHCII CA6 4 4	0.22	529.03	784.02	562.08	0.72	1362.90	6.07	545.40	1.05	3.27	0.69	4.54	1.07	0.07	1.21	0.19	1.45	0.26	0.62	0.15	0.98	0.23	n.d.	0.73	4.43
RHCII CA6 4 5	0.39	949.73	849.84	564.01	0.66	677.47	76.15	153.22	6.18	21.86	5.52	41.04	16.10	4.36	18.17	2.54	15.46	3.13	9.76	1.34	8.01	1.40	1.26	10.48	36.12
RHCII CA6 4 6	0.12	295.66	224.36	271.26	1.21	1620.53	13.75	700.59	2.43	8.69	1.81	8.90	2.48	0.54	2.45	0.71	2.39	0.32	1.43	0.24	0.92	0.03	0.64	3.57	16.28
RHCII CA6 4 7	0.09	214.87	3285.01	308.28	0.09	1120.42	17.26	199.86	1.75	6.06	1.59	10.94	4.11	1.32	3.83	0.93	3.31	0.44	1.82	0.36	2.46	0.34	0.16	1.12	8.36
RHCII CA6 4 8	0.12	294.77	3377.49	573.34	0.17	706.50	52.36	11.77	2.01	7.04	2.38	23.96	12.51	4.21	14.77	2.00	12.39	2.08	5.77	0.82	3.80	0.74	0.12	2.34	8.26
RHCII CA6 3 1	0.31	752.08	2000.43	1872.74	0.94	488.66	60.35	68.47	5.72	26.29	7.12	51.02	21.74	5.19	19.38	2.89	16.64	3.04	8.66	1.45	7.53	1.15	0.35	4.95	17.64
RHCII CA6 3 2	0.05	131.31	1155.90	345.99	0.30	1321.12	3.49	421.78	2.29	6.74	1.17	6.98	2.24	0.46	0.85	0.14	1.47	0.20	0.93	0.18	0.34	0.13	0.14	0.57	0.98
RHCII CA6 3 3	0.14	350.97	2318.14	530.41	0.23	1490.11	5.25	556.76	2.37	7.76	1.16	5.52	1.99	0.20	1.29	0.19	1.13	0.26	0.38	0.05	0.43	0.13	0.78	0.73	2.07
RHCII CA6 3 4	0.36	877.50	2186.55	848.70	0.39	873.12	85.77	229.04	16.77	50.69	13.61	74.01	23.25	5.41	22.44	2.76	21.56	3.25	8.74	1.08	8.89	0.85	0.24	8.73	31.82
RHCII CA6 3 5	0.15	365.99	2902.39	623.77	0.21	758.22	40.85	108.83	7.70	15.04	3.26	36.28	6.83	2.26	6.89	0.90	6.22	1.18	3.17	0.51	2.55	0.38	0.48	2.60	9.43
RHCII CA6 3 6	0.31	748.97	6272.56	2345.83	0.37	676.55	14.69	29.11	4.26	8.06	1.44	12.11	5.84	1.27	3.75	0.52	3.67	0.71	1.85	0.27	1.56	0.23	0.71	0.81	4.15
RHCII CA6 2 1	0.43	1052.44	3523.62	1754.89	0.50	490.13	37.08	71.96	7.93	22.64	4.28	27.05	11.95	1.98	9.93	1.30	8.02	1.58	4.43	0.75	5.01	0.86	0.43	4.04	15.34
RHCII CA6 2 2	0.65	1582.06	3794.69	5448.40	1.44	552.96	37.25	56.81	6.92	19.13	3.89	30.50	11.40	2.52	9.33	1.24	9.02	1.68	4.92	0.82	5.61	0.80	0.60	4.24	13.90
RHCII CA6 2 3	0.40	966.76	3059.52	1956.71	0.64	687.33	35.05	156.01	8.69	23.31	3.01	23.24	7.40	1.75	5.58	1.08	7.03	1.13	3.76	0.47	3.45	0.47	0.25	3.64	12.78
RHCII CA6 2 4	0.07	172.27	1446.00	869.58	0.60	1185.74	12.38	449.25	3.62	9.67	2.08	18.45	6.27	0.97	5.64	0.64	2.72	0.71	1.66	0.28	1.66	0.37	1.42	1.72	8.06
RHCII CA6 2 5	0.04	96.52	1053.76	739.21	0.70	1227.32	6.06	456.48	3.01	9.16	1.95	12.76	4.08	0.47	2.13	0.38	1.88	0.33	0.64	0.05	0.52	0.06	0.10	1.67	7.15
RHCII CA6 2 6	0.33	810.33	3216.83	1093.81	0.34	704.84	43.24	71.13	7.19	22.63	4.54	28.34	10.95	2.80	10.76	1.77	9.26	1.90	4.43	0.83	4.60	0.66	0.08	3.53	12.60
RHCII CA6 1 1	0.05	115.46	772.82	561.83	0.73	1104.63	4.44	380.15	1.36	4.91	0.71	4.76	1.45	0.22	1.69	0.25	1.04	0.27	0.32	0.14	0.32	0.19	0.30	0.27	0.67
RHCII CA6 1 2	0.09	216.94	1296.18	549.52	0.42	1530.26	13.69	655.80	6.41	19.62	3.68	18.32	4.91	1.04	4.28	0.56	2.93	0.69	1.27	0.18	1.10	0.25	0.00	3.36	14.50
RHCII CA6 1 3	0.06	137.83	752.65	449.34	0.60	1235.86	7.04	429.16	2.43	9.55	1.65	8.04	2.55	0.49	2.18	0.30	1.30	0.21	1.04	0.07	0.69	0.16	0.32	1.12	3.61
RHCII CA6 1 4	0.08	200.48	3370.43	539.71	0.16	933.85	19.41	150.10	4.99	9.22	1.51	10.36	3.28	0.83	4.92	0.32	2.77	0.73	1.55	0.38	2.36	0.24	0.17	0.46	4.41
RHCII CA6 1 5	0.27	647.25	1086.62	1286.45	1.18	761.81	40.30	180.56	4.25	13.51	3.23	30.58	15.77	2.89	10.20	1.51	8.68	1.62	5.02	0.95	4.54	0.59	0.10	3.85	15.76
RHCII CA6 1 6	0.11	275.87	3086.36	937.73	0.30	742.08	30.10	70.96	1.48	4.67	1.55	14.76	9.40	1.86	6.55	1.27	7.50	1.00	3.74	0.68	3.18	0.44	0.30	1.50	11.93
Mean	**0.22**	**531.30**	**2566.89**	**1212.92**	**0.54**	**919.10**	**30.35**	**244.36**	**4.90**	**14.63**	**3.19**	**22.57**	**8.43**	**1.99**	**7.75**	**1.11**	**6.80**	**1.23**	**3.52**	**0.55**	**3.28**	**0.50**	**0.43**	**3.03**	**12.31**
Max	**0.65**	**1582.06**	**6805.18**	**5448.40**	**1.44**	**1620.53**	**85.77**	**700.59**	**16.77**	**50.69**	**13.61**	**74.01**	**23.25**	**5.41**	**22.44**	**2.89**	**21.56**	**3.25**	**9.76**	**1.45**	**8.89**	**1.40**	**1.42**	**10.48**	**36.12**
Min	**0.04**	**96.52**	**224.36**	**271.26**	**0.09**	**403.48**	**3.49**	**11.77**	**1.05**	**3.27**	**0.69**	**4.54**	**1.07**	**0.07**	**0.85**	**0.14**	**1.04**	**0.20**	**0.32**	**0.05**	**0.32**	**0.03**	**0.00**	**0.27**	**0.67**

ICP-MS data for crystals from Loc 80 and Loc 25 (ppm)

	Mol % Mg	Mg	Mn	Fe	Fe/Mn	Sr	Y	Ba	La	Ce	Pr	Nd	Sm	Eu	Gd	Tb	Dy	Ho	Er	Tm	Yb	Lu	Pb	Th	U
RHCII CA7 4 1	0.89	2173.81	5211.75	n.d.	-	984.78	36.70	54.44	4.70	10.47	3.29	25.93	12.49	2.76	12.12	1.26	9.92	1.62	4.36	0.79	5.59	0.91	1.29	2.28	8.42
RHCII CA7 4 2	0.20	493.76	2829.14	n.d.	-	1906.64	92.16	57.53	4.83	17.03	5.16	45.16	26.23	7.21	27.42	3.68	22.84	4.03	11.55	1.42	8.71	1.12	0.12	2.45	4.35
RHCII CA7 4 3	0.49	1187.13	2862.48	n.d.	-	1248.09	70.87	65.31	3.10	17.01	3.06	27.28	17.27	3.54	15.53	2.20	14.27	2.74	7.70	1.14	7.11	1.01	0.10	3.44	8.02
RHCII CA7 4 4	0.12	290.99	841.11	n.d.	-	2153.41	16.97	561.53	2.98	8.69	2.51	14.64	8.57	1.62	5.48	0.78	4.53	0.74	2.06	0.28	1.62	0.21	0.05	0.93	6.04
RHCII CA7 4 5	0.85	2076.27	2274.06	n.d.	-	961.29	37.48	110.87	7.03	18.76	4.99	30.20	14.26	3.70	9.90	1.38	10.21	1.42	5.46	0.82	6.03	0.53	0.35	2.94	11.24
RHCII CA7 4 6	0.27	649.35	5287.24	n.d.	-	1016.48	48.10	37.40	2.86	10.66	2.81	33.01	19.07	4.37	18.33	2.46	13.88	1.85	7.17	0.78	5.61	1.00	0.23	1.54	5.19
RHCII CA7 3 1	0.47	1131.57	4868.28	n.d.	-	541.63	24.57	22.21	0.95	5.67	1.50	14.96	8.65	1.82	5.96	0.72	6.11	1.28	3.63	0.79	4.62	0.78	3.64	1.70	8.28
RHCII CA7 3 2	0.45	1088.96	6271.64	n.d.	-	1078.41	19.15	279.32	7.41	22.69	4.54	28.61	10.14	2.94	11.15	1.03	8.35	1.81	3.92	0.46	3.09	0.50	0.19	2.19	10.56
RHCII CA7 3 3	0.74	1804.94	5346.71	n.d.	-	881.38	15.35	160.32	4.80	20.72	3.15	22.01	9.90	1.78	7.62	0.91	5.96	1.20	3.88	0.43	2.86	0.54	0.65	1.44	6.90
RHCII CA7 3 4	0.29	694.63	3275.56	n.d.	-	1172.12	39.35	162.21	5.92	16.45	5.17	36.20	15.01	4.15	15.20	2.18	10.85	2.06	4.09	0.72	3.04	0.59	n.d.	2.58	11.88
RHCII CA7 3 5	1.61	3908.15	4816.98	n.d.	-	920.86	21.27	152.38	20.12	24.10	4.69	22.69	9.76	1.62	5.60	1.10	7.22	1.03	2.93	0.31	2.23	0.30	1.42	2.35	5.35
RHCII CA7 3 6	0.10	254.18	4218.57	n.d.	-	1071.03	20.86	64.81	5.61	8.10	1.49	8.29	6.20	1.14	4.96	0.73	5.00	1.21	2.30	0.40	2.78	0.47	3.34	0.61	0.64
RHCII CA7 2 1	0.62	1513.99	4965.17	n.d.	-	702.49	52.40	78.43	3.85	13.01	4.17	32.08	14.23	4.09	13.25	1.79	10.74	2.31	7.07	1.19	5.28	1.25	0.30	3.85	18.66
RHCII CA7 2 2	0.27	656.29	5164.53	n.d.	-	867.49	38.67	33.73	1.96	7.70	2.39	21.63	10.94	3.17	10.54	1.09	8.83	2.12	5.97	0.79	3.85	0.85	0.83	2.76	11.49
RHCII CA7 2 3	0.18	437.83	1687.46	n.d.	-	1525.62	14.26	405.15	3.17	8.47	1.90	13.23	6.58	1.15	3.03	0.63	2.25	0.64	1.40	0.40	1.90	0.21	n.d.	1.60	7.64
RHCII CA7 2 4	0.56	1366.90	4789.09	n.d.	-	739.82	49.70	76.00	2.76	11.72	2.82	32.34	15.48	4.21	14.66	1.89	11.50	2.69	7.23	1.01	6.27	0.72	0.74	4.81	17.85
RHCII CA7 2 5	1.08	2622.68	4027.84	n.d.	-	790.41	39.45	135.45	3.95	17.14	3.74	28.97	14.95	4.30	10.85	1.35	10.64	2.31	6.78	1.10	6.85	0.88	0.01	5.83	34.86
RHCII CA7 2 6	0.54	1318.69	7248.45	n.d.	-	536.34	24.55	49.88	2.11	5.72	1.70	18.53	7.48	2.56	8.30	1.00	5.81	1.51	4.49	0.65	5.30	0.57	0.43	2.74	15.86
RHCII CA7 2 7	0.29	706.50	1068.83	n.d.	-	1595.85	10.23	901.27	1.88	6.15	1.11	5.59	5.50	1.27	2.29	0.67	2.99	0.60	1.58	0.14	2.16	0.05	0.75	0.60	3.03
RHCII CA7 2 8	0.71	1718.88	2629.89	n.d.	-	575.54	42.99	102.65	3.03	12.96	2.85	37.86	16.32	2.95	13.02	2.05	10.62	2.55	6.60	1.01	5.47	1.02	1.02	7.47	29.83
RHCII CA7 1 1	0.28	668.92	902.12	n.d.	-	1516.20	26.22	875.97	4.49	11.41	2.65	16.40	8.20	2.20	6.66	1.07	7.18	1.36	3.75	0.60	3.46	0.36	0.96	2.57	9.02
RHCII CA7 1 2	0.26	642.02	6031.81	n.d.	-	887.15	28.58	35.07	4.63	11.85	2.20	18.66	8.42	2.05	8.72	1.48	7.01	1.32	3.22	0.71	3.23	0.49	0.04	1.31	6.76
RHCII CA7 1 3	0.57	1382.57	7046.55	n.d.	-	845.04	39.55	32.48	7.82	4.36	2.40	17.17	10.49	3.17	8.82	1.33	8.88	1.68	5.92	0.57	4.47	0.56	1.45	1.20	4.03
RHCII CA7 1 4	0.77	1869.14	4433.20	n.d.	-	1731.91	92.68	169.12	23.69	80.76	19.21	101.93	30.82	8.27	26.27	3.52	21.07	3.83	10.36	1.41	8.08	1.12	0.31	10.85	25.58
RHCII CA7 1 5	0.37	910.27	6226.97	n.d.	-	1891.64	59.88	239.97	7.04	23.76	7.75	74.33	28.35	7.15	23.90	2.99	16.05	2.88	7.59	1.38	6.64	1.21	0.34	4.35	27.95
RHCII CA7 1 6	0.33	791.79	6194.03	n.d.	-	566.94	29.24	28.89	0.86	3.60	1.41	14.36	7.94	2.27	7.12	1.32	7.12	1.59	4.53	0.71	4.90	0.48	0.01	3.50	16.73
RHCII CA7 1 7	0.26	631.36	4959.19	n.d.	-	1116.61	24.21	117.44	3.16	9.88	2.90	24.64	11.37	2.01	8.50	1.03	6.78	1.16	3.70	0.45	2.97	0.49	n.d.	1.35	5.80
RHCII CA7 1 8	0.33	800.89	5410.22	n.d.	-	1415.78	53.38	142.35	6.34	26.59	6.89	52.18	21.54	4.42	18.43	1.98	11.60	2.41	6.92	0.96	5.66	0.69	0.01	4.66	18.29
RHCII CA7 1 9	0.19	456.37	1841.85	n.d.	-	1524.38	29.43	582.83	5.17	14.00	3.36	23.63	10.25	2.30	9.61	1.04	7.17	1.59	4.23	0.59	3.25	0.49	0.11	2.27	9.68
Mean	**0.49**	**1180.99**	**4232.09**			**1129.84**	**37.87**	**197.76**	**5.39**	**15.50**	**3.86**	**29.05**	**13.32**	**3.25**	**11.49**	**1.54**	**9.50**	**1.85**	**5.19**	**0.76**	**4.59**	**0.67**	**0.72**	**2.97**	**12.07**
Max	**1.61**	**3908.15**	**7248.45**			**2153.41**	**92.68**	**901.27**	**23.69**	**80.76**	**19.21**	**101.93**	**30.82**	**8.27**	**27.42**	**3.68**	**22.84**	**4.03**	**11.55**	**1.42**	**8.71**	**1.25**	**3.64**	**10.85**	**34.86**
Min	**0.10**	**254.18**	**841.11**			**536.34**	**10.23**	**22.21**	**0.86**	**3.60**	**1.11**	**5.59**	**5.50**	**1.14**	**2.29**	**0.63**	**2.25**	**0.60**	**1.40**	**0.14**	**1.62**	**0.05**	**0.01**	**0.60**	**0.64**
Mean CA3,5,6,7	**0.29**	**694.37**	**2028.56**			**1182.86**	**38.15**	**215.31**	**5.75**	**16.08**	**3.57**	**24.69**	**9.69**	**2.37**	**9.10**	**1.26**	**7.76**	**1.49**	**4.11**	**0.60**	**3.53**	**0.52**	**0.40**	**3.52**	**11.37**
Max CA3,5,6,7	**1.61**	**3908.15**	**7248.45**			**3209.50**	**111.62**	**901.27**	**23.69**	**80.76**	**19.21**	**101.93**	**30.82**	**8.27**	**27.42**	**4.66**	**22.91**	**5.31**	**11.89**	**1.69**	**10.54**	**1.59**	**3.64**	**18.23**	**40.01**
Min CA3,5,6,7	**0.01**	**31.18**	**40.35**			**403.48**	**3.32**	**11.77**	**0.81**	**0.03**	**0.01**	**0.00**	**0.00**	**0.00**	**0.00**	**0.00**	**0.00**	**0.00**	**0.00**	**0.00**	**0.00**	**0.00**	**0.00**	**0.00**	**0.01**

ICP-MS data for crystals from Loc 80 and Loc 25 (ppm)

	Mol % Mg	Mg	Mn	Fe	Fe/Mn	Sr	Y	Ba	La	Ce	Pr	Nd	Sm	Eu	Gd	Tb	Dy	Ho	Er	Tm	Yb	Lu	Pb	Th	U
Loc 25 4 1	0.94	2283.75	3624.17	n.d.	-	3117.60	9.49	2050.14	9.14	13.17	2.88	14.18	1.42	0.39	1.98	0.29	1.55	0.18	0.55	0.13	1.64	0.20	0.35	3.09	7.59
Loc 25 4 2	3.29	7999.99	2888.52	n.d.	-	2189.18	28.72	1426.70	95.70	64.78	12.96	50.80	10.40	2.24	7.39	1.15	5.86	1.02	3.40	0.38	3.01	0.42	2.21	7.64	17.91
Loc 25 4 3	2.40	5823.87	6655.30	n.d.	-	2784.33	25.97	1775.73	66.11	48.92	11.79	48.37	8.95	2.14	7.08	1.19	5.43	0.85	2.27	0.47	3.41	0.59	0.67	7.39	16.43
Loc 25 4 4	1.00	2433.13	3813.96	n.d.	-	2947.73	9.43	2208.11	12.01	17.77	3.53	15.28	2.42	0.72	1.62	0.26	1.51	0.15	1.28	0.07	1.01	0.27	0.10	5.28	12.20
Loc 25 4 5	2.00	4873.00	3580.63	n.d.	-	2266.36	73.18	1424.55	88.08	90.20	20.74	92.08	18.08	4.65	16.97	2.60	12.78	2.14	7.87	1.16	10.64	2.09	1.06	21.63	46.05
Loc 25 3 3	1.77	4312.78	3237.73	n.d.	-	2218.06	100.83	1152.08	72.24	101.59	26.60	125.62	25.10	5.38	23.42	3.27	18.32	3.10	8.64	1.55	10.40	1.83	0.14	21.87	43.94
Loc 25 3 4	0.70	1706.66	5218.35	n.d.	-	3058.97	10.95	2186.03	15.78	21.47	4.16	17.99	2.22	0.52	2.40	0.41	1.95	0.29	0.96	0.17	1.65	0.14	0.22	4.51	9.13
Loc 25 3 5	1.43	3472.72	n.d.	n.d.	-	2780.37	32.47	1683.43	60.22	71.93	12.89	50.93	9.70	2.39	8.12	1.30	5.37	1.09	2.95	0.40	3.79	0.52	11.03	7.70	16.89
Loc 25 3 6	0.66	1613.70	3434.21	n.d.	-	3012.33	6.44	2087.36	7.68	11.01	2.60	9.95	1.60	0.49	1.25	0.18	1.07	0.20	0.54	0.07	1.07	0.25	0.02	1.91	4.31
Loc 25 2 1	0.57	1393.21	1113.49	n.d.	-	2630.60	5.45	1395.38	4.77	6.41	1.69	6.73	1.04	-0.01	0.58	0.20	0.84	0.20	0.40	0.04	0.92	0.19	0.10	2.08	4.81
Loc 25 2 2	2.64	6424.90	19813.21	n.d.	-	3078.34	41.57	1278.92	118.50	115.94	19.20	80.16	14.05	2.67	9.77	1.29	7.97	1.78	5.01	0.67	4.82	1.02	1.64	12.45	27.59
Loc 25 2 3	0.66	1601.38	10012.82	n.d.	-	2782.75	6.50	1504.54	8.38	10.74	2.19	9.93	1.59	0.16	1.31	0.16	0.81	0.22	0.73	0.11	1.01	0.15	0.04	2.16	5.82
Loc 25 2 4	0.48	1177.41	1095.54	n.d.	-	3117.49	8.25	1454.77	11.72	13.13	3.84	14.00	1.90	0.31	1.62	0.22	0.99	0.25	0.80	0.15	1.05	0.07	0.13	7.05	15.50
Loc 25 2 5	1.86	4527.70	2098.39	n.d.	-	2870.64	101.02	1297.63	60.16	75.74	29.28	126.38	22.28	4.95	16.86	2.45	17.15	3.45	9.47	2.01	16.55	2.40	0.08	39.91	88.27
Loc 25 2 6	1.37	3325.41	1762.86	n.d.	-	2272.85	73.79	1222.57	45.56	60.78	19.68	91.65	19.39	3.68	13.32	1.80	10.84	2.40	8.28	1.45	10.12	1.95	3.67	29.77	68.96
Loc 25 1 1	0.63	1535.14	1114.71	n.d.	-	3005.62	4.29	1592.84	5.44	3.53	2.16	6.85	0.74	0.16	0.57	0.08	0.44	0.12	0.44	0.13	0.71	0.14	0.09	1.77	3.64
Loc 25 1 2	0.59	1433.96	357.48	n.d.	-	2936.65	4.08	1877.95	5.40	2.44	2.05	6.47	0.86	0.24	0.83	0.08	0.97	0.13	0.33	0.04	0.64	0.10	0.04	1.65	4.36
Loc 25 1 3	1.51	3663.49	41302.42	n.d.	-	2063.18	89.80	726.66	81.89	132.40	29.21	134.19	25.37	6.08	19.93	2.63	16.63	3.16	9.30	2.03	12.99	1.89	0.09	28.70	64.64
Loc 25 1 4	0.57	1379.40	162.43	n.d.	-	979.96	28.39	463.81	22.09	10.68	11.60	49.12	8.91	1.57	5.74	0.75	4.49	0.92	2.82	0.56	5.25	0.83	0.05	11.61	26.69
Loc 25 1 5	1.06	2570.66	695.34	n.d.	-	2180.01	63.96	1008.28	41.92	30.05	18.44	86.25	15.65	2.73	11.36	1.53	8.06	2.53	7.19	1.22	8.97	1.47	0.05	26.09	53.62
Loc 25 1 6	0.66	1614.95	4192.55	n.d.	-	2938.88	4.80	1605.91	6.22	5.85	2.01	7.97	0.71	0.14	0.94	0.15	0.65	0.10	0.40	0.09	1.07	0.25	0.09	2.21	4.60
Mean	**1.28**	**3103.20**	**5808.71**			**2630.09**	**34.73**	**1496.35**	**39.95**	**43.26**	**11.40**	**49.76**	**9.16**	**1.98**	**7.29**	**1.05**	**5.89**	**1.16**	**3.51**	**0.62**	**4.80**	**0.80**	**1.04**	**11.74**	**25.86**
Max	**3.29**	**7999.99**	**41302.42**			**3117.60**	**101.02**	**2208.11**	**118.50**	**132.40**	**29.28**	**134.19**	**25.37**	**6.08**	**23.42**	**3.27**	**18.32**	**3.45**	**9.47**	**2.03**	**16.55**	**2.40**	**11.03**	**39.91**	**88.27**
Min	**0.48**	**1177.41**	**162.43**			**979.96**	**4.08**	**463.81**	**4.77**	**2.44**	**1.69**	**6.47**	**0.71**	**-0.01**	**0.57**	**0.08**	**0.44**	**0.10**	**0.33**	**0.04**	**0.64**	**0.07**	**0.02**	**1.65**	**3.64**
Mean all	**0.86**	**2080.23**	**2730.83**	**1133.72**	**3.37**	**1495.07**	**43.48**	**337.68**	**12.01**	**21.50**	**4.60**	**27.30**	**9.82**	**2.43**	**9.62**	**1.38**	**8.42**	**1.62**	**4.45**	**0.65**	**4.01**	**0.59**	**0.50**	**5.94**	**18.86**
Max all	**4.26**	**10350.19**	**41302.42**	**5448.40**	**15.53**	**6010.82**	**155.32**	**2208.11**	**118.50**	**132.40**	**29.28**	**134.19**	**30.82**	**8.27**	**29.10**	**4.66**	**27.90**	**5.53**	**15.32**	**2.19**	**16.55**	**2.40**	**11.03**	**39.91**	**110.94**
Min all	**0.01**	**31.18**	**5.31**	**231.43**	**0.09**	**224.76**	**3.32**	**11.77**	**0.31**	**0.03**	**0.01**	**0.00**	**0.00**	**-0.01**	**0.00**	**0.00**	**0.00**	**0.00**	**0.00**	**0.00**	**0.00**	**0.00**	**0.00**	**0.00**	**0.01**

Appendix 9: Laser ablation ICP-MS analyses of calcite crystals from contemporary lakes in Tanzania

ICP-MS data for crystals from Lake Natron, Lake Ndutu and Lake Makat (ppm)

	Mol % Mg	Mg	Mn	Fe	Fe/Mn	Sr	Y	Ba	La	Ce	Pr	Nd	Sm	Eu	Gd	Tb	Dy	Ho	Er	Tm	Yb	Lu	Pb	Th	U
Lake Natron 4 1	0.13	317.92	363.26	394.02	1.08	1023.24	379.86	51.12	27.29	43.73	9.94	51.02	39.30	9.20	69.02	9.71	73.72	11.95	39.02	4.07	23.54	4.44	0.39	8.86	5.05
Lake Natron 4 2	0.43	1048.12	482.72	1275.05	2.64	825.19	523.74	29.16	9.75	35.67	11.48	116.26	95.29	17.02	139.14	20.51	114.19	19.71	58.54	7.77	41.14	5.30	0.12	12.05	12.33
Lake Natron 4 3	0.18	439.97	1667.20	837.24	0.50	958.40	435.79	88.25	19.40	39.42	9.33	59.02	51.87	8.98	76.71	12.47	79.44	13.50	36.19	5.77	30.94	4.95	0.22	6.79	5.31
Lake Natron 4 4	0.18	430.52	353.23	922.12	2.61	921.83	319.93	116.64	15.54	39.76	7.67	56.78	31.32	9.36	58.54	9.00	61.30	9.89	30.08	4.54	28.29	3.19	0.22	9.13	7.00
Lake Natron 4 5	0.48	1161.92	723.36	1566.66	2.17	582.97	350.43	26.79	6.23	25.56	6.74	63.12	60.71	9.92	89.63	11.57	80.40	12.98	38.99	4.82	34.53	5.30	0.27	9.09	8.34
Lake Natron 3 1	0.04	102.85	550.36	269.57	0.49	2085.32	172.16	615.22	78.72	209.71	33.27	146.73	24.33	3.34	24.44	3.84	30.16	5.22	16.53	2.39	20.98	3.28	0.09	1.65	0.20
Lake Natron 3 2	0.11	271.80	308.90	452.59	1.47	935.20	335.01	87.95	14.18	55.04	13.73	87.84	40.06	8.54	50.93	9.34	59.02	12.61	38.34	6.35	36.10	4.60	0.02	11.07	3.64
Lake Natron 3 3	0.13	315.68	752.92	479.42	0.64	497.88	362.21	22.48	14.15	41.10	11.85	84.14	45.18	9.96	58.87	9.30	69.90	14.81	43.18	5.83	37.31	5.50	0.06	9.42	4.77
Lake Natron 3 4	0.08	196.62	1270.89	658.96	0.52	584.24	126.88	30.81	14.37	23.34	3.36	22.16	14.73	3.58	25.09	3.54	22.45	4.62	12.86	2.05	13.64	2.20	n.d.	1.18	0.97
Lake Natron 2 1	0.13	317.55	272.20	1133.67	4.16	1662.73	62.42	204.13	19.05	27.09	5.27	28.93	9.28	1.08	10.31	1.83	11.40	3.06	5.59	1.25	5.58	0.79	0.30	7.86	5.86
Lake Natron 2 2	0.09	216.88	158.62	657.75	4.15	1389.87	58.15	128.33	4.17	16.43	3.95	22.23	9.96	1.39	8.30	1.79	8.27	1.88	6.45	1.21	6.16	1.15	0.01	7.68	4.99
Lake Natron 2 3	0.06	155.02	336.30	642.59	1.91	1508.45	37.84	179.41	2.18	10.65	2.27	11.81	3.64	0.73	4.71	1.00	6.42	1.73	4.82	1.15	4.78	0.55	0.30	2.26	1.83
Lake Natron 2 4	0.07	176.20	306.04	700.58	2.29	1551.59	42.89	180.44	3.12	11.91	3.08	22.13	3.59	0.26	5.82	0.99	6.96	1.92	7.69	0.70	4.52	1.13	0.01	4.13	2.48
Lake Natron 2 5	0.06	141.22	174.07	576.51	3.31	1559.51	44.81	176.49	2.94	12.29	2.47	15.40	6.69	0.57	5.63	1.29	7.76	1.70	4.08	1.02	5.82	1.01	0.05	3.41	2.63
Lake Natron 1 1	0.12	298.57	1675.68	589.30	0.35	823.84	13.63	3.97	20.53	31.50	2.42	6.14	3.38	1.85	0.93	0.42	3.48	0.51	1.98	0.46	3.64	0.81	0.08	0.53	0.00
Lake Natron 1 2	0.28	683.00	2942.17	1366.28	0.46	369.99	1.66	n.d.	2.60	5.23	0.43	3.04	n.d.	0.48	1.40	0.14	0.76	0.08	0.40	0.06	0.06	0.00	0.09	0.00	0.00
Lake Natron 1 3	0.22	529.04	1354.70	471.19	0.35	528.35	9.81	n.d.	10.21	16.48	1.53	4.34	0.86	0.72	0.64	0.29	1.45	0.38	1.61	0.13	2.54	0.40	0.14	0.71	0.00
Lake Natron 1 4	0.77	1883.19	1115.35	1422.37	1.28	3005.29	19.28	20.39	17.12	27.06	2.60	12.54	3.10	2.45	2.27	0.54	3.81	0.90	2.91	0.33	3.91	0.49	0.27	1.49	0.00
Max	**0.77**	**1883.19**	**2942.17**	**1566.66**	**4.16**	**3005.29**	**523.74**	**615.22**	**78.72**	**209.71**	**33.27**	**146.73**	**95.29**	**17.02**	**139.14**	**20.51**	**114.19**	**19.71**	**58.54**	**7.77**	**41.14**	**5.50**	**0.39**	**12.05**	**12.33**
Min	**0.04**	**102.85**	**158.62**	**269.57**	**0.35**	**369.99**	**1.66**	**3.97**	**2.18**	**5.23**	**0.43**	**3.04**	**0.86**	**0.26**	**0.64**	**0.14**	**0.76**	**0.08**	**0.40**	**0.06**	**0.06**	**0.00**	**0.01**	**0.00**	**0.00**
Average	**0.20**	**482.56**	**822.67**	**800.88**	**1.69**	**1156.33**	**183.14**	**122.60**	**15.64**	**37.33**	**7.30**	**45.20**	**26.08**	**4.97**	**35.13**	**5.42**	**35.60**	**6.52**	**19.40**	**2.77**	**16.86**	**2.50**	**0.16**	**5.41**	**3.63**

ICP-MS data for crystals from Lake Natron, Lake Ndutu and Lake Makat (ppm)

	Mol % Mg	Mg	Mn	Fe	Fe/Mn	Sr	Y	Ba	La	Ce	Pr	Nd	Sm	Eu	Gd	Tb	Dy	Ho	Er	Tm	Yb	Lu	Pb	Th	U
Lake Ndutu 4 1	0.94	2286.26	431.98	2597.13	6.01	7573.53	17.01	1621.21	39.89	59.69	4.75	15.82	2.08	1.18	2.57	0.21	3.31	0.70	2.43	0.22	1.75	0.07	7.56	4.09	5.61
Lake Ndutu 4 2	2.56	6218.46	1171.15	10885.75	9.29	7237.09	12.08	2088.31	34.38	331.28	3.45	11.92	0.07	0.67	2.50	0.58	1.85	0.24	2.05	0.75	1.50	0.31	37.77	10.18	2.70
Lake Ndutu 4 3	0.57	1385.72	861.59	397.79	0.46	8286.07	17.97	1242.55	63.25	146.50	7.58	27.76	2.23	0.55	4.01	0.33	3.22	0.29	2.48	0.27	1.57	0.36	10.06	5.10	1.90
Lake Ndutu 4 4	0.59	1433.43	333.10	1079.32	3.24	5114.77	9.28	1060.06	22.03	56.06	2.52	8.04	0.94	0.26	0.61	0.30	1.38	0.43	0.72	0.20	0.79	0.22	3.82	2.33	5.02
Lake Ndutu 3 1	1.35	3291.14	1879.06	8684.65	4.62	5415.42	23.43	1533.18	85.29	100.30	11.15	42.55	6.32	1.78	5.59	0.87	5.68	1.08	3.30	0.65	1.92	0.38	35.67	13.84	3.12
Lake Ndutu 3 2	1.35	3279.42	2100.13	9670.79	4.60	3554.45	17.33	1390.21	57.18	51.73	9.33	29.13	4.28	0.75	3.75	0.32	4.00	0.61	2.34	0.07	1.34	0.31	35.57	8.74	2.00
Lake Ndutu 3 3	0.88	2140.92	311.75	4825.11	15.48	3453.75	5.30	775.87	17.51	34.54	2.11	6.93	3.97	0.42	1.00	0.18	1.18	0.02	0.69	0.15	0.30	0.31	9.48	3.30	3.92
Lake Ndutu 3 4	0.84	2045.95	482.31	4770.18	9.89	3060.09	9.95	928.89	24.51	66.06	4.27	15.20	0.93	0.38	1.23	0.17	2.03	0.18	1.11	0.19	0.52	0.14	12.10	7.56	6.13
Lake Ndutu 3 5	1.28	3122.91	1121.65	9710.76	8.66	3729.79	13.79	736.58	41.41	82.23	5.54	16.79	0.33	0.78	1.92	0.65	2.03	0.59	1.27	0.25	1.64	0.34	19.03	10.56	2.44
Lake Ndutu 2 1	0.32	789.52	202.06	544.08	2.69	2283.04	4.01	284.15	10.25	13.88	1.99	3.21	1.84	0.83	1.92	0.32	0.25	0.06	0.15	0.15	n.d.	n.d.	1.71	0.66	0.90
Lake Ndutu 2 2	0.65	1586.72	25.68	92.09	3.59	2153.95	2.58	58.71	1.93	5.98	0.46	0.85	n.d.	0.14	n.d.	n.d.	0.04	0.08	0.13	0.09	0.00	n.d.	0.55	0.14	0.11
Lake Ndutu 2 3	0.71	1720.03	4.17	91.40	21.91	2027.13	0.86	3.33	0.12	0.68	0.18	n.d.	n.d.	0.32	n.d.	0.07	n.d.	n.d.	0.21	0.00	n.d.	n.d.	0.15	0.00	0.09
Lake Ndutu 2 4	0.55	1333.39	51.88	390.36	7.52	4198.50	2.72	34.32	6.04	21.88	1.14	2.42	1.43	0.27	n.d.	0.11	n.d.	0.14	0.70	0.11	0.27	n.d.	1.01	0.44	0.08
Lake Ndutu 2 5	0.76	1845.79	680.38	9034.00	13.28	5195.27	19.13	1363.71	65.15	232.66	9.67	26.76	6.48	1.28	5.59	0.80	3.92	0.80	3.07	0.50	2.06	0.34	15.55	5.85	1.49
Lake Ndutu 1 1	0.42	1019.55	269.94	1569.98	5.82	1692.44	37.48	436.39	21.87	47.34	6.21	35.92	9.36	2.17	5.84	1.66	7.35	1.28	4.01	0.60	3.78	0.57	12.76	6.31	0.24
Lake Ndutu 1 2	0.13	309.40	62.20	191.29	3.08	1235.35	30.49	233.38	18.34	29.85	6.54	28.64	9.47	1.66	5.75	1.06	6.72	1.47	6.45	0.68	4.39	0.53	7.75	3.84	0.08
Lake Ndutu 1 3	0.35	860.27	144.40	1125.14	7.79	1783.37	32.95	338.21	19.55	41.88	6.11	28.01	6.56	2.31	7.58	0.99	9.98	1.35	4.40	0.89	3.70	0.65	9.58	5.99	0.16
Lake Ndutu 1 4	0.71	1734.08	449.60	3031.32	6.74	2306.65	31.97	711.11	35.70	82.50	7.45	32.67	9.16	2.43	6.19	0.80	7.47	1.54	4.09	0.93	5.93	0.31	12.46	8.92	0.37
Max	**2.56**	**6218.46**	**2100.13**	**10885.75**	**21.91**	**8286.07**	**37.48**	**2088.31**	**85.29**	**331.28**	**11.15**	**42.55**	**9.47**	**2.43**	**7.58**	**1.66**	**9.98**	**1.54**	**6.45**	**0.93**	**5.93**	**0.65**	**37.77**	**13.84**	**6.13**
Min	**0.13**	**309.40**	**4.17**	**91.40**	**0.46**	**1235.35**	**0.86**	**3.33**	**0.12**	**0.68**	**0.18**	**0.85**	**0.07**	**0.14**	**0.61**	**0.07**	**0.04**	**0.02**	**0.13**	**0.00**	**0.00**	**0.07**	**0.15**	**0.00**	**0.08**
Average	**0.83**	**2022.39**	**587.95**	**3816.17**	**7.48**	**3905.59**	**16.02**	**824.45**	**31.35**	**78.06**	**5.03**	**19.57**	**4.09**	**1.01**	**3.74**	**0.55**	**3.78**	**0.64**	**2.20**	**0.37**	**1.97**	**0.34**	**12.92**	**5.44**	**2.02**

ICP-MS data for crystals from Lake Natron, Lake Ndutu and Lake Makat (ppm)

	Mol % Mg	Mg	Mn	Fe	Fe/Mn	Sr	Y	Ba	La	Ce	Pr	Nd	Sm	Eu	Gd	Tb	Dy	Ho	Er	Tm	Yb	Lu	Pb	Th	U
Lake Makat 4 1	0.06	156.81	25.96	120.59	4.64	3810.79	50.75	370.38	14.41	17.41	6.66	27.38	5.77	3.58	8.26	1.62	8.91	1.58	3.42	0.74	3.80	0.47	0.18	8.15	5.69
Lake Makat 4 2	0.62	1504.16	724.55	1230.24	1.70	5382.10	27.02	517.40	72.32	96.22	10.46	35.89	9.29	2.55	6.46	0.72	5.15	1.07	1.71	0.30	1.66	0.34	4.33	4.71	2.33
Lake Makat 4 3	0.21	507.45	134.52	324.41	2.41	3115.58	41.88	274.76	18.04	27.13	7.08	36.32	7.72	2.45	11.04	1.23	8.83	1.62	5.71	0.76	2.99	0.45	2.85	8.63	3.19
Lake Makat 4 4	0.04	105.27	75.01	313.64	4.18	3350.24	20.70	214.75	11.14	13.78	3.59	16.73	6.49	1.62	2.73	0.46	3.75	1.06	1.26	0.41	3.20	0.44	0.29	1.90	2.32
Lake Makat 4 5	0.14	339.06	206.23	186.04	0.90	3462.39	37.46	235.32	29.55	40.87	7.32	25.82	6.52	1.78	5.58	0.97	4.77	0.75	3.73	0.34	2.50	0.22	1.49	6.19	8.62
Lake Makat 3 1	1.53	3721.39	421.57	3633.06	8.62	2328.52	28.20	783.35	31.33	286.09	6.49	30.73	5.71	1.56	7.08	0.92	5.94	1.22	2.93	0.43	2.82	0.75	15.90	6.90	0.44
Lake Makat 3 2	0.99	2417.95	98.04	590.86	6.03	1987.61	18.50	921.12	21.32	211.32	4.52	18.74	4.00	1.66	4.46	0.70	2.77	0.47	2.63	0.21	1.26	0.44	18.61	5.40	0.06
Lake Makat 3 3	0.37	888.76	29.37	467.79	15.93	1558.13	47.68	456.94	34.38	850.79	7.90	43.50	10.99	3.18	14.08	1.82	9.32	1.44	4.85	0.55	4.97	0.43	4.42	3.16	0.37
Lake Makat 3 4	1.01	2443.35	201.49	2094.27	10.39	1779.53	21.72	551.00	25.13	180.67	5.05	15.79	4.15	0.95	5.61	0.77	3.16	0.76	3.29	0.22	3.87	0.37	11.47	3.77	0.19
Lake Makat 1 1	0.12	289.21	50.92	129.84	2.55	3153.84	33.82	389.58	14.11	9.42	4.49	26.29	6.03	2.06	8.68	1.23	5.07	1.17	4.23	0.45	4.89	0.23	12.26	2.73	0.05
Lake Makat 1 2	0.15	373.06	179.43	39.06	0.22	2133.95	52.40	224.89	21.21	11.17	8.44	49.41	10.66	2.69	10.64	1.91	8.68	1.63	5.18	0.61	5.00	0.89	4.82	3.31	0.52
Lake Makat 1 3	0.05	116.37	n.d.	n.d.	-	1780.19	34.65	218.79	2.51	6.37	1.44	12.40	6.73	1.27	5.74	1.01	4.87	1.17	2.42	0.34	3.27	0.51	4.78	1.37	0.01
Lake Makat 1 4	0.46	1107.95	91.69	574.97	6.27	3324.40	54.14	521.06	32.71	22.43	8.80	43.32	10.32	3.86	12.50	1.64	8.22	1.57	3.87	0.72	4.73	0.81	15.08	4.81	0.24
Lake Makat 1 5	0.79	1920.54	148.77	2440.67	16.41	5171.01	54.12	862.54	51.38	38.56	10.90	56.67	14.19	3.45	14.04	1.57	11.88	1.86	3.28	0.66	4.83	0.36	17.90	4.97	0.12
Max	**1.53**	**3721.39**	**724.55**	**3633.06**	**16.41**	**5382.10**	**54.14**	**921.12**	**72.32**	**850.79**	**10.90**	**56.67**	**14.19**	**3.86**	**14.08**	**1.91**	**11.88**	**1.86**	**5.71**	**0.76**	**5.00**	**0.89**	**18.61**	**8.63**	**8.62**
Min	**0.04**	**105.27**	**25.96**	**39.06**	**0.22**	**1558.13**	**18.50**	**214.75**	**2.51**	**6.37**	**1.44**	**12.40**	**4.00**	**0.95**	**2.73**	**0.46**	**2.77**	**0.47**	**1.26**	**0.21**	**1.26**	**0.22**	**0.18**	**1.37**	**0.01**
Average	**0.47**	**1135.09**	**183.66**	**934.27**	**6.17**	**3024.16**	**37.36**	**467.28**	**27.11**	**129.44**	**6.65**	**31.36**	**7.76**	**2.33**	**8.35**	**1.18**	**6.52**	**1.24**	**3.46**	**0.48**	**3.56**	**0.48**	**8.17**	**4.71**	**1.72**

Appendix 10: XRD Data for relative ordering, reflection ratio, unit cell, and Mol% $CaCO_3$

Dolomite	Peak intensity 015 reflection	Peak intensity 110 reflection	Peak intensity 113 reflection	Relative Order %	Reflection ratio
Upper Bed I dolomite (upper unit) RHCI CA9U	260	746	1506	54.44	0.85
Upper Bed I dolomite (lower unit) RHCI CA9L	248	753	1572	51.45	0.86
Lower Bed I dolomite (top unit) RHCI CA1	257	641	1735	62.63	0.87
Coorong dolomite	150	677	1515	34.61	0.91
Standard dolomite	692	1081	3436	100.00	0.83

Relative order and reflection ratio calculated from XRD peak intensity data.

Upper Bed I dolomite - upper unit RHCI CA9U	**parameter**	**value**	**sigma**	**95% conf**
	a (Å)	4.83	0.00021	0.00047
	c (Å)	16.16	0.00126	0.00278
	cell vol (Å^3)	326	0.0312	0.0688
Upper Bed I dolomite - lower unit RHCI CA9L	**parameter**	**value**	**sigma**	**95% conf**
	a (Å)	4.83	0.00021	0.00046
	c (Å)	16.15	0.00126	0.00277
	cell vol (Å^3)	326	0.0312	0.0687
Lower Bed I dolomite RHCI CA1	**parameter**	**value**	**sigma**	**95% conf**
	a (Å)	4.81	0.00021	0.00046
	c (Å)	16.04	0.00124	0.00273
	cell vol (Å^3)	322	0.0306	0.0675
Coorong dolomite	**parameter**	**value**	**sigma**	**95% conf**
	a (Å)	4.82	0.00021	0.00046
	c (Å)	16.11	0.00125	0.00275
	cell vol (Å^3)	324	0.0309	0.0682
Dolomite standard	**parameter**	**value**	**sigma**	**95% conf**
	a (Å)	4.81	0.00021	0.00046
	c (Å)	16.00	0.00123	0.00271
	cell vol (Å^3)	320	0.0304	0.067

Unit cell data calculated using UNIT CELL (Holland and Redfern, 1997)

	c	c - n_{Ca}	a	a - n_{Ca}	d(104)	d(104) - n_{Ca}	a eff 104	a eff 113	a eff average	a eff - n_{Ca}	c eff	c eff - n_{Ca}	d113	Average nCa	Std Dev	Mol% $CaCO_3$
Upper Bed I dolomite - upper unit RHCI CA9U	16.163	1.185	4.829	1.191	2.906	1.175	4.828	4.831	4.829	1.189	16.156	1.177	2.204	1.183	0.007	59
Upper Bed I dolomite - lower unit RHCI CA9L	16.146	1.165	4.828	1.183	2.904	1.164	4.827	4.828	4.828	1.174	16.146	1.166	2.203	1.170	0.008	59
Lower Bed I dolomite RHCI CA1	16.041	1.043	4.815	1.063	2.891	1.050	4.813	4.815	4.814	1.062	16.045	1.051	2.196	1.054	0.008	53
Coorong	16.111	1.125	4.822	1.127	2.903	1.154	4.826	4.825	4.825	1.154	16.138	1.156	2.201	1.143	0.016	57
Near stoichiometric dolomite	16.003	1.000	4.809	1.014	2.885	1.002	4.807	4.808	4.808	1.008	16.002	1.002	2.201	1.005	0.006	50

Mol % CaCO3 calculated using calculations from McCarthy et. al. (2006)

Appendix 11: Range of trace elements in calcite crystals at different stratigraphic levels.

	Mg	Mn	Sr	Ba	La	Ce	Pr	Nd	Sm	Eu	Gd	Tb	Dy	Ho	Er	Tm	Yb	Lu
Level 4 Upper Bed II (Loc25)	6822.58	41302.42	2137.64	1744.31	113.73	129.96	27.59	127.72	24.66	6.08	22.85	3.19	17.89	3.35	9.14	1.99	15.91	2.33
Level 3 Lower Bed II (RHCII CA3,5,6,7)	3876.97	7248.45	2806.02	889.50	22.88	80.73	19.20	101.93	30.82	8.27	27.42	4.66	22.91	5.31	11.89	1.69	10.54	1.59
Level 2 Upper Bed I (RHCI CA7,10)	9913.52	14395.92	5786.05	730.72	94.49	124.54	17.75	87.45	25.31	6.94	27.74	4.30	26.33	5.16	14.41	2.07	12.93	1.82
Level 1 Lower Bed I (RHCI 104)	6087.79	904.55	1003.04	260.07	20.50	29.92	3.53	20.79	5.77	1.85	6.41	0.73	5.53	1.16	3.37	0.99	4.17	0.55

Appendix 12: Laser Ablation MC-ICP-MS analyses of terrestrial sparry nodules and lacustrine calcite crystals normalised to a NIST glass standard

The U and Pb abundances in sparry nodules and lacustrine calcite crystals were measured using a LA MC ICP-MS at the NERC Isotope Labs, BGS, Keyworth. These data were then used to generate isochrons using a Tera-Wasserberg isochron of each sample using Isoplot 4.12 (Ludwig, 2003). Sparry nodules were chosen for this pilot study as petrographic analyses of the sparry bands had identified, that all of the terrestrial carbonate types, they were least likely to be affected by detrital contamination, and most likely to exhibit closed system behaviour. The samples were all from Tr111 Lower Bed II at the eastern lake margin, 2008 Tr111 CA1, CA4 and CA5. The lacustrine calcite crystals were selected from the lacustrine clays in Lower Bed II, 2008 Loc 80 CA6. The expected age of the sparry nodules and the calcite crystals is constrained by Tuff IF ~1.79 Ma (Hay and Kyser, 2001) and Tuff IIA 1.72 ± 0.003 Ma (Manega, 1993).

Sample preparation and analyses

A thin block, approximately 2-3cm square and 5mm thick, was cut from each sparry nodule using a standard rock saw. These were then polished using a range of Buehler SiC grinding paper from 800, 1200 to 2500. This produced a smooth finish so that the laser housing camera could focus more effectively and ablation pits more easily mapped. Mulitiple positions along a transect from the centre to the edge of each of three specimens of sparry nodules were sampled using the laser. Three crystals were set in resin (Buehler Epxoicure Resin (20-8130-128) and Hardener (20-8132-032)) and were polished using a range of Buehler SiC grinding paper from 800, 1200 to 2400 grade, and finally using 2micron alumina suspension to produce a well polished surface suitable for laser ablation. Each crystal was photographed using transmitted light and cathode-luminescence. Several positions covering a range of CL brightness were sampled from each crystal using the laser.

The specimens were analysed using the same instrument and the same machine parameters as the calcite crystals in Chapter 7 (Table 1).

	Parameters
Rep rate	**10 Hz**
Fluence	**~3.7 joules/cm^2**
Power	**80%**
Carrier gas	**He@ 0.8 l/min**
Aspiration	**0.5ppb ^{205}Tl - ^{203}Tl - ^{235}U in 2% nitric**
Spot size	**100µm diameter round**

Table 1: Individual sample analysis parameters.

NIST 614 and NIST 612 glass reference standard materials for microanalysis of trace elements were used and placed in the laser ablation chamber adjacent to each sample. NIST 614 has uranium content of ~1ppm and NIST 612 has a uranium content of ~40ppm. Each sample was run using NIST 614 and NIST 612 prior to the run and NIST 612 post the carbonate analysis.

Preliminary analysis of the sparry nodules showed high levels of common lead are present on the sample surface during the first ablation with the laser, so that each sampling point needed to be pre-ablated prior to analysis. The initial spike of lead from surface contamination of the sparry nodules and the lacustrine calcite crystals was discarded during the data selection process.

Sparry nodules

The analyses (Table 3) have produced sparry nodule ages with large uncertainties (Figure 1; Table 2) showing that sparry nodules of this age are unsuitable for dating using this technique.

Sample number	**Age**
2008 Tr111 CA5	6.6 ± 6.8 Ma MSWD 2.3
2008 Tr111 CA1	5.3 ± 3.66 Ma MSWD 1.7
2008 Tr111 CA4	7.0 ± 6.1 Ma MSWD 2.9

Table 2: Isochron ages of sparry nodules from Lower Bed II at the eastern lake margin using Laser ablation MC ICP-MS analysis

									Data not common-Pb corrected							
Samples	Signals								Data for Tera-Wasserberg plot				Data for Wetherill plot			
	^{204}Pb in sample cps gc	^{206}Pb mV	^{207}Pb mV	^{238}U mV	Pb ppm	Uppm*	^{206}Pb/^{204}Pb	1σ %	^{238}U/^{206}Pb	1σ %	^{207}Pb/^{206}Pb	1σ %	^{207}Pb/^{235}U	1σ %	^{206}Pb/^{238}U	1σ %	Rho
2008 TR111 CA5 1	3923	0.55	0.37	1.83	1.15	1.00	8.76	5.32	1.02	3.44	0.7905	0.42	107	3.46	0.9819	3.44	0.99
2008 TR111 CA5 2	3604	0.64	0.43	4.40	1.34	2.39	11.09	6.96	2.18	1.39	0.7872	0.34	50	1.43	0.4586	1.39	0.97
2008 TR111 CA5 3	3259	0.42	0.28	3.18	0.87	1.73	8.01	6.61	2.41	2.02	0.7852	0.37	45	2.05	0.4153	2.02	0.98
2008 TR111 CA5 4	3093	0.26	0.17	3.19	0.54	1.73	5.18	3.67	3.91	1.75	0.7900	0.56	28	1.84	0.2558	1.75	0.95
2008 TR111 CA5 5	2454	0.17	0.12	2.16	0.36	1.18	4.42	7.30	3.99	1.51	0.7861	0.79	27	1.70	0.2506	1.51	0.89
2008 TR111 CA5 6	3127	0.31	0.21	2.24	0.64	1.22	6.16	9.61	2.26	1.77	0.7884	0.48	48	1.83	0.4427	1.77	0.97
2008 TR111 CA5 7	8943	1.36	0.92	9.24	2.27	4.89	9.47	3.26	2.68	4.07	0.7873	0.21	41	4.07	0.3736	4.07	1.00
2008 TR111 CA5 8	11062	1.90	1.28	1.49	3.17	0.79	10.70	2.49	0.27	5.66	0.7895	0.10	400	5.66	3.6713	5.66	1.00
2008 TR111 CA5 9	8897	1.41	0.96	1.01	2.36	0.53	9.91	3.21	0.28	4.07	0.7909	0.13	393	4.07	3.6003	4.07	1.00
2008 TR111 CA5 10	26587	6.31	4.27	1.99	10.54	1.05	14.81	5.19	0.13	4.30	0.7892	0.04	866	4.30	7.9550	4.30	1.00
2008 TR111 CA5 11	35082	9.06	6.15	2.58	15.15	1.36	16.12	2.32	0.11	4.00	0.7901	0.15	997	4.00	9.1500	4.00	1.00
2008 TR111 CA1 1	7599	0.89	0.60	10.78	1.49	5.70	7.33	3.08	4.18	4.14	0.7839	0.21	26	4.15	0.2392	4.14	1.00
2008 TR111 CA1 2	10077	1.66	1.12	4.19	2.78	2.22	10.29	4.33	0.88	5.04	0.7863	0.14	123	5.04	1.1385	5.04	1.00
2008 TR111 CA1 3	8348	1.24	0.83	4.34	2.07	2.30	9.25	3.68	1.22	4.69	0.7869	0.18	89	4.69	0.8166	4.69	1.00
2008 TR111 CA1 4	10265	1.68	1.13	3.56	2.81	1.88	10.22	2.08	0.72	4.48	0.7867	0.19	150	4.49	1.3843	4.48	1.00
2008 TR111 CA1 5	8237	1.22	0.82	7.51	2.04	3.97	9.27	3.31	2.05	4.86	0.7842	0.18	53	4.87	0.4873	4.86	1.00
2008 TR111 CA1 6	9082	1.42	0.96	1.21	2.38	0.64	9.77	2.39	0.30	4.38	0.7865	0.19	361	4.38	3.3336	4.38	1.00
2008 TR111 CA1 7	8825	1.31	0.88	0.71	2.19	0.37	9.27	2.19	0.19	4.43	0.7864	0.19	578	4.44	5.3276	4.43	1.00
2008 TR111 CA1 8	7596	0.97	0.65	1.45	1.62	0.77	7.94	1.42	0.52	4.56	0.7868	0.19	210	4.56	1.9358	4.56	1.00
2008 TR111 CA1 9	8150	1.09	0.73	1.95	1.82	1.03	8.32	1.99	0.62	3.99	0.7853	0.17	175	4.00	1.6150	3.99	1.00
2008 TR111 CA1 10	7666	0.94	0.63	1.83	1.57	0.97	7.66	4.62	0.69	4.23	0.7853	0.18	158	4.23	1.4554	4.23	1.00
2008 TR111 CA1 11	6997	0.92	0.62	2.39	1.53	1.26	8.17	3.06	0.80	5.43	0.7840	0.19	136	5.43	1.2539	5.43	1.00
2008 TR111 CA1 12	20366	4.67	3.14	1.81	7.80	0.96	14.30	3.42	0.13	4.33	0.7857	0.16	832	4.33	7.6760	4.33	1.00
2008 TR111 CA4 1	7591	0.69	0.46	1.65	1.15	0.87	5.65	2.54	0.98	4.07	0.7891	0.29	112	4.08	1.0250	4.07	1.00
2008 TR111 CA4 2	7471	0.69	0.47	2.59	1.15	1.37	5.75	2.21	1.49	3.97	0.7915	0.27	73	3.98	0.6713	3.97	1.00
2008 TR111 CA4 5	7227	0.81	0.55	5.57	1.35	2.95	6.98	2.89	2.67	4.13	0.7904	0.24	41	4.13	0.3739	4.13	1.00
2008 TR111 CA4 6	7505	1.11	0.75	4.02	1.85	2.13	9.20	3.77	1.40	4.45	0.7933	0.21	78	4.46	0.7118	4.45	1.00
2008 TR111 CA4 7	9772	1.47	1.00	1.98	2.46	1.05	9.40	2.81	0.51	4.25	0.7929	0.21	212	4.26	1.9423	4.25	1.00
2008 TR111 CA4 8	8734	1.25	0.84	4.41	2.09	2.33	8.92	3.37	1.38	3.98	0.7896	0.19	79	3.99	0.7221	3.98	1.00
2008 TR111 CA4 9	8005	1.01	0.68	3.58	1.68	1.90	7.84	3.69	1.37	4.05	0.7898	0.21	80	4.06	0.7304	4.05	1.00
2008 TR111 CA4 10	5944	0.63	0.42	5.60	1.05	2.96	6.62	2.32	3.26	4.44	0.7867	0.28	33	4.45	0.3069	4.44	1.00
2008 TR111 CA4 11	5892	0.72	0.48	5.98	1.20	3.16	7.58	4.10	3.21	4.47	0.7854	0.32	34	4.49	0.3116	4.47	1.00
2008 TR111 CA4 12	6285	0.98	0.67	4.92	1.63	2.60	9.71	2.65	1.89	3.97	0.7890	0.25	57	3.98	0.5284	3.97	1.00
2008 TR111 CA4 13	4782	0.80	0.54	3.89	1.33	2.06	10.39	4.59	1.68	6.39	0.7908	0.26	65	6.39	0.5953	6.39	1.00
2008 TR111 CA4 14	5192	0.91	0.62	1.87	1.53	0.99	10.99	3.62	0.76	4.18	0.7900	0.21	143	4.19	1.3110	4.18	1.00
2008 TR111 CA4 15	2855	0.30	0.20	6.83	0.51	3.61	6.61	8.93	6.75	7.29	0.7853	0.50	16	7.31	0.1481	7.29	1.00
2008 TR111 CA4 16	4748	0.76	0.51	2.58	1.26	1.36	9.93	4.41	1.01	6.49	0.7897	0.25	107	6.49	0.9864	6.49	1.00
2008 TR111 CA4 17	5285	0.96	0.65	1.90	1.61	1.00	11.36	3.92	0.74	4.43	0.7897	0.17	147	4.44	1.3535	4.43	1.00
2008 TR111 CA4 18	6976	1.25	0.84	1.04	2.08	0.55	11.15	2.51	0.30	4.89	0.7912	0.14	359	4.89	3.2908	4.89	1.00
2008 TR111 CA4 19	6101	1.18	0.80	3.18	1.97	1.68	12.08	5.83	0.94	5.05	0.7903	0.15	116	5.06	1.0665	5.05	1.00
2008 TR111 CA4 20	8863	1.88	1.28	1.62	3.13	0.86	13.21	3.41	0.32	4.42	0.7900	0.10	336	4.42	3.0878	4.42	1.00

Table 3: LA MC ICP-MS analyses of sparry nodules.

The large uncertainties may be the result of open system behaviour, partial leaching of isotopes from clay particles trapped in the calcite lattice, or potential initial uranium disequilibrium. The specimens have high levels of common lead, likely to be due to Pb contamination of trapped detrital clay particles. The specimens have a low abundance of uranium and so radiogenic lead. When using the Tera-Wasserberg isochron plot the age of the sample is determined from the gradient of the linear regression. Ideally, the error ellipses would be as small as possible, and the range of $^{238}U/^{206}Pb$ ratios as large as possible, to produce the most accurate and precise age. The result show a variety of U* from 0.5ppm to ~6ppm and lead concentrations from 0.5ppm to 15ppm, producing very narrow range of $^{238}U/^{206}Pb$ ratios from 0.1 to nearly 7. This poor range of values and large errors has contributed to high uncertainties.

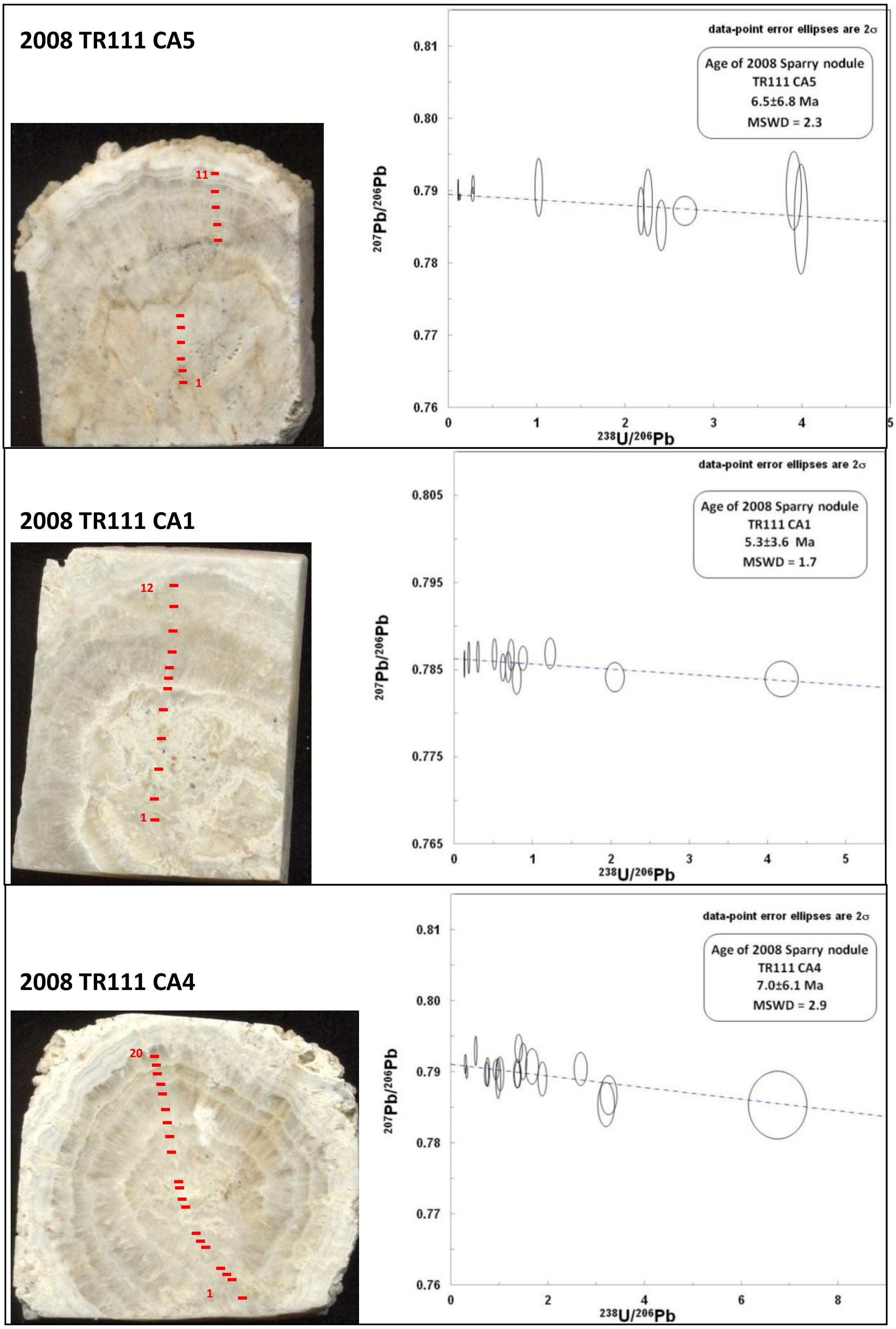

Figure 1: Polished faces of sparry nodules from Lower Bed II (Scale bar 1cm). Tera-Waserburg plots of data from multiple positions per specimens, identifying a narrow range of $^{238}U/^{206}Pb$ ratios for each crystal and high uncertainties

Calcite crystals

The analyses of the lacustrine calcite crystals (Table 4) have produced an age with much smaller uncertainties than those found in the terrestrial specimens (Figure 2), showing that calcite crystals of this age are much more promising prospect for dating using this technique.

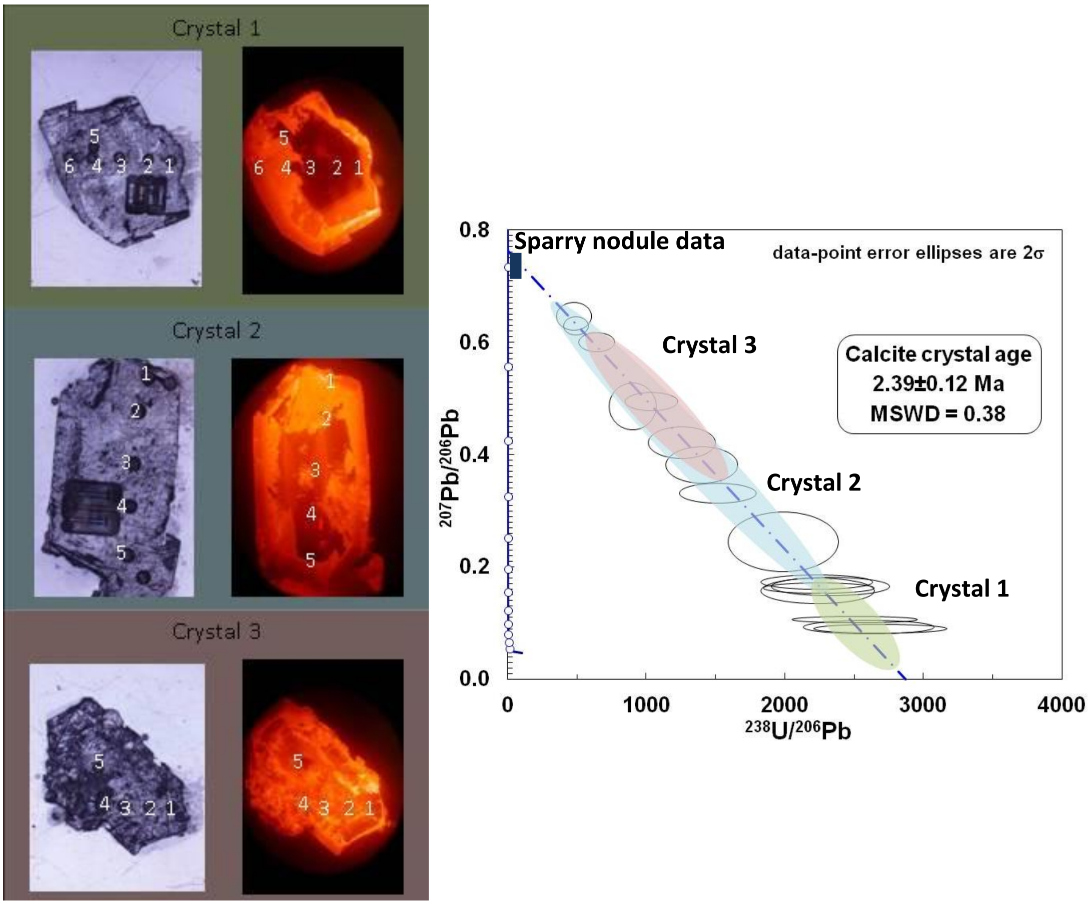

Figure 2: Transmitted light and cathodoluminescence images of three crystals from Lower Bed II with laser ablation pits (FOV 2mm). LA MC-ICP-MS data of three crystals identifying ranges of $^{238}U/^{206}Pb$ ratios for each crystal. Also shown – black box incorporating range of data from first sparry nodules from the lake margin sediments (individual data too small to show –values <7).

As with the sparry nodules, the uncertainties in this data may be the result of open system behaviour, partial leaching of isotopes from clay particles trapped in the calcite lattice, or potential initial uranium disequilibrium. The lacustrine calcite crystals, however, have low levels of common lead, and a much higher abundance of uranium and hence radiogenic lead compared to the sparry nodules. This produces a wide range of $^{238}U/^{206}Pb$ ratios from 480 to 2690 and so the regression line is much better constrained producing an age with very low uncertainties for these young carbonates.

Different materials will respond differently when ablated by the laser, so any difference between the crystallinity of the sample and the standard can create differences in element fractionation. When these samples were analysed, a calcite standard was not available, however subsequently lacustrine crystals have been analysed using this method and normalised to a calcite standard, significantly improving the accuracy of the ages (Chapter 7).

							Data not common-Pb corrected								
Samples							Data for Tera-Wasserberg plot				Data for Wetherill plot				
	^{204}Pb in sample cps gc	^{206}Pb mV	^{207}Pb mV	^{238}U mV	Pb ppm	Uppm*	$^{238}U/^{206}Pb$	1σ %	$^{207}Pb/^{206}Pb$	1σ %	$^{207}Pb/^{235}U$	1σ %	$^{206}Pb/^{238}U$	1σ %	Rho
RHCII CA6 Loc1 1	400	0.02	0.0016	34	0.0178	12	2690	7.28	0.0900	3.63	0.0046	8.14	0.0004	7.28	0.89
RHCII CA6 Loc1 2	327	0.01	0.0011	20	0.0113	7	2506	7.36	0.1063	2.39	0.0059	7.73	0.0004	7.36	0.95
RHCII CA6 Loc1 3	329	0.02	0.0019	40	0.0210	14	2604	7.41	0.0932	5.32	0.0049	9.12	0.0004	7.41	0.81
RHCII CA6 Loc1 4	309	0.03	0.0040	41	0.0258	14	2246	7.31	0.1624	2.46	0.0100	7.71	0.0004	7.31	0.95
RHCII CA6 Loc1 4	294	0.03	0.0045	43	0.0270	15	2232	7.36	0.1728	2.94	0.0107	7.92	0.0004	7.36	0.93
RHCII CA6 Loc1 5	406	0.02	0.0034	36	0.0214	13	2330	7.47	0.1649	4.03	0.0098	8.49	0.0004	7.47	0.88
RHCII CA6 Loc 2 1	538	0.05	0.0060	63	0.0393	22	2236	7.49	0.1574	5.84	0.0097	9.50	0.0004	7.49	0.79
RHCII CA6 Loc 2 2	483	0.12	0.0633	36	0.1015	13	480	10.81	0.6466	1.58	0.1859	10.93	0.0021	10.81	0.99
RHCII CA6 Loc 2 3	475	0.06	0.0115	69	0.0478	24	1990	8.15	0.2446	8.90	0.0169	12.07	0.0005	8.15	0.68
RHCII CA6 Loc 2 4	348	0.04	0.0222	13	0.0373	5	495	7.42	0.6292	1.05	0.1754	7.49	0.0020	7.42	0.99
RHCII CA6 Loc 2 5	569	0.02	0.0055	18	0.0173	6	1516	7.49	0.3313	2.16	0.0301	7.79	0.0007	7.49	0.96
RHCII CA6 Loc 3 1	377	0.03	0.0119	19	0.0254	7	1036	7.52	0.4943	1.38	0.0658	7.65	0.0010	7.52	0.98
RHCII CA6 Loc 3 2	741	0.01	0.0032	4	0.0068	2	902	7.64	0.4858	3.49	0.0742	8.40	0.0011	7.64	0.91
RHCII CA6 Loc 3 3	-11	0.04	0.0176	15	0.0307	5	643	8.14	0.6007	1.17	0.1289	8.22	0.0016	8.14	0.99
RHCII CA6 Loc 3 4	492	0.05	0.0164	38	0.0418	13	1257	7.91	0.4221	2.75	0.0463	8.37	0.0008	7.91	0.94
RHCII CA6 Loc 3 5	528	0.01	0.0038	10	0.0106	4	1400	7.56	0.3822	3.48	0.0376	8.32	0.0007	7.56	0.91

Table 4: LA MC ICP-MS analyses of lacustrine calcite crystals

Appendix 13: Laser ablation MC-ICP-MS U-Pb analyses of lacustrine calcite crystals

Data not common-Pb corrected

Samples	Signals								Data for Tera-Wasserberg plot				Data for Wetherill plot							Ages			
	^{204}Pb in sample cps gc	^{206}Pb mV	^{207}Pb mV	^{238}U mV	Pb ppm	Uppm*	^{206}Pb/^{204}Pb	1σ %	^{238}U/^{206}Pb	1σ %	^{207}Pb/^{206}Pb	1σ %	^{207}Pb/^{235}U	1σ %	^{206}Pb/^{238}U	1σ %	Rho	^{207}Pb/^{206}Pb	2σ abs	^{206}Pb/^{238}U	2σ abs	^{207}Pb/^{235}U	2σ abs
Level 4																							
LOC25 1 1	bd	0.0	0.00	17	0.002	5	bd	bd	1908	1.7	0.3851	3.9	0.028	4.3	0.00052	1.7	0.41	3852	118	3.4	0.1	28	2
LOC25 1 2	bd	0.0	0.00	18	0.003	5	bd	bd	1706	2.9	0.4039	2.4	0.033	3.8	0.00059	2.9	0.77	3924	72	3.8	0.2	33	2
LOC25 1 3	bd	0.1	0.01	284	0.020	83	bd	bd	3658	1.1	0.1414	2.2	0.005	2.5	0.00027	1.1	0.45	2245	76	1.8	0.0	5	0
LOC25 1 4	bd	0.1	0.01	248	0.016	73	bd	bd	3823	0.7	0.0872	3.1	0.003	3.2	0.00026	0.7	0.22	1364	119	1.7	0.0	3	0
LOC25 1 5	bd	0.1	0.01	218	0.015	64	bd	bd	3776	0.9	0.1024	3.3	0.004	3.4	0.00026	0.9	0.25	1667	123	1.7	0.0	4	0
LOC25 1 6	bd	0.0	0.00	32	0.003	9	bd	bd	2736	1.6	0.2301	4.2	0.012	4.5	0.00037	1.6	0.36	3053	135	2.4	0.1	12	1
LOC25 2 1a	bd	0.1	0.05	21	0.01	6	bd	bd	388	3.8	0.7404	1.1	0.263	4.0	0.00258	3.8	0.96	4811	32	16.6	1.3	237	17
LOC25 2 1b	bd	0.1	0.06	21	0.02	6	bd	bd	277	3.9	0.7565	0.9	0.377	4.0	0.00361	3.9	0.97	4842	25	23.3	1.8	325	22
LOC25 2 2a	9095	2.4	1.68	77	0.48	23	17	5	41	5.0	0.8065	0.2	2.683	5.0	0.02413	5.0	1.00	4933	5	153.7	15.1	1324	71
LOC25 2 2b	6124	1.9	1.31	94	0.37	28	19	8	64	4.6	0.8014	0.2	1.722	4.6	0.01558	4.6	1.00	4924	6	99.7	9.1	1017	58
LOC25 2 2c	8534	2.5	1.70	124	0.48	36	18	7	65	2.8	0.8030	0.1	1.698	2.8	0.01534	2.8	1.00	4927	4	98.1	5.5	1008	35
LOC25 2 3a	bd	0.1	0.01	153	0.01	45	bd	bd	3679	1.4	0.1448	2.4	0.005	2.8	0.00027	1.4	0.49	2286	83	1.8	0.0	5	0
LOC25 2 3b	1613	0.1	0.01	190	0.01	56	bd	bd	3312	3.6	0.1969	7.6	0.008	8.4	0.00030	3.6	0.43	2801	249	1.9	0.1	8	1
LOC25 2 4a	17	0.0	0.00	58	0.00	17	bd	bd	3220	1.4	0.1699	5.9	0.007	6.0	0.00031	1.4	0.22	2557	197	2.0	0.1	7	1
LOC25 2 5a	bd	0.1	0.01	237	0.02	70	bd	bd	3942	0.7	0.0803	3.6	0.003	3.7	0.00025	0.7	0.20	1205	142	1.6	0.0	3	0
LOC25 2 5b	bd	0.1	0.01	249	0.02	73	bd	bd	3483	3.5	0.1609	6.8	0.006	7.7	0.00029	3.5	0.45	2465	231	1.9	0.1	6	1
LOC25 2 6a	9	0.1	0.01	219	0.01	64	bd	bd	3737	1.5	0.0986	3.9	0.004	4.1	0.00027	1.5	0.36	1598	144	1.7	0.1	4	0
LOC25 2 6b	277	0.1	0.01	206	0.01	60	15	94	3896	1.5	0.0945	7.1	0.003	7.2	0.00026	1.5	0.21	1519	267	1.7	0.1	3	0
LOC25 3 1a	325	0.1	0.07	40	0.02	12	20	55	511	13.8	0.7109	1.5	0.192	13.9	0.00196	13.8	0.99	4753	44	12.6	3.5	178	44
LOC25 3 1b	95	0.0	0.03	24	0.01	7	bd	bd	652	12.4	0.6899	2.5	0.146	12.6	0.00153	12.4	0.98	4710	71	9.9	2.4	138	32
LOC25 3 2a	4656	1.4	0.95	104	0.28	30	19	4	92	3.3	0.7875	0.2	1.178	3.3	0.01085	3.3	1.00	4899	6	69.5	4.6	790	36
LOC25 3 2b	6817	1.9	1.30	66	0.37	19	17	5	44	7.0	0.8020	0.2	2.522	7.0	0.02280	7.0	1.00	4925	6	145.4	20.1	1278	97
LOC25 3 3a	4164	1.1	0.73	128	0.22	38	17	7	144	4.0	0.7757	0.2	0.744	4.0	0.00696	4.0	1.00	4878	6	44.7	3.6	565	34
LOC25 3 3b	3770	1.2	0.77	122	0.23	36	19	10	136	5.4	0.7811	0.5	0.792	5.5	0.00736	5.4	1.00	4888	14	47.3	5.1	593	48
LOC25 3 4	1422	0.4	0.26	96	0.08	28	18	12	289	5.5	0.7454	0.4	0.356	5.5	0.00346	5.5	1.00	4821	11	22.3	2.4	309	29
LOC25 3 5a	2300	0.7	0.44	67	0.13	20	18	7	127	4.6	0.7765	0.2	0.841	4.6	0.00785	4.6	1.00	4879	4	50.4	4.6	619	42
LOC25 3 5b	1868	0.5	0.34	73	0.10	21	17	18	180	7.2	0.7681	0.2	0.588	7.2	0.00555	7.2	1.00	4864	7	35.7	5.1	470	53
LOC25 3 5c	4468	0.8	0.55	90	0.16	26	11	46	142	13.0	0.7914	0.7	0.770	13.0	0.00706	13.0	1.00	4906	20	45.4	11.8	580	109
LOC25 3 6a	429	0.0	0.02	34	0.01	10	5	26	1240	5.6	0.5566	2.9	0.062	6.3	0.00081	5.6	0.89	4399	84	5.2	0.6	61	7
LOC25 3 6b	496	0.1	0.04	54	0.01	16	8	43	1083	19.5	0.6490	3.9	0.083	19.9	0.00092	19.5	0.98	4622	111	6.0	2.3	81	30
LOC25 4 1a	649	0.1	0.08	38	0.02	11	12	34	379	4.9	0.7637	0.8	0.278	5.0	0.00264	4.9	0.99	4855	22	17.0	1.7	249	22
LOC25 4 1b	195	0.1	0.07	32	0.02	9	33	67	387	6.6	0.7617	1.0	0.272	6.6	0.00259	6.6	0.99	4852	29	16.7	2.2	244	28
LOC25 4 2a	8789	2.3	1.56	49	0.44	14	16	4	27	3.0	0.8027	0.4	4.070	3.0	0.03678	3.0	0.99	4926	12	232.8	13.7	1648	48
LOC25 4 2b	10571	2.4	1.64	50	0.46	15	14	12	27	5.6	0.8051	0.3	4.165	5.6	0.03752	5.6	1.00	4931	8	237.4	26.0	1667	88
LOC25 4 2c	9819	2.8	1.94	50	0.55	15	18	3	23	2.5	0.8055	0.1	4.929	2.5	0.04438	2.5	1.00	4931	3	279.9	13.6	1807	41
LOC25 4 2d	9498	2.8	1.90	48	0.54	14	18	3	23	1.7	0.8072	0.1	4.932	1.7	0.04431	1.7	1.00	4934	4	279.5	9.5	1808	29
LOC25 4 3a	6279	1.8	1.20	71	0.34	21	17	4	52	3.0	0.7988	0.3	2.125	3.0	0.01929	3.0	1.00	4920	8	123.2	7.2	1157	40
LOC25 4 3b	6960	2.0	1.33	76	0.38	22	18	7	49	3.6	0.7942	0.2	2.221	3.7	0.02028	3.6	1.00	4911	4	129.4	9.3	1188	50
LOC25 4 3c	11022	2.7	1.85	70	0.53	21	15	11	33	4.6	0.7964	0.3	3.318	4.6	0.03022	4.6	1.00	4915	8	191.9	17.5	1485	70
LOC25 4 4a	2449	0.7	0.47	50	0.14	15	18	8	93	2.1	0.7879	0.4	1.165	2.1	0.01072	2.1	0.98	4900	12	68.7	2.8	784	23
LOC25 4 5a	4092	1.1	0.76	101	0.22	30	17	10	111	6.8	0.7836	0.3	0.969	6.8	0.00897	6.8	1.00	4892	9	57.6	7.8	688	66
LOC25 4 5b	3622	1.1	0.75	90	0.22	27	19	9	100	4.0	0.7793	0.2	1.076	4.0	0.01001	4.0	1.00	4884	5	64.2	5.1	742	41
LOC25 4 6a	1802	0.1	0.04	15	0.01	4	2	89	302	7.9	0.7637	2.0	0.348	8.1	0.00331	7.9	0.97	4855	56	21.3	3.3	303	42
LOC25 4 6b	164	0.1	0.03	64	0.01	19	22	79	1331	8.8	0.5622	3.0	0.058	9.3	0.00075	8.8	0.95	4413	88	4.8	0.9	57	10
LOC25 4 6c	407	0.1	0.06	16	0.02	5	13	41	230	12.6	0.7794	1.2	0.468	12.7	0.00435	12.6	1.00	4885	35	28.0	7.1	390	79

Data not common-Pb corrected

Samples	Signals								Data for Tera-Wasserberg plot				Data for Wetherill plot					Ages					
	^{204}Pb in sample cps gc	^{206}Pb mV	^{207}Pb mV	^{238}U mV	Pb ppm	Uppm*	$^{206}Pb/^{204}Pb$	1σ %	$^{238}U/^{206}Pb$	1σ %	$^{207}Pb/^{206}Pb$	1σ %	$^{207}Pb/^{235}U$	1σ %	$^{206}Pb/^{238}U$	1σ %	Rho	$^{207}Pb/^{206}Pb$	2σ abs	$^{206}Pb/^{238}U$	2σ abs	$^{207}Pb/^{235}U$	2σ abs
Level 3																							
RHCII CA3 1 3a	240	0.026	0.018	18.0	0.01	7.57	7	41	414	9.9	0.8573	1.4	0.286	10.0	0.00242	9.9	0.99	5020	40	15.6	3.1	255	44
RHCII CA3 1 3b	289	0.034	0.025	14.3	0.02	5.99	7	52	284	5.4	0.9266	1.2	0.450	5.5	0.00353	5.4	0.98	5130	34	22.7	2.4	378	34
RHCII CA3 1 3c	76	0.023	0.014	21.9	0.01	9.22	bd	bd	691	6.9	0.8170	1.2	0.163	7.0	0.00145	6.9	0.98	4952	35	9.3	1.3	153	20
RHCII CA3 1 4a	91	0.044	0.027	47.2	0.02	19.82	bd	bd	769	4.2	0.7852	1.1	0.141	4.3	0.00130	4.2	0.97	4895	31	8.4	0.7	134	11
RHCII CA3 1 4b	178	0.054	0.033	54.5	0.03	22.91	19	79	717	5.3	0.8115	1.1	0.156	5.4	0.00139	5.3	0.98	4942	30	9.0	1.0	147	15
RHCII CA3 1 4c	75	0.037	0.022	41.5	0.02	17.44	bd	bd	798	5.1	0.7779	1.3	0.134	5.3	0.00125	5.1	0.97	4882	37	8.1	0.8	128	13
RHCII CA3 1 5a	12	0.034	0.018	53.0	0.02	22.28	bd	bd	1095	2.5	0.6853	0.9	0.086	2.7	0.00091	2.5	0.94	4700	27	5.9	0.3	84	4
RHCII CA3 1 5b	42	0.032	0.017	54.5	0.02	22.90	bd	bd	1201	1.1	0.6591	1.3	0.076	1.7	0.00083	1.1	0.65	4644	37	5.4	0.1	74	2
RHCII CA3 1 5c	bd	0.038	0.021	51.2	0.02	21.51	bd	bd	972	3.6	0.7144	1.0	0.101	3.7	0.00103	3.6	0.96	4760	29	6.6	0.5	98	7
RHCII CA3 1 6a	315	0.035	0.018	55.6	0.02	23.38	7	29	1112	2.7	0.6864	0.8	0.085	2.8	0.00090	2.7	0.96	4703	23	5.8	0.3	83	4
RHCII CA3 1 6b	94	0.037	0.020	59.7	0.02	25.10	bd	bd	1144	2.9	0.7003	1.3	0.084	3.2	0.00087	2.9	0.91	4731	39	5.6	0.3	82	5
RHCII CA3 1 6c	501	0.033	0.017	52.8	0.02	22.18	4	22	1158	1.0	0.6789	1.1	0.081	1.5	0.00086	1.0	0.66	4687	32	5.6	0.1	79	2
RHCII CA3 2 1	bd	0.009	0.006	13.4	0.01	5.62	bd	bd	984	1.7	0.7383	1.8	0.103	2.4	0.00102	1.7	0.69	4807	50	6.5	0.2	100	5
RHCII CA3 2 2	bd	0.059	0.031	87.0	0.03	36.57	bd	bd	1040	2.3	0.6774	0.8	0.090	2.4	0.00096	2.3	0.94	4683	23	6.2	0.3	87	4
RHCII CA3 2 3a	92	0.072	0.042	84.7	0.04	35.61	49	95	820	3.7	0.7641	0.9	0.128	3.8	0.00122	3.7	0.97	4856	27	7.9	0.6	123	9
RHCII CA3 2 3b	67	0.071	0.041	90.3	0.04	37.96	bd	bd	884	4.1	0.7391	1.0	0.115	4.2	0.00113	4.1	0.97	4809	28	7.3	0.6	111	9
RHCII CA3 2 4	bd	0.010	0.007	4.9	0.01	2.05	bd	bd	346	3.3	0.9114	1.4	0.363	3.6	0.00289	3.3	0.92	5107	40	18.6	1.2	315	19
RHCII CA3 2 5a	bd	0.023	0.008	59.5	0.01	25.01	bd	bd	1914	2.9	0.4465	2.5	0.032	3.8	0.00052	2.9	0.76	4074	73	3.4	0.2	32	2
RHCII CA3 2 5b	bd	0.026	0.008	72.8	0.01	30.58	bd	bd	1980	5.5	0.4099	3.4	0.029	6.5	0.00051	5.5	0.85	3946	102	3.3	0.4	29	4
RHCII CA3 2 5c	bd	0.018	0.007	51.6	0.01	21.69	bd	bd	1904	3.2	0.4574	3.3	0.033	4.6	0.00053	3.2	0.70	4110	97	3.4	0.2	33	3
RHCII CA3 3 1	bd	0.008	0.006	2.7	0.00	1.12	bd	bd	241	7.0	0.8941	3.8	0.512	8.0	0.00415	7.0	0.88	5080	108	26.7	3.7	420	53
RHCII CA3 3 2a	bd	0.012	0.007	10.6	0.01	4.47	bd	bd	636	3.2	0.8077	2.2	0.175	3.9	0.00157	3.2	0.82	4935	63	10.1	0.6	164	12
RHCII CA3 3 2b	bd	0.013	0.008	12.5	0.01	5.24	bd	bd	639	3.0	0.8050	2.2	0.174	3.7	0.00157	3.0	0.80	4931	64	10.1	0.6	163	11
RHCII CA3 3 3	bd	0.011	0.006	16.6	0.01	6.99	bd	bd	1044	2.9	0.6478	2.2	0.086	3.6	0.00096	2.9	0.80	4619	62	6.2	0.4	83	6
RHCII CA3 3 3b	bd	0.010	0.005	14.8	0.01	6.21	bd	bd	1053	3.6	0.6433	3.0	0.084	4.6	0.00095	3.6	0.77	4609	85	6.1	0.4	82	7
RHCII CA3 3 3c	44	0.013	0.007	21.1	0.01	8.88	bd	bd	1089	3.6	0.6604	2.4	0.084	4.3	0.00092	3.6	0.83	4647	70	5.9	0.4	82	7
RHCII CA3 3 4a	bd	0.008	0.003	18.7	0.00	7.87	bd	bd	1656	2.2	0.5138	3.3	0.043	3.9	0.00060	2.2	0.55	4281	97	3.9	0.2	43	3
RHCII CA3 3 4ab	bd	0.007	0.003	17.1	0.00	7.17	bd	bd	1589	2.7	0.5448	4.8	0.047	5.5	0.00063	2.7	0.49	4367	140	4.1	0.2	47	5
RHCII CA3 3 5	bd	0.006	0.004	2.1	0.00	0.88	bd	bd	253	4.3	0.9213	2.6	0.502	5.0	0.00395	4.3	0.86	5122	74	25.4	2.2	413	34
RHCII CA3 3 6	bd	0.013	0.006	29.1	0.01	12.24	bd	bd	1577	2.0	0.5608	2.7	0.049	3.4	0.00063	2.0	0.61	4410	78	4.1	0.2	49	3
RHCII CA3 3 6b	bd	0.013	0.005	29.6	0.01	12.43	bd	bd	1610	1.8	0.5134	3.1	0.044	3.6	0.00062	1.8	0.49	4280	92	4.0	0.1	44	3
RHCII CA3 4 1	bd	0.016	0.004	50.8	0.01	21.36	bd	bd	2225	2.4	0.3450	4.3	0.021	5.0	0.00045	2.4	0.49	3685	133	2.9	0.1	21	2
RHCII CA3 4 2	bd	0.005	0.003	6.9	0.00	2.90	bd	bd	938	4.2	0.8044	3.9	0.118	5.7	0.00107	4.2	0.74	4930	110	6.9	0.6	114	12
RHCII CA3 4 3a	bd	0.039	0.019	79.1	0.02	33.22	bd	bd	1299	14.3	0.5292	7.2	0.056	16.0	0.00077	14.3	0.89	4325	211	5.0	1.4	55	17
RHCII CA3 4 3b	17	0.024	0.005	92.7	0.01	38.94	bd	bd	2703	1.3	0.2649	5.7	0.014	5.8	0.00037	1.3	0.22	3276	178	2.4	0.1	14	2
RHCII CA3 4 3c	bd	0.056	0.032	67.2	0.03	28.24	bd	bd	820	11.5	0.7020	3.7	0.118	12.1	0.00122	11.5	0.95	4735	106	7.9	1.8	113	26
RHCII CA3 4 4b	bd	0.029	0.019	15.6	0.02	6.54	bd	bd	366	7.7	0.8590	1.5	0.324	7.8	0.00273	7.7	0.98	5023	43	17.6	2.7	285	38
RHCII CA3 4 5	bd	0.005	0.004	2.8	0.00	1.16	bd	bd	364	6.2	0.8918	4.0	0.338	7.4	0.00275	6.2	0.84	5076	114	17.7	2.2	296	37
RHCII CA3 4 6	79	0.008	0.005	3.9	0.00	1.66	bd	bd	363	4.0	0.9081	1.9	0.345	4.4	0.00275	4.0	0.91	5101	53	17.7	1.4	301	23
RHCII CA3 4 6b	36	0.007	0.005	4.2	0.00	1.76	bd	bd	407	5.7	0.8103	3.1	0.275	6.5	0.00246	5.7	0.88	4940	88	15.8	1.8	246	28
RHCII CA3 4 6c	bd	0.008	0.005	3.8	0.00	1.61	bd	bd	353	4.6	0.8988	2.4	0.351	5.2	0.00283	4.6	0.88	5087	69	18.2	1.7	306	27

Data not common-Pb corrected

Samples	^{204}Pb in sample cps gc	^{206}Pb mV	^{207}Pb mV	^{238}U mV	Pb ppm	Uppm*	$^{206}Pb/^{204}Pb$	1σ %	$^{238}U/^{206}Pb$	1σ %	$^{207}Pb/^{206}Pb$	1σ %	$^{207}Pb/^{235}U$	1σ %	$^{206}Pb/^{238}U$	1σ %	Rho	$^{207}Pb/^{206}Pb$	2σ abs	$^{206}Pb/^{238}U$	2σ abs	$^{207}Pb/^{235}U$	2σ abs
		Signals							Data for Tera-Wasserberg plot					Data for Wetherill plot						Ages			
RHCII CA5 1 1a	102	0.010	0.004	23.4	0.01	9.81	6	92	1600	7.4	0.4689	4.1	0.040	8.4	0.00063	7.4	0.88	4146	120	4.0	0.6	40	7
RHCII CA5 1 1b	159	0.012	0.004	25.8	0.01	10.83	5	82	1538	9.4	0.4892	5.1	0.044	10.7	0.00065	9.4	0.88	4209	151	4.2	0.8	44	9
RHCII CA5 1 1c	57	0.008	0.003	20.7	0.00	8.69	bd	bd	1855	4.1	0.4741	5.3	0.035	6.7	0.00054	4.1	0.61	4163	156	3.5	0.3	35	5
RHCII CA5 1 2a	bd	0.007	0.003	13.4	0.00	5.65	bd	bd	1367	5.9	0.5118	4.1	0.052	7.2	0.00073	5.9	0.82	4276	121	4.7	0.6	51	7
RHCII CA5 1 2b	334	0.030	0.022	9.7	0.02	4.09	6	51	217	4.3	0.9373	1.0	0.596	4.4	0.00461	4.3	0.98	5146	27	29.7	2.6	475	33
RHCII CA5 1 3	126	0.026	0.012	48.4	0.01	20.35	13	67	1290	4.0	0.5775	2.1	0.062	4.5	0.00078	4.0	0.89	4452	61	5.0	0.4	61	5
RHCII CA5 1 4a	370	0.030	0.012	62.8	0.02	26.41	5	27	1430	5.3	0.5148	2.9	0.050	6.0	0.00070	5.3	0.88	4284	86	4.5	0.5	49	6
RHCII CA5 1 4b	262	0.030	0.012	67.1	0.02	28.20	7	46	1550	5.9	0.4938	3.6	0.044	6.9	0.00065	5.9	0.85	4223	108	4.2	0.5	44	6
RHCII CA5 1 4c	435	0.024	0.010	52.4	0.01	22.01	3	67	1482	2.8	0.5312	3.8	0.049	4.7	0.00067	2.8	0.60	4330	110	4.3	0.2	49	4
RHCII CA5 1 5	207	0.041	0.028	7.1	0.02	3.00	12	73	121	10.1	0.8942	0.7	1.015	10.1	0.00823	10.1	1.00	5080	19	52.9	10.6	711	98
RHCII CA5 1 6a	712	0.141	0.096	25.2	0.08	10.57	12	18	117	9.7	0.8686	0.5	1.024	9.7	0.00855	9.7	1.00	5039	15	54.9	10.6	716	95
RHCII CA5 1 6b	690	0.171	0.118	22.7	0.09	9.53	15	28	91	6.9	0.8852	0.5	1.334	6.9	0.01093	6.9	1.00	5065	13	70.1	9.6	861	77
RHCII CA5 1 6c	618	0.098	0.064	28.5	0.05	11.99	10	17	201	7.0	0.8447	0.6	0.580	7.1	0.00498	7.0	1.00	4999	17	32.0	4.5	465	51
RHCII CA5 2 1a	81	0.018	0.012	18.3	0.01	7.68	bd	bd	671	4.0	0.7876	1.3	0.162	4.2	0.00149	4.0	0.95	4900	36	9.6	0.8	152	12
RHCII CA5 2 1b	10	0.019	0.012	16.9	0.01	7.08	bd	bd	619	2.4	0.8216	1.3	0.183	2.8	0.00161	2.4	0.87	4960	38	10.4	0.5	171	9
RHCII CA5 2 2	82	0.014	0.010	3.4	0.01	1.45	bd	bd	172	2.4	0.9656	1.2	0.776	2.7	0.00583	2.4	0.89	5188	35	37.5	1.8	583	24
RHCII CA5 2 3a	277	0.055	0.039	8.8	0.03	3.69	12	40	110	11.0	0.9142	0.7	1.148	11.0	0.00910	11.0	1.00	5111	19	58.4	12.8	776	113
RHCII CA5 2 3b	123	0.047	0.034	8.6	0.03	3.61	bd	bd	129	3.2	0.9159	0.8	0.980	3.3	0.00776	3.2	0.97	5114	22	49.8	3.2	693	33
RHCII CA5 2 4a	360	0.026	0.011	54.4	0.01	22.85	5	31	1412	3.2	0.5612	0.7	0.055	3.3	0.00071	3.2	0.97	4411	22	4.6	0.3	54	4
RHCII CA5 2 4b	313	0.027	0.012	54.0	0.01	22.71	5	64	1382	2.6	0.5649	1.1	0.056	2.9	0.00072	2.6	0.92	4420	33	4.7	0.2	56	3
RHCII CA5 2 4c	259	0.025	0.011	52.9	0.01	22.24	6	50	1481	1.8	0.5657	1.8	0.053	2.5	0.00068	1.8	0.71	4422	52	4.4	0.2	52	3
RHCII CA5 2 5	136	0.015	0.011	5.1	0.01	2.15	7	81	236	1.7	0.9458	0.8	0.553	1.9	0.00424	1.7	0.90	5159	23	27.3	0.9	447	13
RHCII CA5 2 6a	87	0.014	0.010	6.4	0.01	2.67	bd	bd	296	6.8	0.9235	1.4	0.430	6.9	0.00338	6.8	0.98	5125	40	21.7	3.0	363	42
RHCII CA5 2 6b	206	0.015	0.010	8.0	0.01	3.37	4	46	378	5.3	0.9070	1.4	0.331	5.5	0.00265	5.3	0.97	5100	41	17.1	1.8	291	27
RHCII CA5 2 6c	242	0.013	0.010	4.1	0.01	1.74	3	95	219	5.3	0.9704	2.1	0.610	5.7	0.00456	5.3	0.93	5195	58	29.3	3.1	483	43
RHCII CA5 3 1	bd	0.008	0.003	12.0	0.00	5.06	bd	bd	1116	3.0	0.5711	2.8	0.071	4.1	0.00090	3.0	0.73	4436	82	5.8	0.3	69	5
RHCII CA5 3 2	79	0.014	0.005	31.0	0.01	13.03	bd	bd	1527	3.7	0.5103	2.7	0.046	4.6	0.00065	3.7	0.80	4271	81	4.2	0.3	46	4
RHCII CA5 3 3	bd	0.017	0.006	40.4	0.01	16.96	bd	bd	1652	1.8	0.4881	1.9	0.041	2.6	0.00061	1.8	0.69	4206	56	3.9	0.1	41	2
RHCII CA5 3 4a	24	0.010	0.007	6.1	0.01	2.57	bd	bd	426	3.5	0.8428	1.9	0.272	4.0	0.00234	3.5	0.88	4996	54	15.1	1.1	245	17
RHCII CA5 3 4b	77	0.011	0.007	6.2	0.01	2.59	bd	bd	391	2.0	0.8502	1.8	0.300	2.6	0.00256	2.0	0.74	5008	50	16.5	0.6	266	12
RHCII CA5 3 45	bd	0.017	0.005	46.7	0.01	19.64	bd	bd	1886	1.3	0.4061	1.7	0.030	2.1	0.00053	1.3	0.61	3932	50	3.4	0.1	30	1
RHCII CA5 3 6	83	0.011	0.007	4.5	0.01	1.89	bd	bd	281	5.3	0.8698	3.9	0.426	6.6	0.00356	5.3	0.81	5041	111	22.9	2.4	361	39
RHCII CA5 3 6b	bd	0.011	0.008	3.9	0.01	1.62	bd	bd	240	5.5	0.9177	3.5	0.527	6.5	0.00416	5.5	0.85	5116	98	26.8	3.0	430	45
RHCII CA5 4 1a	bd	0.060	0.039	19.1	0.03	8.04	bd	bd	223	6.5	0.8394	0.6	0.518	6.5	0.00448	6.5	1.00	4990	17	28.8	3.7	424	44
RHCII CA5 4 1b	bd	0.042	0.026	18.7	0.02	7.84	bd	bd	312	2.9	0.8213	0.9	0.363	3.1	0.00320	2.9	0.96	4959	25	20.6	1.2	314	16
RHCII CA5 4 2	bd	0.012	0.006	20.9	0.01	8.78	bd	bd	1236	1.6	0.6424	2.3	0.072	2.8	0.00081	1.6	0.57	4607	68	5.2	0.2	70	4
RHCII CA5 4 3	62	0.010	0.006	13.9	0.01	5.85	bd	bd	966	3.7	0.7472	1.9	0.107	4.1	0.00104	3.7	0.89	4824	54	6.7	0.5	103	8
RHCII CA5 4 4a	bd	0.029	0.018	18.1	0.02	7.62	bd	bd	409	9.8	0.7817	1.4	0.263	9.9	0.00244	9.8	0.99	4889	40	15.7	3.1	237	41
RHCII CA5 4 4b	bd	0.037	0.023	18.1	0.02	7.61	bd	bd	343	7.2	0.8177	1.0	0.328	7.3	0.00291	7.2	0.99	4953	29	18.7	2.7	288	36
RHCII CA5 4 5	bd	0.028	0.009	88.8	0.02	37.32	bd	bd	2199	1.4	0.3940	2.0	0.025	2.4	0.00045	1.4	0.57	3886	60	2.9	0.1	25	1
RHCII CA5 4 5b	bd	0.028	0.009	85.7	0.02	36.00	bd	bd	2099	1.9	0.4293	1.4	0.028	2.4	0.00048	1.9	0.81	4015	42	3.1	0.1	28	1
RHCII CA5 4 6a	95	0.043	0.020	77.1	0.02	32.40	28	93	1248	8.4	0.5865	2.6	0.065	8.7	0.00080	8.4	0.96	4475	74	5.2	0.9	64	11
RHCII CA5 4 6b	51	0.036	0.014	80.0	0.02	33.60	bd	bd	1570	2.4	0.5251	1.6	0.046	2.8	0.00064	2.4	0.83	4313	46	4.1	0.2	46	3

Data not common-Pb corrected

Samples	Signals						Data for Tera-Wasserberg plot						Data for Wetherill plot					Ages					
	^{204}Pb in sample cps gc	^{206}Pb mV	^{207}Pb mV	^{238}U mV	Pb ppm	Uppm*	$^{206}Pb/^{204}Pb$	1σ %	$^{238}U/^{206}Pb$	1σ %	$^{207}Pb/^{206}Pb$	1σ %	$^{207}Pb/^{235}U$	1σ %	$^{206}Pb/^{238}U$	1σ %	Rho	$^{207}Pb/^{206}Pb$	2σ abs	$^{206}Pb/^{238}U$	2σ abs	$^{207}Pb/^{235}U$	2σ abs
RHCII CA6 1 2a	497	0.142	0.096	40.2	0.08	16.91	18	30	202	13.7	0.8543	0.8	0.583	13.8	0.00495	13.7	1.00	5015	23	31.9	8.7	467	98
RHCII CA6 1 2b	72	0.061	0.039	35.7	0.03	14.99	bd	bd	398	11.5	0.8110	1.4	0.281	11.6	0.00251	11.5	0.99	4941	39	16.2	3.7	251	50
RHCII CA6 1 4a	109	0.034	0.013	76.4	0.02	32.12	20	73	1462	4.1	0.5463	2.4	0.052	4.7	0.00068	4.1	0.86	4371	70	4.4	0.4	51	5
RHCII CA6 1 4b	166	0.047	0.018	110.7	0.03	46.51	18	84	1621	4.7	0.4942	4.2	0.042	6.3	0.00062	4.7	0.74	4224	125	4.0	0.4	42	5
RHCII CA6 1 4c	63	0.029	0.013	57.5	0.02	24.18	bd	bd	1403	4.2	0.5800	1.9	0.057	4.6	0.00071	4.2	0.91	4459	55	4.6	0.4	56	5
RHCII CA6 1 5a	421	0.096	0.063	30.5	0.05	12.82	14	23	187	14.8	0.8408	0.9	0.619	14.8	0.00534	14.8	1.00	4992	26	34.3	10.1	489	109
RHCII CA6 1 5b	593	0.130	0.087	23.0	0.07	9.68	14	20	125	5.1	0.8652	0.4	0.957	5.1	0.00802	5.1	1.00	5033	10	51.5	5.2	682	50
RHCII CA6 1 5c	268	0.054	0.033	38.8	0.03	16.31	13	57	488	12.2	0.7788	1.9	0.220	12.4	0.00205	12.2	0.99	4883	55	13.2	3.2	202	44
RHCII CA6 1 6a	688	0.138	0.091	34.4	0.08	14.45	13	14	171	5.8	0.8440	0.5	0.681	5.8	0.00585	5.8	1.00	4998	13	37.6	4.4	527	47
RHCII CA6 1 6b	707	0.121	0.079	41.8	0.07	17.56	11	12	239	6.2	0.8434	0.6	0.486	6.3	0.00418	6.2	1.00	4997	17	26.9	3.3	402	41
RHCII CA6 1 6c	420	0.118	0.076	30.3	0.06	12.73	18	57	178	2.7	0.8288	0.7	0.641	2.8	0.00561	2.7	0.97	4972	21	36.0	1.9	503	22
RHCII CA6 2 1a	662	0.151	0.097	60.1	0.08	25.25	14	20	262	6.3	0.8346	0.6	0.439	6.3	0.00381	6.3	1.00	4982	16	24.5	3.1	369	38
RHCII CA6 2 1b	579	0.159	0.100	78.7	0.09	33.08	17	29	339	5.1	0.8053	0.6	0.328	5.1	0.00295	5.1	0.99	4931	18	19.0	1.9	288	25
RHCII CA6 2 1c	473	0.122	0.078	42.9	0.07	18.04	16	20	251	4.3	0.8460	0.7	0.465	4.3	0.00399	4.3	0.99	5001	21	25.6	2.2	388	28
RHCII CA6 2 2a	548	0.105	0.071	48.8	0.06	20.51	12	20	316	6.6	0.8527	0.8	0.372	6.7	0.00316	6.6	0.99	5012	23	20.4	2.7	321	36
RHCII CA6 2 2b	515	0.101	0.067	56.0	0.06	23.54	12	37	379	5.7	0.8517	1.2	0.310	5.8	0.00264	5.7	0.98	5011	33	17.0	1.9	274	28
RHCII CA6 2 2c	626	0.118	0.079	36.4	0.06	15.28	12	20	210	9.5	0.8691	0.6	0.570	9.5	0.00475	9.5	1.00	5039	18	30.6	5.8	458	68
RHCII CA6 2 3a	404	0.069	0.041	56.1	0.04	23.59	11	24	558	9.5	0.7606	1.3	0.188	9.6	0.00179	9.5	0.99	4850	38	11.5	2.2	175	30
RHCII CA6 2 3b	271	0.066	0.039	56.6	0.04	23.79	15	41	595	8.3	0.7400	1.5	0.172	8.5	0.00168	8.3	0.98	4810	43	10.8	1.8	161	25
RHCII CA6 2 4a	277	0.017	0.007	33.6	0.01	14.11	4	40	1342	5.4	0.5647	2.7	0.058	6.0	0.00075	5.4	0.90	4420	78	4.8	0.5	57	7
RHCII CA6 2 4b	510	0.016	0.006	37.4	0.01	15.70	2	31	1615	2.3	0.5081	3.1	0.043	3.9	0.00062	2.3	0.58	4265	93	4.0	0.2	43	3
RHCII CA6 2 6a	280	0.026	0.010	59.4	0.01	24.95	6	43	1614	2.4	0.5179	2.7	0.044	3.6	0.00062	2.4	0.67	4293	79	4.0	0.2	44	3
RHCII CA6 3 1a	271	0.076	0.042	82.1	0.04	34.49	18	29	733	3.2	0.7113	0.8	0.134	3.3	0.00136	3.2	0.97	4754	23	8.8	0.6	127	8
RHCII CA6 3 1b	237	0.083	0.045	86.0	0.05	36.15	22	63	714	4.9	0.6944	1.3	0.134	5.1	0.00140	4.9	0.97	4719	36	9.0	0.9	128	12
RHCII CA6 3 1c	269	0.071	0.040	77.2	0.04	32.45	16	48	739	3.2	0.7228	0.9	0.135	3.3	0.00135	3.2	0.96	4777	27	8.7	0.6	128	8
RHCII CA6 3 2a	103	0.025	0.017	6.6	0.01	2.79	bd	bd	191	16.5	0.8645	1.6	0.623	16.5	0.00522	16.5	1.00	5032	46	33.6	11.0	492	121
RHCII CA6 3 2b	136	0.012	0.008	6.5	0.01	2.74	bd	bd	368	3.5	0.8309	1.9	0.311	4.0	0.00272	3.5	0.87	4976	55	17.5	1.2	275	19
RHCII CA6 3 2c	78	0.049	0.034	6.9	0.03	2.91	bd	bd	98	7.5	0.8954	0.7	1.264	7.5	0.01024	7.5	1.00	5082	19	65.7	9.8	830	82
RHCII CA6 3 3b	81	0.009	0.005	14.8	0.00	6.21	bd	bd	1160	4.3	0.6565	4.1	0.078	5.9	0.00086	4.3	0.72	4638	119	5.6	0.5	76	9
RHCII CA6 3 4a	264	0.077	0.041	95.9	0.04	40.30	18	47	826	15.7	0.5939	5.7	0.099	16.7	0.00121	15.7	0.94	4493	166	7.8	2.4	96	30
RHCII CA6 3 4b	273	0.036	0.011	103.6	0.02	43.53	8	66	2041	2.2	0.3861	3.1	0.026	3.8	0.00049	2.2	0.59	3856	94	3.2	0.1	26	2
RHCII CA6 3 4c	44	0.112	0.067	88.8	0.06	37.30	bd	bd	547	6.6	0.7581	0.9	0.191	6.6	0.00183	6.6	0.99	4845	25	11.8	1.5	178	21
RHCII CA6 3 5a	136	0.042	0.019	87.3	0.02	36.68	19	70	1393	3.5	0.5817	1.2	0.058	3.7	0.00072	3.5	0.95	4463	35	4.6	0.3	57	4
RHCII CA6 3 5b	179	0.045	0.020	92.8	0.02	38.99	16	78	1437	3.2	0.5772	1.2	0.055	3.4	0.00070	3.2	0.93	4452	36	4.5	0.3	55	4
RHCII CA6 3 5c	85	0.038	0.017	75.0	0.02	31.50	bd	bd	1322	5.7	0.5830	2.1	0.061	6.0	0.00076	5.7	0.94	4466	60	4.9	0.6	60	7
RHCII CA6 3 6a	395	0.139	0.092	40.7	0.08	17.10	22	26	197	9.1	0.8521	0.5	0.596	9.1	0.00508	9.1	1.00	5011	13	32.6	5.9	475	67
RHCII CA6 3 6b	447	0.142	0.093	39.1	0.08	16.42	20	43	194	10.1	0.8420	0.8	0.599	10.1	0.00516	10.1	1.00	4994	23	33.1	6.7	476	74
RHCII CA6 3 6c	509	0.114	0.073	47.0	0.06	19.74	14	37	287	2.6	0.8312	0.7	0.399	2.7	0.00348	2.6	0.97	4976	20	22.4	1.2	341	16
RHCII CA6 4 1	734	0.188	0.122	71.4	0.10	30.00	16	20	261	5.7	0.8351	0.6	0.441	5.8	0.00383	5.7	0.99	4983	17	24.6	2.8	371	35
RHCII CA6 4 2a	95	0.018	0.003	68.3	0.01	28.70	bd	bd	2675	1.5	0.2300	3.7	0.012	4.0	0.00037	1.5	0.39	3052	117	2.4	0.1	12	1
RHCII CA6 4 2b	134	0.019	0.004	70.6	0.01	29.65	9	56	2584	1.6	0.2426	3.5	0.013	3.9	0.00039	1.6	0.40	3137	113	2.5	0.1	13	1
RHCII CA6 4 3a	107	0.044	0.018	94.2	0.02	39.59	26	81	1465	10.1	0.4529	6.6	0.043	12.1	0.00068	10.1	0.84	4095	197	4.4	0.9	42	10
RHCII CA6 4 3b	177	0.058	0.029	88.5	0.03	37.20	bd	bd	1059	5.9	0.6278	1.9	0.082	6.2	0.00094	5.9	0.95	4574	55	6.1	0.7	80	10
RHCII CA6 4 4	bd	0.009	0.004	23.2	0.00	9.77	bd	bd	1776	3.0	0.4976	2.8	0.039	4.1	0.00056	3.0	0.73	4234	83	3.6	0.2	38	3
RHCII CA6 4 5a	bd	0.028	0.008	85.7	0.02	36.00	bd	bd	2052	3.5	0.3818	3.4	0.026	4.9	0.00049	3.5	0.72	3839	103	3.1	0.2	26	2
RHCII CA6 4 5b	9	0.023	0.007	64.7	0.01	27.18	bd	bd	1936	4.1	0.4001	2.7	0.028	4.9	0.00052	4.1	0.83	3909	83	3.3	0.3	29	3
RHCII CA6 4 5c	52	0.035	0.009	105.6	0.02	44.40	bd	bd	2108	5.5	0.3491	5.2	0.023	7.5	0.00047	5.5	0.73	3703	157	3.1	0.3	23	3
RHCII CA6 4 6	136	0.013	0.003	44.7	0.01	18.80	6	63	2388	2.3	0.3260	4.0	0.019	4.6	0.00042	2.3	0.50	3599	122	2.7	0.1	19	2

Data not common-Pb corrected

Samples	Signals								Data for Tera-Wasserberg plot				Data for Wetherill plot							Ages			
	^{204}Pb in sample cps gc	^{206}Pb mV	^{207}Pb mV	^{238}U mV	Pb ppm	Uppm*	$^{206}Pb/^{204}Pb$	1σ %	$^{238}U/^{206}Pb$	1σ %	$^{207}Pb/^{206}Pb$	1σ %	$^{207}Pb/^{235}U$	1σ %	$^{206}Pb/^{238}U$	1σ %	Rho	$^{207}Pb/^{206}Pb$	2σ abs	$^{206}Pb/^{238}U$	2σ abs	$^{207}Pb/^{235}U$	2σ abs
RHCII CA7 1 1a	41	0.009	0.003	24	0.01	15	bd	bd	1951	2.1	0.3995	3.5	0.028	4.1	0.00051	2.1	0.52	3907	105	3.3	0.1	28	2
RHCII CA7 1 1b	bd	0.011	0.005	25	0.01	16	bd	bd	1600	3.8	0.4560	3.9	0.039	5.5	0.00062	3.8	0.70	4105	117	4.0	0.3	39	4
RHCII CA7 1 1c	41	0.008	0.003	23	0.01	15	bd	bd	2126	2.1	0.3665	3.3	0.024	3.9	0.00047	2.1	0.54	3777	99	3.0	0.1	24	2
RHCII CA7 1 2a	bd	0.009	0.004	15	0.01	10	bd	bd	1175	3.8	0.5312	2.1	0.062	4.3	0.00085	3.8	0.88	4330	61	5.5	0.4	61	5
RHCII CA7 1 2b	bd	0.009	0.005	15	0.01	9	bd	bd	1136	4.8	0.5451	3.1	0.066	5.7	0.00088	4.8	0.84	4368	91	5.7	0.5	65	7
RHCII CA7 1 2c	bd	0.011	0.005	21	0.01	13	bd	bd	1373	13.7	0.4701	10.4	0.047	17.2	0.00073	13.7	0.80	4150	309	4.7	1.3	47	16
RHCII CA7 1 3a	2449	0.800	0.561	17	0.62	11	20	13	13	7.6	0.7663	0.1	7.830	7.6	0.07411	7.6	1.00	4860	4	460.9	66.9	2212	128
RHCII CA7 1 3b	1293	0.460	0.321	19	0.36	12	22	10	22	10.9	0.7611	0.3	4.802	10.9	0.04576	10.9	1.00	4851	9	288.4	61.4	1785	169
RHCII CA7 1 3c	3344	1.090	0.766	15	0.85	10	20	4	9	5.2	0.7672	0.2	11.217	5.2	0.10603	5.2	1.00	4862	4	649.7	63.8	2541	92
RHCII CA7 1 3d	3302	1.079	0.758	18	0.84	11	20	4	11	5.6	0.7663	0.1	9.744	5.6	0.09222	5.6	1.00	4860	3	568.6	61.1	2411	99
RHCII CA7 1 4	bd	0.017	0.002	68	0.01	43	bd	bd	2981	0.8	0.1738	5.4	0.008	5.5	0.00034	0.8	0.15	2595	180	2.2	0.0	8	1
RHCII CA7 1 5a	540	0.148	0.099	38	0.12	24	17	18	184	4.6	0.7298	0.4	0.548	4.6	0.00545	4.6	1.00	4791	13	35.0	3.2	444	33
RHCII CA7 1 5b	302	0.100	0.065	41	0.08	26	21	25	292	7.3	0.7045	0.9	0.332	7.4	0.00342	7.3	0.99	4740	26	22.0	3.2	291	37
RHCII CA7 1 5c	591	0.165	0.112	37	0.13	23	17	26	162	1.9	0.7356	0.4	0.628	2.0	0.00619	1.9	0.98	4802	11	39.8	1.5	495	15
RHCII CA7 1 6	bd	0.008	0.002	24	0.01	15	bd	bd	2217	1.6	0.3105	2.3	0.019	2.8	0.00045	1.6	0.57	3523	71	2.9	0.1	19	1
RHCII CA7 1 6b	119	0.007	0.002	22	0.01	14	4	67	2157	1.2	0.3117	3.1	0.020	3.4	0.00046	1.2	0.36	3529	97	3.0	0.1	20	1
RHCII CA7 1 6c	bd	0.009	0.003	27	0.01	17	bd	bd	2269	2.9	0.3217	5.0	0.020	5.8	0.00044	2.9	0.51	3578	153	2.8	0.2	20	2
RHCII CA7 1 7a	373	0.134	0.093	7	0.10	4	22	21	37	1.4	0.7577	0.2	2.836	1.4	0.02714	1.4	0.99	4844	6	172.6	4.8	1365	21
RHCII CA7 1 7b	433	0.118	0.082	6	0.09	4	17	32	37	1.2	0.7584	0.2	2.848	1.2	0.02724	1.2	0.99	4845	6	173.3	4.0	1368	18
RHCII CA7 1 8a	24	0.016	0.004	54	0.01	34	bd	bd	2477	3.2	0.2493	6.4	0.014	7.2	0.00040	3.2	0.45	3181	203	2.6	0.2	14	2
RHCII CA7 1 8b	141	0.016	0.004	56	0.01	35	7	65	2534	2.3	0.2413	6.2	0.013	6.6	0.00039	2.3	0.35	3129	198	2.5	0.1	13	2
RHCII CA7 1 9a	25	0.059	0.041	18	0.05	11	bd	bd	211	9.9	0.6430	5.0	0.420	11.1	0.00474	9.9	0.89	4608	144	30.5	6.0	356	65
RHCII CA7 1 9b	77	0.081	0.055	17	0.06	11	66	62	151	3.8	0.7325	0.3	0.668	3.8	0.00661	3.8	1.00	4796	10	42.5	3.2	519	30
RHCII CA7 2 1	bd	0.015	0.005	42	0.01	26	bd	bd	1921	3.3	0.3619	5.0	0.026	5.9	0.00052	3.3	0.55	3758	151	3.4	0.2	26	3
RHCII CA7 2 2	bd	0.014	0.007	17	0.01	11	bd	bd	897	2.0	0.5896	1.0	0.091	2.2	0.00112	2.0	0.89	4483	30	7.2	0.3	88	4
RHCII CA7 2 2b	bd	0.015	0.009	18	0.01	11	bd	bd	848	2.5	0.5989	1.2	0.097	2.7	0.00118	2.5	0.90	4505	35	7.6	0.4	94	5
RHCII CA7 2 2c	bd	0.012	0.006	15	0.01	9	bd	bd	899	1.7	0.5704	1.9	0.088	2.6	0.00111	1.7	0.66	4434	56	7.2	0.2	85	4
RHCII CA7 2 3a	106	0.090	0.058	37	0.07	23	53	70	290	4.6	0.7066	0.5	0.337	4.7	0.00345	4.6	1.00	4744	13	22.2	2.1	295	24
RHCII CA7 2 3b	102	0.083	0.054	31	0.06	20	51	58	271	2.3	0.7110	0.7	0.361	2.4	0.00368	2.3	0.96	4753	19	23.7	1.1	313	13
RHCII CA7 2 3c	272	0.098	0.064	39	0.08	25	22	32	291	6.4	0.7044	0.7	0.334	6.4	0.00344	6.4	0.99	4740	19	22.1	2.8	293	32
RHCII CA7 2 4a	bd	0.012	0.004	27	0.01	17	bd	bd	1617	3.1	0.4252	3.1	0.036	4.3	0.00062	3.1	0.71	4001	91	4.0	0.2	36	3
RHCII CA7 2 4b	bd	0.011	0.005	21	0.01	13	bd	bd	1395	3.1	0.4620	1.9	0.046	3.6	0.00072	3.1	0.85	4124	55	4.6	0.3	45	3
RHCII CA7 2 4c	bd	0.012	0.004	34	0.01	21	bd	bd	2008	0.6	0.3501	1.6	0.024	1.7	0.00050	0.6	0.33	3707	49	3.2	0.0	24	1
RHCII CA7 2 5a	21	0.076	0.042	69	0.06	43	bd	bd	643	2.8	0.6096	1.2	0.131	3.0	0.00156	2.8	0.92	4531	35	10.0	0.6	125	7
RHCII CA7 2 5b	2	0.067	0.035	71	0.05	45	bd	bd	774	1.0	0.5752	0.6	0.102	1.2	0.00129	1.0	0.86	4447	18	8.3	0.2	99	2
RHCII CA7 2 5c	bd	0.080	0.046	66	0.06	41	bd	bd	582	1.4	0.6282	0.7	0.149	1.6	0.00172	1.4	0.89	4575	21	11.1	0.3	141	4
RHCII CA7 2 6	122	0.013	0.003	45	0.01	28	7	61	2395	1.3	0.2721	3.0	0.016	3.2	0.00042	1.3	0.39	3318	93	2.7	0.1	16	1
RHCII CA7 2 7	104	0.007	0.005	7	0.01	4	4	93	666	6.3	0.6485	2.6	0.134	6.8	0.00150	6.3	0.92	4621	76	9.7	1.2	128	16
RHCII CA7 2 8	bd	0.016	0.003	59	0.01	37	bd	bd	2605	0.8	0.1886	1.4	0.010	1.6	0.00038	0.8	0.51	2730	45	2.5	0.0	10	0
RHCII CA7 3 1a	152	0.040	0.027	25	0.03	16	16	64	444	4.9	0.7218	0.9	0.224	5.0	0.00225	4.9	0.98	4775	25	14.5	1.4	205	18
RHCII CA7 3 1b	144	0.044	0.030	25	0.03	15	19	84	398	5.2	0.7283	1.1	0.252	5.3	0.00251	5.2	0.98	4788	33	16.2	1.7	228	21
RHCII CA7 3 1c	94	0.030	0.019	26	0.02	16	bd	bd	620	1.7	0.6808	0.9	0.151	1.9	0.00161	1.7	0.89	4691	25	10.4	0.4	143	5
RHCII CA7 3 2a	bd	0.022	0.014	17	0.02	10	bd	bd	525	2.6	0.6942	0.8	0.182	2.7	0.00191	2.6	0.95	4719	24	12.3	0.6	170	8
RHCII CA7 3 2b	bd	0.022	0.014	19	0.02	12	bd	bd	597	2.8	0.6895	0.8	0.159	2.9	0.00168	2.8	0.96	4709	24	10.8	0.6	150	8
RHCII CA7 3 2c	86	0.020	0.013	13	0.02	8	bd	bd	472	2.2	0.7153	1.1	0.209	2.5	0.00212	2.2	0.90	4762	31	13.6	0.6	193	9
RHCII CA7 3 3a	327	0.109	0.075	12	0.08	7	21	28	75	5.1	0.7564	0.2	1.382	5.1	0.01325	5.1	1.00	4842	6	84.9	8.6	881	59
RHCII CA7 3 3b	242	0.087	0.060	10	0.07	7	22	31	85	3.3	0.7602	0.4	1.230	3.3	0.01173	3.3	0.99	4849	11	75.2	5.0	814	37
RHCII CA7 3 4a	bd	0.023	0.013	23	0.02	14	bd	bd	719	4.5	0.6386	1.6	0.122	4.7	0.00139	4.5	0.94	4598	45	9.0	0.8	117	10
RHCII CA7 3 4b	4	0.017	0.010	22	0.01	14	bd	bd	924	1.1	0.6040	1.2	0.090	1.6	0.00108	1.1	0.68	4518	35	7.0	0.2	88	3
RHCII CA7 3 4c	bd	0.036	0.024	23	0.03	14	bd	bd	459	3.9	0.7088	1.1	0.213	4.0	0.00218	3.9	0.96	4749	32	14.0	1.1	196	14
RHCII CA7 3 5a	245	0.102	0.066	23	0.08	14	26	27	146	10.1	0.7324	0.5	0.690	10.1	0.00684	10.1	1.00	4796	15	43.9	8.8	533	81
RHCII CA7 3 5b	50	0.068	0.045	28	0.05	17	bd	bd	276	6.9	0.7191	0.8	0.360	6.9	0.00363	6.9	0.99	4769	22	23.3	3.2	312	37
RHCII CA7 3 5c	494	0.152	0.104	16	0.12	10	19	23	71	5.6	0.7470	0.3	1.447	5.6	0.01405	5.6	1.00	4824	10	89.9	10.0	909	66
RHCII CA7 3 6	bd	0.007	0.005	3	0.01	2	bd	bd	236	6.4	0.7706	1.2	0.450	6.5	0.00424	6.4	0.98	4868	35	27.3	3.5	378	40
RHCII CA7 4 1a	bd	0.010	0.005	14	0.01	9	bd	bd	997	2.2	0.5519	1.8	0.076	2.8	0.00100	2.2	0.78	4386	51	6.5	0.3	75	4
RHCII CA7 4 1b	bd	0.011	0.006	15	0.01	9	bd	bd	978	3.7	0.5612	3.0	0.079	4.8	0.00102	3.7	0.78	4411	88	6.6	0.5	77	7
RHCII CA7 4 1c	bd	0.009	0.005	13	0.01	8	bd	bd	969	3.0	0.5726	2.6	0.081	4.0	0.00103	3.0	0.75	4440	76	6.6	0.4	80	6
RHCII CA7 4 2a	91	0.072	0.049	12	0.06	8	49	83	126	4.3	0.7431	0.4	0.811	4.3	0.00792	4.3	1.00	4816	12	50.8	4.3	603	39
RHCII CA7 4 2b	5	0.067	0.045	13	0.05	8	bd	bd	137	3.0	0.7389	0.4	0.743	3.0	0.00729	3.0	0.99	4808	13	46.8	2.8	564	26
RHCII CA7 4 3a	269	0.081	0.054	22	0.06	14	19	28	203	5.5	0.7202	0.7	0.490	5.5	0.00493	5.5	0.99	4772	20	31.7	3.5	405	36
RHCII CA7 4 3b	294	0.103	0.069	23	0.08	15	22	29	163	0.8	0.7289	0.3	0.617	0.9	0.00614	0.8	0.94	4789	9	39.5	0.7	488	7
RHCII CA7 4 3c	177	0.033	0.020	21	0.03	13	11	45	458	7.3	0.6539	2.3	0.197	7.7	0.00218	7.3	0.95	4633	66	14.1	2.1	182	25
RHCII CA7 4 4	bd	0.012	0.006	14	0.01	9	bd	bd	882	3.6	0.6099	1.5	0.095	3.9	0.00113	3.6	0.92	4532	45	7.3	0.5	92	7
RHCII CA7 4 5	112	0.029	0.016	34	0.02	21	16	61	824	7.7	0.5662	3.7	0.095	8.6	0.00121	7.7	0.90	4423	108	7.8	1.2	92	15
RHCII CA7 4 5b	78	0.035	0.020	31	0.03	20	bd	bd	645	5.7	0.6375	1.3	0.136	5.9	0.00155	5.7	0.97	4596	39	10.0	1.1	130	14
RHCII CA7 4 6a	bd	0.015	0.007	33	0.01	21	bd	bd	1651	2.5	0.4391	2.5	0.037	3.5	0.00061	2.5	0.70	4049	75	3.9	0.2	37	3
RHCII CA7 4 6b	88	0.018	0.008	35	0.01	22	bd	bd	1423	4.4	0.4821	3.1	0.047	5.4	0.00070	4.4	0.82	4187	92	4.5	0.4	46	5
RHCII CA7 4 6c	bd	0.012	0.005	30	0.01	19	bd	bd	1746	1.7	0.4152	2.1	0.033	2.8	0.00057	1.7	0.63	3965	64	3.7	0.1	33	2

Data not common-Pb corrected

Samples		Signals						Data for Tera-Wasserberg plot				Data for Wetherill plot					Ages					
	^{204}Pb in sample cps gc	^{206}Pb mV	^{207}Pb mV	^{238}U mV	Pb ppm	Uppm*	$^{206}Pb/^{204}Pb$	1σ %	$^{238}U/^{206}Pb$	1σ %	$^{207}Pb/^{206}Pb$	1σ %	$^{207}Pb/^{235}U$	1σ %	$^{206}Pb/^{238}U$	1σ %	Rho	$^{207}Pb/^{206}Pb$	2σ abs	$^{206}Pb/^{238}U$	2σ abs	$^{207}Pb/^{235}U$	2σ abs
Level 2																							
RHCI 7 1 1	379	0.1	0.07	22	0.02	6	19	40	266	4.8	0.7277	0.8	0.377	4.9	0.00376	4.8	0.99	4786	23	24.2	2.3	325	27
RHCI 7 1 2	368	0.1	0.04	35	0.01	10	12	44	729	6.3	0.6167	1.4	0.117	6.5	0.00137	6.3	0.98	4548	40	8.8	1.1	112	14
RHCI 7 1 2b	3292	0.1	0.07	46	0.02	14	2	86	537	18.3	0.6647	2.3	0.171	18.4	0.00186	18.3	0.99	4656	65	12.0	4.4	160	53
RHCI 7 1 2c	546	0.1	0.03	33	0.01	10	7	37	751	9.0	0.6179	1.0	0.113	9.1	0.00133	9.0	0.99	4551	30	8.6	1.5	109	19
RHCI 7 1 3a	147	0.0	0.01	34	0.01	10	bd	bd	1528	5.5	0.4207	2.9	0.038	6.2	0.00065	5.5	0.89	3985	85	4.2	0.5	38	5
RHCI 7 1 3b	430	0.1	0.03	37	0.01	11	8	22	879	12.3	0.5723	3.5	0.090	12.8	0.00114	12.3	0.96	4439	102	7.3	1.8	87	21
RHCI 7 1 4	434	0.1	0.03	42	0.01	12	10	23	904	4.1	0.5884	1.1	0.090	4.2	0.00111	4.1	0.97	4480	32	7.1	0.6	87	7
RHCI 7 1 5a	439	0.1	0.07	76	0.03	22	18	22	843	2.0	0.6023	0.5	0.098	2.1	0.00119	2.0	0.97	4514	15	7.6	0.3	95	4
RHCI 7 1 6	221	0.1	0.01	107	0.01	31	17	63	2460	3.2	0.2483	5.2	0.014	6.1	0.00041	3.2	0.52	3174	166	2.6	0.2	14	2
RHCI 7 2 1	884	0.2	0.16	16	0.05	5	17	18	96	9.1	0.7723	0.3	1.107	9.1	0.01039	9.1	1.00	4872	9	66.6	12.1	756	93
RHCI 7 2 1b	841	0.2	0.14	15	0.04	5	16	16	104	9.4	0.7655	0.5	1.012	9.4	0.00959	9.4	1.00	4859	14	61.5	11.5	710	92
RHCI 7 2 1b	547	0.1	0.09	43	0.03	13	17	18	381	8.4	0.7028	0.8	0.254	8.4	0.00262	8.4	1.00	4737	24	16.9	2.8	230	34
RHCI 7 2 2	557	0.1	0.09	43	0.03	13	16	20	399	8.4	0.7023	0.9	0.242	8.4	0.00250	8.4	0.99	4736	25	16.1	2.7	220	33
RHCI 7 2 3a	532	0.3	0.16	37	0.05	11	30	77	213	3.4	0.7493	0.6	0.486	3.5	0.00470	3.4	0.98	4828	18	30.2	2.1	402	23
RHCI 7 2 3b	1399	0.4	0.25	32	0.07	9	17	14	122	12.2	0.7618	0.3	0.862	12.2	0.00821	12.2	1.00	4852	9	52.7	12.8	631	109
RHCI 7 2 4a	2189	0.9	0.55	84	0.17	25	24	18	141	10.5	0.7594	0.4	0.741	10.5	0.00708	10.5	1.00	4848	13	45.5	9.5	563	87
RHCI 7 2 4b	2958	0.9	0.61	60	0.18	18	20	9	90	5.1	0.7647	0.3	1.167	5.1	0.01107	5.1	1.00	4857	8	71.0	7.1	785	54
RHCI 7 2 5a	1000	0.3	0.16	40	0.05	12	16	21	253	13.2	0.7259	0.8	0.395	13.2	0.00395	13.2	1.00	4783	24	25.4	6.7	338	73
RHCI 7 2 5b	422	0.2	0.08	82	0.03	24	22	36	766	6.4	0.6167	1.3	0.111	6.6	0.00130	6.4	0.98	4548	37	8.4	1.1	107	13
RHCI 7 2 6	2733	0.8	0.51	33	0.15	10	18	17	60	14.4	0.7690	0.4	1.767	14.4	0.01666	14.4	1.00	4865	12	106.5	30.4	1033	172
RHCI 7 2 6	2733	0.8	0.51	33	0.15	10	18	17	60	14.4	0.7690	0.4	1.767	14.4	0.01666	14.4	1.00	4865	12	106.5	30.4	1033	172
RHCI 7 3 1a	555	0.2	0.11	31	0.04	9	20	22	246	5.2	0.7400	0.4	0.415	5.2	0.00407	5.2	1.00	4810	12	26.2	2.7	352	30
RHCI 7 3 1b	427	0.2	0.12	27	0.04	8	27	38	219	8.7	0.7356	0.9	0.464	8.8	0.00458	8.7	0.99	4802	25	29.4	5.1	387	55
RHCI 7 3 2a	bd	0.0	0.01	68	0.01	20	bd	bd	2173	3.3	0.3316	4.5	0.021	5.6	0.00046	3.3	0.58	3624	139	3.0	0.2	21	2
RHCI 7 3 2b	bd	0.0	0.01	70	0.01	20	bd	bd	2148	2.6	0.3304	3.6	0.021	4.5	0.00047	2.6	0.58	3619	111	3.0	0.2	21	2
RHCI 7 3 2c	bd	0.1	0.02	72	0.01	21	bd	bd	1959	2.2	0.3571	3.9	0.025	4.5	0.00051	2.2	0.48	3737	119	3.3	0.1	25	2
RHCI 7 3 3	218	0.1	0.05	52	0.02	15	25	78	871	1.4	0.6462	0.9	0.102	1.7	0.00115	1.4	0.84	4615	26	7.4	0.2	99	3
RHCI 7 3 4a	280	0.1	0.09	40	0.03	12	32	46	384	6.5	0.6994	0.6	0.251	6.5	0.00261	6.5	1.00	4730	16	16.8	2.2	228	26
RHCI 7 3 4b	554	0.3	0.16	45	0.05	13	29	24	236	10.9	0.7347	0.9	0.429	10.9	0.00423	10.9	1.00	4800	27	27.2	5.9	362	64
RHCI 7 3 5a	1356	0.5	0.31	35	0.09	10	22	14	110	2.6	0.7610	0.3	0.957	2.7	0.00912	2.6	0.99	4851	10	58.5	3.1	682	26
RHCI 7 3 5b	1910	0.6	0.41	29	0.12	9	20	16	70	9.8	0.7768	0.3	1.531	9.8	0.01429	9.8	1.00	4880	10	91.5	17.8	943	114
RHCI 7 3 6a	467	0.2	0.13	55	0.04	16	28	32	375	19.1	0.7002	1.1	0.258	19.1	0.00267	19.1	1.00	4731	32	17.2	6.6	233	77
RHCI 7 3 6b	2141	0.6	0.41	35	0.12	10	18	15	84	3.9	0.7715	0.4	1.269	4.0	0.01193	3.9	1.00	4870	11	76.5	6.0	832	44
RHCI 7 3 6c	3719	1.1	0.77	41	0.22	12	19	7	52	5.2	0.7801	0.3	2.059	5.2	0.01914	5.2	1.00	4886	8	122.2	12.6	1135	69
RHCI 7 4 1	66	0.1	0.02	77	0.01	23	bd	bd	1977	9.3	0.3326	8.7	0.023	12.7	0.00051	9.3	0.73	3629	267	3.3	0.6	23	6
RHCI 7 4 1a	420	0.1	0.05	51	0.02	15	13	34	847	7.5	0.6255	1.2	0.102	7.5	0.00118	7.5	0.99	4568	34	7.6	1.1	98	14
RHCI 7 4 1b	1008	0.2	0.15	34	0.05	10	14	12	206	9.5	0.7400	0.5	0.496	9.5	0.00486	9.5	1.00	4810	15	31.3	5.9	409	62
RHCI 7 4 1c	4436	0.2	0.10	31	0.03	9	2	88	275	1.4	0.7370	0.0	0.369	1.4	0.00363	1.4	1.00	4805	1	23.4	0.6	319	8
RHCI 7 4 2a	bd	0.0	0.02	47	0.01	14	bd	bd	1530	5.4	0.4706	2.8	0.042	6.0	0.00065	5.4	0.89	4152	82	4.2	0.5	42	5
RHCI 7 4 2b	119	0.1	0.03	35	0.01	10	bd	bd	831	15.0	0.6173	3.6	0.102	15.4	0.00120	15.0	0.97	4549	103	7.7	2.3	99	29
RHCI 7 4 3	129	0.1	0.02	113	0.01	33	36	57	2185	2.8	0.3181	3.1	0.020	4.2	0.00046	2.8	0.67	3561	97	2.9	0.2	20	2
RHCI 7 4 5	7	0.1	0.05	65	0.02	19	bd	bd	1069	8.1	0.5808	2.6	0.075	8.5	0.00094	8.1	0.95	4461	75	6.0	1.0	73	12
RHCI 7 4 5b	bd	0.0	0.02	41	0.01	12	bd	bd	1484	3.6	0.4594	2.4	0.043	4.3	0.00067	3.6	0.83	4116	71	4.3	0.3	42	4
RHCI 7 4 6	193	0.1	0.03	80	0.02	24	26	62	1452	3.0	0.4562	1.6	0.043	3.4	0.00069	3.0	0.89	4106	46	4.4	0.3	43	3
RHCI 7 4 4a	169	0.1	0.02	122	0.01	36	28	57	2325	3.3	0.2820	4.6	0.017	5.6	0.00043	3.3	0.58	3374	144	2.8	0.2	17	2
RHCI 7 4 4b	222	0.1	0.02	101	0.01	30	20	37	2069	2.7	0.3392	2.5	0.023	3.7	0.00048	2.7	0.73	3659	77	3.1	0.2	23	2

Data not common-Pb corrected

Samples	Signals								Data for Tera-Wasserberg plot				Data for Wetherill plot					Ages					
	^{204}Pb in sample cps gc	^{206}Pb mV	^{207}Pb mV	^{238}U mV	Pb ppm	Uppm*	^{206}Pb/^{204}Pb	1σ %	^{238}U/^{206}Pb	1σ %	^{207}Pb/^{206}Pb	1σ %	^{207}Pb/^{235}U	1σ %	^{206}Pb/^{238}U	1σ %	Rho	^{207}Pb/^{206}Pb	2σ abs	^{206}Pb/^{238}U	2σ abs	^{207}Pb/^{235}U	2σ abs
RHCI 10 1a 1a	bd	0.0	0.01	34	0.01	10	bd	bd	1726	4.1	0.4004	2.7	0.032	5.0	0.00058	4.1	0.83	3911	83	3.7	0.3	32	3
RHCI 10 1a 1b	313	0.0	0.01	27	0.01	8	6	83	1225	3.4	0.5261	2.3	0.059	4.1	0.00082	3.4	0.83	4316	67	5.3	0.4	58	5
RHCI 10 1a 1c	bd	0.0	0.01	36	0.01	11	bd	bd	1477	7.8	0.4408	4.3	0.041	8.9	0.00068	7.8	0.88	4054	128	4.4	0.7	41	7
RHCI 10 1a 2a	293	0.0	0.01	34	0.01	10	6	61	1780	3.6	0.4098	2.7	0.032	4.5	0.00056	3.6	0.80	3945	81	3.6	0.3	32	3
RHCI 10 1a 2b	bd	0.0	0.01	48	0.01	14	bd	bd	1910	2.9	0.3594	2.2	0.026	3.6	0.00052	2.9	0.79	3747	68	3.4	0.2	26	2
RHCI 10 1a 3a	242	0.1	0.01	114	0.01	33	16	50	2543	2.1	0.2640	2.4	0.014	3.2	0.00039	2.1	0.67	3271	75	2.5	0.1	14	1
RHCI 10 1a 4	bd	0.1	0.03	68	0.01	20	bd	bd	1401	2.9	0.4813	1.5	0.047	3.3	0.00071	2.9	0.89	4185	45	4.6	0.3	47	3
RHCI 10 1a 5	381	0.1	0.06	75	0.02	22	18	40	959	8.6	0.5742	1.7	0.083	8.8	0.00104	8.6	0.98	4444	50	6.7	1.2	81	14
RHCI 10 1a 6a	264	0.1	0.06	34	0.02	10	24	64	471	4.6	0.6724	0.6	0.197	4.7	0.00212	4.6	0.99	4673	17	13.7	1.3	182	15
RHCI 10 1a 6b	209	0.1	0.06	36	0.02	11	31	47	484	4.7	0.6765	0.7	0.193	4.7	0.00207	4.7	0.99	4682	19	13.3	1.2	179	15
RHCI 10 1a 6c	213	0.1	0.07	36	0.02	11	33	52	464	4.3	0.6824	0.7	0.203	4.3	0.00216	4.3	0.99	4694	19	13.9	1.2	187	15
RHCI 10 1b 1a	bd	0.0	0.01	12	0.00	3	bd	bd	1028	6.5	0.6457	2.8	0.087	7.1	0.00097	6.5	0.92	4614	81	6.3	0.8	84	11
RHCI 10 1b 1b	24	0.0	0.01	21	0.00	6	bd	bd	1677	4.0	0.4477	4.9	0.037	6.4	0.00060	4.0	0.63	4078	146	3.8	0.3	37	5
RHCI 10 1b 1c	bd	0.0	0.01	14	0.00	4	bd	bd	1397	6.6	0.5475	4.4	0.054	7.9	0.00072	6.6	0.83	4375	128	4.6	0.6	53	8
RHCI 10 1b 2a	bd	0.0	0.01	23	0.00	7	bd	bd	1341	3.5	0.5121	2.1	0.053	4.1	0.00075	3.5	0.85	4276	63	4.8	0.3	52	4
RHCI 10 1b 3	1170	0.3	0.20	31	0.06	9	16	12	146	9.4	0.7610	0.2	0.716	9.4	0.00683	9.4	1.00	4850	7	43.9	8.2	549	77
RHCI 10 1b 4	13140	3.9	2.62	32	0.76	9	18	10	12	9.0	0.7837	0.1	9.046	9.0	0.08372	9.0	1.00	4892	2	518.3	88.6	2343	152
RHCI 10 1b 5	119	0.0	0.01	33	0.01	10	bd	bd	1485	3.1	0.4638	1.5	0.043	3.4	0.00067	3.1	0.90	4130	44	4.3	0.3	43	3
RHCI 10 2 1	bd	0.0	0.00	13	0.00	4	bd	bd	1743	2.8	0.4460	2.7	0.035	3.9	0.00057	2.8	0.72	4072	80	3.7	0.2	35	3
RHCI 10 2 2a	bd	0.0	0.01	100	0.01	29	bd	bd	2884	0.6	0.1589	5.3	0.008	5.3	0.00035	0.6	0.12	2444	179	2.2	0.0	8	1
RHCI 10 2 2b	bd	0.0	0.01	48	0.01	14	bd	bd	1897	13.8	0.3134	8.0	0.023	16.0	0.00053	13.8	0.87	3538	246	3.4	0.9	23	7
RHCI 10 2 3a	bd	0.1	0.01	107	0.01	31	bd	bd	2791	1.1	0.1840	2.1	0.009	2.4	0.00036	1.1	0.46	2689	70	2.3	0.1	9	0
RHCI 10 2 3b	178	0.1	0.02	73	0.01	22	24	73	1510	8.9	0.4271	6.1	0.039	10.8	0.00066	8.9	0.83	4007	182	4.3	0.8	39	8
RHCI 10 2 4	bd	0.0	0.01	62	0.01	18	bd	bd	2477	2.0	0.2103	4.0	0.012	4.5	0.00040	2.0	0.44	2908	129	2.6	0.1	12	1
RHCI 10 2 4b	62	0.0	0.01	74	0.01	22	bd	bd	2543	1.9	0.2039	3.4	0.011	3.9	0.00039	1.9	0.48	2858	110	2.5	0.1	11	1
RHCI 10 2 4c	bd	0.0	0.01	47	0.01	14	bd	bd	2372	3.8	0.2245	6.2	0.013	7.3	0.00042	3.8	0.52	3013	200	2.7	0.2	13	2
RHCI 10 2 5	86	0.0	0.01	77	0.01	23	31	59	2523	2.3	0.2223	3.6	0.012	4.2	0.00040	2.3	0.55	2997	114	2.6	0.1	12	1
RHCI 10 2 6	bd	0.1	0.02	110	0.02	32	bd	bd	1939	3.5	0.3561	2.6	0.025	4.4	0.00052	3.5	0.80	3733	80	3.3	0.2	25	2
RHCI 10 3 1a	1200	0.4	0.22	68	0.07	20	18	13	245	5.9	0.7309	0.3	0.412	5.9	0.00409	5.9	1.00	4793	7	26.3	3.1	350	34
RHCI 10 3 1b	623	0.3	0.17	83	0.05	24	28	26	396	5.1	0.7011	0.5	0.244	5.2	0.00253	5.1	0.99	4733	16	16.3	1.7	222	20
RHCI 10 3 2	bd	0.1	0.04	84	0.02	25	bd	bd	1200	7.0	0.5262	2.1	0.060	7.3	0.00083	7.0	0.96	4316	61	5.4	0.7	60	8
RHCI 10 3 3	bd	0.0	0.02	62	0.01	18	bd	bd	1645	3.5	0.4214	2.1	0.035	4.0	0.00061	3.5	0.86	3987	62	3.9	0.3	35	3
RHCI 10 3 4a	134	0.0	0.01	26	0.00	8	10	89	1637	2.5	0.4402	3.0	0.037	3.8	0.00061	2.5	0.64	4052	88	3.9	0.2	37	3
RHCI 10 3 4b	bd	0.0	0.02	23	0.01	7	bd	bd	851	12.8	0.5735	3.1	0.093	13.1	0.00118	12.8	0.97	4442	92	7.6	1.9	90	22
RHCI 10 3 4c	bd	0.0	0.00	25	0.00	7	bd	bd	1934	3.7	0.3036	4.0	0.022	5.4	0.00052	3.7	0.68	3489	122	3.3	0.2	22	2
RHCI 10 3 5	bd	0.0	0.00	61	0.01	18	bd	bd	2838	2.3	0.1381	9.4	0.007	9.7	0.00035	2.3	0.23	2204	327	2.3	0.1	7	1
RHCI 10 3 6a	590	0.3	0.18	42	0.05	12	28	39	208	3.5	0.7626	0.3	0.505	3.6	0.00480	3.5	1.00	4853	9	30.9	2.2	415	24
RHCI 10 3 6b	647	0.2	0.13	43	0.04	13	20	40	276	6.9	0.7385	1.2	0.369	7.0	0.00363	6.9	0.99	4807	34	23.3	3.2	319	38
RHCI 10 3 6c	924	0.2	0.15	39	0.05	11	16	16	211	4.9	0.7409	0.6	0.483	4.9	0.00473	4.9	0.99	4812	17	30.4	3.0	400	32
RHCI 10 4 1	69	0.0	0.00	33	0.00	10	bd	bd	2200	2.0	0.2554	5.9	0.016	6.2	0.00045	2.0	0.33	3218	185	2.9	0.1	16	2
RHCI 10 4 2	27	0.0	0.00	59	0.01	17	bd	bd	2599	3.9	0.1986	10.1	0.011	10.8	0.00038	3.9	0.36	2815	329	2.5	0.2	11	2
RHCI 10 4 23a	bd	0.0	0.00	103	0.01	30	bd	bd	3068	3.4	0.1172	11.9	0.005	12.4	0.00033	3.4	0.27	1914	429	2.1	0.1	5	1
RHCI 10 4 3b	bd	0.0	0.00	115	0.01	34	bd	bd	3364	1.7	0.0672	6.4	0.003	6.6	0.00030	1.7	0.25	843	266	1.9	0.1	3	0
RHCI 10 4 4a	bd	0.1	0.03	54	0.01	16	bd	bd	1125	5.2	0.5237	1.8	0.064	5.5	0.00089	5.2	0.94	4309	53	5.7	0.6	63	7
RHCI 10 4 4b	94	0.1	0.05	28	0.02	8	bd	bd	428	14.1	0.6767	1.6	0.218	14.2	0.00234	14.1	0.99	4682	47	15.0	4.2	200	50
RHCI 10 4 5	184	0.0	0.00	56	0.00	16	bd	bd	3270	2.7	0.0644	26.4	0.003	26.5	0.00031	2.7	0.10	755	1114	2.0	0.1	3	1
RHCI 10 4 6a	bd	0.1	0.03	132	0.02	39	bd	bd	2122	5.3	0.3409	5.6	0.022	7.7	0.00047	5.3	0.69	3667	170	3.0	0.3	22	3
RHCI 10 4 6b	bd	0.1	0.00	122	0.01	36	bd	bd	3192	1.5	0.1085	9.2	0.005	9.3	0.00031	1.5	0.16	1775	336	2.0	0.1	5	1

Data not common-Pb corrected

Samples	^{204}Pb in sample cps gc	^{206}Pb mV	^{207}Pb mV	^{238}U mV	Pb ppm	Uppm*	$^{206}Pb/^{204}Pb$	1σ %	$^{238}U/^{206}Pb$	1σ %	$^{207}Pb/^{206}Pb$	1σ %	$^{207}Pb/^{235}U$	1σ %	$^{206}Pb/^{238}U$	1σ %	Rho	$^{207}Pb/^{206}Pb$	2σ abs	$^{206}Pb/^{238}U$	2σ abs	$^{207}Pb/^{235}U$	2σ abs
		Signals							Data for Tera-Wasserberg plot				Data for Wetherill plot					Ages					
Level 1																							
RHCI 104 1 1a	bd	0.1	0.01	193	0.02	57	bd	bd	3013	1.0	0.1264	2.7	0.006	2.9	0.00033	1.0	0.36	2049	95	2.1	0.0	6	0
RHCI 104 1 1b	bd	0.1	0.01	218	0.02	64	bd	bd	2983	1.5	0.1289	2.7	0.006	3.1	0.00034	1.5	0.48	2083	96	2.2	0.1	6	0
RHCI 104 1 1c	3387	0.1	0.02	195	0.02	57	2	97	2485	2.5	0.2567	2.3	0.014	3.4	0.00040	2.5	0.73	3227	74	2.6	0.1	14	1
RHCI 104 1 2a	bd	0.1	0.01	156	0.01	46	bd	bd	2994	0.5	0.1185	2.9	0.005	2.9	0.00033	0.5	0.16	1933	103	2.2	0.0	6	0
RHCI 104 1 2b	bd	0.1	0.01	164	0.01	48	bd	bd	2959	0.5	0.1080	4.7	0.005	4.8	0.00034	0.5	0.11	1766	172	2.2	0.0	5	0
RHCI 104 1 3a	100	0.1	0.02	310	0.03	91	bd	bd	2797	1.4	0.1551	2.3	0.008	2.6	0.00036	1.4	0.52	2403	77	2.3	0.1	8	0
RHCI 104 1 3b	bd	0.2	0.03	286	0.03	84	bd	bd	2537	1.0	0.2071	2.8	0.011	2.9	0.00039	1.0	0.33	2883	89	2.5	0.0	11	1
RHCI 104 1 4a	124	0.2	0.03	334	0.03	98	bd	bd	2653	1.6	0.1806	4.0	0.009	4.3	0.00038	1.6	0.38	2659	132	2.4	0.1	9	1
RHCI 104 1 4b	151	0.2	0.04	321	0.03	94	71	56	2493	2.7	0.2447	4.9	0.014	5.6	0.00040	2.7	0.49	3151	156	2.6	0.1	14	2
RHCI 104 1 4c	2747	0.2	0.03	304	0.03	89	bd	bd	2636	2.6	0.2225	3.5	0.012	4.4	0.00038	2.6	0.59	2999	113	2.4	0.1	12	1
RHCI 104 1 5a	157	0.1	0.02	170	0.02	50	37	89	2451	1.0	0.2635	1.7	0.015	2.0	0.00041	1.0	0.49	3268	55	2.6	0.1	15	1
RHCI 104 1 5b	150	0.1	0.03	180	0.02	53	43	93	2305	1.7	0.3001	2.2	0.018	2.8	0.00043	1.7	0.60	3471	69	2.8	0.1	18	1
RHCI 104 1 5c	1810	0.1	0.02	186	0.02	55	bd	bd	2421	1.0	0.2752	3.6	0.016	3.8	0.00041	1.0	0.26	3336	114	2.7	0.1	16	1
RHCI 104 1 6	bd	0.1	0.02	137	0.01	40	bd	bd	2437	1.4	0.2486	1.4	0.014	2.0	0.00041	1.4	0.71	3176	45	2.6	0.1	14	1
RHCI 104 2 1a	199	0.1	0.01	209	0.02	61	bd	bd	3002	2.1	0.1047	3.8	0.005	4.4	0.00033	2.1	0.48	1709	141	2.1	0.1	5	0
RHCI 104 2 1b	303	0.1	0.01	175	0.02	51	16	79	2855	3.4	0.1243	3.8	0.006	5.1	0.00035	3.4	0.67	2019	134	2.3	0.2	6	1
RHCI 104 2 2a	bd	0.1	0.01	236	0.02	69	bd	bd	3053	2.6	0.0978	5.5	0.004	6.1	0.00033	2.6	0.43	1583	206	2.1	0.1	4	1
RHCI 104 2 2b	81	0.1	0.01	228	0.02	67	bd	bd	2703	2.2	0.1543	6.5	0.008	6.8	0.00037	2.2	0.32	2394	221	2.4	0.1	8	1
RHCI 104 2 3	bd	0.1	0.01	192	0.02	56	bd	bd	2859	1.2	0.1352	4.2	0.007	4.4	0.00035	1.2	0.28	2166	147	2.3	0.1	7	1
RHCI 104 2 4	bd	0.1	0.01	161	0.01	47	bd	bd	2791	1.6	0.1407	4.5	0.007	4.7	0.00036	1.6	0.33	2236	155	2.3	0.1	7	1
RHCI 104 2 5	78	0.1	0.01	176	0.02	52	bd	bd	2772	1.5	0.1393	5.1	0.007	5.3	0.00036	1.5	0.29	2218	177	2.3	0.1	7	1
RHCI 104 2 5b	69	0.1	0.01	178	0.02	52	bd	bd	2856	2.4	0.1110	3.2	0.005	4.0	0.00035	2.4	0.61	1816	115	2.3	0.1	5	0
RHCI 104 2 5c	bd	0.1	0.01	172	0.02	50	bd	bd	2908	1.3	0.1142	4.7	0.005	4.9	0.00034	1.3	0.26	1867	171	2.2	0.1	5	1
RHCI 104 2 6a	116	0.1	0.02	327	0.03	96	77	85	2943	1.5	0.1265	3.8	0.006	4.1	0.00034	1.5	0.37	2049	134	2.2	0.1	6	0
RHCI 104 2 6b	202	0.1	0.01	323	0.03	95	44	59	2962	1.5	0.1221	3.9	0.006	4.1	0.00034	1.5	0.36	1987	137	2.2	0.1	6	0
RHCI 104 3 1a	161	0.2	0.02	413	0.03	121	68	43	3001	1.0	0.1090	1.8	0.005	2.1	0.00033	1.0	0.47	1783	67	2.1	0.0	5	0
RHCI 104 3 1b	bd	0.2	0.03	428	0.04	126	bd	bd	2812	1.4	0.1634	5.7	0.008	5.9	0.00036	1.4	0.24	2491	192	2.3	0.1	8	1
RHCI 104 3 2a	bd	0.1	0.01	147	0.01	43	bd	bd	2509	0.9	0.1739	2.9	0.010	3.1	0.00040	0.9	0.29	2596	98	2.6	0.0	10	1
RHCI 104 3 2b	335	0.1	0.01	145	0.01	43	14	75	2463	3.0	0.1682	5.4	0.009	6.1	0.00041	3.0	0.48	2540	179	2.6	0.2	10	1
RHCI 104 3 3	bd	0.1	0.01	323	0.03	95	bd	bd	2887	0.9	0.1210	3.1	0.006	3.2	0.00035	0.9	0.28	1971	109	2.2	0.0	6	0
RHCI 104 3 4a	296	0.2	0.07	270	0.04	79	45	51	1603	4.2	0.3921	3.1	0.034	5.2	0.00062	4.2	0.81	3879	92	4.0	0.3	34	3
RHCI 104 3 5a	88	0.2	0.02	342	0.03	101	bd	bd	2851	1.3	0.1466	8.2	0.007	8.3	0.00035	1.3	0.15	2306	281	2.3	0.1	7	1
RHCI 104 3 5b	bd	0.2	0.02	356	0.03	105	bd	bd	2686	4.0	0.1581	5.2	0.008	6.6	0.00037	4.0	0.61	2436	176	2.4	0.2	8	1
RHCI 104 3 5c	2003	0.2	0.05	378	0.04	111	7	90	2202	5.3	0.2715	7.4	0.017	9.1	0.00045	5.3	0.58	3315	231	2.9	0.3	17	3
RHCI 104 3 6a	333	0.2	0.03	365	0.03	107	33	42	2594	2.1	0.1876	2.2	0.010	3.1	0.00039	2.1	0.68	2722	74	2.5	0.1	10	1
RHCI 104 3 6b	24	0.2	0.03	320	0.03	94	bd	bd	2403	3.8	0.2306	5.6	0.013	6.8	0.00042	3.8	0.56	3056	180	2.7	0.2	13	2
RHCI 104 4 1a	25	0.1	0.02	308	0.03	90	bd	bd	2787	2.4	0.1478	2.8	0.007	3.7	0.00036	2.4	0.65	2321	97	2.3	0.1	7	1
RHCI 104 4 1b	bd	0.2	0.03	318	0.03	93	bd	bd	2647	2.9	0.1947	6.2	0.010	6.8	0.00038	2.9	0.43	2782	202	2.4	0.1	10	1
RHCI 104 4 2a	86	0.2	0.02	383	0.03	113	bd	bd	2824	1.2	0.1235	3.0	0.006	3.2	0.00035	1.2	0.37	2007	106	2.3	0.1	6	0
RHCI 104 4 2b	bd	0.2	0.03	418	0.04	123	bd	bd	2663	1.7	0.1627	2.2	0.008	2.8	0.00038	1.7	0.60	2484	75	2.4	0.1	9	0
RHCI 104 4 3	20	0.2	0.01	400	0.03	117	bd	bd	3116	0.7	0.0657	3.2	0.003	3.3	0.00032	0.7	0.22	796	134	2.1	0.0	3	0
RHCI 104 4 4a	162	0.1	0.01	272	0.02	80	43	80	3145	1.5	0.0768	4.0	0.003	4.3	0.00032	1.5	0.35	1115	161	2.0	0.1	3	0
RHCI 104 4 4b	126	0.1	0.01	234	0.02	69	46	74	3176	0.8	0.0694	2.2	0.003	2.3	0.00031	0.8	0.33	911	89	2.0	0.0	3	0
RHCI 104 4 5	99	0.2	0.01	404	0.03	119	bd	bd	3195	0.7	0.0841	3.9	0.004	4.0	0.00031	0.7	0.18	1294	153	2.0	0.0	4	0
RHCI 104 4 6	bd	0.1	0.01	309	0.02	91	bd	bd	3149	1.0	0.0698	4.2	0.003	4.3	0.00032	1.0	0.24	921	171	2.0	0.0	3	0

Appendix 14: Isotope dilution data

U-Th-Pb isotopic data

		Compositional Parameters							Sample (Radiogenic + Initial Pb) Isotope Ratios								
Sample	Wt. mg	U ppm	Pb ppm	$^{206}Pb^*$ x10^{-13} mol	mol % $^{206}Pb^*$	Pb^*/Pb_c	Pb_c (pg)	$^{206}Pb/^{204}Pb$	$^{238}U/^{206}Pb$	% err	$^{207}Pb/^{206}Pb$	% err	$^{204}Pb/^{206}Pb$	% err	corr. coef. 8/6-7/6	corr. coef. 8/6-4/6	corr. coef. 7/6-4/6
	(a)	(b)	(b)	(c)	(c)	(c)	(c)	(d)	(e)	(f)	(e)	(f)	(e)	(f)			
RHCI 104 3A	2.34	65	0.0	0.0530	4.1%	0.00	100.68	19	**5324.2**	**10.6**	**0.800091**	**0.8**	0.051114	0.846558	**-0.990707**	-0.936222	0.905480
RHCI 104 3C	3.22	69	0.0	2.8434	70.8%	0.65	96.16	64	**2352.6**	**3.2**	**0.262516**	**7.3**	0.014799	8.744481	**-0.999597**	-0.998628	0.999387
RHCI 104 2	4.76	76	0.1	4.9999	69.2%	0.61	182.57	61	**2100.6**	**1.8**	**0.282308**	**3.6**	0.016041	4.305651	**-0.993954**	-0.990666	0.998010
RHCI 104 1.2	1.84	57	0.2	1.4300	23.6%	0.09	379.00	24	**734.8**	**2.1**	**0.647631**	**0.7**	0.040668	0.770833	**-0.994681**	-0.957547	0.933370
RHCI 104 4a	5.87	60	0.0	4.6468	70.7%	0.66	157.82	64	**2251.0**	**2.0**	**0.269179**	**4.3**	0.015171	5.123204	**-0.999057**	-0.996503	0.998527
RHCI 104 4b	4.44	49	0.04	2.8343	70.9%	0.66	95.50	64	**2301.9**	**3.2**	**0.262496**	**7.3**	0.014753	8.819906	**-0.999833**	-0.998879	0.999439
RHCIICA5 2	4.60	18	0.10	1.0069	15.7%	0.05	442.17	22	**546.2**	**2.0**	**0.709971**	**0.4**	0.044956	0.482190	**-0.988152**	-0.909844	0.842309
RHCIICA5 3	4.84	18	0.19	1.2046	9.9%	0.03	899.83	21	**304.1**	**1.1**	**0.757751**	**0.2**	0.048156	0.223840	**-0.897105**	-0.602240	0.204701
RHCIICA5 1a	2.39	31	0.14	0.8140	17.4%	0.05	316.53	23	**665.9**	**2.8**	**0.694432**	**0.7**	0.043998	0.708115	**-0.994912**	-0.962326	0.932740
RHCIICA5 1b	2.31	11	0.29	0.0583	0.7%	0.00	664.57	19	**132.3**	**1.6**	**0.829370**	**0.1**	0.053096	0.183302	**-0.587111**	-0.251998	-0.575979
RHCIICA5 4b	1.76	45	0.50	1.2846	10.9%	0.03	859.83	21	**284.4**	**1.1**	**0.738163**	**0.2**	0.047605	0.279436	**-0.933492**	-0.551816	0.301542
Loc 25 2	4.44	46	0.16	2.3913	23.6%	0.10	636.23	24	**847.8**	**1.3**	**0.648216**	**0.4**	0.040779	0.468318	**-0.989313**	-0.907676	0.847782
Loc 25 3	4.60	42	0.24	2.3652	15.8%	0.07	1033.00	22	**544.9**	**0.9**	**0.711037**	**0.2**	0.044983	0.261623	**-0.940070**	-0.657172	0.397572
Loc 25 4a	2.23	30	0.05	0.6841	37.8%	0.18	92.19	30	**1605.4**	**7.4**	**0.520006**	**4.8**	0.032253	5.175623	**-0.999945**	-0.998801	0.998453
Loc 25 4b	2.72	44	0.06	1.1911	41.6%	0.21	137.17	32	**1803.9**	**4.6**	**0.494997**	**3.3**	0.030561	3.642913	**-0.999848**	-0.997358	0.996829

U-Th-Pb isotopic data

Sample	Sample (Radiogenic + Initial Pb) Isotope Ratios									
	$^{238}U/^{204}Pb$ (e)	% err (f)	$^{206}Pb/^{204}Pb$ (e)	% err (f)	corr. coef. 8/4-6/4	$^{235}U/^{204}Pb$ (e)	% err (f)	$^{207}Pb/^{204}Pb$ (e)	% err (f)	corr. coef. 5/4-7/4
RHCI 104 3A	104162.869317	11.390014	19.564224	0.846558	0.945080	755.460323	11.390014	15.653160	0.359286	0.126898
RHCI 104 3C	158968.043286	11.965793	67.572525	8.744481	0.999900	1152.944903	11.965793	17.738845	1.471108	0.982592
RHCI 104 2	130954.534669	6.079840	62.342193	4.305651	0.999198	949.771792	6.079840	17.599687	0.736061	0.942558
RHCI 104 1.2	18067.916054	2.871591	24.589337	0.770833	0.976983	131.040877	2.871591	15.924810	0.277957	0.250779
RHCI 104 4a	148377.362996	7.074218	65.915711	5.123204	0.999733	1076.134051	7.074218	17.743149	0.893341	0.960266
RHCI 104 4b	156029.619126	12.055252	67.781750	8.819906	0.999919	1131.633443	12.055252	17.792433	1.511160	0.984658
RHCIICA5 2	12149.745425	2.454376	22.243906	0.482190	0.940643	88.118258	2.454376	15.792525	0.260490	0.157373
RHCIICA5 3	6314.294760	1.198701	20.765649	0.223840	0.714519	45.795581	1.198701	15.735187	0.246834	0.115242
RHCIICA5 1a	15134.623491	3.448140	22.728373	0.708115	0.976007	109.766634	3.448140	15.783318	0.255452	0.183133
RHCIICA5 1b	2492.450279	1.625838	18.833736	0.183302	0.356077	18.076953	1.625838	15.620135	0.251451	0.067221
RHCIICA5 4b	5974.822680	1.266201	21.006312	0.279436	0.695878	43.333498	1.266201	15.506092	0.287525	0.093961
Loc 25 2	20790.401591	1.699637	24.522218	0.468318	0.950116	**150.786202**	**1.699637**	**15.895694**	**0.248919**	**0.177910**
Loc 25 3	12113.210604	1.048706	22.230806	0.261623	0.787181	**87.853283**	**1.048706**	**15.806926**	**0.255875**	**0.151300**
Loc 25 4a	49776.445234	12.523300	31.005013	5.175623	0.999587	**361.012803**	**12.523300**	**16.122783**	**0.493563**	**0.828007**
Loc 25 4b	59027.815854	8.196983	32.721530	3.642913	0.999183	**428.110066**	**8.196983**	**16.197061**	**0.413609**	**0.740857**

(a) Fraction weights from weighing on a microbalance

(b) U and total Pb concentrations subject to uncertainty in weight estimation.

(c) Pb* and Pbc represent radiogenic and common Pb, respectively; mol % ^{206}Pb* with respect to radiogenic, blank and initial common Pb.

(d) Measured ratio corrected for spike and fractionation only. SEM analyses, based on analysis of NBS-981 and NBS-982.

(e) Corrected for fractionation, spike, and blank Pb only.

(f) Errors are 2-sigma, propagated using the algorithms of Schmitz and Schoene (2007).

Appendix 15: $^{234}U/^{238}U$ activity ratios

Sample	234/235	± 2σ %	234/238 (old 8/5)	± 2σ %	[234/238]	[234/238]I t=2.0 Ma	[234/238]I t=1.9 Ma	[234/238]I t=1.80 Ma	[234/238]I t=1.5 Ma	[234/238]I t=1.45 Ma	[234/238]I t=1.40 Ma	[234/238]I t=1.35 Ma	[234/238]I t=1.30 Ma	[234/238]I t=1.25 Ma	[234/238]I t=1.20 Ma	[234/238]I t=1.15 Ma	[234/238]I t=1.0 Ma
Lake Natron	0.007833	0.06	5.681E-05	0.06	1.035E+00												
Lake Makat	0.01115	0.12	8.086E-05	0.12	1.473E+00												
Lake Ndutu	0.009779	0.16	7.093E-05	0.16	1.292E+00												
Level 4 Loc 25	0.007772	0.05	5.636E-05	0.05	1.027E+00	8.676E+00	6.786E+00	5.361E+00	2.868E+00	2.622E+00	2.408E+00	2.223E+00	2.061E+00	1.922E+00	1.800E+00	1.695E+00	1.455E+00
Level 3 RHCII CA5	0.007589	0.06	5.504E-05	0.05	1.003E+00	1.797E+00	1.601E+00	1.453E+00	1.194E+00	1.168E+00	1.146E+00	1.127E+00	1.110E+00	1.096E+00	1.083E+00	1.072E+00	1.047E+00
Level 1 RHCI 104_A	0.007649	0.05	5.547E-05	0.05	1.011E+00	4.050E+00	3.299E+00	2.733E+00	1.742E+00	1.644E+00	1.559E+00	1.486E+00	1.422E+00	1.366E+00	1.318E+00	1.276E+00	1.181E+00
Level 1 RHCI 104_B	0.007650	0.06	5.549E-05	0.06	1.011E+00	4.114E+00	3.348E+00	2.770E+00	1.758E+00	1.658E+00	1.571E+00	1.496E+00	1.431E+00	1.374E+00	1.325E+00	1.282E+00	1.184E+00
Calculation			234/235*137.88		'234/238*(2.83E-06/1.55E-10)	1+([234/238]-1)*EXP(2.83E-06*t(years))											
Constants	238/235 Cowan & Adler 1976		137.88		**Laser ages**		**max age**	**min age**									
	λ234U Cheng et al 2000		2.83E-06		Level 4 (LOC25) Tuff IIC - Tuff IID		1.530	1.430									
	λ238U Jaffey et al 1971		1.55E-10		Level 3 (RHCII CA5) Tuff IF - Tuff IIA		1.790	1.717									
					Level 1 (RHCI 104) Tuff IA - Tuff IB		2.040	1.843									